

Fakultät für Geowissenschaften
Ludwig-Maximilians-Universität München

**Pathways of biomineralization and
microstructure evolution
in brachiopod shells**

by

María del Mar Simonet Roda

Ph.D. Thesis



Pathways of biomineralization and microstructure evolution in brachiopod shells

by

María del Mar Simonet Roda

Ph.D. Thesis

SUBMITTED IN FULFILLMENT OF THE
REQUIREMENT FOR THE DEGREE OF
Dr. rer. nat.



Fakultät für Geowissenschaften
Ludwig-Maximilians-Universität München

Munich, 18th January, 2021

Supervisor: Prof. Dr. Wolfgang W. Schmahl

1. Reviewer: Prof. Dr. Wolfgang W. Schmahl

2. Reviewer: Prof. Dr. Antonio Checa (External examiner)

Date of the Oral Exam: 03.03.2021

*To those who walked this path next to me and without whom this work would not have
been possible. To Catalina.*

“What is a scientist after all? It is a curious man looking through a keyhole, the keyhole of nature, trying to know what’s going on”

Jacques-Yves Cousteau

Abstract

Biomaterials of shells, bones and teeth are composites of minerals and organic tissue components precipitated by organisms. Accordingly, it is very important to understand (1) the relation between the soft and hard tissues in composite materials of living organisms, (2) the resulting micro- and nanostructure of the constituting biomaterials (3) and the function of the minerals of the biomaterialization epithelial cells in producing these materials. Brachiopod shells were selected to be the principal subject of this work as they are major geochemical archives for paleo-environmental reconstruction of sea water conditions.

The shell of modern brachiopods is secreted by the outer mantle epithelium (OME) of the animal. Despite several decades of research, it is still unknown how the mineral is transported from OME cells to the site of mineralization. For brachiopod shells the biomaterialization process was not yet described and often biomaterialization of mollusc shells was used as a reference. In order to understand mineral transport and shell secretion, we investigated the ultrastructure of OME cells and their spatial relation to the growing shell for the terebratulide brachiopod *Magellania venosa* (Chapters 2.1 and 2.2). The animals were chemically fixed and high pressure frozen. We worked with high resolution panorama images formed of up to 350 TEM images. This ensured a general overview as well as a detailed description of the ultrastructure of the OME. We found and described the specific differences between (1) the OME ultrastructure at the commissure and that at central shell regions as well as (2) differences between areas in the central region where active secretion takes place and those areas where secretion is finished. The OME at the commissure consists of several cell layers, while at central shell regions it is single-layered. It is significantly thinner at the central shell region in comparison to the commissure. Especially at sites of actively forming calcite fibres, OME cells are only a few tens of nanometre thin.

Where the mineral deposition takes place, the apical membrane of OME cells is in direct contact with the calcite of the forming fibre. At these sites the extracellular organic membrane at the proximal convex surface of the fibre is absent. When mineral secretion is finished the cells form an extracellular organic membrane which lines the proximal surface of fibres. The extracellular organic membrane is attached to the apical cell membrane via apical hemidesmosomes. Tonofilaments cross the cell, connect apical to basal hemidesmosomes, stabilize the contact between epithelium and fibres and keep the mantle attached to the shell. Furthermore, communication and cooperation of neighbouring OME cells could be proved in this work as individual fibres are secreted by several cooperating cells at the same time (Chapters 2.1 and 2.2).

The extracellular space, the space between the epithelium and the growing fibres, is either absent or very narrow. Quantitative analysis demonstrated that there are no significant differences in the volume fraction of vesicles between secreting and non-secreting regions of the OME. The latter and the extreme reduction in cell thickness at sites of mineral secretion suggest that for *Magellania venosa* shells mineral transport to the sites of mineralization does not occur by transport with organelles such as vesicles but via ion transport mechanisms through the cell membrane.

For the central shell region the previously discussed data was complemented with atomic force microscopy (AFM) and electron backscatter diffraction (EBSD) measurements. In the central region of the shell the fibrous layer is secreted. The fibrous

layer of modern terebratulide brachiopod shells has an overall plywood-like organization with the basic mineral units, the calcite fibres, being assembled with a microstructure resembling an ‘anvil-type’ arrangement (Chapter 2.2). The observations on the TEM images and on etched sample surfaces under AFM lead us to develop a model for calcite fibre secretion and fibre shape formation for *Magellania venosa* is described as a dynamic process coordinated by outer mantle epithelium cells (OME). The secretion process consists of the following steps: (i) local detachment of epithelial cell membrane from the organic membrane of previously formed fibres, (ii) onset of secretion of calcite at these sites, (iii) organic membrane formation along the proximal, convex side of the forming fibre during achievement of the full width of the fibre, (iv) start of membrane secretion at the corners of fibres progressing towards the centre of the fibre, (v) attachment of the cells via apical hemidesmosomes to newly formed organic membrane, and (vi) suspension of calcite secretion at sites where the proximal, organic membrane of the calcite fibre is fully developed and the apical cell membrane is attached to the latter with apical hemidesmosomes.

Thecideide brachiopods are an anomalous group of invertebrates. Their position within the phylogeny of the Brachiopoda and the identification of their origin is still not fully resolved. Studies of morphological features such as shell structure and body size aimed to shed more light on thecideide evolution. However, none of these did provide a definitive answer, possibly because of their complex and diverse evolutionary track. In this thesis (Chapter 2.3) we attempt to trace thecideide shell evolution from a microstructure and texture point of view. We describe for this group of brachiopods the appearance and disappearance of a variety of calcite biocrystals that form the shells and trace these from Late Triassic to Recent times. The results and conclusions are based on EBSD measurements that form the basis of a phylogenetic tree. With this thesis we present a new phylogenetic hypothesis for the evolution of Thecideida. This is the first study that links microstructure and texture results gained from EBSD measurements with phylogenetic analysis and implications derived from phylogenetic evolution.

BSD measurements demonstrated the presence of a large variety of mineral units within thecideide shells throughout the geological record. With geologic time there is a progressive loss of the fibrous layer in favour of highly disordered acicular and granular microstructures. This loss can be seen as a pedomorphic pattern in the complex mosaic of evolutionary changes characterizing thecideide brachiopods. The Upper Jurassic species has transitional forms. The shells are composed of stacks of acicles on the external part of the shell. The fibrous layer is kept only in some regions next to the soft tissue of the animal. The regularity of biocrystal shape, mineral unit size, and the strength of calcite co-orientation decreases from the Late Triassic to Recent species. Even though, since the Upper Jurassic the thecideide shell microstructure shows the same type of mineral unit morphologies made of (i) nanometric to small granules, (ii) acicles, (iii) fibres, (iv) polygonal crystals, (v) large roundish crystals. I deduce from my studies that the change in microstructure and texture of thecideide brachiopods may be related to the ecological strategy to exploit distinct niches and life styles, in particular attachment to hard substrates. The clear and well defined microstructure of this brachiopod group is well distinguishable and can help to unravel the phylogenetic relationships between different taxa.

Brachiopods are one of the very few marine organism groups which have a complete fossil record. First species appeared in early Cambrian. The end-Permian extinction erased the majority of Paleozoic brachiopod taxa and reset taxonomic,

morphological, functional and ecological brachiopod diversity. A few groups survived end-Permian extinction, diversified and occupied new ecological niches. Representatives of these form today the extant orders of the Lingulida, Craniida, Rhynchonellida, and Terebratulida. The Thecideida appeared after the end-Permian crisis, in the Triassic.

The geological record shows that brachiopods were and are able to adopt to many marine environments. Accordingly, a large diversity in body plans as well as morphological, structural and chemical features of their shell became developed. With this thesis I highlight structural features of the shells of selected terebratulide, rhynchonellide, thecideide and craniide taxa. Chapter 2.4 describes the difference in shell structure for brachiopods with different life-styles, highlights the distinctness between the structure of the primary shell layer of Terebratulida, Rhynchonellida and the shell structure of Thecideida. I detail the nanometer scale calcite organization of Rhynchonellide and Terebratulide fibers, describe some advantages of a hierarchical composite hard tissue, address possible determinants for primary, fibrous and columnar shell calcite of Terebratulida and discuss a possible usage of thecideide shell for paleoenvironment reconstruction.

Table of Contents

ABSTRACT	1
TABLE OF CONTENTS	5
LIST OF ABBREVIATIONS	9
CHAPTER 1. INTRODUCTION.....	11
1.1. BIOMINERALIZATION PROCESSES	17
1.2. BRACHIOPOD SHELLS.....	21
1.2.1. Shell Secretion.....	21
1.2.2. Shell Microstructures	22
1.2.3. Importance For The Scientific Realm And Other Science Disciplines.....	25
CHAPTER 2. RESULTS AND DISCUSSION	27
2.2. TEREBRATULIDE BRACHIOPOD SHELL BIOMINERALIZATION BY MANTLE EPITHELIAL CELLS	27
2.1.1 Introduction	29
2.1.2. Materials And Methods	31
2.1.3. Results	36
2.1.4. Discussion	55
2.1.5. Conclusions	61
2.1.6. Author's Contribution	62
Supplementary Material	63
2.2. CALCITE FIBRE FORMATION IN MODERN BRACHIOPOD SHELLS	70
2.2.1. Introduction	72
2.2.2. Materials And Methods	73
2.2.3. Results	76
2.2.4. Discussion	86
2.2.5. Conclusions	91
2.2.6. Author's Contribution	91
Supplementary Material	93
2.3. THE EVOLUTION OF THECIDEIDE MICROSTRUCTURES AND TEXTURES: TRACED FROM TRIASSIC TO HOLOCENE.....	100
2.3.1. Introduction	102
2.3.2. Materials And Methods	103
2.3.3. Results	106
2.3.4. Discussion	117
2.3.5. Conclusions	123
2.3.6. Data Availability Statement	124
Supporting Information	125
2.4. DIVERSITY OF MINERAL AND BIOPOLYMER ASSEMBLY IN MODERN TEREBRATULIDE, RHYNCHONELLIDE, THECIDEIDE AND CRANIIDE BRACHIOPOD SHELLS	140
2.4.1. Introduction	142
2.4.2. Materials, Sample Preparation And Methods	144
2.4.3. Diversity Of Microstructures	146
2.4.4. Diversity Of Biocrystal Morphologies.....	150

2.4.5. Distribution Of Organic Substance Within The Shells	156
2.4.6. The Nanometre And Sub-Micrometre Scale Organization Of Calcite And Biopolymers Within Rhynchonellide And Terebratulide Fibers	161
2.4.7. Modes Of Calcite Assembly In Modern Brachiopod Shells	167
2.4.8. Characteristics Of The Textures.....	174
2.4.9. Are Thecideide Shells Reliable Archives For Present And Past Environment Reconstruction?.....	178
2.4.10. Concluding Summary.....	179
2.4.11. Author's Contribution	185
Supplementary Material	186
CHAPTER 3. CONCLUDING SUMMARY AND OUTLOOK	209
3.1. CONCLUDING SUMMARY.....	209
3.2. OUTLOOK.....	213
BIBLIOGRAPHY.....	217
APPENDICES.....	241
APPENDIX I. MATERIAL DESCRIPTION	241
APPENDIX II. APPLIED METHODS	245
APPENDIX III. SAMPLE PREPARATION PROCEDURES	257
APPENDIX IV. CONTROL TABLES FOR CHEMICAL EXPERIMENTS	259
ACKNOWLEDGMENT.....	273
LIST OF PUBLICATIONS	275
CONFERENCE CONTRIBUTIONS	276

List of Abbreviations

ACC - Amorphous Calcium Carbonate

AFM - Atomic Force Microscopy

BSE - Backscattered electrons

EBSD - Electron Backscatter Diffraction

CL - Cathodoluminescence

FE-SEM - Field Emission-Scanning Electron Microscopy

HPF-FFS - High Pressure Frozen – Freeze Substituted

HR-TEM - High Resolution Transmission Electron Spectroscopy

MUD - Multiple of Uniform Distribution

OME - Outer Mantle Epithelium

SEM - Scanning Electron Microscopy

TEM - Transmission Electron Microscopy

The work presented in this dissertation was done inside the framework of the Innovative Training Network (ITN) Programme “*Brachiopods As SENSITIVE tracers of gLobal mariNe Environment: Insights from alkaline, alkaline Earth metal, and metalloid trace element ratios and isotope systems*” (BASE-LiNE Earth). The research was funded by the European Commission within the Marie Skłodowska-Curie Actions in Horizon 2020 'European Union Funding Programme for Research and Innovation' (H2020-MSCA-ITN-2014; REA Grant Agreement No. 643084).

The main objectives of BASE-LiNE Earth programme were to gain knowledge on (1) the link between brachiopod shells (fossil and recent ones) and marine ecology and biomineralization processes; (2) the pathways and processes of diagenetic alteration; (3) the reliability of time series for trace element ratios (Mg/Ca, Sr/Ca, Li/Ca, Ba/Ca, B/Ca, U/Ca) and their isotope systems (e.g. $d^{26}\text{Mg}$, $d^{44/40}\text{Ca}$, $^{87}\text{Sr}/^{86}\text{Sr}$, $d^{88/86}\text{Sr}$, $d^{53/53}\text{Cr}$, $d^7\text{Li}$, $d^{11}\text{B}$) for the Phanerozoic Ocean (<https://www.baseline-earth.eu/research>).

The analytical work for my PhD studies was done at the LMU in Munich and at the University of Ulm. The studies performed in Munich were related to the first objective of the Base-LiNE Earth programme (see above) and involved the study of modern and living brachiopods: their biological ultrastructure as well as their shell microstructure. Within the specific scientific objectives we collected information and gained important knowledge on the (1) “reliability and sensitivity of carbonate archives to environmental and compositional change in the adjacent water body” (first, second and fourth scientific publications) and (2) “the influence of the brachiopod physiology (vital effect) on biomineralogy, trace element composition and isotope partitioning in their calcitic shells” (<https://www.baseline-earth.eu/research>) (first, second and third scientific publications).

I worked in collaboration with many of the partners and fellows of the ITN (e.g. GEOMAR Helmholtz Centre for Ocean Research, University of Milano, Institut de Physique du Globe de Paris) and with other external institutions. The interdisciplinary concept of BASE-LiNE Earth, composed by researchers with very diverse backgrounds, allowed us to have very rich scientific approaches and discussions when facing the different scientific topics of our research.



Chapter 1. Introduction

Organisms precipitate different minerals through biological mineralization and the products of these processes are called biominerals or biological hard tissue. The relation between the organics and the hard tissues (the biomineral) is of great importance for understanding the impact of vital effects on mineral chemistry and mineral morphology. Out of the 60 different minerals (Table 1.1) in the biosphere that can be produced by organisms (Lowenstam and Weiner, 1989), we focused our research on the most abundant one: calcium carbonate (Table 1.2). Biomineralization processes and biomineralized carbonate hard tissues are the subject of study of this Thesis.

From all the marine organisms that form minerals (e.g. bivalves, gastropods, corals, echinoderms, coccolithophores) brachiopods play an important role, not only in the formation of sedimentary sequences, but also as element and isotope archives for ocean chemistry and paleo-environmental reconstruction.

Brachiopods are bivalved lophophorates, which are sessile marine animals that mineralize low-Mg calcite (subphylum *Rhynchonelliformea* and *Craniiformea*) or Calcium phosphate (subphylum *Linguliformea*) shells. Brachiopods exist since the Early Cambrian, diversified during the Ordovician and are still extant (Carlson, 2016, Harper et al. 2017). Even though these organisms mostly live in shallow marine waters their life style is highly diverse. By the end of the Ordovician, brachiopods had already populated a wide range of marine habitats, had diverse life-styles (from free-living to cemented), and developed different types of shell morphologies and microstructures (e.g. Lowenstam 1961, Veizer et al. 1986, Bates and Brand 1991, Grossman et al. 1996, Carpenter and Lohmann 1995, Peck et al. 1997, Williams 1997, Williams et al. 2000, Cusack et al. 2001, Samtleben et al. 2001, Peck 2007, Angiolini et al. 2009, Harper and Drachen 2010, Nielsen et al. 2013, Roark et al. 2015, Carlson 2016, Harper et al. 2017, Garbelli et al. 2017).

Brachiopod shells consist of two valves connected to each other at the hinge. Unlike bivalve shells that commonly have a bilateral symmetry, with the hinge located in the sagittal plane, each brachiopod valve has a mirror plane, the median plane, which cuts through the valves (Fig. 1.1a-d). Morphologically and crystallographically, the two valves are not mirror images of each other, as it is the case for many bivalves (see Fig. 1.1a-d and Schmahl et al. 2012). Even if at juvenile stages valves are thinner relative to adult ones, brachiopod valves have a quite constant thickness along their length. Shell growth does not occur exclusively at commissural margins, but also takes place along the inner surface of the shell (Rosenberg et al. 1988, Baumgarten 2013).

The internal structures of brachiopods consist of the lophophore or feeding filter system separated from the body cavity (visceral area) by the anterior body wall (Fig. 1.1e). Most of the organs (digestive gland, stomach, gonads, heart...) in the coelom or body cavity are situated on the posterior part, close to the hinge, while the lophophore occupies the major part of the cavity (Fig. 1.1e). The muscular system holds together the two valves and it is confined on the posterior region of the organism, close to the pedicle (Fig. 1.1e). The latter is present in all terebratulide and rhynchonellide brachiopods and it facilitates the attachment to a hard substrate.

The dorsal and ventral mantle epithelium/mantle lobe line the two valves internally (Fig. 1.1e) and are attached to the shell via tonofilaments. The mantle lobe can be divided into three different parts: the outer mantle epithelium (the epithelium in close contact to the shell), the middle layer consisting of connective tissue with varying content of collagen, and the inner mantle epithelium with the cilia.

Table 1.1. Names and chemical compositions of biominerals produced by biologically controlled mineralization and biologically induced processes (Weiner and Dove, 2003).

<i>Name</i>	<i>Formula</i>
<u>Carbonates</u>	
Calcite	CaCO ₃
Mg-calcite	(Mg _x Ca _{1-x})CO ₃
Aragonite	CaCO ₃
Vaterite	CaCO ₃
Monohydrocalcite	CaCO ₃ .H ₂ O
Protodolomite	CaMg(CO ₃) ₂
Hydrocerussite	Pb ₃ (CO ₃) ₂ (OH) ₂
Amorphous Calcium Carbonate (at least 5 forms)	CaCO ₃ .H ₂ O or CaCO ₃
<u>Phosphates</u>	
Octacalcium phosphate	Ca ₈ H ₂ (PO ₄) ₆
Brushite	CaHPO ₄ .2H ₂ O
Francolite	Ca ₁₀ (PO ₄) ₆ F ₂
Carbonated-hydroxylapatite (dahllite)	Ca ₅ (PO ₄ ,CO ₃) ₃ (OH)
Whitlockite	Ca ₁₈ H ₂ (Mg,Fe) ₂ ⁺² (PO ₄) ₁₄
Struvite	Mg(NH ₄)(PO ₄).6H ₂ O
Vivianite	Fe ₃ ⁺² (PO ₄) ₂ .8H ₂ O
Amorphous Calcium Phosphate (at least 6 forms)	variable
Amorphous Calcium Pyrophosphate	Ca ₂ P ₂ O ₇ .2H ₂ O
<u>Sulfates</u>	
Gypsum	CaSO ₄ .2H ₂ O
Barite	BaSO ₄
Celestite	SrSO ₄
Jarosite	KFe ₃ ⁺³ (SO ₄) ₂ (OH) ₆
<u>Sulfides</u>	
Pyrite	FeS ₂
Hydrotroilite	FeS.nH ₂ O
Sphalerite	ZnS
Wurtzite	ZnS
Galena	PbS
Greigite	Fe ₃ S ₄
Mackinawite	(Fe,Ni) ₉ S ₈
Amorphous Pyrrhotite	Fe _{1-x} S (x = 0-0.17)
Acanthite	Ag ₂ S

Table 1.1. Continuation 2/2.

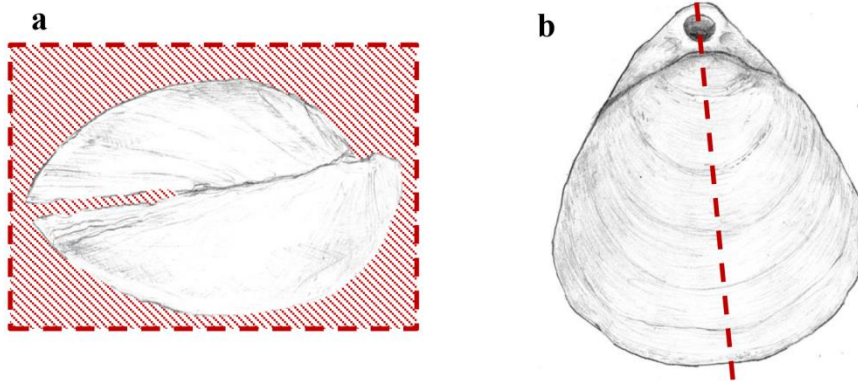
<u>Arsenates</u>	
Orpiment	As ₂ S ₃
<u>Hydrated Silica</u>	
Amorphous Silica	SiO ₂ .nH ₂ O
<u>Chlorides</u>	
Atacamite	Cu ₂ Cl(OH) ₃
<u>Fluorides</u>	
Fluorite	CaF ₂
Hieratite	K ₂ SiF ₆
<u>Metals</u>	
Sulfur	S
<u>Oxides</u>	
Magnetite	Fe ₃ O ₄
Amorphous Ilmenite	F ⁺² TiO ₃
Amorphous Iron Oxide	Fe ₂ O ₃
Amorphous Manganese Oxide	MnO ₄
<u>Hydroxides and Hydrous Oxides</u>	
Goethite	α-FeOOH
Lepidocrocite	γ-FeOOH
Ferrihydrite	5Fe ₂ O ₃ ·9H ₂ O
Todorokite	(Mn ⁺² CaMg)Mn ₃ ⁺⁴ O ₇ ·H ₂ O
Birnessite	Na ₄ Mn ₁₄ O ₂₇ ·9H ₂ O
<u>Organic Crystals*</u>	
Earlandite	Ca ₃ (C ₆ H ₅ O ₂) ₂ ·4H ₂ O
Whewellite CaC ₂ O ₄ ·H ₂ O	CaC ₂ O ₄ ·H ₂ O
Weddelite	CaC ₂ O ₄ ·(2+X)H ₂ O (X<0.5)
Glushinskite	MgC ₂ O ₄ ·4H ₂ O
Manganese Oxalate (unnamed)	Mn ₂ C ₂ O ₄ ·2H ₂ O
Sodium urate	C ₅ H ₃ N ₄ NaO ₃
Uric Acid	C ₅ H ₄ N ₄ O ₃
Ca tartrate	C ₄ H ₄ CaO ₆
Ca malate	C ₄ H ₄ CaO ₅
Paraffin Hydrocarbon	
Guanine	C ₅ H ₃ (NH ₂)N ₄ O

* by the convention of Lowenstam and Weiner (1989)

Table 1.2. Calcium carbonate biominerals in some organisms, summarized from Mann (2001).

Minerals	Formula	Organisms
Calcite	CaCO ₃	Coccolithophores Foraminifera Trilobites Mollusks Crustaceans Brachiopod Birds Mammals
Mg-calcite	(Mg, Ca)CO ₃	Octocorals Echinoderms
Aragonite	CaCO ₃	Scleractinian corals Mollusks Gastropods Cephalopods Otolith
Amorphous	CaCO ₃ ·nH ₂ O	Crustacean Plants
Vaterite	CaCO ₃	Gastropods Ascidians

Rhynchonellata brachiopod *Magellania venosa*



Bivalve *Venerupis decussata*

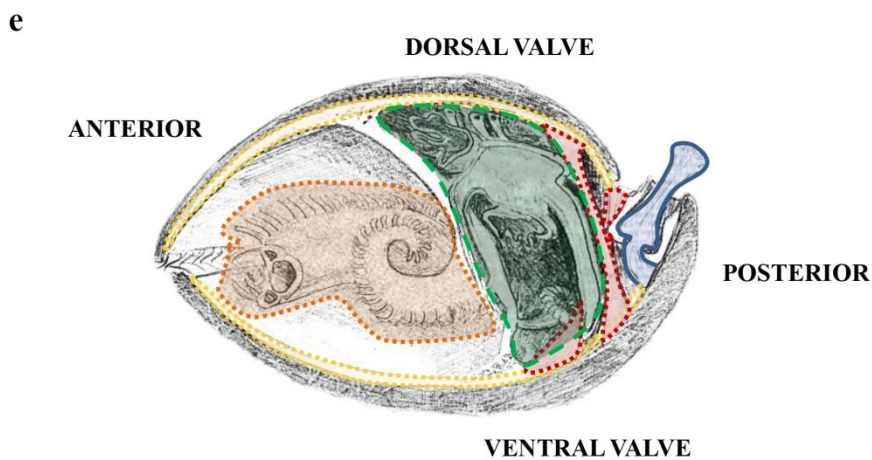
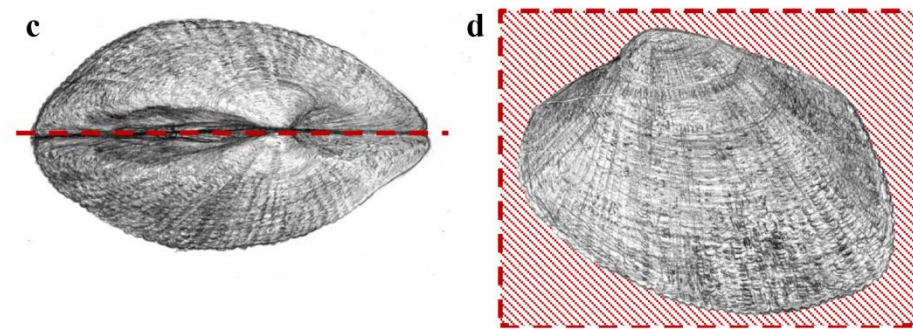


Figure 1.1. (a-d) Comparison of the Rhynchonellata brachiopod *Magellania venosa* (a and b) and the Bivalve *Venerupis decussata* (c and d). The red dashed and diagonal red lines mark the mirror symmetry planes in both animals. For brachiopods, the mirror plane cuts the valves perpendicular to the plane defined by the valve commissures when they are closed and cross from the anterior to the posterior region through the pedicle (a and b). For most bivalves it is the opposite, the mirror plane is the same as the one defined by the commissures of the closed valves (a and d). (e) Scheme of a half section of an articulate terebratulide brachiopod (modified from Harper 2005 by Holmer; original drawn by Lisa Belhage, Geological Museum, Copenhagen). The dorsal and ventral valves as well as the anterior and posterior region are indicated. Some of the main internal regions are marked in colour: the mantle epithelium (yellow), the lophophore (orange), body cavity (green), muscular system (red) and pedicle (blue). The draws were done by Eloy Manzanero Criado, freelance Palaeoartist.

There are five extant brachiopod orders: Lingulidae, Craniidae, Rhynchonellidae, Thecideidae and Terebratulidae. They are highly distinct differing in soft-tissue anatomy, shell morphology, shell chemistry and shell texture and microstructure. Some of the differences can be observed not only on the micrometer scale but also on the micro-, and nanometer scale. Due to the complexity of the characteristics given above, most studies described the mentioned hierarchical structure for only one species per study (e.g. Williams 1973, Schmahl 2004, Griesshaber et al. 2007, Cusack and Williams 2007, Perez-Huerta et al. 2007, Goetz et al. 2009, Merkel et al. 2009, Schmahl et al. 2012, Gaspard et al. 2016, Ye et al. 2018a).

An important part of this dissertation refers to thecideid brachiopods, the last brachiopod order to appear in the fossil record (Carlson, 2016). Thecideide are a very special group among Brachiopoda. Their position and connections within the brachiopod phylogeny is still under debate as well as their origin (Williams 1973, Carlson 2016). They are small bodied animals and live cemented to hard substrates in cryptic habitats, a life-style and a living environment that contrasts significantly with most terebratulide and rhynchonellide extant brachiopods (Williams 1973, Carlson 2016, Baumgarten et al. 2013, Ye et al. 2018a, 2018b).

1.1. Biomineralization processes

“The term biomineralization or biological biomineralization defines those processes by which organisms form minerals”

(Lowenstam and Weiner 1989)

“Biomineralization links soft organic tissues, which are compositionally akin to the atmosphere and oceans, with the hard materials of the solid Earth. It provides organisms with skeletons and shells while they are alive, and when they die these are deposited as sediment in environments from river plains to the deep ocean floor. It is also these hard, resistant products of life which are mainly responsible for the Earth’s fossil record.”

(Leadbeater and Riding 1986)

“Biomineralization is by definition a multidisciplinary field that draws on researchers from biology, chemistry, geology, material science, and beyond.”

(L.A. Estroff, 2008)

Through cellular activity organisms convert ions in solution into solid minerals (Simkiss and Wilbur, 1989). The minerals that result from these processes are called biominerals, which form minerals when combined with an organic substance. The presence of the organic component is the main difference to the inorganic mineral equivalents. However, biominerals as well as inorganic minerals have often defined morphologies, crystallography, trace elements and isotopic composition. One specific characteristic of biocomposite materials is that they are highly controlled from nano- to micrometer scale levels, leading to hierarchical hybrid composite complex structures with multifunctional properties (Schmahl et al, 2012).

In nature we find an extensive amount of examples of biominerals precipitated by plants, bacteria, molluscs, brachiopods... Also vertebrates mineralize biominerals, such as calcium phosphate to produce bones and teeth (Lowenstam and Weiner, 1989). Biominerals are often adapted to specific functional purposes. Therefore, these minerals play an important role in many organisms’ structures as they give them stability and mobility [e.g. calcium phosphate in vertebrates skeletons, calcium oxalate in plants (chlorophyte) (Lowenstam and Weiner, 1989) silicates in algae and diatoms], protection (e.g. calcium carbonate or calcium phosphate forming shells), tools for living (e.g. calcium phosphate of vertebrate teeth or calcium carbonate in fish otoliths, magnetite in magnetotactic bacteria) and many more.

Porter (2011) and Cohen et al. (2011) place the first evidence of biomineral formation starting at about 750 Mya and Maloof et al. (2010) suggest that around 630 Mya sponge organisms may have formed the first calcite skeletons. However, most animal lineages started to biomineralize at the end of the Precambrian and at the beginning of the Cambrian (541 Mya). From this moment on, that many phyla started to form a huge diversity of biomaterials (Knoll, 2003). Hence, understanding all aspects of biominerals is important in order to understand better the evolution of life.

About one half of the known biogenic mineral species are silica, iron oxides, metal sulphides, sulphates and oxalate biominerals. Biominerals with calcium ion as a major

component comprise the other half of the known biogenic minerals (Lowenstam and Weiner 1989). This is as a consequence of organisms developing the ability to manipulate this ion started very early in the evolution of life. Calcium carbonate minerals are the most abundant biogenic minerals on the Earth in terms of: (1) quantities produced and (2) the widespread distribution among many different taxa in combination with proteins and organic polymers such as collagen and chitin (Lowenstam and Weiner 1989, Vinn, 2013).

Biom mineralization processes can be grouped into two different concepts depending on the degree of biological control (Lowenstam, 1981): “biologically induced” (Lowenstam 1981) and “organic matrix-mediated”, known as well as “biologically controlled” biological mineral formation (Mann 1983).

Biologically induced mineralization takes place mainly when microbial metabolic processes interact with the surrounding environment (Fortin et al. 1997, Braissant et al. 2007 and Decho, 2010). This type of process occurs when the cell surface acts as a template for mineral nucleation and growth (Weiner and Dove 2003). Within this concept we can distinguish *induced* and *influenced* mineralization. *Induced* mineral formation occurs when the biochemical conditions that induce the mineral precipitation, are the product of microbial activities (Dupraz et al. 2009, Decho, 2010). *Influenced* mineral formation refers to the processes where the driving forces for precipitation come from the passive interaction between the extracellular polymers and the geochemistry of the environment (Dupraz et al. 2009, Decho, 2010). The degree of biological control of these systems is still under debate. During the last years many studies pointed out that induced or influenced biom mineralization are not passive precipitation, showing that the bacteria (including their walls and extracellular polymeric substances) have a real influence in several aspects of the biom mineral formation (e.g., Lian et al. 2006, Sánchez-Román et al. 2007, Tourney and Ngwenya, 2009, Shirakawa et al. 2011, Ercole et al. 2012, Oppenheimer-Shaanan et al. 2016, Yin et al. 2020). The biologically induced mineralization is a common mineralization concept among the Monera, Fungi and Protista kingdoms (Lowenstam and Weiner 1989) (Fig. 2).

Biologically controlled mineralization was defined by Mann (1983) as a regulated process, based on genetic predetermination (Simkiss and Wilbur, 1989), that produces materials with specific biological structures and functions such as shells, bones, teeth. Due to the high biological control over mineral growth, the understanding of biologically controlled mineralization is of special interest for materials with engineering applications (Boskey, 1998, Sarikaya, 1999). This type of mineralization can be categorized as being either an *extra-*, *inter-*, or *intracellular* process (Lowenstam and Weiner 1989). Practically all these processes, regardless whether inside or outside of the cell, occur in an isolated or closed environment (Weiner and Dove 2003). The mineralization is biologically controlled when the process is organic matrix-mediated and the nucleation, growth and morphology of the deposited mineral is directed by cells (Weiner and Dove 2003).

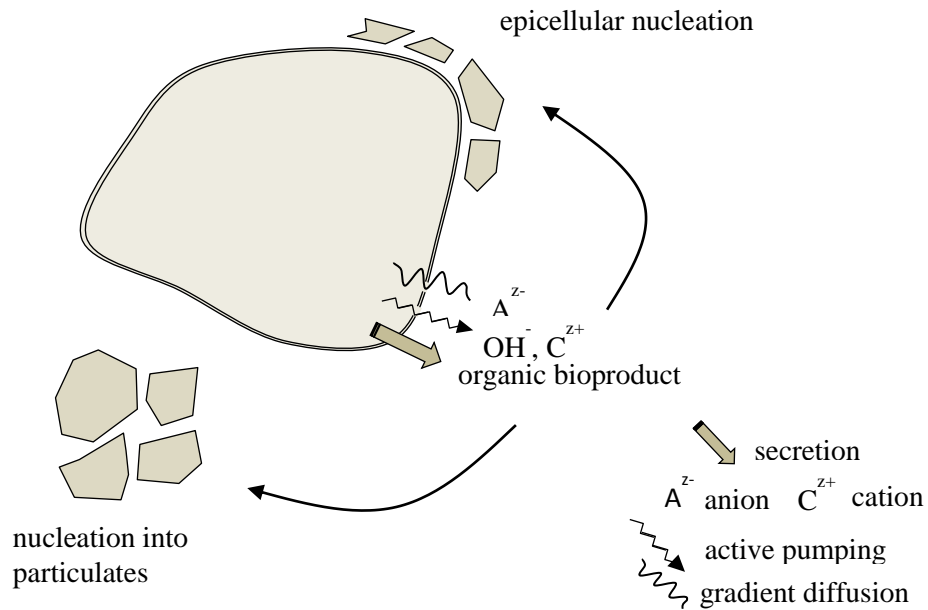


Figure 2. Scheme of biologically induced mineralization modified from Weiner and Dove (2003).

Intercellular mineralization occurs when the isolated site of mineralization is the epidermis of the individual (Mann, 2001). It can be found in communities of single-celled organisms and the processes take place until the mineral fills the intercellular spaces. It is the surface of a cell or organism that directs the polymorph and shape of the precipitated biomineral (Weiner and Dove 2003) (Fig 3).

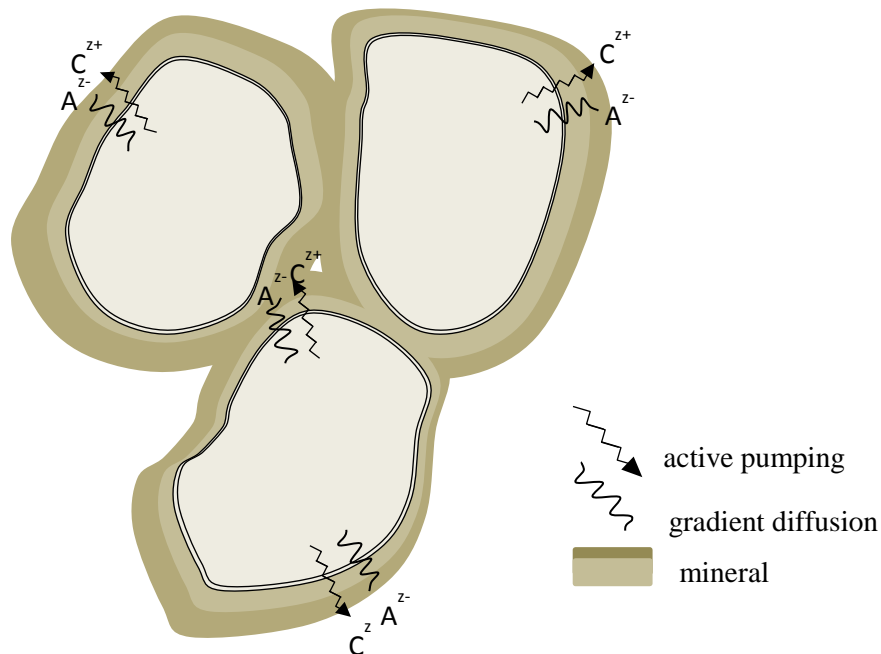


Figure 3. Scheme of biologically controlled intercellular mineralization modified after Weiner and Dove (2003).

Intracellular mineralization occurs when specialized vesicles direct the nucleation of the biomineral within the cell (Weiner and Dove 2003). This is the case for echinoderms, coccoliths or some foraminifera and silica mineralizing algae (Fig 4).

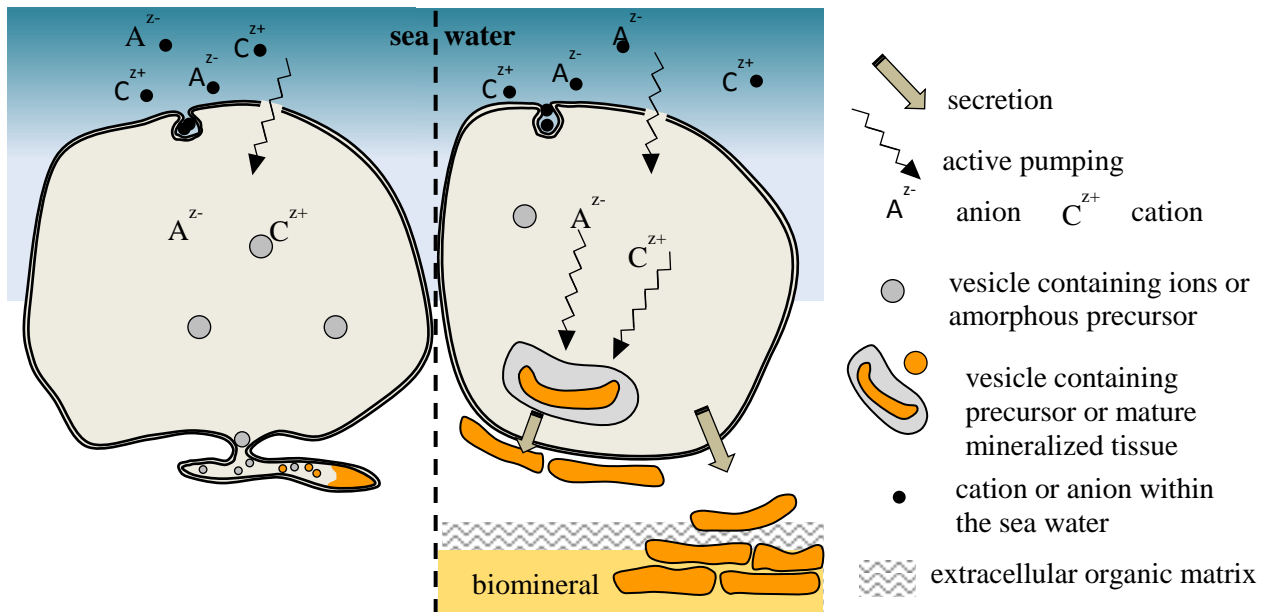


Figure 4. Schemes of biologically controlled intracellular mineralization based on Weiner and Dove (2003) and Weiner and Addadi (2011).

Extracellular mineralization takes place when the cell secretes an extracellular organic matrix that is subsequently mineralized (Weiner and Dove 2003). The organic framework regulates and organizes functions for the biomineral formation (Weiner and Dove 2003). The transfer of mineral or ions to the extracellular matrix can be done by (1) active pumps of ions to the site of mineralization (Simks, 1986) or by (2) vesicles, filled with cations, which are exported through the cell membrane and take precursor compounds to the organic matrix (Weiner and Dove 2003) (Fig.5).

For this study the process of *extracellular mineralization* is of major interest as it is the predominant biological hard tissue forming process for mollusk shells (Gregoire et al. 1955, Crenshaw 1980, Weiner and Traub 1980, 1984, Falini et al. 1996, Pereira-Mouries et al. 2002, Weiss et al. 2002, Gotliv et al. 2003, Weiner and Addadi 2011). For brachiopod shells the biomineralization process was not yet described and often biomineralization of mollusk shells was used as a reference. Accordingly, the studies of this thesis aimed to understand, in one hand, how the mineralization in modern brachiopod shells takes place and, in the other hand, if there is any analogy with the biomineralization process of mollusc shells.

The classical mechanisms of the extracellular mineralization process are still under discussion and every new study brings new light for understanding the complexity of this way of mineralizing shells (e.g. Roer 1980, Aizenberg et al. 1996, Greenaway et al. 1995, Wheatly 1999, 2001, Ziegler et al. 2002, 2004, Politi et al. 2008, Gal et al. 2014, Weiner and Addadi et al. 2011, Simonet Roda et al. 2019).

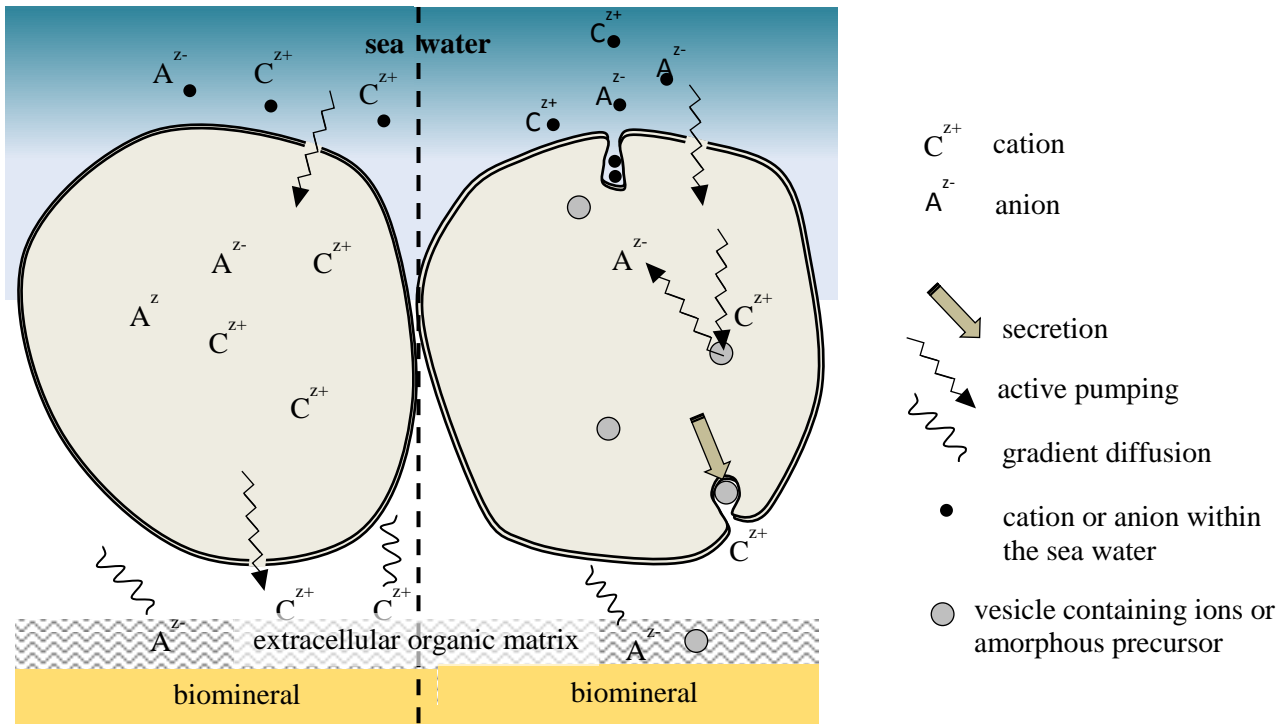


Figure 5. Schemes of biologically controlled extracellular mineralization based on Weiner and Dove (2003) and Weiner and Addadi (2011).

1.2. Brachiopod shells

1.2.1. Shell secretion

Williams and co-workers investigated shell formation for modern rhynchonellide - *Hemithiris psittacea*, *Notosaria nigricans*, *Waltonia inconspicua*- and terebratulide - *Laquens californicus*, *Macandrevia cranium*, *Megerlia truncata*, *Terebratalia transversa*, *Terebratella inconspicua*- (Williams 1953, 1966, 1968a, 1968b, 1973, 1997 and Williams et al. 1997, 2000) brachiopods. The mantle epithelium of brachiopods is the one in charge of the secretion of the different shell layers, being the “biological filter” or guide between the sea water and the shell. The area where the mineralization of the shell takes place is called extracellular space.

According to Williams, TEM and SEM observations show that secretory cells of the brachiopod epithelium are formed within a ‘generative zone’ of the mantle epithelium: the mantle groove that separates the inner and outer lobes of the mantle edge. Williams postulated that the epithelial cells of the mantle lobes act like ‘a conveyor belt’ (e.g. Williams 1966, 1973, Williams et al. 1997). This model relies on the notion that the generative zone of the mantle constantly produces new cells and, therefore, existing cells have to move away. Consequently, Williams suggested (Williams 1966, 1968, 1997) that mantle epithelial cells are capable of performing many secretory tasks and secrete all layers of a brachiopod shell: the periostracum, the extracellular matrix, the calcite of the primary layer, the calcite of the fibrous and that of the columnar shell layer (Williams et al. 1968b). The energy that is required for

physiological changes that epithelial cells must perform when switching between the different secretory tasks was not determined (Williams 1966, 1968).

The fibrous and columnar shell layers of modern rhynchonellide and terebratulide brachiopods are hybrid composites where an extracellular biopolymer matrix is mineralized with calcite; both secreted by outer mantle epithelium (OME) cells. The organic components are formed within the cell or at the apical cell membrane, they cross through the cell membrane at the side of the shell, and they are released into the shell as networks of fibrils or as extracellular organic membranes (Simonet Roda et al. 2019b). As mentioned above, the precursor of the mineralized shell can follow two possible routes of cellular transport: (1) Transport of mineral loaded vesicles that fuse with the apical cell membrane and deposit their content at the sites of mineralization; or (2) transport of ions that cross from the cell to the growing shell. Despite many decades of research, there is still no definitive evidence whether brachiopod shell mineralization occurs via one or another way. Nevertheless, there is general consensus that there is a tight cellular control for brachiopod hard tissue formation.

1.2.2. Shell microstructures

Through geological time brachiopods have developed different types of shell microstructures (Ye et al. 2020). For this dissertation we defined the term “microstructure” based on electron backscattered diffraction (EBSD) measurements. This technique allowed us to determine grain morphology, size, mode of co-orientation/misorientation, co-orientation/misorientation strength and crystallite orientation based on physical measurements. The term ‘texture’ relates to the orientation of a crystal within a material while the term ‘microstructure’ is the sum of all grain sizes, grain morphologies, crystallite co- and misorientations in a given material (Simonet Roda et al. 2020a).

The studies presented in this dissertation were done on modern and fossil specimens of brachiopod with calcitic shells. From the five different extant orders four (Craniidae, Rhynchonellidae, Thecideidae and Terebratulidae) secrete calcitic shell and within them terebratulide and rhynchonellide brachiopods are the most abundant.

Modern terebratulide and rhynchonellide brachiopod shells consist of up to four shell layers: the periostracum situated in the outermost part that is followed inward by up three mineralized layers: the primary, the fibrous and, in some species, the columnar layer (Figure 6). Each shell layer has a specific microstructure (e.g. Schmahl et al. 2004, Schmahl et al. 2008, Griesshaber et al. 2009, Goetz et al. 2009, Goetz et al. 2011, Schmahl et al. 2012, Gaspard and Nouet 2016, Ye et al. 2018, Simonet Roda 2020b) (Fig. 6).

For the primary layer, EBSD measurements show that it consists of an array of interdigitating, irregularly shaped micrometre sized calcite units (Goetz et al. 2011). According to TEM results of Griesshaber et al. (2009) the non-punctate primary shell layer of modern brachiopods does not contain organic material. However, as some organics, e.g. chitin, do not become contrasted by conventional contrasting methods, some organic components might be present within the primary layer. Going inward, there is the fibrous shell layer consisting of arrays of calcite fibres. This layer comprises sub-layers where the stacks of fibres are differently oriented (Merkel et al. 2007, Schmahl et al. 2008, Griesshaber et al. 2009). In contrast to the primary layer, there are

biopolymers occluded within the fibrous shell layer of brachiopods. The organic components can be found inside the individual fibres forming a nanometer scale network of fibrils (Casella et al. 2018). In addition, thick organic membranes line each fibre at their proximal, convex surface (Simonet Roda et al. 2019b). The specific shape and way of packing of the fibres implicates their full encasing by organic substance (Simonet Roda et al. 2019b). In the innermost region of the shell we can find the tertiary or columnar layer. This layer is characterized by long, thick calcite prisms. The upper part of the columnar layer, adjacent to the fibrous layer, is formed by a band of small columnar calcite crystals (1–5 µm). These crystals compete at growth when increasing their width as they grow towards the inner part of this layer, forming the large “pillars” (Goetz et al. 2009). In this layer the organic content is minor (Fig. 6).

Thecideide shell microstructure is complicated and rare and “the full taxonomic potential of shell microstructures remains to be realized” (Baker, 2006, p. 1938). Nowadays we know that it consists of only one mineralized layer with a heterogranular microstructure (Simonet Roda et al. 2020a) also called “acicular primary layer” (Williams, 1997, Williams and Cusack 2007) (Fig. 6). The latter term may be confusing as it compares it to the common primary layer (the external one and the first to be secreted during brachiopod growth) of terebratulide and rhynchonellide brachiopods.

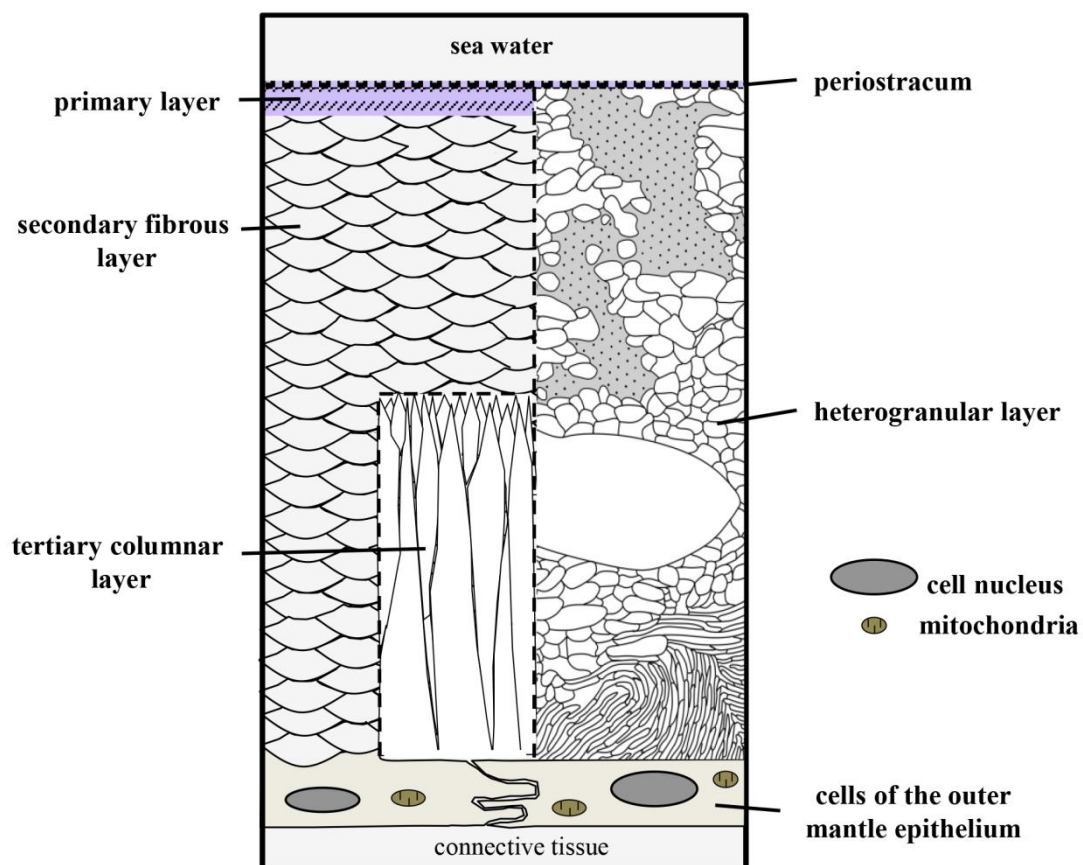


Figure 6. Diagram, based on Williams (1997), Schmahl et al. (2012), and Simonet Roda et al. (2020), showing the different types of shell microstructures of modern terebratulide, rhynchonellide and thecideide brachiopods.

The description and name of the thecideide shell microstructure was classically done under the frame of the primary shell layer. It was named as the “subclass” primary

acicular layer, pointing out the presence of acicular crystallites (Figure 6, Williams, 1973 and 1997). Recent studies redefine the thecideide microstructures by comparing the shell of modern and fossil specimens with the common primary layer of terebratulides (Simonet Roda et al., 2020a and 2020b). These studies define the microstructure as a non-primary heterogranular microstructure where bigger crystals with different morphologies – acicular, polygonal, roundish and granular - are embedded in a matrix of nanocrystallites. The organic material within the shell is very abundant and follows the growth lines that are often perpendicular to the longitudinal axis of the acicular crystallites (Simonet Roda et al., 2020a).

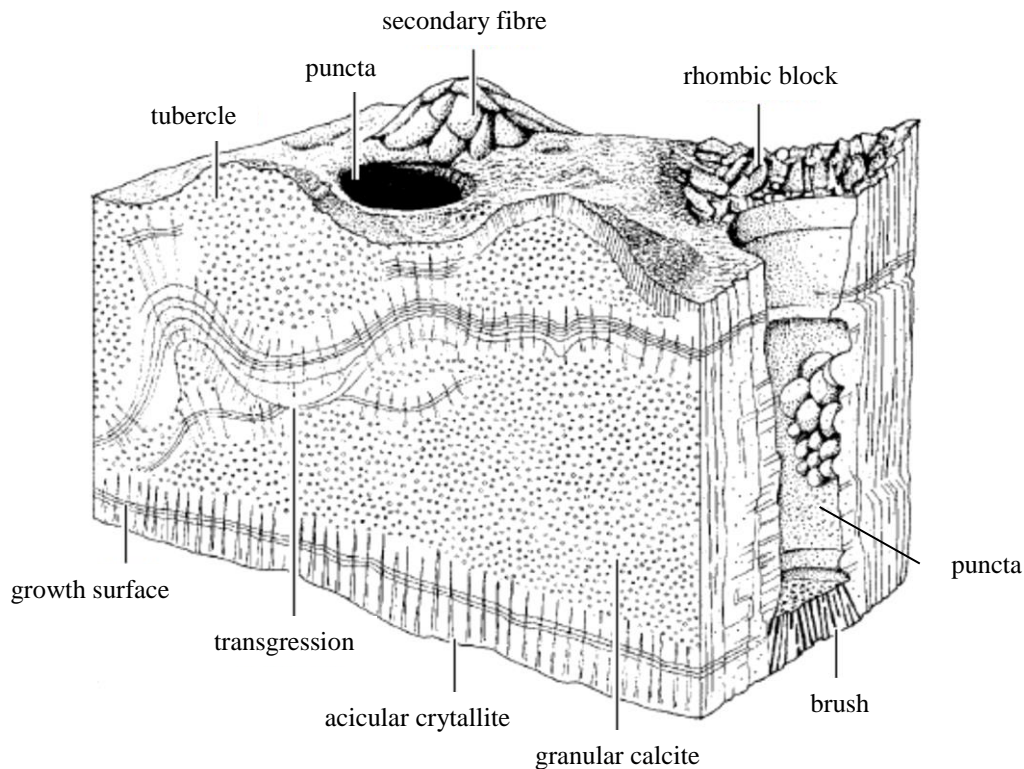


Figure 7. Diagram from Williams (1973) showing a sectioned block of the shell of the thecideide genus *Thecidellina* x 640 magnification. In the scheme we can observe some of the characteristic features of the thecideide microstructure. The puncta in this genus has an average diameter of 25 μm .

Thecideids show a particular evolution of their shell microstructure which involves the progressive loss of the secondary fibrous layer - which became restricted to isolated patches mainly on the brachiopods teeth - in favour of an “acicular” microstructure starting from the Jurassic-Cretaceous (e.g. Baker 2006, Williams and Carlson 2007, Simonet Roda et al. 2020a). Baker 2006 clarifies that the loss of the fibrous fabric as an evolutionary change occurred at different rates among the different Thecideid subfamilies. In the Lacazellinae and Thecideinae, the fibres are suppressed by the Late Jurassic but in the Thecidellinae they are persisting up to the Cretaceous (Baker 2006).

1.2.3. Importance for the scientific realm and other science disciplines

The interest of marine invertebrate shells is wide, comprising different scientific fields. For Earth scientist they are very useful tools for understanding the evolution of the water masses. The sea water conditions will be reflected to some extent in the calcitic shells of marine organisms as it is the environment where they live and grow. This makes them to be very important archives for reconstruction of paleo-environments and climates as well as of ocean and sea water conditions (e.g. Rowell and Grant 1987, Carpenter and Lohmann 1995, Grossman et al. 1996, Veizer et al. 1999, Brand et al. 2003, Parkinson et al. 2005).

The combination of mineral and organic components gives them some advantages relative to inorganic materials, such as strength and flexibility (e.g. Griesshaber et al. 2005, Schmahl et al. 2012). These properties make biominerals very interesting for medical and material sciences. Understanding the biomineralization processes and natural biomaterials leads to a better approach in mimicking the processes in laboratory to create similar materials. Within the last decades biominerals have been used as model systems for new synthetic biomimetic materials (e.g. Sarikaya, 1994, and Sarikaya, 2002, Mayer, 2005, Nindijasari et al. 2015, Greiner et al. 2018, Yin et al. 2019). The development of new biomimetic materials is of great importance for pharmaceutical and medical applications (e.g. Jackson et al. 1988, Saenz et al. 1999, Kamat et al. 2000, Queiroz et al. 2001, Srivastav 2011, Rezaie et al. 2015, Devi et al. 2017, Khan and Chen 2019).

“Consequently, biomineralization involves biologists, chemists, and geologists in interdisciplinary studies at one of the interfaces between Earth and life.”

(Leadbeater and Riding 1986)

Chapter 2. Results and Discussion

2.2. Terebratulide brachiopod shell biomineralization by mantle epithelial cells

Journal of Structural Biology 207 (2019) 136–157



Contents lists available at ScienceDirect

Journal of Structural Biology

journal homepage: www.elsevier.com/locate/yjsbi



Terebratulide brachiopod shell biomineralization by mantle epithelial cells

M. Simonet Roda^{a,*}, A. Ziegler^b, E. Griesshaber^a, X. Yin^a, U. Rupp^b, M. Greiner^a, D. Henkel^c, V. Häussermann^{d,e}, A. Eisenhauer^c, J. Laudien^f, W.W. Schmahl^g



^a Department of Earth and Environmental Sciences, LMU, 80333 München, Germany

^b Central Facility for Electron Microscopy, University of Ulm, 89069 Ulm, Germany

^c Marine Biogeochemistry/Marine Systems, GEOMAR Helmholtz Centre for Ocean Research, 24148 Kiel, Germany

^d Pontificia Universidad Católica de Valparaíso, Facultad de Recursos Naturales, Escuela de Ciencias del Mar, Avda. Brasil, 2950 Valparaíso, Chile

^e Huiñay Scientific Field Station, Puerto Montt, Chile

^f Alfred-Wegener-Institut Helmholtz Zentrum für Polar- und Meeresforschung, 27568 Bremerhaven, Germany

ARTICLE INFO

Keywords:
Transcellular ion transport
Ultrastructure
Amorphous calcium carbonate
ACC
Isotope fractionation
Marine invertebrates

ABSTRACT

To understand mineral transport pathways for shell secretion and to assess differences in cellular activity during mineralization, we imaged with TEM and FE-SEM ultrastructural characteristics of outer mantle epithelium (OME) cells. Imaging was carried out on *Magellania venosa* shells embedded/etched, chemically fixed/decalcified and high-pressure frozen/freeze-substituted samples from the commissure, central shell portions and from puncta. Imaging results are complemented with morphometric evaluations of volume fractions of membrane-bound organelles.

At the commissure the OME consists of several layers of cells. These cells form oblique extensions that, in cross-section, are round below the primary layer and flat underneath fibres. At the commissure the OME is multi-cell layered, in central shell regions it is single-cell layered. When actively secreting shell carbonate extrapallial space is lacking, because OME cells are in direct contact with the calcite of the forming fibres. Upon termination of secretion, OME cells attach via apical hemidesmosomes to extracellular matrix membranes that line the proximal surface of fibres. At the commissure volume fractions for vesicles, mitochondria and lysosomes are higher relative to single-cell layered regions, whereas for endoplasmic-reticulum and Golgi apparatus there is no difference.

FE-SEM, TEM imaging reveals the lack of extrapallial space between OME cells and developing fibres. In addition, there is no indication for an amorphous precursor within fibres when these are in active secretion mode. Accordingly, our results do not support transport of minerals by vesicles from cells to sites of mineralization, rather by transfer of carbonate ions via transport mechanisms associated with OME cell membranes.

Citation: Simonet Roda, M., Ziegler, A., Griesshaber, E., Yin, X., Rupp, U., Greiner, M., Henkel, D., Häussermann, V., Eisenhauer, A., Laudien, J. and Schmahl, W.W. 2019 : Terebratulide brachiopod shell biomineralization by mantle epithelial cells. *Journal of Structural Biology*, 207, 136-157.

2.1. Terebratulide brachiopod shell biomineralization by mantle epithelial cells

Simonet Roda M.* (1), Ziegler A. (2), Griesshaber, E. (1), Yin X. (1), Rupp U. (2), Greiner M. (1), Henkel D. (3), Häussermann V. (4), Eisenhauer A. (3), Laudien J. (5), and Schmahl W. W. (1)

¹ Department of Earth and Environmental Sciences, LMU, 80333 München, Germany

² Central Facility for Electron Microscopy, University of Ulm, 89069 Ulm, Germany

³ Marine Biogeochemistry/Marine Systems, GEOMAR Helmholtz Centre for Ocean Research, 24148 Kiel, Germany

⁴ Pontificia Universidad Católica de Valparaíso, Facultad de Recursos Naturales, Escuela de Ciencias del Mar, Avda. Brasil 2950, Valparaíso, Chile and Huinay Scientific Field Station, Puerto Montt, Chile

⁵ Alfred-Wegener-Institut Helmholtz-Zentrum für Polar- und Meeresforschung, 27568, Bremerhaven, Germany

*Corresponding author: simonet@lrz.uni-muenchen.de

Abstract

To understand mineral transport pathways for shell secretion and to assess differences in cellular activity during mineralization, we imaged with TEM and FE-SEM ultrastructural characteristics of outer mantle epithelium (OME) cells. Imaging was carried out on *Magellania venosa* shells embedded/etched, chemically fixed/decalcified and high-pressure frozen/freeze-substituted samples from the commissure, central shell portions and from puncta. Imaging results are complemented with morphometric evaluations of volume fractions of membrane-bound organelles.

At the commissure the OME consists of several layers of cells. These cells form oblique extensions that, in cross-section, are round below the primary layer and flat underneath fibres. At the commissure the OME is multi-cell layered, in central shell regions it is single-cell layered. When actively secreting shell carbonate extrapallial space is lacking, because OME cells are in direct contact with the calcite of the forming fibres. Upon termination of secretion, OME cells attach via apical hemidesmosomes to extracellular matrix membranes that line the proximal surface of fibres. At the commissure volume fractions for vesicles, mitochondria and lysosomes are higher relative to single-cell layered regions, whereas for endoplasmic-reticulum and Golgi apparatus there is no difference.

FE-SEM, TEM imaging reveals the lack of extrapallial space between OME cells and developing fibres. In addition, there is no indication for an amorphous precursor within fibres when these are in active secretion mode. Accordingly, our results do not support transport of minerals by vesicles from cells to sites of mineralization, rather by transfer of carbonate ions via transport mechanisms associated with OME cell membranes.

Keywords: transcellular ion transport, ultrastructure, amorphous calcium carbonate, ACC, isotope fractionation, marine invertebrates

2.1.1 Introduction

Brachiopods are shell-forming sessile marine invertebrates that have existed from the Early Cambrian and are still extant (e.g. Lowenstam, 1961, Veizer et al., 1986, Peck et al. 1997, Samtleben et al., 2001, Carlson 2016, Cross et al. 2018). They mineralize low-Mg calcite or Ca-phosphate shells and populate a wide range of marine habitats (e.g. Bates and Brand, 1991; Grossman et al., 1996; Carpenter and Lohmann, 1995; Williams et al. 2000, Cusack et al. 2001; Peck 2007; Angiolini et al., 2009; Lee et al. 2011; Roark et al., 2015; Garbelli et al., 2017; Temereva and Kuzmina 2017).

Brachiopod shells consist of two valves that are connected to each other at the hinge. Unlike mollusc shells each brachiopod valve has a mirror plane, the median plane, that cuts through the valves. The two valves are not mirror images of each other. Brachiopod valves have a quite constant thickness along their length. As juvenile valves are thinner relative to adult ones, valve growth does not occur exclusively at commissural margins, it takes also place along inner shell surfaces (Rosenberg et al. 1988, Baumgarten 2013).

Modern terebratulide and rhynchonellide brachiopod shells consist of up to four shell layers: the outermost periostracum that is followed inward by up to three mineralized layers: the primary, the fibrous and, where developed, the columnar layer. Each shell layer has a specific microstructure (e.g. Schmahl et al. 2004, Griesshaber et al. 2007, Schmahl et al. 2008, Griesshaber et al. 2009, Goetz et al. 2009, Goetz et al. 2011, Schmahl et al. 2012, Gaspard and Nouet 2016, Ye et al. 2018a, 2018b, Simonet Roda et al. 2019). EBSD measurements show that the primary layer consists of an array of interdigitating, irregularly shaped micrometre sized calcite units (Goetz et al. 2011). Organic substance is not incorporated within the primary layer (Griesshaber et al. 2009). Arrays of calcite fibres form the proximal part of both brachiopod valves. EBSD results prove that the fibrous shell portion consists of sub-layers. The latter are formed of differently oriented stacks of parallel calcite fibres (Merkel et al. 2007, Schmahl et al. 2008, Griesshaber et al. 2009). In contrast to the primary layer, in the fibrous shell layer biopolymers are incorporated and are developed as membranes or fibrils (Casella et al. 2018a, Simonet Roda et al. 2019). A thin network of fibrils exists within each fibre (Casella et al. 2018a, 2018b), while organic membranes separate adjacent calcite fibres (Williams 1966, 1968a, 1968b, 1997). The membranes are secreted only onto the proximal, convex side of the fibres and are not fully encasing them (Simonet Roda et al. 2019). The specific shape and mode of packing of the fibres implicates that they are enveloped by organic substance.

The calcite fibres in modern brachiopods are single crystals (Schmahl et al., 2004, 2008, 2012, Griesshaber et al. 2007, Goetz et al. 2009, Ye et al. 2018a, 2018b). Mild selective etching of these biocrystals produces nanoscale surface morphologies that do not reflect a simple inorganic rhombohedral calcite crystallography, but instead give the appearance of a nanoparticulate mesocrystalline structure consisting of globular units in the 50-100 nm size range (Cusack et al. 2008, Schmahl et al. 2008, 2012, Simonet Roda et al. 2019). For nacre tablets of the gastropod *Phorcus turbinatus* Macías-Sánchez et al. (2017) described as well a globular appearance of the mineral units. However, the authors demonstrated that granularity of the biomineral is not related to the secretion process, but is rather the consequence of the transformation from the precursor to the crystallized mineral. According to Macías-Sánchez et al. (2017) transformation to aragonitic nacre in *Phorcus turbinatus* takes place via an interface-coupled dissolution-

reprecipitation mechanism, where, in the presence of water, the original structure of the amorphous mineral is reshaped by the regrowth of the newly-formed crystalline phase. This induces the globular appearance of the crystallized carbonate biomaterial.

Modern rhynchonellide (*Notosaria nigricans*, *Calloria inconspicua*, *Hemithiris psittacea*) and terebratulide (*Laquens californicus*, *Macandrevia cranium*, *Megerlia truncata*, *Terebratalia transversa*, *Terebratella inconspicua*; Williams 1966, 1968a, 1968b, 1997, Williams et al. 2000) brachiopod shell formation was investigated by Williams and co-workers. From TEM and SEM observations the authors deduced a model for shell secretion and proposed that secretory cells of brachiopods are formed within a ‘generative zone’ of the mantle epithelium: the mantle groove. The latter separates the inner and outer lobes of the mantle edge. Williams postulated (e.g. Williams 1966) that epithelial cells of the mantle lobes move like ‘conveyor belts’. This idea relies on the notion that the generative zone of the mantle epithelium constantly produces new cells, hence, existing cells need to make space and to move away. In agreement with the ‘conveyor belt’ idea, Williams postulated (Williams 1966, 1968a, 1968b, 1997) that epithelial cells are capable of performing many secretory tasks and, hence, to secrete all layers of a brachiopod shell: the periostracum, the calcite of the primary layer, the extracellular matrix, the calcite of the fibrous layer and the calcite and extracellular matrix of the columnar shell layer. However, the impetus that is required for the physiological changes that brachiopod epithelial cells must undergo when switching between the many and very different secretory tasks is up to now not determined.

The fibrous and columnar shell layers of modern rhynchonellide and terebratulide brachiopods is a hybrid composite where an extracellular biopolymer matrix is reinforced by calcite. Both material components are secreted by outer mantle epithelium (OME) cells. The organic component is formed within the cells: biopolymers are packed into organelles; these fuse with the apical OME cell membrane and release their content to the shell (e.g. Rothman and Wieland 1996, Bonifacino and Glick 2004). For the mineral component two routes of transport from the cell to the site of mineralization might be possible: (1) Transport of material as ions that cross through the cell to the sites of mineralization, or (2) transport of mineral loaded intracellular vesicles that fuse with apical cell membranes and deposit their content at sites of active shell secretion. Despite many decades of cell biological and biochemical research, up to now, there is no definitive evidence whether brachiopod shell mineralization occurs via mineral filled vesicles or by membrane-protein-aided ion transport. Nonetheless, there is general consensus that hard tissue formation occurs under tight cellular control.

Accordingly, the focus of this study is the investigation of brachiopod shell mineralization, in particular, calcite fibre secretion in modern terebratulide brachiopod shells. We started our work with the hypothesis that brachiopod calcite is formed by aggregation of ACC nanoparticles, which are exocytosed by epithelial cells, attach to the developing fibre and crystallize in-situ. Therefore, we conducted an ultrastructural study of outer mantle epithelium (OME) cells that are in direct contact with the growing shell at: (i) the commissure, (ii) central valve sections, and (iii) at and within endopuncta. We describe and visualize ultrastructural differences of the OME at the above mentioned shell regions, substantiate these with quantitative morphometric data of organelle distribution patterns in epithelial cells and propose a conceptual model for mineral transport from OME cells to the sites of calcification. Our starting working hypothesis was not substantiated by our results.

In a broader perspective, we aim with this study for shelled organisms for an up to date understanding of material transport from epithelial cells to the sites of hard tissue formation. This is not only of major importance from a biomineralization perspective. As modern and fossil brachiopods are proxies for climate dynamics and environmental change, it is essential to assess and to evaluate physiological mechanisms that induce fractionation of shell forming isotopes and elements (e.g. Wefer and Berger 1991, Bates and Brand 1991, Auclair et al. 2003, Parkinson et al. 2005, Brand et al. 2011). As it has been shown for corals and coccolithophorides, fractionation might arise as a consequence of the mode of material transport to the sites of mineral formation, which is either by ion or by vesicular transport or is possibly a combination of both (e.g. Böhm et al. 2006, Langer et al. 2007, Mejia et al. 2018).

2.1.2. Materials and methods

Materials

In this study we investigated the terebratulide brachiopod *Magellania venosa*. The animals were obtained from Comau Fjord, southern Chile. The brachiopods were taken from 21 meters depth, from waters with an average water temperature of 11 °C and 30.3‰ salinity.

Great care was taken that the investigated animals secreted shell material up to the very start of sample preparation. A stock of 150 to 200 brachiopods were transported live from Comau Fjord, Chile, to GEOMAR, Kiel, Germany, where they were kept in aquaria for three and a half years. In 2018 the brachiopods were transferred to aquaria at AWI in Bremerhaven, Germany, and are still living there today. The brachiopods that were selected for this study lived in the aquaria for more than 6 months prior to the start of sample preparation and had, thus, enough time to adjust to the new living conditions. Within the aquaria the brachiopods were monitored constantly with infrared cameras for observing them opening and closing their valves. Dead animals were discarded immediately. The aquaria were checked for dead animals twice a week.

Brachiopods that we investigated in this study had their valves open. We regard this as a sign that they were constantly filtering, hence feeding and actively secreting shell material. *Magellania venosa* is a fast growing brachiopod. Shell secretion was also checked with the measurement of an increase in shell size, the latter was checked every three months. The brachiopods adopted well to their new living conditions as they spawned twice per year. Prior to transfer into the fixation solution or preparation for high-pressure freezing it was checked whether the investigated specimens were still alive by having them open and close their valves. Animals that were chemically fixed had a longitudinal axis length between 5 and 7 millimetres. Brachiopods that were used for high-pressure freezing had a longitudinal axis length of about 4-5 millimetres. According to Baumgarten et al. (2013), the *Magellania venosa* specimens of the size we used in our study are still juveniles and, thus, have a higher shell growth rate than adults. We investigated in this study eight *Magellania venosa* specimens.

Methods

Chemical fixation and decalcification

For transmission and scanning electron microscopical imaging of the organic phase within the hard tissue and the ultrastructure of mantle epithelial cells we fixed 20 shell

pieces that were taken from central shell portions and from the commissure of both valves. All 20 shell pieces contained shell material and adjacent OME. We followed fixation procedures described in Karnovsky 1965 and Seidl and Ziegler 2012. In order to assure best fixation results of the soft tissue we checked the effect of two fixation solutions. The difference between the two fixation solutions was given by the used concentrations of paraformaldehyde and glutaraldehyde. Fixation solution A was prepared by mixing equal volumes of filtered seawater from the culture of *Magellania venosa* containing 2% paraformaldehyde and 2% glutaraldehyde with a solution of 0.35 mol L⁻¹ saccharose and 0.17 mol L⁻¹ NaCl in 0.2 mol L⁻¹ Na-cacodylate buffer (pH 7.7). Fixation solution B was prepared in the same way, however, with higher concentrations of paraformaldehyde (3.2%) and glutaraldehyde (4%) in the filtered seawater. The quality of soft tissue preservation was checked in TEM at 8000 times magnification. We did not find any difference in structure preservation, irrespective which solution was used. Occasionally we found the OME ruptured or/and slightly detached from the shell. We attribute these features to mechanical impact at shell dissection. These samples were investigated (cut and imaged with FE-SEM and TEM) as well, but were not taken into account for the interpretation of our results. All 20 shell pieces (containing hard and soft tissue) were fixed for 17 hours at 4 °C.

Of the 20 specimens, 8, taken from both valves, were decalcified for 14 days in a solution containing 0.25 mol L⁻¹ HEPES, 0.05 mol L⁻¹ EDTA and 1% glutaraldehyde (Fabritius et al. 2005, Seidl and Ziegler 2012). The simultaneous decalcification and fixation ensures that the organic matrix emerges slowly, is exposed to the solution and is immediately fixed by aldehyde. Subsequent to decalcification the samples were washed three times with 0.1M Na-cacodylate buffer (7.7 pH) and postfixed in the same buffer for one hour containing 1% OsO₄ and 0.9% K₄Fe(CN)₆·3H₂O. After washing with bi-distilled water the samples were dehydrated in an ascending series of isopropanol solutions (30, 50, 70 and 90%) and were contrasted with 2% uranyl acetate (in 100 % ethanol for 30 minutes, washed 3 times for 30 minutes each in 100% isopropanol and two times for 5 minutes in propylenoxid).

Finally all 20 shell pieces were embedded in EPON resin and were cut with an ultramicrotome for imaging in TEM and FE-SEM as thin sections or as block-faces, respectively.

High-pressure freezing and freeze-substitution

High-pressure freezing enhances significantly the quality of morphological preservation of soft tissue samples for electron microscopical observation (Giddings 2003). *Magellania venosa* not larger than 6 mm in length were dissected in the seawater of the culture. Pieces of shell with the mantle epithelium attached to the shell were cut from the commissure and the central shell portion of both valves. Samples were transferred to hexadecane and placed in aluminium planchets with an outer diameter of 3 mm and a 200µm deep cavity, and covered with the flat side of another planchet. Samples were then high-pressure frozen with a Wohlwend HPF Compact 01 high-pressure freezer within 30 ms at a pressure of 2.3 x 10⁸ Pa.

Some of the high-pressure frozen samples were, in addition, subsequently freeze-substituted. The substitution medium enhances further ultrastructural features of biological soft tissues (Walther and Ziegler 2002). The planchet sandwiches were opened and freeze-substituted overnight in 0.2% OsO₄, 0.1% uranyl acetate and 5%

H₂O in acetone from -90°C to 20°C following the protocol described in Walter and Ziegler, 2002. Finally, the samples were embedded in EPON resin and cut by using a diamond trimming knife (Diatome,) and a Reichert Ultracut ultra microtome.

In a further procedure some of the high-pressure frozen, freeze-substituted and EPON embedded samples were decalcified for two weeks with 0.25 mol L⁻¹ HEPES, 0.05 mol L⁻¹ EDTA. The samples were then re-embedded in EPON. This procedure facilitated better thin sectioning for TEM imaging.

In order to visualize simultaneously epithelial cells, organic matrices and shell mineral with FE-SEM we used chemically fixed but non-decalcified as well as high-pressure frozen and freeze-substituted samples, all of them embedded in EPON resin. Samples were mounted on 3 mm thick cylindrical aluminium rods using super glue, were cut (Reichert Ultracut ultramicrotome) with glass and polished with diamond knives (Diatome). Samples were then coated with 4 nm of carbon and imaged with a Hitachi S5200 FE-SEM. After imaging the carbon layer was removed, sample surfaces were re-polished, etched and fixed simultaneously for 40 seconds with a solution containing 0.1 M HEPES (pH = 9.0) and 2.5 % glutaraldehyde. Samples were then treated with 100 % isopropanol 3 times for 10 seconds each and critical point dried in a BAL-TEC CPD 030 devise. After coating with 4 nm carbon the dried samples were imaged again with a Hitachi S5200FE-SEM.

Sample preparation for microstructure characterisation

Electron Backscatter Diffraction (EBSD) measurements were done on even surfaces of high-pressure frozen and freeze-substituted samples, embedded in EPON resin. The used sample preparation for high-pressure freezing, freeze-substitution and embedding in EPON is described in the sections above. For the required even surfaces, samples were cut and polished with a diamond microtome knife and were subsequently coated with 4-6 nm of carbon.

Transmission electron microscopy

Ultrathin 60 nm thick sections were cut from chemically fixed and high-pressure frozen and freeze-substituted and decalcified samples using a diamond knife and an ultramicrotome. The sections were placed on carbon stabilized Formvar-coated copper hole grids and stained with 0.3% lead citrated.

A Zeiss 912 TEM equipped with an Omega energy filter, a goniometer stage and a 2k x 2k pixel camera was used to image the sections at 8000 times magnification and 120 kV acceleration voltage using only elastically scattered electrons. To screen a large area of the outer mantle epithelium at high resolution, up to 60 panorama images were recorded at rectangular grids, each of these containing between 250 and 300 high-quality individual images. These were then aligned using the TRS software and formed the composite panorama images. Up to 20 composite images were used for structural and numerical analysis.

Field emission scanning electron microscopy

Non-decalcified animals were chemically fixed as a whole (Fabritius and Ziegler 2003, Fabritius et al., 2005) . Small pieces of the shell were embedded in EPON resin and knife polished with successively advancing the knife to the surface of the sample to

70, 40, 20, 10 and 5 nm, repeating each polishing step 15 times. Samples were mounted on aluminium holders using self-adhesive carbon pads and conductive glue and were coated with 4 nm of carbon using a BAF 300 BAL-TEC coating machine. Samples were analysed with a Hitachi S5200 field emission scanning electron microscope (FE-SEM) using the converted backscattered electron signal to obtain so called composite rich images (Walther, 2008) with 20 μ A emission current and 4kV acceleration voltage in analysis mode of the microscope. Secondary electrons from the sample were suppressed by 100% so that only the backscatter electron signal was used for imaging.

Electron backscatter diffraction

EBSD measurements were carried out on a Hitachi SU5000 field emission SEM, equipped with an Oxford EBSD detector. The SEM was operated at 15 to 20 kV and measurements were indexed with the CHANNEL 5 HKL software. In this study crystal orientation information is presented with band contrast measurement, colour-coded crystal orientation images and corresponding pole figures. EBSD band contrast represents the pattern quality of the EBSD-Kikuchi diffraction pattern, where a strong EBSD signal yields a bright image point when a crystal is scanned. An absent signal results from organic material or the presence of amorphous mineral. Co-orientation statistics are derived from pole figures obtained from EBSD scans. A measure of crystal co-orientation is given by the MUD value, a value defined as the multiple of uniform (random) distribution. Thus, high MUD values indicate a high crystal co-orientation, whereas low MUD values reflect a low to random co-orientation, respectively. For further information see Griesshaber et al. 2013, Griesshaber et al. 2017, Casella et al. 2018a, 2018c.

Morphometry

In this study we aim for a comprehensive understanding of the ultrastructure of OME cells that are in close contact with the growing shell. We investigate the relation between OME cells and actively secreted calcite fibres. Accordingly, our intention was to image large portions of the OME with very high quality TEM and SEM images and perform a statistical evaluation of organelle distribution patterns for a large portion of the OME. To achieve the latter we recorded 60 TEM panorama images. Each panorama image covered both, shell calcite and OME cells and consisted of 250 and 300 individual very high-quality TEM images. The individual TEM images were aligned to each other and formed the TEM panorama images. Of these 60 panorama images we selected 18 for numerical analysis. Of the 18 panorama images we selected 48 areas of interest, with each area of interest covering many OME cells depicted in very high resolution. The statistical evaluation was performed for two animals. We did not perform the statistical evaluation in 3D, as the intention was to cover large portions of the OME. A 3D statistical evaluation is carried out currently in a further study. OME volumes are selected on the basis of our imaging and statistical results obtained from the 2D statistical evaluation.

Throughout this study we compare for the central shell region two types of outer mantle epithelia:

OME that is connected by hemidesmosomes within the apical OME cell membrane to the extracellular organic membrane lining at the proximal convex surface of the fibres. We use the abbreviation *cr-a: central shell region with OME - attached*.

OME where both the extracellular organic membrane at the convex proximal side of the fibres as well as the apical hemidesmosomes are absent. In this case the apical cell-membrane delineates the compartment into which the cell secretes all components of the shell-forming mineral. We use the abbreviation *cr-s: central shell region with OME - secreting*. For further description see Simonet Roda et al. (2019). These two epithelia alternate at about the cross-sectional size scale for a calcite fibre, i.e. at about 7-9 micrometres.

We also examined the *thin epithelium at the puncta (pt)* and regard it as an epithelium that is not involved in mineral secretion. We consider the epithelium at and within the puncta as a reference the secreting epithelia.

Furthermore, we compare the multi-cell layered OME underneath the calcite fibres at the inner commissure (*abbreviation: com*) with the single-cell layered OME below central shell regiona (*abbreviation: cr-all*).

Volume fractions of various organelles were determined by counting randomly positioned points on predefined structures (classes) within test fields using the open source software JMicroVision Image analysis system (Roduit, 2008). Twelve different classes were defined as: *cytoplasm, nucleus, mitochondria, lysosomes-endosomes, vesicles, Golgi apparatus, rough endoplasmic reticulum, smooth endoplasmic reticulum, glycogen, multivesicular bodies, others, and extracellular space*. The number of random points was set either to 250 or 500 depending on the size of the test field. Test areas were defined using the implemented “area editor” so that regions outside of the epithelium were at a minimum. Evolution plots created by the software were used to evaluate if calculated volume fractions of organelles are representative.

For each test field the length of the epithelium “ E_L (μm)” and the test field area “ A_T (μm^2)” were determined and the percentages of the various classes “ A_p (%)” in “ A_T ” were measured.

The absolute area “ $A_O(i)$ ” of each class i was calculated by

$$A_O(i) = A_T * (A_p(i)/100) (\mu\text{m}^2)$$

The areas of the extracellular space and of the nucleus were excluded by calculating the area of the cytoplasm “ A_C ” within the test field by

$$A_C = (\sum_{classes\ i=1}^{16} A_O(i)) - A_O(\text{nucleus}) - A_O(\text{extracellular space}) (\mu\text{m}^2)$$

The volume fraction of each class “ $V_O(i)$ ” of the cytoplasm without the nucleus equals the area fraction “ $A(i)$ ” and was calculated by

$$V_O(i) = A(i) = (A_O(i) / A_C) * 100 (\%)$$

From the area fraction “ $A(i)$ ” of classes i , we calculated the absolute volume $V_A(i)$ of classes i per $10 \mu\text{m}^2$ epithelium area by

$$V_A(i) (\mu\text{m}^3/\mu\text{m}^2) = A_O(i) / E_L * 10 (\mu\text{m}^2 / \mu\text{m})$$

For measuring the area of cell membranes as well as for the outer membrane of the mitochondria we followed the method of Merz (1967). As the region of the OME near the shell rim (commissure) contains numerous long extensions it was not possible to distinguish the apical cell membrane from the basal one. Therefore, we distinguished a distal from a proximal cell membrane, with the latter most probably containing both apical and lateral membrane compartments. The Merz grid plugin for ImageJ/Fiji (Research Services Branch, National Institute of Mental Health, Bethesda, MD, USA) was used to superimpose an array of coherent semicircular lines to the images. The profile length " L_p " of the cell membrane and the outer membrane of the mitochondria was determined by counting the intersections of the Merz grid lines with the membranes inside the test fields. L_p was calculated by:

$$L_p = N d (\mu\text{m})$$

with " N " as the number of intersections between the grid lines and the membranes and " d " the diameter of the semicircles in each test field.

L_p was normalized to $1 \mu\text{m}$ epithelium length by

$$L = L_p/E_L$$

with " E_L " the epithelial length within the test field.

The areas of the membranes " A_M " per μm^2 area of epithelium was calculated by

$$A_M = L \times 1.273 (\mu\text{m}^2) \text{ (Merz, 1967).}$$

Statistical analysis

GraphPad Prism software, version 6.00, for Mac (GraphPad Software, La Jolla California USA, www.graphpad.com) was used for statistical analysis and graphical representation. Mean values and standard deviations were calculated for the volume fractions $V_O(i)$, the absolute volume of each class normalized to $10 \mu\text{m}^2$ of epithelium V_A , and the membrane areas normalized to one square micrometer epithelium A_M for the distal and proximal cell membrane, and the outer membrane of the mitochondria. One way ANOVA was used to test the significance of differences in the mean values for the volume fraction $V_O(i)$ and area per $10 \mu\text{m}$ epithelial length of classes $A_O(i)$. To account for multiple comparisons, Sidiak's multiple comparisons tests were used to assign significant differences between the mean values for the mineral secreting central region (cr-s), the non-secreting attached areas (where the OME is attached to the organic membrane at the convex proximal side of the fibre) of the central shell region (cr-a) and the puncta (pt). T-tests were used to test for significant differences between the mean values of the pooled central regions.

2.1.3. Results

The shell

The schematic presentation shown in Fig. 2.1.1 depicts the different layers of the shell of modern *Magellania venosa* as well as the topological relation of the mantle epithelium to the growing shell. The scheme is true to scale for an approximately 10 mm large *Magellania venosa*. Fig. S2.1.1 indicates on cross-sections through the two

valves those shell portions that were investigated in this study: the commissure and the central shell region (Fig. S2.1.1B).

The valves of *Magellania venosa* (Fig. S2.1.1A) consist of an outer organic layer, the periostracum, and two mineralized layers, the primary and the fibrous shell layers. The periostracum in *Magellania venosa* (Figs. 2.1.1, 2.1.2A) is a reticular structure that contains thin branching septae and large hollow spheres, the latter being similar to those observed in the periostracum of the bivalve *Mytilus edulis* (Wählich et al. 2014). Along the proximal side of the periostracum, small spherical structures with a dense (osmiophilic) core fuse with one another. At its distal side the reticular structure of the periostracum is connected to a flat and thin sheet that carries numerous small rods (Fig. 2.1.2A) and is interrupted by large pores (Fig. 2.1.2A). At its proximal side the periostracum of *Magellania venosa* is lined by a porous basal layer (red rectangles in Fig. 2.1.2A), hence, there is access from an outer medium to the puncta.

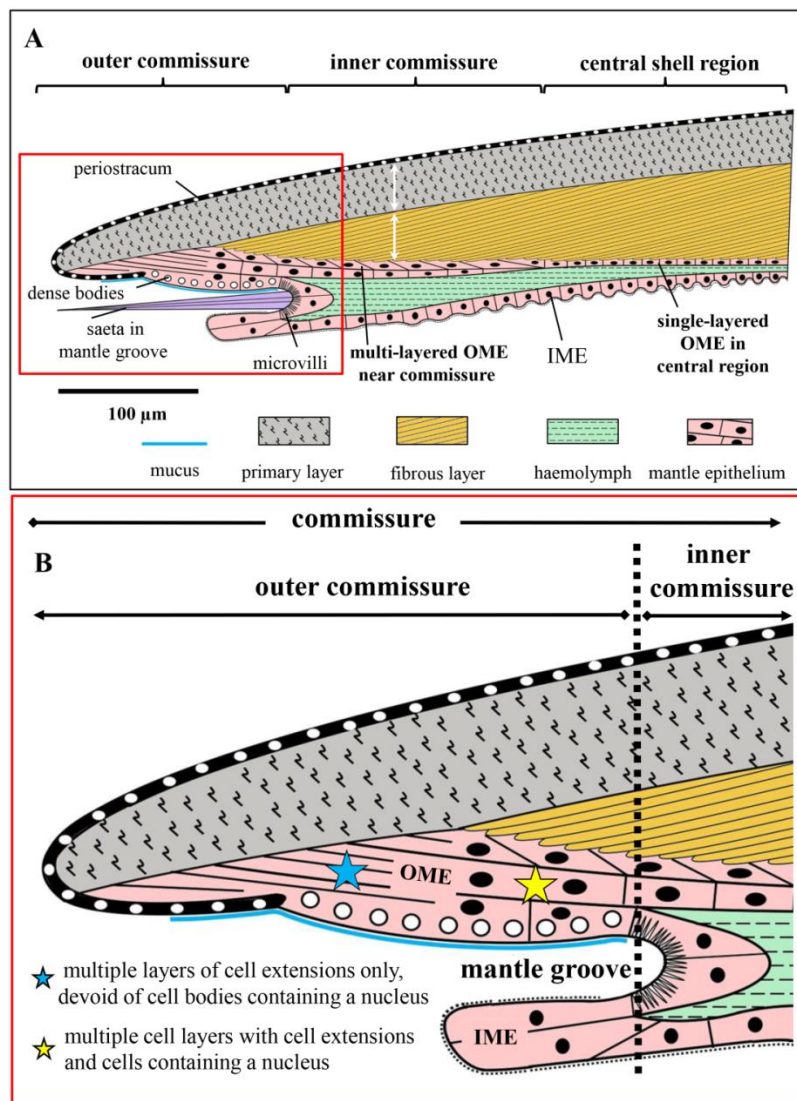


Figure 2.1.1. Scheme showing the different layers of the shell of *Magellania venosa* and the topologic relation between the mantle epithelium and the shell. The scheme is true to scale for a 10 mm large specimen. A) The shell of *Magellania venosa* consists of three layers, the periostracum, the mineralized primary layer and the mineralized fibrous (secondary) layer. The mantle epithelium is subdivided into two regions: the outer (OME) and inner mantle epithelium

(IME). B) Region of the commissure enlarged from A (red rectangle in A). Based on ultrastructural characteristics we can distinguish different portions of the OME: (i) the OME at the outer commissure below the primary layer, (ii) the OME at the outer commissure below the first row of fibres, (iii) the OME at the inner commissure below the fibres and (iv) the OME below central shell portions. Within the commissure the OME is multi-layered, while at the central shell region the OME consists of a single layer of cells. For an about 10 mm large *M. venosa* the transition from multi-layered to single-layered OME is about 350 to 400 μm away from the tip of the commissure. The OME at the outermost portion of the commissure at the primary layer consists of cell extensions (blue star) only, while, still within the outer commissure but below the fibres, the OME consists of cell extensions and cells with a nucleus (yellow star).

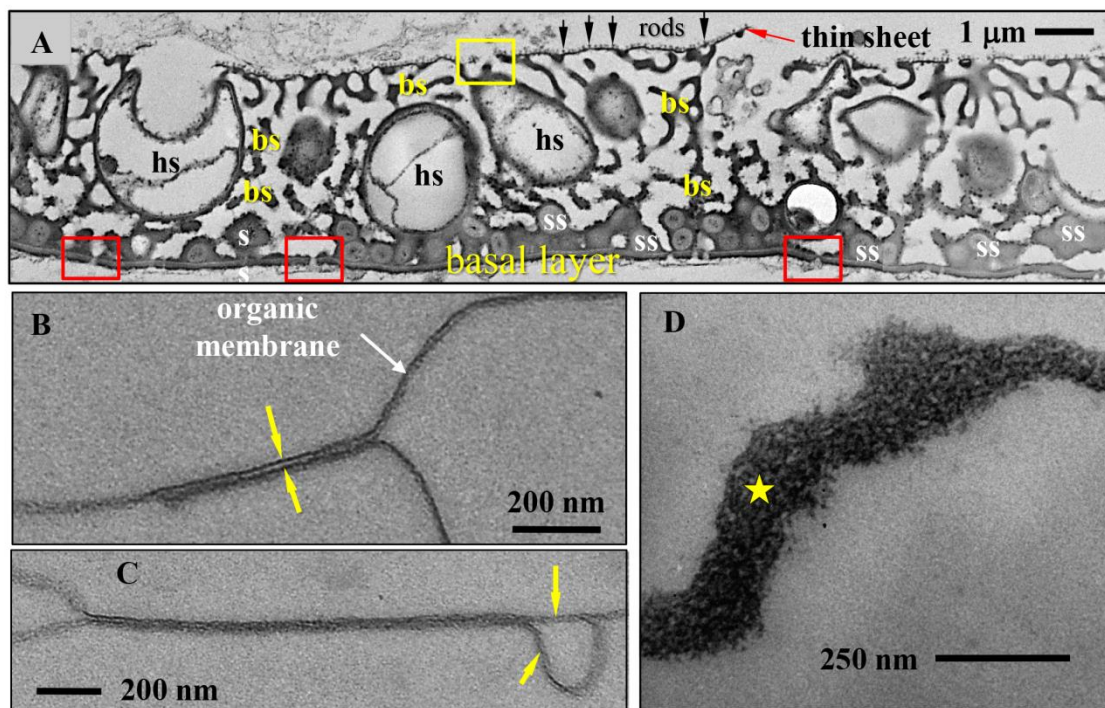


Figure 2.1.2. TEM micrographs showing ultrastructural features of the periostracum (A), and the fibrous shell layer (B to d) of *Magellania venosa*. A) Periostracum of a chemically fixed and decalcified sample. Thin branching septae (bs) form a reticular structure interrupted by large hollow spheres (hs). In the proximal area, small osmiophilic spherical structures (ss) fuse with one another and with a basal layer of the periostracum. The basal layer contains small pores (red rectangles). Apically the periostracum has a thin flat sheet that carries numerous small rods at its distal side (black arrows) and is interrupted by large pores (yellow rectangles). B, C) Often two organic membranes overlap at fibre corners (for further information see Fig. S2.1.2). D) Tangential cut through an organic membrane between two fibres showing the porosity of these membranes.

The primary shell layer (Fig. 2.1.1), is secreted at the outer commissure (Simonet Roda et al. 2019) and consists of micrometre sized, irregularly shaped, interdigitating calcite units (Goetz et al. 2011). In a 10 mm long *Magellania venosa* shell, secretion of fibres (Fig. 2.1.1) starts about 100 μm away from the outer commissure. The fibrous shell layer has a plywood structure as it comprises differently oriented stacks of parallel-assembled calcite fibres (this study and Goetz et al. 2009, Griesshaber et al.

2009, Schmahl et al. 2012). A brachiopod fibre has in cross section four sides: one convex proximal side and three concave sides, the latter located distally or laterally (Fig. S2.1.2A, Simonet Roda et al. 2019, Ye et al. 2018a, 2018b). Each fibre is lined by an organic membrane, however, only at its convex, proximal surface (Simonet Roda et al. 2019). TEM micrographs of high-pressure frozen and decalcified samples show occasionally branching of organic membranes at lateral fibre corners (Figs. 2.1.2B, 2.1.2C, S2.1.2C to S2.1.2G). This takes place when a new membrane attaches to a pre-existing membrane, resulting in double-plied membrane sections in many but not all cases. Since the membrane has only one open margin per double-plied membrane corner, an artefactual origin of the branching, e.g. by rupturing the membrane apart during sample preparation, can be excluded. In *Magellania venosa* the extracellular organic membrane is porous; porosity becomes well visible when the membrane is sectioned tangentially (Fig. 2.1.2D and Nindiyasari et al., 2015, Griesshaber et al. 2017).

The mantle epithelium

The mantle epithelium in *Magellania venosa* (Fig. 2.1.1) consists of an **outer** (OME, Figs. 2.1.3 to 2.1.11) and an **inner** (IME, Figs. S2.1.3, S2.1.4) section. Based on ultrastructural differences we are able to distinguish between the outer mantle epithelium that is present at the **commissure** (mainly below the primary layer and the first few rows of fibres, Figs. 2.1.1, 2.1.4 to 2.1.7, S2.1.3 to S2.1.6) and the epithelium at **central shell portions** (here, only below the fibres, Figs. 2.1.1, 2.1.8 to 2.1.10, S2.1.7). Moreover, **within the commissure**, we differentiate between the OME at the **outer commissure**, an OME section where we cannot distinguish between OME cells and IME cells on the basis of their ultrastructural characteristics (Fig. 2.1.1A), and the OME at the **inner commissure** where the OME and IME are separated by a haemolymph space (Fig. 2.1.1A).

At the commissure the OME is multi-layered, while below central shell portions it is single-layered (Fig. 2.1.1A). In an about 10 cm long *Magellania venosa* shell, the transition from multi-layered to single-layered OME is about 350 to 400 μm away from the tip of the shell (Fig. 2.1.1A). At the commissure and below the first row of fibres the thickness of the OME can exceed 30 μm (Fig. 2.1.1B). It is thicker than the mantle epithelium underneath the primary layer at the very tip of the commissure (Figs. 2.1.1A-B). At the inner commissure, within the multi-layered OME portion, the thickness of the fibrous layer is about the same as that of the primary layer (white arrows in Fig. 2.1.1A). This indicates that mineral deposition in this part of the commissure has similar rates for both the primary and the fibrous layers, respectively. When secretion of the fibres starts the thickness of the primary layer cannot be changed any more. With increasing distance x from the commissure (Fig. 2.1.1A), the thickness d of the fibrous layer increases, however, towards the central shell regions the corresponding thickness increment ($\Delta d/\Delta x$) decreases. This indicates that the rate in mineral deposition (biomineral formation per time increment) decreases from the commissure to central shell regions. In *Magellania venosa* the angle between the fibres and the OME is about 10 degrees.

The mantle epithelium at the commissure

Figures 2.1.3 to 2.1.7 and figures S2.1.3 to S2.1.6 show ultrastructural features of the OME at the commissure. The periostracum and the primary shell layer are secreted at the outer commissure (Figs. 2.1.3, 2.1.4A-B). OME cells consist here of long cell

extensions and are devoid of cell bodies containing a nucleus (Figs. 2.1.1B, 2.1.3, 2.1.4A). We distinguish between distal and proximal cell extensions (Fig. 2.1.4A). Distal extensions are close to the calcite of the primary layer, and are devoid of cell organelles such as endoplasmic reticulum, Golgi apparatus or mitochondria, but contain numerous very dense spherical bodies with 300 to 400 nm in diameter (sb in Fig. 2.1.4A). Proximal extensions (Fig. 2.1.4A) are in the vicinity of the forming periostracum (Fig. 2.1.4B). Although the content of organelles of proximal extensions is similar to that of the distal ones, dense spherical bodies in the proximal extensions are more irregular in shape and density. Distal and proximal extensions are separated from each other by a layer of degraded cell extensions (dce in Fig. 2.1.4A, Fig. 2.1.3) that contain much cell debris.

The periostracum is secreted at the proximal side of the mantle epithelium by proximal cell extensions (Figs. 2.1.3, 2.1.4A-B). It develops within a shallow pouch of the epithelium (outlined with a yellow dashed line in Fig. 2.1.4B) and is covered by a layer of irregularly distributed material, most likely consisting of mucous polysaccharides (blue star in Fig. 2.1.4B). Within the pouch at the beginning of the periostracum irregular and partly dense secretions can be observed (yellow star Fig. 2.1.4B). Dense or osmiophilic material lies extracellularly between the tips of two extensions and the basal layer (red arrows in Fig. 2.1.4B) of the periostracum.

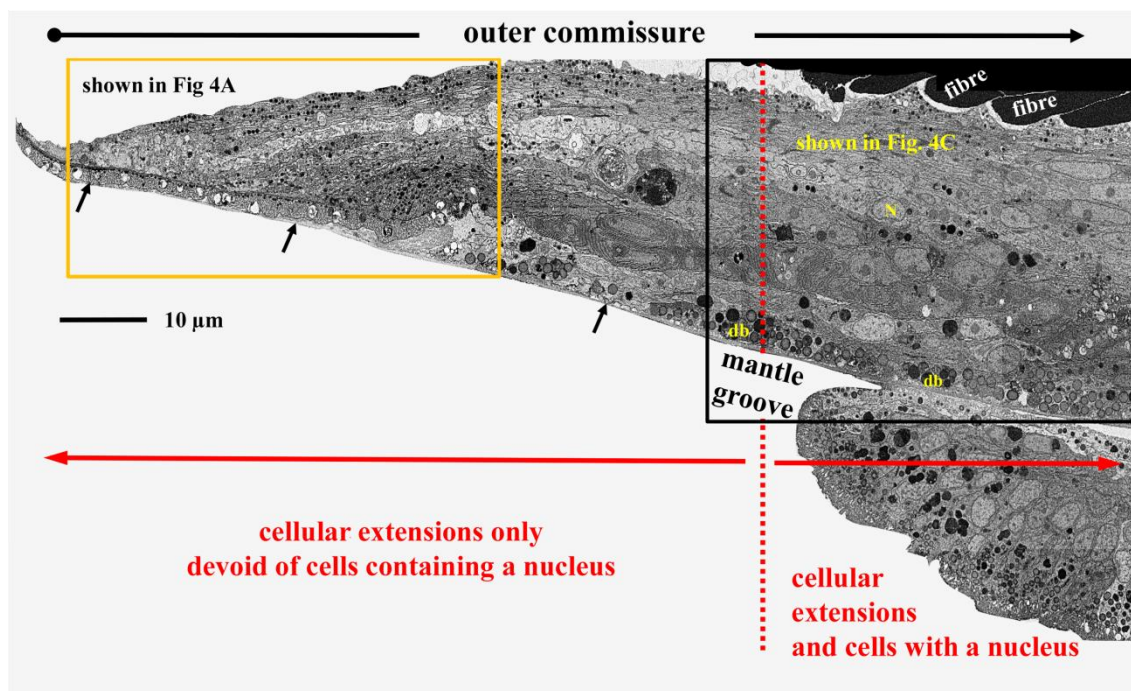


Figure 2.1.3. FE-SEM panorama image (aligned sequence of micrographs) of an embedded and polished sample depicting the outer mantle epithelium (OME) at the **outer commissure below the primary shell portion and the first rows of fibres**. The contrast is reversed. The red arrow pointing to the left indicates OME portions that consist of cellular extensions only present at the outermost part of the commissure. Towards inner commissure regions (red arrow pointing to the right) the OME contains cellular extensions as well as cells having a nucleus (N). At inner commissure regions there is a high abundance of dense bodies (db) at the proximal side of the OME. Subimages of Figure 5 are shown in Figures 6A and 6C, respectively. Black arrows point to the presence of a mucus layer.

Cell extensions below the primary layer have their origin in cell bodies that contain a nucleus and are situated in the multi-cellular portion of the mantle epithelium (blue and yellow stars in figure 2.1.1B, right-hand upper part of Fig. 2.1.4C). This part of the multicellular region (the part of the OME at the outer commissure where cell extensions contain a nucleus) is close to the site where the secretion of fibres starts (Figs. 2.1.4C, Fig. 2.1.1). Due to the absence of a mantle cavity or an extracellular matrix a clear borderline between the OME and IME is not observable (Figs. S2.1.3, 2.1.4C). Close to the appearance of fibres the mantle epithelium forms a groove (Fig. 2.1.3). At the base of the latter setae are formed (Figs. 2.1.1, S2.1.3). From the tip of the commissure to the base of the mantle groove a 400 nm thick mucus layer covers the periostracum (black arrows in Figs. 2.1.3 and 2.1.4A and blue star in Fig. 2.1.4B).

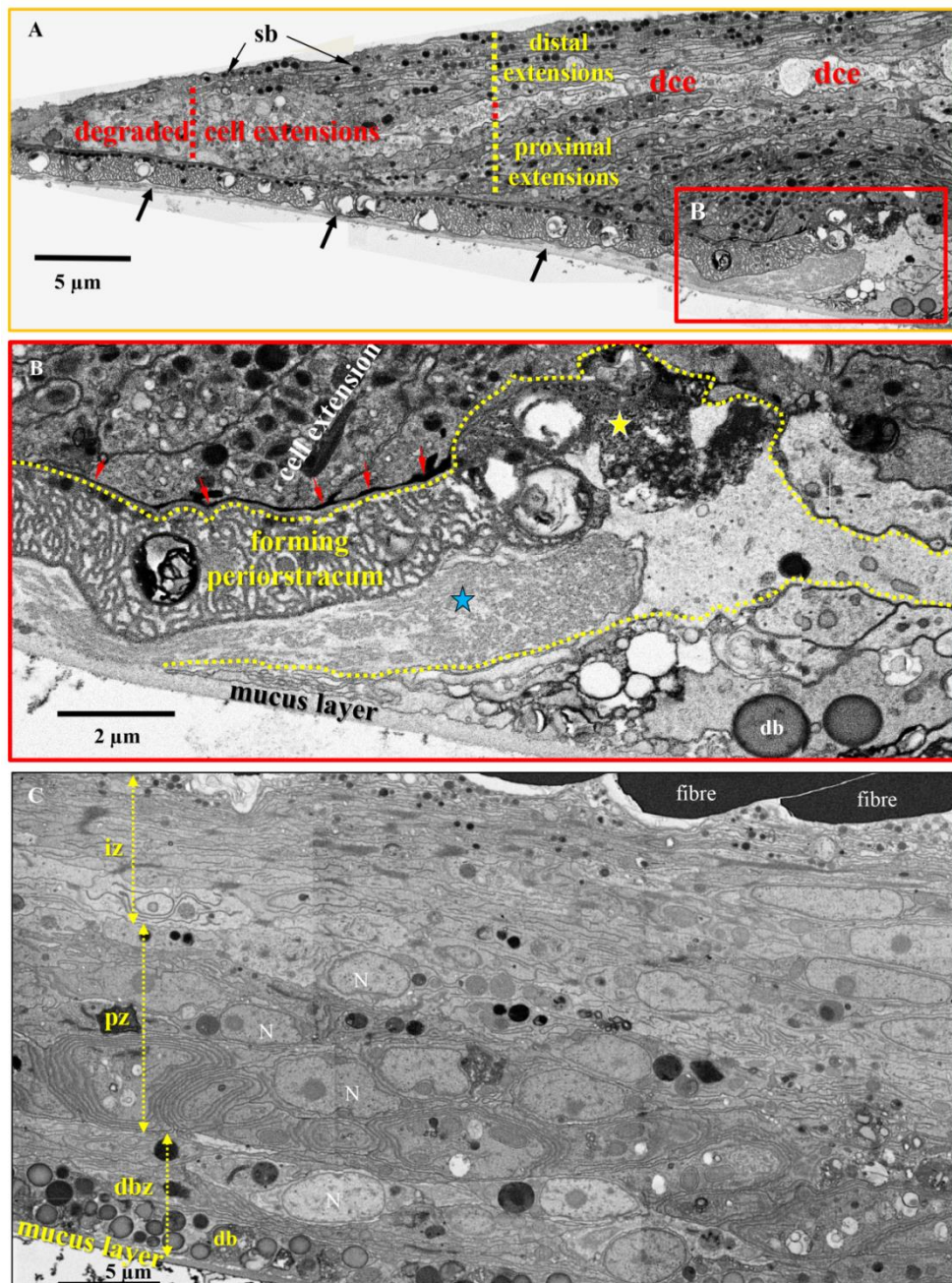


Figure 2.1.4. FE-SEM micrographs of embedded and polished samples depicting the outer mantle epithelium (OME) at the **outer commissure**. The contrast is reversed. A) Detail, marked

with an orange rectangle in Figure 5, consists of cell extensions, distal at the primary layer and proximal near the periostracum. Between these is a region formed of degraded cell extensions (dce). Small dense bodies (sb) are present at proximal and distal extension sites. B) Zoom into the region that is marked with a red rectangle in A, depicting the site of periostracum formation within a shallow pouch (outlined with a dashed yellow line in B). Dense extracellular material occurs between the periostracum and the OME. Red arrows in (B) point to the basal layer of the periostracum. Blue star in B: mucus material close to the forming periostracum; yellow star in B: irregular and partly dense secretions close to the forming periostracum. C) Multi-cellular mantle epithelium below fibres at the outer commissure. Due to ultrastructural differences we distinguish different regions within the epithelium: the apical zone (az) consists of thin cell extensions only; the inner zone (iz) consists of larger extensions; the proximal zone (pz) contains cells with a nucleus (N) and the distal proximal zone (dbz) contains many large dense bodies (db) in addition to cell bodies with a nucleus.

The inner mantle epithelium (IME) begins proximal of the mantle groove (Figs. 2.1.1, S2.1.3, S2.1.4). It consists of a single layer of cells that carry numerous microvilli like extensions and cilia at their apical side (Fig. S2.1.4). IME cells contain many large dense bodies and organelles of the lyso-endosomal pathway of varying sizes as well as endoplasmic reticulum and many mitochondria (Figs. S2.1.3, S2.1.4).

The OME at the commissure underneath the first few fibres (Figs. 2.1.1B, 2.1.3, 2.1.4C) is characterized by many cell extensions and by elongated cells containing a nucleus. This is in contrast to the OME at the very outer commissure, which consists of cell extensions only; OME cells here secrete solely the primary layer of the shell. The cell extensions below the fibres run obliquely towards the tip of the commissure and attach with their distal ends to the fibres (Fig. 2.1.5A and 2.1.6A). Within the commissure, but below the fibres (Fig. 2.1.6C), the mantle epithelium is zoned. We distinguish a distal zone, an inner zone, a proximal zone and a dense body zone (Figs. 2.1.4C, 2.1.5A, 2.1.6A). Within the commissure, but where OME and IME are separated by hemolymph space, we also find a zonation; however, here the dense body zone and the mucus layer are lacking (Fig. 2.1.7A).

The **distal zone** (dz, in Figs. 2.1.5A, 2.1.6A, 2.1.7A) consists of the outermost layer of cellular extensions. Cellular profiles are flat, are up to about 1000 nm thick and line the convex proximal side of the fibres (Figs. 2.1.5A-B, 2.1.6A-C, 2.1.7A). We often observe very thin cells at these cellular extensions (e.g. Figs. 2.1.5B, 2.1.6B-C, 2.1.7A). In most cases, more than one cellular profile occurs directly below a single calcite fibre (e.g. Fig. 2.1.5B). Organelles in the distal zone are rare (Figs. 2.1.5A, 2.1.6A, 2.1.7A). OME cells are connected to organic membranes of the fibres via apical hemidesmosomes (Fig. 2.1.7B). These are abundant, are very small and can be seen best in obliquely cut sections as dense plaques (black arrows in Fig. 2.1.7B). In regions where an organic matrix is absent cell extensions are always covered with a thin surface coat (black arrows in Fig. 2.1.7C). Adherence junctions resembling adhesion belts connect apical cell extensions with each other (Fig. 2.1.7D). In high-pressure frozen and freeze-substituted shell and polished samples we see that OME cells are in very close contact with the calcite of the fibres (Fig. S2.1.5 and in more detail see Simonet Roda et al. 2019).

Within the **inner zone** (Figs. 2.1.4C, 2.1.5A, 2.1.6A, 2.1.7A), cell extensions and the shape of most of the cell profiles are round in cross section (Figs. 2.1.5B, 2.1.6C) and their thickness increases from the the distal zone towards the proximal side of the inner zone (Figs. 2.1.5A, 2.1.6A, 2.1.7A). In the proximal part of the inner zone

lysosomes are the most common organelles, rough endoplasmic reticulum and vesicles are present but not as common, while mitochondria, multivesicular bodies and Golgi stacks are very rare. In most cases cell extensions are devoid of nuclei (Figs. 2.1.5A, 2.1.6A, 2.1.7A). Widened intercellular spaces filled with electron dense material are common and occasionally contain extracellular vesicles (yellow circles in Fig. 2.1.7E).

Within the *proximal zone* (Figs. 2.1.5A, 2.1.6A, 2.1.7A) we find cell bodies that contain a nucleus. Cells here are elongated in horizontal direction and have round profiles in cross section. In addition to nuclei, cells within the proximal zone are very rich in organelles, in particular mitochondria, long cisternae of rough endoplasmic reticulum, Golgi apparatus and organelles of the endo-lysosomal pathway including multivesicular bodies (Figs. 2.1.4C, 2.1.5-7). Smooth endoplasmic reticulum and glycogen are rare. The cells are connected to each other by gap junctions (Fig. 2.1.7, Fig. 2.1.10).

The *most proximal, dense body zone* occurs only in the *outer commissure* and is formed of cells containing many large and spherical dense bodies (*dense body zone*, dbz in Figs. 2.1.4C, 2.1.5A, 2.1.6A). In the dense body zone the apical side of the cells faces seawater. Spherical dense bodies occur only between the end of the pouch where the periostracum is secreted and the base of the mantle groove just above the mucus layer. Near the base of the mantle groove the epithelium separates into the outer and the inner mantle epithelium. The dense body layer is continuous with the inner mantle epithelium.

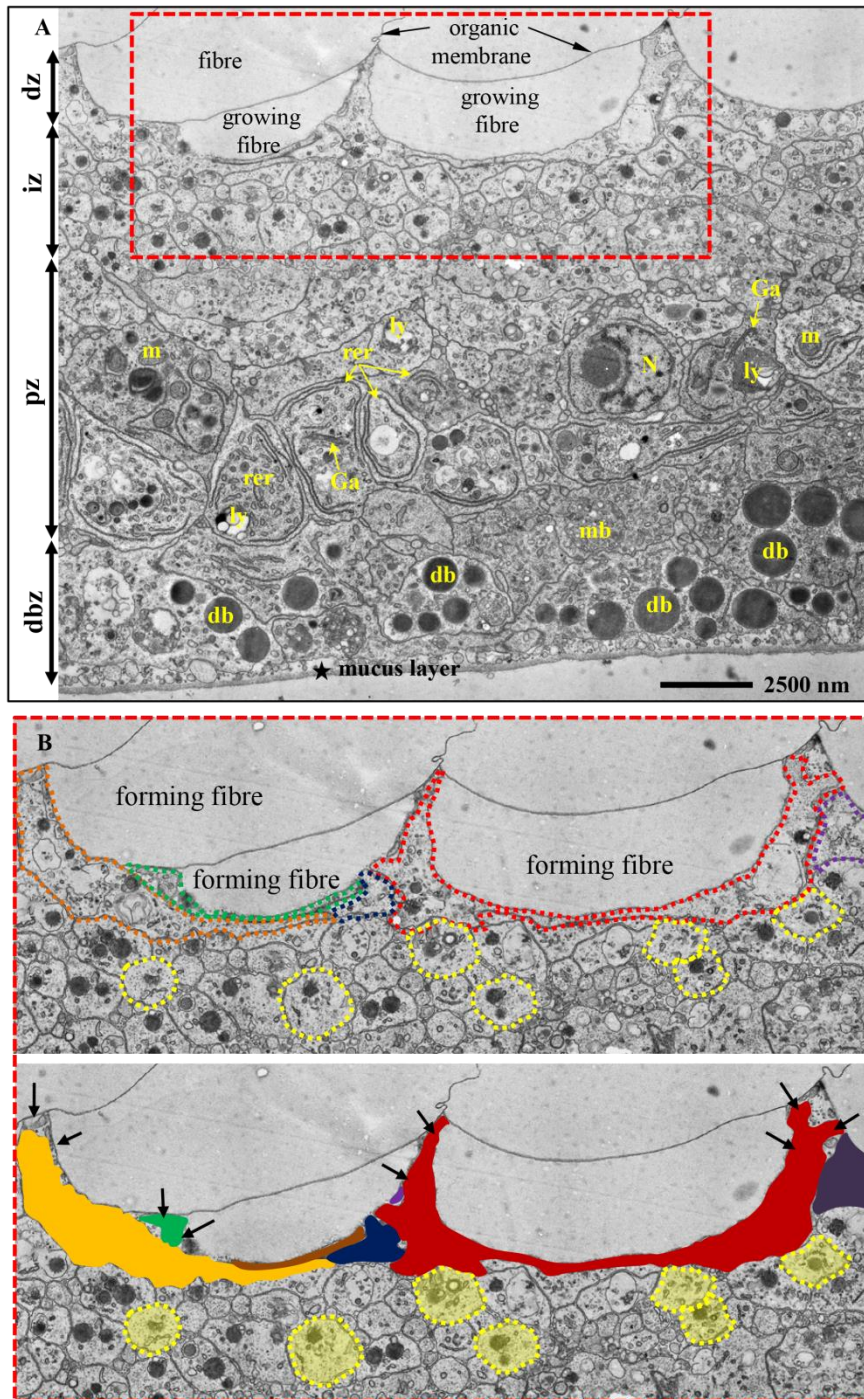


Figure 2.1.5. TEM micrographs of a chemically fixed and demineralized sample depicting a perpendicular cut through fibres, cells and cellular extensions at the **outer commissure**. A) Four regions can be distinguished: The distal zone (dz), the region that is in contact with the fibres consists of small extensions; organelles are absent. Within the inner zone (iz) of the epithelium cellular extensions increase in size and contain organelles such as Golgi apparatus (Ga), mitochondria (m) and rough endoplasmic reticulum (rer). The proximal zone (pz) contains many cell bodies; organelles are abundant, especially nuclei and mitochondria. The most proximal zone (dbz) is characterized by the presence of dense bodies (db). Ly: lysosome; mb: multivesicular body. B) A cell extension is attached to a few fibres, e.g. for the cell outlined in red in to 5 fibres. The shape of the cell extension that is in direct contact to the growing fibre adapts to the profile of the fibre, while further below cell extension profiles are round (outlined in yellow in B).

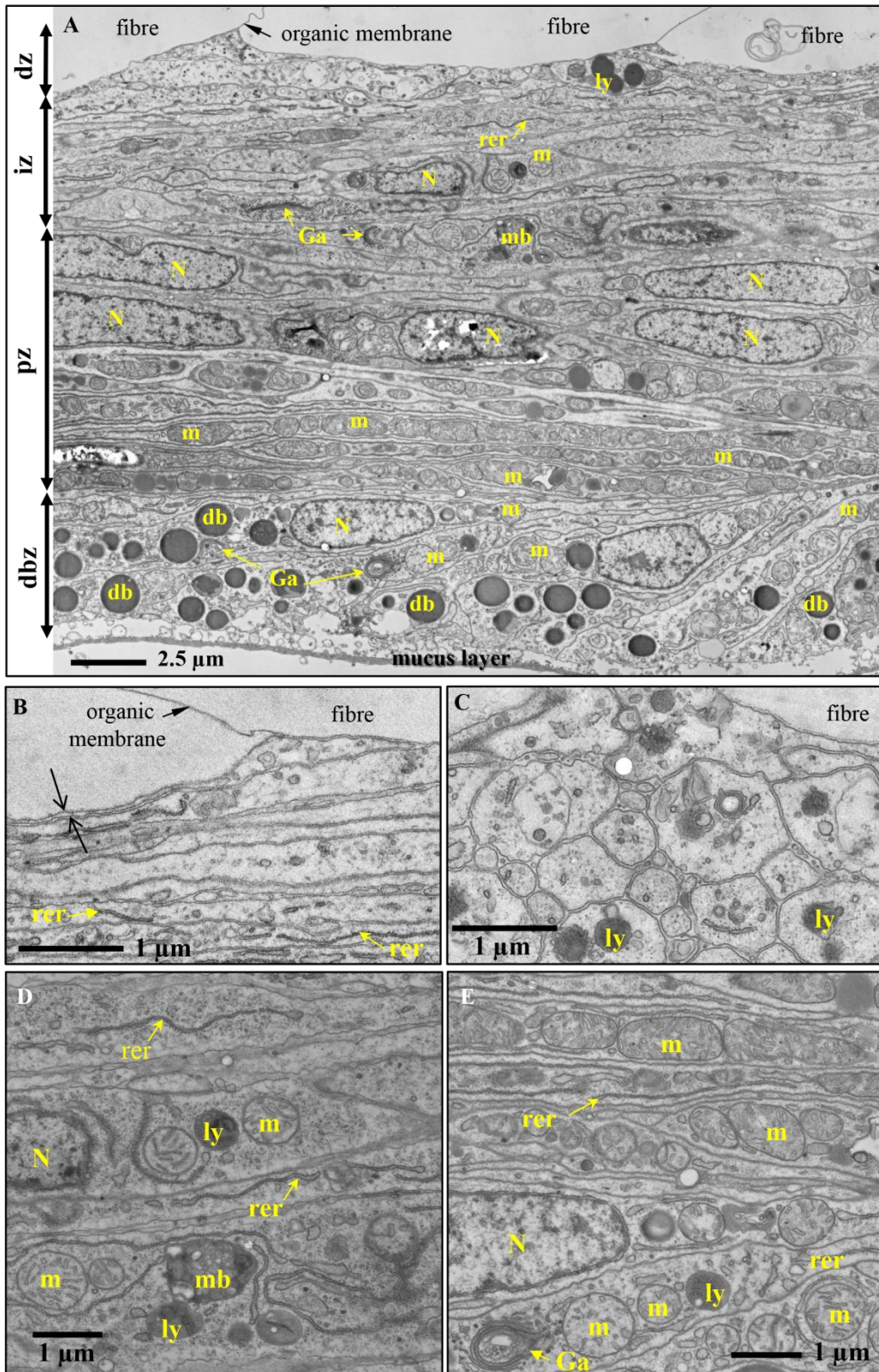


Figure 2.1.6. TEM micrograph of chemically fixed and demineralized samples depicting fibres, cellular extensions and cells at the **outer commissure**. A) Calcite fibres are cut in longitudinal direction. Within the epithelium we distinguish four different regions: the distal zone (dz), the region that is in contact with the fibres consists mainly of small extensions; organelles are rare. Within the inner zone (iz) of the epithelium cellular extensions increase in size and contain organelles such as Golgi apparatus (Ga), mitochondria (m) and rough endoplasmic reticulum (rer). The proximal zone (pz) contains many cell bodies; organelles are abundant, especially

nuclei and mitochondria. In the most proximal zone (dbz) dense bodies (db) are abundant. B), C), D), E) TEM micrographs of chemically fixed OME samples taken from the outer commissure but below the first few fibres. B), D) Longitudinal, C), E) transversal cut. Next to the calcite of the fibres (B, C) we see cellular extensions only, while the epithelium portion further proximally (D, E) is abundant in organelles. Ga: Golgi apparatus; ly: lysosome; m: mitochondria; mb: multivesicular body; N: nucleus; rer: rough endoplasmic reticulum.

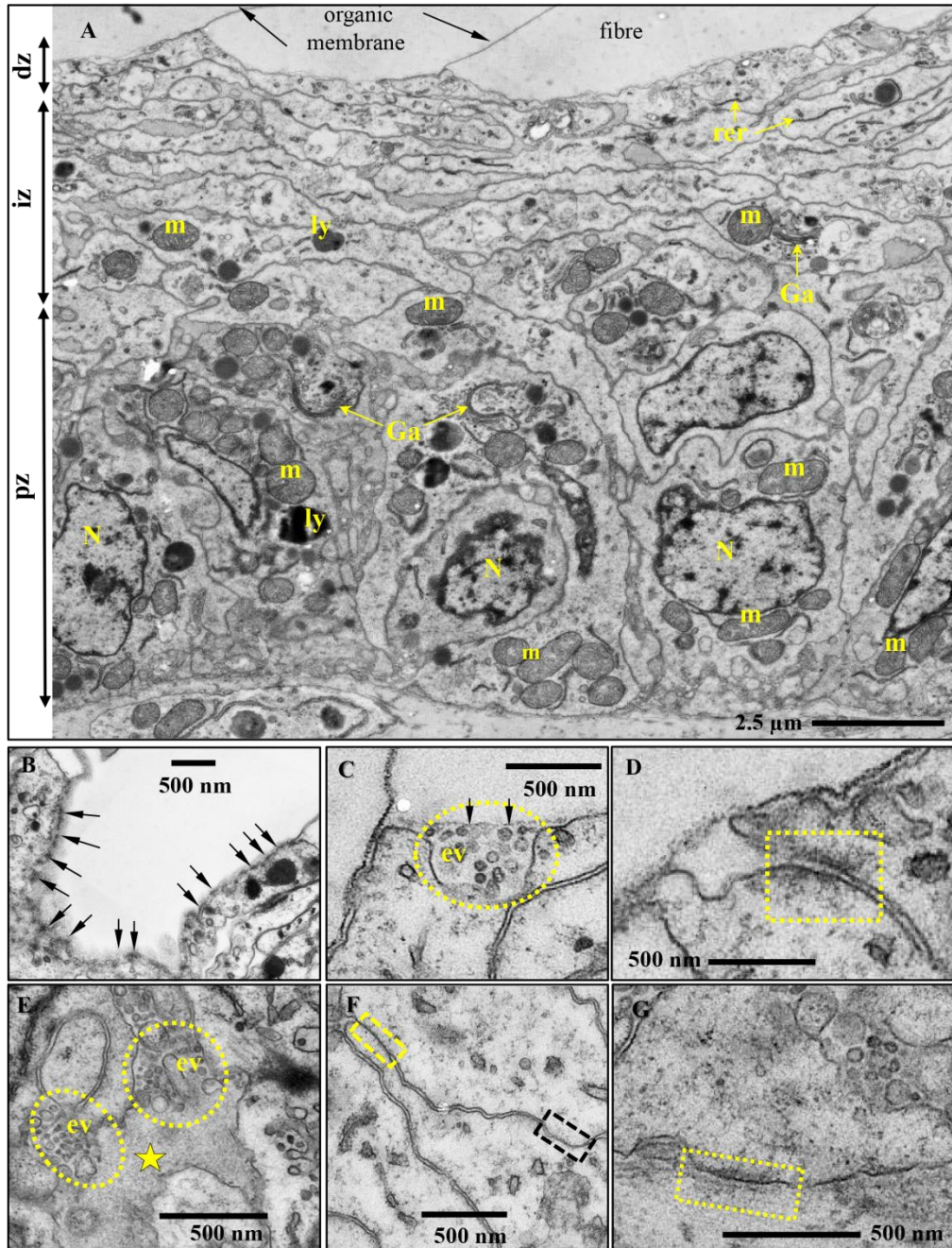


Figure 2.1.7. TEM micrographs of chemically fixed samples taken from the **inner commissure** of *Magellania venosa*. A) The OME is sectioned at an angle to the longitudinal axes of cell extensions. We can distinguish a distal zone (dz), an inner zone (iz) and a proximal zone (pz). Apical cell extensions are elongated and follow the curvature of the fibre. The distal zone consists of numerous small cellular extensions, is devoid of cells with a nucleus and other large organelles. Organelles like mitochondria (m), lysosomes (ly) and Golgi apparatus (Ga) appear in the inner zone; organelle content increases towards the proximal zone at the base of the

epithelium; here we find cells with a nucleus (N). B) Oblique cut through a most distal cell extension where apical hemidesmosomes appear as dark plaques (black arrows in B). C) Enlargement showing extracellular vesicles (iv, dashed yellow line) present in the most distal portion of the OME. Regions not attached to the organic membrane have a faint surface coat at their apical side (black arrows in C). D) Enlargement depicting an apical adherence junction resembling an adhesion belt (yellow dashed rectangle). E) Areas with electron dense extracellular material (yellow star) are abundant in distal portions of the OME. These regions contain extracellular vesicles (ev). F) Gap junctions between cells are indicated with black and yellow dashed rectangles. G) Basal hemidesmosomes (yellow dashed rectangle).

The mantle epithelium at central shell regions

In a 10 mm long *Magellania venosa* shell, about 350 to 400 μm away from the tip of the commissure, the OME changes from a multi-layered to a very thin single-layered epithelium (Fig. 2.1.1A). Cell thicknesses vary, even within a single cell (Figs. 2.1.8 A to E, S2.1.7). In thick cell portions, the OME is about 1-3 μm thick and organelles such as the nucleus, mitochondria, rough endoplasmic reticulum and glycogen are abundant. Neighbouring cells form extended interdigitations between each other (Fig. 2.1.9), resulting in an increase of the basal plasma membrane surface area. Many gap junctions between cells can be observed (Fig. 2.1.7F, Fig. 2.1.10A-C).

However, cells at central shell regions can also be extremely thin, as thin as 20 nm (Figs. 2.1.8D-F). In these cases they are devoid of cell organelles (Figs. 2.1.8C-E, S2.1.7) and are mainly below shell portions where the organic membrane of the calcite fibres is not yet developed (Figs. 2.1.8C-D), thus at sites of active shell secretion. In addition, these thin cells at these sites are covered by a surface coat (Fig. 2.1.8E).

Thick cells or cell portions are connected to the organic membrane that lines the proximal convex surface of fibres via hemidesmosomes present within the apical cell membrane. At the intracellular side the hemidesmosomes bind to tonofilaments (Figs. 2.1.8C-D, F, S2.1.7), the latter consisting of a bundle of thin filaments (marked with a 't' in Fig. 2.1.10D). The tonofilaments bind at the basal side of the cells again to hemidesmosomes. In comparison with the commissure, hemidesmosomes below central shell portions are much thicker. In addition, in high-pressure frozen and freeze-substitution samples we observe that at and near hemidesmosomes OME cells have often two basal plasma membranes (Figs. 2.1.10D-E).

At sites where the organic membrane at the proximal, convex surface of a fibre is absent, OME cells do not contain any hemidesmosomes nor tonofilaments (Figs. 2.1.8A-C, S2.1.7). At these sites calcite secretion is active and material is transported from OME cells to adjacent, newly forming fibres. There is a constant alternation between OME portions that are attached to the organic membrane of fibres and those OME regions where apical cell membranes are detached from fibres (e.g. red dotted line in Fig. 2.1.8A). Analysing an epithelial length of 189 μm we find that 14 regions with a total length of 98 μm are attached to the shell via hemidesmosomes and 10 regions, with a total length of 91 μm , are not. Thus, at a given time, about 50% of the OME is not secreting mineral; while the other ~50% of the OME is involved in fibre mineralization (this study and Simonet Roda et al. 2019).

The mantle epithelium in endopuncta

The shell of *Magellania venosa* contains endopuncta (Figs. 2.1.11, S2.1.8); these cross the shell from the mantle epithelium to almost the periostracum and, hence, traverse both mineralized shell layers. Between the periostracum and an endopunctum the shell forms a sieve plate containing numerous channels radiating from the lumen of the punctum to the periostracum (Figs. 2.1.11A). TEM micrographs of decalcified and chemically fixed samples show that these channels are filled with organic material. The channels are continuous with a hyaline layer present at the distal portion of the punctum, between the sieve plate and numerous microvilli-like cellular extensions of distal punctum cells (Figs. 2.1.11B-C). The distal region of the punctum (Figs. 2.1.11A-B), the punctum portion that is in the primary layer, is filled with cells rich in lipid droplets, mitochondria, lysosomes and multivesicular bodies. This indicates high metabolic activity in these regions of the punctum. Towards the median region of endopuncta (Fig. 2.1.11D), there is a change to a thin, about 1,5 μm thick, single layer of elongated cells; here neighbouring cells overlap with one another (Figs. 2.1.11E and S2.1.8). Cells within this part of endopuncta contain glycogen, lysosomes, rough endoplasmic reticulum, nuclei and mitochondria; vesicles are rare. At proximal endopuncta regions, the epithelium connects to OME cells (not shown). As the diameter of endopuncta does not decrease with time, cells that line their walls are not secreting mineral. Accordingly, we take morphological characteristics and organelle distribution patterns of OME cells as a reference for comparison with the mineralizing cells encountered at the commissure and the central shell regions.

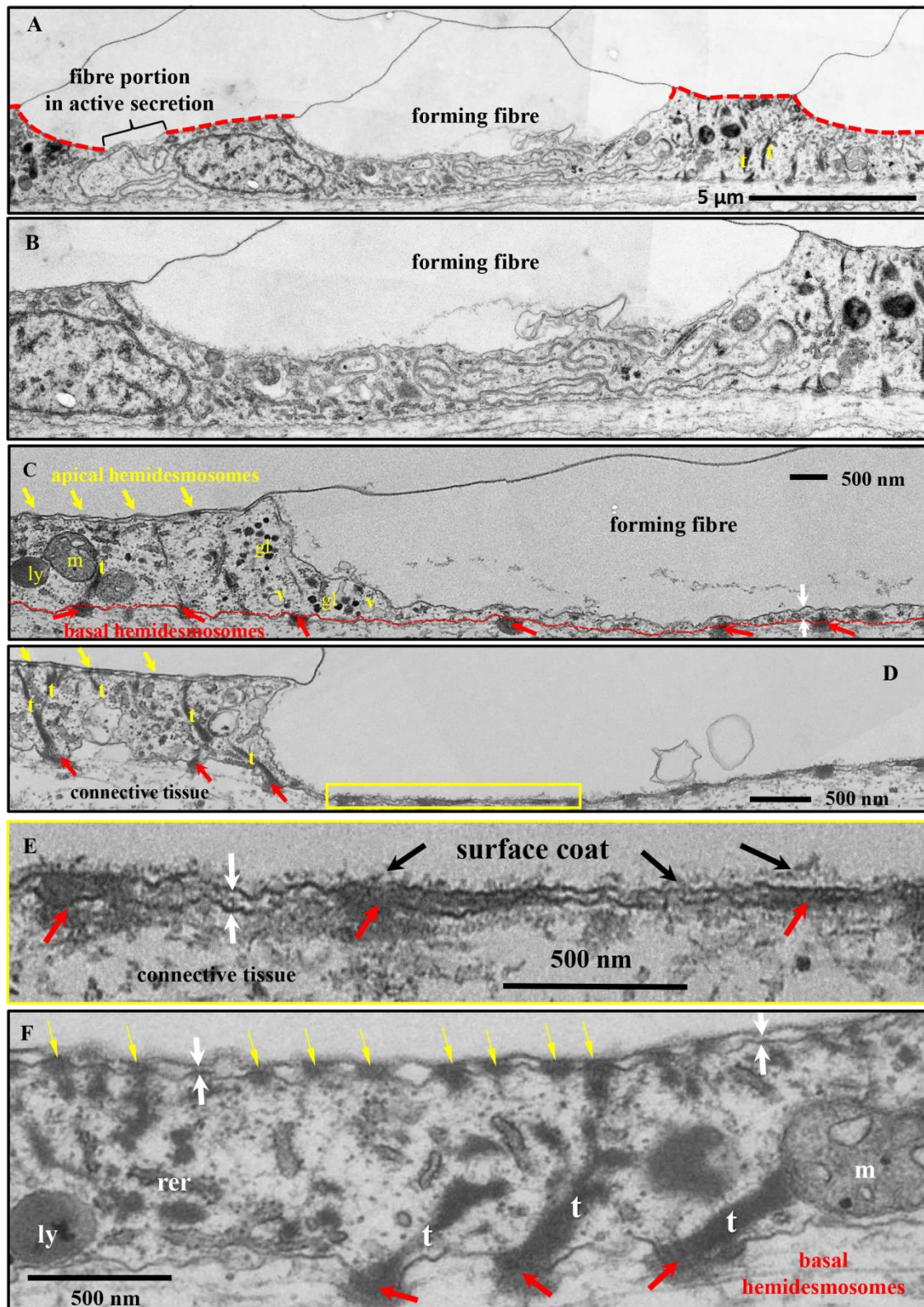


Figure 2.1.8. Aligned arrays of TEM micrographs taken on chemically fixed and decalcified samples obtained from **central shell portions**. Fibres are sectioned transversally. Indicated with a red dotted line are those fibre portions that are not in the state of active secretion. Fibre secretion is finished with the formation of an organic lining along the proximal, convex surface of a fibre. Hence, at sites where the apical cell membrane is attached to the organic membrane lining a fibre portion (red dotted line) OME cells are not producing mineral. The connection between the apical cell membrane and the organic membrane that lines the proximal, convex

surface of a fibre occurs via apical hemidesmosomes (yellow arrows in C, D, F). Tonofilaments (C, D, F) within the cells connect apical hemidesmosomes to basal hemidesmosomes (red arrows in C, D, E, F), with the latter being attached to the basal lamina of the OME. Apical hemidesmosomes are small, while basal ones are large (e.g. F). At sites where fibre secretion is active there are neither tonofilaments nor apical hemidesmosomes within cells (A, B, C, D). We observe a thin coat on the surface of cells (black arrows in E). Actively secreting OME cells below fibres from the central shell region are very thin and highly elongated (white arrows in C, E, F).

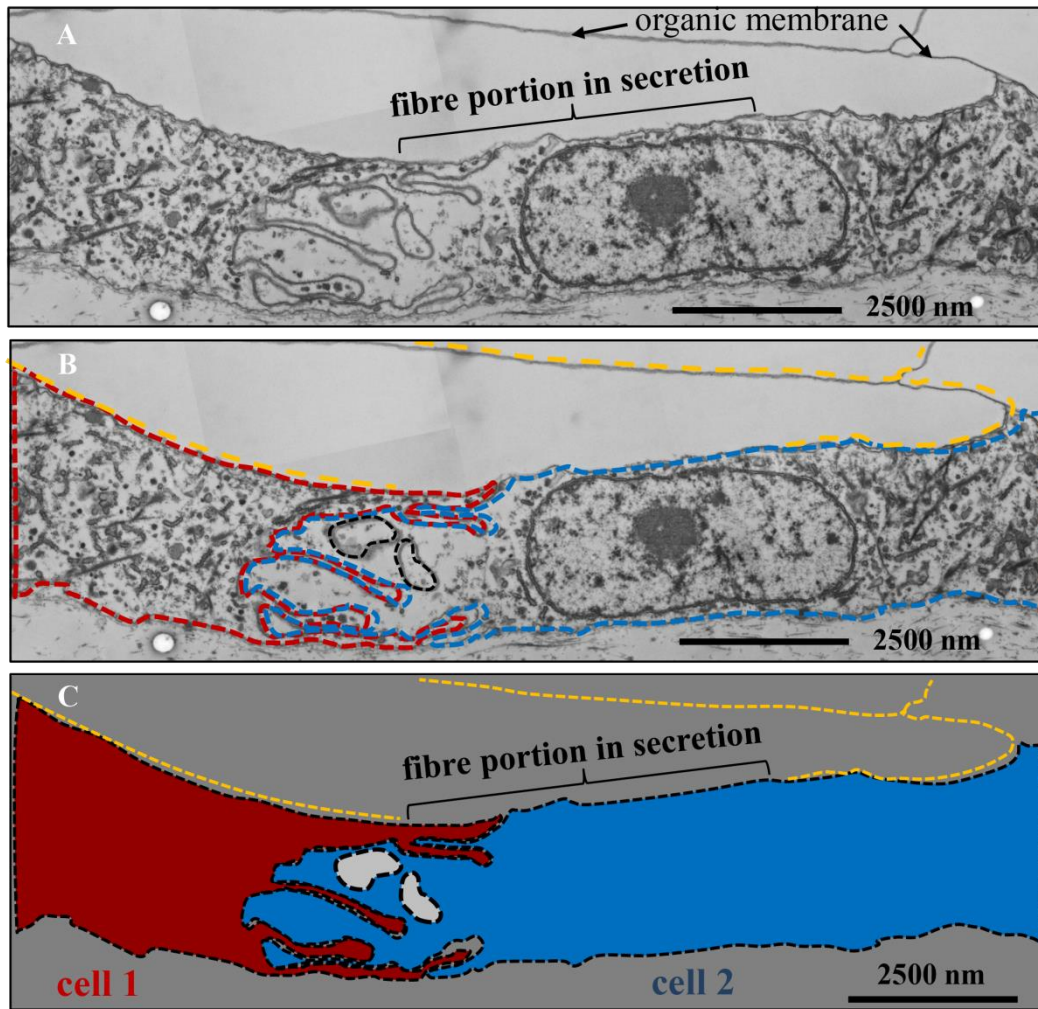


Figure 2.1.9. Topological relation of OME cells to fibres in central shell portions of *Magellania venosa*. A, B, C) TEM panorama micrographs of chemically fixed and decalcified samples depicting the ultrastructure of OME cells below transversally sectioned fibres. At sites of ongoing fibre formation the organic membrane along the proximal, convex surface of the fibre is not yet secreted. There is no one-by-one relationship between a fibre and a cell, generally at least two cells contribute to the secretion of the same fibre.

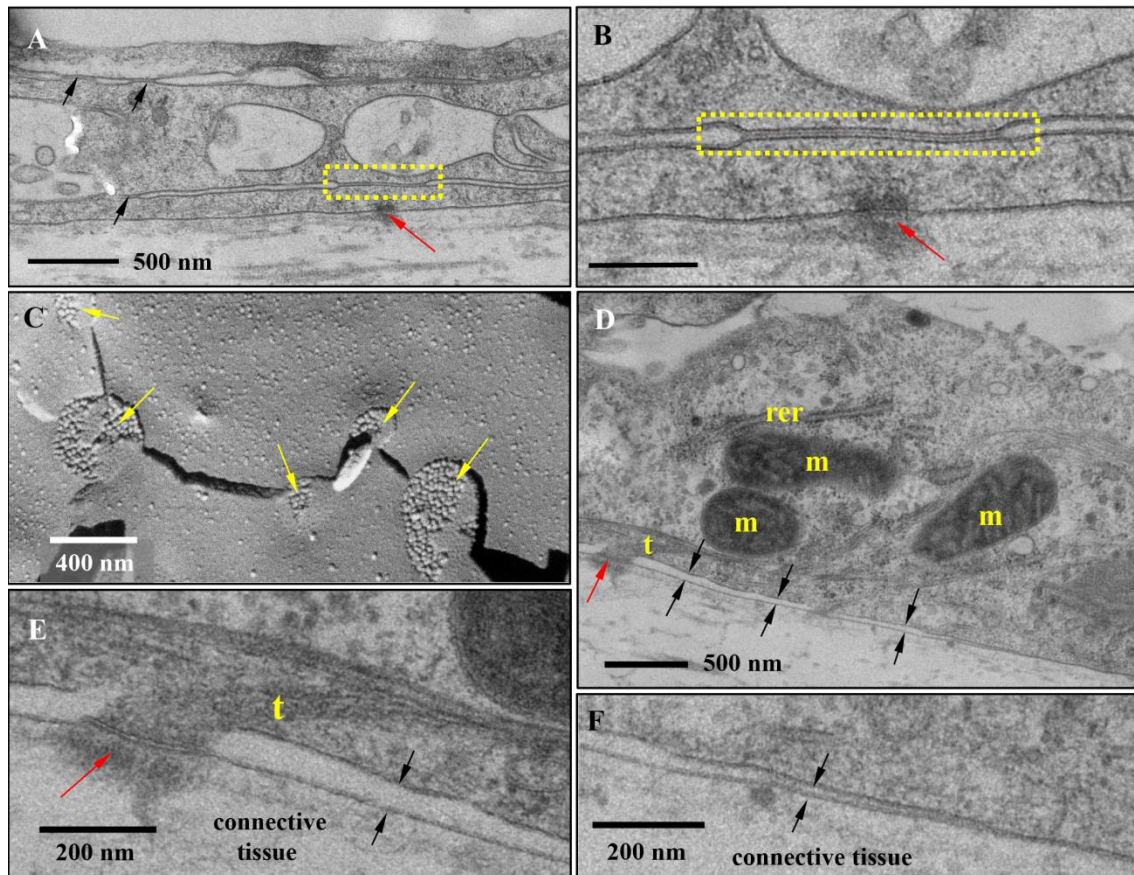


Figure 2.1.10. TEM micrographs recorded from high-pressure frozen OME samples taken from the **central shell region**. The tissue is freeze-substituted (A, B and D-F) or freeze fractured (C). A, B) Many gap junctions can be observed (black arrows and yellow rectangles in A and B). Large hemidesmosomes (red arrows in A, B, D, E) attach the basal membrane of the epithelium to the basal lamina and to tonofilaments (marked with a yellow t in D and E). C) Cryo-SEM image showing 5 gap junctions between two adjoining cells (yellow arrows in C). D) OME cells with two basal membranes (black arrows); rer, rough endoplasmic reticulum; m, mitochondria.

Patterns of organelle distribution in OME cells

Results obtained from morphometric analyses are presented in Table 2.1.1 and 2.1.2 and Figures 2.1.12 and S2.1.9. Tables 2.1.1 and 2.1.2 provide means and standard deviations for the volume fractions and the volume per $10 \mu\text{m}^2$ epithelium, respectively, for mitochondria, organelles of the endo-lysosomes pathway including multivesicular bodies, intracellular vesicles, Golgi apparatus, rough and smooth endoplasmic reticula and glycogen (Fig. S2.1.6). Values are given for: (i) the central shell region where the OME is attached to the organic membrane of the fibres, (ii) areas of the central region where the OME is not attached to the organic membrane of fibres and, as an additional control, (iii) the lateral walls of the median regions of the puncta, that do not secrete mineral, (iv) the two central regions pooled together, and (v) the multi-layered inner region of the OME near the commissure. The different stages of the endosomes and lysosomes including multi-vesicular bodies were pooled in the class “endo-lysosomes”. Dark and light vesicles that are not very close to a Golgi apparatus were assigned to the class “intracellular vesicles”. Golgi cisternae and those vesicles that are near the cisternae comprise the class “Golgi apparatus”.

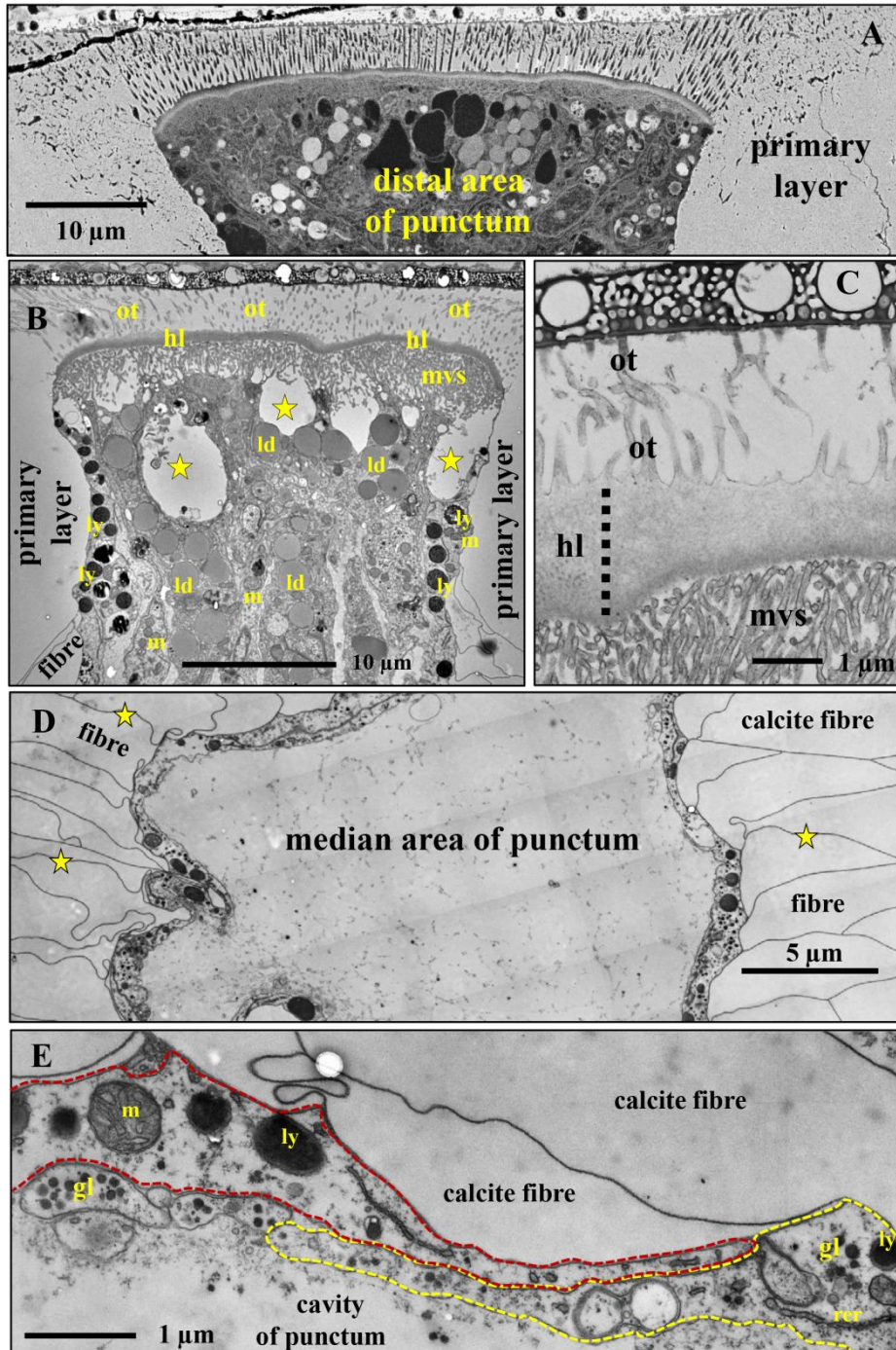


Figure 2.1.11. FE-SEM (A) and TEM (B to E) micrographs of the periostracum, the primary shell layer and an endopunctum in the shell of *Magellania venosa*. A) FE-SEM image of a high-pressure frozen, freeze-substituted but not decalcified shell portion taken on a polished surface showing the primary layer below the periostracum and organic tissue at the uppermost part of a punctum. Above the punctum the shell contains numerous channels radiating from the lumen of the punctum into the periostracum. Apically puncta are completely filled with OME cells. B), C) TEM micrographs of chemically fixed and decalcified samples depicting the uppermost portion of the primary layer above a punctum and the transition to the periostracum. There are channels through the calcite of the primary layer. These are extracellular organic tubes (ot) and are attached to an extracellular hyaline layer (hl) just above microvilli-like cellular extensions (mvs). Within punctum cells, most abundant are lipid droplets (ld), lysosomes (ly) and mitochondria (m). D) and E) TEM micrographs of chemically fixed and decalcified sample depicting the median portion of a punctum traversing a stack of fibres. The surface of the

punctum is lined by a very thin layer of single, but overlapping cells (E, see also Fig. A8). Most abundant are: lysosomes (ly), mitochondria (m), glycogen (gl), rough endoplasmic reticulum (rer).

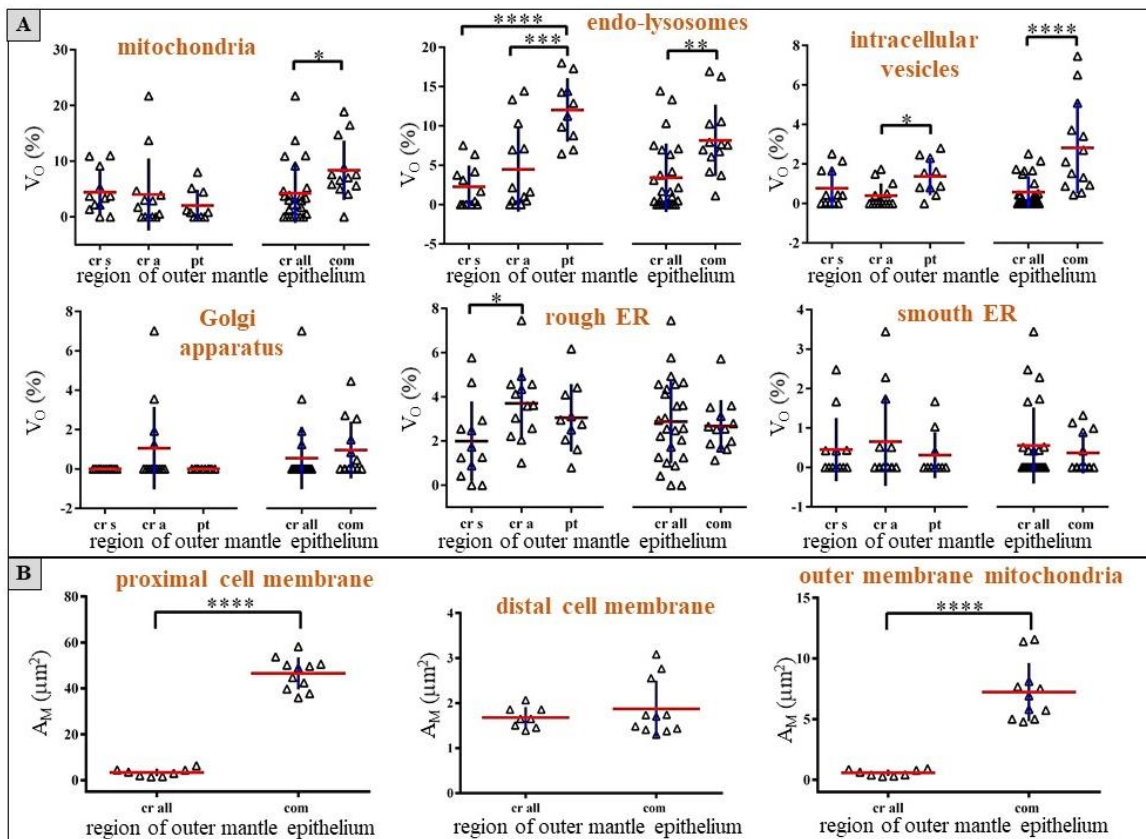


Figure 2.1.12. Volume fraction of membrane-bound organelles. (A) mitochondria, endo-lysosomes, intracellular vesicles, Golgi apparatus, and rough and smooth ER in different regions of the outer mantle epithelium: central shell region that can secrete mineral (cr s), central shell region not involved in secretion (cr a), punctum (pt), secreting and not secreting central shell portions (cr all), commissure (com). (B) Membrane area per $10 \mu\text{m}^2$ of the apical and proximal cell membrane and membrane area of the outer membrane of mitochondria for the central shell portion (secreting and not secreting: cr all) and the commissure (com). Results are plotted with the mean (indicated with horizontal red lines in the graphs) and the standard deviation (indicated with vertical lines in the graphs). Stars indicate significant differences of mean values for a given organelle between different outer mantle epithelium regions: *: $P \leq 0.05$; **: $P \leq 0.01$; ***: $P \leq 0.001$; ****: $P \leq 0.0001$.

The comparison of the volume fractions of membrane bound organelles in different regions of the outer mantle epithelium (Fig. 2.1.12) reveals that the values for the investigated organelles between the two central shell regions (OME attached and OME not attached to the organic membrane of the fibre) are similar, except for the rough endoplasmic reticulum. The difference for the latter is statistically significant and is 1.9 times higher in the OME region that is attached to the organic membrane of the fibre. In the lateral walls of puncta, values for the class endo-lysosomes are significantly higher in comparison to values found for the two central shell regions (OME attached and not attached to the organic membrane of the fibre). Volume fractions of mitochondria, endo-lysosomes and intracellular vesicles are significantly higher in the commissure

than in the central region, by factors of 2.0 (mitochondria), 2.4 (endo-lysosomes) and 4.7 (intracellular vesicles), respectively.

Since the rate of epithelial mineral transport should be considered across a unit of epithelium area we have normalized the absolute volume of organelles and glycogen to an epithelium area of $10 \mu\text{m}^2$ (Fig. S2.1.9). In the case of central shell regions the value for rough endoplasmatic reticulum for OME membranes that are attached to the organic membrane of the fibres is significantly higher than where OME membranes are not attached to fibres, as well as for the epithelium of the lateral walls of the puncta. For all organelles shown in Figure A9 the difference between the commissure and central region is significant; values are always higher in the commissure (Figs. S2.1.9). As the distribution of glycogen is concerned, it is abundant in many epithelial cells, except those present at the commissure (Table 2.1.1 and 2.1.2). In the central shell section, for OME portions that are not attached to the organic membrane of the fibres, the volume fraction for glycogen is higher than in cells that line the lateral walls of the puncta (Table 2.1.1).

The comparison of the mean value of the distal cell membrane area per square μm of epithelium (Fig. 2.1.12) between the central shell region ($1.3 \pm 2 \mu\text{m}^2$) (mean \pm SD), and the commissure, ($1.5 \pm 0.5 \mu\text{m}^2$), yields no significant difference within standard deviations. However, the proximal cell membrane area ($36.5 \pm 5.5 \mu\text{m}^2$) in the commissure is significantly higher than the membrane area ($2.6 \pm 1.3 \mu\text{m}^2$) in the central shell region. The membrane area of mitochondria per square μm of epithelium of $5.7 \pm 1.9 \mu\text{m}^2$ in the commissure is significantly higher than the membrane area of $0.5 \pm 0.2 \mu\text{m}^2$ in the central shell region.

Table 2.1.1. Mean values m and their standard deviations σ for the volume fraction of organelles (in %) in the different regions of the outer mantle epithelium. n is the number of test-fields used for the calculations. “central region all” contains the values of the test-fields of “central region secreting” and “central region attached”; er: endoplasmic reticulum .

organelle volume fraction (V_o)	central region secreting		central region attached		puncta		central region all		commissure	
	m	σ	m	σ	m	σ	m	σ	m	σ
mitochondria	4.0	6.5	4.4	3.9	2.1	2.8	4.2	5.3	8.3	5.3
endo-lysosomes	2.3	2.7	4.5	5.3	12.0	4.0	3.4	4.3	8.2	4.5
vesicles	0.8	0.9	0.4	0.6	1.4	0.9	0.6	0.8	2.8	2.3
Golgi apparatus	0.0	0.0	1.1	2.1	0.0	0.0	0.5	1.6	1	1.4
rough er	3.7	1.6	2	1.8	3.1	1.5	2.9	1.9	2.7	1.2
smooth er	0.7	1.1	0.5	0.8	0.3	0.6	0.6	1	0.4	0.5
glycogen	1.2	1	0.8	0.9	0.3	0.6	1.0	1	0.0	0.0
N	13		12		10		25		13	

Table 2.1.2. Mean values m and their standard deviations σ for the volume of organelles (in μm^3) per $10 \mu\text{m}^2$ epithelial area (V_A) in the different regions of the outer mantle epithelium. Values are given with standard deviation. n is the number of test-fields used for the calculations. “central region all” contains the values of the test-fields of “central region secreting” and “central region attached”; er: endoplasmic reticulum.

organelle volume per $10 \mu\text{m}^2$ epithelial area (V_A)	central region secreting		central region attached		puncta		central region all		commissure	
	m	σ	m	σ	m	σ	m	σ	m	σ
mitochondria	0.5	1	0.6	0.7	0.2	0.2	0.6	0.8	8.9	4.9
endo-lysosomes	0.3	0.3	0.8	1.2	1.0	0.6	0.6	0.9	9.4	5.8
vesicles	0.1	0.1	0.1	0.1	0.1	0.1	0.1	0.1	3.4	3.0
Golgi apparatus	0.1	0.1	0.0	0.0	0.0	0.0	0.0	0.1	0.5	1
rough er	0.6	0.4	0.2	0.2	0.2	0.1	0.4	0.4	3	1.1
smooth er	0.1	0.1	0.1	0.1	0.0	0.0	0.1	0.1	0.4	0.6
glycogen	0.2	0.3	0.1	0.1	0.0	0.1	0.1	0.2	0.0	0.0
N	13		12		10		25		13	

2.1.4. Discussion

Cell proliferation and differentiation

Williams (Williams1968a, 1968b) suggested that in Brachiopoda the generative zone of the mantle epithelium is located at the commissure, at the bottom of the mantle groove. As new cells are permanently produced within the generative zone, Williams postulated the “conveyor belt” model. This model is based on the notion that, due to permanent cell formation, cells need to move away from the mantle groove and develop anteriorly the OME and posteriorly the IME. As a consequence, OME cells have to undergo a sequence of proliferation events: the secretion of the mucous layer, that of the periostracum and of the mineralized shell layers. However, neither the idea of a proliferation zone located at the base of the mantle groove nor the conveyor belt model is based on firm observations or experiments.

For gastropods and bivalves Kniprath (1975, 1978), using ^3H -thymidine labelling, has shown that mitotic cell divisions occur at any site within the OME. The authors did not find an indication of growth centres within the OME. Accordingly, Kniprath concluded that epithelial cells of these molluscs do not change their function and stay in place for secretion of just one structural entity of the shell throughout their lives. In contrast, using a BrdU immunohistochemical method, Fang et al. (2008) observed for the bivalve *Pinctada fucata* that cell divisions were concentrated at a central region of the OME. This indicates, that, depending on the investigated metabolic system, there might be differences in cell proliferation patterns.

For *Magellania venosa* we have not observed any stages of mitosis. This points to the fact that mitosis events might be rare in modern terebratulide brachiopods. It is also in agreement with the observed growth rate of 15 to 18 mm per year for juvenile *Magellania venosa* (Baumgarten, 2013) which corresponds, when assuming a mean cell length of $10 \mu\text{m}$, to about 40-50 cell divisions per day along the median plane of the animal. However, as the mitotic process can be quite fast, observations of these in TEM

sections should be rare, and accordingly, sites of cell proliferation in *M. venosa* might so far be undetected. With regard to the conveyor belt mechanism postulated by Williams, it should be noted that in primary shell layer regions of *M. venosa* cell extensions become degraded between the distal ones that secrete the mineral and the proximal ones that secrete the periostracum. This might indicate cell re-differentiation during shell growth and the changing of cell function depending on the type of material they secrete.

According to Williams, regions of the OME at the inner commissure become later part of the mantle epithelium at central shell portions. This implies, that the OME either re-organizes itself from a multi- to a single-layered epithelium or OME cells migrate relative to the calcite fibres towards the shell edge where they differentiate from central-region type cells to commissure type cells. However, the statistically significant higher abundance of organelles of the endo-lysosomal pathway in the commissure in comparison to the abundance of organelles in OME cells at the central shell region and the presence of dense material between cells within the inner commissure strongly argue for a re-organization of OME cells and not for cell migration. Our results indicate that in *Magellania venosa* cell re-organisation takes place between the commissure and the central shell region, where the OME decreases in thickness and successively reduces the number of the long cellular extensions, eventually forming a single cell-layered epithelium devoid of cell extensions.

In both shell regions, the outer commissure and the central shell portion, OME cells connect by hemidesmosomes apically to the organic membranes of the fibres and basally to a thin basal lamina of the OME. At the commissure, apical and basal hemidesmosomes are very small, while they are considerably larger at the central shell portion, particularly the basal hemidesmosomes. This difference can be explained by the presence of large tonofilaments in the mantle epithelium at the central shell portion connecting apical to basal hemidesmosomes. Apparently the tonofilaments together with the hemidesmosomes help to stabilize the position and the shape of epithelial cells that are in direct contact to the fibres. At the commissure tonofilaments cannot occur due to the large number of cellular extensions between the shell and the basal lamina of the OME. Most likely more than one of these large cellular extensions originate from a single cell. Due to its multi-layered structure and the large size of the epithelium, additional stabilization of the OME at the commissure appears to be unimportant.

Cryo-preparation of OME cells revealed some additional aspects of OME ultrastructure. High-pressure frozen and freeze-substituted samples of the OME reveal that the tonofilaments are composed of thin fibrils (Fig. 2.1.10E). As the tonofilaments are connected to hemidesmosomes, these fibrils represent intermediate filaments that are known to sustain tensile forces particularly well (Kreplak and Fudge, 2007) Another unexpected feature is the presence of two plasma membranes at the basal side of OME cells located close to hemidesmosomes (Figs. 2.1.10D-F). This is a new finding for modern brachiopods, to our knowledge, such double cell membranes have up to now been reported only once in the hematophagous insect *Rhodnius prolixu* (Lane and Harrison, 1979).

Calcite fibre secretion

Simonet Roda et al. (2019) showed that in periodic alternation on the order of 7-9 micrometers about 50 % of the OME is attached to the organic membranes that cover the proximal, convex surface of the calcite fibres. This part of epithelium is in very

close contact to the shell, leaving little (i.e. very few nanometers) or no room for an extrapallial space. At these sites, mineral deposition does not take place. It takes place when the cells have detached from the organic membrane that lines the basal surface of the fibres. At these regions, we find that more than one cell is located below the forming fibre Figs. 2.1.5 and 2.1.9. This observation contradicts claims of Williams (Williams 1966, 1968b), who reported that a fibre is formed by one cell only (described for *Notosaria nigricans* and *Hemithiris psittacea*). Secretion of a fibre by more than one cell requires tight cooperation and coordination of neighbouring OME cells as these secrete the mineral and the organic membrane (Simonet Roda et al. 2019). The strong interdigitations of neighbouring cells (Fig. 2.1.9) and the very large number of gap junctions between adjacent epithelial cells (Figs. 2.1.10A- C) substantiates the need for cell communication and/or exchange of small metabolites.

The tight attachment of apical OME cell membranes to forming fibres raises the question of the dimension of the extrapallial space, the space between the mineral secreting region of the cells and the forming fibre. An answer to this question is important as the width of the extrapallial space affects the mechanism that adds mineral to the growing shell. It is known for molluscs that the extrapallial space between the OME and the shell is only a few tens of nanometers (e.g. about 90 nm in the bivalve *Neotrigonia*, Checa et al. 2014, *Nodipecten nodosus*, Audino et al. 2015). Since mineral may dissolve during sample preparation, we investigated polished samples of resin embedded shells that have been high-pressure frozen and freeze-substituted (this study and Simonet Roda et al., 2019), where both, the mineral and the adjacent outer mantle epithelium are well preserved. These experiments show that at the growing fibres at sites of mineral deposition the outer mantle epithelium is in direct contact with the calcite fibre, without any extrapallial space in between.

Mineral transport

Research over the last decades indicated that in shelled organisms hard tissue formation might occur via an amorphous precursor (e.g. Beniash et al. 1997, 1999, Weiss et al. 2002, Addadi et al. 2003, Weiner et al. 2003, Politi et al. 2004, 2008, Nassif et al. 2005, Nudelman et al. 2008, Jacob et al. 2011, Cartwright et al. 2012, DeVol et al. 2015, Macías-Sánchez et al. 2017, Rousseau, 2018).

In order to test if calcite deposition in *Magellania venosa* fibres takes place via amorphous calcium carbonate (ACC) we performed etching experiments on high-pressure frozen, freeze-substituted and microtome polished surfaces, with shell mineral and the OME being preserved in a native state (Fig. S2.1.5). It is known that ACC has a ten times higher solubility than crystalline calcium carbonate and dissolves readily at pH values higher than 7.0 (Brečević and Nielsen, 1989). In previous studies, we have used this characteristic to distinguish between calcite and amorphous Ca-carbonate mineral phases (Seidl and Ziegler, 2012; Seidl et al., 2012). Etching of *Magellania venosa* shell samples at a pH of 9 with the mineral of the shell and the OME being in closest contact to each other showed no mineral dissolution between the forming fibre and the OME (Fig. S2.1.5). We find only between fibres a thin layer of mineral that dissolved (compare Fig. S2.1.5A-B). We did not find any evidence for the presence of an amorphous precursor at the growing front of fibres. This suggests that the mineral is deposited here directly as calcite rather than via a precursor amorphous phase (ACC). With the applied type of sample preparation crystallization of ACC at preparation can be excluded, since, after shock-freezing the sample remains free of liquid-state water as

well as during freeze-substitution, embedding and polishing. This is experimentally verified by our etching experiments, when comparing the micrograph recorded before etching (Fig. S2.1.5A) with that after etching at a pH of 9 (Fig. S2.1.5B).

Corresponding to our conclusions that we inferred from etching experiments, high-resolution, low-kV EBSD analysis also did not show any ACC between the fibres and the cells of the outer mantle epithelium (Fig. S2.1.10). The EBSD signal is a diffraction signal that originates from backscattering at lattice planes of crystallized material. Hence, when the electron beam hits lattice planes we obtain a Kikuchi pattern (EBSD signal), while in the case of an amorphous mineral or biopolymers there will be no diffraction at lattice planes and, hence, an EBSD signal will not be formed. We conducted high-resolution EBSD measurements with a step size of about 100 nm (Figs. S2.1.10B-C) on high-pressure frozen and freeze-substituted *Magellania venosa* fibres that are in direct contact to OME cells (Fig. S2.1.10A). We did not find any signs for the presence of an amorphous precursor in any fibres at 100 nm resolution. In contrast, as the EBSD measurement, notably the band contrast, in Fig. S2.1.10 shows, the mineral at the growing face of fibres directly next to OME cells is crystallized calcite.

Ultrastructural results of the OME given in this study and the experiments reported by Simonet Roda et al. (2019) allow conclusions about the mechanism of mineral transport from OME cells to the forming fibres. As mentioned in the introduction, transport and deposition of calcium carbonate may occur either via vesicles and exocytosis to the site of mineral deposition (e.g. Aizenberg et al. 1996, Politi et al. 2008, Weiner and Addadi 2011, Gal et al. 2014) or via ion transport across cell membranes (e.g. Greenaway et al., 1995; Roer, 1980; Wheatly, 1999, Wheatly et al., 2001; Ziegler et al., 2002, 2004) and through the cytoplasm; either with calcium binding proteins or intracellular compartments like the endoplasmic reticulum (e.g.; Ziegler, 2002, Hagedorn and Ziegler 2002; Hagedorn et al., 2003; Ahearn, 2004, Ziegler et al., 2005). The compartmentalization is essential as it ensures that high toxic concentrations of ionized calcium in the cytosole are avoided. It was the nanogranular appearance of etch patterns of brachiopod biocalcite in the 50-100 nm size range (Cusack et al. 2008, Schmahl et al. 2008, Simonet Roda et al. 2019), which originally appeared to support the paradigm of biocalcite growth by successive attachment of 50-100 nm nanoparticles. As the fibres of modern *Magellania venosa* are single crystals, the particles - if they exist - need to be ACC which crystallizes homoepitaxially on a substrate crystal. Accordingly, we originally expected to find ACC-filled vesicles of 50-100 nm diameter, which form in the epithelial cells, are exocytosed to attach to the mineral. However, in our high-resolution TEM images there is no positive or direct indication for such a mechanism. Moreover, in the extremely thin epithelial cells of the central shell region (as thin as 20 nm) we did not find organelles or vesicles that would transport solid mineral from cells to the sites of mineralization.

Nevertheless, we observed in OME cells at the commissure small vesicles between the outermost flat cell extensions and the fibrous shell layer. These could be interpreted as exosomes containing mineral and/or organic material that possibly contribute to the formation of the calcite fibres. Contradicting this interpretation is that we do not observe any multivesicular bodies containing exosomes within the OME cells, which are necessary for the secretion of exosomes into extracellular space. Hence, the above mentioned extracellular vesicles are most likely the result of degradation of the long cell extensions, and these are abundant at the commissure. Furthermore, we regard it very

unlikely that mechanisms for mineral transport are different between the commissure and the central shell region.

The thin cellular extensions underneath sites of mineral secretion, their direct contact to the forming fibres and the absence of ACC at the growing face of the fibres argue strongly for a vesicle independent mechanism of mineral transport for both, the commissure and the central shell region. Hence, in accord to our findings we propose for modern *Magellania venosa* a transcellular transport of calcium and hydrogen carbonate ions across the OME and the direct formation of calcite at the growing fibre. For the central shell region, this hypothesis is well supported by the extremely thin epithelial cells at sites of mineral secretion. The thinning of these cells diminishes the need of maintaining high calcium gradients within the cytosol and reduces toxic effects on calcium dependent signalling, cytoskeleton stability, and the function of mitochondria. The results of our morphometric analysis support as well transport of ions to sites of shell secretion. OME cells at the commissure have an about twice as high volume fraction of mitochondria than those within the central shell region, what points to a higher energy consumption of the cells at the commissure. When we compare values of absolute mitochondria volume we find a 15 times higher value for the commissure than for the central region, and for the mitochondrial outer membrane area an 11 times higher value, respectively. This difference is significant. However, it should be kept in mind that additional functions, such as secretion of the periostracum, that of the mucous layer, degradation of cellular extensions and the possibly higher energy costs for higher proliferation rates, evoke as well an increased volume fraction of mitochondria.

Hence, how is then mineral transported to the site of calcification in the modern brachiopod *Magellania venosa* ? On the basis of our findings and results reported in literature (Roer, 1980; Roer and Dillaman, 1984; Giraud-Guille, 1984; Cameron and Wood, 1985; Ziegler, 1997; Wheatly, 1999, Wheatly et al., 2001; Hagedorn and Ziegler 2002; Hagedorn et al., 2003; Ziegler et al., 2004) we developed a conceptual model (Figure 13) for ionized calcium, carbonate and proton transport for the modern brachiopod *Magellania venosa*. Observations gained in this study that favour a plasma membrane aided ion transport mechanism for shell formation in *Magellania venosa* are: (i) the presence of very thin cell regions at sites of mineral secretion. These thin cells do not require a compartmentation of calcium in the cytoplasm of the cell; (ii) the absence of an amorphous carbonate phase in fibres that are in direct contact with OME cells, hence, fibres that are in active secretion; (iii) the absent or very narrow extrapallial space between the apical membrane of OME cells and the growing fibres, which leaves no space for mineral transport by vesicles; (iv) the lack of evidence for the presence of vesicles transporting ACC.

The major steps of our model are (Figure 2.1.13): (1) Ionized calcium enters the cell passively through calcium channels along the steep inwardly directed electrochemical gradient; (2) From the cytoplasm calcium is transported across the apical cell membrane by a Ca^{2+} -transport ATPase and an $\text{Na}^+/\text{Ca}^{2+}$ -exchange mechanism. Carbonate ions are formed by cell metabolism or/and (3) enter the cell through a $\text{HCO}_3^-/\text{Cl}^-$ exchange or a $\text{HCO}_3^-/\text{Na}^+$ co-transport mechanism. (4) Hydrogen carbonate is transported by a $\text{HCO}_3^-/\text{Na}^+$ co-transporter or/and a $\text{HCO}_3^-/\text{Cl}^-$ exchanger across the apical cell membrane. (5) At the site of mineralization Ca^{2+} reacts with HCO_3^- to CaCO_3 releasing one H^+ . To our knowledge there is no transporter which is able to transport protons against its electrochemical gradient from the outside of the cell

into the cytoplasm as indicated by the (X) in Figure 2.1.13. However, mineralization can only proceed if the proton is removed into the cytosol to maintain an alkaline pH at the site of mineralization (to reduce the solubility of CaCO_3). Numerous studies on a range of different CaCO_3 mineralizing organisms have shown the presence of carbonic anhydrases in the mineralized tissue and/or expression of the protein in the mineralizing epithelial cells (e.g. Cameron and Wood, 1985, Miyamoto et al. 1996, Yu et al. 2006, Tambutté et al. 2007, Marie et al. 2008, Moya et al. 2008, Ziegler 2008) including brachiopods (Isowa et al. 2015). Carbonic anhydrases catalyse the formation of H_2O and CO_2 from H^+ and HCO_3^- as well as the reverse reaction. H_2O can pass back into the cell by aquaporin channels. The passage of the non-polar CO_2 through the membrane is possible by passive diffusion (e.g. Misser et al. 2008), but there are also indications for the existence of CO_2 channels (Endeward et al. 2017). Inside the cell the CO_2 is transformed with water into H^+ and HCO_3^- . The carbonic anhydrase process is indicated as (6) in Fig. 2.1.13. (7) The proton is transported from the cytoplasm to the haemolymph by a V-type H^+ -ATPase. (8) The inwardly directed sodium gradient is maintained by the $3\text{Na}^+ / 2\text{K}^+$ transport-ATPase located in the basolateral cell membrane.

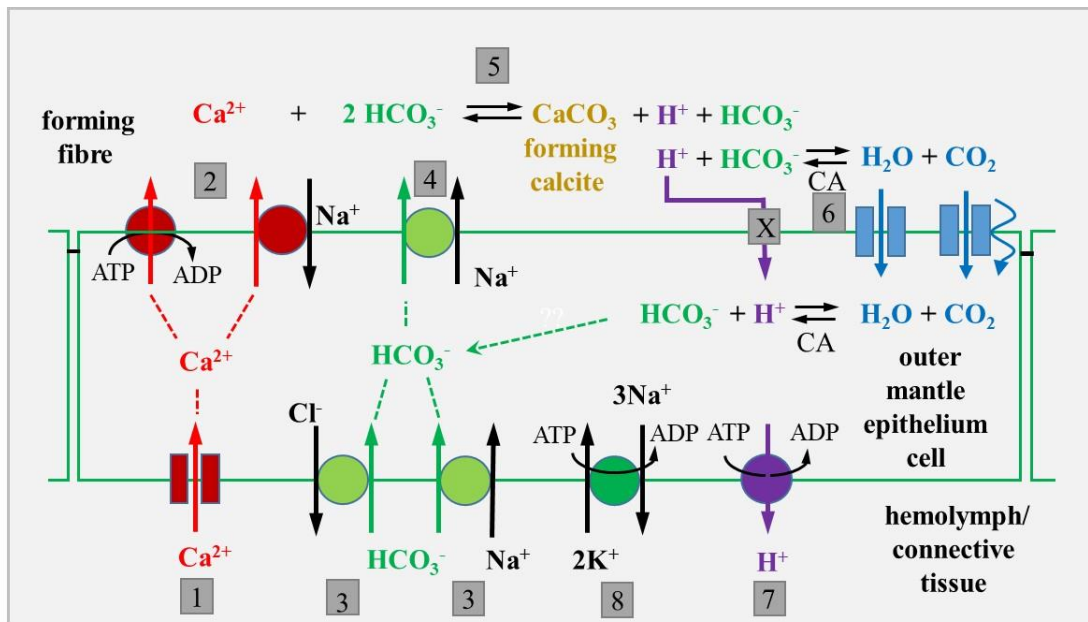


Figure 2.1.13. Major steps of a conceptual model for calcite secretion in the modern brachiopod *Magellania venosa*. (1) Ionized calcium diffuses into the cell through channels along the inwardly directed electrochemical gradient, (2) Ca^{2+} is transported out of the cell, across the apical plasma membrane to the forming fibre, by a Ca^{2+} -transport ATPase or/and a $\text{Na}^+/\text{Ca}^{2+}$ -exchange mechanism. Carbonate is formed by cell metabolism; but it also enters the cell as HCO_3^- through a (3) $\text{HCO}_3^-/\text{Cl}^-$ exchange or a $\text{HCO}_3^-/\text{Na}^+$ co-transport mechanism. (4) HCO_3^- is transported across the apical cell membrane by a $\text{HCO}_3^-/\text{Na}^+$ co-transport mechanism or/and a $\text{HCO}_3^-/\text{Cl}^-$ exchanger (the latter not shown in the model). (5) At the site of mineralization Ca^{2+} reacts with HCO_3^- to form CaCO_3 and releasing H^+ . (X) To our knowledge there are no proton transporters capable to bring protons from the outside to the inside of the cell against its electrochemical gradient. (6) Carbonic anhydrase catalyses the formation of H_2O and CO_2 from the proton and HCO_3^- ; H_2O enters the cell through aquaporin channels and CO_2 diffuses back through the cell membrane into the cytoplasm. In the cytosole the carbonic anhydrase catalyses the reaction back to hydrogencarbonate and a proton. The HCO_3^- is recycled and (8) the proton is transported into the hemolymph by a V-type H^+ -ATPase. (8) The inwardly directed sodium gradient is maintained by the $3\text{Na}^+ / 2\text{K}^+$ transport-ATPase within the basolateral membrane.

Passage of ionized calcium through specific channels in the cell membrane or/and into intracellular stores plays a major role in cell signalling events and triggers many cell physiological processes (e.g. Grover and Khan 1992, Simkiss, 1996, Carafoli 2004, Berridge 2005, Clapham 2007). Transcellular calcium ion transport is intrinsic to many epithelial cells. *Non-mineralising epithelial cells* of vertebrate kidney (Kumar, 1995; Moor and Bonny, 2016), the gill and antennal gland epithelium of Crustacea (Flik et al., 1994; Lucu, 1994; Neufeld and Cameron, 1993; Wheatly et al., 2007). Also for *mineralizing epithelial cells*, e.g. those that secrete the mineral in crustacean cuticle (Roer and Dillaman, 1984, Greenaway et al., 1995; Wheatly, 1999, Wheatly et al. 2001; Ziegler et al., 2004), in corals (e.g. Allemand et al. 2004, Böhm et al. 2006, Marshall et al. 2007, Tambutté et al. 2011, Pretet et al. 2013, Fallini et al. 2015, Inoue et al. 2015, Gothmann et al. 2016, Mejía et al. 2018), coccolitophorides (e.g. Gusonne et al. 2006, Langer et al. 2007, McClelland et al. 2017, Hermoso et al., 2017, Yin et al. 2017, Toyofuku et al. 2017, Liu 2018) and foraminifera (e.g. Bentov et al. 2009, De Nooijer et al. 2014, Toyofuku et al. 2017). To our opinion, it is well conceivable that transport of ionized Ca across cell membranes might take place as well at shell mineralization in shell secreting organisms.

2.1.5. Conclusions

The shell of modern brachiopods is secreted by the outer mantle epithelium (OME) of the animal. Despite several decades of research, it is still unknown how the mineral is transported from OME cells to the site of mineralization. In order to understand mineral transport and shell secretion, we investigated the ultrastructure of OME cells and their spatial relation to the growing shell. We deduce the following conclusions from our results:

1. The ultrastructure of the OME at the commissure differs significantly from that at central shell regions. The OME at the commissure consists of several cell layers, while at central shell regions it is single-layered.
2. At the commissure, cells form long, lateral extensions towards the shell. These are thin, flat, and in direct contact with the calcite fibres, while proximally they are roundish in cross section.
3. At central shell regions OME cells are considerably thinner in comparison to cells at the commissure. Especially at forming calcite fibres cells are only a few tens of nm thick.
4. Mineral deposition takes only place at sites where the apical membrane of OME cells is in direct contact to the calcite of the fibre. Mineral secretion is terminated with the formation of an organic (likely proteinaceous) membrane which lines the proximal surface of fibres. At these sites, apical hemidesmosomes connect apical cell membranes to the organic lining of the fibres. Tonofilaments connect apical to basal hemidesmosomes. This stabilizes the contact of epithelium and fibres and keeps the mantle in place.
5. Individual fibres are secreted by several cells at the same time. This requires communication and tight cooperation of neighbouring OME cells for the coordinated secretion of organic membrane and mineral, explaining the high abundance of gap junctions between cells.
6. There is not any observation in the cell ultrastructure in our study that can be taken as evidence for a vesicular transport based mineralization process. On the contrary, the absent or very narrow (in the range of nanometers) space between the epithelium and the growing fibres, together with the absence of significant

differences in the volume fraction of vesicles between secreting and non-secreting regions of the OME, as well as the extreme reduction in cell thickness at sites of mineral secretion suggests, that in modern *Magellania venosa* (and likely in all Rhynchonellida and Terebratulida forming the fibrous microstructure) mineral transport to the sites of mineralization occurs via ion transport mechanisms through the cell membrane and not by transport of mineral by organelles such as vesicles.

2.1.6. Author's Contribution

MSR and AZ performed all EM analytical work: biochemical preparation, FE-SEM, TEM, imaging and morphometry data analysis. UR helped with TEM imaging and evaluation of morphometric data sets. AZ, EG, MSR wrote the manuscript. WS, AE, XY, MG contributed to the final version of the manuscript. VH, JL, DH took care of sampling, transport and culturing of live *Magellania venosa*.

Acknowledgments

We thank two anonymous referees for their thoughtful reviews and helpful comments. Very many thanks to Florian Böhm for reading and discussing the manuscript. We thank Renate Kunz of the Central Facility for Electron Microscopy of Ulm University for technical support and assistance. This is a BASE-LINE Earth project with the funding of the European Union's Horizon 2020 research and innovation program under grant agreement No. 643084. In part this work was supported by the Deutsche Forschungsgemeinschaft (Zi 368/11-1).

Supplementary material

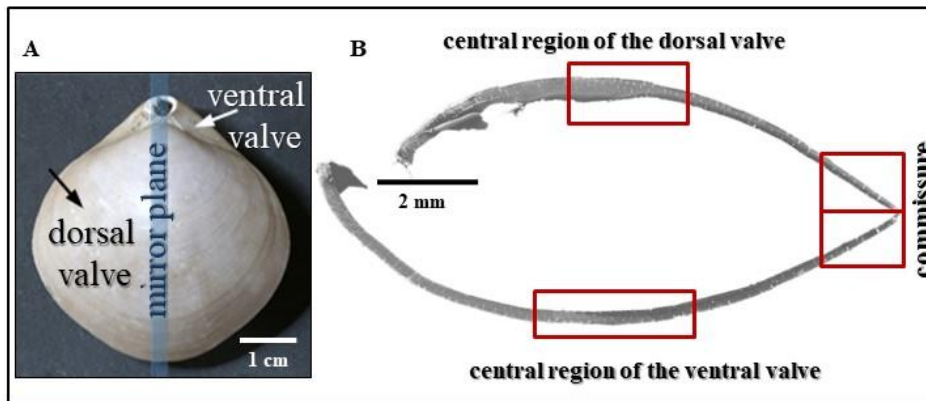


Figure S2.1.1. The shell of the modern brachiopod *Magellania venosa* (A). B) SEM micrograph of a longitudinal section through the shell showing the two valves and shell portions that were investigated in this study: the commissure and the central shell region.

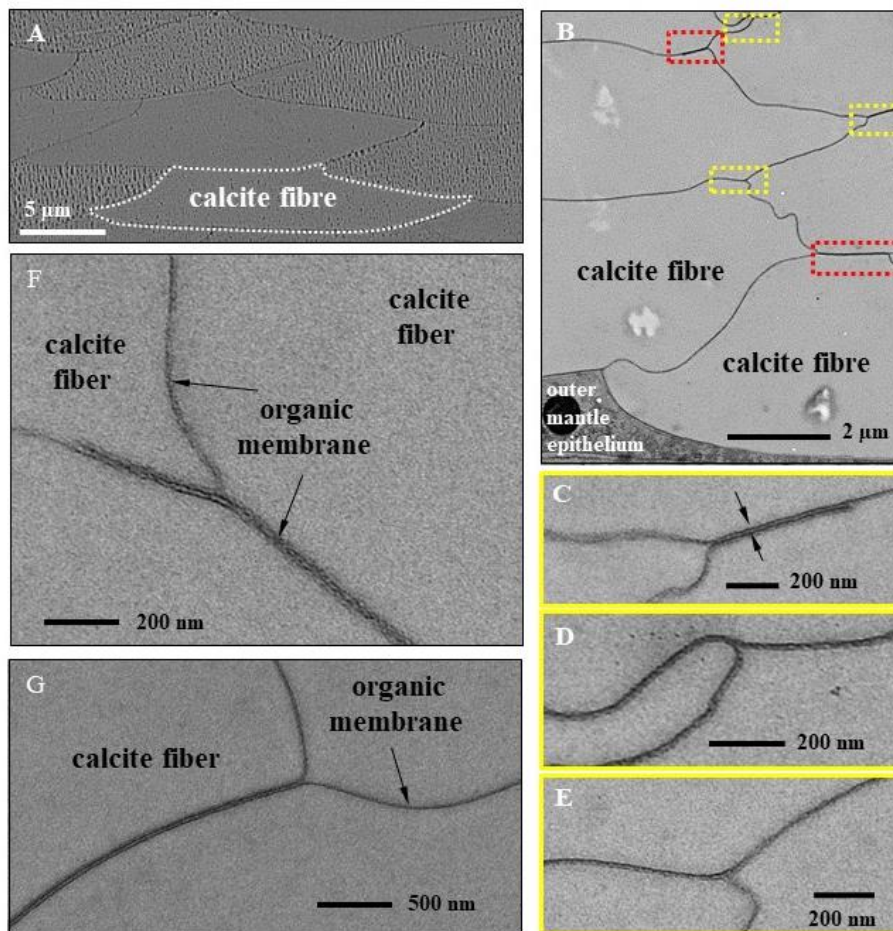


Figure S2.1.2. FE-SEM and TEM micrographs of microtome polished high-pressure frozen freeze-substituted samples showing the shape of calcite fibres in cross-section (SEM image in A), organic membranes between the fibres (TEM image in B) and the occasional presence of double-plied membranes at fiber corners (TEM images in C to G). Membrane portions highlighted in red in Fig. S2B are shown enlarged in Figs. 2B and 2C.

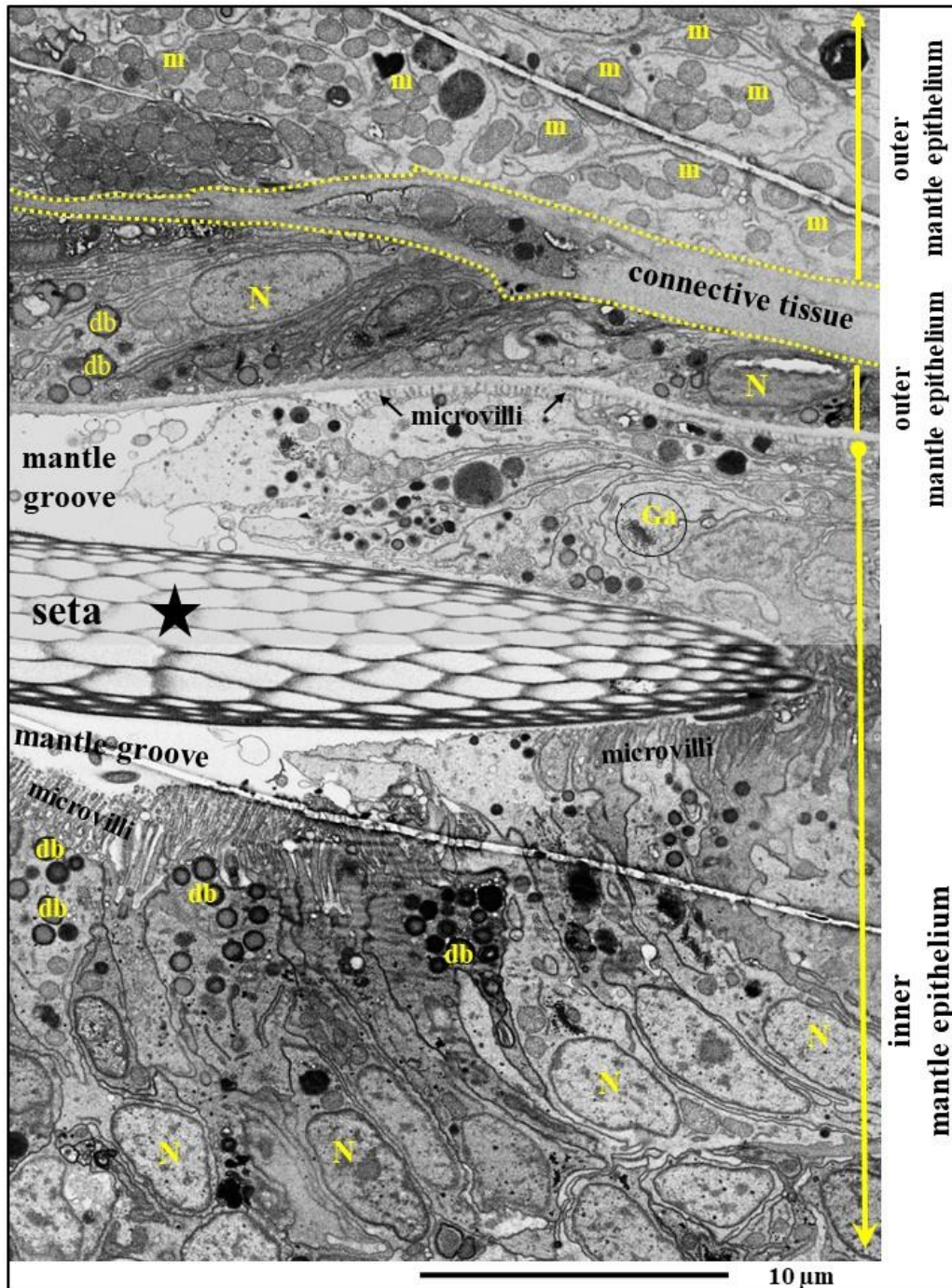


Figure S2.1.3. FE-SEM micrograph of an embedded and polished sample showing the inner mantle epithelium (IME) at the base of the mantle groove with a protruding seta (black star). The contrast is reversed. The seta, secreted by the surrounding IME cells, was cut obliquely. IME cells have long microvilli-like extensions at their apical side and contain many dense bodies (db). Golgi apparatus: (Ga), mitochondria: (m), nucleus: (N).

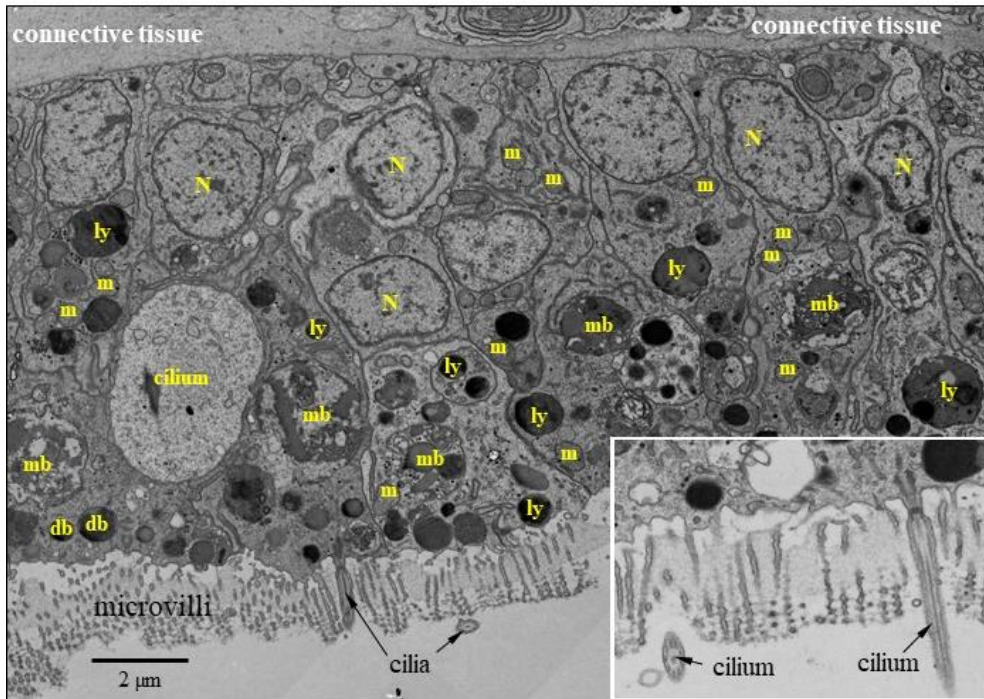


Figure S2.1.4. TEM micrograph of the ultrastructure of the IME at the **inner commissure**. It consists of a single layer of cells; these carry microvilli like extensions and cilia. The cells contain many organelles: nuclei (N), mitochondria (m), lysosomes (ly), multivesicular bodies (mb), dense bodies (db).

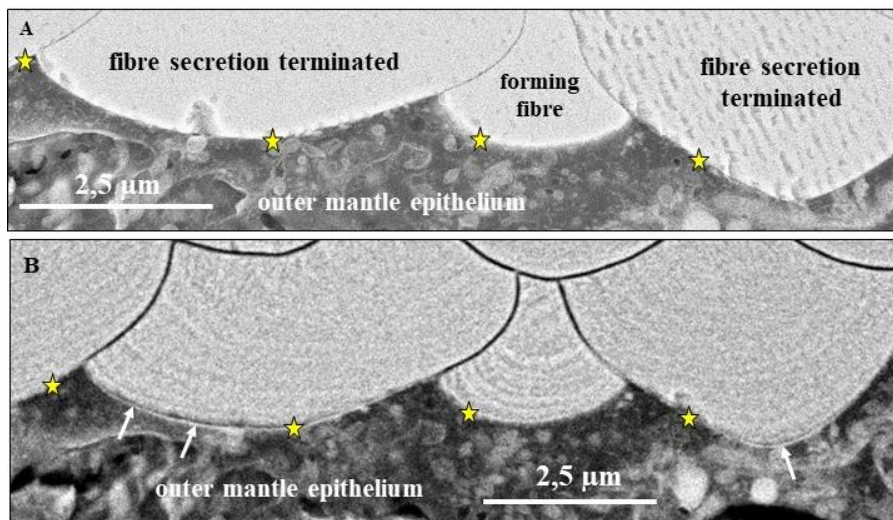


Figure S2.1.5. FE-SEM and TEM micrographs of calcite fibres and outer mantle epithelial cells at the **commissure** depicting the close contact of OME cells to the growing fibres. See also Simonet Roda et al. 2019. A) high-pressure frozen and freeze-substituted shell portion. B) high-pressure frozen/ freeze-substituted and additionally etched shell piece of modern *Magellania venosa*. Etching was done at a pH of 9, for 40 seconds and with a 0.1 molar HEPES and 2,5% Glutaraldehyde solution and subsequent critical point drying. The sample shown in (A) was only polished, not etched neither critical point dried. Outer mantle epithelium cells are in very close contact to the calcite of the fibres (yellow stars in A). Etching removes soluble material between calcite fibres. However, no material is etched away between forming fibre and the subjacent epithelium (yellow stars in B). White arrows in B point to the presence of the organic membrane that covers the proximal surface of a fibre when fibre secretions is terminated.

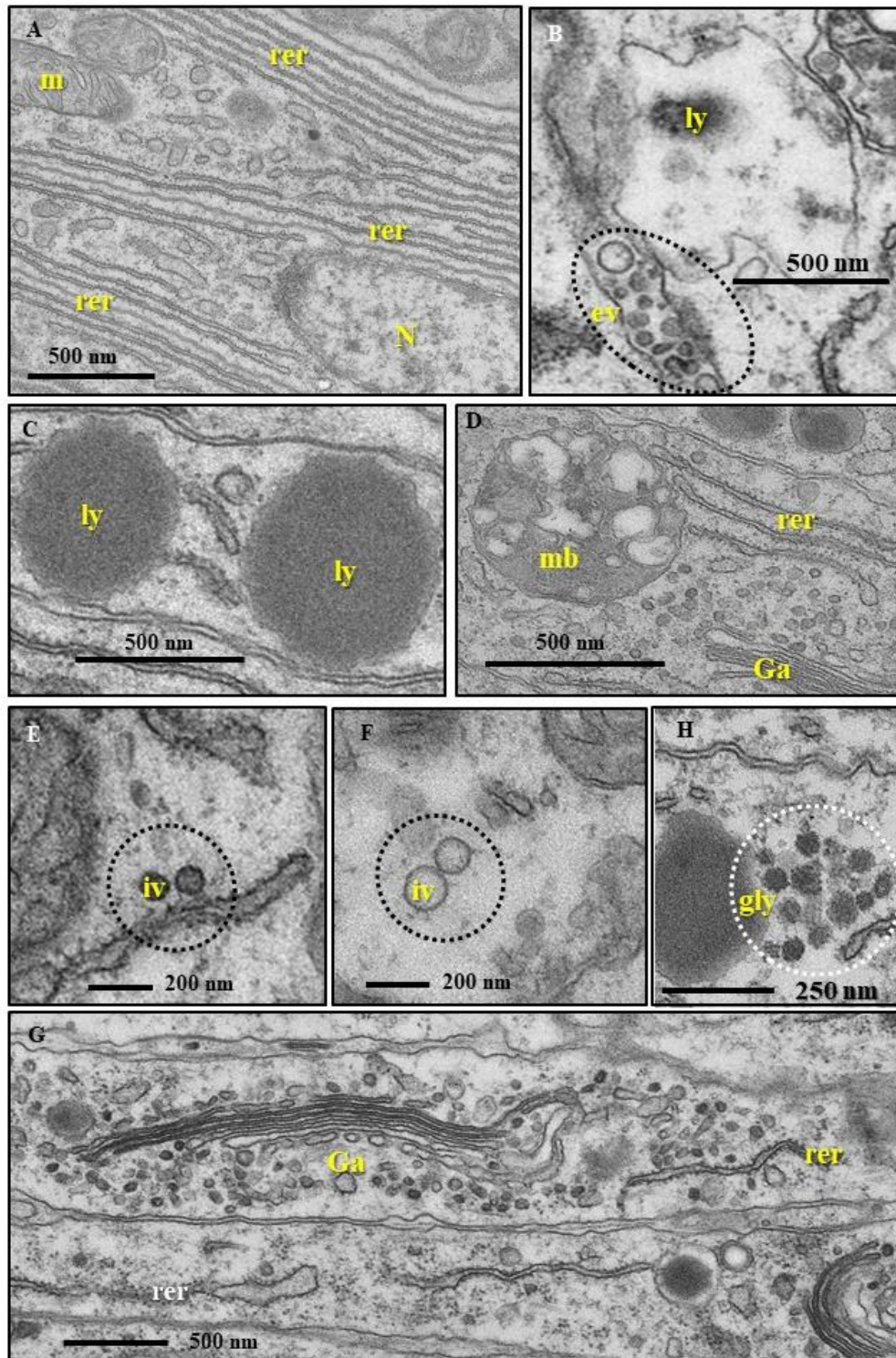


Figure S2.1.6. TEM micrographs from outer mantle epithelium that lines the shell at the **inner commissure** (A-F, G) and at the central region (H). The images depict examples of organelles and glycogen that were subject to the morphometric analysis. A) Mitochondria (m) and rough endoplasmic reticulum (rer). B-D) examples of lysosomes (ly in B and C) and a multivesicular body (mb in D) as combined in the class endo-lysosomes of the morphometric analysis; ev, extracellular vesicles and dashed black line in B. E, F) Intracellular vesicles (iv) are either filled with densely stained material (E) or appear light (F). G) an example of the Golgi apparatus with surrounding Golgi vesicles as combined to the class Golgi apparatus. H) Example of glycogen (gl).

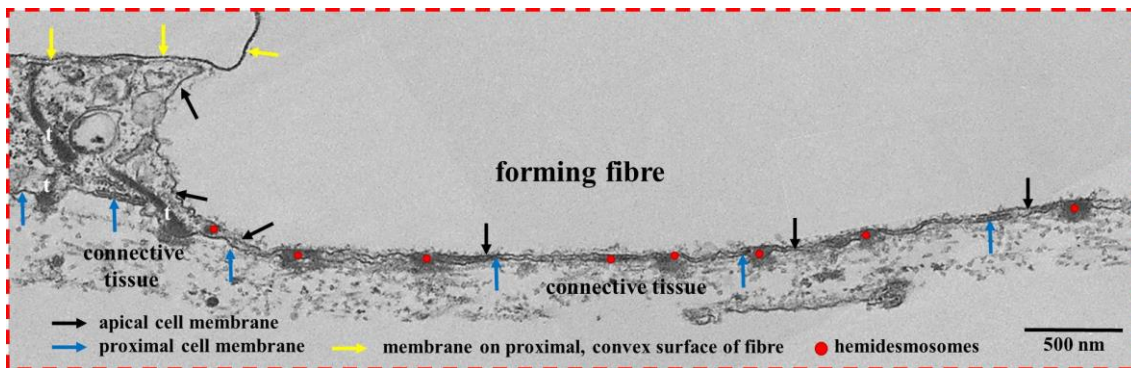


Figure S2.1.7. TEM micrograph taken on chemically fixed and decalcified samples from **central shell portions** depicting the position of apical (black arrows) and proximal (blue arrows) OME cell membranes. Yellow arrows point to the organic membrane that is present at the proximal, convex surface of a fibre (yellow arrows). With the formation of this membrane secretion of mineral ceases at this site of the OME cells. OME cells are attached to the organic membrane lining the fibres via apical hemidesmosomes, the latter are connected via tonofilaments (t) to basal hemidesmosomes (red dots) and the basal lamina of OME cells.

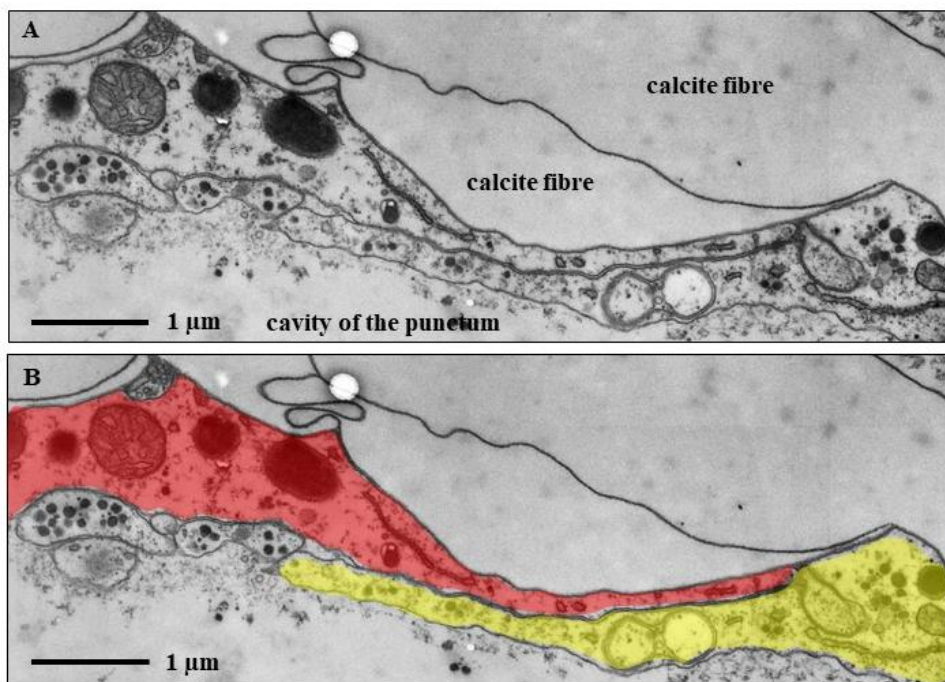


Figure S2.1.8. TEM micrograph of a chemically fixed and decalcified sample depicting the cavity within the median portion of a punctum. The surface of the punctum is lined by a very thin layer of single, but overlapping (A, B) cells. For further information see Fig. 11.

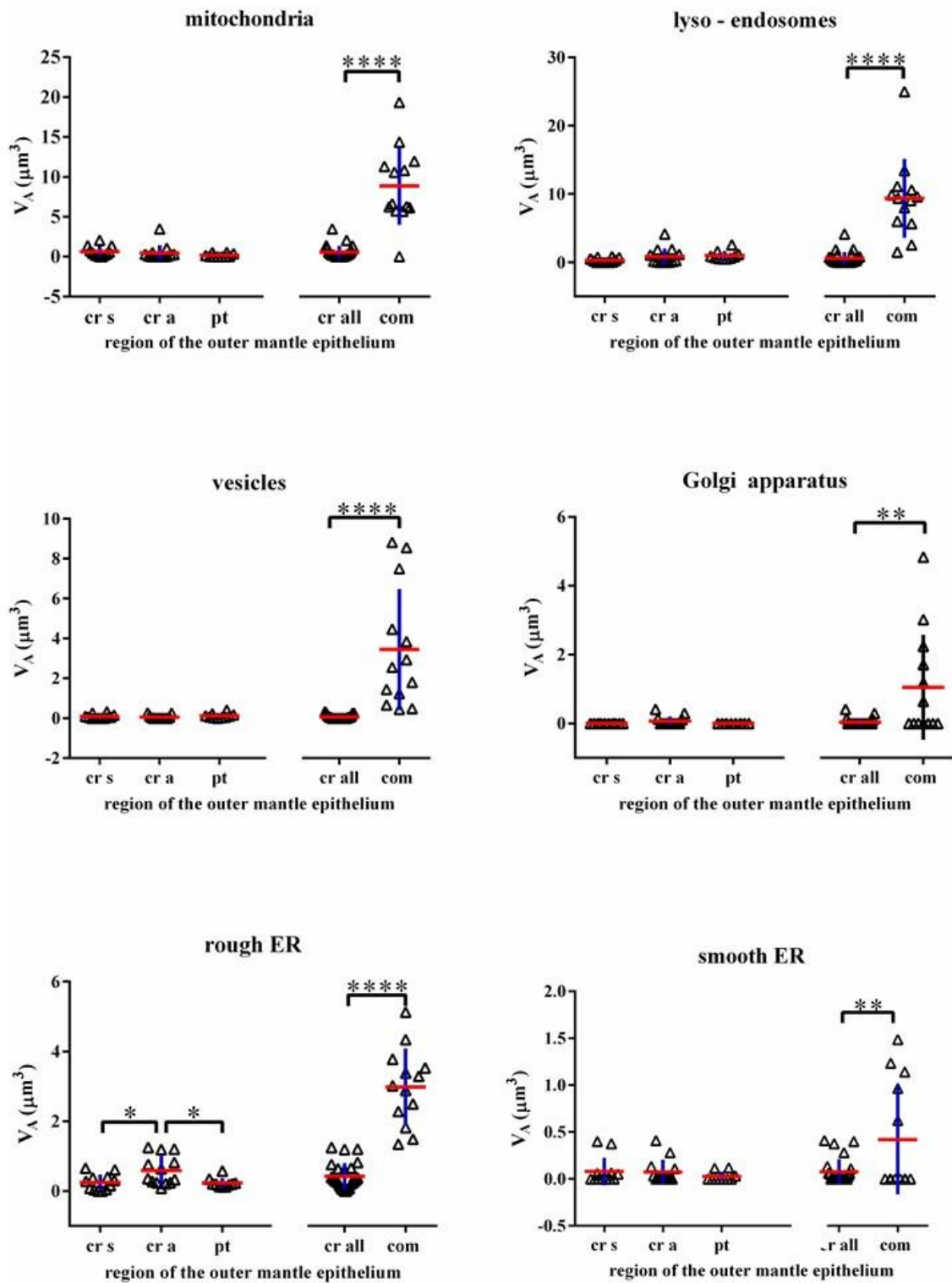


Figure S2.1.9. Volume of organelles (mitochondria, vesicles, rough endoplasmatic reticulum, endo-lysosomes, Golgi apparatus, smooth endoplasmatic reticulum) in the cells of $10 \mu\text{m}^2$ of the outer mantle epithelium for different OME regions: Results are plotted with the mean (indicated with horizontal red lines in the graphs) and the standard deviation (indicated with vertical lines in the graphs). Stars indicate significant differences of mean values for a given organelle between different outer mantle epithelium regions: *: $P \leq 0.05$; **: $P \leq 0.01$; ***: $P \leq 0.001$; ****: $P \leq 0.0002$.

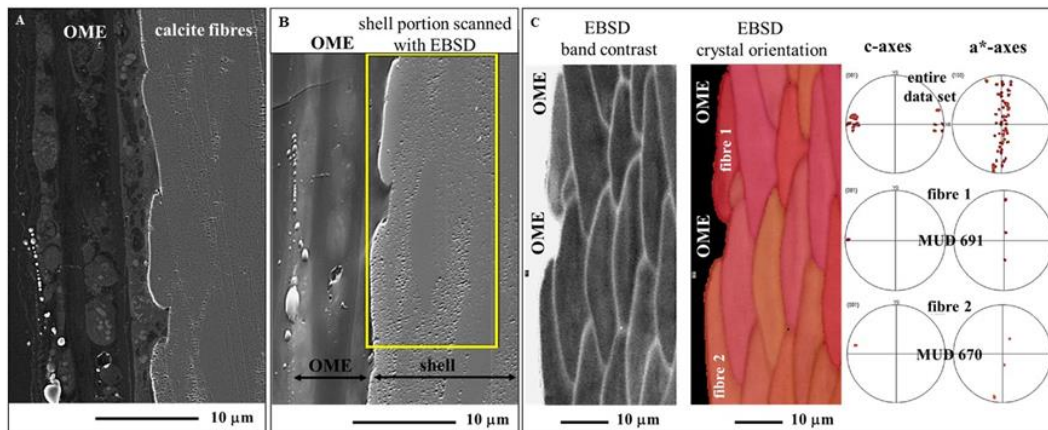


Figure S2.1.10. BSE (A), SE (B) and EBSD band contrast (grey scale) and color-coded orientation images and corresponding pole figures (C) of a high-pressure frozen and freeze-substituted shell section of *Magellania venosa*. Figure A demonstrates the closeness of the OME to the growing fibres. Figure B gives the shell and OME portion that was scanned with EBSD. Figure C shows with EBSD maps and corresponding pole figures the arrangement of calcite crystals in a transversely cut stack of fibres. The EBSD band contrast measurement image depicts the borders between adjacent fibres (light grey, note, for a better visualization, in this image the grey levels are reversed) within the shell. The orientation measurement (in color) shows that all fibres, also those in direct contact to the OME, consist of crystalline calcite only. The amorphous carbonate precursor would easily be detected with EBSD, as not crystallized material does not give a diffraction pattern, hence regions with ACC would not give any EBSD signals. The used step size for the measurement was 100 nm. The uniformity in color depicts the high degree of calcite c-axis co-orientation within the scanned shell portion (upper pole figure) as well as in individual fibres (the lower two pole figures). MUD values are an indication for crystal co-orientation strength. Each calcite fibre is a single crystal, the latter reflected by the high MUD value of individual fibres, 670, 691, respectively. The MUD value for an inorganic calcite crystal precipitated from solution scatters between 710 and 720 (see Nindiyasari et al. 2015).

2.2. Calcite fibre formation in modern brachiopod shells

www.nature.com/scientificreports

SCIENTIFIC REPORTS

OPEN Calcite fibre formation in modern brachiopod shells

Maria Simonet Roda¹, Erika Griesshaber¹, Andreas Ziegler², Ulrich Rupp², Xiaofei Yin¹, Daniela Henkel³, Vreni Häussermann^{4,5}, Jürgen Laudien⁶, Uwe Brand⁷, Anton Eisenhauer³, Antonio G. Checa^{8,9} & Wolfgang W. Schmahl¹

Received: 12 October 2018

Accepted: 19 November 2018

Published online: 24 January 2019

The fibrous calcite layer of modern brachiopod shells is a hybrid composite material and forms a substantial part of the hard tissue. We investigated how cells of the outer mantle epithelium (OME) secrete calcite material and generate the characteristic fibre morphology and composite microstructure of the shell. We employed AFM, FE-SEM, and TEM imaging of embedded/etched, chemically fixed/decalfied and high-pressure frozen/freeze substituted samples. Calcite fibres are secreted by outer mantle epithelium (OME) cells. Biometric analysis of TEM micrographs indicates that about 50% of these cells are attached via hemidesmosomes to an extracellular organic membrane present at the proximal, convex surface of the fibres. At these sites, mineral secretion is not active. Instead, ion transport from OME cells to developing fibres occurs at regions of closest contact between cells and fibres, however only at sites where the extracellular membrane at the proximal fibre surface is not developed yet. Fibre formation requires the cooperation of several adjacent OME cells. It is a spatially and temporally changing process comprising of detachment of OME cells from the extracellular organic membrane, mineral secretion at detachment sites, termination of secretion with formation of the extracellular organic membrane, and attachment of cells via hemidesmosomes to this membrane.

Citation: Simonet Roda, M., Griesshaber, E., Ziegler, A., Rupp, U., Yin, X., Henkel, D., Häussermann, V., Laudien, J., Brand, U., Eisenhauer, A., Checa, A.G. and Schmahl, W.W. 2019: Calcite fibre formation in modern brachiopod shells. *Scientific Reports*, 9, 598.

2.2. Calcite fibre formation in modern brachiopod shells

Simonet Roda M. *(1), Griesshaber E. (1), Ziegler A. (2), Rupp U. (2), Yin X. (1), Henkel D. (3), Häussermann V. (4), Laudien J. (5), Brand U. (6), Eisenhauer A. (3), Checa A.G. (7), and Schmahl W.W. (1)

¹Department of Earth and Environmental Sciences, LMU, 80333 München, Germany

²Central Facility for Electron Microscopy, University of Ulm, 89069 Ulm, Germany

³Marine Biogeochemistry/Marine Systems, GEOMAR Helmholtz Centre for Ocean Research, 24148 Kiel, Germany

⁴Pontificia Universidad Católica de Valparaíso, Facultad de Recursos Naturales, Escuela de Ciencias del Mar, Avda. Brasil 2950, Valparaíso, Chile and Huinay Scientific Field Station, Puerto Montt, Chile

⁵Alfred-Wegener-Institut Helmholtz-Zentrum für Polar- und Meeresforschung, 24148, Bremerhaven, Germany

⁶Department of Earth Sciences, Brock University, 1812 Sir Isaac Brock Way, St. Catharines, Ontario, L2S 3A1, Canada

⁷Departamento de Estratigrafía y Paleontología, Facultad de Ciencias Universidad de Granada, 18071 Granada, Spain, and Instituto Andaluz de Ciencias de la Tierra, CSIC-Universidad de Granada, 18100, Armilla, Spain.

*Corresponding author: simonet@lrz.uni-muenchen.de

Abstract

The fibrous layer of modern brachiopod shells forms a substantial part of the hard tissue. It consists of arrays of calcite fibres that are assembled into differently-oriented stacks. To understand calcite fibre formation and shape development, we investigated fibre morphology, internal structure and mineral deposition by AFM, FE-SEM, TEM imaging of embedded/etched, chemically fixed/decalcified and high-pressure frozen/freeze substituted samples.

Calcite fibres are secreted by outer mantle epithelium (OME) cells. Biometric analysis of TEM micrographs indicates that about 50 % of these cells are attached via hemidesmosomes to an organic membrane present at the proximal, convex surface of a fibre. At these sites, mineral secretion is not active. Instead, ion transport from OME cells to developing fibres occurs at points of closest contact between OME cells and fibres, and only at sites where the membrane at the proximal fibre surface is not developed.

Fibre formation requires the cooperation of several adjacent OME cells. It is a spatially and temporally changing process comprising of detachment of OME cells from the organic membrane, secretion of mineral at detachment sites, termination of secretion with formation of organic membrane, attachment of cells via hemidesmosomes to newly formed membrane, and suspension of secretion at attachment sites.

Key words: modern brachiopod *Magellania venosa*, AFM, FE-SEM, TEM, outer mantle epithelium (OME) cells, fibre morphology, nanometric biocalcite crystallites (NBC)

2.2.1. Introduction

Brachiopods are extant shell-forming, marine, sessile organisms abundant throughout the Phanerozoic, particularly during the Paleozoic when they dominated the marine benthic ecosystem. They are of interest to modern and paleo-environment research, as they cover most of the geological record and live in a wide range of marine habitats (e.g. Veizer et al., 1986; Bates and Brand, 1991; Grossman et al., 1991; Carpenter and Lohmann, 1995; Grossman et al. 1996; Richardson, 1997; Veizer et al., 1999; Veizer et al., 2000; Logan, 2007; Angiolini et al., 2009; Nielsen et al., 2013; Roark et al., 2015; Veizer and Prokoph, 2015; Rollion-Bard et al. 2016; Garbelli, 2017; Henkes et al., 2018; Reddin et al. 2018; Stigall, 2018). Their shells consist mainly of low-Mg calcite, which is assumed to crystallize in equilibrium with seawater with only small or negligible “vital effects”.

Modern terebratulide and rhynchonellide brachiopod shells consist of up to three mineralized shell layers: the outer primary, the inner fibrous, and, where developed, an innermost columnar layer (Griesshaber et al. 2009; Goetz et al. 2009 and 2011; Schmahl et al., 2012). In two-layered shells the fibrous layer forms an extensive part of the shell. The fibres are hundreds of micrometers long and mostly single-crystalline mineral units (Schmahl et al., 2004; Griesshaber et al., 2007). They have four surfaces: a proximal convex surface at their base, concave surfaces at their two lateral sides and a concave surface at their apical side. The shape of brachiopod fibres is unique and well developed in the Lower Cambrian, when the orders Protorthida, Orthida and Pentamerida of the class Rhynchonellata emerged with shells having fibrous microstructures (William et al. 2000; Carlson, 2016). In recent brachiopods, the morphology and dimension of fibres are characteristic for a given brachiopod species and are evolutionarily adapted to the animal's habitat (Ye et al., 2018a and 2018b).

Brachiopod shells are also of interest to material science, as these are important prototypes for bioinspired light-weight and energy-efficient hybrid materials. In these materials, advantageous mechanical properties of one component not only compensate for adverse properties of other's (e.g. Studart. 2012; Naleway et al., 2015; Niebel et al., 2016), but additional gain is derived from the overall composite nature of the biological hard tissue (e.g. Richie, 2011). The mineral component provides high elastic modulus and high compressive strength, while its inferior tensile strength and brittleness is compensated by the high tensile strength and pliability of the organic matrix. The hierarchical nature of the composite hard tissue provides overall toughness and fracture toughness (Meyers et al., 2008; Dunlop and Fratzl, 2010; Barthelat and Mirkhalaf, 2013; Wegst et al., 2014).

Fibrous biological composites are an important class of materials (e.g. Studart. 2012; Naleway et al., 2015; Niebel et al., 2016). Aragonite or calcite fibres are embedded in a pliant biopolymer matrix (e.g. Weiner et al. 1983; Levi-Kalisman et al., 2001; Gaspard et al., 2008; Checa et al., 2009; Dunlop and Fratzl, 2010; Maier et al., 2014; Nindiyasari et al., 2015; Wang et al., 2015; Checa et al., 2016; Griesshaber et al., 2017), the latter being always cross-linked within the hard tissue (e.g. Studart. 2012; Naleway et al., 2015; Niebel et al., 2016). This enables the fibres to transmit high forces to each other via the matrix, while remaining immobile and stationary. Accordingly, in fibrous composite materials (man-made or biological) the matrix is always pliant and flexible. Biopolymer matrices are plasticized with water (Naleway et al., 2015; Niebel

et al., 2016), whereas, when the matrix is a mineral, the latter is always softer relative to the hardness of the constituting fibres (Goezt et al., 2014).

In biological carbonate hard-tissue the fibres are not simple rods, as it is often the case in man-made fibrous composite materials. Instead, they have highly variable lengths and thicknesses, have elaborate morphologies (Ye et al., 2018a and 2018b) and are interleaved in three dimension (Studart, 2013; Studart and Erb, 2014). Most biological carbonate hard tissue is subject to compressive, bending and shearing forces. As fibres within a matrix cannot be reorganized once they endure these forces, they must be properly packed and oriented within the hard tissue from the onset of their formation. This is accomplished by the formation of stacks of parallel fibres, with the stacks twisted in a plywood-like arrangement. This ensures that all components of the composite are interleaved in three dimension and on all length scales (Weiner and Wagner, 1998; Schmahl et al., 2008; Schmahl et al., 2012; Pan, 2014; Studart and Erb, 2014).

Shell formation of brachiopods has been described based mostly on macroscopic morphological observations (Rudwick, 1959; Rudwick, 1970; McGhee, 1980; Williams et al., 2000). Williams and co-workers (Williams, 1953, 1966, 1968a, 1968b, 1968c and 1997) investigated shell development of modern rhynchonellide and terebratulide brachiopods and postulated that the same mantle epithelium cell performs several secretory operations and is capable of secreting all shell layers. This concept is based on the notion that mantle epithelium cells migrate during the secretory process. As new cells are supposed to be constantly produced in the mantle groove, previously formed cells have to move away from the generative zone in a “conveyor-belt” manner. Hence, according to Williams et al., an individual epithelial cell secretes the periostracum first, then the calcite of the primary layer, and subsequently and in sequence, the calcite of the fibrous layer together with the organic sheath, which surrounds the calcite of the fibre (Williams, 1968a, 1968b and 1968c). Furthermore, due to the presumed similarity in cross-section between a fibre and the outline of a cell, Williams assumed that each cell secreted only one fibre.

Few investigations have looked at the construction of the fibre composite material of brachiopod shells by epithelial cells in any detail. Specifically, the mechanism that leads to fibre mineralization and generation of the specific morphology of a fibre is still unknown. In this study, we present the first model that describes fibre secretion as well as fibre shape formation for modern terebratulide brachiopods. We demonstrate for the terebratulide species *Magellania venosa*, (i) the very close spatial relationship of the outer mantle epithelium with the calcite fibres, (ii) the tight control of the outer mantle epithelium cells on fibre secretion, and, (iii) describe the sequence of processes that take place with brachiopod fibre formation.

2.2.2. Materials and Methods

Materials

We investigated fibre shell formation of the modern brachiopod *Magellania venosa* from Comau Fjord in southern Chile. Brachiopods were taken at about 21 m depth from waters with an average temperature of 11°C and 30.3 ‰ salinity. Samples that were chemically fixed and decalcified had a longitudinal axis length between 5 and 7 mm;

shells that were fixed by high pressure freezing and subsequent freeze substitution had a longitudinal axis length of about 4-5 mm.

Methods and sample preparation

Chemical fixation and decalcification

A total of 8 small samples of the shell with the mantle tissue attached were first dissected from central and commissure regions of both ventral and dorsal valves. We used two different fixation media. Fixation medium A was prepared by mixing equal volumes of filtered seawater from the culture of *Magellania venosa* containing 2% paraformaldehyde and 2% glutaraldehyde with a solution of 0.35 mol L⁻¹ saccharose and 0.17 mol L⁻¹ NaCl in 0.2 mol L⁻¹ Na-cacodylate buffer (pH 7.7). Fixation medium B was prepared in the same way, however, with 3.2% paraformaldehyde and 4% glutaraldehyde in the filtered seawater. No differences in preservation of the structures was observed between the fixation procedures and media. After 17 hours in fixation solution at 4 °C, 8 samples, one from each region and valve of the animals, were decalcified for 14 days in a solution containing 0.25 mol L⁻¹ HEPES, 0.05 mol L⁻¹ EDTA and 1.0 v/v % glutaraldehyde stabilized at a pH of 8.0. All samples were washed three times with 0.1M Na-cacodylate buffer (7.7 pH) and postfixed in the same buffer containing 1% OsO₄ and 0.9% K₄Fe(CN)₆·3H₂O for one hour. After washing with bi-distilled water, the samples were dehydrated in an ascending series of isopropanol solutions (30, 50, 70 and 90%), and contrasted with 2% uranyl acetate (in 100 % ethanol) for 30 minutes, washed 3 times for 30 minutes each in 100% isopropanol and two times for 5 minutes in propyleneoxide and subsequently embedded in EPON resin.

High pressure freezing and freeze substitution

M. venosa individuals no longer than 6 mm were dissected in culture seawater. With scalpels pieces of shell with the mantle epithelium attached were cut from the commissure and central region of dorsal and ventral valves. Samples were transferred to hexadecane and placed in aluminium planchets with an outer diameter of 3 mm and a 200 µm deep cavity, and covered with the flat side of planchets. Samples were then high pressure frozen with a Wohlwend HPF Compact 01 high-pressure freezer (Engineering Office M. Wohlwend GmbH) within 30 ms at a pressure of 2.3 x 10⁸ Pa. The planchet sandwiches were then opened and freeze substituted overnight in 0.2% OsO₄, 0.1% uranyl acetate and 5% H₂O in acetone ranging from -90°C to 20°C (Walther and Ziegler, 2002). Samples were then embedded in EPON resin. Embedded samples were cut open using a diamond trimming knife (Diatome, Liechtenstein) and a Reichert Ultracut ultra microtome (Leica) to expose the mineralised shell.

Transmission Electron Microscopy

Ultra-thin 60 nm sections were cut from chemically-fixed and decalcified samples using a diamond knife and the ultra-microtome. The sections were placed on carbon stabilized Formvar-coated copper hole grids and stained with 0.3% lead citrate. A Zeiss 912 TEM (Zeiss, Jena, Germany) equipped with an Omega energy filter, a goniometer stage and a 2k x 2k pixel camera (TRS, Moorenweis, Germany) was used to image the sections at 8000 times magnification with a 120 kV acceleration voltage using only elastically scattered electrons. To screen a large area of the outer mantle epithelium at high resolution up to 300 images were recorded at rectangular grids. The images were then aligned into large composite images using the TRS software. These composite images were used for structural and numerical analysis.

Sample preparation for AFM imaging

For Atomic Force Microscopy (AFM) imaging shell pieces of modern *Magellania venosa* shells were cut in longitudinal section from the umbo to the commissure and embedded in epoxy resin. Embedded sample surfaces were polished in 5 sequential mechanical steps down to a grain size of 1 μm . For the final step, etch-polishing was applied for three hours with a colloidal alumina suspension in a vibratory polisher. Subsequently, the samples were washed in Milli-Q water in an ultrasonic bath and rinsed with 80% ethanol.

Atomic Force Microscopy

Samples were measured in contact mode with a JPK NanoWizard II AFM using silicon cantilevers. The measurements of height, lateral and vertical deflection traces were processed with the NanoWizard® IP image processing software and Gwyddion free and open source software. We used the “Gold” scale for colour. The height trace shows the surface height of the measured area while lateral and vertical deflection traces are the result of the interaction between the cantilever tip and the sample surface. With lateral deflection traces, we observed the different components within the shell (e.g., the organic membrane of the calcite fibres has a different interaction with the cantilever tip than the calcite of the fibres). We show all AFM results with vertical as well as lateral deflection trace measurements.

Sample preparation for microstructure characterisation

For Electron Backscatter Diffraction (EBSD) analyses 5 x 5 mm pieces were cut out of the shell and embedded in epoxy resin. The surface of the embedded samples was subjected to several sequential mechanical grinding and polishing steps down to a grain size of 1 μm . The final step consisted of polishing with colloidal alumina (particle size ~ 0.06 μm) in a vibratory polisher. Finally, samples were coated with 4-6 nm of carbon.

Electron backscatter diffraction

EBSD measurements were carried out on a Hitachi SU5000 field emission SEM, equipped with an Oxford EBSD detector. The SEM was operated at 20 kV and measurements were indexed with the CHANNEL 5 HKL software. In this study information obtained from EBSD measurements is presented as band contrast measurement images. EBSD band contrast represents the signal strength of the EBSD-Kikuchi diffraction pattern in each measurement point and is displayed as a grey-scale component of EBSD scanning maps. The strength of the EBSD signal is high when a crystal is detected (bright), whereas it is weak or absent when a polymer is scanned (dark/black).

Field Emission Scanning Electron Microscopy

Non-decalcified EPON resin embedded samples of high pressure frozen and freeze-substituted shell as well as chemically fixed shells, were knife polished by successively advancing the knife for 70, 40, 20, 10 and 5 nm 15 times for each step (Fabritius et al., 2005). Samples were then mounted on aluminium holders using self-adhesive carbon pads and conductive glue and coated with 4 nm of carbon using a BAF 300 (BAL-TEC, Balzers, Liechtenstein). Samples were analysed with a Hitachi S5200 field emission scanning electron microscope (FE-SEM). For chemically fixed samples we used the secondary electron signal at 4kV. To obtain material density contrast at high resolution for the high pressure frozen/freeze substituted samples, we used the converted backscattered electron signal to obtain so-called composite-rich images (Walther, 2008)

at 4kV acceleration voltage and 20 μ A emission current in analysis mode of the microscope. To test if the fibrous layer contained highly soluble mineral phases (e.g., an amorphous precursor phase of calcite) we first removed the 4 nm carbon layer using a diamond knife. The sample was then etched and organic material fixed simultaneously for 40 seconds using a 0.1 M HEPES (pH = 9.0) and 2.5 % glutaraldehyde solution. Immediately after etching, the samples were dehydrated in 100% isopropanol 3 times for 10 seconds and were critical point dried in a BAL-TEC CPD 030 (Liechtenstein) device. The dried samples were coated with 3 nm platinum. Then, the same regions of the sample were imaged again in the Hitachi S5200 FE-SEM.

Assessment of secreting and non-secreting OME portions

For distinguishing between secreting and non-secreting portions of the outer mantle epithelium (OME) we used several large TEM composite images from chemically fixed samples recorded at central shell regions. We measured the length of the outer mantle epithelium that is attached to the shell by apical hemidesmosomes and where two membranes could be observed such as at the apical membrane of the epithelial cells and the organic membrane at the proximal side of fibres (non-secreting parts of the epithelium). The length of these regions was compared, in perpendicular and longitudinal sections, with the length of those epithelium portions where the membrane lines the proximal side of the fibres as well as where apical hemidesmosomes are absent (secreting parts of the epithelium). For measurements, we used the open source software JMicroVision. The epithelial lengths were measured in basal parts of the epithelium where the cells are in contact with the basal lamina.

2.2.3. Results

The scheme in Figure 2.2.1a was deduced from our FE-SEM and TEM observations and depicts the spatial relationship between the different shell layers of the modern brachiopod *Magellania venosa* and their topological relation to the outer and inner mantle epithelia (OME, IME).

The shell of *Magellania venosa* (Dixon, 1789) consists of the periostracum, a purely organic layer, and two mineralized layers, the primary and the fibrous layer (Fig. 2.2.1a). All three layers are secreted by the outer mantle epithelium (OME) cells of the animal. The primary shell layer, located between the periostracum and the fibrous shell portion (Figs. 2.2.1a-b, S2.2.1a, S2.2.2a) is secreted near the commissure and ceases to grow in thickness when the fibres (Fig. 2.2.1a) start to develop. Hence, growth of the shell extension occurs by secretion of the primary layer at the commissure, while growth in shell thickness takes mainly place with secretion of fibres some tens of micrometers away from the commissure (Fig. 2.2.1a). The fibres (Figs. 2.2.1b, 2.2.2, S2.2.1b, S2.2.2) in *Magellania venosa* have four sides: one convex side facing proximally, two concave sides facing laterally and one concave side facing distally. The fibres are separated from each other by an organic membrane (Figs. 2.2.3, S2.2.1a-b, S2.2.2f), but this membrane does not form a sheath around individual calcite fibre's. Instead, the membrane lines only the proximal, convex surface of a fibre (Figs. 2.2.3, S2.2.1b, S2.2.2f). The specific shape and mode of packing of the fibres implicates the full encasing of the calcite of a fibre by an organic sheath.

AFM images (Figs. 2.2.1b, 2.2.3a, S2.2.1a, S2.2.2d) visualize the transition from the primary to the fibrous shell layer. There is no distinct or sharp boundary between the primary layer calcite and the adjacent secondary-layer fibres but rather a smooth

transition (Figs. 2.2.3a, S2.2.1a, S2.2.2d). Mineral units that are next to or close to the primary layer portion of the shell do not show the characteristic blade-shaped morphology of a brachiopod fibre (white stars in Fig. S2.2.4b). Instead, they are rather irregular in shape and elongated in cross-section. They are, however, already lined along their proximal, convex side by an organic membrane (white arrows in Figs. 2.2.3a, S2.2.2d). Occasionally short segments of organic membrane might become visible within the transition zone between the primary and fibrous shell layers (white arrows in Fig. S2.2.4a-b). Some distance away from this transition region, fibre morphology becomes more regular and cross-sections of fibres increase in size (yellow stars in Fig. S2.2.4b). The calcite within fibres (Figs. 2.2.2, 2.2.3, S2.2.2, S2.2.3) consists of highly structured nanometric biocalcite crystallites (NBC) often aligned in curved rows, along growth lines, following the convex proximal surface of the fibre (white arrows in Fig. 2.2.2a).

Figure 2.2.4 shows FE-SEM micrographs of polished surfaces of chemically fixed (Fig. 2.2.4a) and high-pressure frozen and freeze-substituted (Fig. 2.2.4b-f) shell portions embedded in EPON resin. High pressure freezing followed by freeze-substitution in acetone containing OsO₄ and uranyl acetate ensures minimal shrinkage of the soft tissue and negligible dissolution of the calcite during preparation. We find that the outer mantle epithelium is always in close contact with the proximal, convex side of the fibres. On the basal side, mantle epithelium cells are connected to the basal lamina of the connective tissue and haemolymph by large hemidesmosomes (red dots in Fig. 2.2.4a). In high pressure frozen and freeze-substituted samples, at sites of mineral secretion, apical cell membrane cannot be distinguished from basal surfaces of fibres (Fig. 2.2.4c and e). This indicates that in *Magellania venosa* extrapallial space between fibres and OME cells is either absent or only a few nanometers wide.

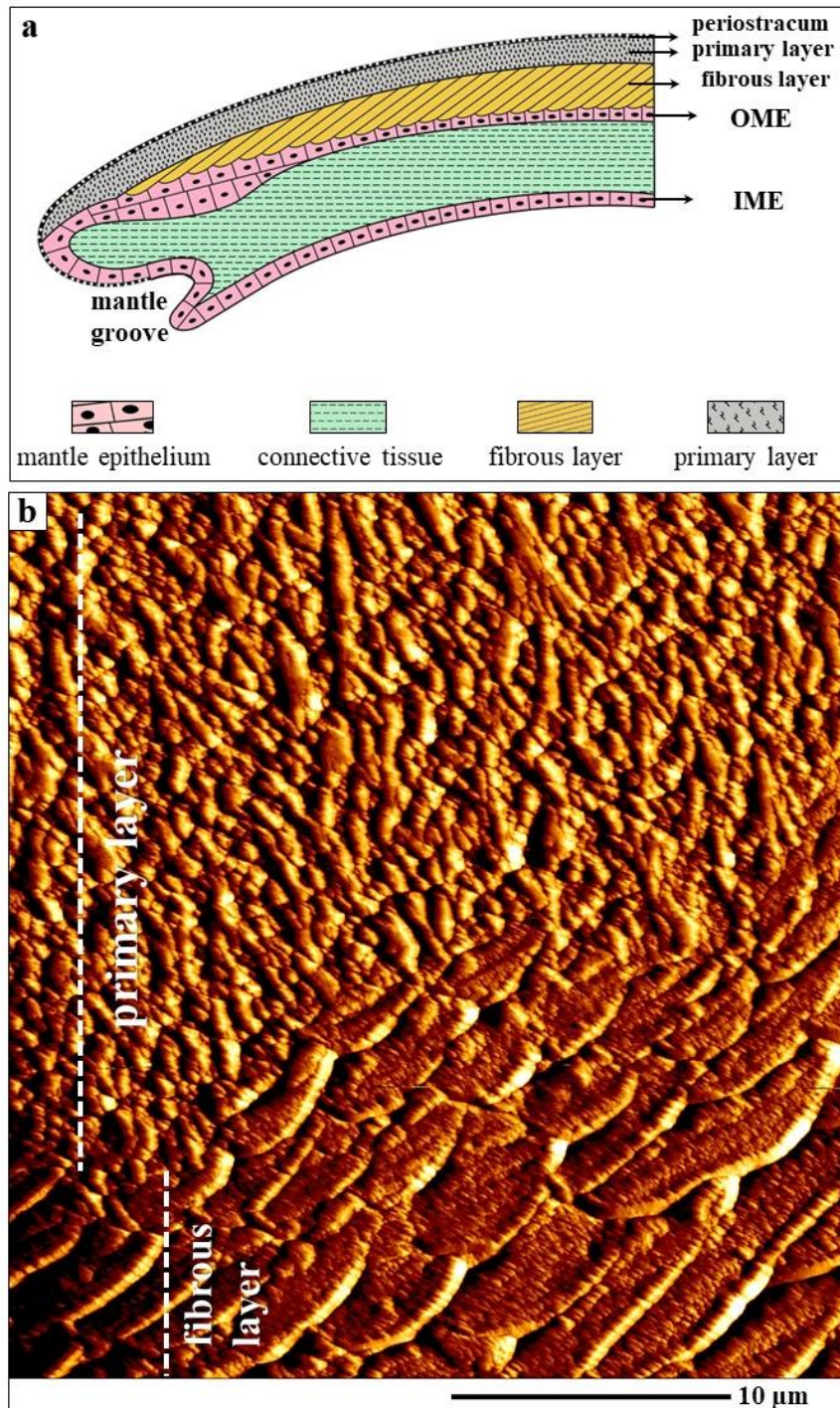


Figure 2.2.1. The different shell layers of the modern terebratulide brachiopod *Magellania venosa*. **a**, Schematic deduced from our FE-SEM and TEM results depicting the position of the periostracum, the two mineralized shell layers and the location of the mantle epithelium. The schematic shows the spatial relationship between the outer (OME) and inner (IME) mantle epithelium as well as the connective tissue in the growing shell. **b**, AFM vertical deflection image visualizing the structure of the outward primary and inward fibrous shell layer. The corresponding lateral deflection image is shown in Figure S2.2.2a; for additional information see Figure S2.2.1a. The fibres are sectioned transversely. Clearly visible is the transitional area between the primary and fibrous shell layers.

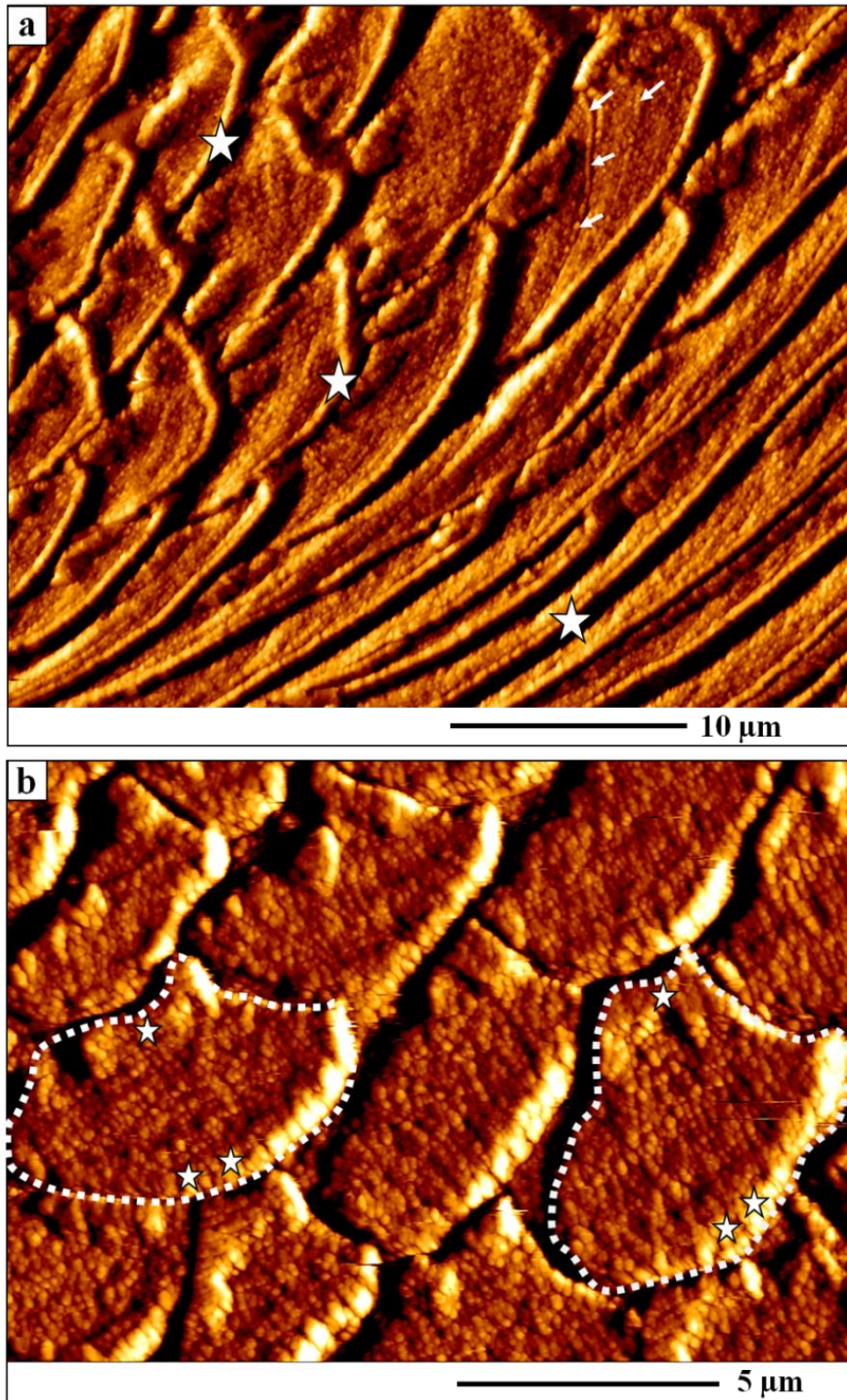


Figure 2.2.2. AFM vertical deflection images depicting the shape of longitudinally and transversely cut fibres as well as the internal structures of fibres of the modern brachiopod *Magellania venosa*. The corresponding lateral deflection images are shown in Figure S2.2.2. **a)** Nanometric biocalcite crystallites (NBC) constitute a fibre. These are often strung in rows (white arrows in a) following the convex shape of the proximal, convex basal part of a fibre and depict growth lines. White stars point to the organic membrane that lines the proximal, convex surface of fibres. **b)** One star indicates the apical, concave part of a fibre; two stars point to the proximal, convex portion of a fibre.

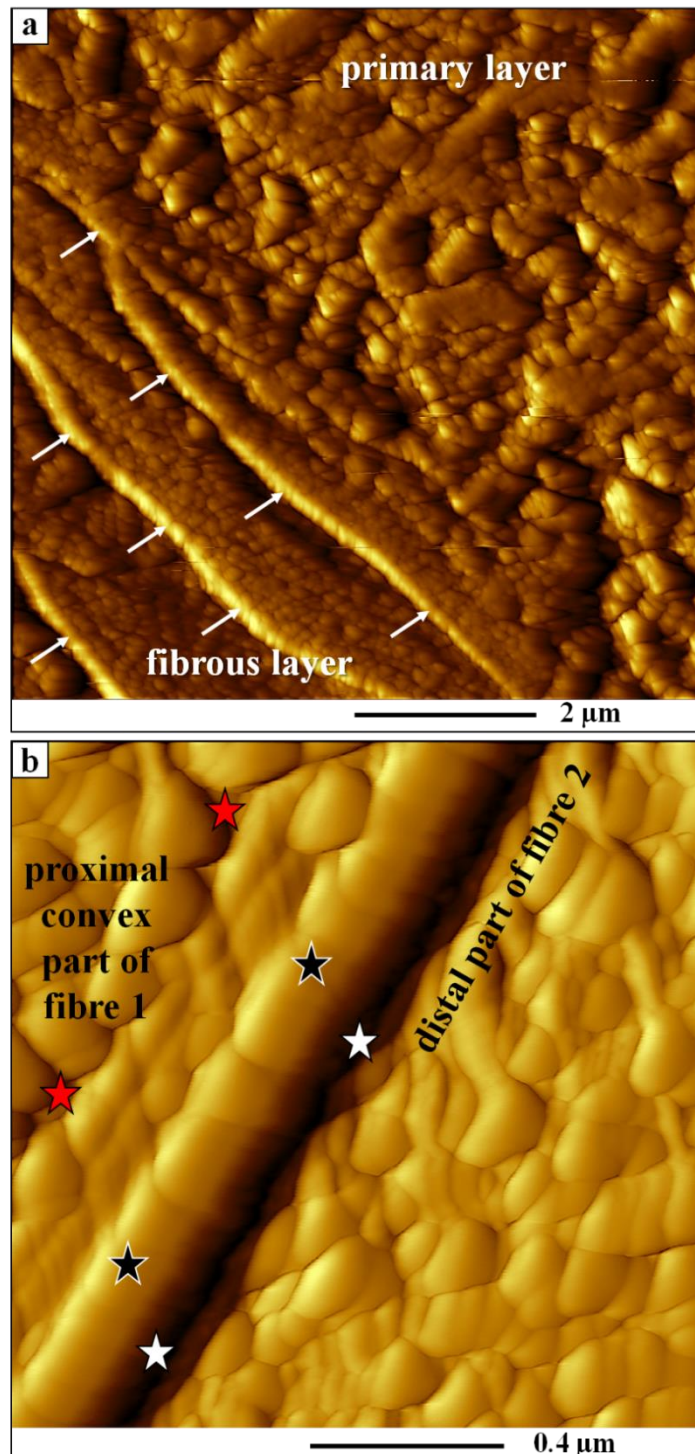


Figure 2.2.3. AFM vertical deflection images depicting the internal structure of primary and fibrous shell portions of *Magellania venosa*. Corresponding lateral deflection images are shown in Figure S2.2.2. **a**, Close-up of the primary layer and the first three rows of adjacent fibres visualizing the gradual changeover from primary to fibrous calcite shell layers. **b**, Biopolymer membrane tightly attached to the calcite of a fibre along its proximal, convex surface. The organic membrane (black stars) is between two adjacent fibres (red and white stars) and in each case the biopolymer lines the basal (proximal), convex portion of the fibre.

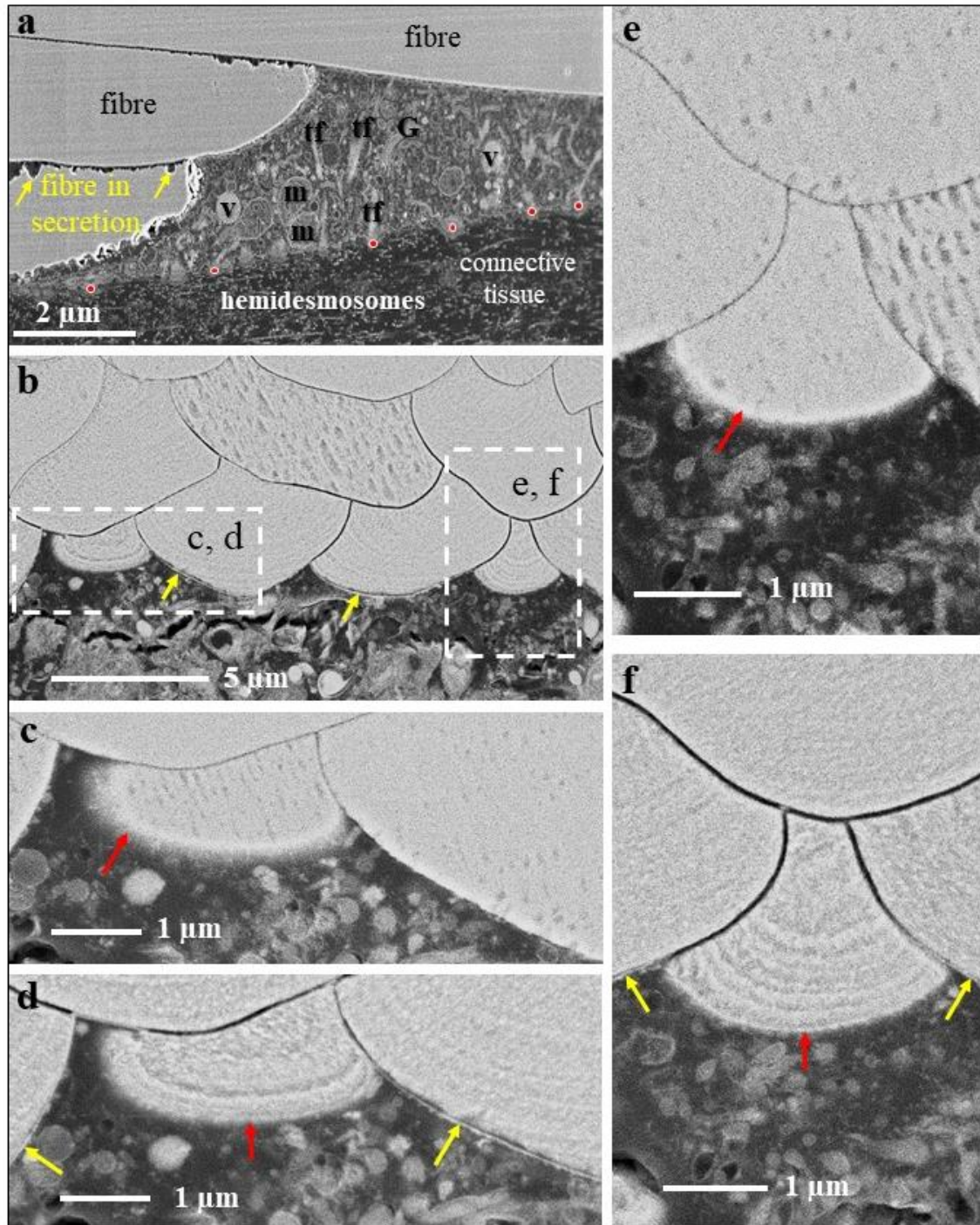


Figure 2.2.4. FE-SEM micrographs of polished surfaces of chemically fixed (a), high-pressure frozen and freeze-substituted (b to f) and etched (d, f) shell pieces of *Magellania venosa*. Samples in 4b, 4d and 4f were etched at a pH of 9, for 40 seconds with a 0.1 molar HEPES and 2,5% glutaraldehyde solution and critical point dried. Samples in 4e and 4c were polished but not etched nor critical point dried. Micrographs were recorded using secondary electron (at 4kV; Fig. 2.2.4a) and converted backscattered electron (at 4 kV; Fig. 2.2.4d-f) signals, respectively. **a-f**. Outer mantle epithelium (OME) cells are always in very close contact to the calcite of the fibres. It is well visible that at some cell – calcite interfaces the biopolymer lining of the fibre is not developed (red arrows in c, e, d, f). These are the sites where fibre formation is still in progress. In contrast, at sites where the biopolymer membrane along the proximal, convex surface of a fibre is well observable (yellow arrows in b, d, f), fibre mineralization is complete. At their basal side, epithelial cells are connected to the connective tissue by basal

hemidesmosomes (red dots in a). Samples (c) and (d) are high-pressure frozen, freeze-substituted, embedded in EPON resin and polished with a diamond knife; samples (d) and (f) are, in addition, etched for possible detection and visualization of amorphous calcium carbonate. G: Golgi apparatus, m: mitochondria, t: tonofilaments, v: vesicles.

As Figures 2.2.4c and 2.2.4e visualize, in *unetched* samples, the organic membrane that lines the proximal, convex side of a fibre cannot be distinguished from the calcite of the fibre. However, when *etched*, the membrane becomes visible (yellow arrows in Fig. 2.2.4b, d and f). Hence, there is a close connection between the membrane that lines the calcite of the fibres, in that the organic membrane is an integral part of fibres. The close connection between fibre calcite and membrane lining is clearly visible in our AFM images (Fig. 2.2.3b; black and red stars at the basal, convex surface of a fibre). In unetched samples (Fig. 2.2.4c and e) the organic membrane is not visible in FE-SEM images as during freeze-substitution OsO_4 and uranyl acetate have no access to them. In etched samples, the contact between the organic membrane lining is at the proximal, convex part of a fibre and the distal section of the adjacent fibre in low relief (Figs. 2.2.3b, 2.2.4e and c, S2.2.2). This might be due to higher solubility of the mineral at distal fibre surfaces and can be explained by inhibition of calcite crystal growth at these sites. This leads to the formation of nanocrystalline calcite with higher solubility.

In *chemically-fixed* samples with fibres still in formation, we observe irregular dissolution of the calcite at fibre margins (yellow arrows in Fig. 2.2.4a). However, in *high pressure frozen and freeze-substituted* samples these dissolution features are not present (Fig. 2.2.4c and e). Accordingly, etching of high pressure frozen and freeze-substituted shell portions with an aqueous solution at a pH of 9 containing 0.1 molar HEPES and 2,5% glutaraldehyde does not result in dissolution of the mineral (amorphous or crystalline) of the developing fibres. Hence, the dissolution features that we observed in the chemically fixed samples (Fig. 2.2.4a) can be traced back to the effect of aqueous solutions that were used in the course of that preparation method, and they do not indicate a possible presence of an amorphous precursor, amorphous calcium carbonate (ACC), within the fibres. Furthermore, we do not find selective dissolution of the calcite between epithelial cells and at the sites of mineral secretion (red arrows in Fig. 2.2.4d and f). ACC readily dissolves at a pH of 9, this is a good indication that the calcite of fibres forms directly and most probably not via a disordered mineral phase, such as amorphous calcium carbonate.

TEM imaging of chemically fixed and decalcified shell samples (Figs. 2.2.5 - 7) allows us to investigate the ultrastructure of OME cells, the organelle distribution within them, and the topological relation of OME cells to organic membrane that lines the proximal, convex surface of adjacent fibres.

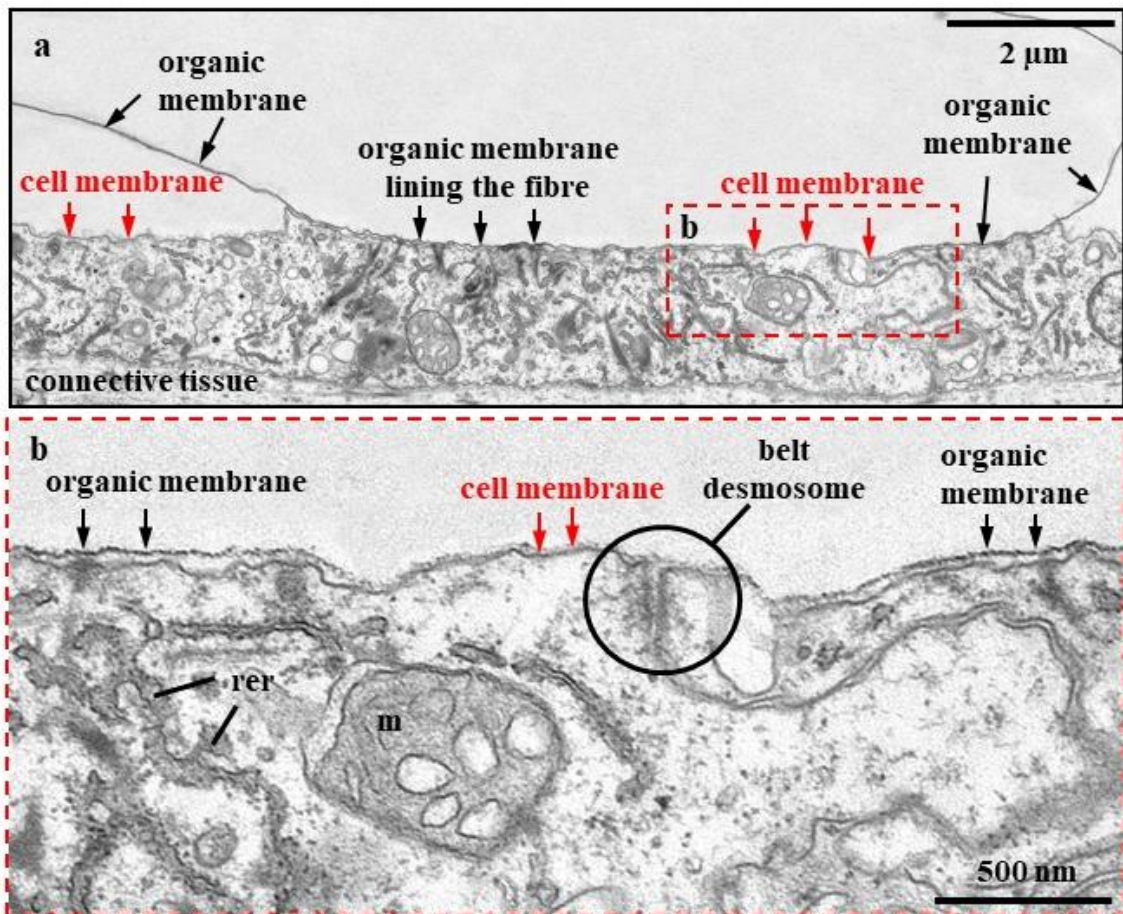


Figure 2.2.5. TEM micrographs of chemically fixed and decalcified contact between epithelium and shell calcite in modern *Magellania venosa*. **a**, Mineral formation ceases with the secretion of an organic membrane covering the proximal, convex part of the fibre (black arrows). At these sites, we see two membranes: (i) the apical cell membrane of the attaching OME cell (red arrows), and (ii) the organic membrane lining the basal portion of the fibre (black arrows in **b**). **b**, Site of active fibre secretion, there is only one membrane present and visible, namely the apical membrane of the OME cell (red arrows in **a** and **b**), which is tightly attached to the calcite of the forming fibre. Neighbouring cells are connected to each other by belt desmosomes. Note the absence of tonofilaments in cells below those parts of the fibre that are actively secreting. rer: rough endoplasmatic reticulum, m: mitochondria.

Apical membranes of OME cells are always present in the investigated samples, in contrast to membrane that lines the basal (proximal), convex surface of fibres. We find regions where the organic membrane lining at the basal (proximal) surface of the fibre is lacking (red arrows in Fig. 2.2.6a), is incomplete (Figs. 2.2.5 and 2.2.7), or is fully developed (black arrows in Fig. 2.2.6b). When membranes are present, apical cell and organic membranes, at the basal surface of the fibres, OME cells are attached to the organic membrane of the fibres via apical hemidesmosomes (green arrows in Fig. 2.2.6b). At sites where the organic membrane at the proximal, convex surface of the fibre is lacking, OME cells do not contain any hemidesmosomes or tonofilaments (Figs. 2.2.5b, 2.2.6a). At these sites, mineral transport from OME cells to adjacent fibres, thus active secretion, is a process still in progress. Analysing an epithelial length of 189 μm we find that 14 regions with a total length of 98 μm are attached to the shell via hemidesmosomes and 10 regions with a total length of 91 μm are not (Fig. S2.2.5-c).

Thus, at a given time, about 52 % of the OME is not secreting mineral and only a maximum of about 48 % of the OME is involved in fibre mineralization.

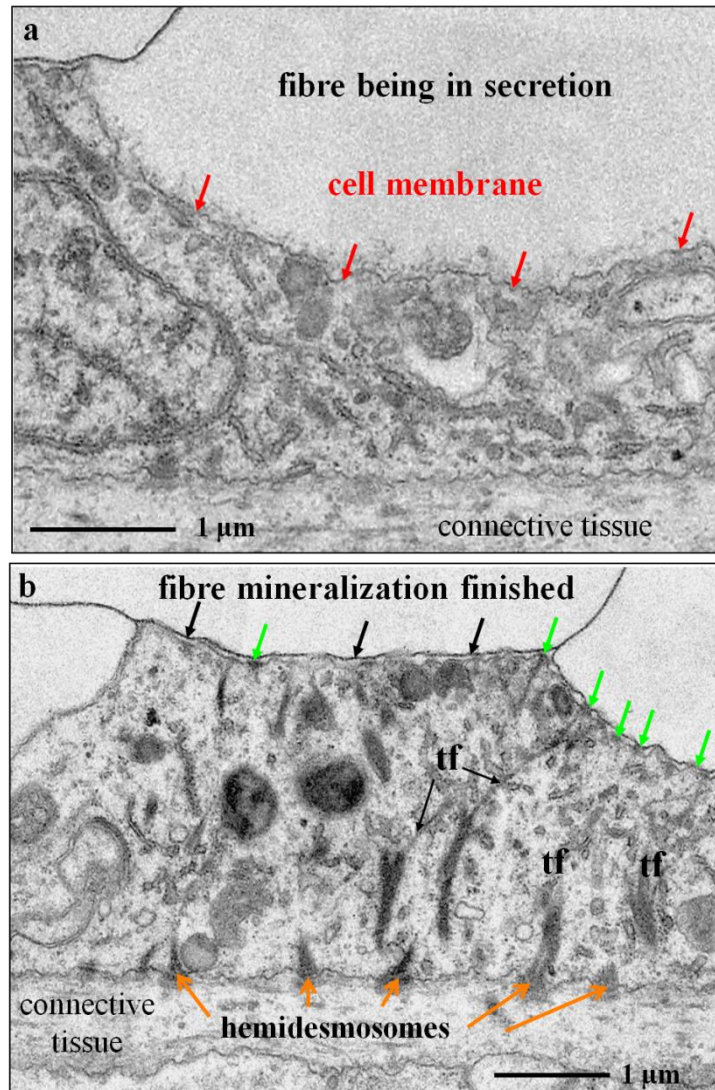


Figure 2.2.6. TEM micrographs of chemically fixed and decalcified contact between epithelium and fibre calcite in modern *Magellania venosa*. Samples were taken from the central region of the shell. **a**, With ongoing mineralization, the membrane lining the proximal, convex part of the fibre is not yet developed (red arrows). **b**, Apical cell membrane attached to organic membranes of the fibres by apical hemidesmosomes (green arrows), the latter being connected to basal hemidesmosomes (orange arrows) via tonofilaments (tf). Cells below fibres in the process of active mineral secretion do not contain any tonofilaments.

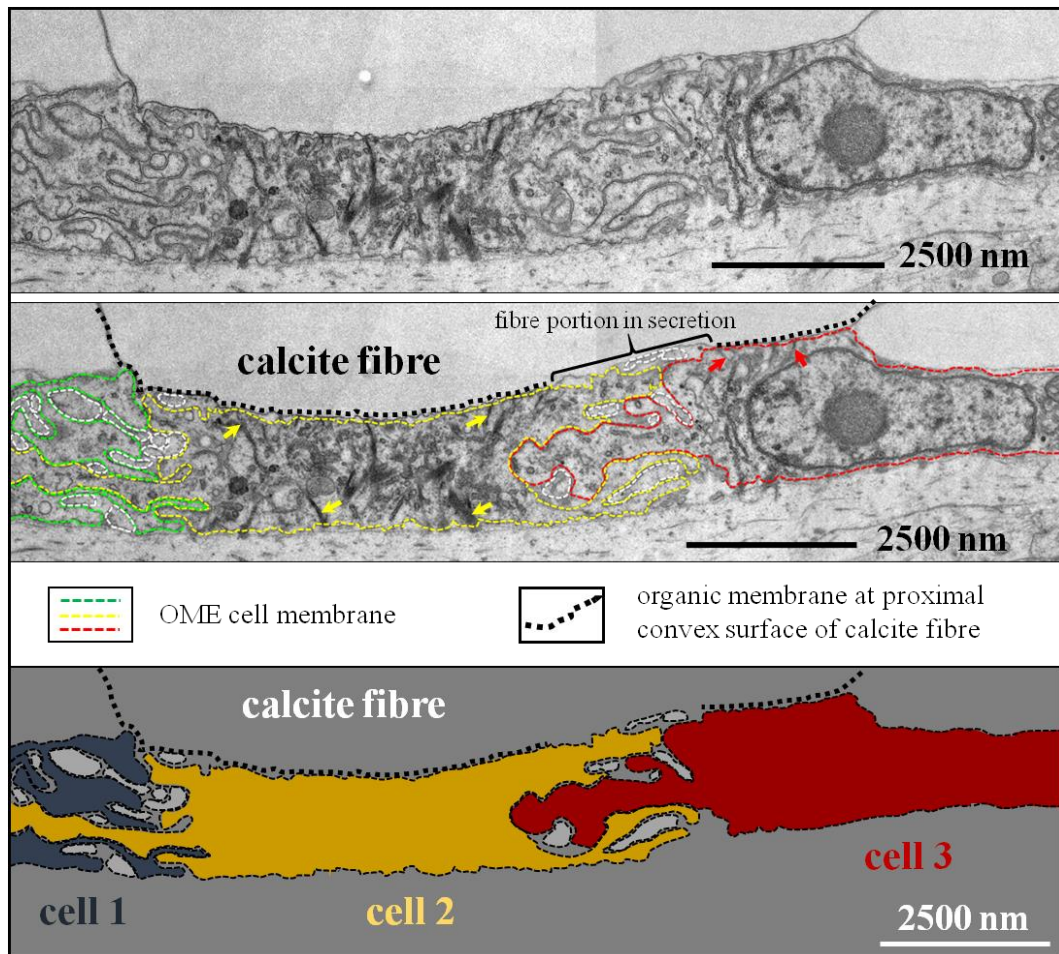


Figure 2.2.7. TEM micrographs and deduced schematic showing the interlinkage of three cells below an almost fully secreted fibre. Well visible are tonofilaments within cells 2 and 3 (yellow and red arrows) that connect the apical cell membrane to the organic membrane at the proximal, convex side of the fibre by hemidesmosomes.

In contrast to observations by Williams and co-workers (Williams, 1966, 1968a, 1968b, 1968c, 1997 and Williams et al 2000), we do not find a one-by-one relationship between epithelial cells and fibres. Instead, we often observe either one cell below two or more fibres or interdigitating epithelial cells below one fibre (Fig. 2.2.7). In regions where the organic membrane at the proximal, convex side of the fibre is not fully developed, cross sections through fibres reveal that secretion of the organic membrane starts at the two lateral corners of the fibre (Fig. 2.2.5a) and progresses from here until the proximal, convex surface of the fibre is fully covered with an organic lining. The formation of the basal membrane lining at the convex side of the fibre represents the terminal step in fibre secretion. It also separates the outer mantle epithelium cell from the compartment in which the fibre is mineralized. Where the fibre basal membrane is absent, the compartment in which calcite mineralization takes place is in direct contact with cell membranes, such that either by pumps or ion exchange mineral components can be transported into the compartment of calcite crystallization.

2.2.4. Discussion

*Fibre secretion and microstructure generation in *Magellania venosa**

Elongated, cylindrical mineral units are structural elements in bivalve, gastropod and brachiopod shells and are either prismatic-columnar, foliated, fibrous or acicular in shape (e.g. Carter et al., 1990a, 1990b and 2012). Even though prismatic-columnar, foliated and acicular microstructures prevail, in some classes of the phyla Mollusca and Brachiopoda assemblies of fibres are of major importance to the overall structure of the hard tissue and may constitute entire shell layers. Fibrous microstructures prevail in the shell of Mytiloidea and Cavolinioidea (Mollusca) and in Rhynchonellata and Terebratulida (Brachiopoda). In most cases fibres are made of calcite (with the exception of the shells of the marine cavolinioidean gastropods, where they are made of aragonite) and vary in shape and dimension depending on the taxa.

Rudwick (1959 and 1970), Rosenberg (1988) and Rowel and Grant (1987) described shell architecture and growth in modern and fossil brachiopods. Williams and co-workers (Williams, 1953, 1966, 1968a, 1968b, 1968c and 1997; Williams et al., 2000) investigated brachiopod shell mineralization and hypothesized from SEM and TEM observations that (i) the same cell of the outer mantle epithelium lobe is able to perform different secretory tasks and secretes sequentially all layers of the shell, (ii) based on similar cross-sections between fibre and outline of the cell, a fibre is formed by one cell only, and (iii) each fibre is entirely encased by an organic membrane.

In our study, we did not observe any features to support these findings. Instead, we observed that near the commissure, the OME consists of many cell layers, while, further away towards central shell portions, OME cells form a single layer (for a detailed study see Simonet-Roda et al., 2019). We did not find any similarities in cross-section dimensions between cells and fibres. Cross sections of OME cells varied and we observed roundish as well as elongated cross-sections of mantle epithelial cells (Simonet-Roda et al., 2019). Instead, we found that neighbouring cells, each of them attached to the same fibre cooperate in fibre secretion (Simonet-Roda et al., 2019) (Fig. 2.2.7 this study and Simonet-Roda et al., 2019). We further observed that epithelial cells are only in contact with the proximal, convex side of the fibre and never in contact with their concave sides (not even in puncta). Thus, the membrane, that is formed in the final step of fibre secretion, is exclusively deposited onto the basal, convex surface of a fibre. It is the matrix membrane located between fibres, or the extracellular matrix within the shell (Figs. 2.2.5a, 2.2.6b, S2.2.1b, S2.2.2f, S2.2.3a). The interlocked packing of fibres with their concave-convex morphology leads to the perception that each fibre is sheathed by an individual membrane. In modern brachiopod shells, only one of the four surfaces of any individual fibre is lined by an organic membrane.

Most biological as well as bioinspired structural materials are composites of soft and hard components. They consist of a soft polymer scaffold that is reinforced by hard minerals (in the case of biological hard tissue) or/and ceramics (in the case of biomimetic/bioinspired hard materials). Even though biological and biomimetic hard tissues share this basic material property, their mode of fabrication is quite distinct. Synthetic composites formed by freeze-casting have structures, architectures and even material properties that are to some extent comparable to those of biological composites (Deville et al., 2006; Corni et al., 2012; Wegst et al., 2015). However, a basic difference unique to biologic composites is that fabrication of synthetic composites occurs in at

least two steps. First, the scaffold is formed and, in a subsequent step, the scaffold is reinforced with another material (Deville et al., 2006; Wegst et al., 2015) (Figure 1 in Deville et al., 2006, Figure 5 in Wegst et al., 2015). The generation of biological hard tissue follows a different pathway. It is a layer-by-layer formational process comprising the sequential deposition of mineral and, when and where needed, secretion of a biopolymer membrane, or vice versa. The latter are, for example, the polymer lining at the convex surface of a brachiopod fibre at termination of fibre formation (this study) or an interlamellar or surface membrane during molluscan nacre growth (Cartwright and Checa, 2007; Checa, 2018).

When brachiopod fibre and nacreous tablet formation are compared, significant differences emerge in biopolymer/mineral deposition and, hence, microstructure generation. In the case of modern brachiopod fibres, during secretion, mantle epithelium cells are always in direct contact with the mineral (this study), whereas in molluscs the nacreous tablets are never in direct contact with epithelial cells. There is always an interlamellar (in bivalves) or surface (in gastropods) membrane between secreting mantle cells and the growing aragonite platelets (Checa, 2018 and references therein). In bivalve nacre, the aragonite is always deposited between a few (two or three), and in gastropod nacre even between many (a few tens) interlamellar membranes (Figures 7A, 7B, 7F, 7G in Checa, 2018). When brachiopod fibres form, secretion of the biopolymer membrane covering the convex surface of the fibre is the last and *terminal step in fibre growth*. In contrast, when nacre forms, *aragonite tablet formation is started* with the consecutive self-assembly by liquid crystallization of interlamellar membranes. This leads to the formation of compartments that become successively infiltrated by aragonite and ultimately filled with nacreous tablets (e.g. Figures 7A, 7F, 7C in Checa, 2018 and references therein). Accordingly, we find modern brachiopod shell and molluscan nacre development as two divergent microstructure generation processes (Fig. S2.2.7a and Checa, 2018). One is biologically controlled through direct cellular contact and activity with the mineral as it is the case for brachiopods, and physically controlled through the self-organization of extracellular matrix membranes as it is the case for molluscan nacre (this study, Fig. S2.2.7a and Checa, 2018).

In summary, in many man-made biomimetic composites the eventually mineralized organic matrix is fully developed prior to mineral infiltration. Formation of molluscan nacre resembles to some extent the formation of biomimetic composites, as it occurs through progressive mineralization of a preformed biopolymer matrix. However, nacre growth is a dynamic process as the mineralization front advances with ongoing shell growth. During shell growth, extracellular matrix formation progresses steadily and is successively mineralized. Brachiopod fibre formation is a strictly layer-by-layer deposition process, where both, secretion of the mineral and the biopolymer is controlled and co-ordinated by mantle epithelial cells (Fig. S2.2.7a).

Fibre shape generation in *Magellania venosa*

Brachiopod fibrous layer microstructure, such as fibre morphology and their arrangement in stacks, is characteristic of modern terebratulide and rhynchonellide brachiopod shells (see the compilation of Ye et al., 2018a and 2018b). It differs from that in other biological hard tissues, for example, calcite fibres in *Mytilus edulis* shells (Fig. S2.2.6). In the latter, fibre shape is more cylindrical and the mode of interlocking is less regular (Fig. S2.2.6b, Griesshaber et al., 2013). The mode of assembly of fibres in modern brachiopod shells shows similarities to the “brick-wall” arrangement of

nacreous tablets in bivalve nacre (Fig. S2.2.7b). Hence, the staggered, “brick-wall”, organization of basic mineral units, irrespective of these being tablets or fibres, is obviously a type of microstructure that is of high value to many shelled organisms and was and is utilized in very different aquatic habitats. Furthermore, it was developed within the geologic record by many organisms of different phylae. Hence, basic mineral unit (fibre, tablet) morphology and mode of interlinkage is essential to the organism, as an adequately constructed shell guarantees protection of the soft tissue and, thus, survival of the organism in its chosen habitat (e.g. Wählich et al., 2014).

Observations on the unique morphology of brachiopod fibres led us to develop a model for fibre shape generation (Fig. 2.2.8) and fibre elongation (Fig. 2.2.9) for the shell of *Magellania venosa*. This model may be applicable to other modern and fossil terebratulide and rhynchonellide brachiopod species with a fibrous microstructure shell. Our model is based on the following observations: (i) only about 50% of the epithelium secretes mineral at any given time as the remaining part of the epithelium is tightly attached to the shell via hemidesmosomes and therefore cannot secrete any mineral. (ii) The extrapallial space either does not exist or is very narrow and indicates that mineral secretion is under tight cellular control. (iii) At large epithelial lengths, sites of mineral secretion alternate with sites that do not secrete any mineral. (iv) Only the convex part of any individual fibre is covered with an organic membrane. (v) Secretion of the organic lining of the proximal convex surface of the fibre proceeds from the sides to the central part.

Fibre formation starts with the disintegration of apical hemidesmosomes and the detachment of a small region of the outer mantle epithelium from the organic membrane lining, a previously secreted and finished portion of a fibre (black arrows in Fig. 2.2.8, sketch 1). This induces mineral accretion at this site by the underlying cell or cells. In cross section, this detached region appears to be small at the beginning. However, it increases in size and thickness with progressive fibre growth (Fig. 2.2.8, sketch 1). Once the fibre has reached its full width, the underlining epithelial cells start with the secretion of the membrane that lines the basal surface of the fibre, and it starts at the corners of the growing fibre. With ongoing secretion, the proximal convex surface of the growing fibre is lined with a membrane until full coverage is achieved of the convex fibre surface (blue arrows in Fig. 2.2.8, sketch 2). Once the latter is completed, apical OME cell membrane attaches itself immediately via apical hemidesmosomes to organic membrane at the proximal side of the fibre (Fig. 2.2.8). Even though the sites between the epithelial cell membrane are still in direct contact with the calcite of the fibre and carry on with mineral secretion (Figs. 2.2.5a, 2.2.7, 2.2.8 sketch 2). The attachment of mantle epithelia to membrane portions at the proximal convex surface of the fibres is essential for stabilization of the whole secretion system. This is essential for fibres and sections that are still actively in the secretion process. Additional proof for the above described model of fibre growth was observed AFM images. The striation patterns observed on cross-sections of transversely and longitudinally cut fibres (white arrows in Fig. 2.2.2a) supports the incremental addition of mineral to the growing fibre by successively retreating OME cells. Mineral secretion ceases when the organic membrane forming at the two corners of a fibre merges (Figs. 2.2.5, 2.2.7, 2.2.8 sketch 2), and the membrane lining fully covers the proximal, convex fibre surface.

We did not observe a one-to-one relationship between epithelial cells and calcite fibres, hence, each epithelial cell may contribute to the formation of many fibres when the shell grows in thickness. Figure 2.2.9 shows a model for fibre elongation and depicts

a sequence of four moments in time (Fig. 2.2.9 sketches 1-4). The model emphasises how individual fibres are formed by many cells with each cell being engaged in the secretion of just a short segment of a fibre (e.g., Fig. S2.2.5). We depict three individual cells (A-C in Fig. 2.2.9) contributing from right to left to the elongation of three different fibres. In our model, individual epithelial cells do not move along the inner shell surface, nor does our model imply sliding of the cells as fibre grows across the shell. Instead, elongation of fibres is brought about by repeated changes in sites where (i) regions of a cell secrete the organic membrane at the proximal, convex surface of a fibre (blue lines in Fig. 2.2.9), (ii) stay attached to it and (iii) elongate the fibre by mineral secretion after detachment from the organic membrane.

Hence, when the shell grows in thickness, each epithelial cell contributes to the formation of many fibres and cooperates with its neighbours. In the native state, cells assume a near hexagonal pattern, so that each cell has to cooperate with up to 5 neighboring cells and, thus each cell is able to contribute to the formation of more than two fibres at a given time. Furthermore, each cell simultaneously can secrete calcium carbonate as well as biopolymers; hence, there are areas of a cell that secrete calcium carbonate, while other regions of the same cell produce organic material. The extent of these carbonate and biopolymer secreting regions changes with time during the secretion of brachiopod fibres.

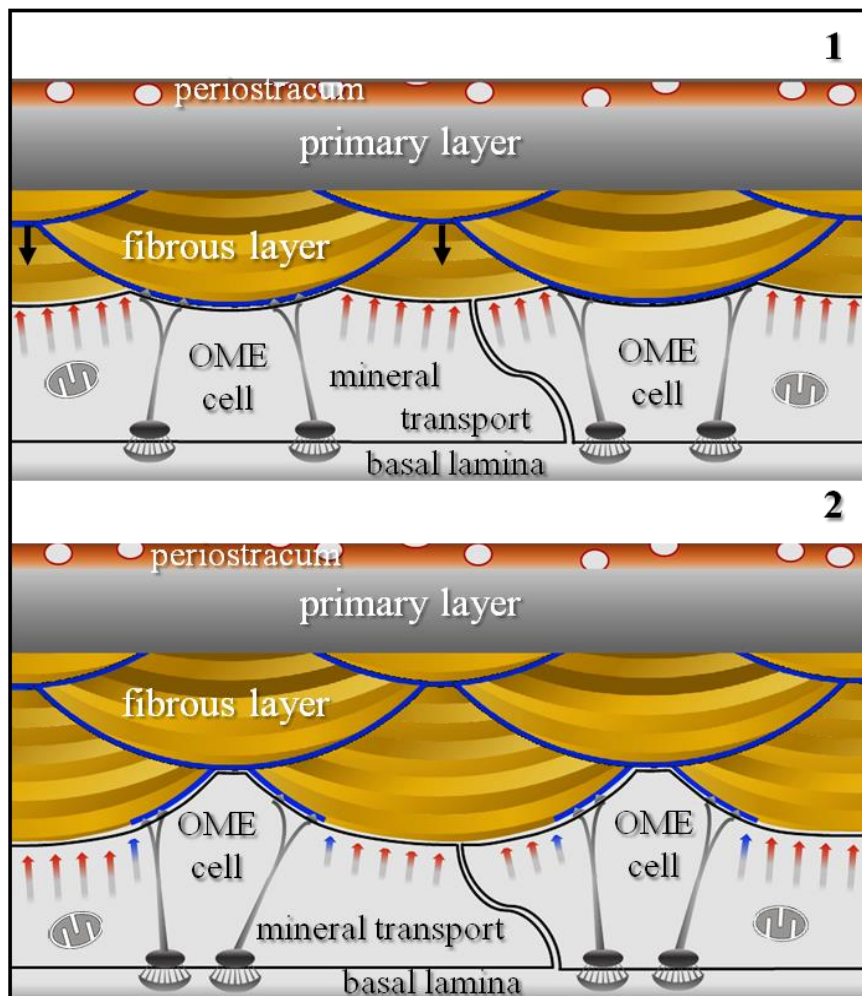


Figure 2.2.8. Schematic model illustrating calcite fibre shape formation for terebratulide and possibly rhynchonellide brachiopods. We see a stack of transversely cut fibres. Prior to fibre

secretion OME cell membranes are in close contact with the organic membrane lining present along the proximal surface of fibres. Detachment of epithelial cells from this membrane lining induces mineral secretion and starts fibre growth (black arrows in schematic 1). When fibres have reached their full width, OME cells start to secrete the organic membrane lining (blue arrows in schematic 2), and when finished, will completely line the basal convex part of the fibre (blue stars in schematic 2).

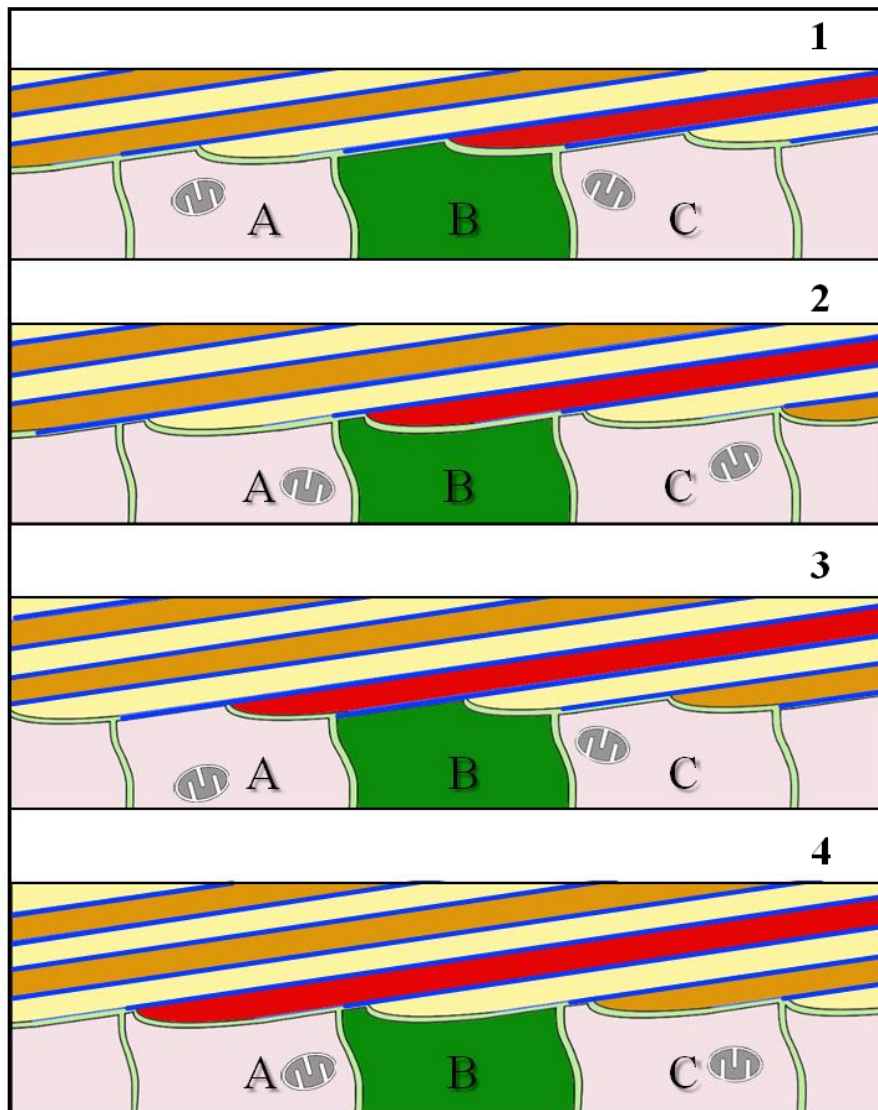


Figure 2.2.9. Schematic model illustrating calcite fibre elongation for terebratulide and rhynchonellide brachiopods. A stack of longitudinally cut fibres is shown. Fibre growth occurs through the coordinated interaction of neighbouring cells (A to C). These are stationary and secrete both, the organic basal lining as well as the calcite of the fibre, and this in the required proportion necessary for the developing fibre (stages 1 to 4). Elongation of fibres takes place by repeated changes in the position of cells relative to fibres: (i) attached either to the organic membrane lining the convex surface of the fibre or (ii) to the calcite of the fibre. The organic membrane lining the fibre is indicated with blue lines. Due to the lack of a one-by-one relationship between epithelial cells and calcite fibres, as the shell grows in thickness, each epithelial cell contributes to the formation of more than one fibre and secretes both calcium carbonate and organic material at different portions.

2.2.5. Conclusions

Our results show that fibre secretion and fibre shape formation in the modern brachiopod *Magellania venosa* is a dynamic process. It requires a sequence of actions induced and coordinated by outer mantle epithelium cells (OME) in close contact with the forming fibre.

We reach the following conclusions for the development of calcite fibres in the shell of the modern brachiopod *Magellania venosa*:

1. It is shown for the first time that extrapallial space between the fibres and the outer mantle epithelium is either non-existent or is extremely narrow and only a few nanometers wide. This indicates that fibre formation in *Magellania venosa* is under tight cellular contact and control.
2. More than one cell may contribute to the formation of a fibre at the same time; hence, fibre secretion, growth and shape generation requires communication of adjacent cells.
3. The extracellular organic membrane is secreted only onto the proximal, convex surface of a fibre.
4. Fibres are not individually and fully sheathed by separate organic membranes.
5. Secretion of calcite by epithelial cells occurs only at sites where the extracellular organic membrane at the proximal, convex surface of the fibre is absent, and fibres consist of nanometric biocalcite crystallites (NBC).
6. Once the extracellular membrane at the base of fibres is secreted, cells of the outer mantle epithelium are attached to these by apical hemidesmosomes. This keeps the OME close to the shell and stabilizes those fibre regions that are still actively secreting.
7. A brachiopod fibre is formed by a sequence of processes occurring at the apical OME cell membrane, by (i) local detachment of epithelial cell membrane from the organic membrane of previously formed fibres, (ii) onset of secretion of calcite at these sites, (iii) organic membrane formation along the proximal, convex side of the forming fibre during achievement of the full width of the fibre, (iv) start of membrane secretion at the corners of fibres progressing towards the centre of the fibre, (v) attachment of the cells via apical hemidesmosomes to newly formed organic membrane, and by (vi) suspension of calcite secretion at sites where the proximal, organic membrane of the fibre is fully developed and the apical cell membrane is attached to the latter with apical hemidesmosomes.
8. The fibrous layer of terebratulide brachiopod shells is a fibre composite material that has an overall plywood-like organization with the basic mineral units, the fibres, being assembled in a microstructure resembling the ‘anvil-type’ arrangement of calcite fibres in bivalves as well as the ‘brick wall’ arrangement of aragonite tablets in bivalve nacre.

2.2.6. Author’s Contribution

MSR and AZ performed all EM analytical work: biochemical preparation, FE-SEM, TEM, imaging and morphometry data analysis. UR helped with TEM imaging and evaluation of morphometric data sets. MSR performed all AFM imaging. EG, AZ, MSR wrote the manuscript. UB, AC, WS, AE, XY contributed to the final version of the manuscript. VH, JL, DH took care of sampling, transport and culturing of live *Magellania venosa*. The authors declare no competing interests.

Data availability

The datasets generated during and/or analysed during the current study are available from the corresponding author on request.

Acknowledgements

We thank Renate Kunz and C.H. of the Central Facility for Electron Microscopy of Ulm University for technical support and assistance. This is a BASE-LINE Earth project supported by the European Union's Horizon 2020 research and innovation program under grant agreement No. 643084.

Supplementary material

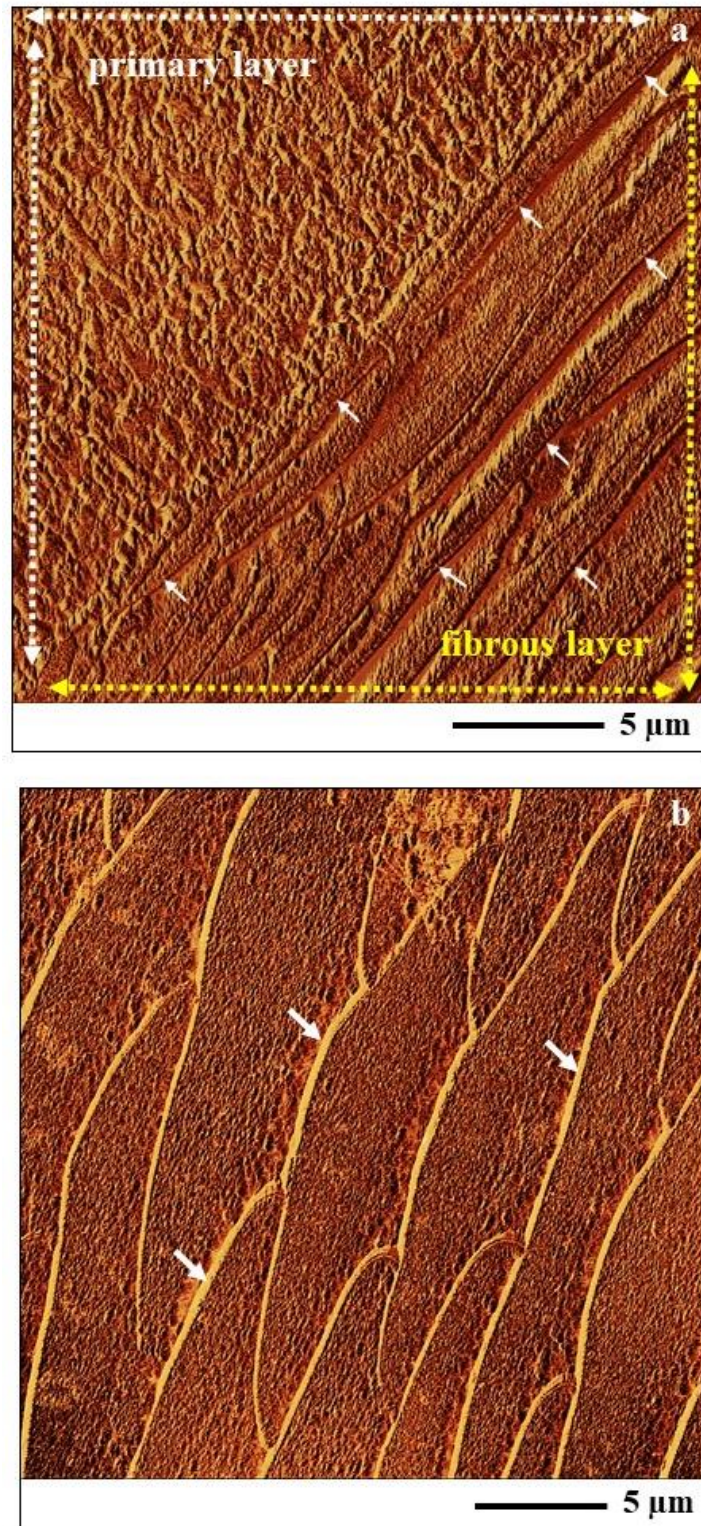


Figure S2.2.1. AFM lateral deflection images showing structural characteristics of the primary and the fibrous shell layers of the modern brachiopod *Magellania venosa*. Well visible is the smooth transition from the primary into the fibrous shell portion (a) as well as the organic membrane lining the proximal, convex surface of fibres (white arrows in a and b).

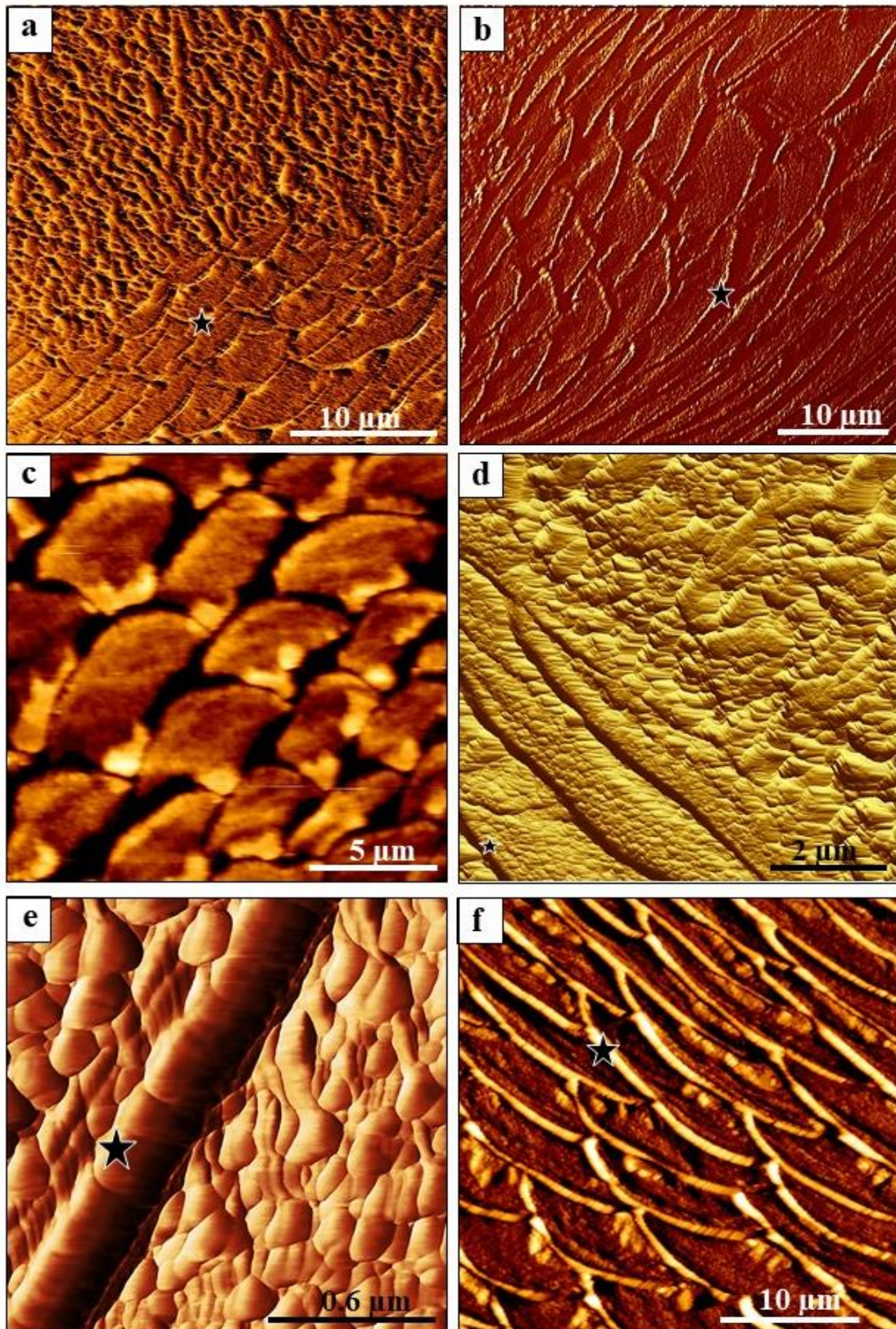


Figure S2.2.2. AFM lateral (a, b and d to f) and vertical (c) deflection images of the primary shell layer (a), the transition from the primary into the fibrous shell layer (a) and of stacks of fibres (a to f) within the fibrous shell layer. Corresponding vertical deflection images are shown in 1b, 2 and 3. The convex, proximal part of each fibre is always lined by an organic membrane (black star in a, b, d, e, f).

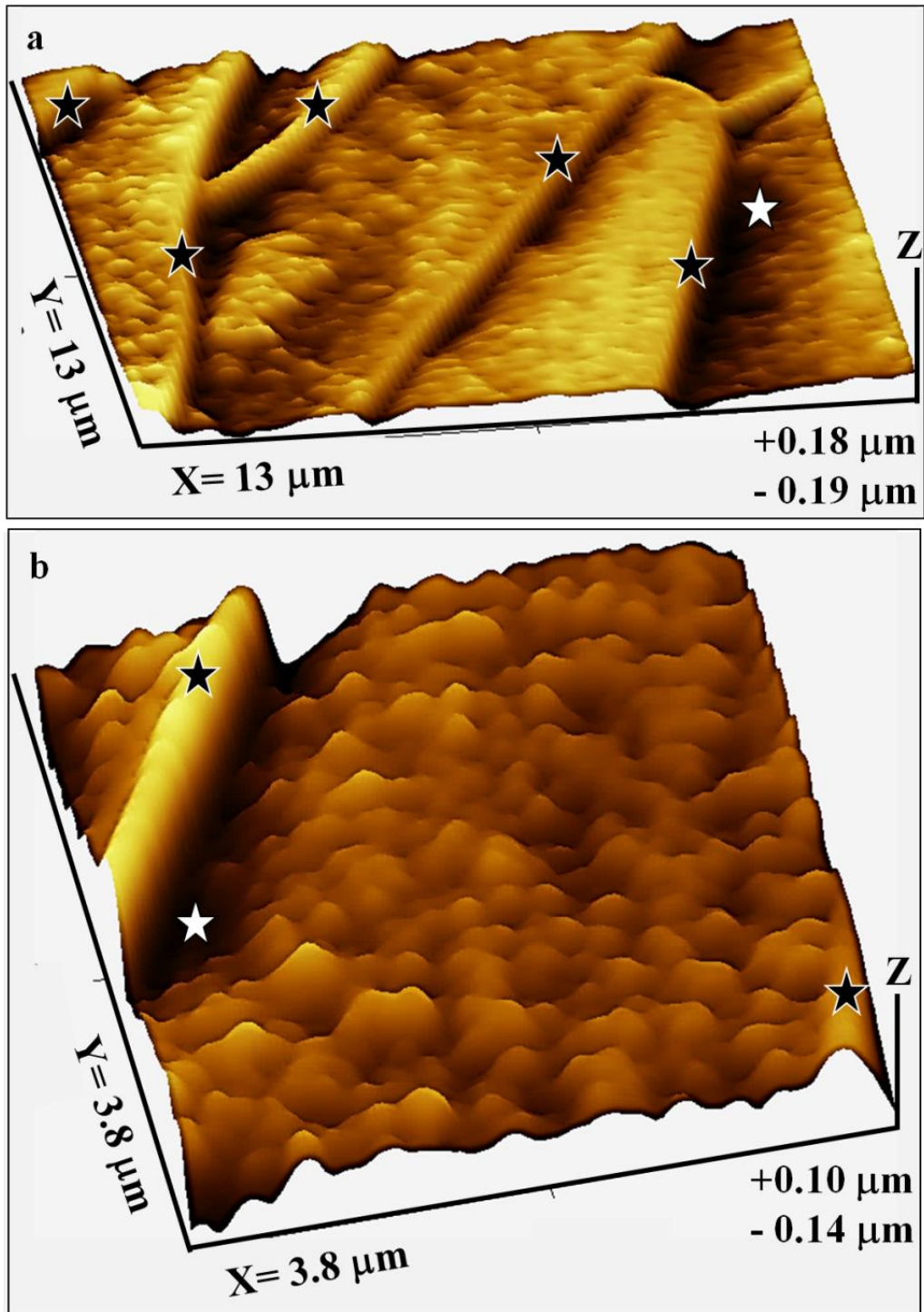


Figure S2.2.3. 3D representation of AFM height trace images of stacks of longitudinally cut calcite fibres. Well visible is the organic membrane lining at the proximal, convex part of a fibre (black stars in a, b), as well as the absence of any organic lining (membrane) along the apical portion of a fibre (white star in a, b). Instead, calcite fibres are not fully sheathed by an organic membrane, but are partially covered.

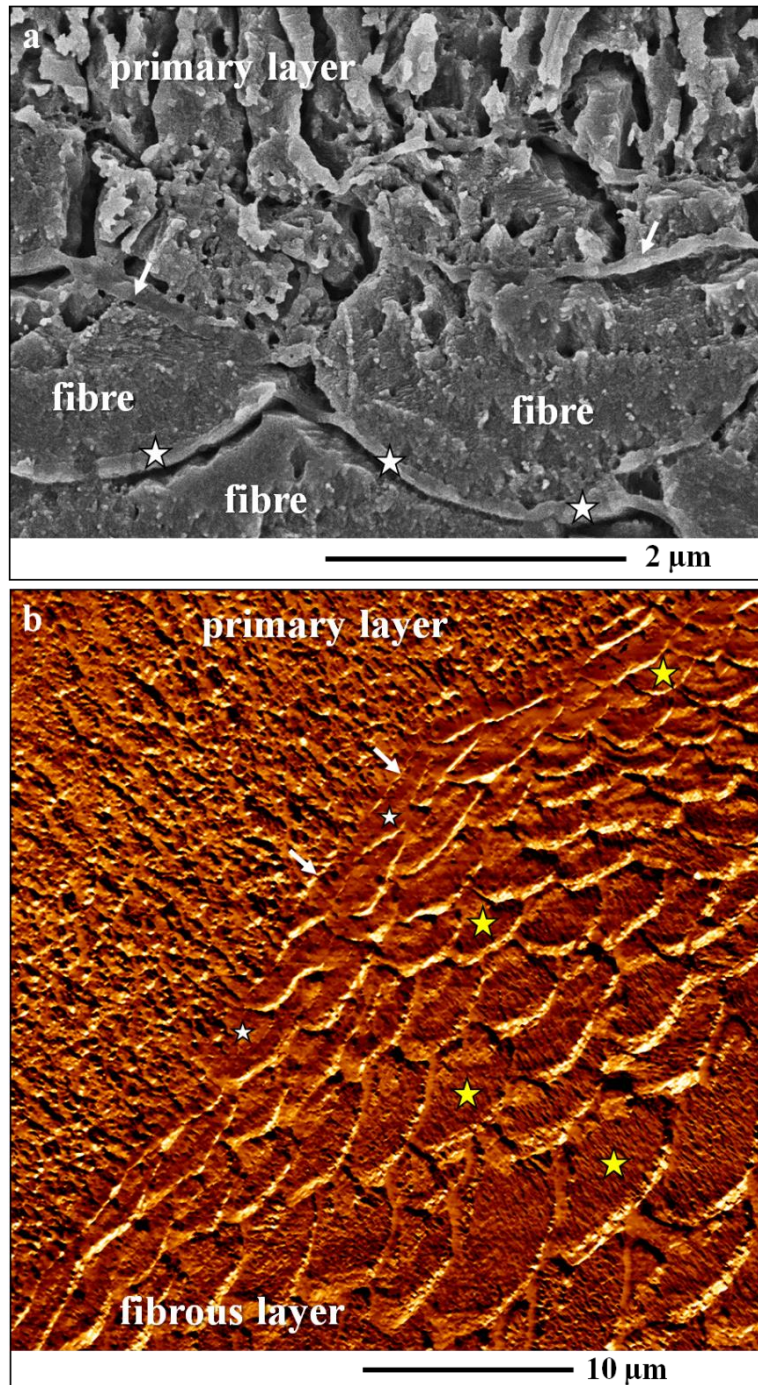


Figure S2.2.4. FE-SEM (a) and AFM lateral vertical deflection (b) images of primary and fibrous shell portions of *Magellania venosa*. The sample in (a) was microtome cut and polished, subsequently etched for 180 seconds at a pH of 6.5 and critical point dried. Both images depict the transition from the primary to the fibrous shell layer. We do not see a continuous membrane between the two shell layers; the transition from one layer into the other appears to be gradual. However, we see occasional inclusions of short sections of biopolymer membranes (white arrows in a and b) within the transitional zone from one shell layer to the other. White stars in (a) point to the proximal organic lining of the fibres. At the transition from the primary to the fibrous shell portion the shape of the fibres is not well developed (white stars in b). Mature fibres with their characteristic morphology and size appear a few rows away from the transition between the primary to the fibrous shell fabrics (yellow stars in b).

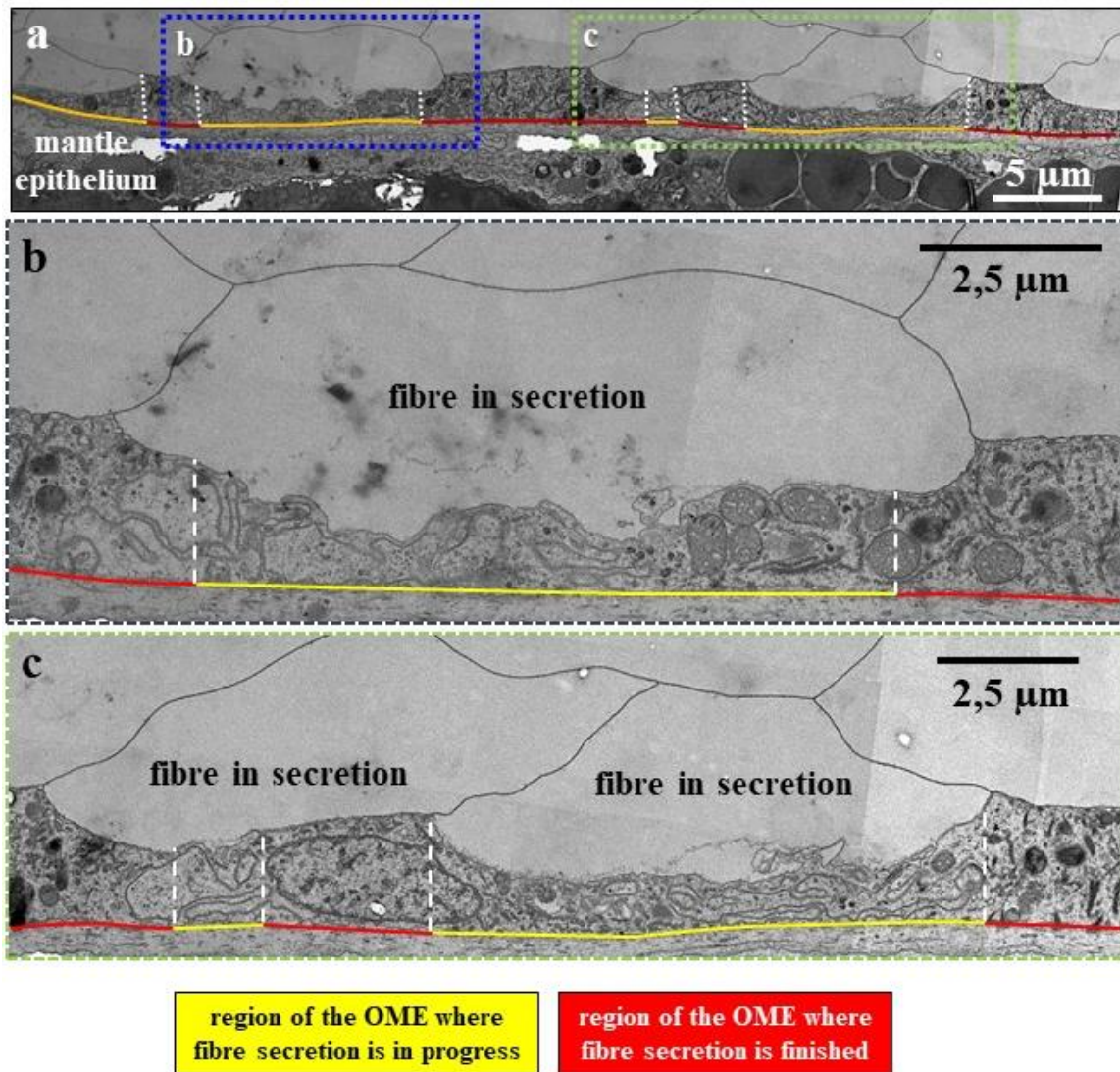


Figure S2.2.5. TEM micrographs of a chemically fixed shell sample from the ventral valve of *Magellania venosa*. **a, b, c**, Alternating shell portions where secretion is completed (indicated with red lines) with fibre portions that are in actively secreting (indicated with yellow lines). Mineral deposition ceases with secretion of the membrane lining at the proximal, convex side of the fibre.

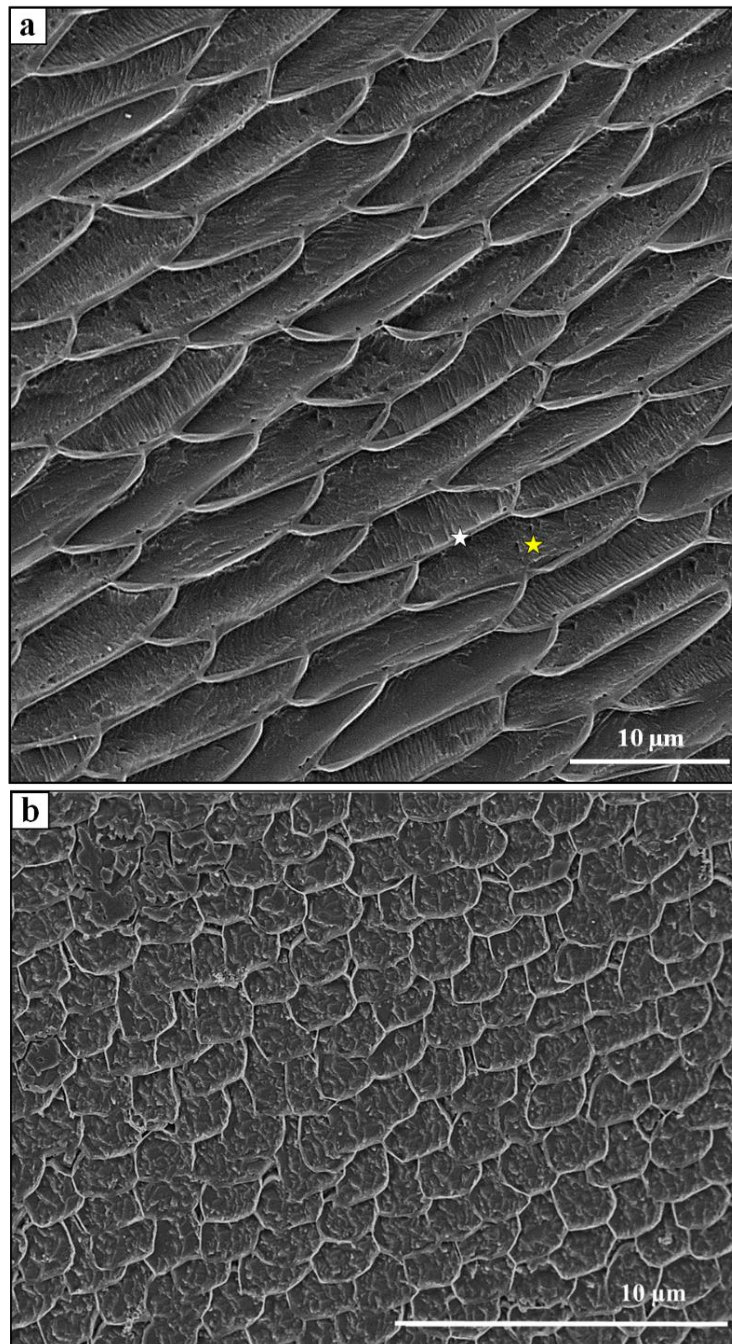


Figure S2.2.6. Mode of fibre assembly into stacks in the shell of the terebratulide brachiopod *Magellania venosa* (**a**), and in the calcitic shell portion of the bivalve *Mytilus edulis* (**b**). The samples were microtome cut and polished, subsequently etched for 180 seconds and critical point dried. Due to the concave-convex morphology of the brachiopod fibre and their interlocked packing into stacks, a biopolymer membrane (white star in a) is always present between two calcite fibres (yellow star in a). This gives the impression that a fibre is surrounded by an organic sheath, however, this is not the case. **b**, Cross-section through a stack of calcite fibres in the calcitic shell layer of *Mytilus edulis*. Fibre morphology, regularity in shape and extent of encasing of the calcite with an organic sheath is significantly different from that in the modern brachiopod *Magellania venosa*.

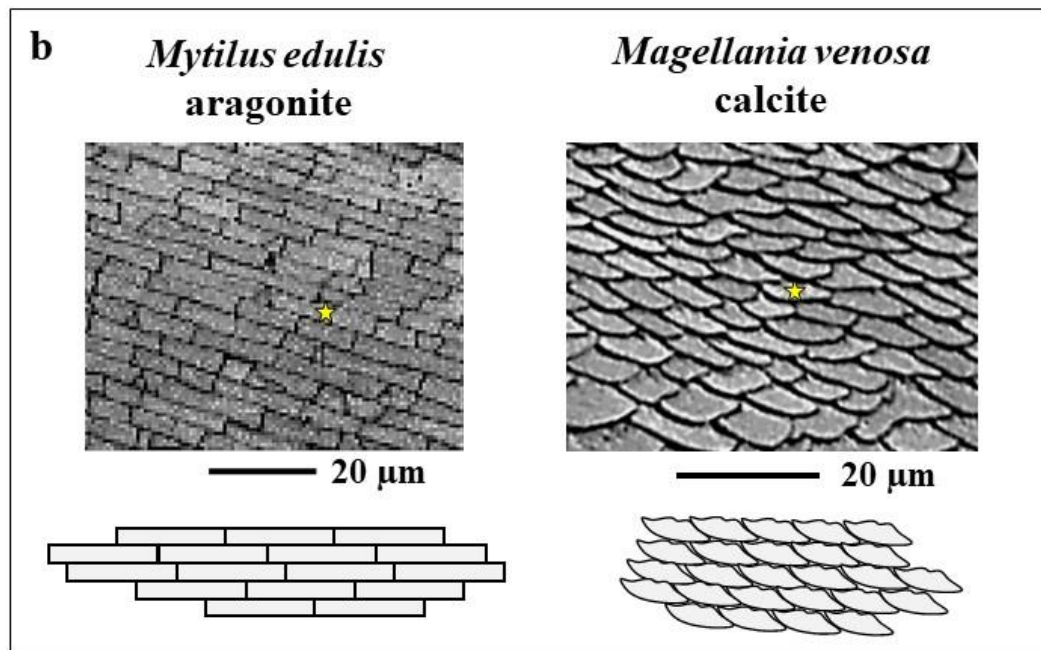
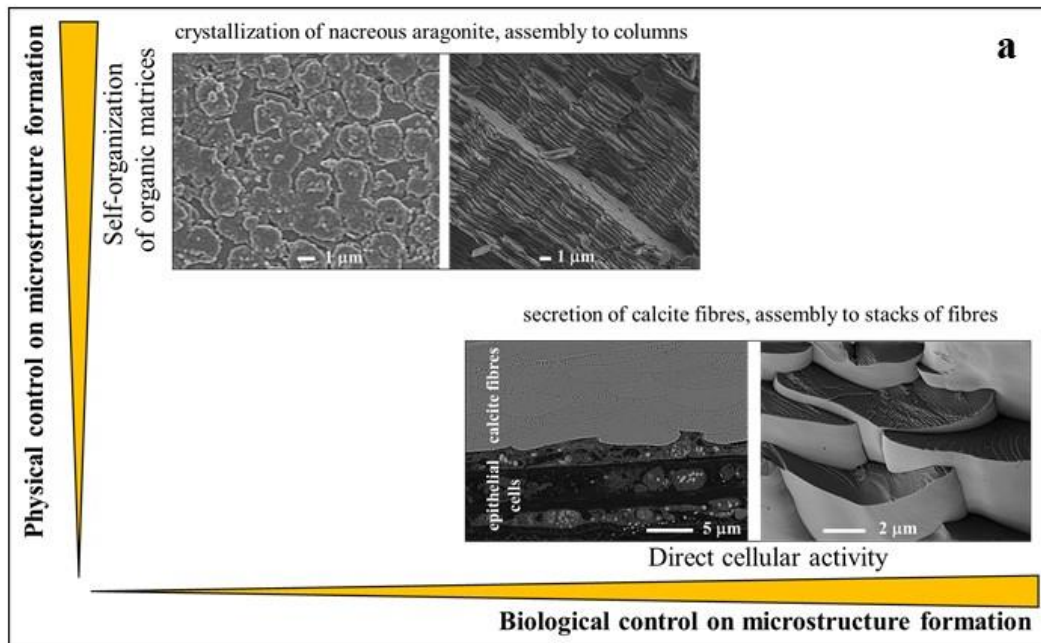


Figure S2.2.7. Processes involved in the fabrication of mollusc nacreous and brachiopod fibrous microstructures. Scheme in (a) is modified after Figure 10 in Checa et al. 2018. a, Whereas the nacreous aragonite mineral assembly takes place in self-organized organic matrices and the mineral unit, and shell microstructure formation is mainly controlled by physical determinants (Checa et al. 2018). Brachiopod shell microstructure formation is mainly biologically controlled as fibre secretion occurs at direct cellular contact. b, EBSD band contrast measurement image and corresponding schematic visualizing the mode of mineral unit assembly and interlocking in bivalve aragonite (*Mytilus edulis* nacreous tablets) and brachiopod calcite (*Magellania venosa* calcite fibres). A “brick-wall” arrangement of mineral units not only occurs in bivalve nacre, it is similar to the stacking mode of calcite fibres in the modern terebratulide brachiopod *Magellania venosa*. Yellow stars in (b) point to the basic mineral unit (tablet, fibre) that was chosen as a model unit for the schematics shown below the EBSD band contrast images.

2.3. The evolution of thecideide microstructures and textures: traced from Triassic to Holocene

ACTION	STATUS	ID	TITLE	SUBMITTED	DECISIONED
	AE: Owen, Alan EIC: Doyle, Peter ADM: Stouge, Svend ADM: Doyle, Peter PROD: Doyle, Peter	0974- LET-OA- 09-20.R1	The evolution of thecideide microstructures and textures: traced from Triassic to Holocene View Submission	09-Dec-2020	22-Jan-2021
	<ul style="list-style-type: none">Accept (22-Jan-2021)				

2.3. The evolution of thecideide microstructures and textures: traced from Triassic to Holocene

Simonet Roda M. *(1), Griesshaber E. (1), Angiolini L. (2), Harper D.A.T. (3), Jansen U. (4), Bitner M.A. (5), Henkel D. (6), Manzanero E. (7), Müller T. (8), Tomašových A. (8), Eisenhauer A. (6), and Schmahl W.W. (1)

1. Department of Earth and Environmental Sciences, LMU München, Munich, Germany
2. Dipartimento di Scienze della Terra "A. Desio", Università degli Studi di Milano, Milano, Italy
3. Department of Earth Science, Durham University, Durham, United Kingdom
4. Senckenberg Forschungsinstitut und Naturkundemuseum Frankfurt, Frankfurt am Main, Germany
5. Institute of Paleobiology, Polish Academy of Sciences, Warsaw, Poland
6. GEOMAR-Helmholtz Centre for Ocean Research, Kiel, Germany
7. Universidad Nacional de Educación a Distancia, UNED Madrid, Spain
8. Geological Institute SAS, Bratislava, Slovakia

*Corresponding author: simonet@lrz.uni-muenchen.de

Abstract

Thecideide brachiopods are an anomalous group of invertebrates. In this study we discuss the evolution of thecideide brachiopods from the Triassic to the Holocene and base our results and conclusions on microstructure and texture measurements gained from electron backscatter diffraction (EBSD). In fossil and Recent thecideide shells, we observe the following mineral units: (i) nanometric to small granules, (ii) acicles, (iii) fibres, (iv) polygonal crystals, (v) large roundish crystals. We trace for thecideide shells the change of mineral unit characteristics such as morphology, size, orientation, arrangement and distribution pattern. Triassic thecideide shells contain extensive sections formed of fibres interspersed with large, roundish crystals. Upper Cretaceous to Pleistocene thecideide hard tissues consist of a matrix of minute to small grains reinforced by acicles and small polygonal crystals. Recent thecideide species form their shell of mineral units that show a wide range of shapes, sizes and arrangements. We find from Late Triassic to Recent a gradual decrease in mineral unit size, regularity of mineral unit morphology and orientation, as well as calcite co-orientation strength. While crystallite co-orientation strength is the highest for fibrous microstructures, it is strikingly low for taxa that form their shell out of nanogranular to acicular mineral units. Our results indicate that Upper Jurassic species represent transitional forms between ancient taxa with fibrous shells and Recent forms that construct their shells of acicles and granules. We attribute the observed changes in microstructure and texture to be an adaptation to a different habitat and life-style associated with cementation to hard substrates.

Keywords: Brachiopoda, shell microstructure evolution, thecideides, calcite crystals, calcite fibre, EBSD

2.3.1. Introduction

In this study, we describe and trace through time the evolution of shell microstructure and texture for a single order of rhynchonelliform brachiopods, the Thecideida. These brachiopods form a very outstanding group within the Phylum Brachiopoda as obvious connections to other rhynchonelliform orders are still equivocal (Dagys 1972; Williams 1973; Frisia 1990; Carlson 2016). Thecideide brachiopods are the last brachiopod order to appear in the fossil record (e.g. Carlson 2016). Extinct and extant thecideide species are small-bodied animals that, with the exception of very few cases (e.g. Backhaus 1959; Krawczyński, 2008), lived and live cemented to hard substrates in cryptic habitats. This life-style and living environment contrasts with that of most other extinct and extant Rhynchonelliformea but it is common in Craniiformea (Williams 1973; Carlson 2016; Baumgarten et al. 2013; Ye et al. 2018a, 2018b).

Even though the literature is replete with studies locating the Thecideida in higher-taxa classifications, their position within the phylogeny of the Brachiopoda as well as the identification of their origin are still unclear. To shed more light on thecideide evolution, previous studies concentrated on (i) shell size and macroscale morphological features (Elliott 1953; Rudwick 1970), (ii) shell structure characteristics (Williams 1973), (iii) the combined interpretation of ontogenetic, morphological and shell structural properties (Baker 1990) and (iv) characteristics of body size (Carlson 1995, 2007). However, even though well executed, none of these studies provided a definitive answer to either thecideide origin or to their phylogenetic relationships with other taxa, resulting most probably from their very complex and diverse evolutionary track. It is, for example, still unclear whether strophomenates, davidsonioids, spiriferides, terebratulides or other brachiopod taxa are the ancestors of the Thecideida (e.g. Pajaud 1970; Grant 1972; Williams 1973; MacKinnon 1974; Baker 1990, 2006; Lüter 2005; Cohen 2007; Carlson 2016).

The studies of Baker (2006) Williams & Carlson (2007) suggest that thecideide shell structures changed over time. This involved: (i.) the loss of fibres, (ii.) restriction of fibres to small and isolated patches in the shell, e.g. to the cardinalia, (iii.) replacement of fibres by arrangements of acicular mineral units. These changes occurred at different rates among the thecideide subfamilies; fibres were suppressed by the Late Jurassic in the Lacazellinae and Thecideinae, but persisted up until the Cretaceous in the Thecidellinae (Baker 2006).

Williams and co-workers referred to the microstructure of thecideide brachiopods as 'Primary-Acicular-Shell-Layer-Type' structure (Williams 1997), a microstructure that is developed in the outermost shell portions of all the other Rhynchonelliformea. According to Williams (1997) the primary shell layer calcite is of nanometric size, has a granular morphology and contrasts significantly in dimension and morphology to other mineral units such as fibres and columns (e.g. Williams 1997; Williams & Cusack 2007). Microstructure and texture measurements carried out with high-resolution EBSD have shown that the primary shell layer of rhynchonelliform brachiopods (e.g. Goetz et al. 2011, and references therein) is neither nanocrystalline nor nanogranular, but consists of large (not nanogranular) interdigitating mesocrystals. These are tens of micrometre-sized dendritic calcite units that, due to their specific dendritic morphology, are interwoven in three dimensions (see Goetz et al. 2011, Figs. 4 and 5). In addition, primary shell layer mineral units of recent rhynchonelliform brachiopods are not encased by organic material, in contrast to the mineral units in the fibrous and columnar

layers (e.g. Griesshaber et al. 2009, Goetz et al. 2009, Goetz et al. 2011, Simonet Roda et al. 2019b). As described in this study and shown by Simonet Roda et al. (submitted), the microstructure and texture of the primary shell layer of the other rhynchonelliform brachiopods is distinct from the microstructure and texture that we find in recent thecideide brachiopod shells. Simonet Roda et al. (submitted) redefined the microstructure of recent thecideide brachiopod shells as a ‘NON-Primary-Layer-Type’ structure. Recent thecideides have heterogranular microstructures, where large crystals with different morphologies are embedded in a matrix of nano- to microcrystallites and organic substance (Simonet Roda et al. submitted).

In this study, we describe the appearance and disappearance of a variety of crystal morphologies in fossil and recent thecideide species and trace shell structure evolution from a microstructural and textural point of view. We base our results on crystal orientation measurements and not only on SEM images of fractured or etched shell surfaces (e.g. Williams, 1973, 1997). By using electron-backscatter diffraction imaging (EBSD), we are able to give an overview of the different types of mineral units that form the shell of the investigated thecideide species, from the Triassic to Recent, and describe the changeover from one mineral unit type to another. In addition, we reveal the different textures of the investigated thecideide species, a study that, to the knowledge of the authors, has not been done yet.

Accordingly, we present here biomineral unit type, size, morphology, orientation, and their distribution pattern within the shell, strength of calcite co-orientation within as well as between mineral units for species of both thecideide superfamilies, the Thecospiroidea and the Thecideoidea; for selected specimens of taxa of the families Thecospiridae, Bactryniidae, Thecidellinidae and Thecideidae. The Thecospiridae, Bactryniidae, Thecidellinidae originated in the Late Triassic, representatives of Thecideidae are present since the Early Jurassic. Thecospiridae and Bactryniidae became extinct in Late Triassic and Late Jurassic respectively, while species of the families Thecidellinidae and Thecideidae are still extant.

2.3.2. Materials and Methods

Materials

In this study we show microstructure and texture results for 11 thecideide brachiopods (Table 2.3.1 and Table S2.3.1) that were chosen from a large set of samples. Each specimen represents a species and a distinct geological time interval between Late Triassic and present (Table 2.3.1 and Table S2.3.1). The illustrated specimens are housed in the collections of Ludwig Maximilian University, Munich (numbers prefixed E, LMU and UF) and Museo di Paleontologia, Dipartimento di Scienze della Terra, Università degli Studi, di Milano (numbers prefixed MPU) (see Fig. S2.3.1). For *Thecidea papillata* and *Lacazella mediterranea* we investigated an Upper Cretaceous and Paleocene as well as an Upper Eocene and Upper Oligocene specimen, respectively.

The shells were cut along the symmetry plane, from the umbo to the anterior shell margin. Special care was taken in order to avoid the investigation of regions of poorly preserved or/and shell. Shell surfaces that were scanned with EBSD were checked, prior to EBSD measurements, for diagenetic alteration with five screening methods: light, laser confocal, cathodoluminescence, SEM microscopy and electron dispersive

spectroscopy (EDS). The last of these was used for the detection of Mn and Fe enrichments within the shells, as these might indicate diagenetically altered shell portions. EBSD measurements were carried out only on those surfaces that showed excellent preservation. With the exception of *Neothecidella ulmensis*, we performed three or four EBSD measurements on each fossil shell and 22 on the shell of the modern thecideid species *Pajaudina atlantica*. As *Neothecidella ulmensis* appears to be a transitional form between fibrous and acicular microstructures we investigated this species in great detail and measured six large EBSD scans, of which we show here four measurements.

Table 2.3.1. Overview of the investigated thecideid species, their age and provenance.

Families	Species	Age	Location
Thecospiridae	<i>Thecospira tenuistriata</i> Bittner, 1890	Late Triassic	Alpe di Specie, Italy
Thecospiridae	<i>Thecospira tyrolensis</i> (Loretz, 1875)	Late Triassic	Alpe di Specie, Italy
Bactryniidae	<i>Bactrynum bicarinatum</i> Emmrich, 1855	Late Triassic	Eiberg, Austria
Thecideidae	<i>Neothecidella ulmensis</i> (Quenstedt, 1858)	Late Jurassic (middle Oxfordian)	Baltów, Poland
Thecideidae	<i>Thecidiopsis digitata</i> (Sowerby, 1823)	Late Cretaceous	Petersberg, Maastricht, Netherlands
Thecideidae	<i>Thecidea papillata</i> (Schlotheim, 1813)	Late Cretaceous	Symphorien, Mons, Belgium
Thecideidae	<i>Thecidea papillata</i> (Schlotheim, 1813)	Paleocene	Ciply, Mons, Belgium
Thecideidae	<i>Lacazella mediterranea</i> (Risso, 1826)	Late Eocene	Dnipropetrovsk, Ukraine
Thecideidae	<i>Lacazella mediterranea</i> (Risso, 1826)	Late Oligocene	Peyrere Aquitaine Basin, France
Thecidellinidae	<i>Thecidellina</i> sp.	Pleistocene	Curaçao, Caribbean
Thecideidae	<i>Pajaudina atlantica</i> Logan, 1988	Recent	Palma, Canary Islands, Spain

Methods

For all analytical techniques performed in this study, the shells were embedded in epoxy resin and sample surfaces were polished with a sequence of five mechanical grinding and polishing steps. The last step was etch-polishing with colloidal aluminium in a vibratory polisher. For the measurements, all samples were coated with 4–6 nm of carbon.

EBSD and EDS measurements and SE, BSE imaging were carried out on a Hitachi SU5000 FE-SEM, equipped with a Nordlys II EBSD detector and an Oxford Instruments 80 mm² X-Max SDD energy dispersive spectrometer. EBSD measurements were carried out with a step size of 0.4 to 0.5 micrometres. Data acquisition and evaluation were achieved with the Oxford Instruments AZTec and CHANNEL 5 HKL software, respectively.

Microstructures are presented with grey-scaled EBSD band contrast measurement and colour-coded EBSD orientation maps, respectively. The colouring code is indicated either in the figure or is stated in the relevant figure caption. Similar colours indicate similar, distinct colours highlight different crystallite orientations, respectively. Band contrast images depict the signal strength of each measurement point. High signal strengths correspond to light grey colours and indicate strong diffraction at the crystal lattice. Faint grey or dark colours are indicative of non-diffracting substances, e.g. polymers, or an overlap of minute crystallites that could not be indexed automatically with the EBSD software.

The *texture* is presented with pole figures that give density distributions of the measured orientation data. For density distributions, we use the lowest possible setting for half width and cluster size: a half width of five and a cluster size of three degrees. The half width controls the extent of the spread of the poles over the surface of the project sphere; a cluster comprises data with the same orientation. Calcite co-orientation strength within as well as between mineral units is derived from density distributions of the measured EBSD data and is given with MUD values. The MUD (multiple of uniform (random) distribution) value is calculated with the Oxford Instruments CHANNEL 5 EBSD software. A high MUD indicates high crystal co-orientation, while low MUD values reflect a low to random crystallite or/and mineral unit co-orientation strength. For further information see Schwartz et al. (2000), Schmahl et al. (2004), Griesshaber et al. (2012) and Griesshaber et al. (2017).

Microstructure determination is based on quantitative results measured with the EBSD detector. Therefore, grain morphology, size, orientation, mode of co-orientation/misorientation, co-orientation/misorientation strengths are based on measurements and not on SEM images. The term 'texture' relates to the varieties of crystal orientations within a material and is illustrated with pole figures. The term 'microstructure' refers to the sum of grains, their sizes, morphologies, modes of interlinkage, co- and misorientations and is highlighted with EBSD maps.

For AFM imaging, shell pieces were cut in longitudinal section from the umbo to the commissure and embedded in epoxy resin. Embedded sample surfaces were polished in 5 sequential mechanical steps down to a grain size of 1 µm. For the final step, etch-polishing was applied for three hours with a colloidal alumina suspension in a vibratory polisher. Subsequently, the samples were washed in Milli-Q water in ultrasonic bath and subsequently rinsed with 80% ethanol.

In order to expose the distribution of biopolymers and mineral units, shell pieces were glued onto aluminium rods. First, even sample surfaces were obtained by cutting and polishing the samples with glass and diamond knives in an ultramicrotome. Subsequently, sample surfaces were etched slightly and organic material was chemically fixed. Simultaneous etching of the calcite and fixation of organic substance was done by using a 0.1M HEPES (pH = 6.5) and 2.5 % glutaraldehyde solution that

was applied to the sample for 180 seconds. Etching and fixation was followed by dehydration in 100 % isopropanol three times and immediate critical point drying. The dried samples were coated for SEM imaging with 6 nm platinum.

A phylogenetic tree was constructed for the Order Thecideida. For this purpose the software TreeSearch (Brazeau et al. 2019) was selected and the data matrix of Jaecks & Carlson (2001) was adopted. The latter was complemented with information on shell microstructure and texture from the taxa analysed for this study and the inclusion of *Neothecidella ulmensis* (Table S2.3.2). For the calculations, we applied implied weighting and chose a default value of 4 for concavity for the Thecideida.

In the text we refer to the term ‘mineral unit’. *Mineral units* in biological structural materials are the biocrystals; in thecideide brachiopod shells biocrystals/mineral units are *fibres, acicles granules, grains*. In this study we use terms such as *minute, small, large* mineral units. A *minute* mineral unit is a sub- to very few micrometre-scale entity, *small* mineral units have 2D extensions of very few micrometres, *large* mineral units have 2D sizes of very few tens of micrometres.

2.3.3. Results

Figure 2.3.1 presents the stratigraphical range and the thecideide species that were investigated in this study. EBSD results are shown in Figs. 2.3.2-10, S2.3.1-16.

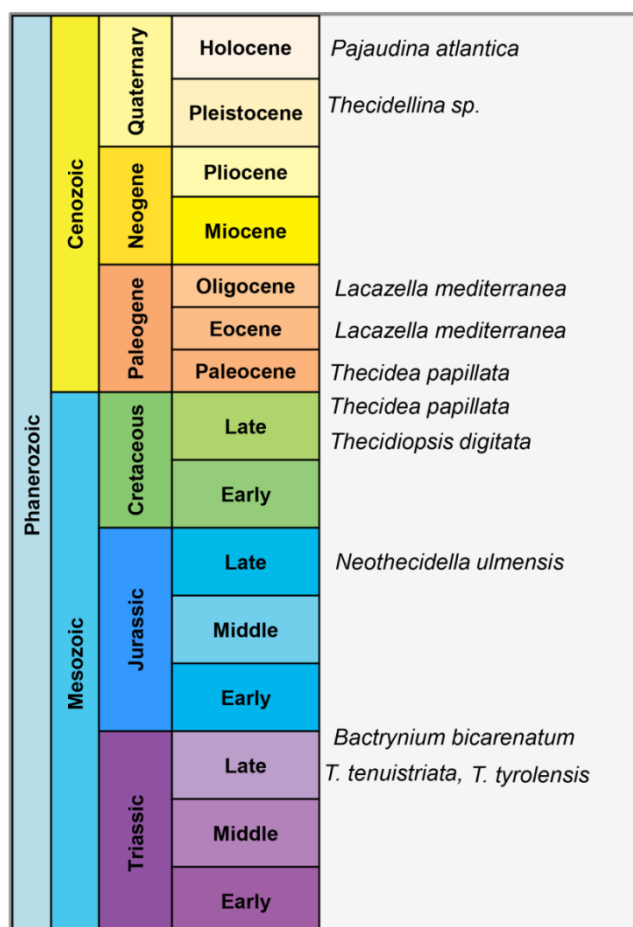


Figure 2.3.1. Stratigraphical distribution of the thecideide species investigated in this study.

We observe five different biomineral units in the investigated shells. Based on morphology and size we can distinguish fibrous, granular, acicular, small-polygonal and large-rounded biocrystals. The shell of the Upper Triassic *Bactrynum bicarinatum* Emmrich, 1855 (Fig. 2.3.2A, S2.3.5) contains well-preserved stacks of fibres. Their morphology is very similar to the fibre shape that builds the secondary layer of fossil and extant rhynchonellide and terebratulide species (Crippa et al. 2016; Ye et al. 2018a, 2018b; Griesshaber et al. 2007; Schmahl et al. 2012). However, the size of the fibres differs, such that in this thecideide species the fibres are larger in cross-sections relative to what is observed in recent rhynchonellides and terebratulides (Figs. 2.3.2, S2.3.1B, S2.3.7 cf. Ye et al. 2018a, 2018b).

In addition, we found well-preserved stacks of fibres in the shell of the Upper Triassic thecideide brachiopod *Thecospira tenuistriata* Bittner, 1890 (Figs. 2.3.2B, S2.3.1, S2.3.6-7), depicting clearly the typical secondary layer morphology of fibres also seen in fossil and extant rhynchonellide and terebratulide brachiopod shells. However, close EBSD examination (Figs. S2.3.1B, S2.3.7) reveals that *T. tenuistriata* developed fibres with two sizes: thick fibres (left- and right hand side in Fig. S2.3.1B) and thin fibres (central portion of Fig. S2.3.1B). Cross-section morphologies of the large fibres are distorted, are rather polygonal and do not show a blade-shaped cross-section of the smaller fibres (Fig. S2.3.1B). In addition to fibres, we located for both Upper Triassic species (*B. bicarinatum* and *T. tenuistriata*) another biomineral unit: polygonally shaped crystals, often with roundish morphologies; in most cases large in size (shown by yellow stars in Figs. 2.3.2A-B and S2.3.1).

Calcite crystal co-orientation/misorientation is expressed with MUD values and is given for each EBSD measurement (Figs. 2.3.2-10). MUD values are multiples of uniform orientation, thus, an MUD of 1 indicates a random orientation of crystallites, an MUD of above 700 is indicative for perfect crystallite co-orientation, e.g. single crystals grown from solution (e.g. Greiner et al. 2018; Yin et al. 2019). For the shells of Recent terebratulide and rhynchonellide brachiopods we obtain MUD values that are larger than 60 (Casella et al. 2018); most values scatter between 80 and 100 (Griesshaber et al. 2017). Calcite co-orientation strength for the shell of *B. bicarinatum* is increased, with an MUD value of 51. In the shell of *T. tenuistriata* crystal co-orientation strength is significantly lower, MUD values scatter between 22 (Fig. 2.3.2B) 14 and 18 (Fig. S2.3.1).

The shell of the Upper Jurassic thecideide brachiopod *Neothecidella ulmensis* (Quenstedt, 1858) comprises both fibres and acicles (Figs. 2.3.3, S2.3.2-4, S2.3.8). Shell portions next to the soft tissue of the animal (innermost shell layers) consist of fibres aligned in parallel, while the outer shell is formed of acicles (Figs. 2.3.3, S2.3.3-4, S2.3.8). We conducted six large EBSD scans on shell cross-sections and observed these two microstructures in all cases and did not detect any polygonal biocrystals. MUD values for entire scans, comprising both fibres and acicles, are increased and scatter between 30 and 40 (Fig. 2.3.3). However, if calculated individually for the different microstructures, then calcite co-orientation strength is higher for the fibres (MUD: 65, Fig. S2.3.3, MUD: 42, Fig. S2.3.4), relative to that for the acicular shell part (MUD 15/25, Fig. S2.3.3; MUD: 11, Fig. S2.3.4). Accordingly, calcite co-orientation strengths decrease with the generation of acicular microstructures, a feature already observable for the shell of the Upper Jurassic thecideide species *N. ulmensis*.

In summary, fibres occur in all investigated Triassic and Jurassic species. In addition to fibres, Triassic taxa contain also polygonal to roundish mineral units. However, these are not developed in the shells of Upper Jurassic species. In the latter, polygonal to roundish mineral units are replaced by acicles. Calcite co-orientation strength is increased for the shell of Triassic *B. bicarinatum*, it is low for Triassic *T. tenuistriata*, and is only slightly decreased relative to *B. bicarinatum*, for the Upper Jurassic *N. ulmensis*.

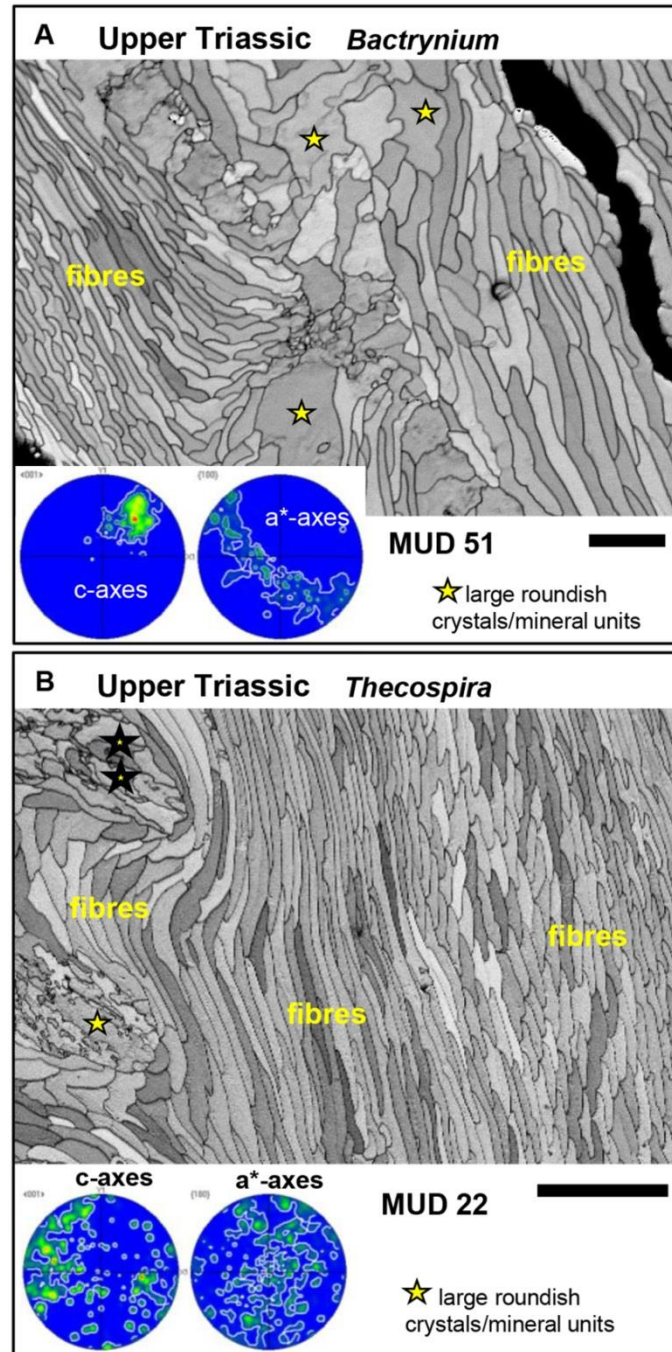


Figure 2.3.2. EBSD band contrast images and associated pole figures depicting characteristics of the microstructure and texture of the Triassic thecideide brachiopods *Bactrynum bicarinatum* (A) (E100-18-17) and *Thecospira tenuistriata* (B) (MPU5784-4), respectively. Stacks of longitudinally and transversely cut fibres are well visible as well as the large roundish calcite units/biocrystals. Scale bars represent 20 and 50 μm in A and B respectively.

Acicular and granular microstructures dominate thecideide taxa from the Late Cretaceous to Holocene (Figs. 2.3.4-10, S2.3.9 to S2.3.16). Calcite co-orientation strengths are very low, MUD values are below 15; for the shell of *Thecidiopsis digitata* (Sowerby, 1823) the MUD value is as low as 3.5 (Fig. 2.3.4). Acicle sizes vary and scatter between micrometre and sub-micrometre sizes (e.g. *Thecidea papillata* (Schlotheim, 1813), Figs 2.3.5-6); the acicles are always embedded in a matrix of nanometric to micrometre-sized granules. In addition to acicles, polygonal crystals appear (Paleocene *T. papillata* (Schlotheim, 1813) Figure 2.3.6; Eocene and Oligocene *L. mediterranea* (Risso, 1826) Figures 2.3.7 and 2.3.8; Pleistocene *Thecidellina* sp. Fig. 2.3.9, however, these are significantly smaller in size relative to those that we found in Triassic taxa (e.g. in the shell of *B. bicarinatum* (Fig. 2.3.2A)). As stated in the methods section, all samples were carefully checked with different screening methods for possible diagenetic overprint. Accordingly, we do not consider these polygonal crystals as a result of diagenetic alteration, but rather as an original feature of the microstructure of these thecideide species (Paleocene *T. papillata*; Eocene *L. mediterranea*; Pleistocene *Thecidellina* sp.). In contrast to Triassic and Jurassic thecideides, the shells of Cretaceous, Paleogene and Pleistocene thecideide taxa are formed by numerous mineral units with different sizes and shapes. These are assembled following very little to almost random structural order (Figs. 2.3.4-9, S2.3.9-13), and very low calcite crystallite and mineral unit co-orientation strength (MUD values 3.5, 15, 10, 8). In summary, following the Late Jurassic, a marked loss of fibrous calcite can be observed. If at all present in thecideide shells, fibres are limited to particular parts of the shell, e.g. to articulatory structures.

In *T. papillata* (Late Cretaceous and Paleocene, Figs. 2.3.5-6, S2.3.10-11) and in the Oligocene *L. mediterranea* (Figs. 2.3.8, S2.3.12), we see an alternation in the orientation of stacks of more or less aligned acicles. This resembles, to some degree, the stack alternation of co-aligned fibres in Recent terebratulide and rhynchonellide brachiopod shells (Griesshaber et al. 2007, 2017, Ye et al. 2018a, 2018b; Ye et al. submitted).

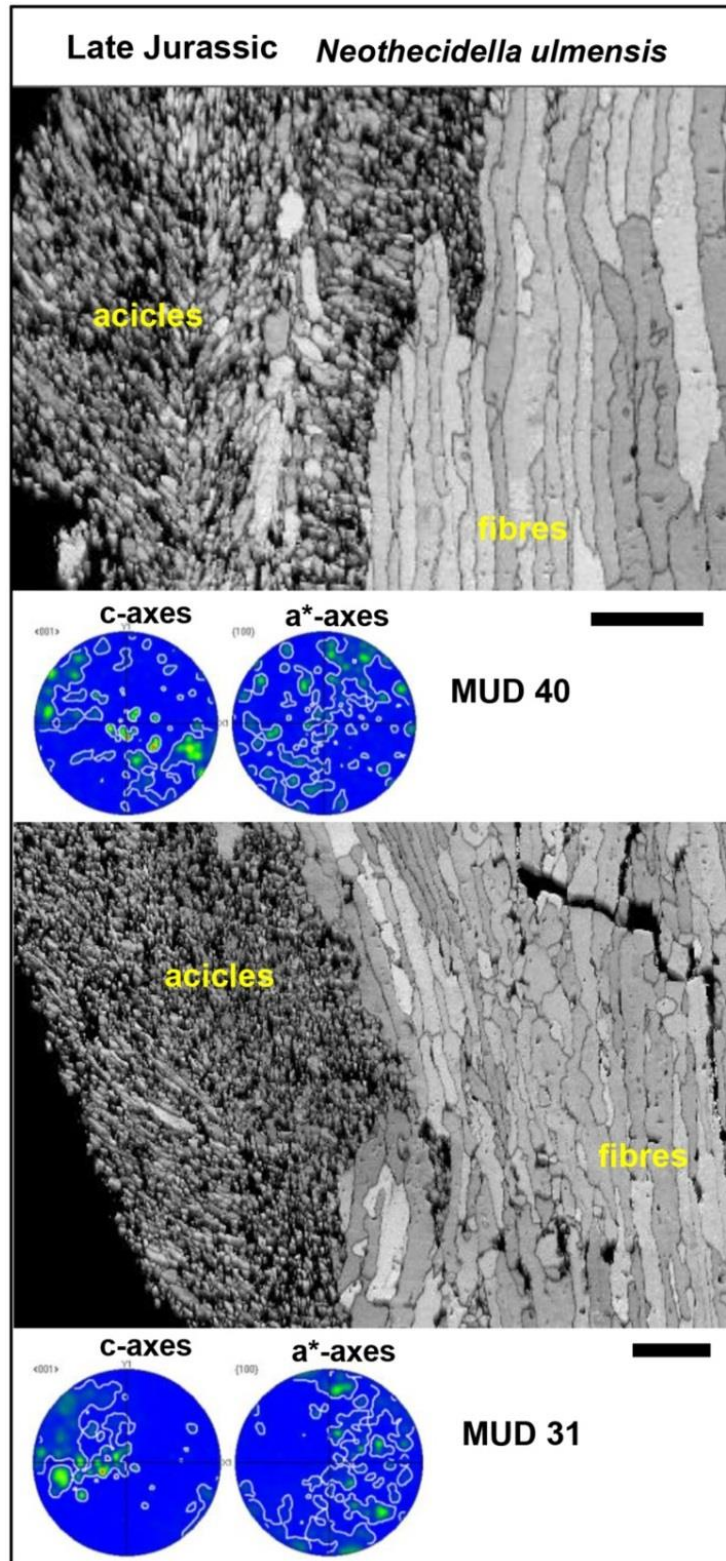


Figure 2.3.3. EBSD band contrast images of two measurements at different shell parts and associated pole figures depicting characteristics of the microstructure and texture of the Jurassic thecideide brachiopod *Neothecidella ulmensis* (LMU-NU01). An additional measurement is given in Fig. S2.3.4. Note fibrous (often with amalgamated fibres) as well as acicular shell portions. The stack of fibres is cut longitudinally while the acicles are cut diagonally. Scale bars represent 20 μm .

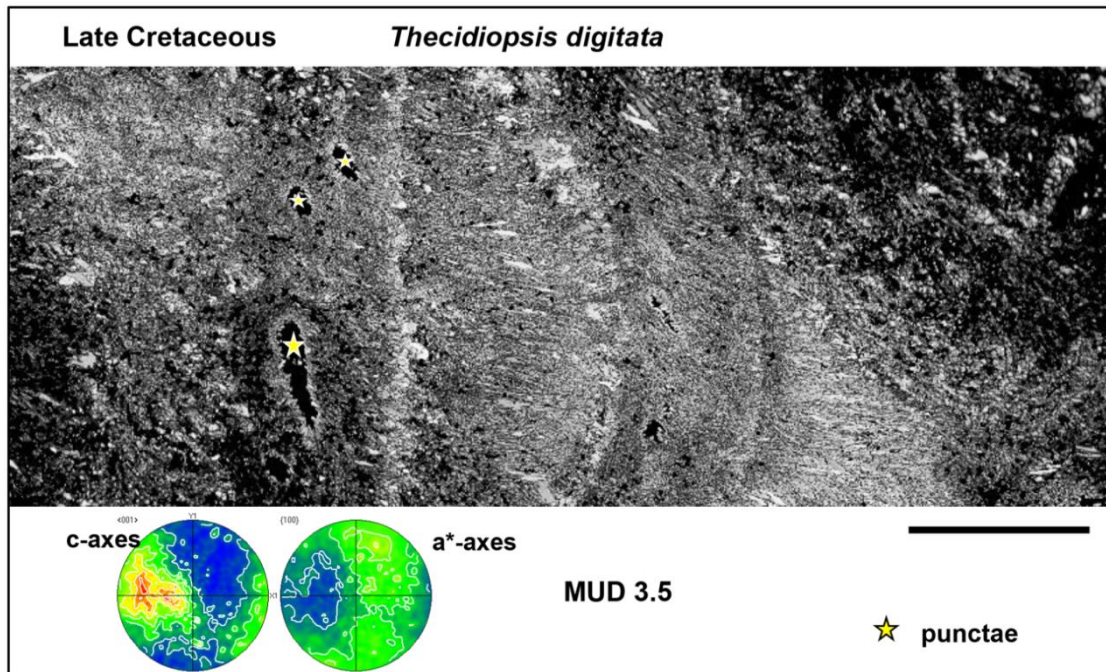


Figure 2.3.4. EBSD band contrast image and associated pole figure visualizing the microstructure and texture of the Upper Cretaceous thecideide brachiopod *Thecidiopsis digitata* (LMU-TD01). Note the matrix of small to nanometre-sized calcite crystallites containing occluded small acicles and some small pseudo-polygonal crystals. The calcite that comprises the shell is poorly co-aligned, see the low MUD value of 3.5. Yellow stars indicate the location of punctae. Scale bar represents 20 μm .

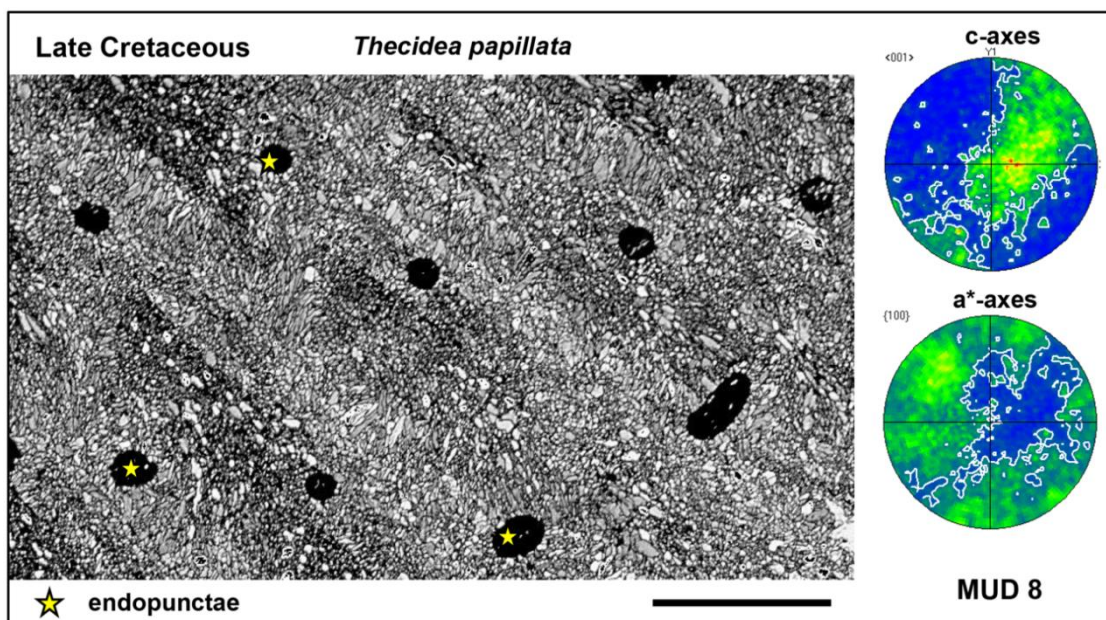


Figure 2.3.5. EBSD band contrast image and associated pole figure visualizing the microstructure and texture of the Cretaceous thecideide brachiopod *Thecidea papillata* (LMU-TPLC01). The shell consists of acicles embedded in a matrix of small to nanometre-sized calcite granules and small polygonal crystals. Calcite co-orientation strength is very low (MUD value of 8). Note that endopunctae (some marked by stars) are not filled. Scale bar represents 100 μm .

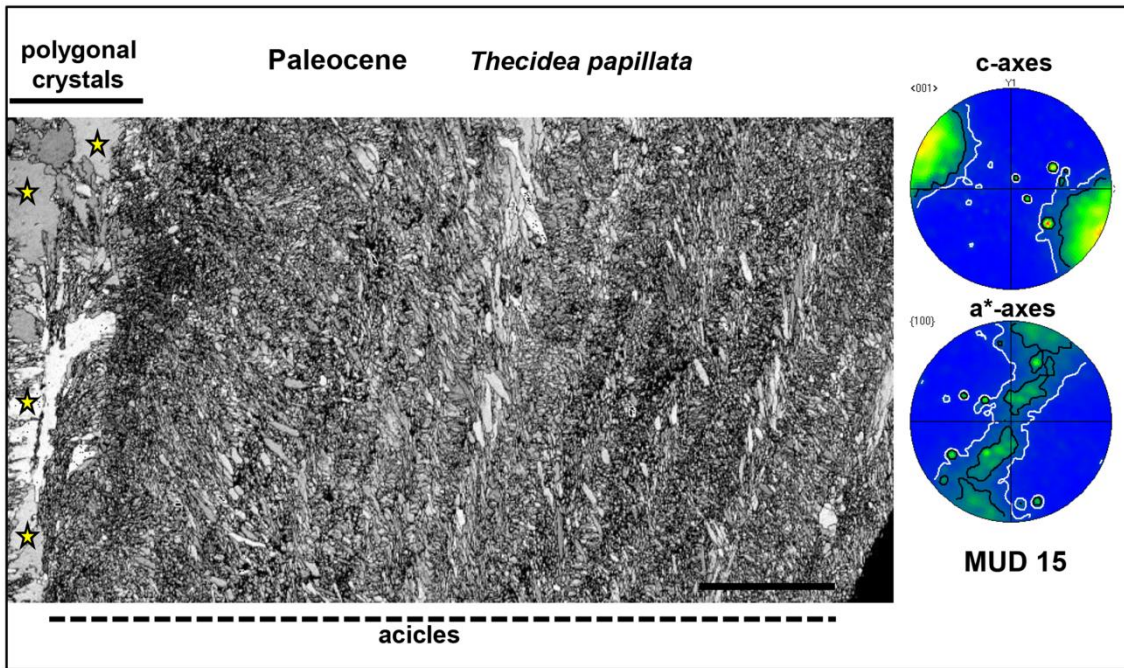


Figure 2.3.6. EBSD band contrast image and associated pole figure visualizing the microstructure and texture of the Paleocene thecideide brachiopod *Thecidea papillata* (LMU-TPP01). The shell consists of a matrix of nanograins interspersed with little co-aligned acicles and some irregularly shaped, large calcite crystals (see yellow stars on the left-hand side of the image). Scale bar represents 100 μm .

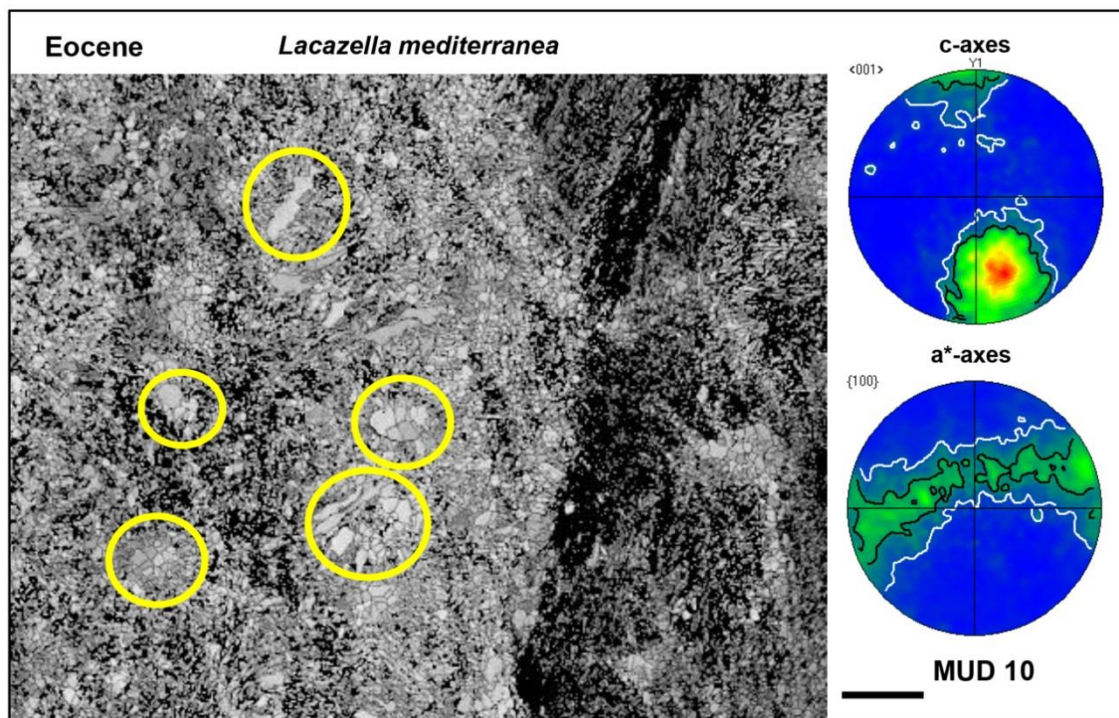


Figure 2.3.7. EBSD band contrast images and associated pole figures depicting the microstructure and texture of the Eocene thecideide brachiopod *Lacazella mediterranea* (LMU-LME01). The microstructure of the shell is nanogranular interspersed with small polygonal calcite crystals (circled). Note very low co-orientation of calcite; MUD 10. Scale bar represents 50 μm .

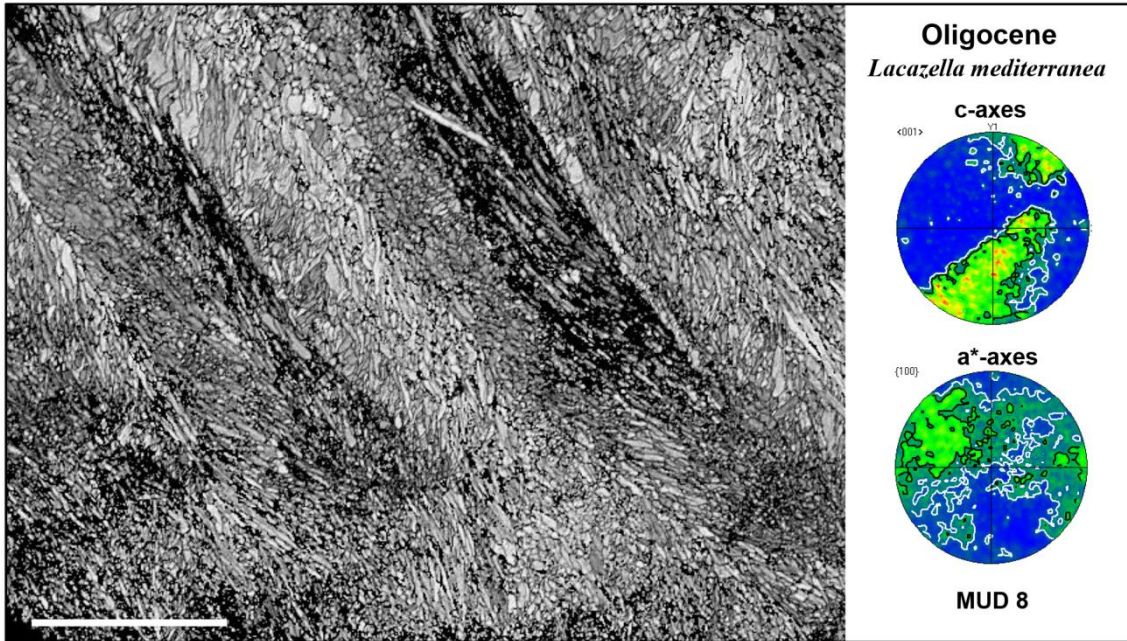


Figure 2.3.8. EBSD band contrast images and associated pole figure depicting the microstructure and texture of the Oligocene thecideide brachiopod *Lacazella mediterranea* (LMU-LMO01). The microstructure is acicular, the acicles are poorly co-oriented. Scale bar represents 100 μm .

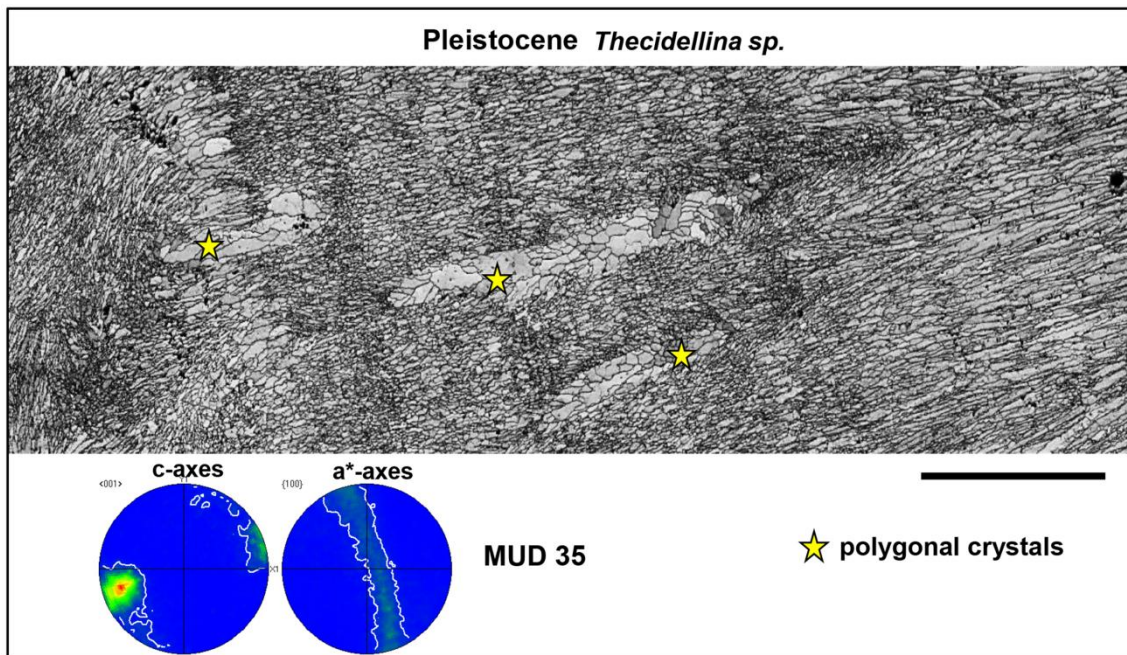


Figure 2.3.9. EBSD band contrast image and associated pole figure depicting the microstructure and texture of the Pleistocene thecideide brachiopod *Thecidellina* sp. (UF 325201). Large stacks of acicles form the shell, interspersed with patches consisting of mainly small polygonal calcite crystals (shown by yellow stars). As the pole figure and the slightly elevated MUD value of 35 shows, co-orientation strength of calcite is slightly increased in the shell of this thecideide species. Scale bar represents 50 μm .

Figures 2.3.10-11, S2.3.14-16 display the microstructure and texture of the Recent thecideide brachiopod *Pajaudina atlantica*. Figure 2.3.10 presents microstructure and texture results, Figure 2.3.11 depicts internal features of the shell such as the shapes of mineral units and the occlusion of organic membranes. We observe a large variety of mineral unit sizes and shapes: nanometre/micrometre-sized acicles, granules, polygonal crystals; all more or less randomly oriented within the shell. There is a considerable amount of organic matter intercalated into the shell of *P. atlantica*, generally developed as membranes or thin films (Fig. 2.3.11). The distribution pattern of organic matter is also not structured, it is more or less randomly intercalated into the calcite, a characteristic that contrasts significantly to the distribution of organic matrices in fibrous and columnar shell layers of other Recent rhynchonelliform brachiopods. While in the latter organic membranes encase fibres and columns (e.g. Simonet Roda et al. 2019a, 2019b), the mineral units of the primary shell layer are not sheathed by organic material. In Recent terebratulide and rhynchonellide brachiopod shells the primary layer consists of large, dendritic mesocrystals that interdigitate in 3D (Goetz *et al.* 2011).

Clearly visible in *P. atlantica* is the large diversity in mineral unit size and morphology (Figs. 2.3.10, 2.3.11A-C), the interlinkage of mineral units (white stars in Fig. 2.3.11B) and the presence of organic membranes/organic films that are occluded within the shell (white arrows) in Figs. 2.3.11C-F).

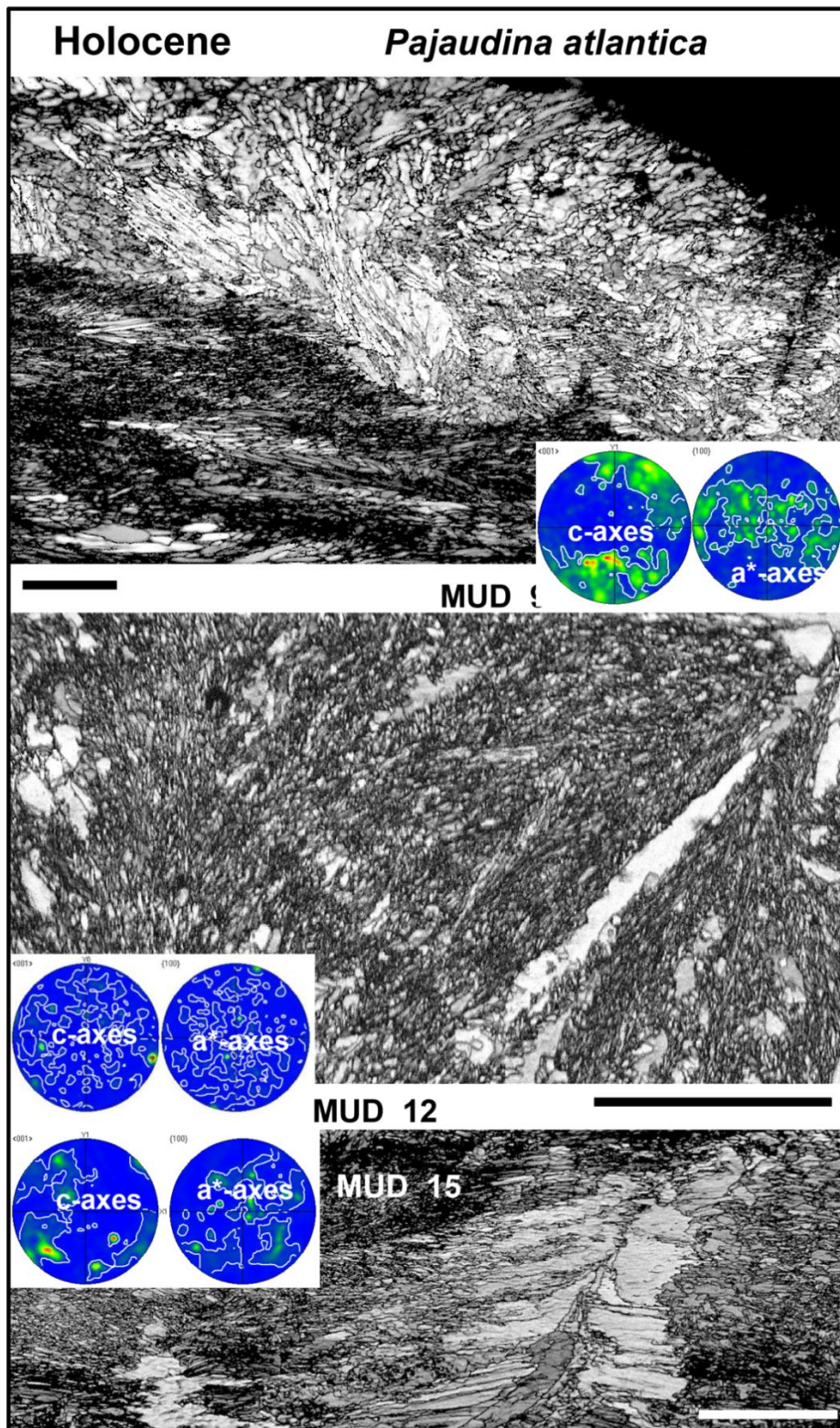


Figure 2.3.10. EBSD band contrast image and associated pole figure depicting the microstructure and texture of the Recent thecideide brachiopod *Pajaudina atlantica* (LMU-PA008, LMU-PA0010 and LMU-PA09 from top to bottom respectively). The shell of this brachiopod species includes all types of biocrystals: nanogranules, granules, acicles, small polygonal crystals and large polygonal crystals. Calcite co-orientation strength is low. Scale bars represent 20 μm for A and 50 μm for B and C.

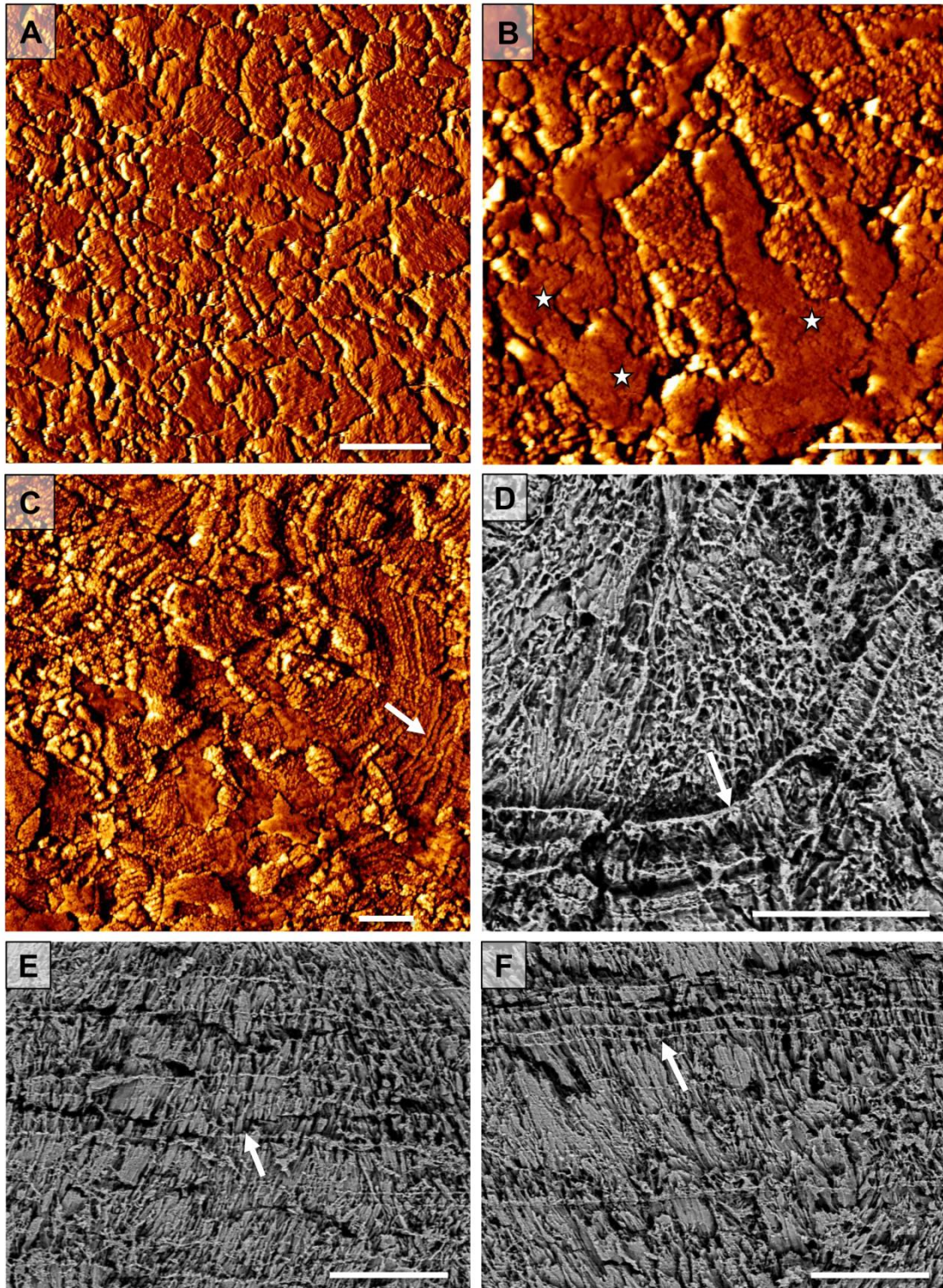


Figure 2.3.11. Internal structural characteristics of the shell of the Recent thecideide brachiopod *Pajaudina atlantica*. Figs. 2.3.11-C show AFM images (LMU-PA010), Figs. 2.3.11D-E depict SEM images of polished and etched surfaces (LMU-PA011). The organic substance is chemically fixed. The presence of organic membranes/organic films occluded within the shell is pointed by white arrows. The white stars (1B) indicate the interlinkage of the mineral units. Scale bars represent 2.5 μm for A to C and 10 μm for D to F.

2.3.4. Discussion

Change in microstructure and texture

The aim of this study is to trace the evolution of thecideide microstructure and texture from the Triassic to Recent times (Figs. 2.3.12-14). The change in shell fabric involves the loss of fibres and large roundish crystals/mineral units and implies the introduction of acicles and granules. Thus, we see over time a change from large (micrometre-sized) biomineral units to small (sub-micrometre, nanometre-sized) biocrystals together with a reduction in microstructural order (see compilation of MUD values in Fig. 2.3.14). We observe a transition of thecideide shell fabric from co-aligned and well-assembled mineral units to almost unaligned biocrystals (Figs. 2.3.12, 2.3.14). The shells of Upper Triassic species consist of fibres and large roundish calcite crystals. The Upper Cretaceous to Pleistocene species built their shells of acicles, small sized granules and small polygonal to irregularly shaped biocrystals. However, despite a significant change in microstructure, Upper Cretaceous to Pleistocene species still retain some microstructural regularity within their shells. Nevertheless, this microstructural regularity is not present in the shell of the Recent thecideide species *Pajaudina atlantica* and *Kakanuiella chathamensis* Lüter, 2005. These taxa have highly disordered, almost random shell microstructures and form their shell of a large variety of mineral units that are of highly irregular shapes and sizes (Lüter 2005). Thus, disorder in microstructure, texture and mineral unit characteristic is typical of some thecideid brachiopods, especially those living in a specific environment and following specific life-styles. In summary, we find a decrease over time in: 1) biomineral shape regularity, 2) biomineral unit size and 3) strength of biomineral unit co-orientation. All these microstructural characteristics are the least ordered in the shell of the Recent species *Pajaudina atlantica* and *Kakanuiella chathamensis*, characteristics that contrast significantly to microstructure/texture patterns of most fossil and extant rhynchonellate brachiopods. In the latter, the fibrous layer comprises well-developed stacks of co-aligned calcite fibres and, when present in the shell, the columnar layer consists of large co-aligned calcite columns (Ye et al. 2018a, 2018b). In most of the Rhynchonellata, these characteristics of microstructural elements did not vary significantly from the Triassic to Recent (Ye et al. 2018a, 2018b).

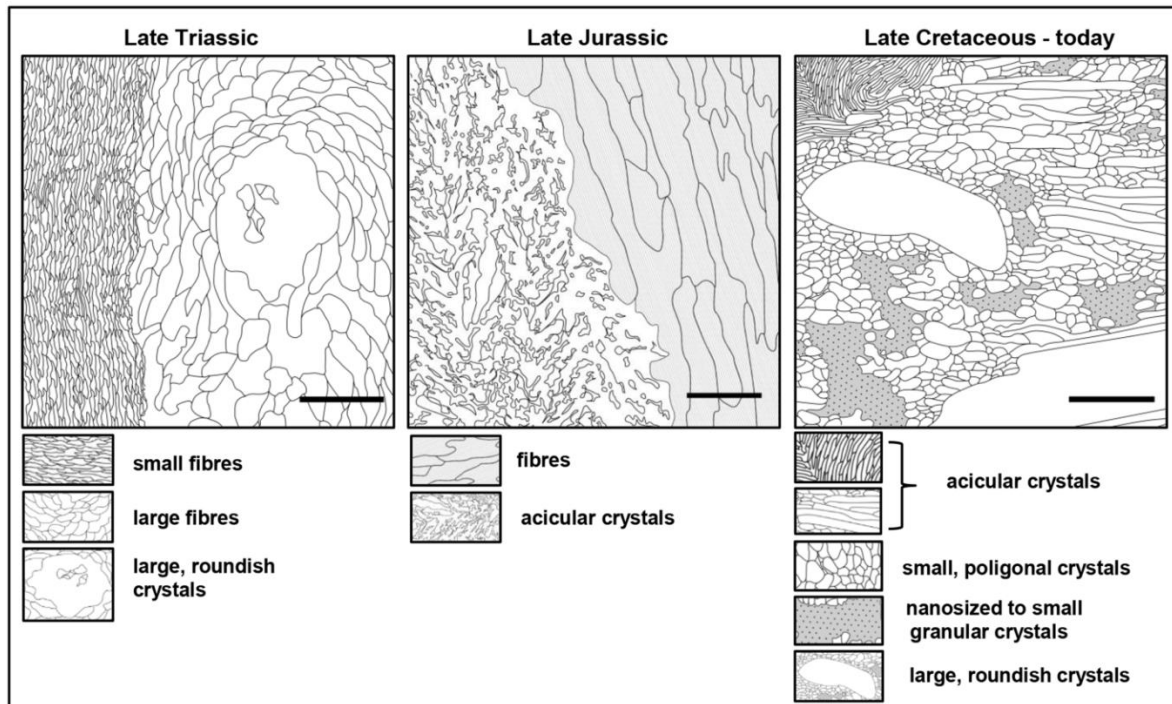


Figure 2.3.12. Microstructure features of thecideide brachiopods characteristic for different geological intervals. Scale bars represent: 50 μm for the Late Triassic example, 20 μm for the Late Jurassic example and 40 μm for the Late Cretaceous – Recent example.

The shell of the Upper Jurassic species *Neothecidella ulmensis* forms a special case as it consists of fibres as well as acicles and is formed exclusively of these two types of biocrystals. Both microstructures are present in the shell with a high crystal co-orientation strength; especially the calcite of the fibrous shell layer (MUDs of 42 and 65). Crystal co-orientation strength within the acicular shell portion of *Neothecidella ulmensis* is increased, MUD values are 25, 15 and 11, but not as high as in the fibrous shell layer. This finding does not support the inference of Jaecks & Carlson (2001) that the acicular microstructure is complementary to the fibres. Those taxa that have an acicular microstructure have a reduced fibrous layer, e. g. *Neothecidella ulmensis*. The Upper Jurassic *Neothecidella ulmensis* could be a possible link between those thecideides that fabricated their shells with fibres and large roundish crystals and those that formed their shells from small acicles and granules. In addition, *Neothecidella ulmensis* illustrates that up to Late Jurassic thecideides were able to secrete fibres, a capability that was lost in the Early Cretaceous (this study and Baker 2006). Indeed, the Lower Cretaceous *Neothecidella parviserrata* is described as having fibres limited to teeth or to tooth ridges only. Fibres in the dorsal valve of *Neothecidella parviserrata* are completely suppressed (Baker & Laurie 1978). The *Neothecidella* lineage appears to confirm the suggestion of Williams (1973) that fibres might become suppressed around the Jurassic-Cretaceous boundary.

The shell microstructure of Recent thecideides was previously described as having a structure/microstructure similar to that of the primary layer of other rhynchonelliform taxa (Baker 2006; Williams & Cusack 2007). The present study indicates that this is not the case (also Simonet Roda et al. submitted). EBSD measurements indicate that the microstructure and texture of the primary shell layer of most Recent rhynchonelliform brachiopods is an assemblage of interdigitating dendrites, micrometre sized calcite mesocrystals (Goetz et al. 2011; Schmahl et al. 2012; Ye et al. 2018a, 2018b). Dendritic

mineral unit arrangements are easily detected with EBSD, even in 2D (Goetz *et al.* 2011, Griesshaber *et al.* 2017), and are distinct from microstructures that are formed by any kind of stacked mineral unit assemblages. Furthermore, neither SEM nor TEM observations were able to detect any organic components within or surrounding mineral units of the primary layer (e.g. Griesshaber *et al.* 2009). These features contrast to structural characteristics of Recent thecideide shells, e.g. that of *Pajaudina atlantica* (Simonet Roda *et al.* submitted), where we do not find any dendritic mesocrystals, nor organic sheaths encasing the mineral units (Simonet Roda *et al.* submitted). However, we find organic membranes intercalated within Recent thecideide shells (Fig. 2.3.11).

Even though the shell fabric of Recent thecideides differs significantly from the other extant Rhynchonelliformea, the occurrence of fibrous layers in Upper Triassic to Cretaceous species, the presence of endopunctae with perforated canopies in several genera, and the capacity to resorb shell (Baker 2006 and reference therein), makes the thecideide shell fabric more similar to that of the Rhynchonellata and less akin to the Strophomenata shell microstructures - even though the latter also have a complex shell fabric, that consists of laminae of aligned blades (Garbelli *et al.* 2014; Ye *et al.* submitted). Accordingly, as outlined above, we wish to emphasize with this study that, on the basis of shell fabric and microstructure, it is very difficult to envisage a link between thecideides and strophomenates, as was previously suggested by Williams (1973), Baker (2006) and Carlson (2016).

An important feature of thecideide and terebratulide brachiopod shells is the occurrence of endopunctae. In longitudinal sections, these are canal-like structures that cross the shell in terebratulides from the innermost fibrous to the primary shell layer (Williams 1997). In thecideides, endopunctae are often suppressed (Baker & Laurie 1978), however, if present, they cross the heterogranular microstructure from innermost to outermost shell regions. In the studied samples we see endopunctae only in the shells of the Cretaceous *Thecidiopsis digitata* and *Thecidea papillata* (Figs. 2.3.4-5). In living rhynchonelliform brachiopods the walls and the basal region of endopunctae are covered by living cells (Williams 1997, Simonet-Roda *et al.* 2019a, Fig. 2.3.11). With the degradation of organic material, endopunctae could become filled with diagenetic calcite, this might lead to misinterpretation and be seen as brachiopod shell calcite with specific crystal morphologies, sizes and orientation. In this study we investigated the shell material with great care for any diagenetic overprint, and therefore avoided the misinterpretation of secondary calcite within endopunctae. In addition, based on structural patterns and MUD values, EBSD measurements and the analysis of orientation data provide reliable indications for the identification of diagenetic calcite within shell material (Casella *et al.* 2018), which was not observed here.

Phylogenetic implications

We present here an updated phylogenetic hypothesis to illustrate the evolution of the thecideides (Fig. 2.3.13). This is not the main purpose of the paper, however it provides a template to map and interpret changes in shell fabric through time against the evolution of the group. For the construction of the tree the data matrix of Jaecks & Carlson (2001) was modified with the addition of information on the shell microstructure from the taxa analysed here and the inclusion of *Neothecidella ulmensis* (Table S2.3.2). The tree was constructed by TreeSearch (Brazeau *et al.* 2019) using implied weighting, the default value of 4 for concavity and a number of characters in the

terebratulide outgroup that were coded as inapplicable. The search produced a single, unique tree (Fig. 2.3.13).

The tree replicates some of the anomalous placements of taxa, indicated on a strict consensus tree based on a reweighted analysis with terebratulide outgroups (Fig. 5 in Jaecks and Carlson 2001). For example the positions of *Bittnerella*, *Pamirotheca* and *Agerinella* are similarly misaligned with respect to the *Treatise* classification of the superfamily (Baker 2006). These and other anomalies may be rectified by a more extensive study of shell fabrics across the entire group.

Using the terebratulides as an outgroup, the basal taxon is *Thecidella* and not *Eudesella* as was the case in the original analysis of Jaecks & Carlson (2001). *Eudesella* is still, nevertheless nearby, in the lower part of the tree. This hypothesised phylogeny indicates that the Hungarithecidae and Thecospirellidae are ancestral to both Thecidellinidae and Thecideidae. There is no evidence, however, that the Hungarithecidae are ancestral to Thecidellinidae, and the Thecospirellidae are ancestral to Lacazellinae, as suggested by Baker & Logan (2011) on morphological evidence. However, in the upper part of the tree, the thecospirellid *Bittnerella* is linked to most taxa of the Lacazellinae.

Jaecks & Carlson (2001) demonstrated that the reduction or loss of the fibrous microstructure in most of the Thecideidae is a derived feature. Taxa near the root of the tree have a continuous inner fibrous layer, whereas most derived taxa have fibrous layers that are reduced or absent, with the exception of *Neothecidella ulmensis* which maintains a continuous fibrous layer, as confirmed by our microstructural analysis. Another exception is the Upper Cretaceous *Eolacazella longirostrea*, which is rather low in the tree, but has a completely suppressed fibrous layer.

The pattern is more complex in the Thecidellinidae, as *Ancorellina* and *Stentorina*, near the root of the tree, have a continuous fibrous layer. However, *Rioulina* and *Eothecidellina* are more derived and have a continuous fibrous lining. Accordingly, the reduction or loss of the fibrous layer probably occurred more than twice.

This analysis does not support the suggestion of Baker & Logan (2011) that Thecidellinidae emerged as a sister group to the Thecideidae in the Late Triassic, as *Thecidella* appears as an outgroup, but the position of *Moorellina*, may be in agreement with the authors suggestion. Further phylogenetic analyses require detailed shell microstructure and texture data like those provided in this study, for more thecideide taxa, in order to unravel their phylogenetic relationships. Besides the appearance of acicular microstructure and the reduction/loss of the fibres, which according to Jaecks & Carlson (2001) are derived features, the different types of granular microstructures, the large roundish as well as the small polygonal crystals and the MUD values described here, should be further investigated, especially in the early stocks. This is the first study that links microstructure and texture results gained from EBSD measurements and data evaluation to phylogenetic analysis and their implications.

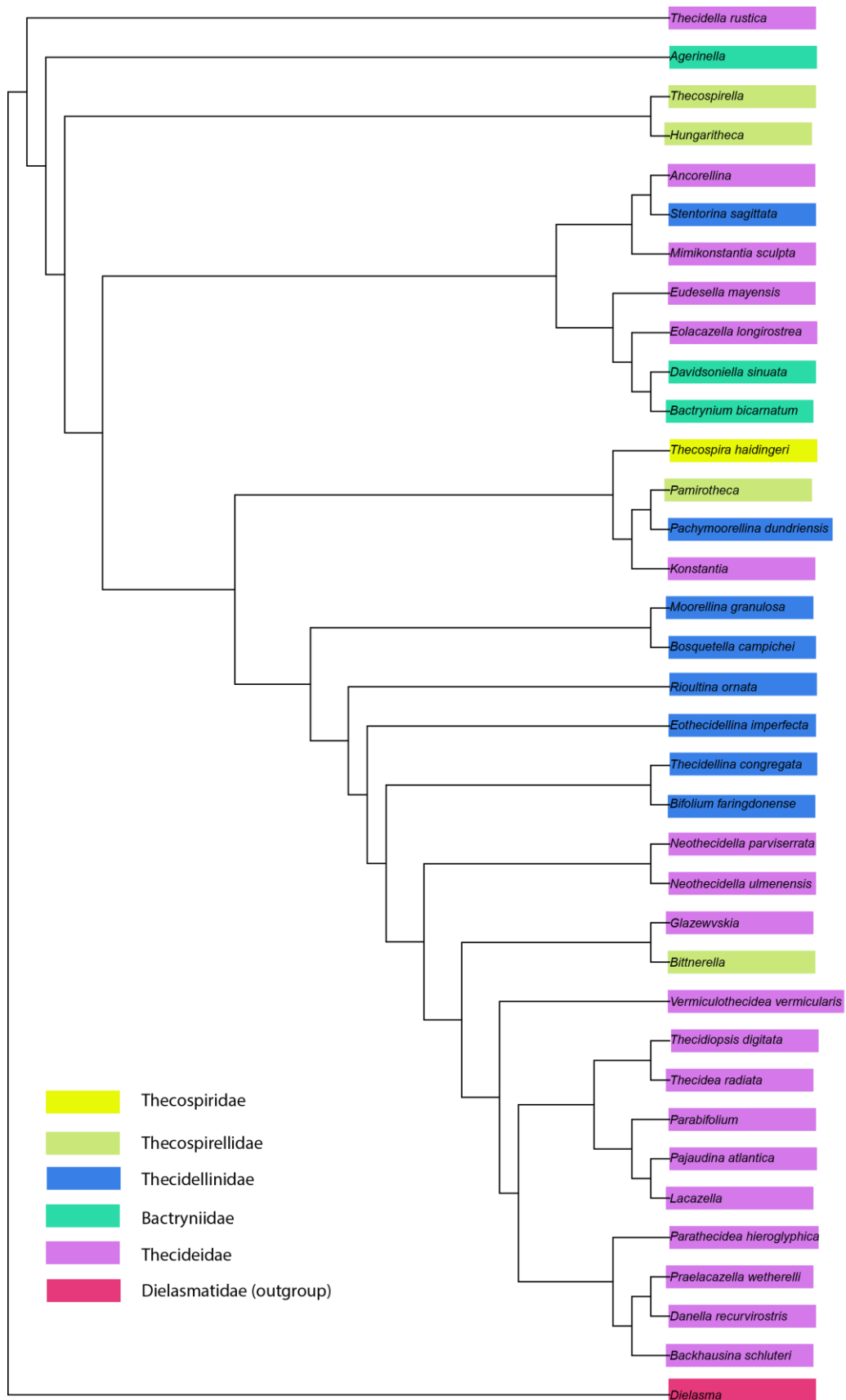


Figure 2.3.13. The phylogenetic tree is based on the characters and character states given by Jaecks & Carlson (2001) and was obtained with the addition of microstructure and texture results obtained in this study and the inclusion of the thecideide species *Neothecidella ulmenensis*.

The tree was constructed using TreeSearch (Brazeau et al. 2019), details are given in the text.

Is the change in microstructure an expression of adaptation to a different life-style and living environment?

Brachiopods dominated global marine benthic habitats until the end of the Permian, when the largest mass extinction of marine biota in the Earth's geological history affected the phylum severely. About 90% of the species went extinct and brachiopod evolution was completely reset (e.g. He et al. 2019). However, even though the causes that led to this biotic crisis are still debated, a main feature of the End-Permian event was the massive extinction among the Rhynchonelliformea, especially the clades that produced a laminar shell layer, the Strophomenata, and the selective survival of species secreting a shell consisting of fibres, the Rhynchonellata (Garbelli et al. 2017). The emergence of thecideides is not strictly related to the End-Permian extinction as they appeared about 20 million years after this event (e.g. Baker 2006). However, as benthic palaeocommunities were increasingly dominated by bivalves during the Triassic and Jurassic and, as free-living and pedicle-attached rhynchonellide and terebratulide brachiopods became less common (e.g. Clapham & Bottjer 2007; Liow et al. 2015), the emerging thecideides developed shell cementation to the substrate. Thecideides are found today and in the fossil record in cryptic habitats, caves or/and surfaces below rock overhangs and are associated, in contrast to most other fossil and extant rhynchonelliform brachiopods, cemented to hard substrates. Their growth is confined to small body sizes. It is well established that the composite nature and hierarchical component organization of structural biomaterials allows for the development of many hard tissue design concepts (e.g. Mayer 2005; Fratzl & Weinkamer 2007; Dunlop & Fratzl 2010). Accordingly, Recent carbonate biological structural materials exhibit a vast diversity of microstructure and texture patterns (e.g. Huber et al. 2015; Griesshaber et al. 2017; Casella et al. 2018; Checa 2018; Checa et al. 2018; Seidl et al. 2018; Checa et al. 2019), where both, almost unaligned as well as highly co-aligned crystal assemblies are utilized, if necessary. Thus, both, a high order as well as a high disorder in biomineral unit arrangement and crystallite orientation is advantageous in certain circumstances for the organism. Microstructure and texture patterns influence directly mechanical properties of structural materials. Different environments, e.g. high energy settings in shallow waters or substrates in quieter, deeper waters with higher water loads, require shells with different amounts of hardness, stiffness, toughness, tensile strengths and ductility. These characteristics are imparted by the mineral-biopolymer arrangement within the hard tissue and reflect directly conditions that are defined by a given habitat (Seidl et al. 2012; Huber et al. 2015; Griesshaber et al. 2017; Ye et al. 2018a, 2018b; Seidl et al. 2018).

Accordingly, we infer that the evolution of thecideide shell microstructures and textures, the change from fibres to acicles, the switch from large mineral units to small and granular biominerals, the transition from an ordered to a highly disordered microstructure and texture reflect their success in colonizing hard substrates by cementation and the occupation of niches not yet taken by bivalves or/and rhynchonellide and terebratulide brachiopods. Several observations support these hypotheses: (1) Taxa that had a similar life strategy in the Palaeozoic, cementation to hard substrates (e.g. some taxa of the Class Strophomenata), had a laminar and not a fibrous fabric (McGhee 1999; Williams *et al.* 2000; Ye et al. submitted). Fibrous assemblies appear to be less suitable for a cemented life-style; (2) the Craniiformea also

lived and live cemented to hard substrates and form shells with a distinct organocarbonate tabular laminar fabric (Williams 1997); (3) the granular-acicular fabric can possibly be secreted more easily and rapidly relative to the formation of fibres and columns; (4) secretion of small mineral units, acicles and granules, might make it easier to attach to uneven substrate surfaces. We can support the last suggestion based on the study of the microstructure of other shell-attached benthic organisms such as the Recent oyster *Magallana gigas* [formerly *Crassostrea gigas* (Thunberg, 1793)] which lives cemented to many types of substrates (MacDonald 2010). Our EBSD measurements show that for attachment, *M. gigas* secretes a shell layer of variable thickness, that consists of minute to small, irregularly sized, shaped and oriented calcite crystals (Figs. S2.3.17-18). Crystal co-orientation strength within the layer that attaches to the substrate is low; it is significantly less than the co-orientation strength of calcite in the adjacent foliated shell portion (Fig. S2.3.17). The many different orientations and the small size of those crystallites that touch the surface of the substrate makes it easier for the oyster to adjust to the surface roughnesses.

Rudwick (1968) and Pajaud (1974) showed that the attachment scar on the ventral valve in some Triassic and Cretaceous thecideides became obsolete in larger specimens (as the ventral valve increased in convexity and the dorsal valve in concavity) and suggested that such individuals were secondarily free-lying in adult stages. In contrast, Recent thecideides are permanently cemented to substrate. The gradual shift from fibrous to acicular structures seems to coincide with an overall shift in the living strategy of thecideides towards a permanent attachment. For example, the Upper Triassic *Bactrynum bicarinatum*, also investigated in this study, is very common in offshore mudstones of the Eiberg Member of the Kössen Formation (Northern Calcareous Alps, Austria) where a free-lying life habit can be expected (see also Michalik 1976).

In transitional forms (e.g. *Neothecidella ulmensis*) the fibrous layer is partly replaced by stacks of acicles. Acicles always form outer shell portions, while the arrays of fibres are always next to the soft tissue of the animal. The progressive loss of fibres in favour of a more disordered acicular and granular microstructures is a loss which is a derived feature according to Baker (2006). This can be considered as part of the complex mosaic of paedomorphic and peramorphic patterns of evolutionary changes observed for the thecideides (Carlson 2016).

2.3.5. Conclusions

EBSM measurements have demonstrated the large variety of mineral units that form thecideide shells from Late Triassic to Recent times. These range from fibres through acicles to granules which are irregularly shaped and sized calcite biocrystals. Thecideide biomineral units and their arrangements differ significantly from those of terebratulide and rhychonellide species. Based on our analyses, we draw the following conclusions:

1. The regularity of biocrystal shape, mineral unit size, and the strength of calcite co-orientation decreases from the Late Triassic to Recent species.
2. The shell of Upper Jurassic species represent transitional forms and are composed of stacks of acicles on external shell portions and of a remnant of the fibrous layer next to the soft tissue of the animal.
3. The change in microstructure and texture may be interpreted as an ecological strategy to exploit distinct habitats and life styles, in particular attachment to

- hard substrates, as confirmed by a microstructural comparison with recent bivalves that live attached to rock substrates.
- The progressive loss of the fibrous layer in favour of highly disordered acicular and granular microstructures can be seen as a pedomorphic pattern in the complex mosaic of evolutionary changes characterizing thecideide brachiopods.
 - Detailed shell microstructure and texture data gained from EBSD measurements are needed from more thecideid taxa in order to unravel their phylogenetic relationships.

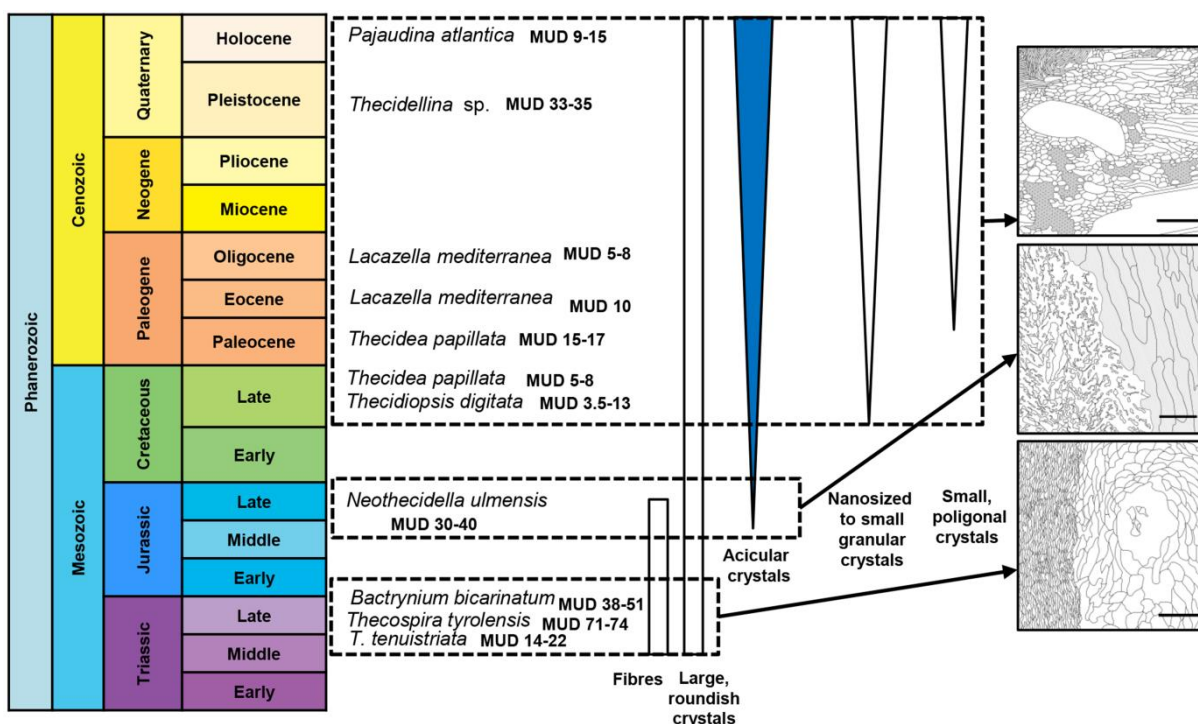


Figure 2.3.14. Summary of the investigated suite of thecideide brachiopods, their stratigraphical distribution and schematic illustrations of the main microstructure characteristics of their shells. See scale bars values in Figure 2.3.12.

2.3.6. Data availability statement

Additional data, that support the findings of this study, are available from the Supporting Information of this article and from the corresponding author upon reasonable request.

Acknowledgements.

This project has received funding from the European Union's Horizon 2020 research and innovation programme under grant agreement No 643084. We thank Prof. Dr. A. Checa (Department of Stratigraphy and Paleontology, University of Granada, Spain) for the *Magallana gigas* sample. D. A. T. Harper thanks Martin Smith (Department of Earth Sciences, Durham University, UK) for his help implementing the TreeSearch algorithm. We would like to thank the two anonymous reviewers for their constructive comments, which improved the text.

Supporting Information

Table S2.3.1 Sample numbers for the illustrated material.

Species	Age	Original location	Number	Repository
Thecospira tenuistriata Bittner, 1890	Late Triassic	Alpe di Specie, Italy	MPU5784-4 MPU5804	Museo di Paleontologia Dipartimento di Scienze della Terra Università degli Studi di Milano
Thecospira tyrolensis (Loretz, 1875)	Late Triassic	Alpe di Specie, Italy	MPU5484-4	Museo di Paleontologia Dipartimento di Scienze della Terra Università degli Studi di Milano
Bactrynum bicarinatum (Emmrich, 1855)	Late Triassic	Elberg Austria	E100-18-17	Ludwig Maximilian University of Munich
Neothecidella ulmensis (Quenstedt, 1858)	Late Jurassic (middle Oxfordian)	Bałtów, Poland	LMU-NU01	Ludwig Maximilian University of Munich
Thecidiopsis digitata (Sowerby, 1823)	Late Cretaceous	Petersberg, Maastricht, Netherlands	LMU-TD01	Ludwig Maximilian University of Munich
Thecidea papillata (Schlotheim, 1813)	Late Cretaceous	Symphorien, Mons, Belgium	LMU-TPLC01	Ludwig Maximilian University of Munich
Thecidea papillata (Schlotheim, 1813)	Paleocene	Ciply near Mons, Belgium	LMU-TPP01	Ludwig Maximilian University of Munich
Lacazella mediterranea (Risso, 1826)	Late Eocene	Dnipropetrovsk, Ukraine	LMU-LME01	Ludwig Maximilian University of Munich
Lacazella mediterranea (Risso, 1826)	Late Oligocene	Peyrere Aquitaine Basin, France	LMU-LMO01	Ludwig Maximilian University of Munich
Thecidellina sp.	Pleistocene	Curaçao, Caribbean	UF 325201	Ludwig Maximilian University of Munich
Pajaudina atlantica Logan, 1988	Recent	Palma, Canary Islands, Spain	LMU-PA008	Ludwig Maximilian University of Munich
			LMU-PA009	
			LMU-PA010	
			LMU-PA011	

Table S2.3.2. The character matrix and taxa used for construction of the phylogenetic tree (see also Figure 13), based on the characters and character states described by Jaecks & Carlson (2001) with the addition of microstructure and texture results obtained in this study and the inclusion of the thecideide species *Neothecidella ulmensis*. Character numbers referring to microstructure and texture and character states are as follows:

38. Dorsal valve, extent of fibrous layer. 0 = covers entire valve; 1 = partial coverage; 2 = partial coverage, limited to sockets and/ or cardinal process; 3 = absent.

39. Ventral valve, extent of fibrous layer. 0 = covers entire valve; 1 = partial coverage; 2 = partial coverage, teeth only; 3 = absent.

40. Dorsal valve granular calcite. 0 = absent; 1 = present.

43. Ventral valve acicular calcite. 0 = absent; 1 = present.

41. Ventral valve granular calcite. 0 = absent; 1 = present.

50. Secondary fabric type. 0 = non-fibrous; 1 = fibrous

42. Dorsal valve acicular calcite. 0 = absent; 1 = present.

	1	2	3	4	5	6	7	8	9	10	11	12	13	14	15	16	17	18	19	20	21	22	23	24	25	26	27	28	29	30	
Dielasma	1	0	2	?	?	0	1	0	?	0	0	1	0	1	1	0	0	0	0	0	0	0	0	0	0	0	?	2	0	?	?
Backhausina schluteri	0	3	3	1	?	0	0	3	0	3	2	2	1	1	1	2	0	2	?	0	0	?	?	?	1	3	2	2	1	2	
Agerinella	0	3	5	1	?	0	0	3	1	0	0	?	0	?	?	2	?	?	?	?	?	?	?	?	1	?	2	?	1	0	
Bactrynum bicarnatum	0	1	2	?	1	0	0	?	?	?	?	1	0	0	0	0	?	?	1	?	?	1	?	?	?	1	4	2	?	1	
Bifolium faringdonense	0	0	4	1	3	0	0	3	0	2	3	1	0	1	0	1	1	1	2	1	1	0	0	1	1	1	2	2	2	0	
Bitternella	0	3	?	1	1	0	0	?	?	?	3	0	0	1	1	1	1	1	?	?	?	?	?	?	1	?	2	?	1	1	
Bosquetella campichei	0	0	0	2	1	0	0	0	?	0	0	0	0	1	?	?	?	1	?	3	2	?	?	?	1	1	2	0	2	0	
Danella recurvirostris	0	1	0	2	1	0	0	0	?	2	3	1	0	?	?	2	1	2	2	3	1	1	?	?	1	2	2	1	1	2	
Davidsoniella sinuata	0	1	5	2	1	0	0	?	1	2	3	2	0	0	0	1	2	1	2	2	?	2	?	1	0	2	2	0	1	0	
Eothecidellina imperfecta	0	3	4	1	2	0	0	?	1	4	2	1	0	1	?	1	1	1	1	?	?	2	?	?	1	3	2	0	1	0	
Eudesella mayensis	0	0	3	1	3	0	0	3	0	2	3	0	0	0	0	1	1	0	2	1	2	0	0	0	1	2	1	?	1	0	
Glazewvskia	0	4	1	1	2	0	0	3	0	2	3	0	0	1	1	1	2	1	2	1	1	?	?	?	1	1	2	?	1	1	
Konstantia	0	3	3	?	?	0	0	?	0	0	0	?	0	?	?	?	?	?	?	?	?	?	?	?	1	?	2	?	1	1	
Lacazella	0	0	0	3	3	0	0	3	0	3	3	2	0	1	1	1	2	2	2	3	?	0	0	2	1	4	2	2	1	2	
Mimikonstantia sculpta	0	3	3	1	2	0	0	?	1	1	1	1	0	0	0	2	2	1	0	1	?	4	?	1	1	1	?	0	1	0	
Moorellina granulosa	0	3	0	3	3	0	0	3	0	0	0	2	0	1	1	1	1	0	2	?	?	0	0	1	1	4	2	?	2	0	
Neothecidella ulmensis	1	0	6	1	?	0	0	1	1	3	1	1	0	1	1	1	?	0	0	2	1	?	?	?	1	1	1	1	1	0	
Neothecidella parviserrata	0	0	4	1	?	0	0	1	0	2	2	2	0	?	?	1	2	2	2	2	?	0	0	?	1	4	1	1	1	0	
Pachymoorellina dundriensis	0	1	1	3	3	0	0	2	0	4	3	2	0	1	1	0	1	1	1	3	2	1	?	1	1	1	2	0	1	0	
Pajaudina atlantica	0	3	3	1	2	0	0	3	0	3	3	2	0	1	1	1	1	1	2	2	2	0	0	2	1	2	1	2	1	2	
Pamirotheca	0	1	2	2	1	0	0	?	?	?	1	?	0	1	1	?	?	1	?	?	?	?	?	?	1	?	?	0	1	0	

Parabifolium	0	0	4	1	?	0	0	1	0	2	2	2	0	?	?	?	?	?	?	?	?	?	?	1	4	2	?	1	2		
Parathecidea hieroglyphica	0	3	3	2	1	0	0	3	0	2	3	2	0	1	1	2	1	1	2	3	2	0	0	0	1	3	2	2	1	1	
Praelacazella wetherelli	0	4	4	1	2	0	0	3	0	2	3	0	0	?	?	2	1	2	2	2	2	0	0	2	1	3	2	2	1	2	
Rioutlina ornata	0	3	0	2	1	0	0	3	0	2	2	2	0	1	1	2	1	1	?	2	1	?	?	?	1	1	?	0	1	0	
Thecidea radiata	0	0	0	0	0	0	0	3	0	2	2	2	1	1	1	1	1	1	2	3	2	0	0	3	0	2	2	2	1	1	
Thecidella rustica	0	3	5	1	3	0	0	0	?	0	0	0	0	1	?	3	1	0	0	2	?	2	?	1	1	3	2	0	1	0	
Thecidellina congregata	0	0	1	3	3	0	0	3	0	2	2	1	0	1	?	1	1	1	0	2	1	2	2	?	1	1	2	2	1	0	
Thecidiopsis digitata	0	3	3	3	3	0	0	3	0	2	3	2	0	?	?	1	1	1	2	3	2	0	0	3	1	3	2	2	1	1	
Thecospira haidingeri	0	3	3	2	1	?	0	2	0	4	?	1	0	1	?	0	0	2	0	?	?	?	?	?	1	3	?	0	0	0	
Hungaritheca	0	0	2	1	?	0	0	?	?	?	?	?	0	1	1	1	?	?	1	0	?	?	?	?	?	1	1	2	?	1	0
Thecospirella	0	3	2	1	?	0	0	?	?	?	?	3	0	1	1	1	1	1	1	?	?	?	?	?	?	1	?	2	?	1	0
Vermiculothecidea vermicularis	0	3	0	2	1	0	0	3	0	2	3	2	0	?	?	?	1	1	?	1	2	?	?	?	1	3	2	1	1	2	
Eolacazella longirostrea	0	3	0	2	?	0	0	?	?	2	?	2	0	0	0	4	1	1	2	3	2	0	0	2	1	3	?	0	1	2	
Stentorina sagittata	0	4	3	1	2	0	0	1	1	4	2	0	0	?	?	2	2	2	1	2	?	?	?	?	1	4	2	1	1	0	
Ancorellina	0	4	1	2	2	0	0	2	1	?	?	?	0	0	2	0	2	0	2	0	?	?	?	?	?	1	3	2	?	1	?

Table S2.3.2 *continued*. The used matrix and taxa for construction of the phylogenetic tree (see also Figure 2.3.13).

	31	32	33	34	35	36	37	38	39	40	41	42	43	44	45	46	47	48	49	50	51	52	53	54
Dielasma	?	?	?	?	0	1	?	0	0	0	0	0	0	0	2	0	?	0	1	0	?	?	?	
Backhausina schluteri	0	?	?	3	0	0	1	?	?	?	?	?	?	0	3	0	1	0	1	1	?	?	?	1
Agerinella	0	0	0	?	?	1	?	?	?	?	?	?	?	0	3	0	?	0	1	1	?	?	?	?
Bactrynum bicarnatum	0	0	0	1	0	1	?	0	0	0	0	0	0	4	0	1	0	1	1	2	0	?	0	
Bifolium faringdonense	0	0	0	2	0	0	0	2	2	0	0	1	1	0	1	0	1	0	1	1	1	0	1	0
Bitternella	0	0	0	1	?	0	?	?	2	0	0	?	?	0	?	0	1	0	1	1	?	?	?	?
Bosquetella campichei	0	0	0	1	0	0	0	2	0	0	1	1	0	0	1	0	1	0	1	1	1	?	?	0
Danella recurvirostris	2	0	0	3	0	0	1	?	?	?	?	?	?	0	3	0	1	0	1	1	2	0	1	1
Davidsoniella sinuata	0	0	0	2	0	1	0	0	0	0	0	0	0	4	0	1	0	1	1	2	0	5	0	
Eothecidellina imperfecta	0	0	0	2	0	0	0	2	0	0	0	0	0	0	1	0	1	0	1	1	1	0	1	0
Eudesella mayensis	0	?	?	0	1	0	0	0	0	0	0	0	0	4	0	0	0	1	1	1	?	?	0	0

Glazewvskia	0	?	?	3	0	0	?	?	?	?	?	?	?	0	3	0	1	0	1	1	?	?	?	0
Konstantia	0	1	0	0	1	?	?	?	?	?	?	?	?	0	1	0	1	0	1	1	1	0	0	?
Lacazella	2	0	0	3	0	0	1	2	2	1	1	1	1	0	3	0	1	0	1	0	2	1	1	0
Mimikonstantia sculpta	0	1	0	0	0	0	0	0	0	1	1	0	0	0	1	0	2	0	1	1	1	?	0	0
Moorellina granulosa	0	0	0	5	0	0	0	0	0	0	0	0	0	0	1	0	1	0	1	1	1	?	?	0
Neothecidella ulmenensis	0	0	0	1	0	0	0	0	2	0	0	1	1	0	3	0	1	0	1	1	2	0	5	?
Neothecidella parviserrata	0	0	0	1	0	0	0	2	2	0	0	1	1	0	3	0	1	0	1	1	2	0	5	?
Pachymoorellina dundriensis	0	0	0	0	1	0	0	1	1	0	0	0	1	0	1	0	1	0	1	0	1	0	0	0
Pajaudina atlantica	2	0	0	3	0	1	1	2	2	1	1	1	1	0	3	0	1	0	1	1	2	1	3	?
Pamirotheca	0	0	0	?	?	0	?	?	?	0	0	?	?	0	?	0	1	0	1	1	?	?	?	0
Parabifolium	?	0	0	3	0	0	?	?	?	?	?	?	?	0	3	0	?	0	1	1	?	?	?	0
Parathecidea hieroglyphica	0	?	?	3	0	?	?	?	?	0	?	?	?	0	2	0	1	0	1	1	?	?	?	0
Praelacazella wetherelli	2	0	0	4	0	0	1	2	0	0	1	1	0	0	3	0	1	0	1	1	2	0	5	?
Rioutina ornata	0	0	0	1	1	0	0	0	0	0	0	0	0	0	1	0	1	0	1	1	1	0	1	0
Thecidea radiata	0	0	0	3	0	0	1	3	3	1	1	1	1	0	2	0	1	0	0	0	1	1	3	0
Thecidella rustica	0	0	0	0	0	1	0	0	0	0	0	0	0	0	3	0	1	0	1	3	2	0	0	0
Thecidellina congregata	0	0	0	1	0	0	0	2	2	1	1	1	1	0	1	0	1	0	1	1	0	0	1	0
Thecidiopsis digitata	0	0	1	3	0	0	1	2	1	1	1	1	1	0	2	0	1	0	1	0	1	1	5	0
Thecospira haidingeri	0	0	0	0	0	0	0	0	0	0	0	0	0	0	0	1	1	1	1	1	1	0	0	0
Hungaritheca	0	0	0	?	?	?	?	?	?	?	?	?	?	0	1	1	1	0	1	1	?	?	?	?
Thecospirella	0	?	?	0	0	1	?	?	?	?	?	?	?	0	0	1	1	0	1	1	?	?	?	?
Vermiculothecidea vermicularis	1	0	0	1	0	0	0	?	?	?	?	?	?	0	3	0	1	0	1	1	?	?	?	0
Eolacazella longirostrea	?	?	?	3	1	1	0	3	3	0	0	0	0	0	3	0	1	0	1	1	2	1	?	0
Stentorina sagittata	0	0	0	5	0	1	?	0	0	0	0	?	?	0	1	0	1	0	1	1	?	?	?	0
Ancorellina	0	0	0	0	0	0	?	0	0	?	?	?	?	0	2	0	1	0	1	1	?	?	?	0

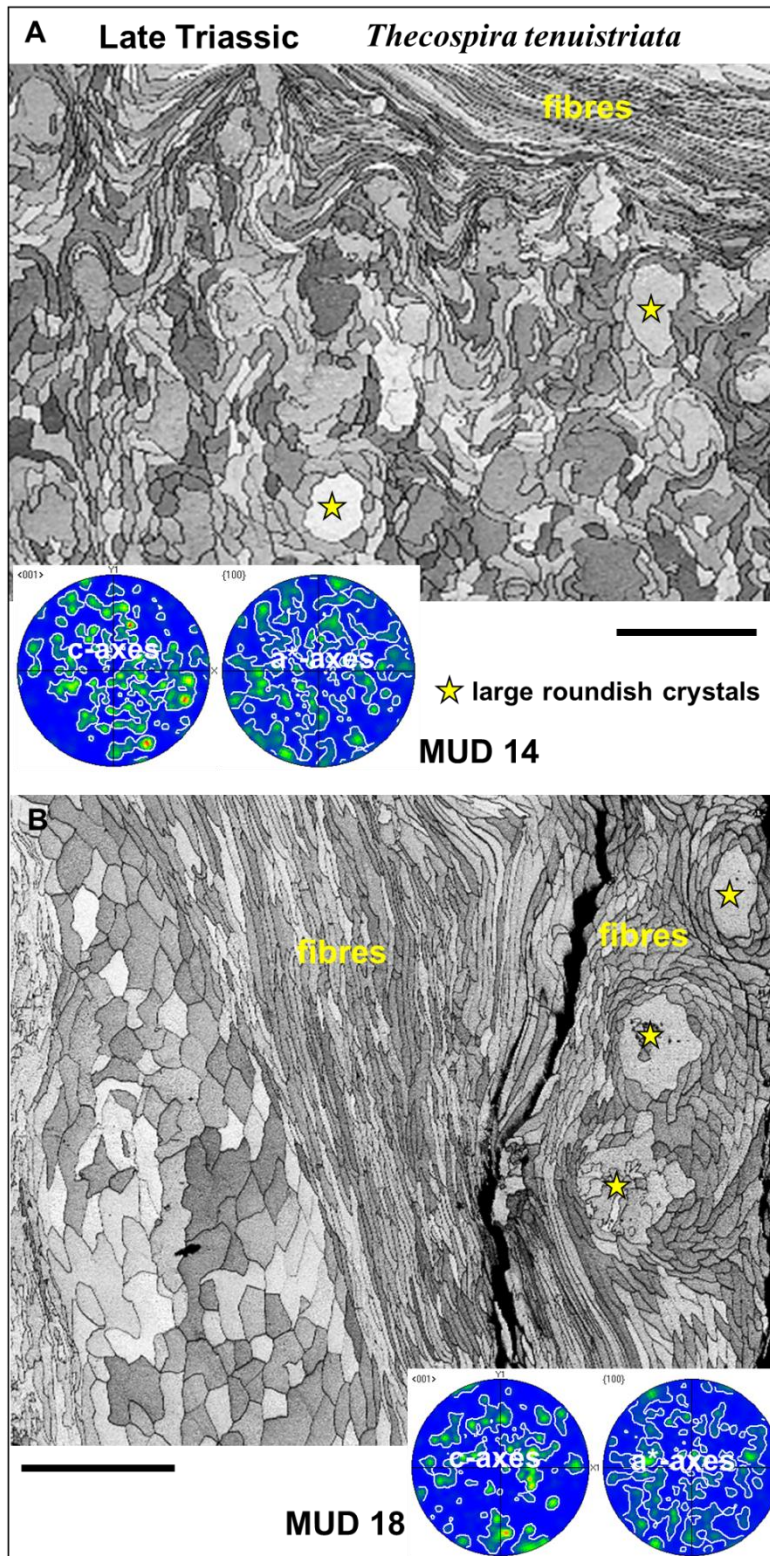
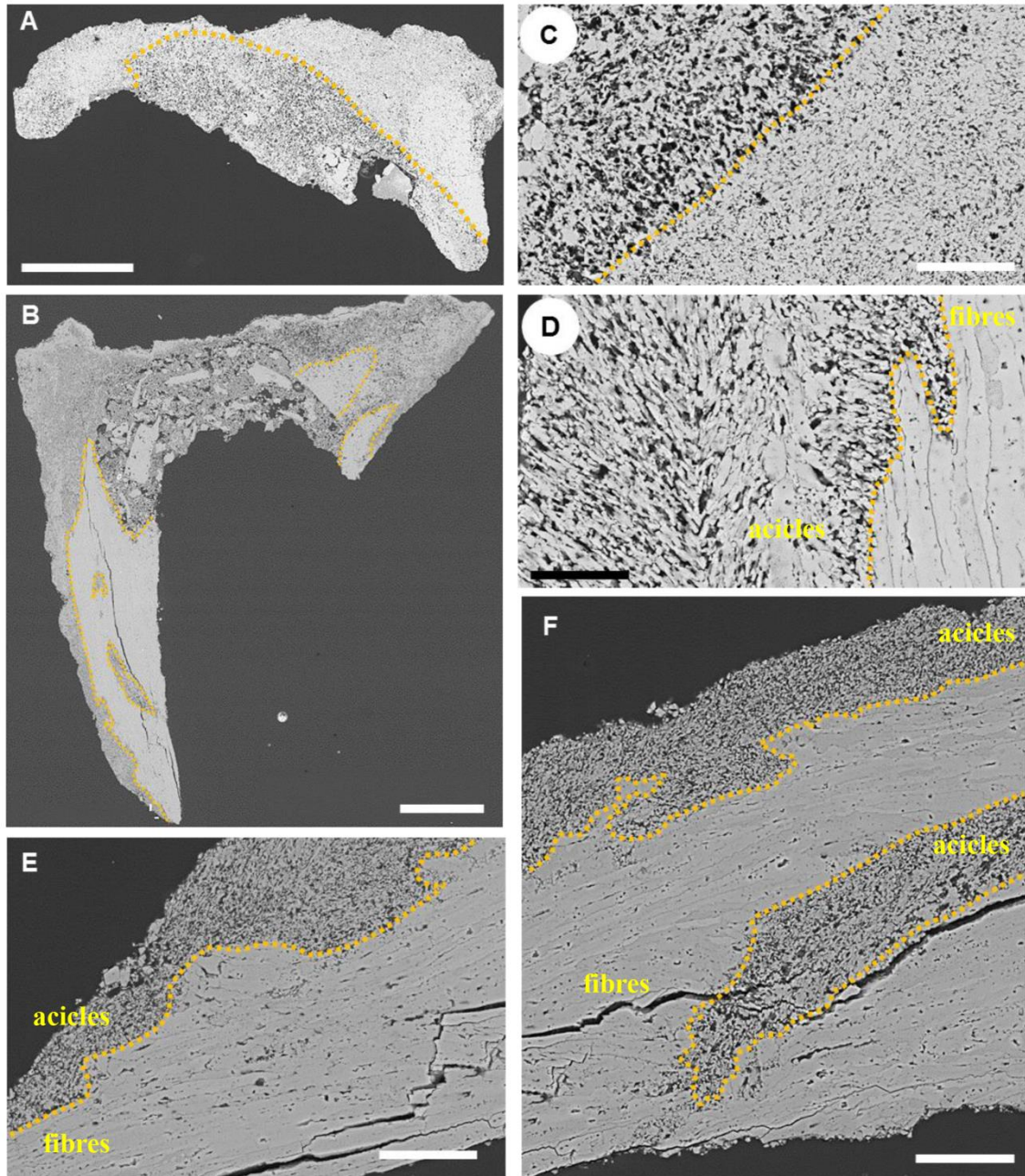


Figure S2.3.1. EBSD band contrast measurement image of the shell microstructure of the Triassic thecideide brachiopod *Thecospira tenuistriata* (MPU5804). The shell comprises small and large fibres and large rounded calcite units (yellow stars). Scale bars represent 100 μm .



Figures S2.3.2. BSE images of shell portions of the Jurassic thecideide brachiopod *Neothecidella ulmensis* (LMU-NU01). Two microstructures form the shell of this species: (i) acicles and (ii) fibres. Figures (A) and (B) show the distribution of the two microstructures in the dorsal (A) and ventral (B) valve, respectively. Acicular and fibrous shell portions are well distinguishable, see dashed yellow line. (D), (E) and (F) are detailed images of the contact between acicular and fibrous shell layers and the interdigitation of these. Scale bar represent 250 μm for A and B, 50 μm for C, E and F and 20 μm for D.

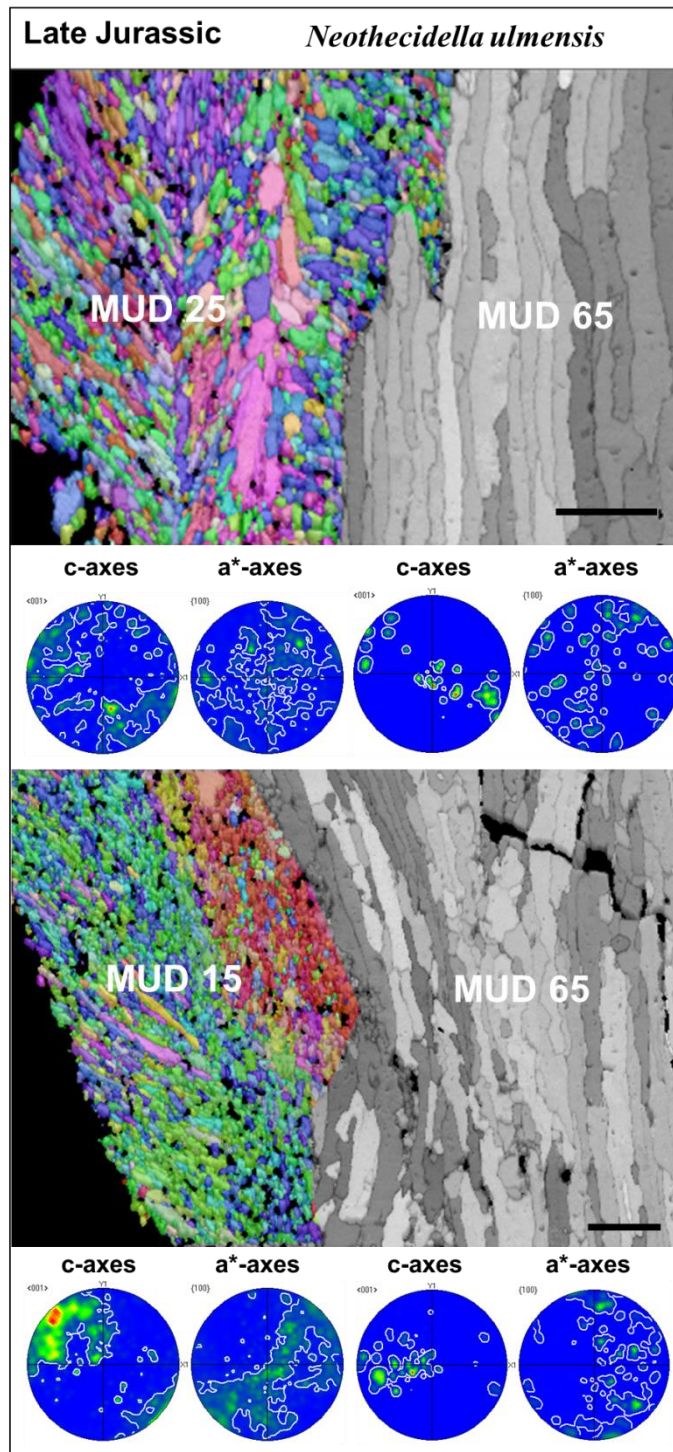


Figure S2.3.3. Calcite orientation (shown colour-coded) and band-contrast measurement images (shown grey-scaled) in the Jurassic thecideide brachiopod *Neothecidella ulmensis* (LMU-NU01) visualizing shell portions consisting of acicles (coloured) and of fibres (in grey), respectively. As the MUD values show co-orientation strength in the fibrous shell portion is higher (grey scaled), relative to acicular shell layers (coloured). Scale bars represent 20 μm .

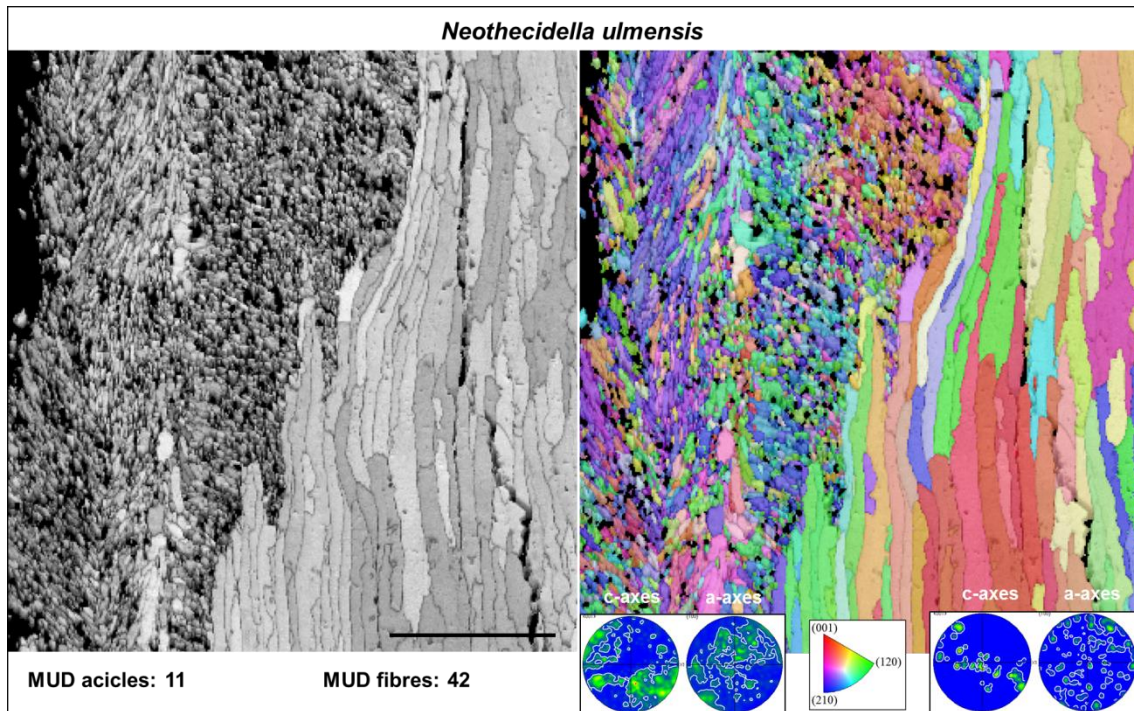


Figure S2.3.4. A further EBSD scan made on the shell of *Neothecidella ulmensis* (LMU-NU01) depicting calcite orientation (in color), band contrast measurement (grey-scaled) images, pole figures and giving MUD values for the acicular and fibrous shell portions. Scale bar represents 50 μm . The EBSD color code is given by the IPF triangle situated between the pole figures.

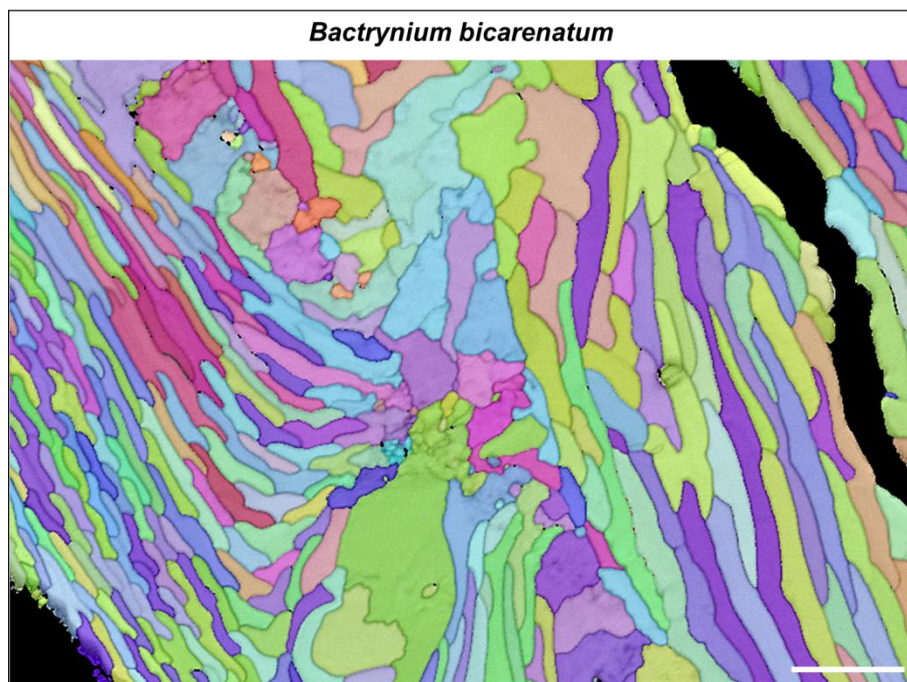


Figure S2.3.5. Orientation pattern of calcite shown colour-coded and derived from EBSD measurements for the shell of the Triassic thecideide brachiopod *B. bicarinatum* (E100-18-17). The EBSD colour code is given by the IPF triangle shown in Fig. S2.3.4. Scale bars represent 50 μm .

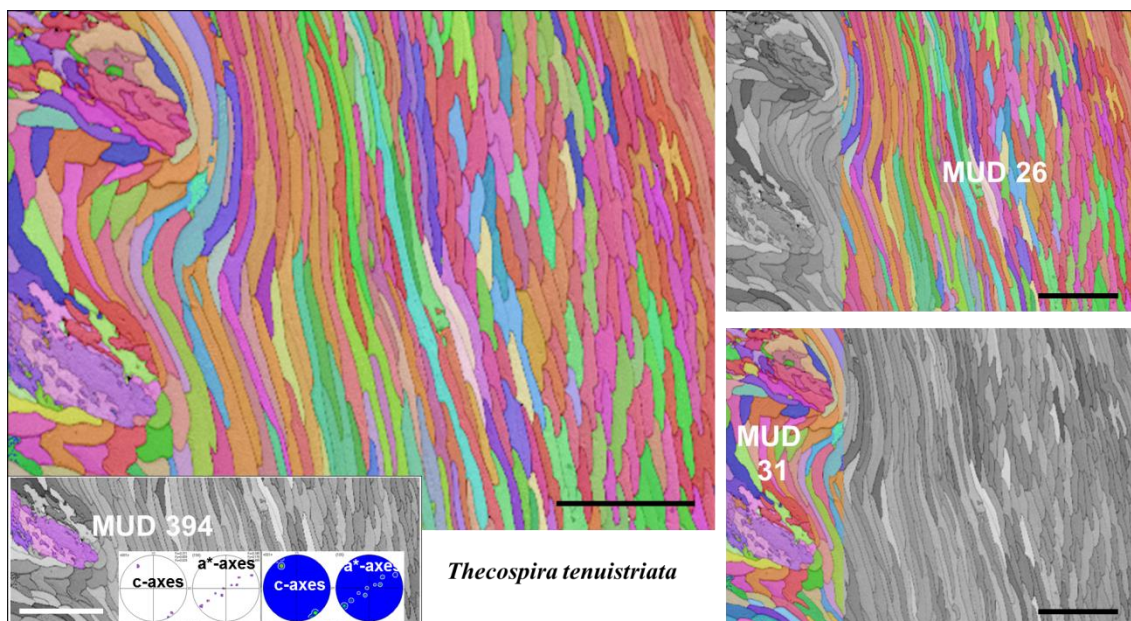


Figure S2.3.6. Orientation pattern of calcite shown colour-coded and derived from EBSD measurements for the shell of the Triassic thecideide brachiopod *Thecospira tenuistriata* (MPU5784-4). The MUD value for the array of fibres is 26; 31 for fibres and the large roundish calcite crystals and 394 for an individual large roundish calcite unit. The EBSD colour code is given by the IPF triangle shown in Fig. S2.3.4. Scale bars represent 50 μm .

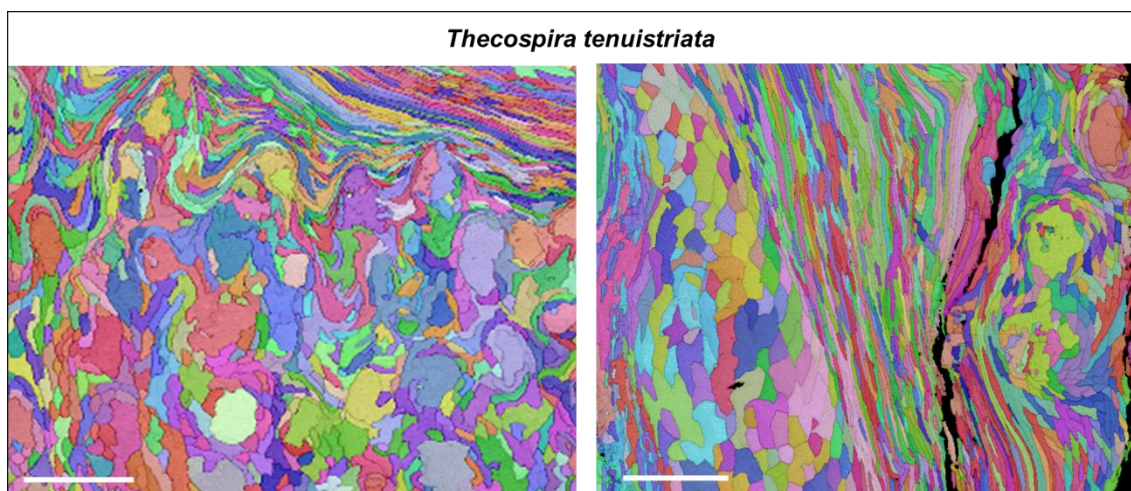


Figure S2.3.7. Orientation pattern of calcite shown colour-coded and derived from EBSD measurements for the shell of the Triassic thecideide brachiopod *T. tenuistriata* (MPU5804). The EBSD colour code is given by the IPF triangle shown in Fig. S2.3.4. Scale bars represent 100 μm .

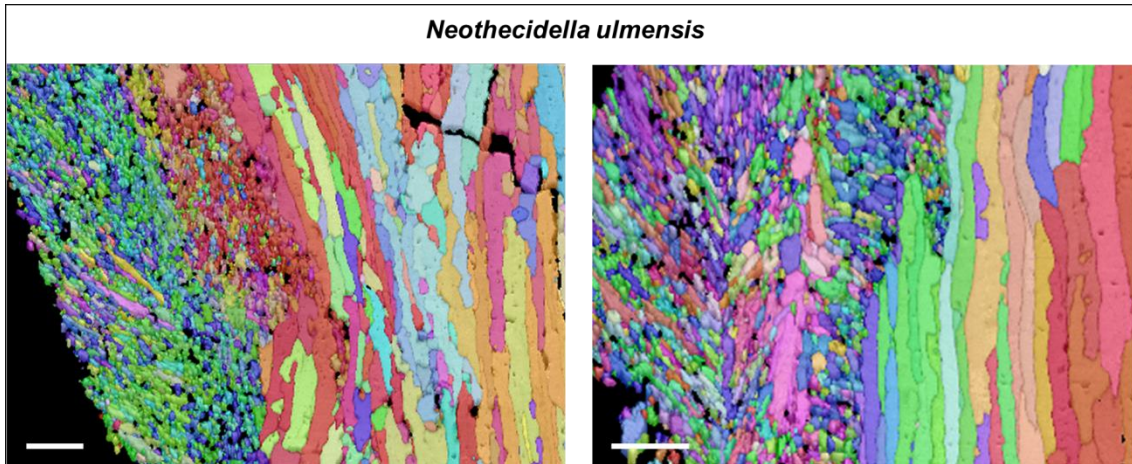


Figure S2.3.8. Orientation pattern of calcite shown colour-coded and derived from EBSD measurements for the shell of the Jurassic thecideide brachiopod *N. ulmensis* (LMU-NU01). The EBSD colour code is given by the IPF triangle shown in Fig. S2.3.4. Scale bars represent 20 μm .

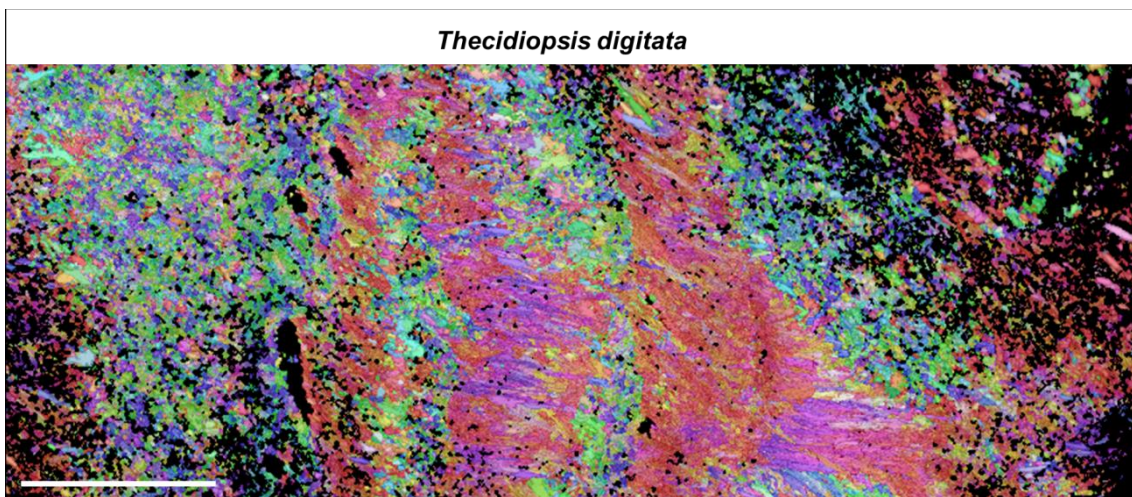


Figure S2.3.9. Orientation pattern of calcite shown colour-coded and derived from EBSD measurements for the shell of the Cretaceous thecideide brachiopod *T. digitata* (LMU-TD01). The EBSD colour code is given by the IPF triangle shown in Fig. S2.3.4. Scale bar represents 200 μm .

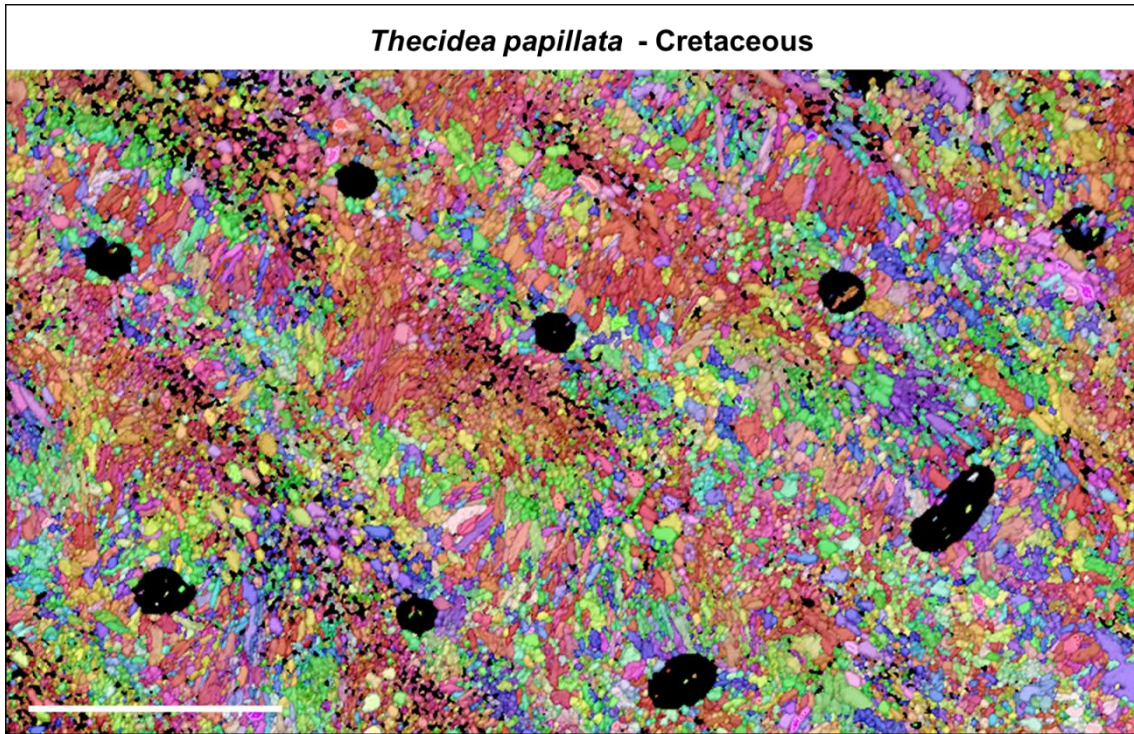


Figure S10. Orientation pattern of calcite shown colour-coded and derived from EBSD measurements for the shell of the Cretaceous thecideide brachiopod *T. papillata* (LMU-TPLC01). The EBSD colour code is given by the IPF triangle shown in Fig. S2.3.4. Scale bar represents 100 μm .

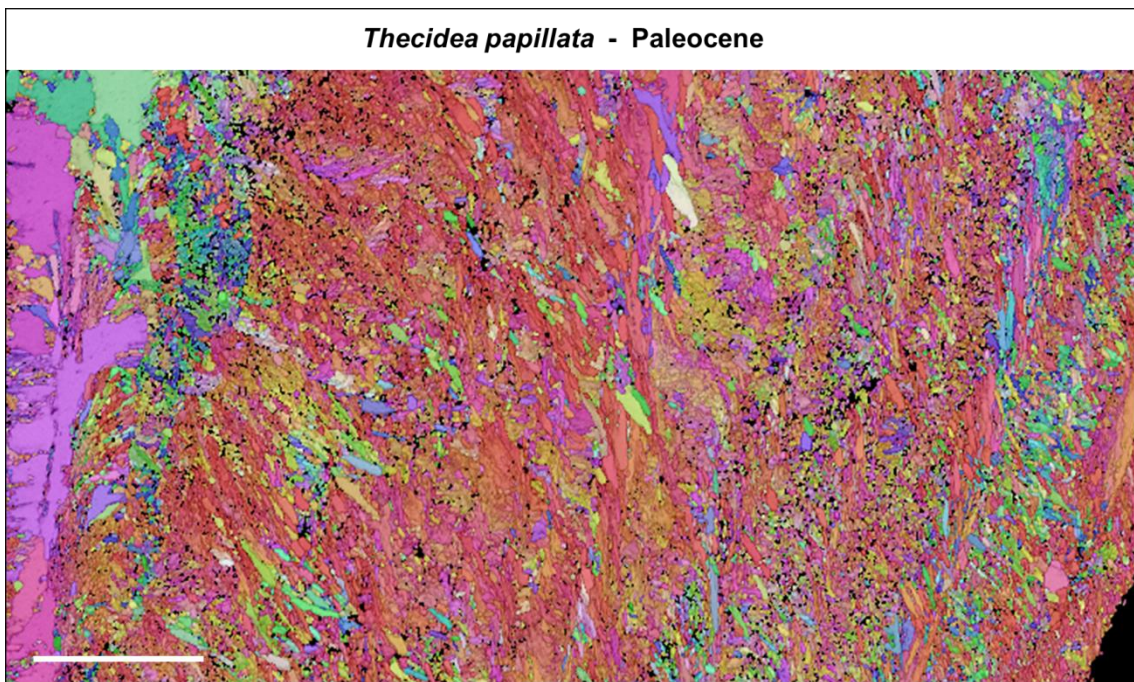


Figure S2.3.11. Orientation pattern of calcite shown colour-coded and derived from EBSD measurements for the shell of the Paleocene thecideide brachiopod *T. papillata* (LMU-TPP01). The EBSD colour code is given by the IPF triangle shown in Fig. S2.3.4. Scale bar represents 100 μm .

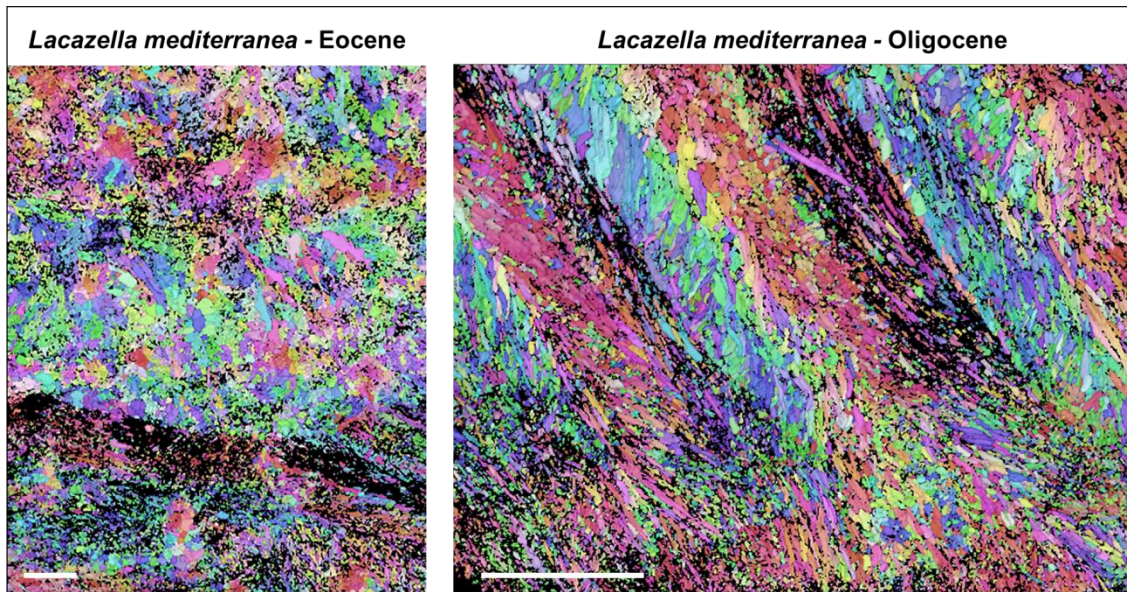


Figure S2.3.12. Orientation pattern of calcite shown colour-coded and derived from EBSD measurements for the shell of the Eocene and Oligocene thecideide brachiopod *L. mediterranea* (LMU-LME01 and LMU-LMO01 respectively). The EBSD colour code is given by the IPF triangle shown in Fig. S2.3.4. Scale bars represent 50 μm for the Eocene sample and 100 μm for Oligocene one.

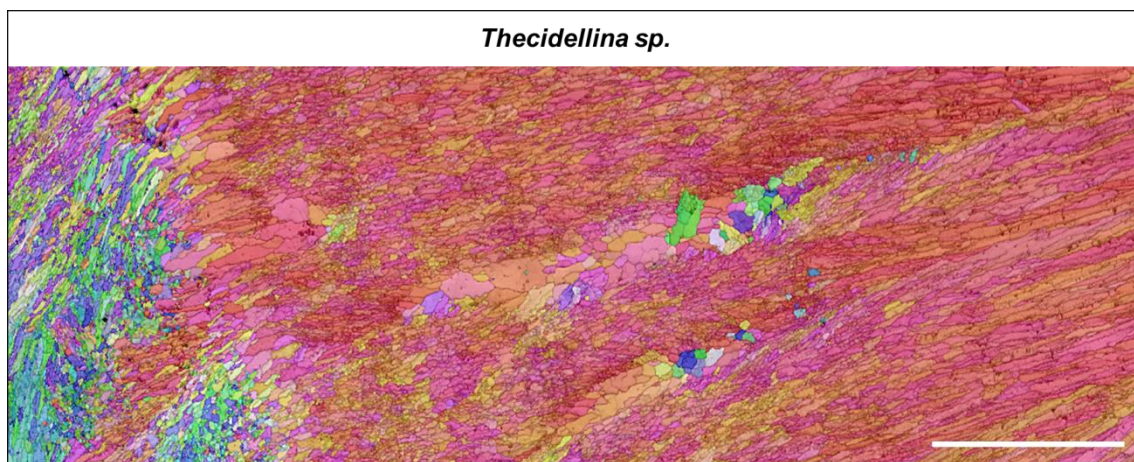


Figure S2.3.13. Orientation pattern of calcite shown colour-coded and derived from EBSD measurements for the shell of the Pleistocene thecideide brachiopod *Thecidellina* sp. (UF 325201). The EBSD colour code is given by the IPF triangle shown in Fig. S2.3.4. Scale bar represents 100 μm .

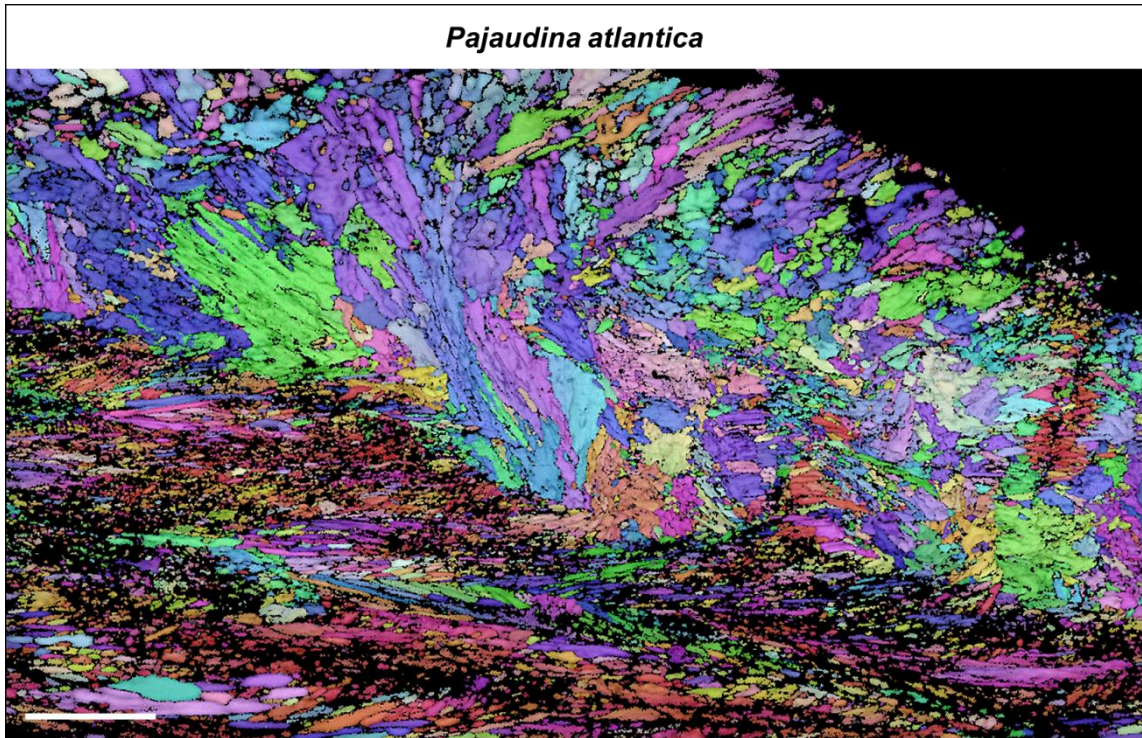


Figure S2.3.14. Orientation pattern of calcite shown colour-coded and derived from EBSD measurements for the shell of the Recent thecideide brachiopod *P. atlantica* (LMU-PA008). The EBSD colour code is given by the IPF triangle shown in Fig. S2.3.4. Scale bar represents 20 μm .

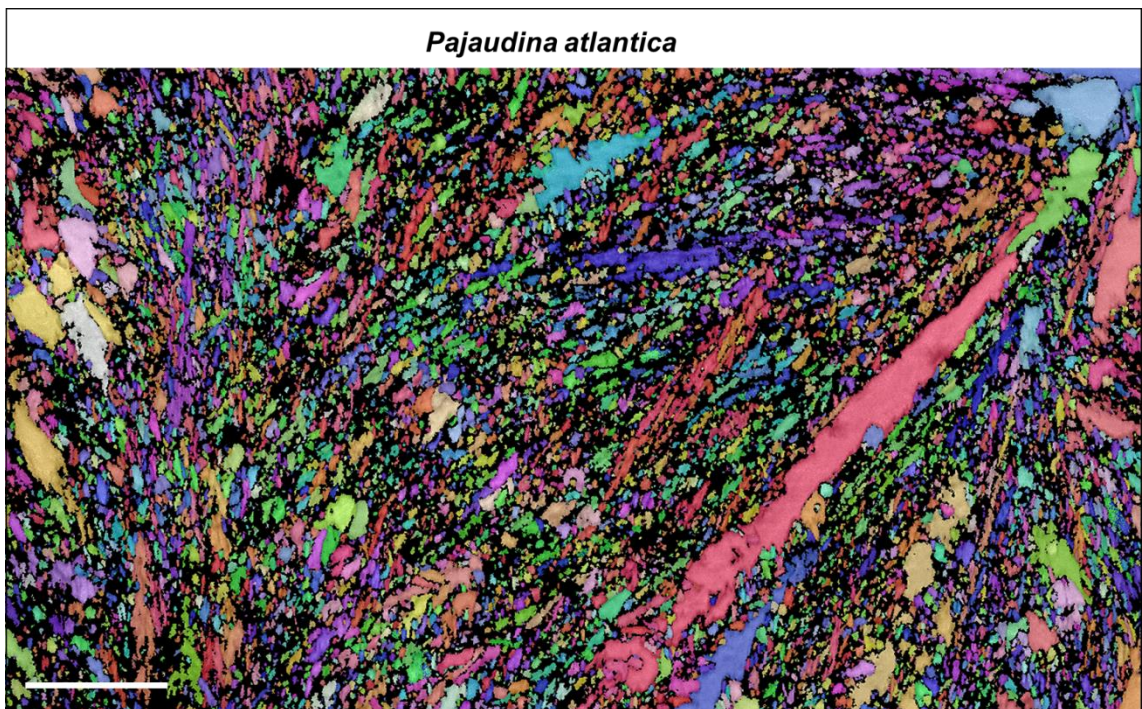


Figure S2.3.15. Orientation pattern of calcite shown colour-coded and derived from EBSD measurements for the shell of the Recent thecideide brachiopod *P. atlantica* (LMU-PA010). The EBSD colour code is given by the IPF triangle shown in Fig. S2.3.4. Scale bar represents 20 μm .

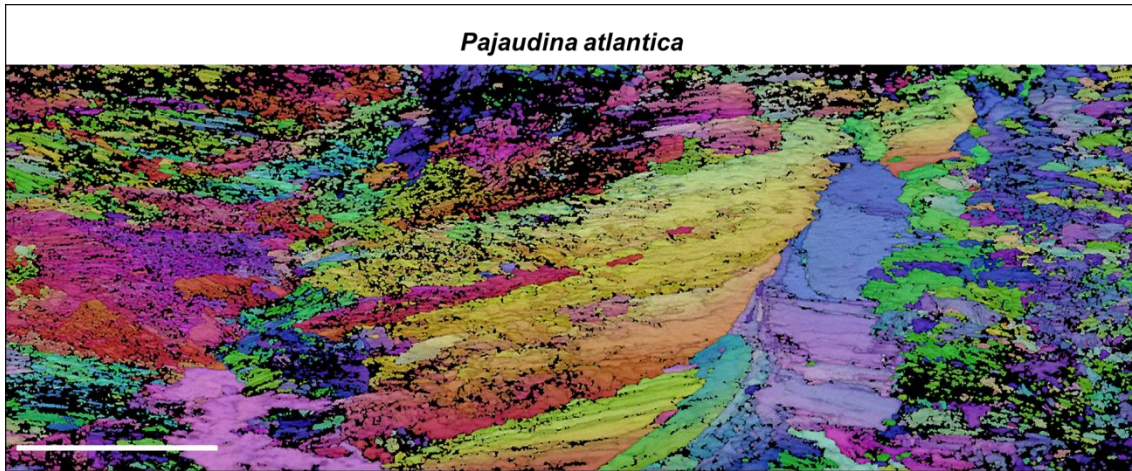


Figure S2.3.16. Orientation pattern of calcite shown colour-coded and derived from EBSD measurements for the shell of the Recent thecideide brachiopod *P. atlantica* (LMU-PA009). The EBSD colour code is given by the IPF triangle shown in Fig. S2.3.4. Scale bar represents 50 μm .

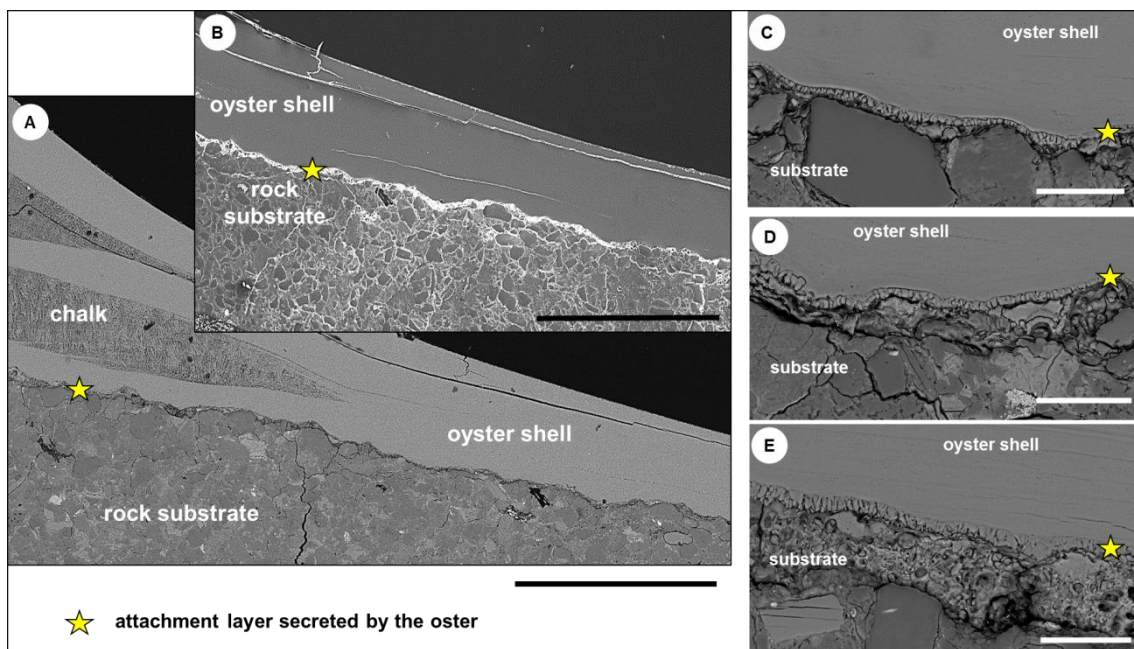


Figure S2.3.17. BSE images depicting the attachment of the shell of the oyster *Magallana gigas* onto the substrate. Attachment is made by a thin mineralized layer (yellow star in all images) secreted by the animal. The thickness of the attachment layer varies, depending on the roughness of the substrate. Scale bars represent 1mm for A-B and 50 μm for C-E.

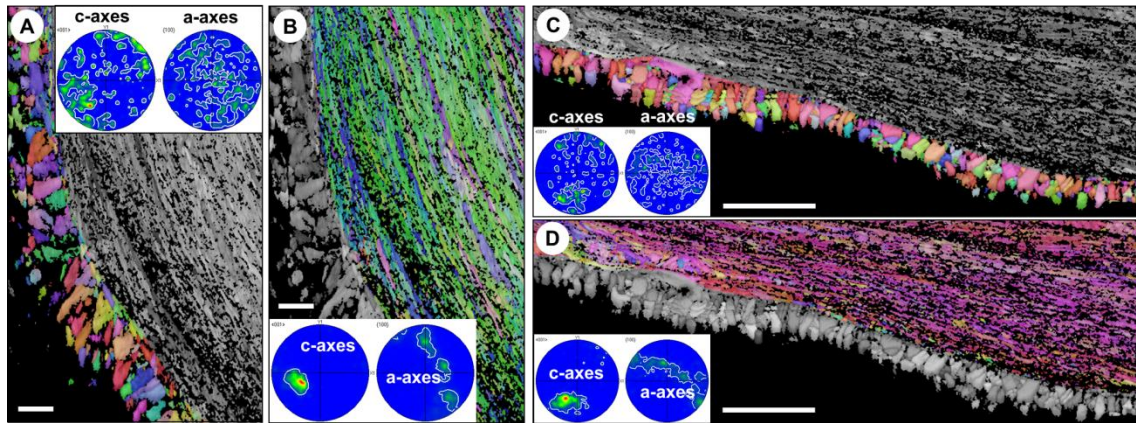


Figure S2.3.18. Orientation pattern of calcite shown with colour-coded EBSD maps and density distributions of associated pole figures for the attachment layer (A and C) and foliated calcite (B and D) of *Magallana gigas* shell. There is a significant difference in microstructure and texture: The strength of calcite co-orientation is low (MUD values 19, 21) within the attachment layer, while it is significantly higher (MUD values 38, 44) in the foliated calcite shell portion. Scale bars represent 10 μm for A-B and 20 μm for C-D.

2.4. Diversity of mineral and biopolymer assembly in modern terebratulide, rhynchonellide, thecideide and craniide brachiopod shells

MABI-D-20-00572 - Submission Confirmation [↗](#)



From Marine Biology (MABI) <em@editorialmanager.com> on 2020-12-02 18:38

[✉ Detalles](#)

Dear Mrs. Simonet Roda,

Thank you for submitting your manuscript, Diversity of mineral and biopolymer assembly in modern terebratulide, rhynchonellide, thecideide and craniide brachiopod shells, to Marine Biology.

The submission id is: MABI-D-20-00572

Please refer to this number in any future correspondence.

2.4. Diversity of mineral and biopolymer assembly in modern terebratulide, rhynchonellide, thecideide and craniide brachiopod shells

Simonet Roda M.*(1), Griesshaber E. (1), Angiolini L. (2), Rollion-Bard C. (3), Milner S. (3), Ye F. (4), Henkel D. (5), Häussermann V. (6), Eisenhauer A. (5), Brand U. (7), Gnägi H. (8), and Schmahl W.W. (1)

1. Department of Earth and Environmental Sciences, LMU Munich, Germany

2. Dipartimento di Scienze della Terra "A. Desio", Università degli Studi di Milano, Milano, Italy

3. Université de Paris, Institut de physique du globe de Paris, CNRS, F-75005 Paris, France

4. University of Wollongong, School of Earth, Atmospheric and Life Sciences, Wollongong NSW 2522, Australia

5. GEOMAR-Helmholtz Centre for Ocean Research, Marine Biogeochemistry/Marine Geosystems, Kiel, Germany

6. Huinay Scientific Field Station, Casilla, Puerto Montt, Chile

7. Earth Sciences Department, Brock University, St. Cathrines, Ontario, L2S 3A1, Canada

8. Diatome Ltd, Helmstraße 1, CH-2560 Nidau, Switzerland

*Corresponding author: simonet@lrz.uni-muenchen.de

Abstract

Biological hard tissues are a rich source of design concepts for the generation of advanced materials. They represent the most important library of information on the evolution of life and its environmental conditions. Biology constructs its structural material bottom-up. It is a fabrication principle that is intrinsic to tissues secreted by organisms. It emerged early in the geological record, with the start of biological mineralization.

The phylum Brachiopoda is one of the few marine animal groups that have a complete fossil record from early Cambrian to recent times. Throughout this entire time period Brachiopoda secreted phosphate and carbonate shells and populated many and highly diverse marine habitats. This required significant metabolic flexibility that is adaptation of soft and hard tissue to specific marine environments and living conditions.

In this article we review main modes of mineral and biopolymer organization for recent, carbonate shell producing, brachiopods. We describe and juxtapose shell tissue characteristics for taxa of the orders Rhynchonellida, Terebratulida, Thecideida and Craniida. We highlight calcite and organic matrix assembly on nano-, micro- and micrometer scale based on results obtained with electron backscatter diffraction (EBSD), AFM (Atomic Force Microscopy), FE-SEM (Field Emission Scanning Electron Microscopy) and STEM (Scanning Transmission Electron Microscopy). We show differences in composite hard tissue organization for taxa having different life styles, highlight, in particular, thecideide shell characteristics, visualize the nanostructure of and calcite assembly in rhynchonellide fibers and discuss for representatives of Rhynchonelliformea the feasibility to use the shells as archives for proxies for paleoenvironment reconstruction.

2.4.1. Introduction

Brachiopods are a phylum of sessile marine organisms which secrete either phosphatic (Linguliformea) or calcareous (Craniiformea, Rhynchonelliiformea) shells. Brachiopods are one of the very few marine organism groups which have a complete fossil record (Carlson 2016, Harper et al. 2017). First species of both phosphate as well as carbonate shells producing orders appeared in early Cambrian, already at the very start of biological tissue formation. During the Ordovician, the phylum diversified significantly (e.g. Carlson 2016, Harper et al. 2017), what initiated that by the end of the Ordovician major differences were developed in life-styles and, with this, shell structure and morphology (e.g. Williams 1997, Harper and Drachen 2010, Harper et al. 2015, Harper et al. 2017). The end-Permian extinction erased the majority of Paleozoic brachiopod taxa and impacted severely taxonomic, morphological, functional and ecological brachiopod diversity (Carlson 2016). Some groups survived end-Permian extinction, diversified, occupied new ecological niches and form today the extant orders of the Lingulida, Craniida, Rhynchonellida, and Terebratulida. The Thecideida appeared after the end-Permian crisis, in the Triassic. Representatives of the five extant brachiopod orders populate today mainly shallow to moderately deep, rarely very deep, sea floor environments and live in a wide range of marine habitats (e.g. Williams 1973, Peck et al. 1997, Williams et al. 2000, Williams and Carlson 2007, Bittner 2000, Peck 2001, Williams and Cusack 2007, Peck 2007, Peck and Harper 2010, Cross et al. 2015, Carlson 2016, Finnegan et al. 2016, Cross et al. 2016, Harper et al. 2017, Ye et al. 2018a, 2018b, Cross et al. 2018, Ye et al. 2019).

The geological record shows that brachiopods were and are able to adopt to many marine environments (see the references above). They live in open ocean as well as in sheltered, cryptic habitats, settle within as well as on sediment or/and rock surfaces. When living on the sea floor, brachiopods are either attached to it by a pedicle or lie free or are cemented with their ventral valve to the sediment/rock substrate. Representatives of the five extant brachiopod orders have different modes of larval development, differ significantly in soft-tissue anatomy, shell morphology, shell chemistry, shell microstructure, texture, amount, type and fabric of organic substance intercalated into the shell. Thus, we find today large diversity in brachiopod body plans as well as morphological, structural and chemical features of their shell.

In this review we focus on modern calcite shelled brachiopods and detail shell structural characteristics. We do not summarize shell morphology or shell chemistry. The aim of this article is to give a comprehensive overview of microstructure, texture, biopolymer content and distribution for representatives of all four extant calcite shell producing brachiopod orders: the Terebratulida, Rhynchonellida, Thecideida and Craniida. We discuss in total 20 modern brachiopod taxa (Table S1): 2 rhynchonellide, one craniide, three thecideide and 14 terebratulide species. We base our review on measurements gained with electron backscatter diffraction (EBSD), AFM, STEM and FE-SEM imaging of fractured and etched shell cross-section surfaces. Studies of the last decades address modern brachiopod shell structure, microstructure, texture (e.g. Williams 1973, Williams 1997, Williams and Cusack 2007, Schmahl et al. 2004, Griesshaber et al. 2007, Cusack and Williams 2007, England et al. 2007, Perez-Huerta et al. 2007, Schmahl et al. 2008, Cusack et al. 2008, Goetz et al. 2009, Merkel et al. 2007, Merkel et al. 2009, Goetz et al. 2011, Schmahl et al. 2012, Gaspard and Nouet 2016, Ye et al. 2018a, 2018b). However, these rarely deal with the composite nature of

the shell and concentrate on either one or only very few, in general, rhynchonellide, terebratulide species. Especially shell microstructure, texture of the Thecideida and Craniida is little characterized.

In this contribution we highlight the following:

- (i) Difference in microstructure and texture for representatives of the different calcite-shelled orders.
- (ii) Difference in shell microstructure and texture between species that attach by a pedicle and those that live cemented with a valve to the substrate/sediment, respectively.
- (iii) Difference in shell structure between thecideide species and the primary shell-layer of rhynchonellide and terebratulide taxa. As thecideide shell microstructure and texture is up to now little investigated, we place specific attention to the shell structure of these brachiopods.
- (iv) The mode of organic substance intercalation into different shell layers of rhynchonellide and terebratulide as well as into the shell of thecideide and craniide species, respectively.
- (v) The nanometre scale structure of modern rhynchonellide, terebratulide fibers as reference for the assessment of overprint of fossil equivalents. It is known by now that for a reliable assessment of alteration it is necessary to investigate the nanometre scale crystallite assembly of the biogenic archive as well (Casella et al. 2018). Paleoenvironment reconstruction based on brachiopod archives relies strongly on the preservation state of the fibrous shell layer. Accordingly, we place major attention on the fibers and summarize the present knowledge of nanocrystalline calcite assembly in the fibrous layer of rhynchonellide and terebratulide shells.

This review is divided into seven chapters:

Subsequent to an introduction we show in chapter 1 the distinctness in shell calcite organization for representatives of Terebratulida, Rhynchonellida, Thecideida and Craniida.

As second we describe characteristics of the biocrystals and subsequently, in chapter 3, the pattern of organic substance within the shells.

In chapter 4 we discuss nanometre scale structural features of terebratulide and rhynchonellide shell fibers and highlight in particular (i) their hierarchical internal structuring and (ii) demonstrate that fibers incorporate a network of thin organic fibrils.

The fifth chapter details for terebratulide, rhynchonellide, thecideide and craniide representatives patterns of calcite assembly in the shells and describes characteristics of the texture. We show that shells of modern, calcitic brachiopods are constructed of only five types of basic mineral units: dendrites, fibers, columns, platelets and polygonal biocrystals.

Chapter 6 discusses modern thecideide shells in greater detail and describes differences/similarities in shell chemistry of thecideide and terebratulid species.

We end our review with a concluding summary (chapter 7) where we address: (i) microstructural adaptation to environments, (ii) the advantage of a hierarchical and composite hard tissue microstructure, (iii) determinants of microstructure and texture

fabrication, (iv) characteristics of thecideide shell microstructures and their applicability for paleoenvironment reconstruction.

2.4.2. Materials, sample preparation and methods

Materials

We investigated the following modern brachiopod specimens (Table S1): *Megerlia truncata* (Linnaeus, 1767), (Terebratulida), *Magellania venosa* (Dixon, 1789) (Terebratulida), *Terebratulina septentrionalis* (Couthouy, 1838) (Terebratulida), *Terebratalia transversa* (Sowerby, 1846) (Terebratulida), *Magellania flavescens* (Lamarck, 1819) (Terebratulina), *Terebratulina crossei* (Davidson, 1882) (Terebratulina), *Terebratalia palustris* (Linnaeus, 1767) (Terebratulina), *Calloria inconspicua* (Sowerby, 1846) (Terebratulida), *Magasella sanguinea* (Leach, 1814) (Terebratulida), *Laqueus rubellus* (Sowerby, 1870) (Terebratulida), *Liothyrella uva* (Broderip, 1833) (Terebratulida), *Liothyrella neozelanica* (Thomson 1918) (Terebratulida), *Gryphus vitreus* (Born, 1778) (Terebratulida), *Magellania fragilis* (Smith, 1907) (Terebratulida), *Terebratulina retusa* (Linnaeus, 1758) (Terebratulida), *Notosaria nigricans* (Sowerby, 1846) (Rhynchonellida), *Neorhynchia strebeli* (Dall, 1908) (Rhynchonellida), *Kakanuiella chathamensis* Lüter, 2005 (Thecideia), *Pajaudina atlantica* Logan, 1988 (Thecidea), *Thecidellina blochmanni* (Dall 1920) (Thecidea), *Novocrania anomala* (Müller, 1776) (Craniida).

Methods and sample preparation

For visualizing the distribution pattern of organic substance within the shells, we etched shell cross-sections. First even surfaces were obtained by cutting and polishing the samples with glass and diamond knives. The surfaces were then etched with a 0.1 M HEPES (pH=6.5) and 2.5% glutaraldehyde solution for 90 and 120 seconds. Etching was terminated by rinsing the samples three times in 100% isopropanol for 10 seconds each. Subsequently, samples were critical point dried, coated and imaged at 4kV with a Hitachi SU5000 FE-SEM.

Electron backscatter diffraction (EBSD)

Microstructure and texture characterization is based on Electron Backscatter Diffraction (EBSD) measurements. Shell samples were embedded in epoxy resin, subjected to several sequential mechanical grinding and polishing steps. The final step consisted of etch-polishing with colloidal alumina in a vibratory polisher. For EBSD measurements the samples were coated with 4-6 nm of carbon; measurements were carried out on a Hitachi SU5000 field emission SEM, equipped with an Oxford EBSD detector. The SEM was operated at 20 kV, Kikuchi patterns were indexed with the CHANNEL 5 HKL software. Information obtained from EBSD measurements is presented as band contrast measurement images and as colour-coded crystal orientation maps with corresponding pole figures; the latter giving either individual data points or, in the contoured version, the strength of the clustering of poles. When contouring, we use the lowest possible degree for half width and cluster size, a half width of five and a cluster size of three degrees, respectively. The half width controls the extent of the

spread of the poles over the surface of the project sphere. A cluster comprises data with the same orientation.

EBSD band contrast gives the signal strength of the EBSD-Kikuchi diffraction pattern and is displayed as a grey-scale component in a map. The strength of the EBSD signal is high when a crystal is detected (bright in the map), whereas it is weak or absent when a polymer, such as organic matter, is scanned (dark/black in the map). Co-orientation statistics are derived from pole figures and are given by the MUD (multiple of uniform (random) distribution) values. The MUD value measures texture sharpness in the scanned area; a high MUD value indicates high crystal co-orientation, while a low MUD value reflects a low co-orientation, i.e. high misorientation.

Imaging with SEM

For SEM imaging samples were coated with 4-6 nm of Pt/Pd, images were taken with a Hitachi SU5000 at 4kV and show secondary electron contrasts.

Imaging with AFM

The sub-micrometre and nanostructure of brachiopod shell calcite was visualized with atomic force microscopy (AFM). Samples were measured in contact mode with a JPK NanoWizard II AFM using silicon cantilevers. The measurements of lateral and vertical deflection traces were processed with the NanoWizard® IP image processing software and Gwyddion free and open source software. We used the “Gold” scale for colour. The lateral and vertical deflection traces are the result of the interaction between the cantilever tip and the sample surface.

Imaging with STEM

Magellania venosa shell fibers were imaged with a STEM detector attached to a Hitachi SU5000 field emission SEM. 40 to 80 nm thin sections were cut of fresh shells using a Reichert Ultracut S and an Ultra-type diamond knife (Diatome). Sections were mounted on copper EM grids (Plano) and imaged with a HAADF Annular SEM STEM detector (Deben).

Geochemical analyses - Oxygen isotope analysis by Ion Microprobe

Oxygen isotope composition of two specimens of the modern brachiopod *P. atlantica* and one specimen of the modern brachiopod *M. venosa* was analysed by ion microprobe. We investigated primarily the ventral valves for both species. To assess the variability in oxygen isotope composition, transects through the shells were performed from outermost to innermost shell portions; 20 μm spots were shot with a step size between two spots of 50 μm . Prior to analyses, the valves were cut from anterior to posterior shell regions into halves. One half was embedded into epoxy resin and polished with diamond paste down to 1 μm . Measurements were carried out at CRPG (Centre de Recherches Pétrographiques et Géochimiques, Nancy, France) and followed closely the technique described by Rollion-Bard et al. (2007). A Cameca IMS 1280-HR2 was used for measurements. Instrumental mass fractionation (IMF) was corrected for by normalizing the results gained on the samples with two in-house calcite reference materials, BRET ($\delta^{18}\text{O}=-10.87\text{‰}$ V-PDB, Rollion-Bard and Marin-Carbonne 2011) and CCciAg ($\delta^{18}\text{O}=-11.61\text{‰}$ V-PDB). IMF was also corrected for the effect Mg content with the correction of $-0.3 \times \text{MgO \% wt}$ (Rollion-Bard and Marin-Carbonne 2011). The

internal $2\sigma_n$ error was less than $\pm 0.1\%$. External reproducibility (1σ), based on replicates of the calcite in-house reference materials, was ± 0.13 and 0.28% , depending on the analytical session. The total error for each $\delta^{18}\text{O}$ value takes into account the external reproducibility and the internal error. All $\delta^{18}\text{O}$ values are reported in ‰ and are given relative to V-PDB (Vienna Pee Dee Belemnite) international standard.

Geochemical analyses - Trace and minor element compositions by laser ablation coupled to an ICP-MS (Inductively Coupled Plasma Mass Spectrometry)

The method described in Rollion-Bard et al. (2019) was applied for the measurements of trace and minor element compositions. An Analyte G2 Excimer laser ablation system (193 nm), coupled to a quadrupole Agilent 7900 series (LA-Q-ICP-MS) was operated at a repetition rate of 5 Hz and an energy fluence of 3.7 mJ/cm^2 . Samples were analyzed using a laser spot of $40\mu\text{m}$ diameter. The isotopes ^7Li , ^{23}Na , ^{24}Mg , ^{25}Mg , ^{27}Al , ^{44}Ca , and ^{88}Sr were monitored. Measurements of NIST glass standard 610 and 612 were acquired before and after each run of 10 to 20 analyses, depending on the shell thickness. The overall precision (Relative Standard Deviation, RSD) of the element ratios, calculated adding the errors in quadrature, are based on repeated measurements of NIST 612 glass. RSD was 10% for Li/Ca in *M. venosa*, 20% for Li/Ca in *P. atlantica* and 2% for Na/Ca, 4% for Mg/Ca and 2% for Sr/Ca in both species.

In this study we use for fibers, columns, acicles, granules also the terms mineral units or biocrystals. The outermost, mineralized, shell layer of terebratulide and rhynchonellide shell we call, in correspondence with the used terminology, primary or outer shell layer. For the secondary and tertiary shell layers we use the terms fibrous (secondary) and columnar (tertiary). It has been shown for three-layered modern brachiopods that fibrous layers alternate with columnar layers (Goetz et al. 2009); accordingly, a successive numbering of the two inner shell layers (secondary, tertiary) is not applicable. Even though, when we refer to the different shell layers, we use our terminology and give in parenthesis ‘secondary/tertiary’, the conventional brachiopod shell layer terminology.

2.4.3. Diversity of microstructures

EBSD band contrast measurement images highlight the distinctness and diversity of biocrystal shapes, sizes and microstructures that we find for modern rhynchonellide and terebratulide (Fig. 2.4.1) and thecideide (Fig. 2.4.2A) and craniide (Fig. 2.4.2B) shells.

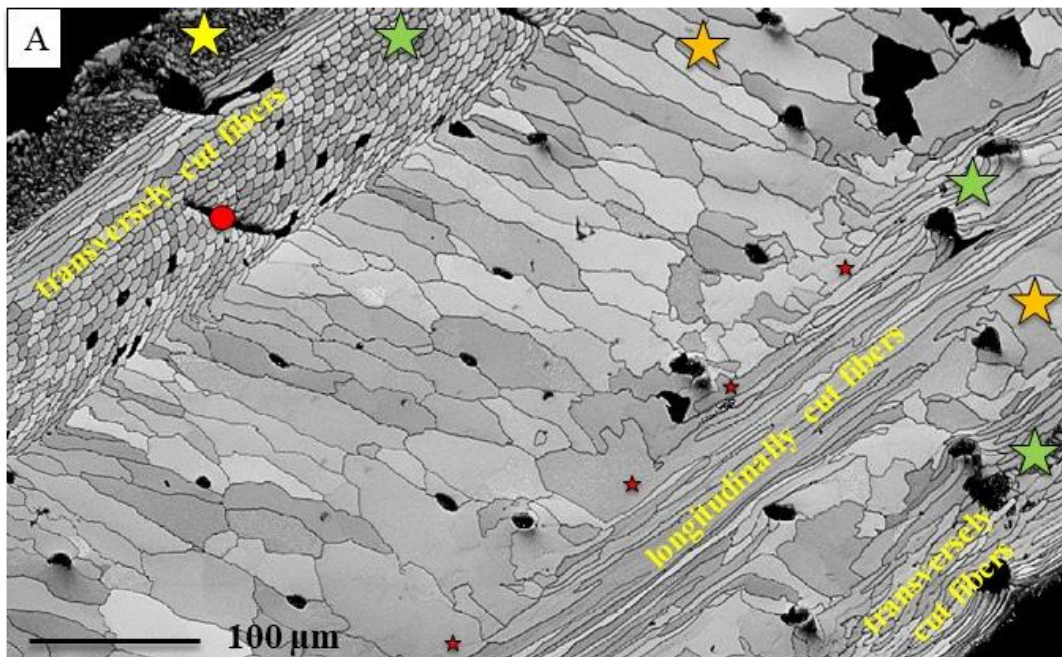
Depending on the species, modern rhynchonellide and terebratulide valves consist of four layers: an outer organic layer, the periostracum and, at most, three mineralized shell layers, the primary, fibrous (secondary) and columnar (tertiary) shell layers. Even though all three mineralized shell layers are distinct in microstructure (Fig. 2.4.1), the calcite in all layers has a systematic pattern of crystallographic preferred orientation, a well-ordered structure (this study and Schmahl et al. 2004, Griesshaber et al. 2007, Cusack et al. 2008, Goetz et al. 2009, Griesshaber et al. 2009, Ye et al. 2018a, 2018b).

The degree of ordering of calcite mineral units is low, even close to almost random, in modern thecideide and craniide shells (chapter 5 and Simonet Roda et al. 2020). Modern thecideides form their shell of mineral units that have a multitude of sizes and shapes (Fig. 2.4.2A). These are assembled in the shell without any obvious arrangement. Modern craniides form most of their shell of mainly one type, small (2 to

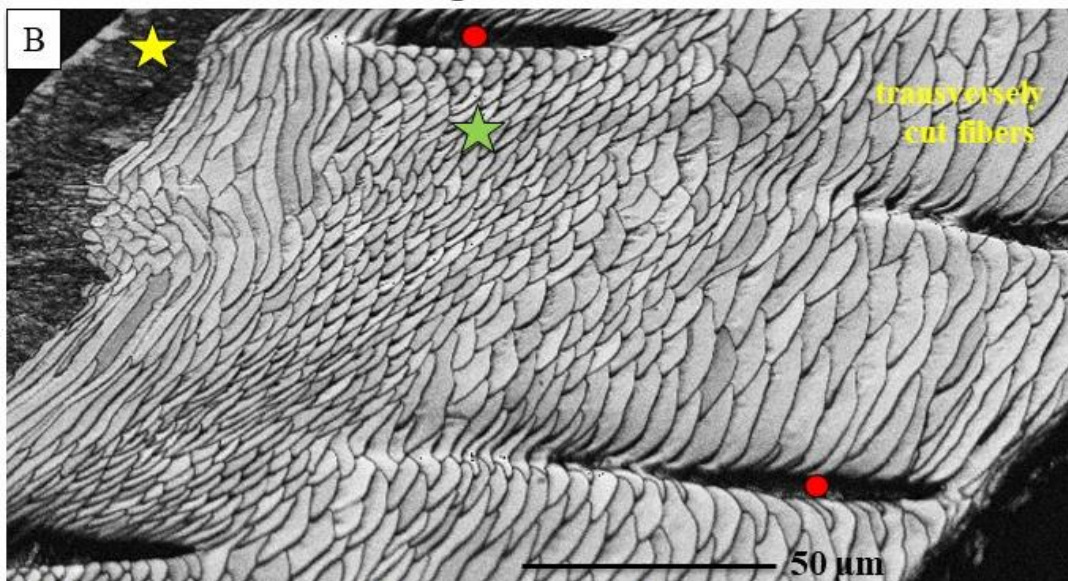
4 μ m times 400 to 600 nm in cross-section) tablet-resembling mineral units (Fig. 2.4.2B) and arrange these to stacks of thin (400 to 500 nm in cross-section), often curved, calcite layers. Being tablet-shaped, the mineral units in craniide shells are addressed as ‘semi-nacre’ structures (Williams and Wright 1970, England et al. 2007, Perez-Huerta et al. 2007). We will show in chapter 5 (Figs. 2.4.21, S2.4.19) that even though craniide shells are formed of tablets, the latter have nothing to do with the tablets and their arrangement to columnar and sheeted nacre that we find in modern and fossil mollusc shells.

We show in this review that craniide shells have the weakest texture; the crystals are the least co-oriented. Calcite in thecideide shells has a slightly higher preferred orientation. The highest crystallographic preferred orientation is in the columnar shell layer of Terebratulida. Relative to the columns, slightly reduced in co-orientation strength, is the primary shell layer of Rhynchonellida and Terebratulida. The fibrous shell layer of Rhynchonellida and Terebratulida has always a lower preferred orientation, relative to that of the primary and the columnar shell layers, respectively.

Liothyrella neozelanica

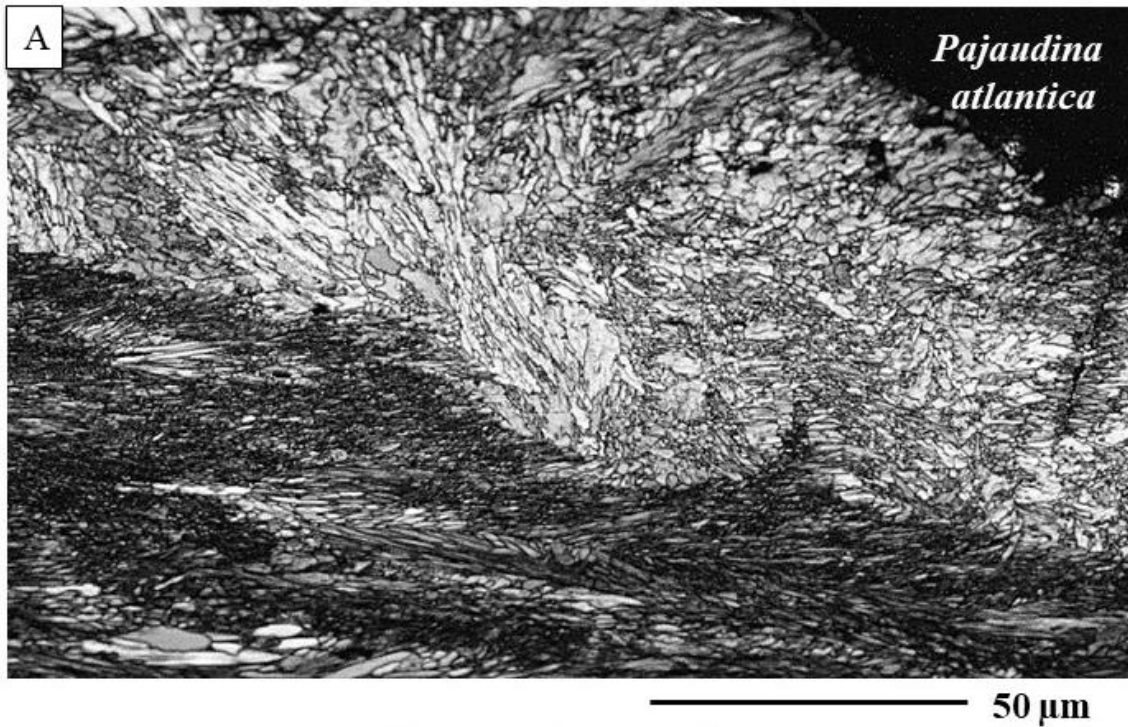


Magellania venosa



★ primary layer ★ fibres ★ columns ● puncta

Figure 2.4.1. EBSD band contrast measurement images depicting shell microstructure of *L. neozelanica* (A) and *M. venosa* (B). Note the significant difference between (i) the primary (yellow star in A and B) and the two other mineralized shell layers and, (ii), especially for the shell of *L. neozelanica*, in mineral unit (biocrystal) size and morphology. Note further the alternation of fibers (green star in A) and columns (orange star in A) within the innermost mineralized layer of the shell of *L. neozelanica* (see also Goetz et al. 2011, Ye et al. 2018a). Red dots in A and B indicate puncta. The change-over from columns to fibers is smooth; an organic membrane delineating fibrous and columnar shell layers is absent (red stars in A).



Novocrania anomala

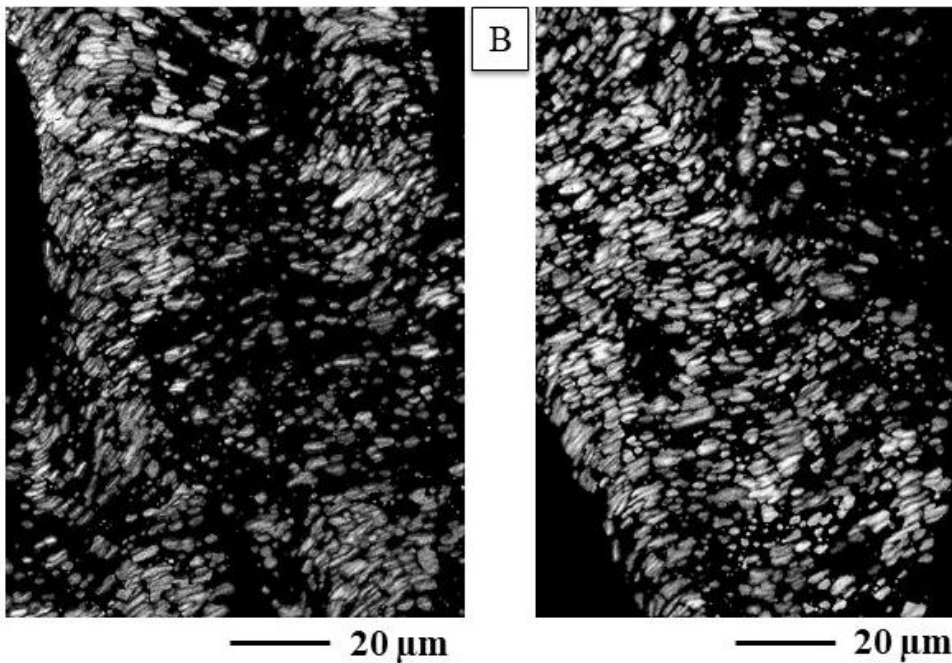


Figure 2.4.2. EBSD band contrast measurement images depicting shell microstructure of *P. atlantica* (A) and *N. anomala* (B). The shell of *P. atlantica* consists of a multitude of differently shaped and sized calcite crystals that comprise the shell without any obvious systematic assembly pattern. In contrast, calcite in *N. anomala* forms small tabular mineral units that form thin layers. The latter undulate often and assemble to stacks.

2.4.4. Diversity of biocrystal morphologies

Figures 2.4.3-6 and supplementary information Figures S2.4.1-6 visualize morphological differences of biocrystals that form rhynchonellide, terebratulide, thecideide and craniide shells. We show characteristics on micrometre, submicrometre scale levels. The primary shell layer of rhynchonellides, terebratulides (Figs. 2.4.3A-B, S2.4.1-3) consists of interdigitating mineral units. These are often larger-sized at the base of the primary layer, next to the fibers (yellow star in Figs. 2.4.3A, S2.4.4B) and decrease in size generally towards outer primary layer regions (Fig. 2.4.3A). However, we often observe that the outermost primary shell layer section is seamed by a row of large crystals (yellow arrows in Fig. S2.4.3). The very tip of the valves of Rhynchonellida and Terebratulida is also always formed of primary layer calcite (Fig. S2.4.3).

The transition from the primary to the fibrous shell layer is smooth (Fig. S2.4.2B), an organic membrane that would delineate the two shell layers is absent. The primary shell layer of rhynchonellide and terebratulide brachiopod shells is not nanogranular, it does not consist of an assembly of nanogranules as described previously by Williams (Williams 1973). This shell layer has a very specific structure and is devoid of intercalations of organic material. Large fractal-like, irregularly shaped and differently oriented mineral units interdigitate in 3D and constitute the layer (Fig. 2.4.15C and Goetz et al. 2011). The specific mode of interlinkage of the fractal-shaped mineral units creates the impression that this part of the shell is nanogranular.

In all rhynchonellides and terebratulides, the layer next to the primary shell layer is formed by an assembly of fibers (Figs. 2.4.3C-D, S2.4.1, S2.4.3-4) being within a well-structured network of organic membranes, the extracellular biopolymer matrix. The membranes are about 100 to 120 nm thick (chapters 3 and 4). Individual fibers are not fully encased by organic substance, only one surface of the fiber is covered by an organic lining. Within the fibrous shell layer the fibers form stacks consisting of, more or less, parallel arrays of fibers (Fig. 2.4.4A-B and Griesshaber et al. 2007, 2009, Goetz et al. 2011). The stacks change their orientation within the layer by a few tens of degrees; thus in 2D cuts we find diagonally, transversely and longitudinally cut fibers (Figs. S2.4.4B, S2.4.1). The arrangement pattern of the stacks is comparable to a twisted plywood structure. When cut in cross-section, the convex-concave morphology of the fibers and their staggered arrangement is a significant characteristic for terebratulide and rhynchonellide brachiopod shells (Fig. 2.4.3C and Simonet Roda et al. 2019a, 2019b) and differs significantly from fibrous assemblies of other biological hard tissues, e.g. calcite fibers in *Mytilus edulis* shells. It has been shown by Ye et al. 2018a, 2018b that fiber length, roundness and convexity of modern rhynchonellides and terebratulides can be related to ontogenetic developments and environmental conditions.

Calcite fibers in brachiopod shell are curved (Fig. S2.4.4A), especially at punctae. The calcite in modern brachiopod fibers consists of 200 to 400 nm sized units that are further substructured (chapter 4). In cross-section the calcite within an individual fiber is arranged to thin, 80 to 100 nm sized, layers (Figs. 2.4.3D, S2.4.4C).

When developed in the shell, the columnar shell layer is formed of large, prism-shaped entities, so called columns (Figs. 2.4.3E, S2.4.5). The columns are delineated from each other by organic membranes, have often irregular morphologies (Fig. S2.4.5) and interdigitate slightly (yellow/magenta stars in Fig. S2.4.5). The transition between

the columns and the fibers is smooth, especially between columns and longitudinally cut fibers (Fig. S2.4.5). It is most remarkable that calcite crystallites within the columns have rhombohedral morphology (Fig. 2.4.3F), resembling the morphology of inorganic calcite precipitated from solution. Goetz et al. 2009 and Schmahl et al. 2012 describe brachiopod column growth in detail and find that columns form through a competitive growth process (Fig. S2.4.5B). Competitive growth is based on the fact that the calcite c-axis is the fastest direction of growth and that only those crystals that have their c-axes parallel to the main growth direction of the shell extend in size. Crystals that have their c-axes inclined to the plane of nucleation are hindered in growth as they abut with their neighbors.

Modern craniide and thecideide species form their shell with entirely different structural patterns (Figs. 2.4.4-6, S2.4.6). The craniids (Figs. 2.4.4, 2.4.5C-F, S2.4.6) secrete sequences of 300 to 500 nm thin layers consisting of tabular calcite crystallites, when imaged with SEM (Figs. 2.4.5C, 2.4.6C-F) or scanned with EBSD (Fig. 2.4.4C) in cross-section. The layers are very often curved (Figs. S2.4.6C-D). Their curvature is easily obtained as the constituting platelet-shaped crystallites (Fig. 2.4.4C) do not interdigitate, are only slightly misoriented to each other, as required by the curvature of the layer. In surface view individual crystals vary significantly in size (Figs. 2.4.5D-F) and have a spiral aspect (Figs. 2.4.5D-F, S2.4.6G).

Modern thecideides form their shell of a multitude of differently sized and shaped mineral units (Figs. 2.4.6, 2.4.5A-B) that assemble the shell without any obvious regularity or assembly pattern (Fig. 2.4.6). We observe occasionally that mineral units interlink (white stars in Fig. 2.4.6D), however, their interlinkage is dissimilar to the interdigitation of dendrites of the primary shell layer.

Liothyrella uva

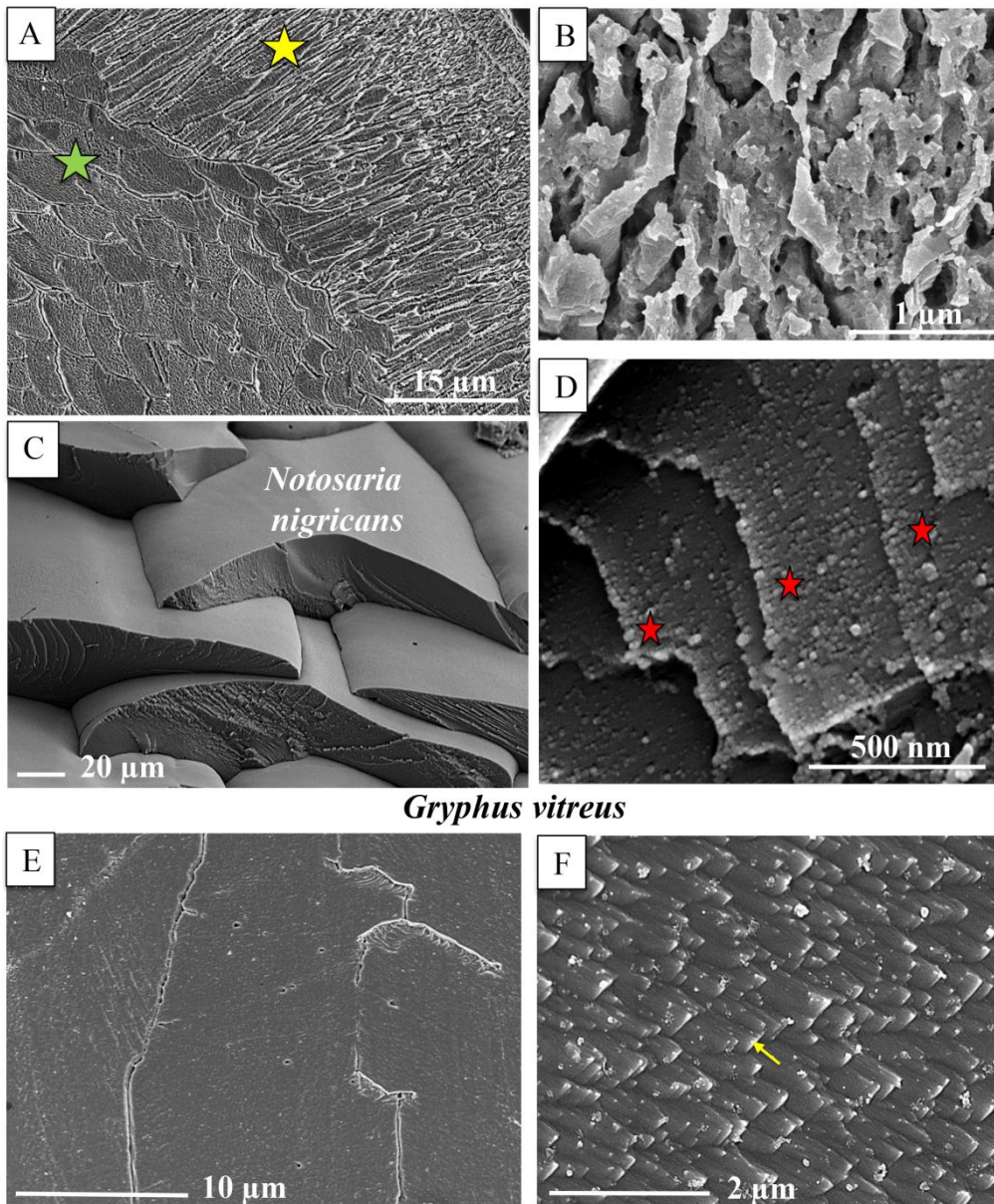


Figure 2.4.3. SEM images taken on microtome knife polished and etched (A, B, E, F) as well as on fractured surfaces (C, D) of the different shell layers of *Liothyrella uva* (A, B), *Notosaria nigricans* (C, D) and *Gryphus vitreus* (E, F). (A, B) primary shell layer, (C, D) fibrous shell layer, (E, F) columnar shell layer. Note the difference in submicronscale structure for the different shell layers: (B) irregularly shaped units comprise the primary layer, (D) sequences of layers (red stars in D) with nanosized entities form the fibers, (F) calcite crystals with rhombohedral morphologies constitute the columns.

Novocrania anomala

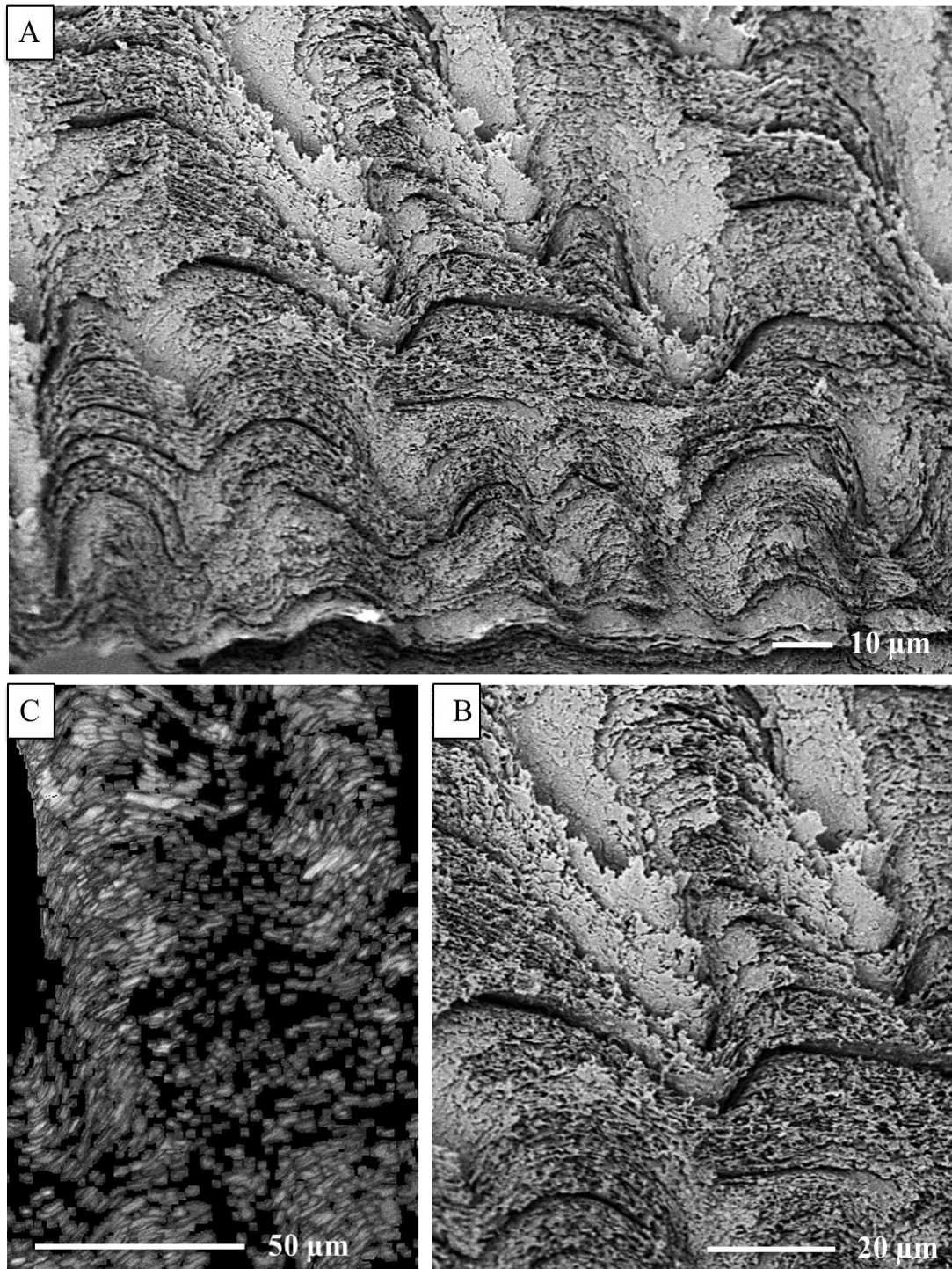
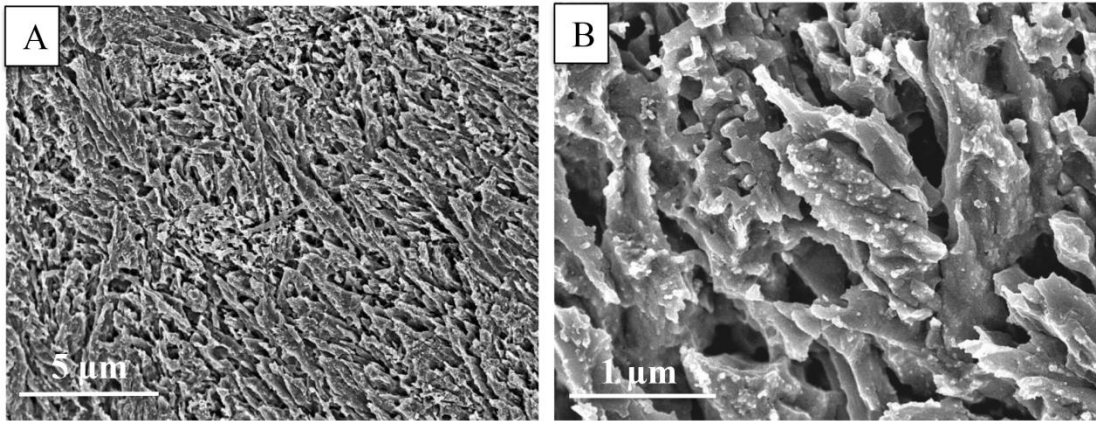


Figure 2.4.4. SEM images (A, B) and EBSD band contrast measurement image (C) depicting the shell structure of modern *Novocrania anomala*. Shell calcite consists of a sequence of thin, curved calcite layers (Figs. 2.4.4A-B), the latter comprising strings of platelet-shaped calcite crystallites (Fig. 2.4.4C).

Kakanuiella chathamensis



Novocrania anomala

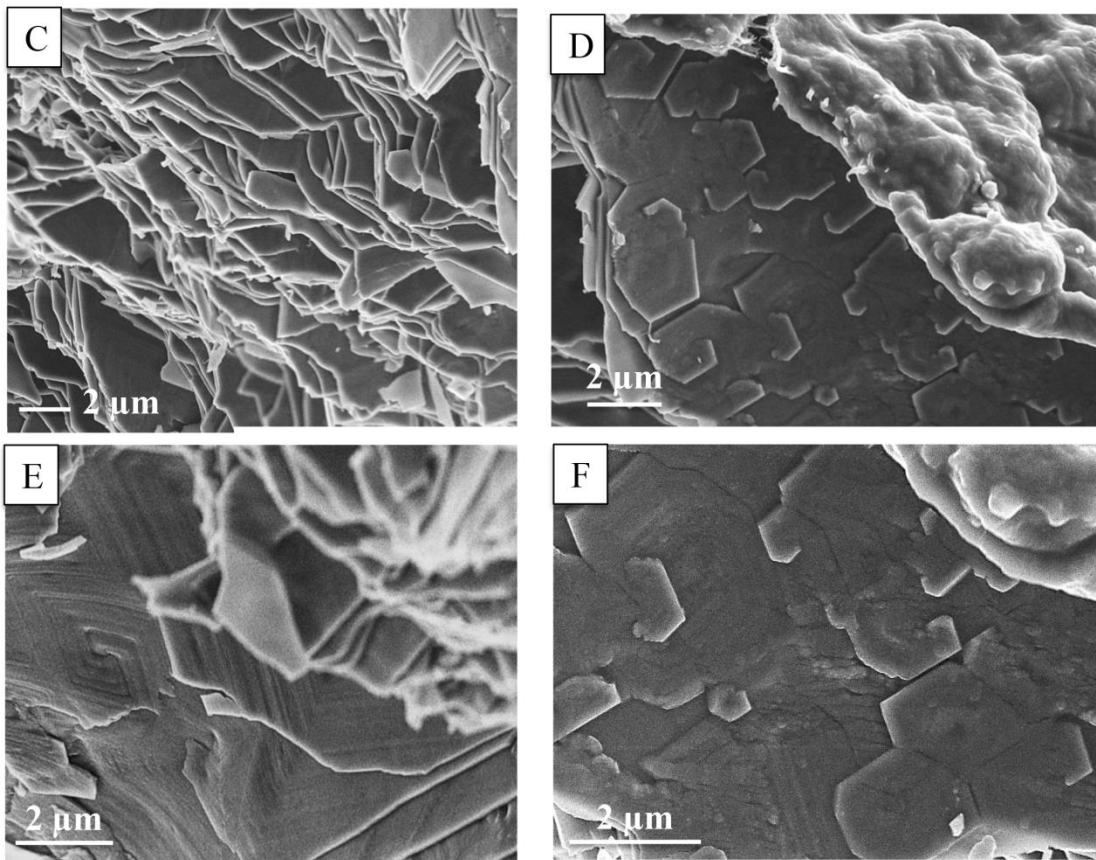


Figure 2.4.5. SEM images taken on microtome knife polished and etched (A, B) and fractured surfaces (C to F) of the shell of the thecideide species *K. chathamensis* (A, B) and the shell of the craniide specimen *N. anomala* (D to F). The shell of *K. chathamensis* consists of an assembly of interdigitating calcite units (B); *N. anomala* shells are formed of stacks of more or less parallel calcite layers (C). In surface view individual crystals within the layers exhibit a spiral internal structure (D, E, F).

Pajaudina atlantica

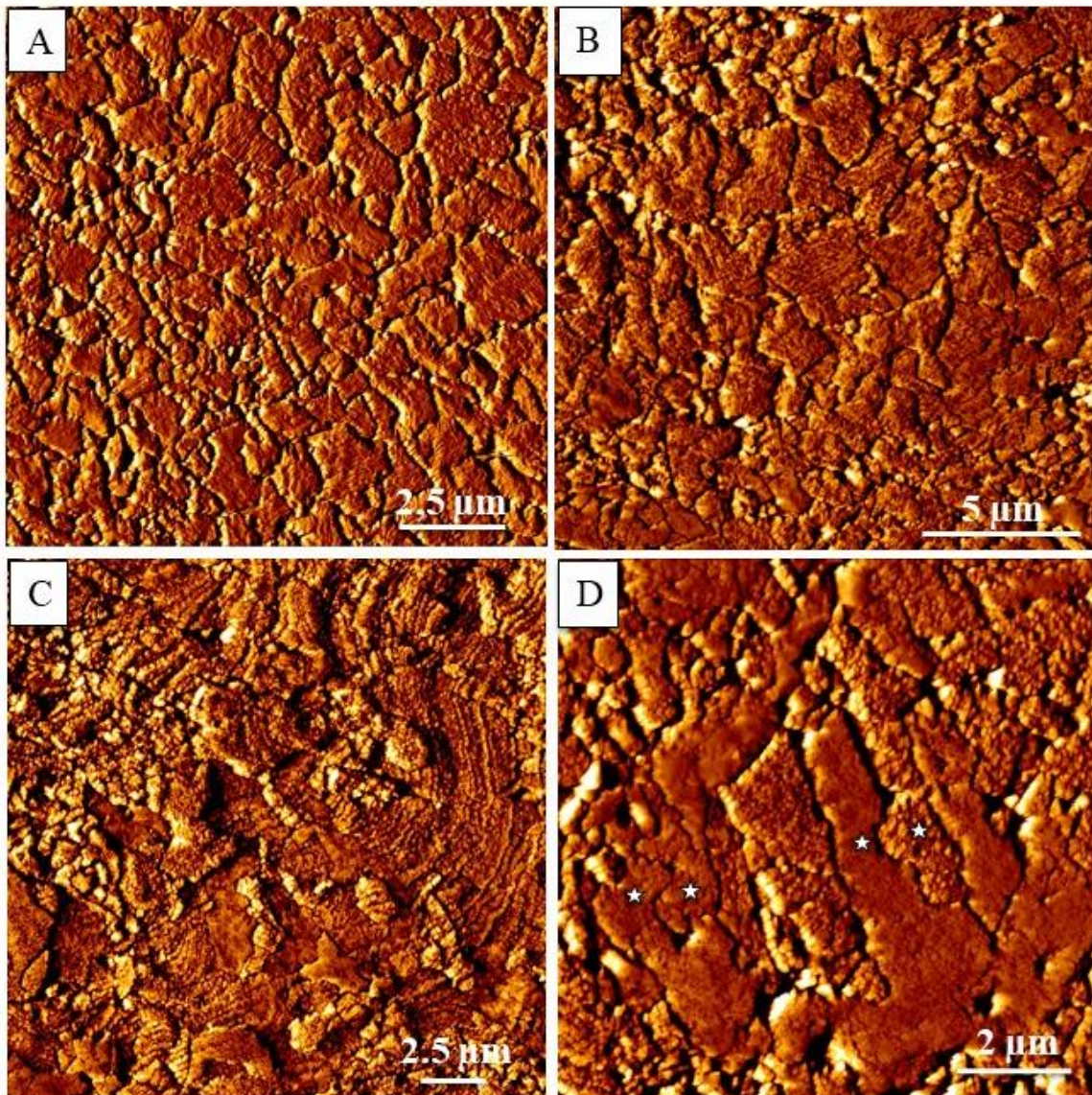


Figure 2.4.6. Vertical deflection AFM images depicting the mineral units that comprise the shell of thecideide *P. atlantica*. There is no regularity in crystal morphology, neither crystal size (A to D). Neighboring mineral units/crystals might interdigitate (see white stars in D).

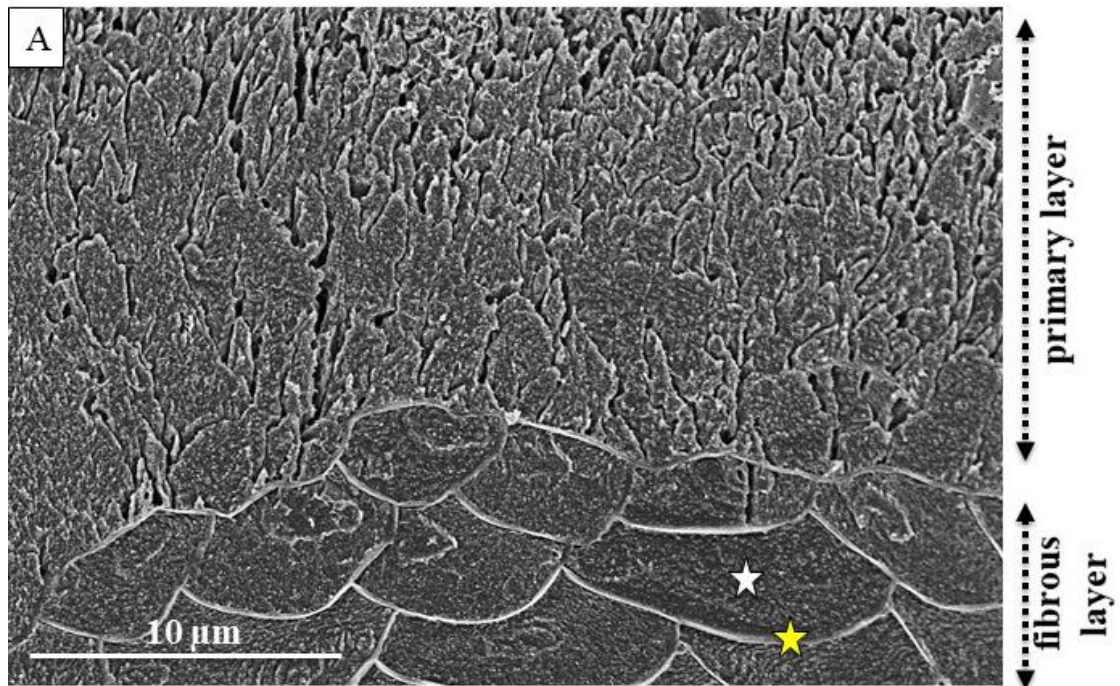
.4.5. Distribution of organic substance within the shells

The distribution pattern of organic substance is not only distinct for representatives of the four calcite shell-forming brachiopod orders, it varies also for the different shell layers of species of Terebratulida and Rhynchonellida. Figures 2.4.7-10 and supplementary information Figures S2.4.7-11 highlight the mode of distribution of organic biopolymers within the shells.

The fibrous shell layer of the Terebratulida and Rhynchonellida as well as the shell of *N. anomala*, Craniida, contain much organic substance. In these genera the organic substance is developed as an extracellular biopolymer matrix (Figs. 2.4.7B, 2.4.8, 2.4.9C-E, S2.4.7A, S2.4.8B-C) that delineates neighboring fibers in Terebratulida, Rhynchonellida and neighboring layers in Craniida.

The primary shell layer of Terebratulida and Rhynchonellida is devoid of organic substance (Figs. 2.4.7A, S2.4.7A). The columnar shell layer occludes biopolymers, here as well developed as membranes and delineating neighboring columns (Figs. 2.4.9A, S2.4.8A-B), however, as the columns are generally large in size and not as thin and platy as the fibers, there is in total less organic substance occluded into the columnar layer when compared to the fibrous layer. In cross-section (Figs. 2.4.8A-B, S2.4.7B-D, 2.4.9A-B) organic membranes vary in thickness between 50 and 150 nm and appear to be compact (Figs. 2.4.8A-B, 2.4.9A-B). However, in surface views (Figs. 2.4.8C-F, S2.4.8A) it becomes visible that they have a rather porous fabric. Organic membranes delineate also calcite layers in the shell of *N. anomala* (Figs. 2.4.9C-E, S2.4.8B-C). Membrane thickness in craniide shells is well below 100 nm, on average it varies between 20 to 40 nm. In the shell of terebratulides, rhynchonellides and craniides the distribution of organic substance is patterned as it is an extracellular matrix, whereas in modern thecideides there is no obvious regularity in the distribution of organic substance within the shells (Figs. 2.4.10, S2.4.9 to S2.4.11). Organic material in the latter is developed predominantly as a network of fibrils (e.g. Fig. 2.4.10B, E, F) and, to a lesser extent, as thin membranes (Figs. 2.4.10A-D). Their mode of occlusion into and distribution within the shell is random (Figs. white arrows in S2.4.9-11).

Terebratalia transversa



Liothyrella uva

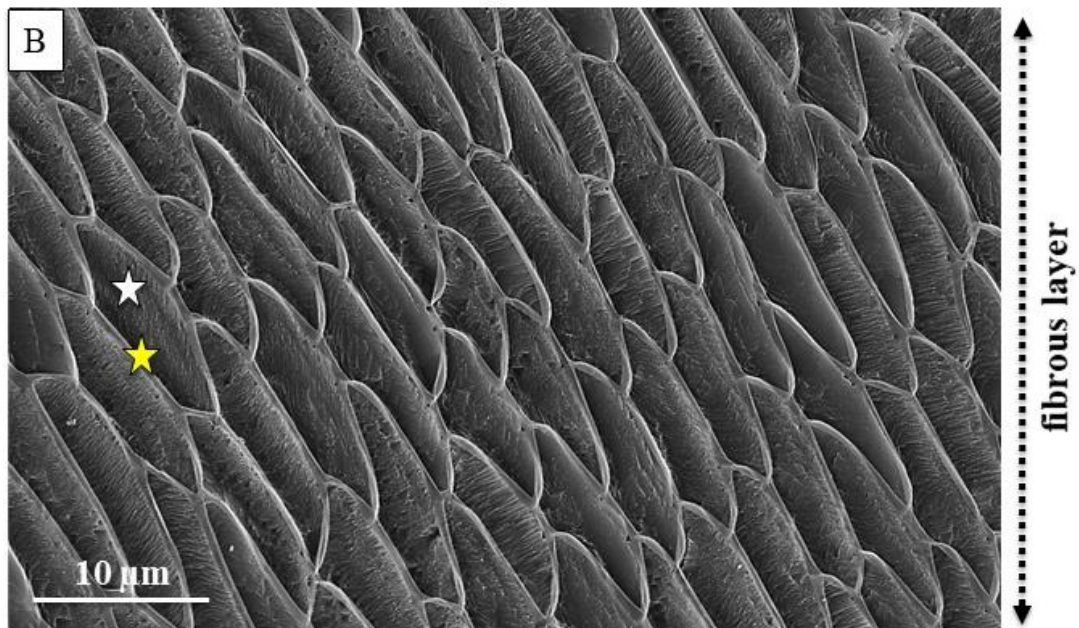
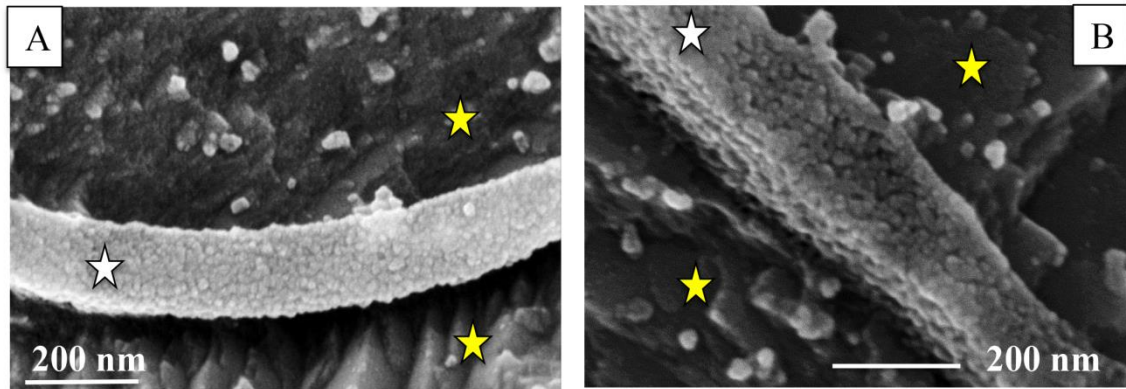
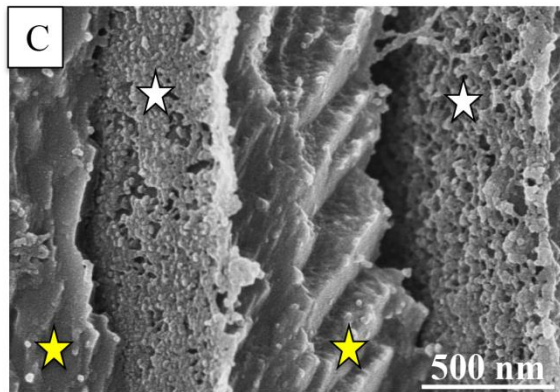


Figure 2.4.7. SEM images of microtome knife polished and etched surfaces of the primary and fibrous shell layer of *T. transversa* (A) and the fibrous layer of *L. uva* (B). The primary layer does not occlude organic substance (A). An extracellular matrix is present within the fibrous layer formed of an assembly of organic membranes (yellow star in A, B), separating neighboring calcite fibers (white star in A, B).

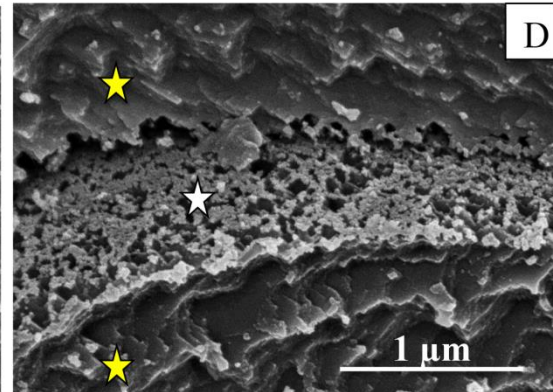
Terebratalia transversa



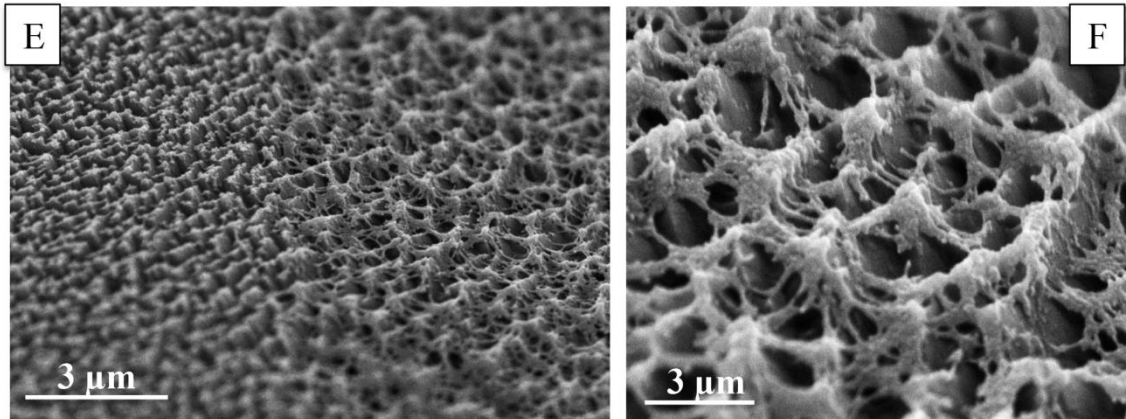
Liothyrella uva



Laquens rubellus



Laquens rubellus



★ fiber calcite ☆ biopolymer

Figure 2.4.8. SEM images taken on microtome knife polished and etched shell cross-sections visualizing biopolymer membranes (white stars in A to D) between fibers (yellow stars in A to D) and their fabric (C to F). Fig. 2.4.7C is modified after Griesshaber et al. 2017.

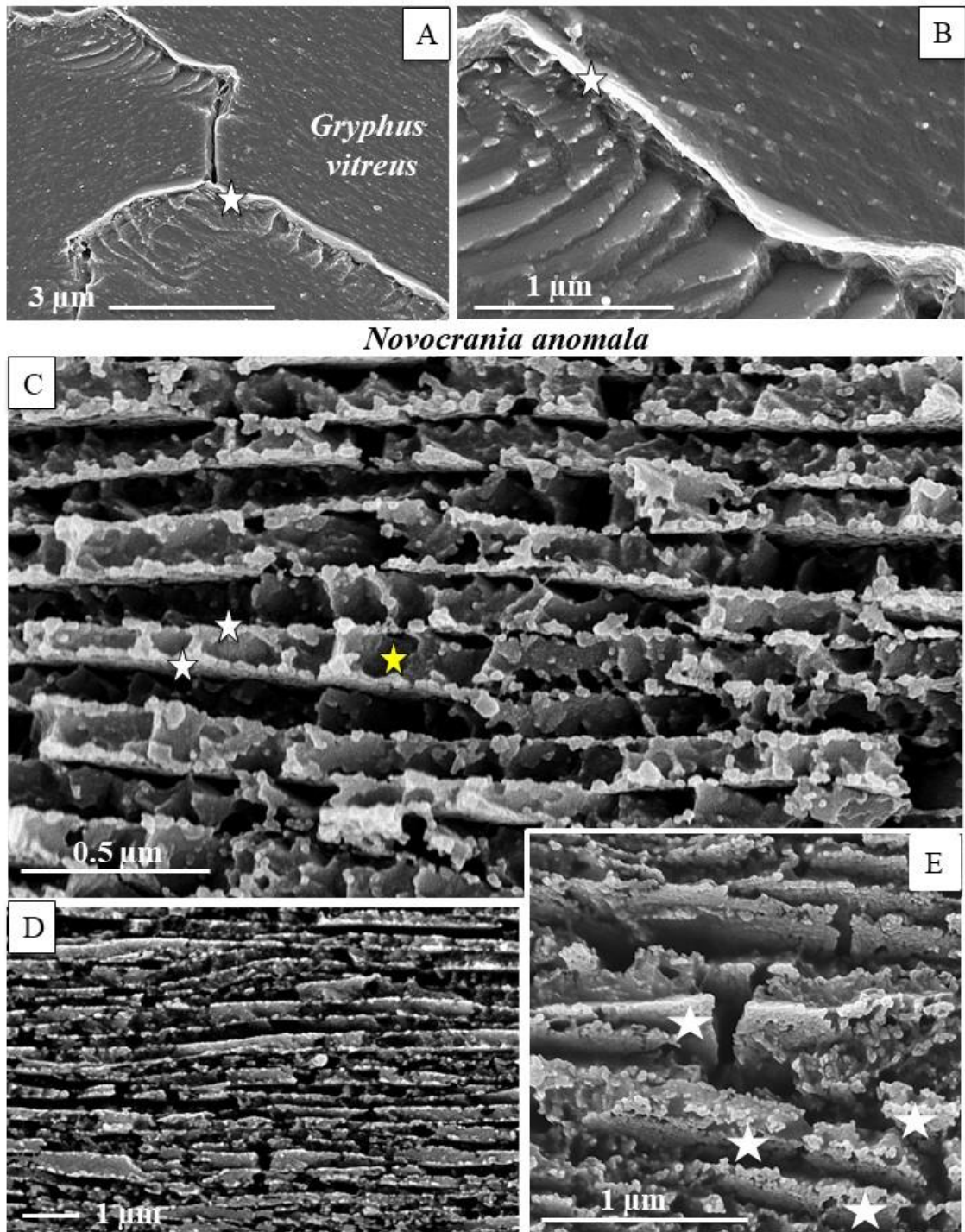


Figure 2.4.9. SEM images taken on microtome knife polished and etched shell cross-sections depicting membranes between columns (A, B) and delineating sequences of calcite layers (C to E). White stars in A, B, C, E point to organic membranes within the shells; the yellow star in C draws attention to the calcite between two organic linings.

Pajaudina atlantica

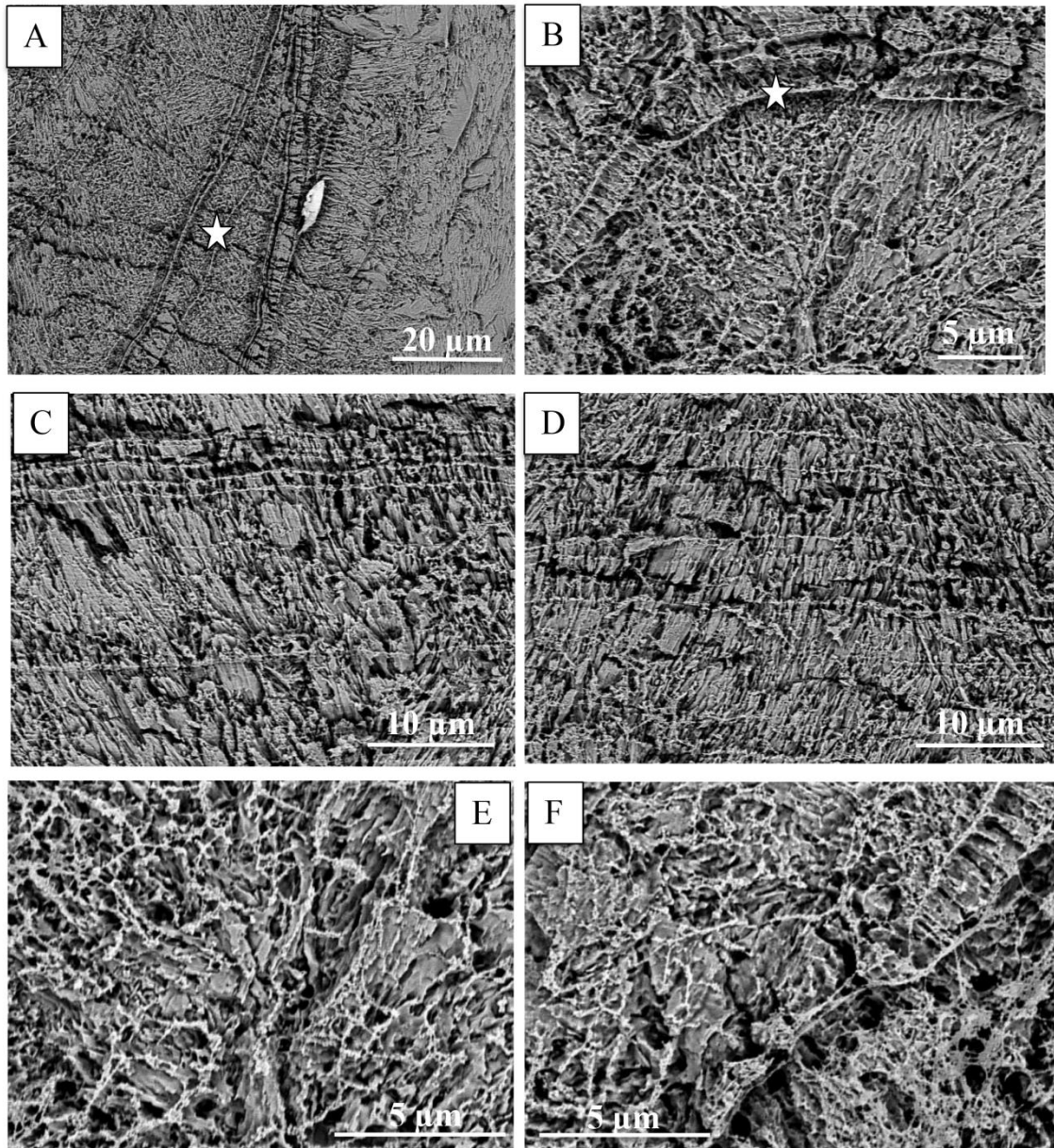


Figure 2.4.10. SEM images taken on microtome knife polished and etched shell cross-sections visualizing the distribution pattern of organic substance in the thecideide shell. Thecideides occlude much organic substance into shell calcite. This is developed as thin membranes (white star in A, B and figures A to D) and as networks of fibrils (E, F). Note that both membranes and fibrils are very irregularly distributed within shell calcite.

2.4.6. The nanometre and sub-micrometre scale organization of calcite and biopolymers within rhynchonellide and terebratulide fibers

Understanding how diagenetic overprint influences microstructural archival data is of fundamental importance in palaeoecological and palaeoclimatological studies (Immenhauser et al. 2016). Of particular interest is the identification of a low degree of overprint. Severe overprint is easily recognized due to the more or less complete destruction of the hard tissue microstructure and texture and shell recrystallization (e.g. Figs. 10C, 11E in Casella et al. 2018). Previous studies have shown that identification of an altered nanostructure is of immense importance. Structural characteristics might be preserved on the micrometre scale, however, the nanostructure of the hard tissue can be completely reset by alteration (Fig. 2.4.4C in Casella et al. 2018).

As the fibrous shell layer of rhynchonellide and terebratulide brachiopods is regarded to be appropriate archival material for environment reconstruction, we focused on the nano- and submicrometre scale characterization of the fibers (Figs. 2.4.11-14, S2.4.12-15). Modern brachiopod fibers are hierarchical composites where biopolymers and calcite are interlinked on at least four scale levels: (i) the individual fiber, (ii) calcite layers within a fiber, (iii) strings of calcite nanocrystals forming a calcite layer, (iv) the nanoparticulate calcite crystal. Simonet Roda et al. 2019a, 2019b investigated in great detail fiber secretion and fiber organization for the modern terebratulide *Magellania venosa* and showed that individual fibers are not fully sheathed by an organic membrane, as described previously. Only one surface of a fiber is covered by an organic membrane, the proximal surface of the fiber (white stars in Fig. 2.4.11C-D, and Simonet Roda et al. 2019a, 2019b). The specific mode of fiber organization in the shell layer creates the impression that an individual fiber is fully sheathed by organic substance. At fiber secretion mantle epithelial cells are in direct contact with the calcite of the forming fiber (Simonet Roda 2019b). Calcite nucleation for new fiber formation starts at the proximal surface of the proximal membrane of a previously secreted fiber (yellow arrows in Fig. 2.4.11A). Ongoing fiber growth is given by the successive accretion of thin calcite layers (Fig. S2.4.12) to previous layers within the fiber (see the striation of all fibers in Fig. 2.4.11A, sketch shown in Fig. 2.4.11B). Fiber growth is terminated with the secretion of a membrane (white star in Fig. 2.4.11C-E) along the proximal surface of the fiber. Modern rhynchonellide and terebratulid fiber calcite is not devoid of organic substance. As the AFM image in Figure 2.4.11F highlights, the calcite of a fiber occludes a very thin network of organic fibrils. These are placed between the thin calcite layers that constitute a fiber.

When etched at a pH of 6.5 with an 0.1 M HEPES solution we observe for many terebratulid and rhynchonellid species a structural sub-division of fibers into a porous/spongy apical (white dots in Fig. 2.4.12A, C-G) and a dense proximal region (red dots in Fig. 2.4.12A, C-E, white arrows in Fig. 2.4.12B). Obviously material that etches easily (ACC or remains of specific biopolymers) is etched away; this material is predominantly concentrated at the apical region of the fiber.

The calcite of the fibers consists of 200 to 400 nm sized calcite crystallites, that often show rhombohedral morphologies (Figs. 2.4.13A-B, S2.4.13, S2.4.14). These crystallites are further structured. STEM images of Figure 2.4.13D-F made on 60 to 80 nm thin microtome cuts of shell calcite (Fig. 2.4.13C) visualize, that the fibers are nanostructured; see the patchiness within individual fibers. The calcite of a fiber

consists of 50 to 80 nm thin layers (yellow star and black arrows in Fig. 2.4.14A, yellow stars in Fig. 2.4.14B-C), that are formed of 40 to 60 nm sized calcite crystallites (yellow arrows in Fig. 2.4.14A-C). It is very important to note that SE images shown in Figure 2.4.14A-B are taken on fractured and not on etched surfaces. Thus Fig. 2.4.14A depicts the nanometric particles that comprise the calcite of the fibers. Calcite crystalites of both the nanometric particles as well as of the thin layers that constitute the fibers is highly co-oriented (Fig. S8C in Simonet Roda et al. 2019b). Hence, the occluded organic network does not cause much or any misorientation between the crystallites in the fiber.

Modern thecideides and rhynchonellides/terebratulides differ significantly in mineral unit morphology, presence of extracellular matrix and microstructure. Even though, as Figure S2.4.15 shows, the submicrometre scale structure of crystallites that constitute the mineral units is very similar for the species of the two taxa.

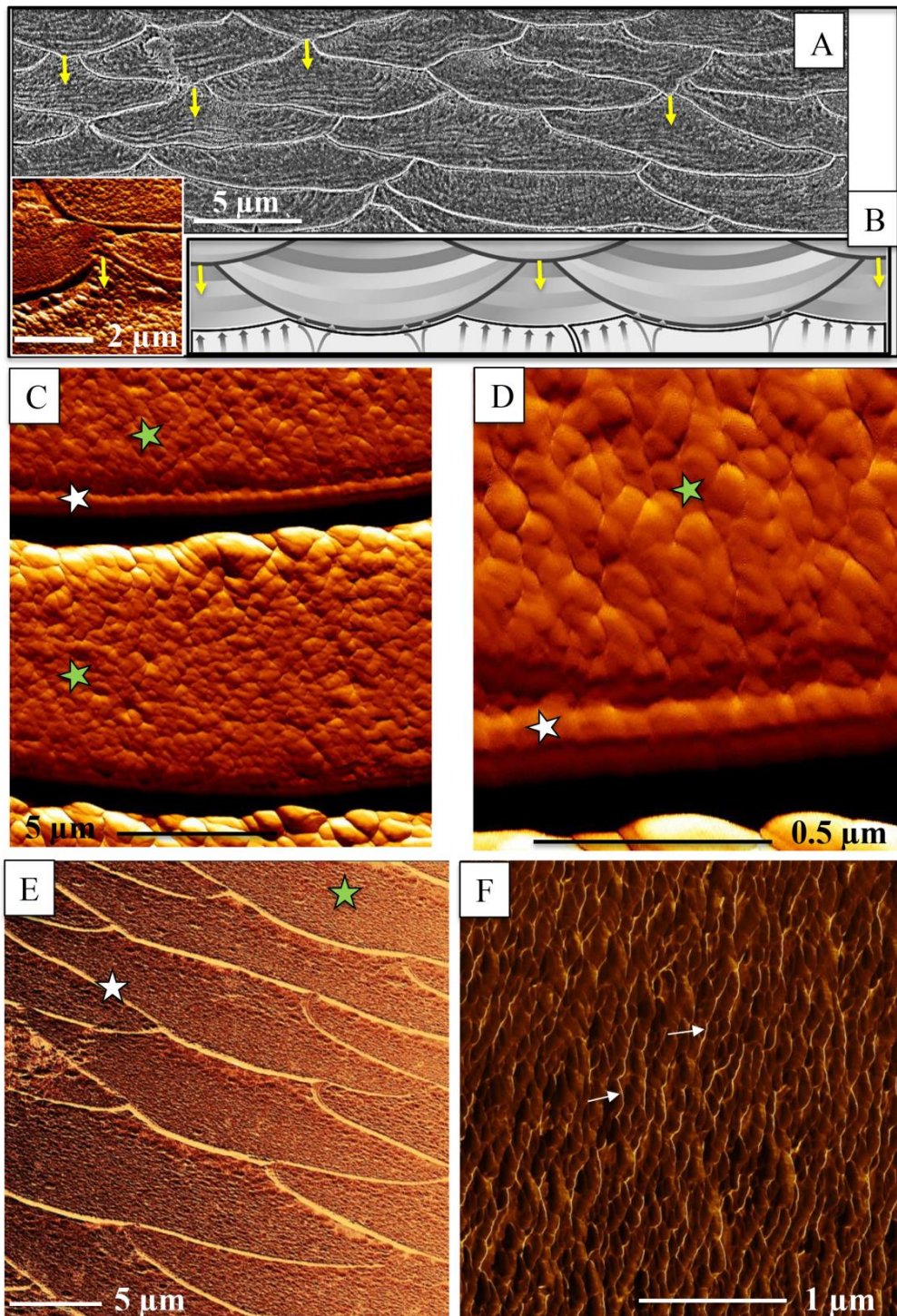


Figure 2.4.11. Transverse cut through calcite fibers of *Notosaria nigricans* (A) and *Magellania venosa* (C to F). (A): SEM image taken on a microtome polished and etched surface, (B): sketch depicting successive growth of the fibers by addition of discrete calcite layers, modified after Simonet Roda et al. 2019. See the striation within the fibers (Fig. 2.4.11A); this indicates the presence of calcite layers in individual fibers. Insert in (A): AFM image indicating the start of fiber calcite nucleation and growth; this image is shown in full size in Fig. 2.4.12D. Fig. 2.4.11C-11D are lateral deflection AFM images depicting in high-resolution neighboring fibers, the calcite (green star) and the proximal, fiber growth terminating, membrane (white star) on the proximal surface of the fiber. Fig. 2.4.11C-D visualize that the apical surface of a fiber is not covered by an organic membrane, in contrast to its basal, proximal surface. (E): vertical deflection AFM image depicting the extracellular matrix within the fibrous shell layer, F: lateral

deflection AFM image demonstrating the presence of a thin organic network within the fibers (white arrows in F, figure modified after Casella et al. 2019). White stars in C, D, E point to organic membranes, green stars in C, D, E draw attention to the calcite.

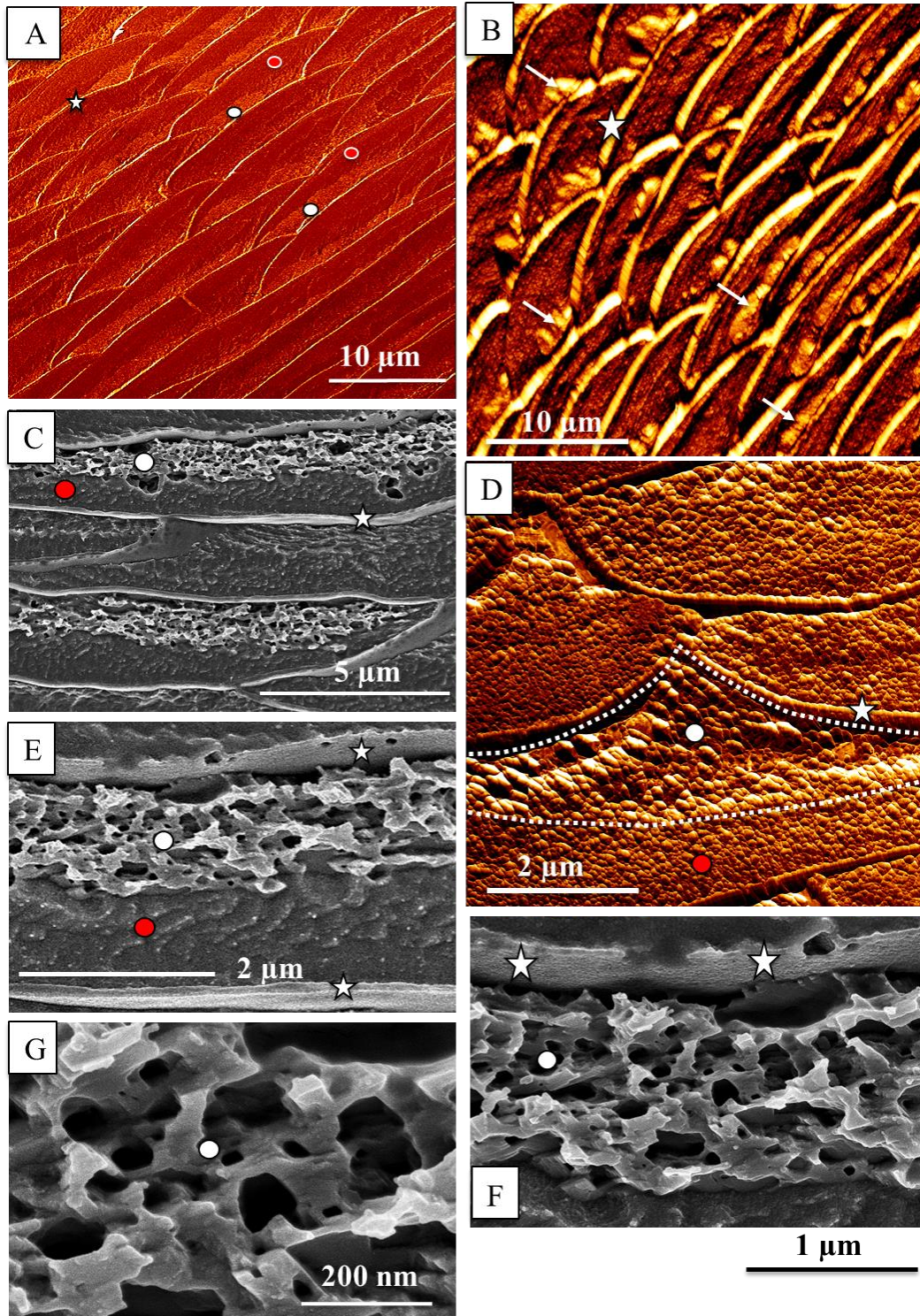


Figure 2.4.12. When etched at a pH of 6.5 with an 0.1 M HEPES solution the calcite within fibers exhibits a porous, spongy, apical (white dots in A, C, D, E, F, G, white arrows in B) and a dense, proximal (red dots in A, C, D, E) region. (A): lateral deflection AFM image; (B, D): vertical deflection AFM image; figures C, E, F, G: SEM images of microtome knife polished and etched surfaces. White stars in A, B, C, D, E, F point to the organic membrane at the proximal surface of the fiber.

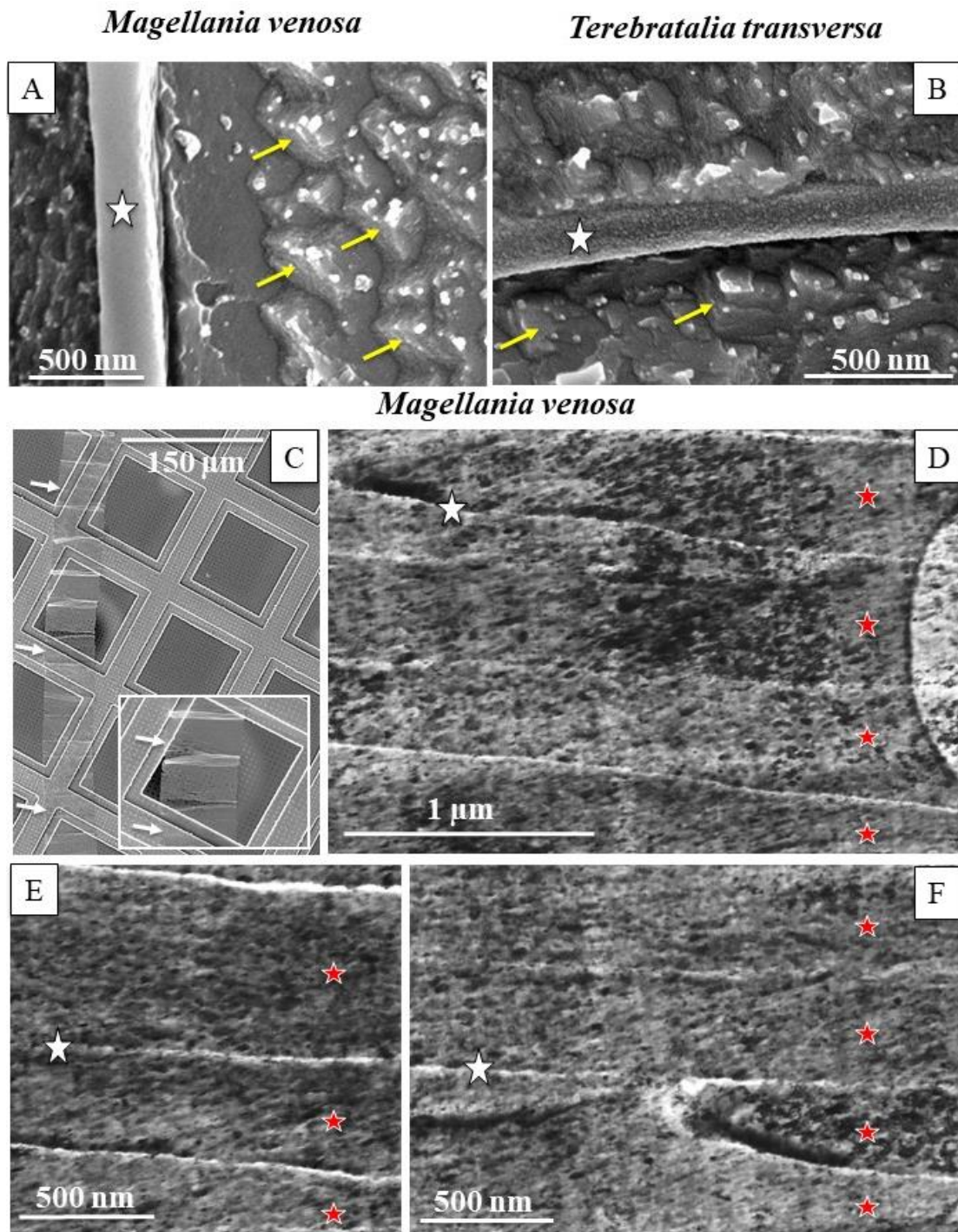


Figure 2.4.13. Submicrometre to nanometre scale structuring of calcite fibers visualized with SEM images of microtome polished and etched surfaces (A, B) and STEM imaging of 60 to 80 nm thin sections (C) cut of the calcite of the fibers (D, E, F). The white star in A, B, D, E, F points to the organic membrane between adjacent fibers. Calcite fibers consist of 200-400 nm sized crystals (A, B); very striking, these often have rhombohedral morphologies (yellow arrows in A, B). The patchiness visualized with STEM imaging (D, E, F) indicates that the calcite of brachiopod fibers is structured further and consists of about 50 to 100 nm sized well aligned crystallites. Red stars in D, E, F indicate individual fibers.

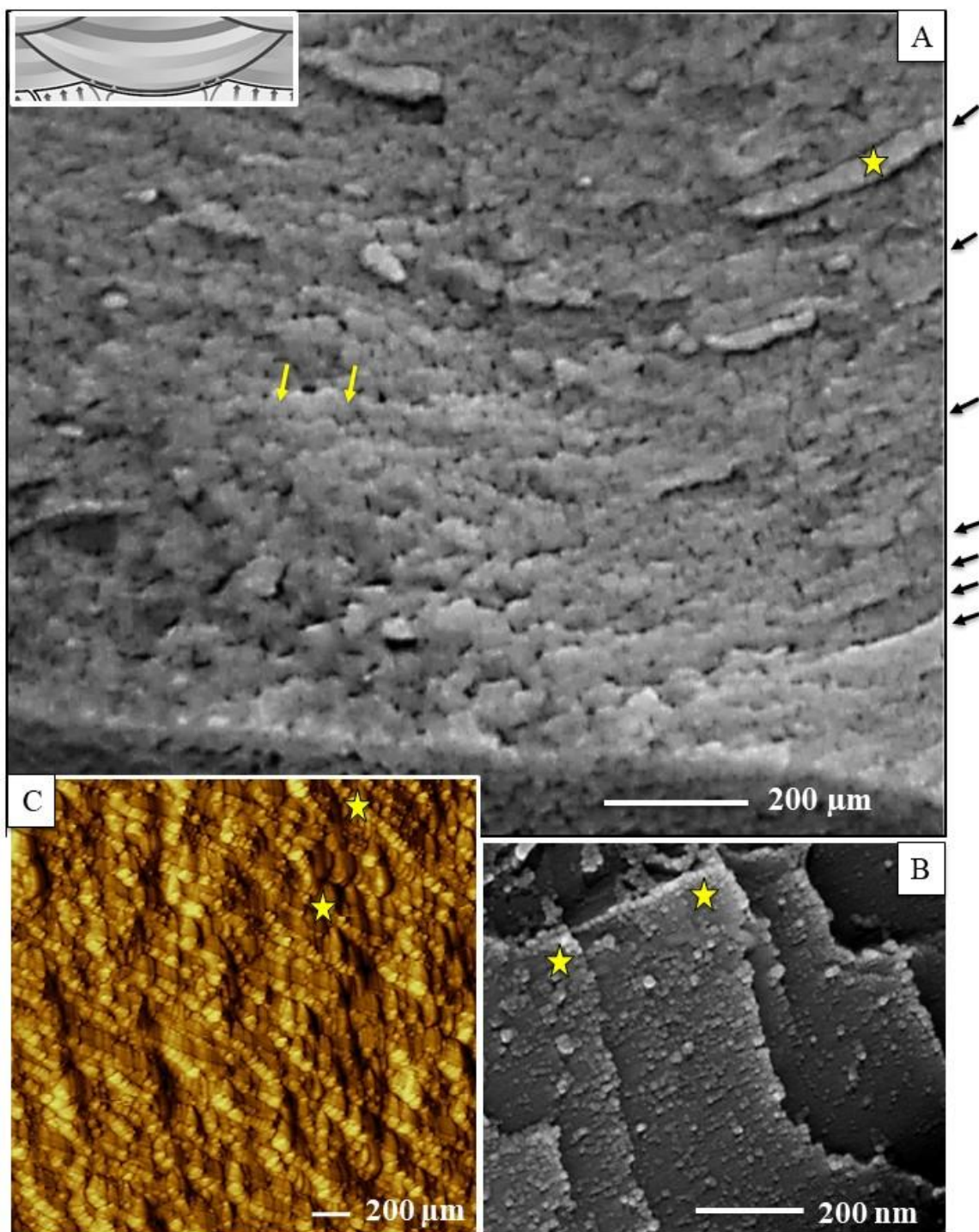


Figure 2.4.14. The nanoscale structure of a cross-sectioned calcite fiber visualized with SEM images of fractured surfaces (A, B) and a vertical deflection AFM image (C). Well visible are the, in cross-section, 80 to 100 nm sized layers (black arrows in A, yellow stars in B, C) that form a fiber and the 50 to 100 nm sized crystallites that constitute a calcite layer (B and C, yellow arrows in A). It is important to note that the SEM images shown in A and B are taken on fractured and not on etched surfaces, thus the imaged surfaces are not modified by etching or other chemical means at sample preparation.

2.4.7. Modes of calcite assembly in modern brachiopod shells

Shell calcite assembly patterns for representatives of the four extant calcite secreting brachiopod orders are given in Figs. 2.4.15-19, S2.4.16-19.

Modern Rhynchonellida and Terebratulida produce three calcite material fabrics which have similar textures, however, distinct crystal morphologies (Figs. 2.4.15-17) and calcite co-orientation strength (Figs. 2.4.21 and 2.4.22). It has been demonstrated in previous studies (Goetz et al. 2011, Schmahl et al. 2012) and as shown in Figs. 2.4.15A-C and 2.4.16A that the primary shell layer of modern Rhynchonellida and Terebratulida is not nanogranular. The primary shell layer is formed of an array of concave/convex calcite grains (yellow stars in Fig. 2.4.15A-B and Goetz et al. 2011) that have dendritic morphologies (Fig. 2.4.3B). These interdigitate strongly (Fig. 2.4.15C) and generate recesses and protrusions of abutting crystals without any cavities in or between the dendrites. The interface topology of these mineral units ranges from a few tens of nanometres to a few tens of micrometres. This gives the nanoscale structure to the material fabric. The dendritic grains show a spread of crystallographic orientation of several degrees and can thus be referred to as being mesocrystals; individual mesocrystals have sizes in one dimension of 20 or even more micrometres (Fig. 2.4.15C), thus are not nanometre sized grains. The preferred crystallographic orientation of the primary shell layer is very similar to that of the adjacent fibrous shell layer (Fig. 2.4.16), even though these two layers are formed of biocrystals with very different crystal morphologies and grain boundary topologies. Neither with SEM nor TEM could we identify organic substance (membranes, network of fibrils) between the mesocrystals of the primary shell layer.

The primary shell layer is developed in all modern rhynchonellide and terebratulide shells, accordingly, it is very important for the animal, irrespective of differences in environments the different brachiopods live in. The primary shell layer together with the periostracum is the protective cap of inner shell layers and of the soft tissue against external impact. The interlocked nature of the dendrites effects the high hardness (Vickers hardness) of the material that is about twice as hard as non-biological calcite (Griesshaber et al. 2007, Schmahl et al. 2008). Just for comparison, the hardness of the fibrous shell layer is significantly lower and is, more or less, that of calcite precipitated from solution (Tretsch 1950). Primary shell layer material with its specific structure forms also the tip of the two valves (Fig. S2.4.3A).

The fibrous layer of modern rhynchonellide and terebratulide shells is fabricated to be pliant and tough. These properties are obtained with the composite nature of the fibers, their hierarchy and their specific mode of organization. Individual fibers are hierarchical mesocrystal composites and vary in length, 3D dimension and 3D fiber morphology (Ye et al. 2018a, 2018b). Fibers of all modern terebratulid and rhynchonellide shells have one concave, proximal, and three convex, apical, surfaces, respectively. The specific morphology of fibers allows their staggered arrangement and facilitates their interlocked packing (Figs. 2.4.1B, 2.4.3C). The internal organization of calcite within a fiber (Fig. 2.4.14) evokes their conchoidal mode of fracture. A further, unique, feature of brachiopod fibers is that they can bend and retain crystallographic orientation for calcite for the entire length of the fiber (Figs. 2.4.15D, S2.4.4A). Thus, even though the morphological orientation of the fiber changes, calcite lattice orientation remains coherent. Often morphological fiber axis and orientation of calcite c-axes that constitute the fibers are different. Neighboring fibers are generally co-

oriented due to stacking formation (see similarity in color in Fig. 2.4.15D: mainly green colors on the left and mainly blue colors on the right hand side of the image, respectively). Even though, differing significantly in crystal morphology and microstructure relative to the primary shell layer, the fibrous shell layer as well has a strong axial fiber texture (compare EBSD maps and pole figures of the different shell layers in Figs. 2.4.15, S2.4.16).

The columnar shell layer was investigated for *Gryphus vitreus* and *Liothyrella neozelanica* (Figs. 2.4.17, S2.4.16B, S2.4.17). Similar to the primary and the fibrous shell layer, the columnar shell layer has also a strong axial fiber texture (see the pole figures in Figs. 17, S16A, S17), although the morphology of the columns is distinct to that of the fibers and of the dendrites. Calcite within individual columns is very co-oriented, it is almost single crystalline; MUD values scatter between 650 and 720 (Fig. 2.4.17). However, even though very similar in microstructure and texture, we find one difference between the columnar layers of *G. vitreus* and that of *L. neozelanica*. In *L. neozelanica* shells there is always an alternation between columns and fibers, generally, longitudinally cut fibers (Fig. 2.4.17B, Griesshaber et al. 2009, Goetz et al. 2009). This is never observed for *G. vitreus* (Figs. 2.4.17A, S2.4.17). The ratio between the extent of the fibrous and the columnar shell layer can vary significantly for *G. vitreus*, even in the same specimen (Figs. S2.4.17A, S2.4.17B). Occasionally the fibrous layer might dominate the extent of the cross-section of the shell (Fig. S2.4.17B) with the columns being very little developed (Fig. S2.4.17B). The transition between fibers and columns is very smooth for both *L. neozelanica* (Fig. 2.4.17) as well as *G. vitreus* (Fig. S2.4.17B). The calcite of the columns nucleates topotactically (Fig. 2.4.17C) onto the membrane lining on the proximal surface of a fiber.

The microstructure and texture of representatives of extant calcite shelled brachiopod orders that live cemented to substrate (Thecideida Figs. 2.4.18, S2.4.18; Craniida Fig. 2.4.19) is distinct to what we find for the Terebratulida and Rhynchonellida. Structural order is more or less absent for the shells of both taxa, especially for the shells of species of Craniida. There is, however, one difference between the shells of the two taxa. While modern Thecideida form their shells of crystals having a large diversity in shape and size, the Craniida build their shells of mainly one mineral unit type, thin calcite platelets (Fig. 2.4.19). These string and form thin layers; arrays of layers form the shell. However, neither in individual layers, nor for arrays of layers do we observe structural order.

Williams and Wright (1970), England et al. (2007), Perez-Huerta et al. (2007) addressed the platelets in the shell of Craniida as 'semi-nacre'. Even though tablet shaped, *Novocrania anomala* platelets have nothing to do with nacre tablets or/and nacreous microstructures of mollusc shells (Fig. S2.4.19). Neither the carbonate phase, nor the dimension of the platelets, nor crystal co-orientation strength, nor the microstructure nor the texture of craniide shells can be compared to the nacre of bivalves, gastropods, cephalopods (Fig. S2.4.19). Nacreous assemblies in molluscs are formed of aragonite, have sheeted or columnar microstructure, high aragonite co-orientation strengths (e.g. MUD values of 185, 130, 102 compared to an MUD of 15 in *N. anomala*) and a strong fiber texture (Fig. S2.4.19 and Griesshaber et al. 2013, Casella et al. 2018, Peters et al. 2020). Even though formed of platelets, we do not find the latter characteristics for the shell of *N. anomala*. The use of platelets in craniide and mollusc shells should be rather regarded as biological convergence, such as for example the development of fibers for shell construction in brachiopod and bivalve shells.

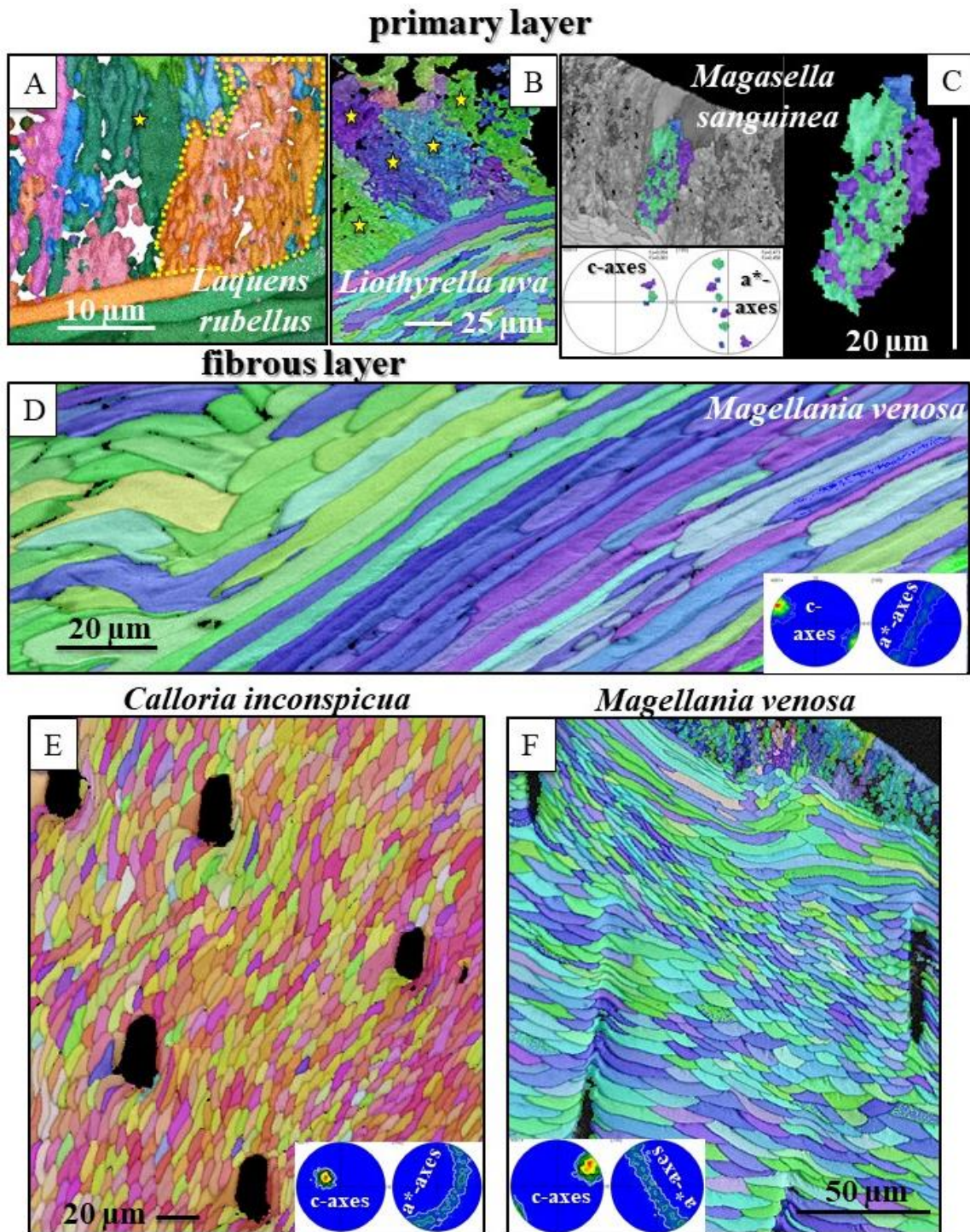


Figure 2.4.15. The microstructure (EBSD maps) and texture (pole figures) of the primary and fibrous shell layer of terebratulid brachiopods. The primary shell layer of modern terebratulid and rhychonellide brachiopods is not nanocrystalline, in contrast, it consists of large, several micrometre sized, units that are highly interdigitated in 3D (A, B, C). The primary shell layer has a fractal-like, dendritic, microstructure. (C) Three interveaved dendritic crystals with slightly different orientations; see the pole figure in (C). The fibrous shell layer consists of, more or less, parallel arrays of fibers. These arrays change often orientation; accordingly, in 2D views the fibers are then cut longitudinally or transversely (D). Brachiopod fibers can be curved (lefthand-side of figure 2.4.15D), often at punctae. The used color-code for A and E is given in Fig. S2.4.16, for B, C, D, F in Fig. S2.4.17.

Magasella sanguinea

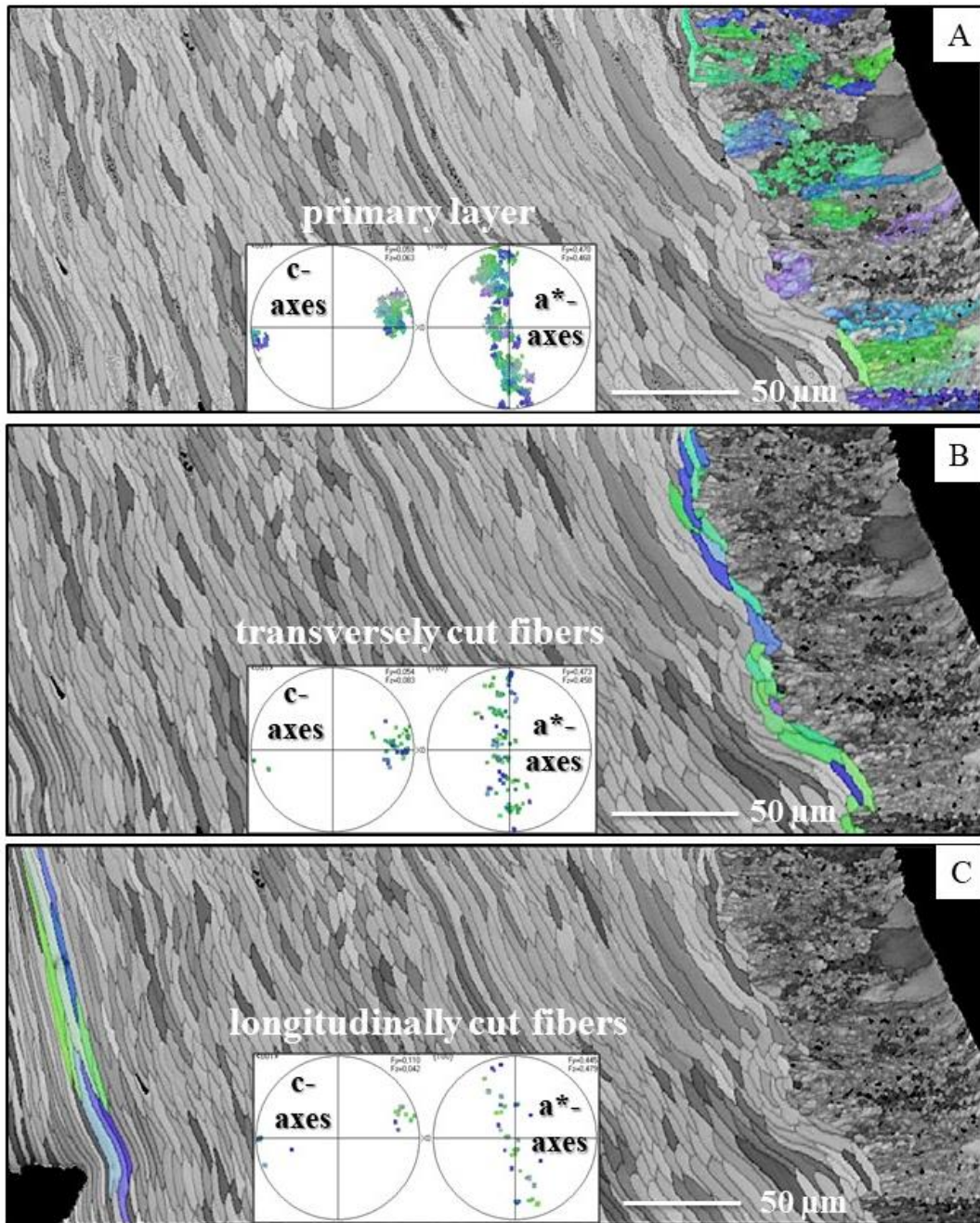


Figure 2.4.16. EBSD band contrast and color-coded orientation measurement on a cross-section through the valve of *Magasella sanguinea*. (A) shown in color are dendritic crystals of the primary shell layer and their orientation; (B) shown in color orientation of adjacent fibers; (C) orientation of fibers close to inner shell margin. Pole figures in A, B, C give the texture of those shell portions that are highlighted in color. Note that there is no difference in calcite orientation between the primary and fibrous shell layers even though crystal morphologies (dendrites, fibers) comprising the two layers are very distinct. Note in (A) tens of micrometre large dendritic units that form the primary shell layer. The used color-code is given in Fig. S2.4.17.

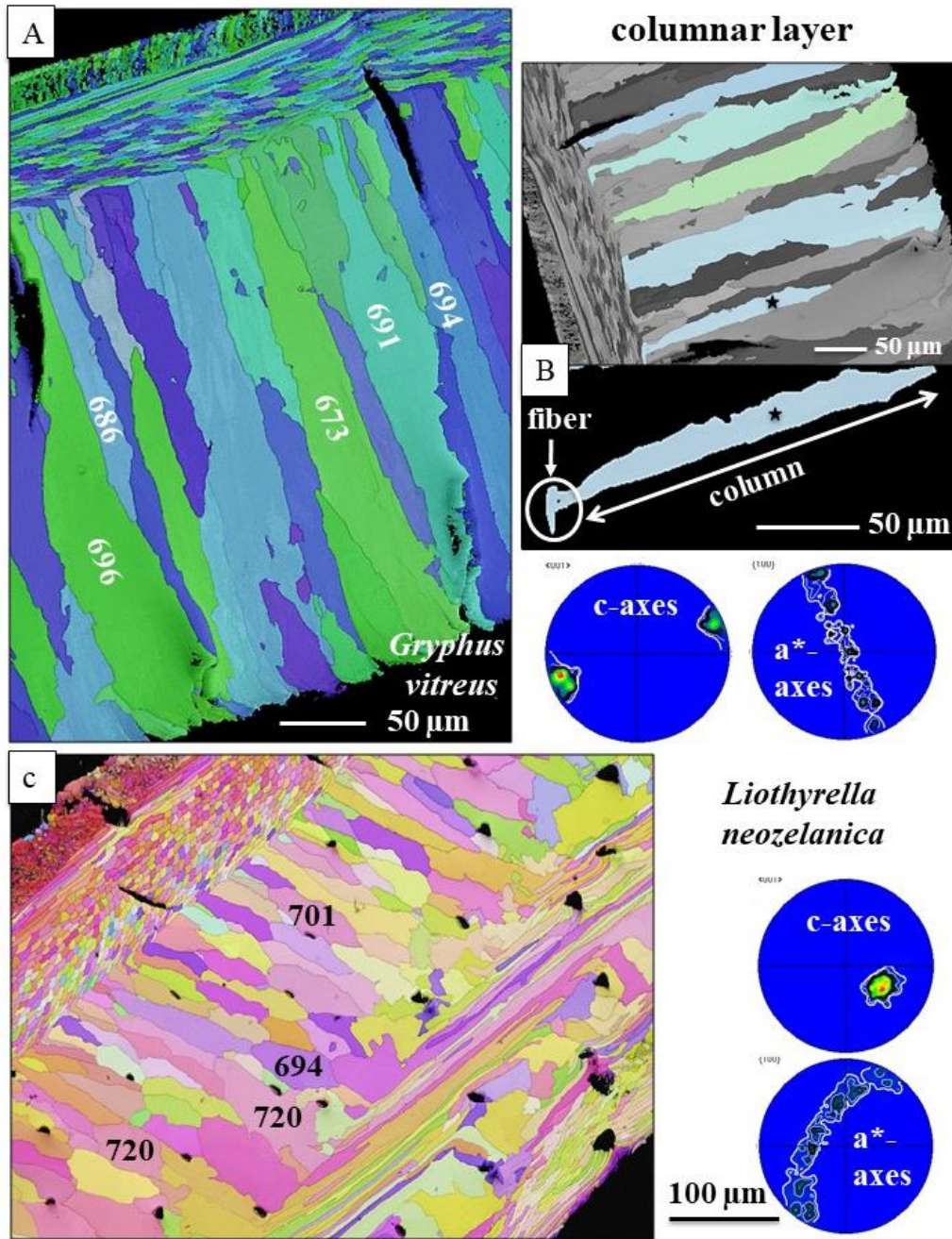


Figure 2.4.17. Columnar shell layer microstructure (EBSD maps) and texture (pole figures) deduced from EBSD measurements. *Gryphus vitreus* (A, B) and *Liothyrella neozelanica* (C) have a columnar shell layer consisting of large irregularly shaped, prism-like units. The columns nucleate epitactically on the proximal membrane covering the basal surface of a fiber; white circle in (B). In *L. neozelanica* we find an alternation between columns and fibers (C), a feature that is not present in the shell of *G. vitreus* (A), see also Goetz et al. 2009, Ye et al. 2018a. For both taxa c- and a*-axes are highly co-oriented (see the pole figures and the very high MUD values); an axial texture prevails: all c-axes of a map point to predominantly one direction, while a-axes orientations scatter on a great circle. Numbers given in black in the columns are MUD values; MUD values are similar to those of single crystalline calcite grown from solution (Yin et al. 2019). The used color-codes are given in supplementary information figures S2.4.16 and S2.4.17. For A and E the color code is in Fig. S2.4.16, for B, C, D, F and in Fig. S2.4.17, respectively. The used color-code for A and B is given in Fig. S2.4.17, C in Fig. S2.4.16.

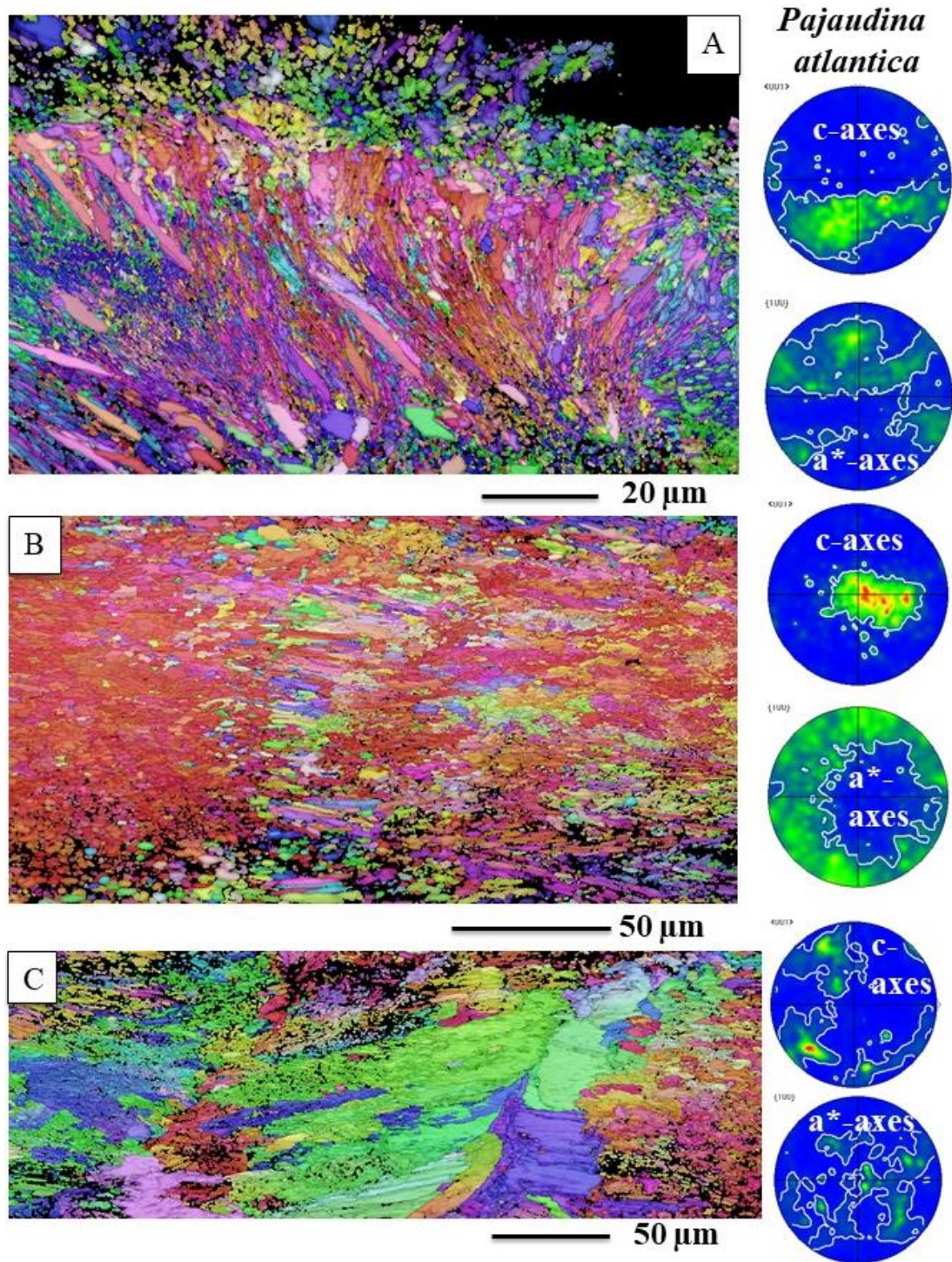


Figure 2.4.18. Microstructure and texture of shell calcite of the thecideide brachiopod *Pajaudina atlantica*, deduced from EBSD measurements. It is well visible that modern thecideide shells consist of a multitude of irregularly shaped, sized and assembled calcite units (A, B, C). These have a very little co-orientation strength, thus, the shell has a weak texture (see pole figures). The color-code for A and C is given in Fig. S2.4.17, for B in Fig. S2.4.16.

Novocrania anomala

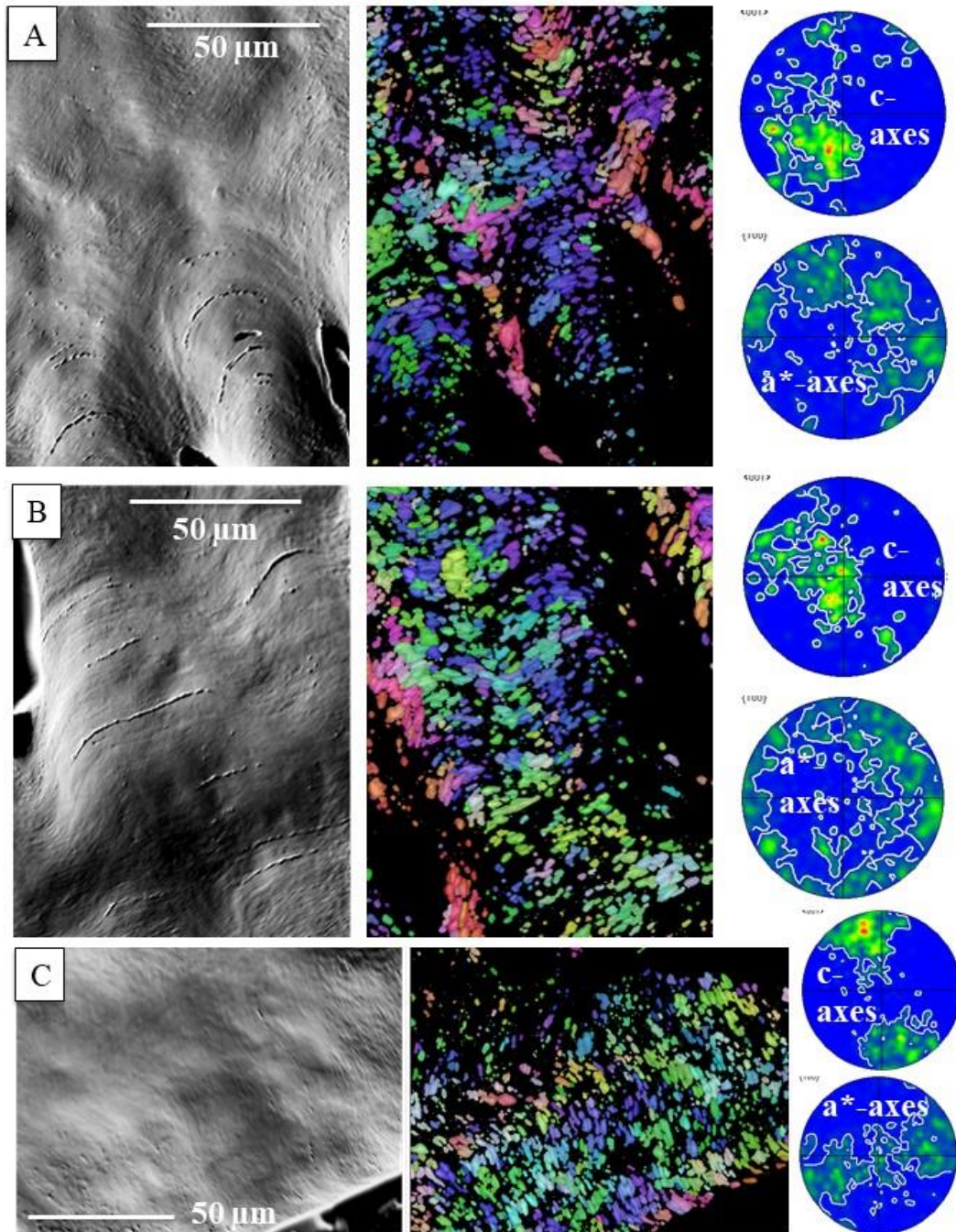


Figure 2.4.19. Microstructure and texture of shell calcite of modern *N. anomala* deduced from EBSD measurements. Comparable to the texture of the modern thecideide brachiopod *P. atlantica*, the texture of *N. anomala* is also very weak, calcite crystallites are very little co-oriented. However, crystallite/mineral unit morphology is not as diverse/random as it is the case for the shell of *P. atlantica*. The color-code for the figure is given in Fig. S2.4.16.

2.4.8. Characteristics of the textures

This review is based on more than 100 EBSD measurements (Table 2.4.1); accordingly, we can attempt to deduce texture patterns for shell calcite of the investigated representatives of Terebratulida, Rhynchonellida, Thecideida and Craniida (Figs. 2.4.20-22).

EBSD links the molecular with the macro scale (Figs. 2.4.20A); it connects the orientation of planes formed by a particular ion in the crystal (Fig. 2.4.20B) with the macro scale architecture of the skeleton (Fig. 2.4.20A, C). This holds for the layered shells of Terebratulida and Rhynchonellida where we find a sharp, axial texture, irrespective if an EBSD measurement scans over (i) different or (ii) just one layer in the shell. For the shells of Rhynchonellida and Terebratulida the texture of the valves is such that calcite c-axes are more or less perpendicular to the surface of the valves and rotate with their curvature (Fig. 2.4.20A and Schmahl et al. 2004). It is known by now that this is an intrinsic feature of carbonate shells (brachiopods, molluscs) and teeth. The valves have an uniaxial fiber texture, while the hinge shows a bimodal distribution pattern of calcite c-axes (Fig. 2.4.20C and Griesshaber et al. 2007).

Is the texture of terebratulide species with three mineralized layers (*L. neozelanica*, *G. vitreus*) compared to each other (Fig. 2.4.21A-C), we find the following characteristics: (i) the columnar layer has the strongest calcite co-orientation strength, thus the strongest texture and is followed (ii) in calcite co-orientation strength by the primary shell layer; (iii) the fibrous shell has the weakest texture, the least co-orientation strength of calcite crystallites, when compared to the columnar and to the primary shell layer, respectively. For both, *G. vitreus* and *L. neozelanica* we investigated six specimens each and show in Fig. 2.4.21 pole figures and MUD values for two specimens per taxon. We observed always that the calcite in the shell of *G. vitreus* has a stronger texture (for all shell layers a higher MUD value, Figs. 2.4.21A-C) when compared with the texture strength of *L. neozelanica* shells (lower MUD values for all shell layers, Figs. 2.4.21A-C).

For the shells of Craniida and Thecideida texture strength decreases significantly (Figs. 2.4.21D-E); for both taxa we investigated several specimens but show per taxon two examples. The pole figures show that the thecideide shells have an axial texture as well, similar to terebratulide and rhynchonellide taxa, however, calcite co-orientation strength is very low (see MUD values in Fig. 2.4.21D), thus the shell has a weak texture (compare pole figures and MUD values of Fig. 2.4.21A-D). The craniide species *N. anomala* forms its shell with the least textured calcite (Fig. 2.4.21E, see MUD values), even though, the calcite does not have a completely random distribution, there is still in the shell some overall pattern of calcite orientation.

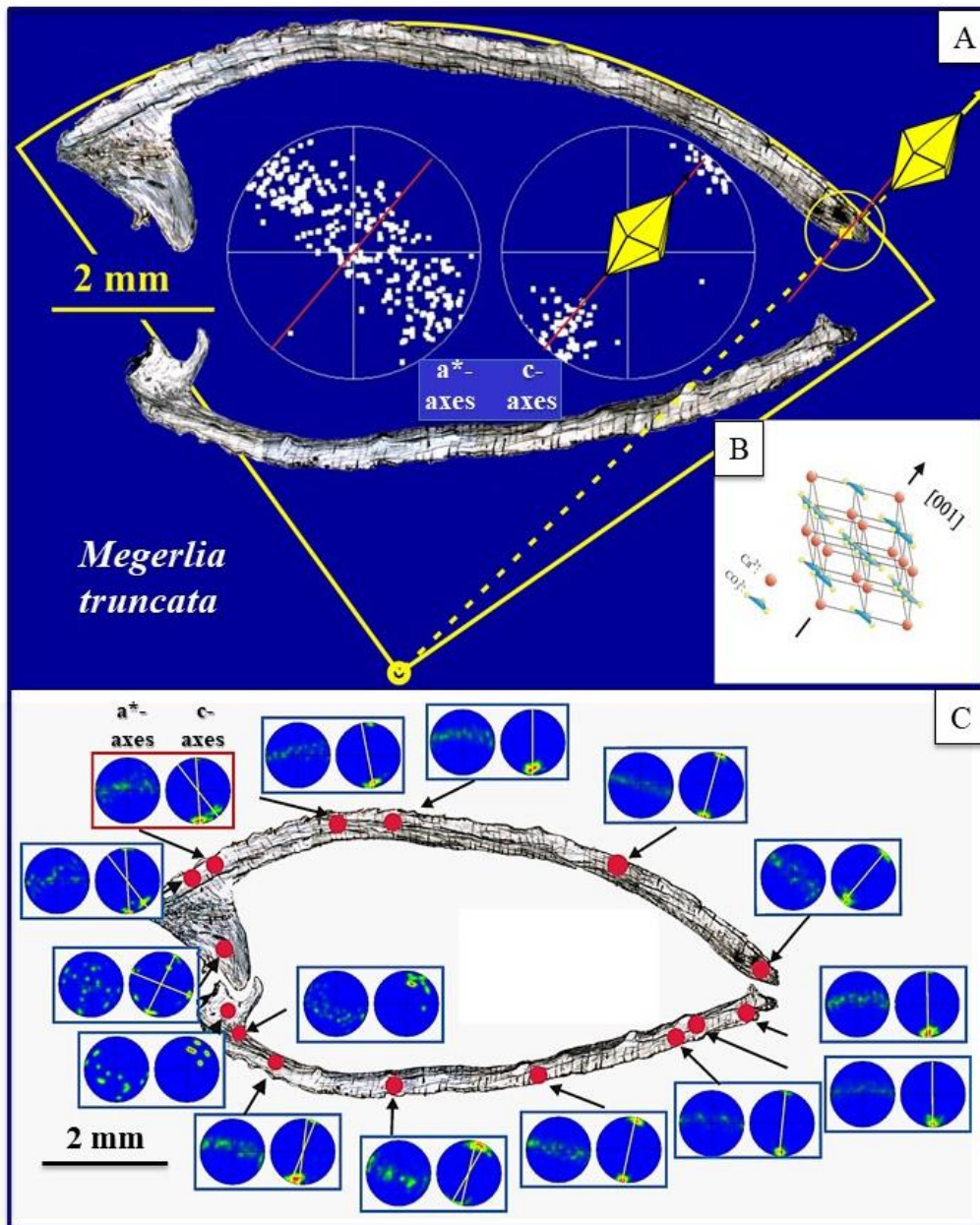


Figure 2.4.20. Pattern of calcite c- and a*-axes orientation measured on a cross-section through the median plane of both valves of the terebratulide species *Megerlia truncata*. Calcite c-axes are parallel to the radius of the curvature of the shell, perpendicular to the shell surface (A and Schmahl et al. 2004) and rotate with the curvature of the shell vault (B and Griesshaber et al. 2007). The valves have a sharp axial fiber texture, while at the hinge a bimodal distribution of c-axes is present (B and Griesshaber et al. 2007).

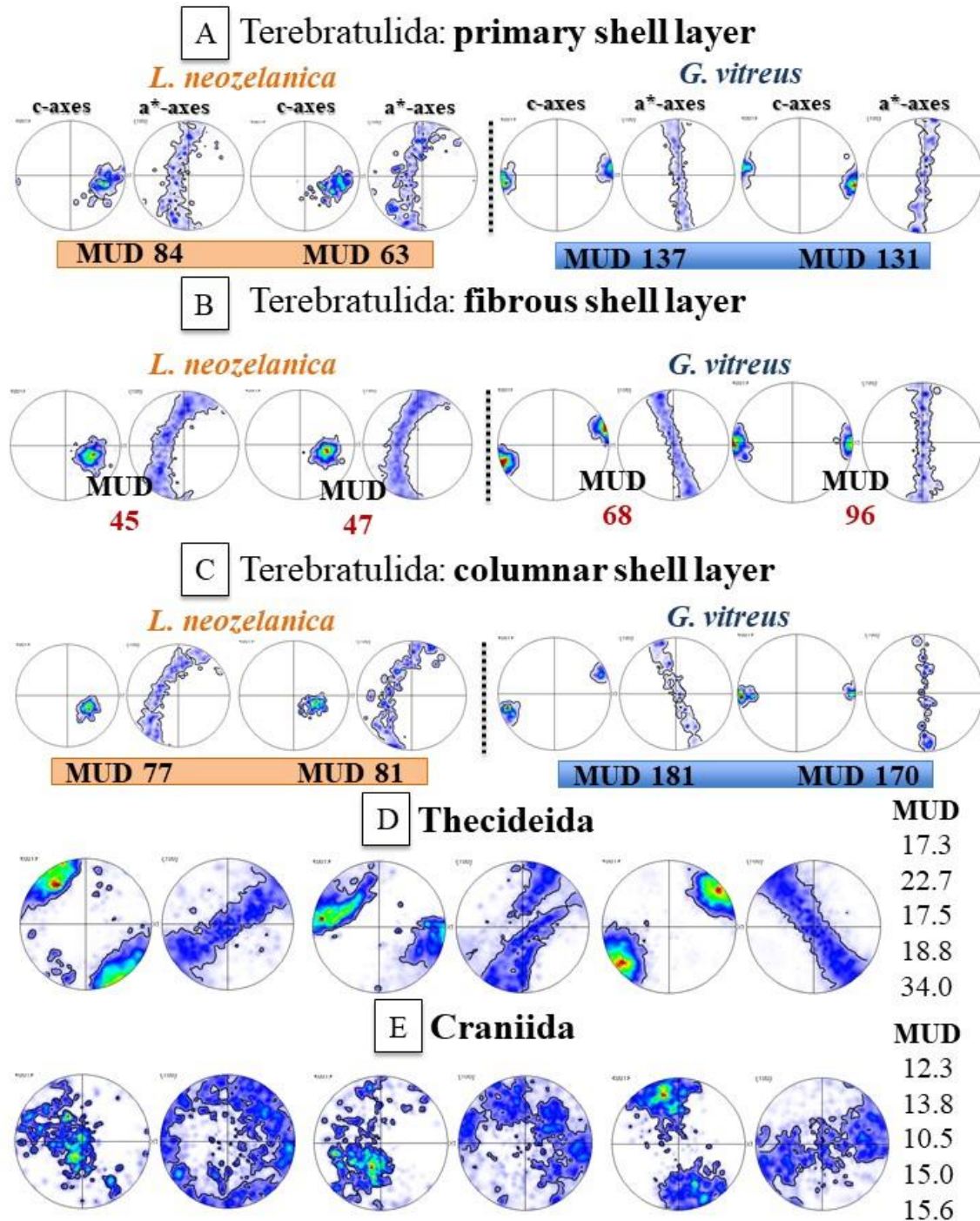


Figure 2.4.21. Comparison between terebratulide, thecideide and craniide shell texture. MUD values give calcite co-orientation strengths; for definition see the methods section. At a half width of 5 and a cluster size of 3 an MUD of 1 indicates random crystal orientation, while an MUD above 700 indicates more or less single crystallinity. For *G. vitreus* and *L. neozelanica* we show the texture of two specimens, for the Thecideida and Craniida for three specimens each. We can deduce the following: (i) relative to the terebratulide species, calcite crystals in the shells of the thecideide and the craniide species are significantly less co-aligned, (ii) the least co-aligned is the calcite in craniid shells. (iii) There is a huge difference in calcite co-orientation strength between *L. neozelanica* and *G. vitreus*. (iv) For both species the fibrous layer has the least calcite co-orientation strength. (v) Calcite co-orientation is highest for the columnar layer, but (vi) it is also high for the primary shell layer.

Figure 2.4.22 compares texture strength of the primary and the fibrous shell layer for taxa that form their shell of only two mineralized layers. We observe that (i) for the same specimen calcite in the primary shell layer is always more co-oriented, has always the strongest texture, relative to the fibrous shell layer. (ii) texture strength differs for the different species, for both the primary and the fibrous shell layers. The largest difference one can observe for *Calloria inconspicua* (MUD 370 and 65) and *Magasella sanguinea* (MUD 47 and 27) (Fig. 2.4.22). Both species live in the same environment; Doubtful Sound, New Zealand.

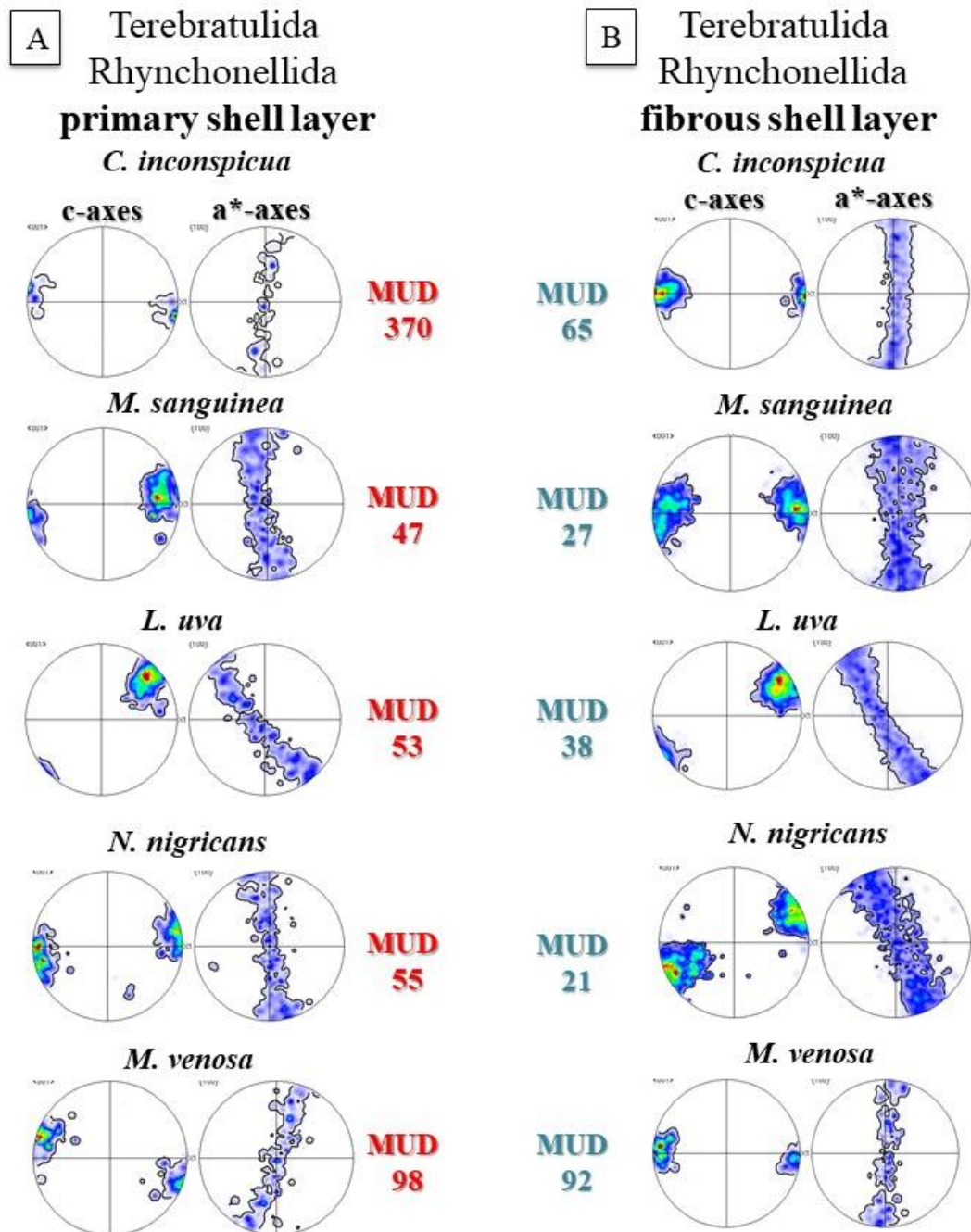


Figure 2.4.22. Comparison in crystal orientation strength between species with a primary and a fibrous shell layer. We see the following: (i) calcite co-orientation in the primary shell layer is

always increased, relative to the fibrous layer. (ii) There is a large difference in calcite co-orientation strength for the different modern terebratulide and rhynchonellide taxa.

2.4.9. Are thecideide shells reliable archives for present and past environment reconstruction ?

Paleoclimate and paleoenvironment reconstructions are based on analysis of geochemical proxies performed on archives such as biogenic hard tissues and cements (e.g. Brand et al. 2011). Shells of Terebratulida and Rhynchonellida are one of the most used biogenic structural materials for paleoenvironment reconstruction as they cover almost the entire geologic record, are wide-spread in many and distinct marine habitats and, most of them, secrete low-Mg calcite shells (Al-Aasm and Veizer 1982, Veizer et al. 1999, Brand et al. 2003, Brand et al. 2011, Auclair et al. 2003, Parkinson et al. 2005, Von Allmen et al. 2010, Payne and Clapham 2012; Cross et al. 2015, Immenhauser et al. 2015, 2016, Garbelli et al., 2012, Garbelli et al. 2014, Ye et al. 2019).

Thecideide brachiopods are the last brachiopod order to appear in the fossil record (e.g. Pajaud 1970, Grant 1972, Williams 1973, MacKinnon 1973, Baker 1990, Baker 2006, Lüter 2005, Cohen 2007, Carlson 2016). In contrast to Rhynchonellida and Terebratulida, thecideides are small-bodied, thick-shelled animals that live in tropical and warm seas in cryptic habitats cemented to rocky substrates (e.g. Rudwick 1970, Baker 1990, Richardson 1997, Carlson 1995, 2007, Nebelsick et al. 2011, Simonet Roda et al. 2020). Williams and co-workers (Williams 1973, 1997, Baker 2006, Williams and Carlson 2007) addressed thecideide shell microstructure as being similar to the primary layer microstructure of Rhynchonellida and Terebratulida. Would this be the case, then, thecideide shells could not be considered to be reliable archives, as geochemical work demonstrated that the primary shell layer of rhynchonellide and terebratulide shells is not precipitated in equilibrium with ambient seawater (Carpenter and Lohmann 1991, Carpenter and Lohmann 1995, Parkinson et al. 2005, Brand et al. 2011, Rollion-Bard et al. 2019). In this review we focus on this issue and complement our microstructural work (chapters 1 to 5) with geochemical analyses obtained on a terebratulide (*M. venosa*) and a thecideide (*P. atlantica*) species (Figs. S2.4.20-21 and Milner Garcia 2018).

For **terebratulide** *M. venosa*, the $\delta^{18}\text{O}$ signature of the primary shell layer is strongly depleted in ^{18}O relative to the equilibrium field (Fig. S2.4.20B), a feature attributed to kinetic and physiological effects (Auclair et al. 2003). Towards inner shell surfaces $\delta^{18}\text{O}$ values become heavier, at innermost shell sections, formed of fibers, $\delta^{18}\text{O}$ values are close or within the equilibrium field (Fig. S2.4.20B). Water temperature at sampling location of *M. venosa* is 3.5°C and accounts for a $\delta^{18}\text{O}$ variation of 1‰. Accordingly, the observed variation in $\delta^{18}\text{O}$ for the fibrous layer of *M. venosa* is due to physiological and kinetic effects (see also discussions in Yamamoto et al. 2010, Yamamoto et al. 2013, Taganayaki et al. 2013, Bajnai et al. 2018, Brand et al. 2019, Rollion-Bard et al, 2019, Ye et al. 2019). For **thecideide** *P. atlantica*, $\delta^{18}\text{O}$ results diverge from what we find for *M. venosa* (Fig. S2.4.20A). Furthermore, we find for *P. atlantica* differences in $\delta^{18}\text{O}$ between ventral and dorsal valves (Fig. S2.4.20A). In the ventral valve $\delta^{18}\text{O}$ values fluctuate close to the field of equilibrium with seawater, while $\delta^{18}\text{O}$ values of the dorsal valve scatter fully within the range of values that span the equilibrium field (Fig. S2.4.20A). Water temperature at sampling of *P. atlantica* was 3.7 °C and accounts for a variability in $\delta^{18}\text{O}$ of 58 to 77% of the overall shell $\delta^{18}\text{O}$ value. The remaining can be attributed to kinetic effects. For transects through the

ventral valve we find that outer shell layers of *P. atlantica* are depleted in ^{18}O relative to equilibrium values, while inner shell portions are secreted in equilibrium with ambient seawater (Fig. S2.4.20A). As the overall variability across the transect through the valve is not in agreement with the temperature range of 3.7°C , we can assume that kinetic effects affect mainly outer and to a lesser degree inner shell sections; a result that is in concert with $\delta^{18}\text{O}$ measurements of Brand et al. 2003. Hence, inner shell calcite of *P. atlantica* incorporates oxygen isotopes, more or less, in equilibrium with ambient seawater.

Mg concentration across shell transects of terebratulide *M. venosa* follows a characteristic trend: high Mg-contents in the primary shell layer that decrease in the fibrous layer, however, increase again at innermost shell surfaces (Fig. S2.4.21); a well-known trend described already previously (e.g. Griesshaber et al. 2007, Romanin et al. 2018, Rollion-Bard et al. 2019). Mg content in thecideide *P. atlantica* (Fig. S2.4.21) is also structured and in concentration distinct to what we observe for *M. venosa* shells: (i) the Mg/Ca ratio in *P. atlantica* is significantly higher relative to values that we find for *M. venosa* (Fig. S2.4.21), (ii) within the outer half of the shell (in cross-section) Mg/Ca ratios fluctuate between 50 to 90 mmol/mol, while Mg contents increases within the inner half of the shell and varies between 80 to 120 mmol/mol (Fig. S2.4.21).

Sr distribution in *M. venosa* resembles that of magnesium (Fig. S2.4.21). As Sr/Ca values are negatively correlated with oxygen isotope compositions, an influence of precipitation rate is indicated (this study and Ullman et al, 2017; Romanin et al., 2018; Rollion-Bard et al, 2019). Indeed, kinetic effects tend to decrease the value of $\delta^{18}\text{O}$ in carbonate (McConnaughey, 1989; Zeebe and Wolf-Gladrow, 2001; Beck et al, 2005; Rollion-Bard et al, 2011), while an increase in precipitation rate tends to rise the incorporation of Sr into the calcite lattice (Gabitov and Watson, 2006; DePaolo, 2011). In *P. atlantica* Sr is homogenous within the shell, Sr/Ca ratios scatter between 1.9 and 2.1 mmol/mol across the cross-section through the shell (Fig. S2.4.21 and for other thecideides Lowenstam 1961; Delaney et al. 1989; Carpenter and Lohmann 1991; Carpenter and Lohmann 1993, Brand et al. 2003).

Li distribution in the shell of *M. venosa* (Fig. S2.4.21) is comparable to that of Sr. The primary layer has the highest values and is followed by a drop in Li contents in the fibrous shell layer (this study and Rollion-Bard et al, 2019). In *P. atlantica* as well Li contents are higher in outer, relative to inner portions, however, the decrease in *P. atlantica* is significantly less marked, when compared to the trend in Li contents in *M. venosa*.

Na concentration distribution in *M. venosa* cross-sections through the valve follows closely the trend of Li (Fig. S2.4.21). The primary shell layer is enriched in Na, relative to inner shell regions. Such a trend is observable for Na contents along cross-sections through *P. atlantica* valves as well (Fig. 2.4.21), however, significantly less pronounced.

2.4.10. Concluding summary

In chapters one to five we present: (i) the diversity of calcite crystal assembly solutions utilized for shell formation by representatives of extant calcite secreting

brachiopod orders and (ii) summarize the current knowledge on brachiopod shell structure, microstructure and texture.

In this chapter we place our findings in a broader perspective and discuss the following: (i) adaptation of microstructure and texture to environments, (ii) advantage gained from a composite nature and hierarchical architecture, (iii) recognition of determinants of microstructure fabrication, (iv) illustration of the stand-alone microstructure of modern thecideides.

Microstructure, texture, life-style and environment

Modern, calcite secreting brachiopods mineralize and grow continuously; valves grow in both, length and thickness (Williams 1966, Rosenberg et al. 1988, Baumgarten et al. 2014).

The shells of all extant calcite secreting brachiopod species consist of two, differently sized valves. Size difference between valves is most pronounced for species of cementing taxa (Craniida, Thecideida), while for species of taxa living attached to substrate by a pedicle (Terebratulida, Rhynchonellida) the difference in ventral and dorsal valve dimensions is less marked.

Thecideida and Craniida live in sheltered/cryptic habitats, in contrast to Terebratulida and Rhynchonellida, that live predominantly in open marine environments. Shells of cementing taxa are small (below 1.5 x 1.5 cm), especially the shells of the Thecideida. The latter form 2 to 3 mm thick shells with dimensions well below 1 x 1 cm. Shell size of not cementing taxa is significantly larger. For terebratulide and rhynchonellide adult animals shell sizes range from about 1 to about 10 cm. E. g. *Magellania venosa* has the highest growth performance recorded for a rhynchonelliform brachiopod (Baumgarten et al. 2014), shell sizes reach easily 10 cm in length. Nonetheless, most modern terebratulide and rhynchonellide species secrete 1 to 3 mm thick shells in the size range of up to 5 to 6 cm in length. Thus shell size variation for taxa that live in open marine water and that are attached to substrate by a pedicle is large, in contrast to taxa that live in cryptic habitats and are cemented to substrate.

As shown in Figures 2.4.15-18 and 2.4.21 there are major differences in shell microstructure and texture between taxa that live in cryptic habitats and taxa that live in open marine environments. Species that live cemented to substrate form their shell of little co-ordinated, almost untextured calcite (Figs. 2.4.21D-E), while those that attach to substrate by a pedicle secrete shells with well to even highly textured calcite (Fig. 2.4.21A-C). The above described variation is the only adaptation to environmental conditions that we can deduce from our microstructure and texture data. Peck and Harper (2010) investigated size variations of Terebratulida and Rhynchonellida with latitude and depth. For Terebratulida the study could establish a relationship between shell size and environmental conditions (latitude and depth), while for Rhynchonellida trends between these characteristics were not observable.

However, when focussing only on fibers, characteristic relationships emerge between structural features of the fibers and environmental and ontogenetic conditions for both Terebratulida as well as Rhynchonellida (Ye et al. 2018a, b). Ye et al. investigated for adult specimens of six modern brachiopod species living in three different habitats (Antarctica, the Pacific at New Zealand, Mediterranean Sea) fiber convexity, roundness and length and could establish the following: (i) lack of difference

in morphometric characteristics between fibers in ventral and dorsal valves. Accordingly, a specific brachiopod secretes only one type of fiber. (ii) connection between morphological characteristics of fibers and ontogenetic development and (iii) link between fiber morphometry and environmental conditions. The latter is present when the comparison is made between species of similar genus that live in water with similar salinity but different temperature and carbonate saturation state. Accordingly, modern terebratulide and rhynchonellide brachiopods respond to changes in temperature and carbonate saturation state but tolerate variations in salinity.

Composite nature and hierarchical architecture

Calcium and hydrogen carbonate is abundant in seawater and is readily available to marine organisms. However, the pure carbonate phases, calcite and aragonite, are useless as shell construction materials as they are very brittle and break easily. For obtaining a protective and functional hard tissue the biomineral has to be functionalized, already at the very start of its formation.

Organisms employ a bottom-up construction process for fabrication of their hard tissues. As secreted by cells, the first-formed entities have to be small, even though the final product, the hard tissue, needs to be macro-sized. This is reached by utilizing hierarchical assembly principles (e.g. Dunlop and Fratzl 2010, Staudart 2012, Wegst et al. 2014) and fabricating biomaterials with hierarchical architectures. E.g. for modern rhynchonellide and terebratulide fibrous shell layers we find at least 5 levels of hierarchy: nanometric calcite crystals (Fig. 2.4.14A), 50 to 100 nm sized calcite layers within fibers (Figs. 2.4.14B-C, 2.4.11A and S2.4.12), individual fibers (Figs. 2.4.11C, S2.4.4A), stacks of parallel fibers (Fig. S2.4.4) the fibrous layer of the shell layer (Fig. S2.4.1). The entire shell would then be the sixth level of hierarchy.

For being protective and functional, the biomaterial has to be functionalized. This occurs, in general, with the formation of a composite hard tissue. Very many, but not all carbonate biological hard tissues (e.g. the primary shell layer of Rhynchonellida and Terebratulida) are composites of mineral and biopolymer components, and this, on all length scales of the hard tissue; from organic membrane bound and mineral/ion filled vesicles to the macro-scale level of the shell. The latter consists of layers formed of a mineral component that occludes an extracellular matrix (e.g. the fibrous and columnar shell layers of Rhynchonelliformea or the calcite layers within the shell of Craniida). The amount of organic substance occluded into the mineral depends on the specific requirement to the composite hard tissue. E. g. *Lingula anatina* burries itself quickly with its two valves into the sediment, thus it needs very flexible but resilient valves. Organic matter content of *L. anatina* valves varies between 30 to 32 wt. % (this study). In contrast, organic substance content of *G. vitreus* and *L. neozelanica* is between 2 to 3 wt. % (this study).

On rare occasions, it is not the composite nature that enhances the overall material properties of the hard tissue, it is the microstructure. We find this for the primary shell layer of rhynchonellide and terebratulid brachiopods. The strongly and tightly interdigitating dendrites form the specific material property characteristics of this layer, the nanoscale topology of grain boundaries, the jigsaw topology of the polycrystalline assembly. The specific microstructure gives the high microhardness of this shell layer, relative to that of the significantly softer adjacent fibrous layer (Griesshaber et al. 2007) and increases its abrasion resistivity.

When the biologically secreted mineral is functionalized with biopolymers the organic components become occluded into the mineral. The composite biocalcite is very different from the non-biologic counterpart, it can be bent, even strongly twisted, without breaking (Fig. S2.4.4A in this study, Griesshaber et al. 2005, Fig. 9H in Checa 2018, and Checa et al. 2019). Accordingly, the biologic and the non-biologic calcite have very little in common: only the crystal structure and the gross chemical composition.

An important feature that distinguishes biogenic and non-biogenic calcite is the absence of (104) cleavage and the increased hardness of the biocalcite, relative to its non-biogenic counterpart. When not, the result of a specific microstructure, increase in hardness is given by the composite nature of the biomaterial, the intercalation of organic substance into the biomineral (Merkel et al. 2009, Schmahl et al. 2012). The mineral component provides compressive and bending strength, hardness and abrasion resistance; the organic component contributes morphogenetic control, tensile strength, flexibility and ductility. The extracellular matrix is a dominant feature of the fibrous shell layer. It enables that this shell layer is deformation tolerant, as (i) it allows for dislodged fibers, (ii) it stops crack propagation and (iii) blunts cracks.

The fibres in brachiopod shells are not simple rods. They are highly variable in roundness, convexity, lengths and thicknesses (Ye et al. 2018a, Ye et al. 2018b), have elaborate morphologies and are interleaved in three dimension. Biological carbonate hard tissues are subject to compressive, bending and shearing forces. As fibres within an organic matrix cannot be reorganized once they endure these forces, they must be properly packed and oriented within the hard tissue from the very beginning of their formation. This is accomplished by the formation of stacks of parallel fibres and the stacks being twisted in a plywood-like arrangement (Figs. S2.4.1, S2.4.4B). Stack formation is what we see for all investigated fibrous layers of modern brachiopods. Brachiopod fibers have very different morphologies to bivalve fibers, e.g. calcite fibers in *Mytilus edulis* shells (Fig. S6 in Simonet Roda et al. 2019b, Griesshaber et al. 2013). Brachiopod fiber morphology is specific and unique (Fig. 2.4.7B and Simonet Roda et al. 2019b). The one convex and the three concave sides allow for staggered arrangement and an interleaved packing in the stack (Figs. 2.4.3C, 2.4.7B, 2.4.11A-C, 2.4.12B, 2.4.15F). The latter and the twisted plywood arrangement ensures that all components of the fibrous composite are interleaved in three dimension and on all length scales. Simonet Roda et al. 2019b noted that brachiopod fiber arrangements resemble tablet arrangements of sheeted nacreous aragonite in bivalve shells (Fig. S7 in Simonet Roda et al. 2019b). Accordingly, the staggered and twisted plywood architectures generate very successful shell microstructures, irrespective of these forming bivalve nacreous or brachiopod fibrous layers. Two-layered brachiopod shells consist of a stiff, hard and resilient protective cap, the primary layer, constructed as a thin, surface sheet. Adjacent is a massive, ductile but tough layer, the fibrous layer consisting of a fiber composite material (e.g. Figs. 2.4.15F, S2.4.3A and Schmahl et al. 2012).

Determinants of microstructure and texture

EBSD measurements of the last two decades demonstrated that brachiopod shells of the four extant calcite secreting orders are formed of five types of biomineral units, of the following biocrystals: (i) dendrites, (ii) fibers, (iii) columns (Rhynchonellida, Terebratulida), (iv) predominantly platelets (Craniida), (v) polygonal crystals (Thecideida). Fibers and platelets are intimately associated with an extracellular

biopolymer matrix. Columnar layers of Terebratulida and polygonal crystals assemblies of Thecideida contain also organic matrices, however, the fabric of these is less regular, especially that of thecideide shells. The matrix of thecideide shells is formed of submicrometre sized polygonal calcite crystallites that are interfused with micrometre sized or even tens of micrometre sized crystals. Randomly distributed organic membranes and networks of organic fibrils strengthen the cohesion of the shell material (Figs. 2.4.18, S2.4.9, S2.4.11).

A very interesting case is the columnar shell layer of Terebratulida that intercalate organic membranes, delineating neighboring columns; form, however, through a competitive growth process. Thus, what is the determinant that influences columnar layer microstructure formation? (i) the organic matrix? or (ii) crystal competition at growth? Checa 2018 describes determinants of microstructure formation in mollusc shells and demonstrates that microstructure fabrication can be influenced by (i) mainly physical, (ii) mainly chemical or (iii) by both physical as well as chemical determinants. The latter is the case for the columnar shell layer of modern Terebratulid brachiopod shells. The main determinant of column formation is growth competition, supported, however, by a membraneous organic matrix.

Column- and prism-shaped biocrystals that form through crystal competition are the closest analogues to non-biologic carbonate (see the rhombohedral morphology of calcite crystals within a column in Fig. 2.4.3F and von Allmen et al. 2010). In addition to brachiopod columns, further prominent examples of biocarbonates formed through competitive growth are myostracal shell layers of bivalves (Crippa et al. 2020a, 2020b) and the shells of cephalopods (e.g. *Argonauta argo*: Stevens et al. 2017). The latter biomaterials consist of prisms comprising highly co-oriented aragonite or calcite crystals and very high MUD values for individual prisms (MUD > 700). High co-orientation strength of crystallites and high MUD values are characteristics of non-biological calcite and aragonite precipitated from solution (e.g. Yin et al. 2019).

Castro-Claros et al. 2020 investigated for the bivalves *Anomia ephippium* and *Ostrea stentina* calcium transport to myostracal and non-myostracal shell layers. The authors observe that at mineralization of the myostracum mantle cells are not in contact with the myostracal shell, while when the ostracum and hypostracum are mineralized, mantle cells are directly next to the latter shell layers. Castro-Claros et al. 2020 suggest for these two bivalves two modes of shell secretion: (i) Ca transport by vesicles at myostracal prism formation and (ii) mineralization in direct contact with mantle cells at ostracum, hypostracum formation. Thus, these organisms utilize different mineralization processes when they form their shell.

The two modes of shell mineralization are mirrored by differences in carbonate microstructure. Myostracal aragonite assembly resembles that of the non-biological mineral counterpart, while ostracum, hypostracum shell microstructures are highly sophisticated, hierarchical and very diverse. Simonet Roda et al. (2019a, 2019b) demonstrated that the primary shell layer of the terebratulide brachiopod *Magellania venosa* is secreted by cell extensions only, the latter devoid of nuclei. In contrast, the mineralization of fibers occurs through mantle epithelial cells with cells containing nuclei and other organelles. As shown in this review, the primary and the fibrous shell layers have highly distinct microstructures and biopolymer contents. The highly distinct microstructure of the columnar shell layer indicates that a further mode of mineralization is applied when the columnar shell layer is secreted: competitive growth.

The latter is not dependent on the morphology and microstructure characteristic controlling influence of an organic component.

Modern thecideide shells: a stand-alone microstructure

Modern terebratulide and rhynchonellide brachiopods form layered shells. Discriminants between the layers are the microstructures of the mineral and the fabric of the organic components. In the shell of these taxa the molecular arrangement of ions in the calcite is linked to the macroscopic morphology of the shell via the orientation pattern of calcite *c*- and *a**-axes (Fig. 2.4.20A and Schmahl et al. 2004). Both calcite crystallites as well as the occluded organic components have well organized structures and fabrics.

These characteristics we do not find for modern thecideide shells (this study and Goetz et al. 2009). The hierarchical architecture of terebratulide and rhynchonellide shell calcite (at least 6 levels of hierarchy) is not detectable for modern thecideide shells. The latter form composite shells, however, both the calcite and the organic components are present in the shell with very little ordered arrangements.

A further distinction between modern thecideide and terebratulide/rhynchonellide shells is the distribution pattern of organic substance within the shell. With the exception of the primary shell layer, terebratulide and rhynchonellide fibrous and columnar calcite occludes an extracellular matrix that delineates the mineral units (fibres, columns) from each other. In addition, we know that the fibers intercalate a very low amount of organic substance in form of a network of fibrils (Figs. 2.4.11F). Accordingly, in terebratulide/rhynchonellide shells the distribution pattern of organic substance is also structured and hierarchical, a further feature that we do not observe for modern thecideide shells. In the latter, much organic substance is intercalated into the calcite (membranes, fibrils) however, without any structured distribution pattern, e.g. an extracellular matrix filled with mineral. The mineral component in modern thecideide shells consists of a groundmass of calcite nanocrystals into that irregularly shaped micrometre sized crystals are interspersed (Figs. 2.4.18, S2.4.18). The calcite crystals do not have a dendritic structure as it is the case for the primary shell layer of terebratulides and rhynchonellides; we also do not see such a strong interdigitation of neighboring crystals, as it is the case for the primary shell layer. The organic substance in thecideide shells serves rather as reinforcement not as a matrix (Figs. S2.4.9-11).

Our study demonstrates that the microstructure and texture of modern thecideides is a stand-alone structure, specific to this brachiopod order. It is dissimilar to the microstructure and texture of the primary layer of modern rhynchonellide and terebratulide brachiopods. The primary shell layer of the latter brachiopod genera consists of interlocked dendrites, is devoid of organic substance (this study and Griesshaber et al. 2009, Goetz et al. 2011) and has a strong texture (Fig. 2.4.16A; high MUD values Fig. 2.4.22A), in contrast to all structural characteristics that we find for the hard tissues of modern Thecideida (Fig. 2.4.21D).

Our geochemical results substantiate as well the distinctness between thecideide and terebratulide shells: (i.) *P. atlantica* (thecideide) secretes high-Mg calcite, *M. venosa* (terebratulide) forms its shell of low-Mg calcite, (ii) the range in Li, Na, Mg, Sr concentration is larger for *M. venosa* shells, in comparison to what we observe for *P. atlantica* valves. Even though, oxygen isotope results for inner ventral valve sections of *P. atlantica* (thecideide) fall within the $\delta^{18}\text{O}$ equilibrium zone (Fig. S2.4.20 and Brand

et al. 2003). This result could be interpreted that parts of thecideide shells might be appropriate to be used as archives for environment reconstruction. However, the drawback is that thecideide shell fabric is not sub-structured into layers, sections, regions. Thus, the problem is, where in the thecideide shell do we base the distinction between outer and inner shell portions, between valve sections precipitated in equilibrium or in disequilibrium with ambient seawater. Even if this distinction could be made for thecideide shells, localization between different shell portions will vary for each specimen and in some cases might not be possible. In addition, due to their high-Mg calcite shells, thecideides are more prone to diagenetic overprint, relative to low-Mg calcite shelled brachiopods. Thus, in contrast to terebratulides and rhynchonellides, their unstructured shell fabric does not allow for a distinction between (i) overprinted shells that lost their pristine microstructure due to diagenesis or simply (ii) the always present little organized shell fabric, which is an intrinsic feature of representatives of modern thecideide taxa.

2.4.11. Author's Contribution

Erika Griesshaber and Maria Simonet Roda had the original idea for the article. Maria Simonet Roda and Erika Griesshaber performed the analytical work: EBSD, AFM, FE-SEM, STEM, imaging and data analysis. Helmut Gnägi provided the microtome sections for STEM imaging, Uwe Brand, Lucia Angiollini, Facheng Ye, Daniela Henkel and Vreni Häusermann provided the shell samples. Claire Rollion-Bard, Sara Milner provided the geochemical data. Anton Eisenhauer, Wolfgang W. Schmahl contributed to the discussion. All authors contributed to the final version of the manuscript. The authors declare no competing interests.

Data availability

The datasets generated during and/or analysed during the current study are available from the corresponding author on request.

Acknowledgements

This project has received funding from the European Union's Horizon 2020 research and innovation programme under grant agreement No 643084 and the German Research Council Programme GR 9/1234.

We very much thank Prof. A. Logan, Prof. U. Brand, Prof. A. Angiollini, Prof. E. M. Harper, Dr. A. Bitner, Dr. V. Häusermann, Dr. D. Henkel, Dr. H. Jurikova, Dr. C. Lüter for the many brachiopod specimens they gave us. We thank Dr. Fitriana Nindiyasari and Julia Huber for microtome preparation and etching of many shell samples; Moritz Zenkert for conventional preparation of some brachiopod shells for EBSD measurements. We thank Dr. D. Henkel and Dr. H. Jurikova for taking care of culturing modern *Magellania venosa* and *Pajaudina atlantica* in aquaria at GEOMAR Helmholtz Zentrum für Meeresforschung, Kiel, Germany. We want to express our thanks to Prof. P. Walter and Dr. Andreas Ziegler for letting us to use for many years the entire laboratory equipment at the Center for Electron Microscopy, University of Ulm.

Supplementary Material

Table S2.4.1. Investigated species, number of investigated specimens, sampling localities and number of EBSD scans per species.

Species	No. investigated specimens	Locality	No. EBSD scans
Terebratulida			
<i>Megerlia truncata</i>	4	Marseille Med. Sea	6
<i>Magellania venosa</i>	10	Punta Arenas Chile	8
<i>Terebratalia septentrionalis</i>	5	Gulf of Maine USA	4
<i>Terebratalia transversa</i>	3	San Juan Islands USA	4
<i>Calloria inconspicua</i>	3	Doubtfull Sound NZ	4
<i>Magasella sanguinea</i>	2	Doubtfull Sound NZ	3
<i>Laquens rubellus</i>	1	Sagami Bay Japan	2
<i>Liothyrella uva</i>	5	Signy Bay Antarctica	6
<i>Liothyrella neozelanica</i>	6	Doubtfull Sound NZ	6
<i>Gryphus vitreus</i>	6	Thyrrhenian Sea Italy	6
<i>Terebratalina crossei</i>	1	Otsuchi Bay Japan	2
<i>Terebratalina retusa</i>	1	Skagerrak, Norway	2
<i>Terebratalia palustris</i>	1	California USA	2
<i>Magellania flavescens</i>	1	Westerport Bay Australia	4
Rhynchonellida			
<i>Notosaria nigricans</i>	4	Doubtfull Sound NZ	8
<i>Neorhynchia strebeli</i>	1	Weddell Sea Antarctica	2
Thecideida			
<i>Pajaudina atlantica</i>	8	Canary Islands Spain	12
<i>Thecidellina blochmanni</i>	1	Europa Is. Indian Ocean	6
<i>Kakamiella chathamensis</i>	4	Chatham Rise NZ	8
Craniida			
<i>Novocrania anomala</i>	3	Marseille Med. Sea	16

Notosaria nigricans

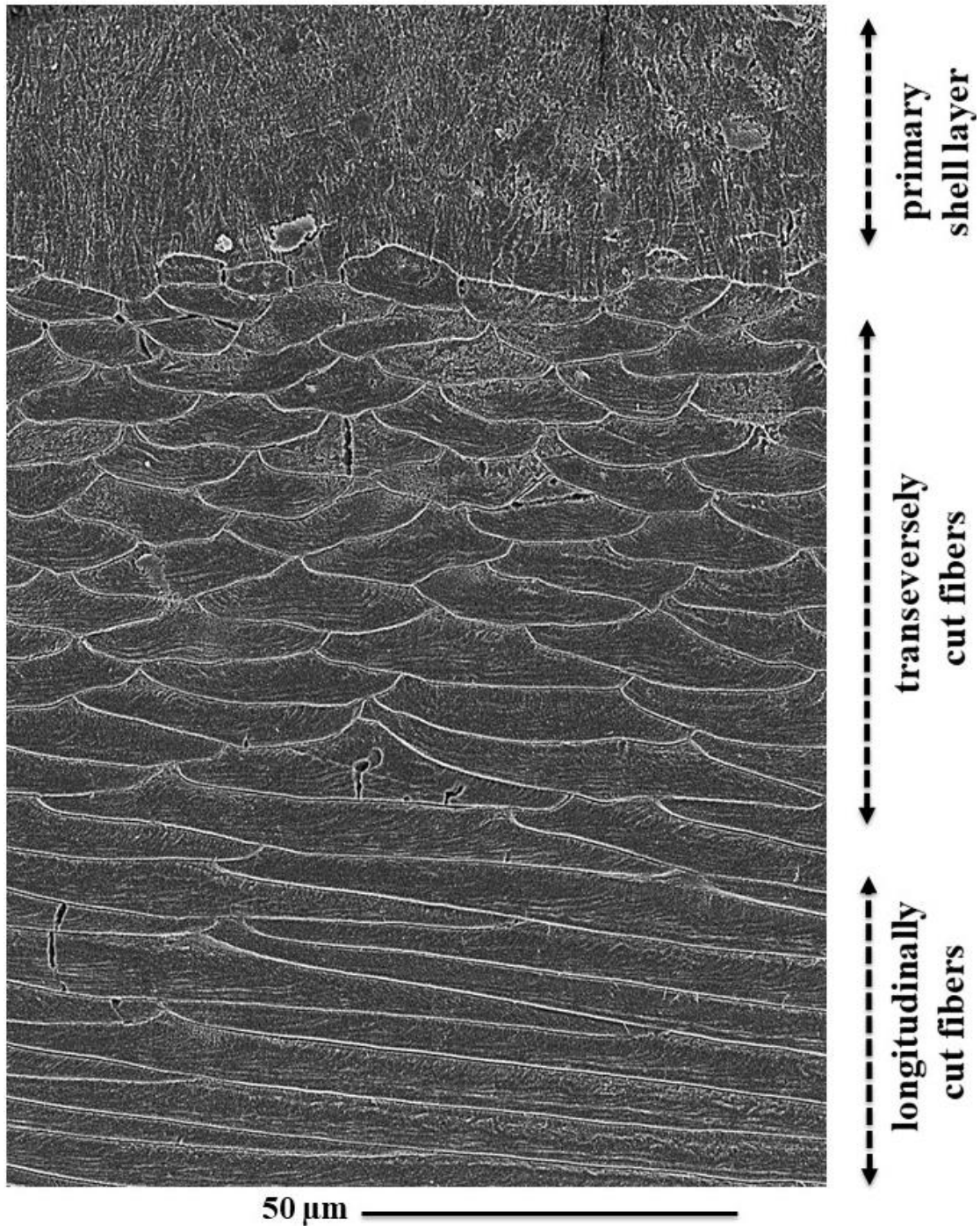
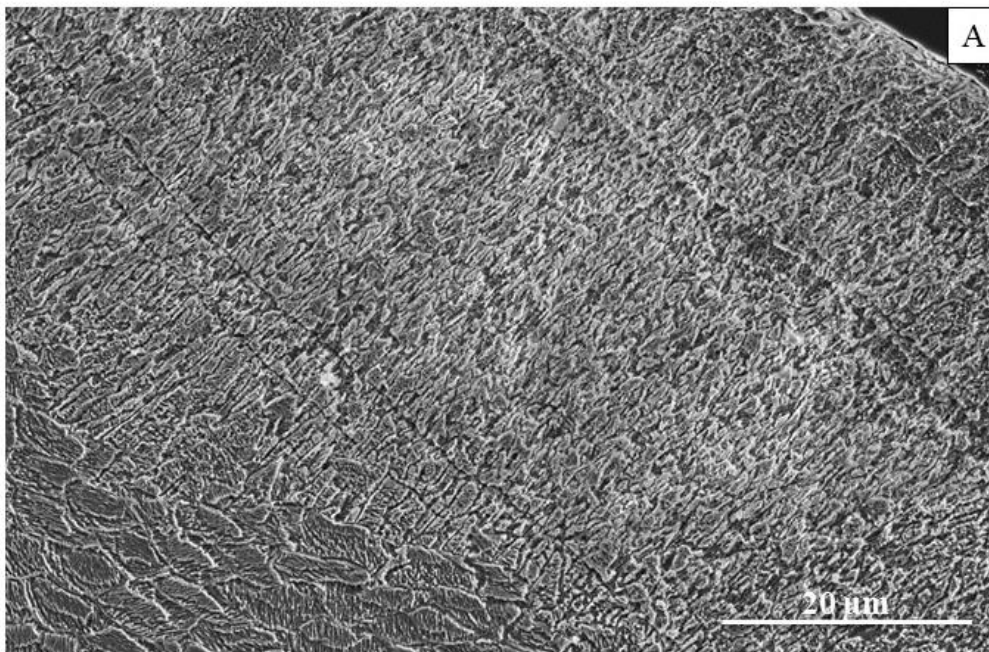


Figure S2.4.1. The primary and fibrous shell layers of *Notosatia nigricans*. SEM image of a microtome knife polished and etched cross-section through the shell. Well visible is the lack of an organic matrix in the primary and its presence in the fibrous shell layer, respectively. Note the stacks of transversely and longitudinally cut fibers. Well visible in most fibers is a striation, indicative of the mode of calcite secretion within the fibers: deposition of thin calcite layers in a fiber; see also Fig. 2.4.3D and Simonet Roda et al. 2019b.

Liothyrella uva



Magellania venosa

Magellania venosa

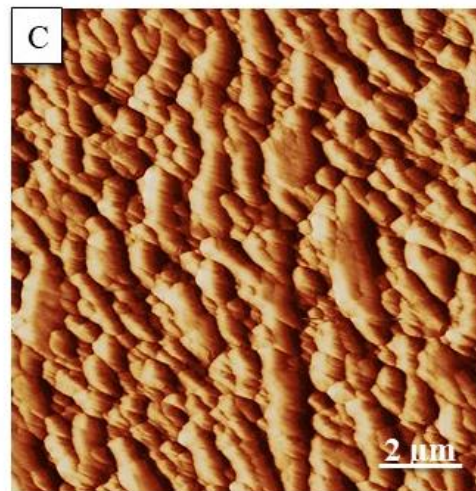
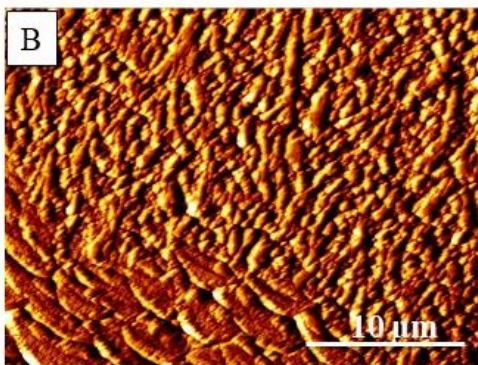
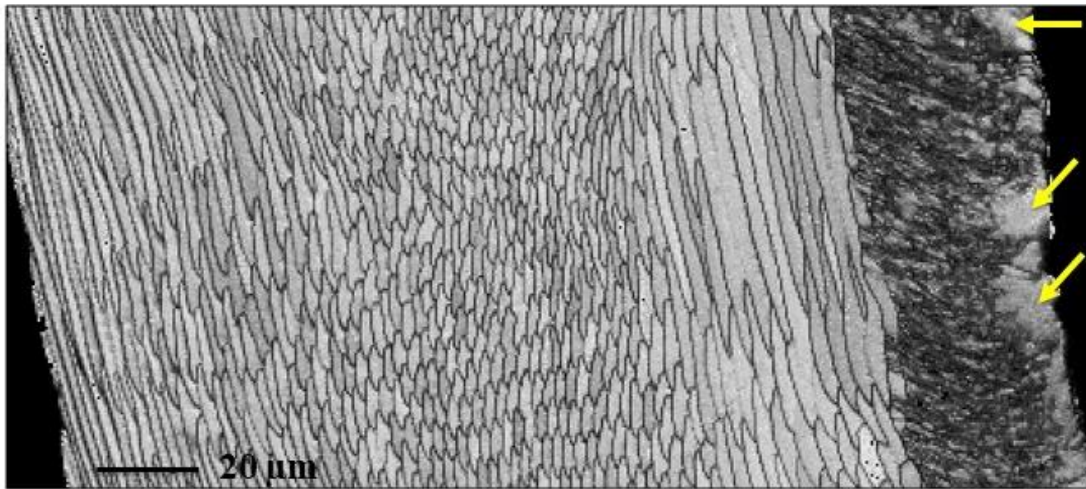
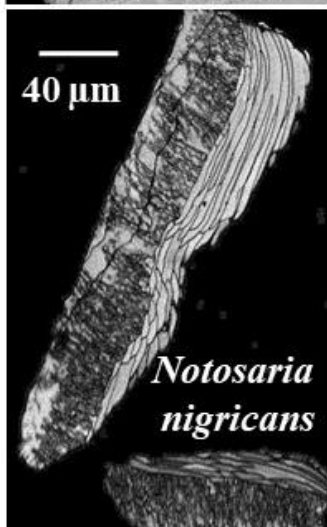
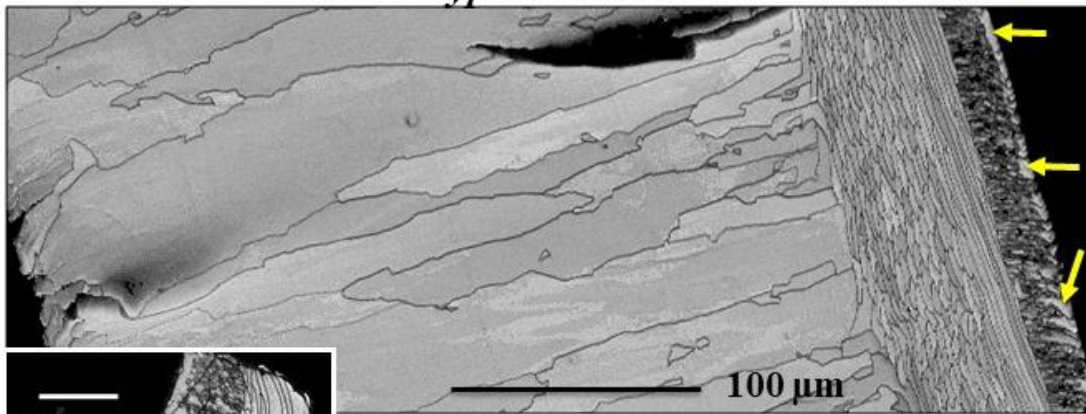


Figure S2.4.2. The internal structure of the primary shell layer of terebratulid shells visualized with an SEM image of an etched surface (A) and AFM vertical deflection images (B, C).

Calloria inconspicua



Gryphus vitreus



Magellania venosa

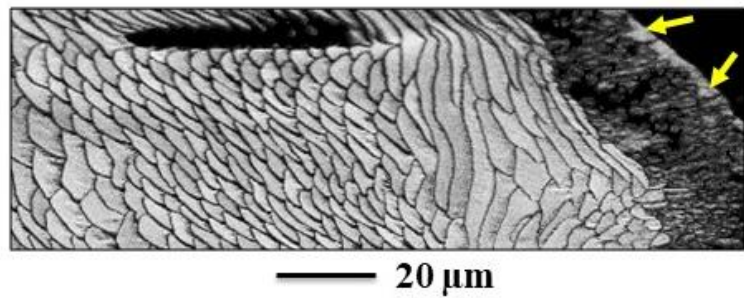


Figure S2.4.3. EBSD band contrast measurement images through cross-sections of terebratulid brachiopod shells. Note: (i) for *Calloria incinspicua* the cut through differently oriented stacks of fibers and (ii) the string of large/larger crystallites (yellow arrows) that seam outermost primary layer surfaces. The very tip of the valves consists always of primary layer type material with its characteristic microstructure and texture.

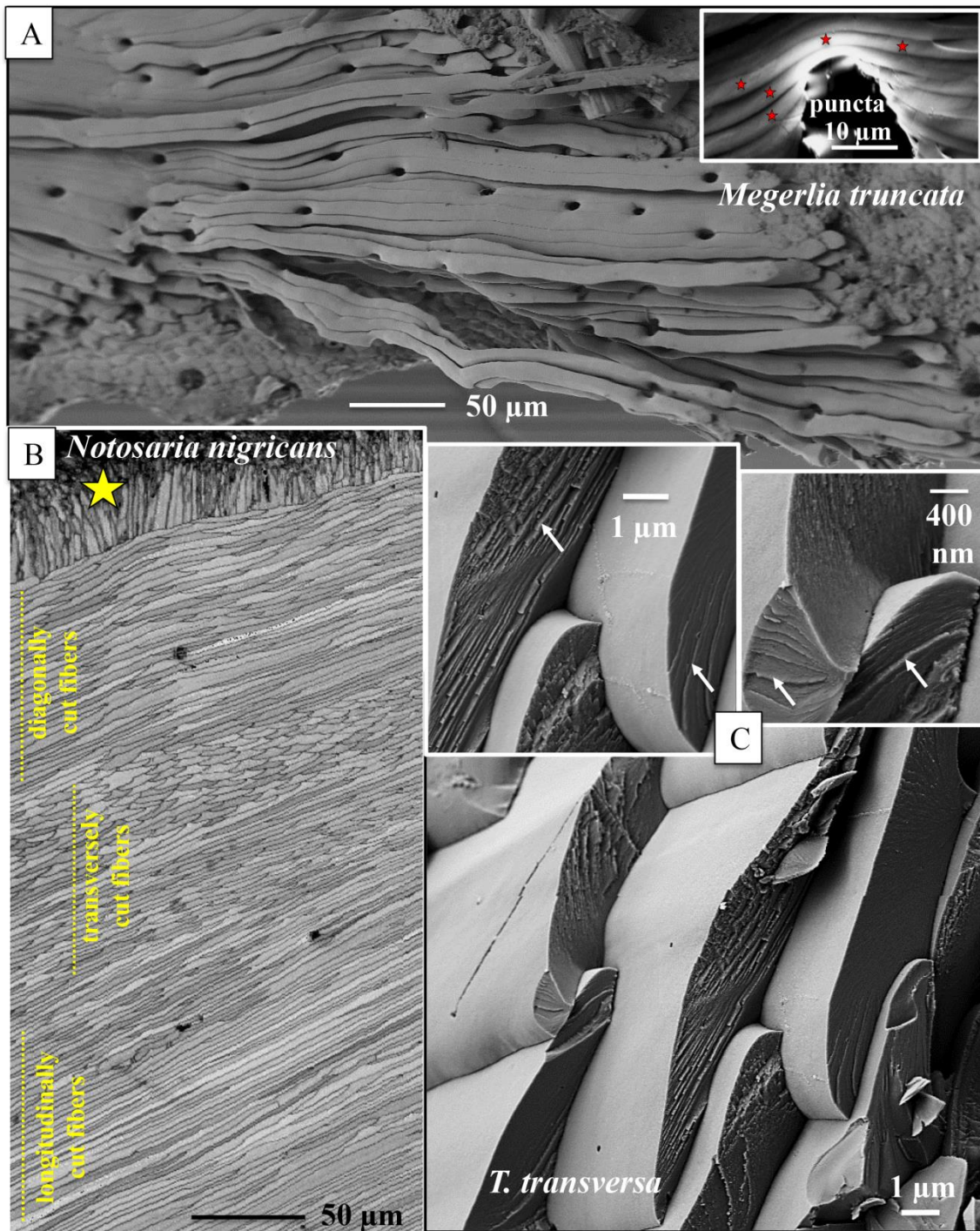


Figure S2.4.4. The fibrous shell layer of *M. truncata*, *N. nigricans* and *T. transversa*. (A, C): SEM images of fractured surfaces. (B): EBSD band contrast measurement on a cross-section through the primary and the fibrous shell layer. Well visible are in (B): (i) the differently oriented stacks of, more or less, parallel fibers and (ii) a row of large, primary layer, crystals (yellow star in B) at the transition from the fibrous to the primary shell layer. (C): the staggered arrangement of fibers in a stack; the sequence of thin calcite layers within individual fibers. Insert in (A): note the bending of fibers (red stars). It is remarkable that at these instances the calcite lattice remains constant, even though the morphological axis of the fiber changes direction.

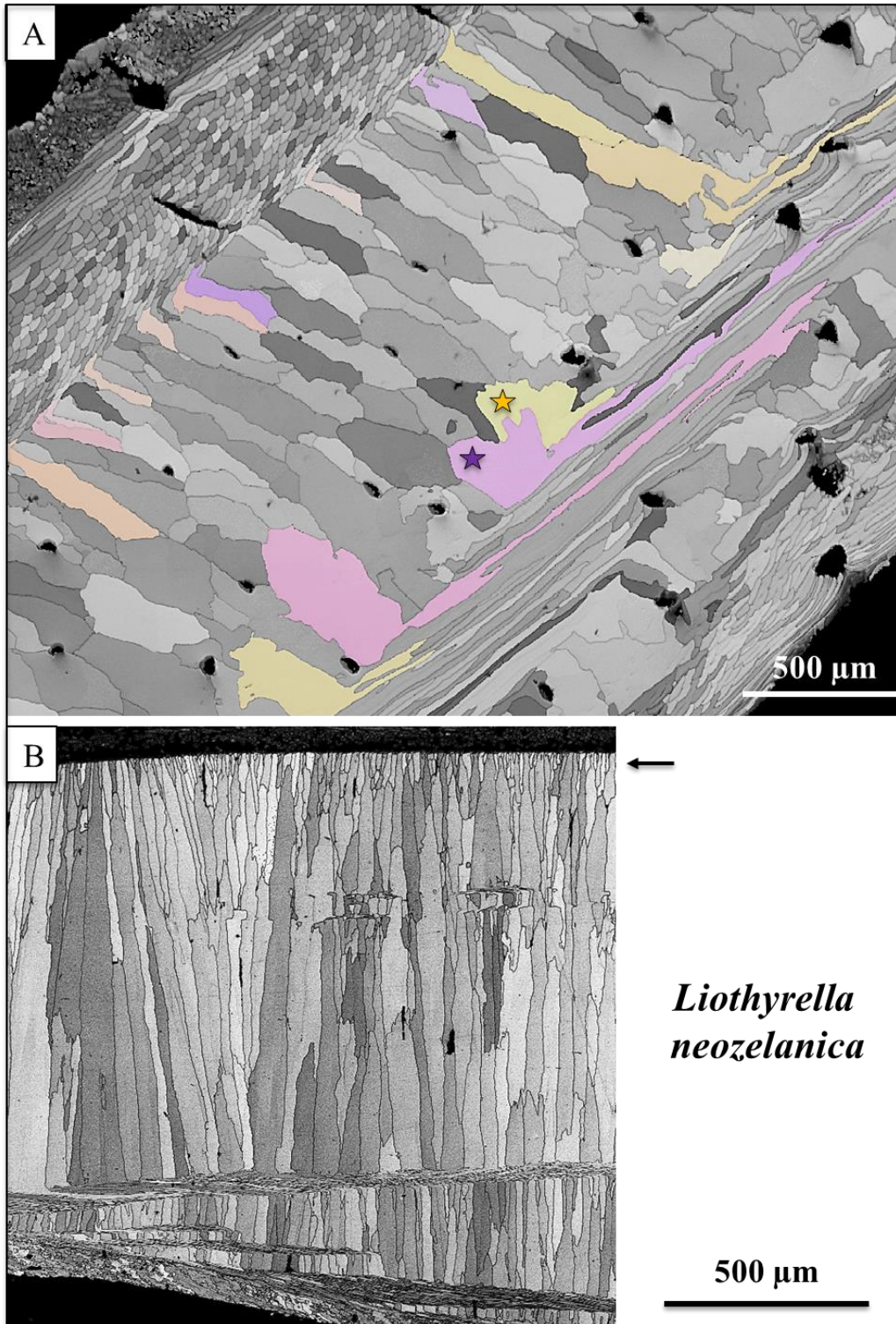


Figure S2.4.5. EBSD band contrast (grey) measurement images (A, B) of a cross-section through the shell of *L. neozelanica*. Figs. S2.4.5A, B show two different cuts through the shell for (i) a better visualization of column morphology and (ii) the change-over from the columnar to the fibrous microstructure. Columns have highly irregular morphologies and might interdigitate (e. g. the two columns marked with a yellow and magenta star). The cross-over from columns to fibers is smooth. As it is well visible in (B), columns form through competitive growth; see the first-formed small-sized columns (black arrow in (B)) that develop with increasing growth to large columnar units; for a more detailed description see Goetz et al. 2009, Schmahl et al. 2012. The color-code for A is given in Fig. S2.4.16.

Novocrania anomala

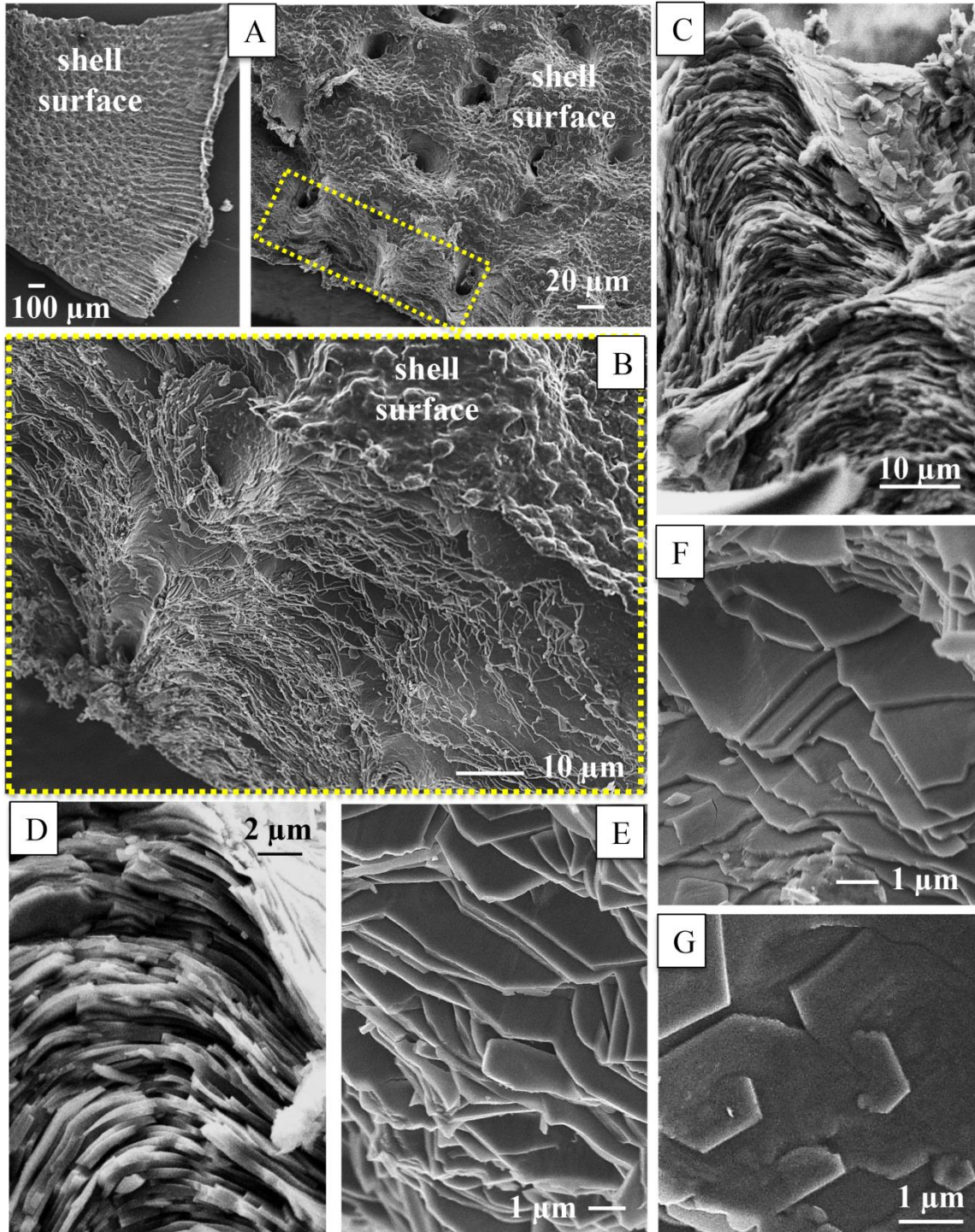


Figure S2.4.6. Sequence of calcite layers (C, D, E, F) in the shell of *N. anomala* (A, B) depicted with SEM images of fractured surfaces. The layers are often curved (C) and have uniform sizes; cross-sections of individual layers are 400 to 500 nm (E, F). Calcite crystals in these show spiral growth (G). Shell portion shown in (B) is indicated with a yellow, dashed rectangle in (A).

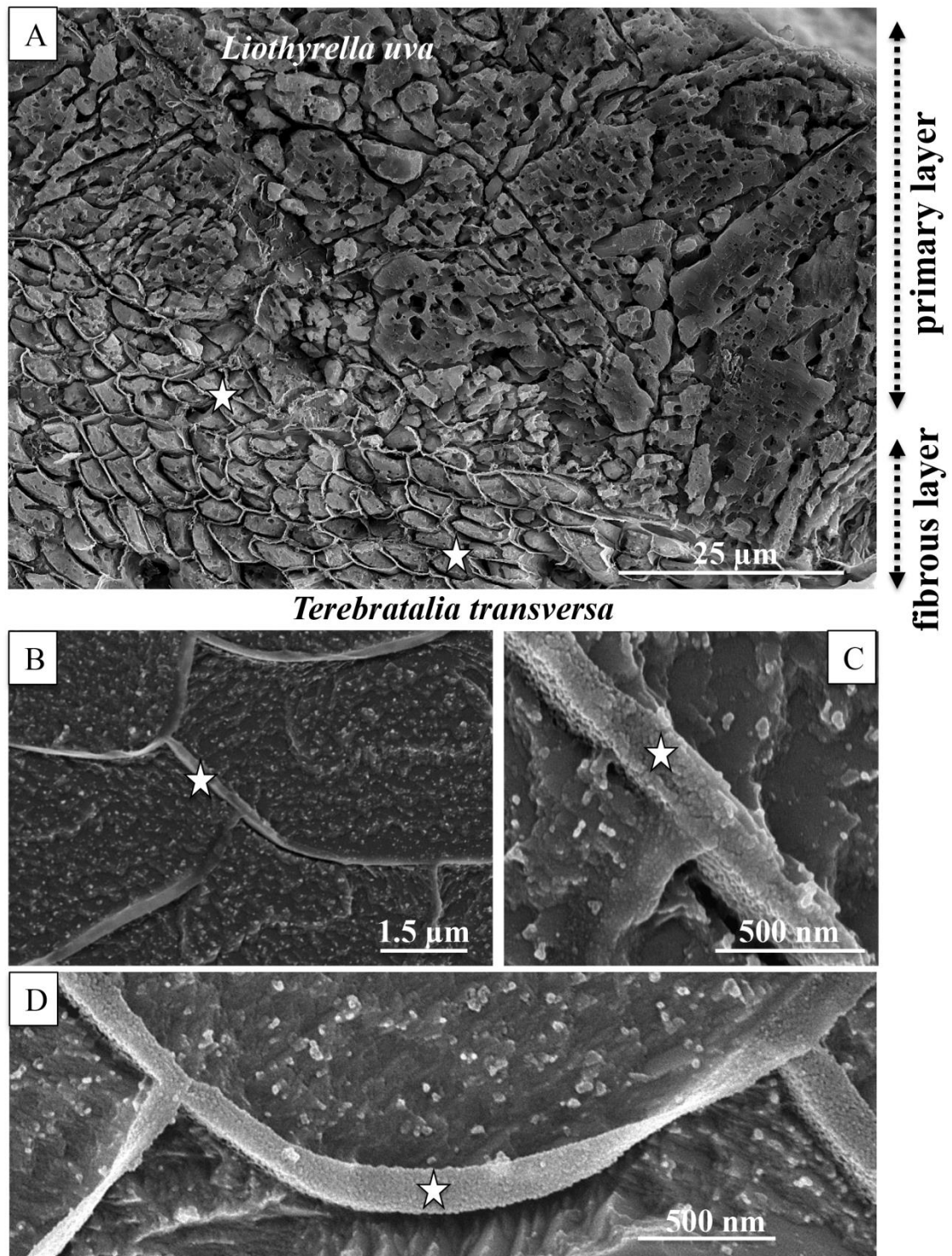


Figure S2.4.7. SEM images of microtome knife polished and etched shell surfaces of *L. uva* and *T. transversa*. Well visible is the absence of biopolyme matrices in the primary (A) and their marked presence in the fibrous shell layer, respectively (A, B).

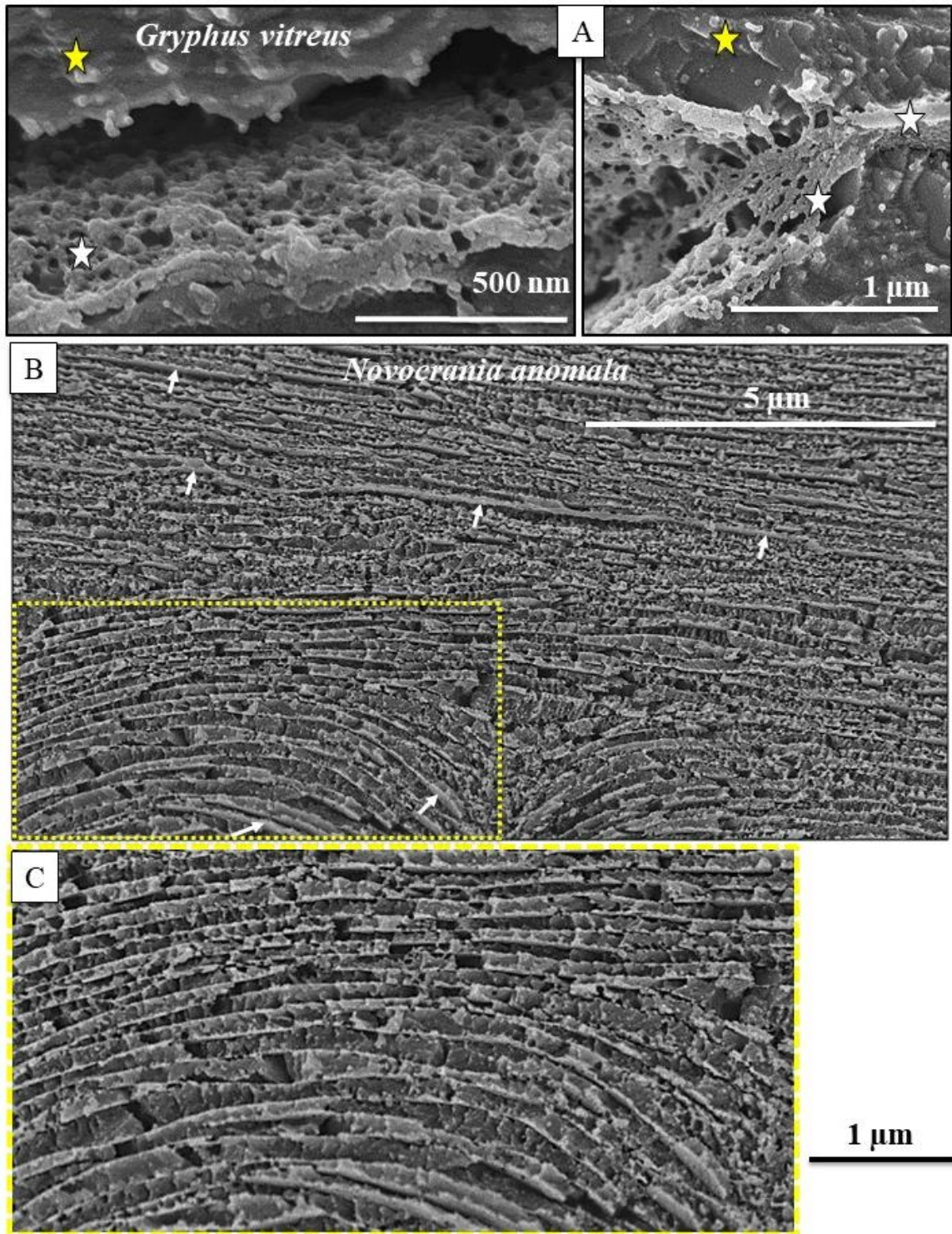


Figure S2.4.8. SEM images of microtome knife polished and etched shell surfaces of *G. vitreus* (A) and *N. anomala* (B). Biopolymer membranes (white star) between columns (yellow star) in the shell of *G. vitreus*. Sequences of calcite layers in *N. anomala* (B, C); note their bending (e.g. C). Neighboring layers are delineated by organic membranes (white arrows in B). Shell portion shown in (C) is indicated with a yellow, dashed rectangle in (B).

Pajaudina atlantica

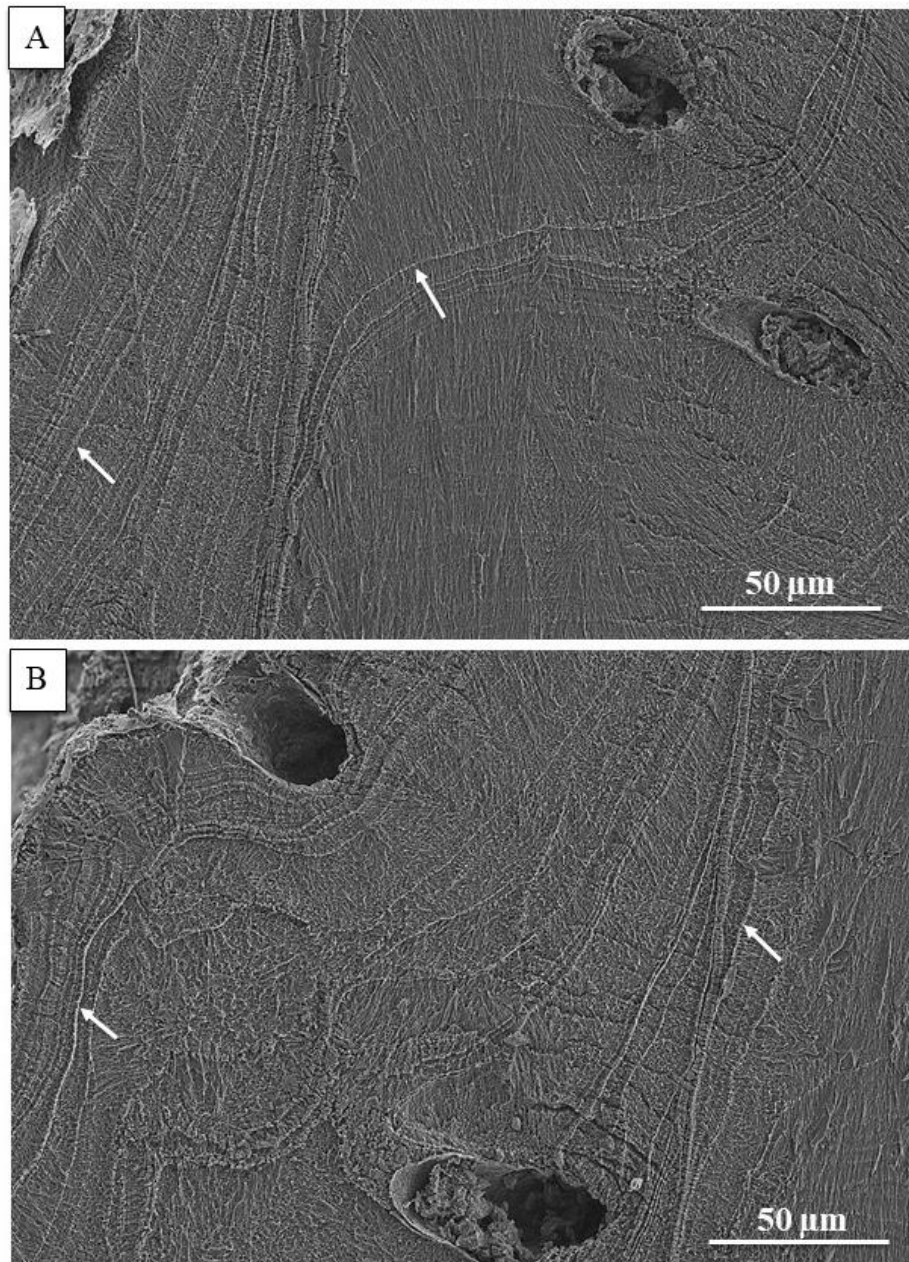


Figure S2.4.9. SEM images of microtome knife polished and etched shell surfaces of *P. atlantica*. Organic membranes are occluded within the shell (white arrows in A, B), however, their distribution is random.

Pajaudina atlantica

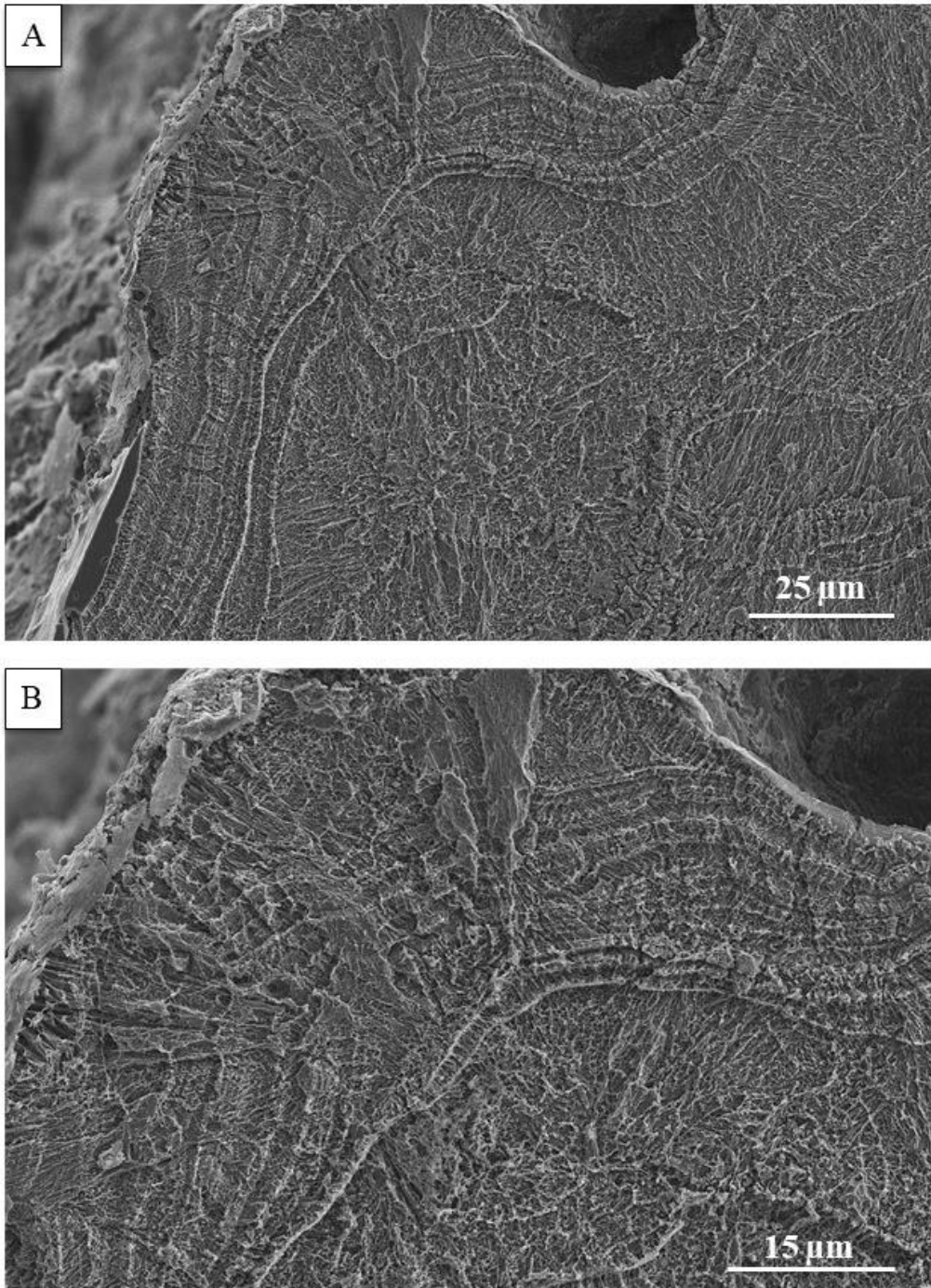


Figure S2.4.10. SEM images of microtome knife polished and etched shell surfaces of *P. atlantica* visualizing the distribution of organic membranes and biopolymer fibrous networks within the shell.

Pajaudina atlantica

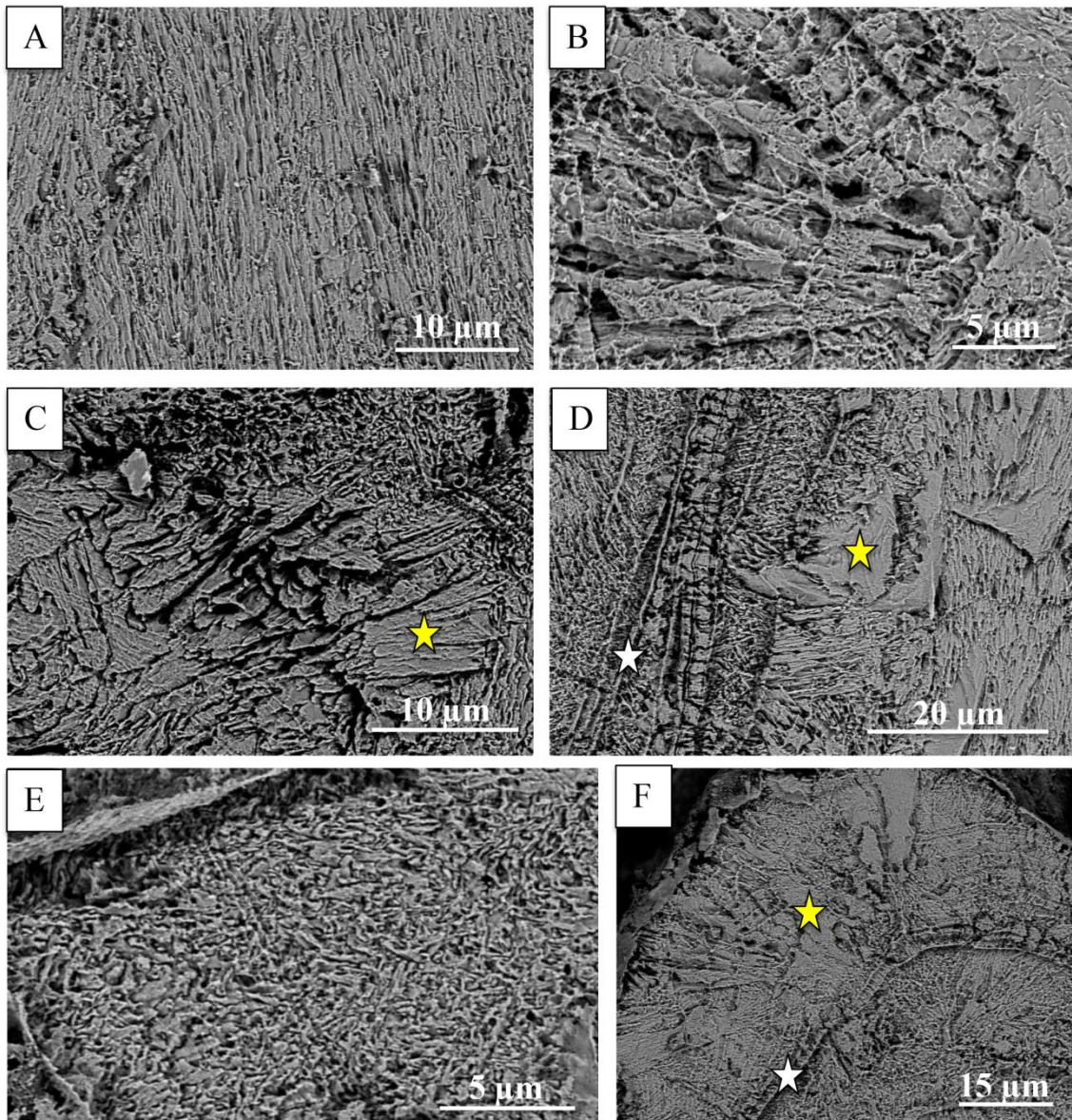


Figure S2.4.11. SEM images of microtome knife polished and etched shell surfaces of *P. atlantica* depicting variously sized and shaped mineral units within the shell. Yellow stars in C, D, F point to larger crystals; the white star in D draws the attention to an aggregation of organic membranes occluded within the shell.

Notosaria nigricans

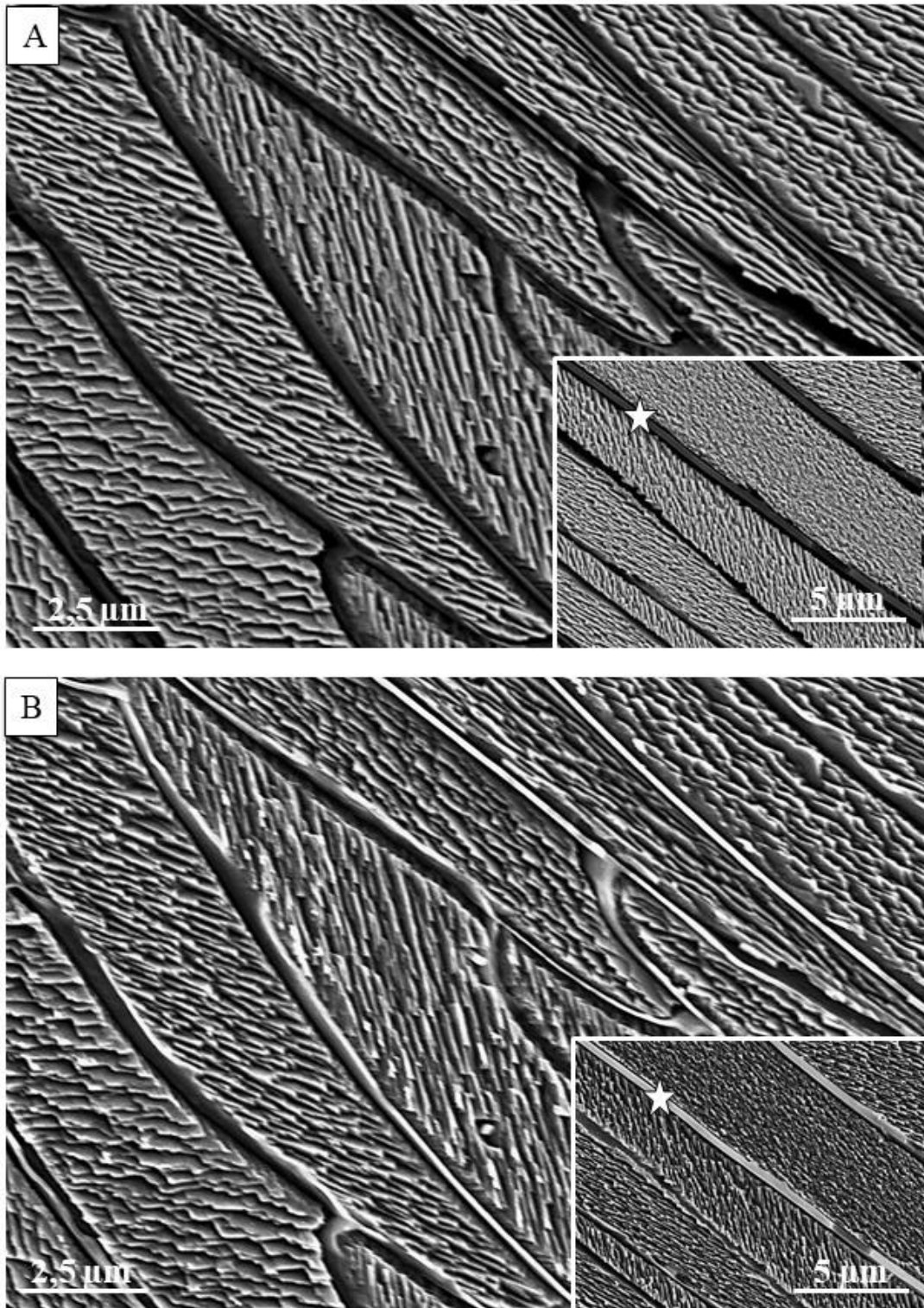
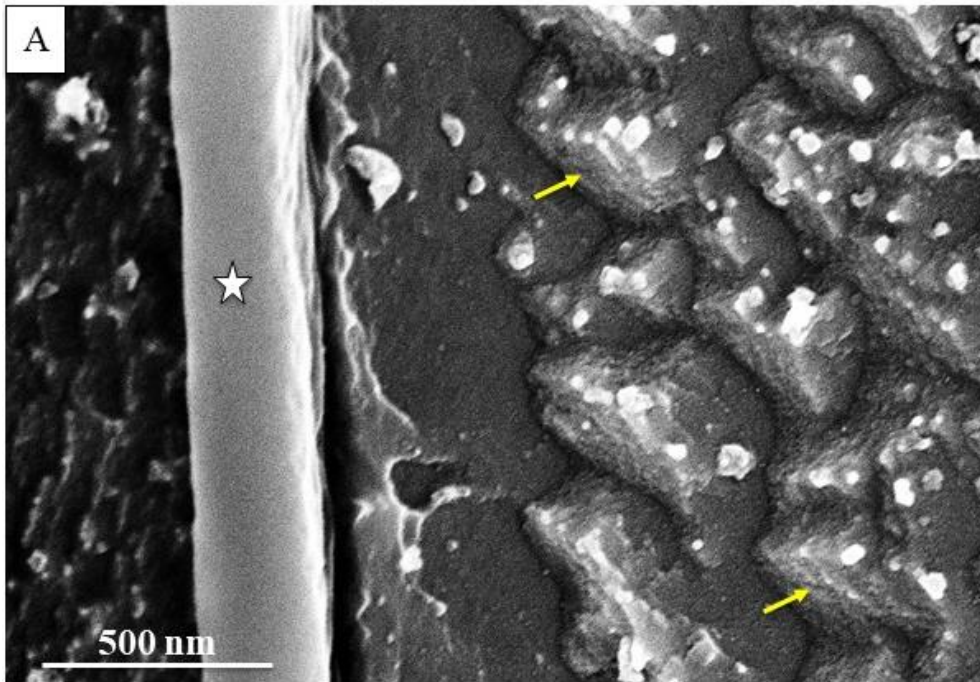


Figure S2.4.12. SEM images of microtome knife polished and etched surfaces of fibers in *N. nigricans*. Well visible is the layered structure of the fibers, the high co-alignment of individual layers within the fibers and the membrane at always the proximal surface of a fiber (white star in inserts in A, B).

Magellania venosa



Terebratalia transversa

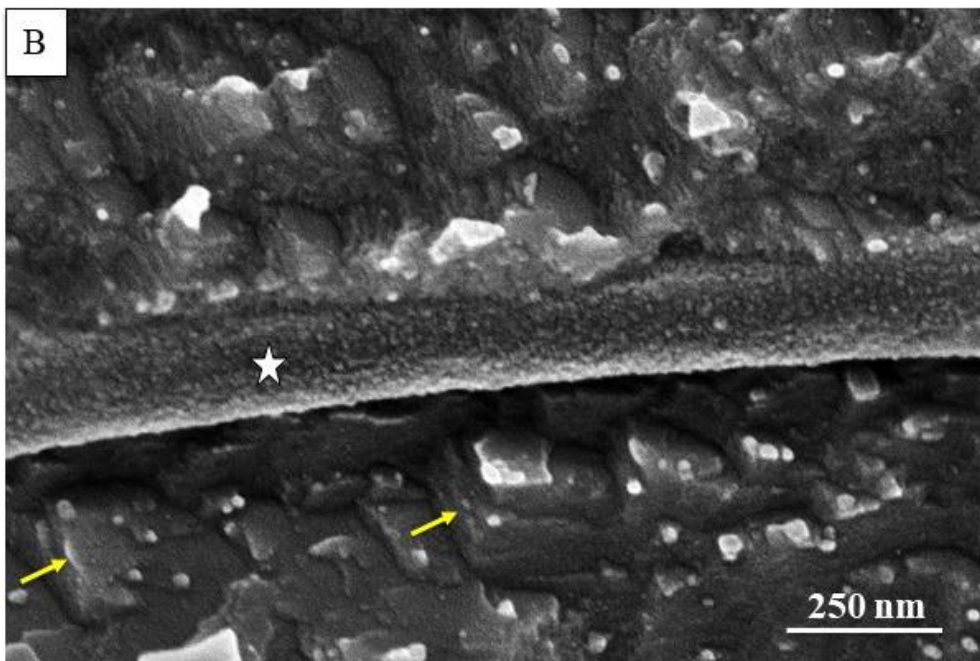


Figure S2.4.13. The rhombohedral shape (yellow arrow) of biocrystals in *M. venosa* and *T. transversa*. SEM images of microtome knife polished and etched shell surfaces. White stars point to the occluded biopolymer membrane.

Liothyrella neozelanica

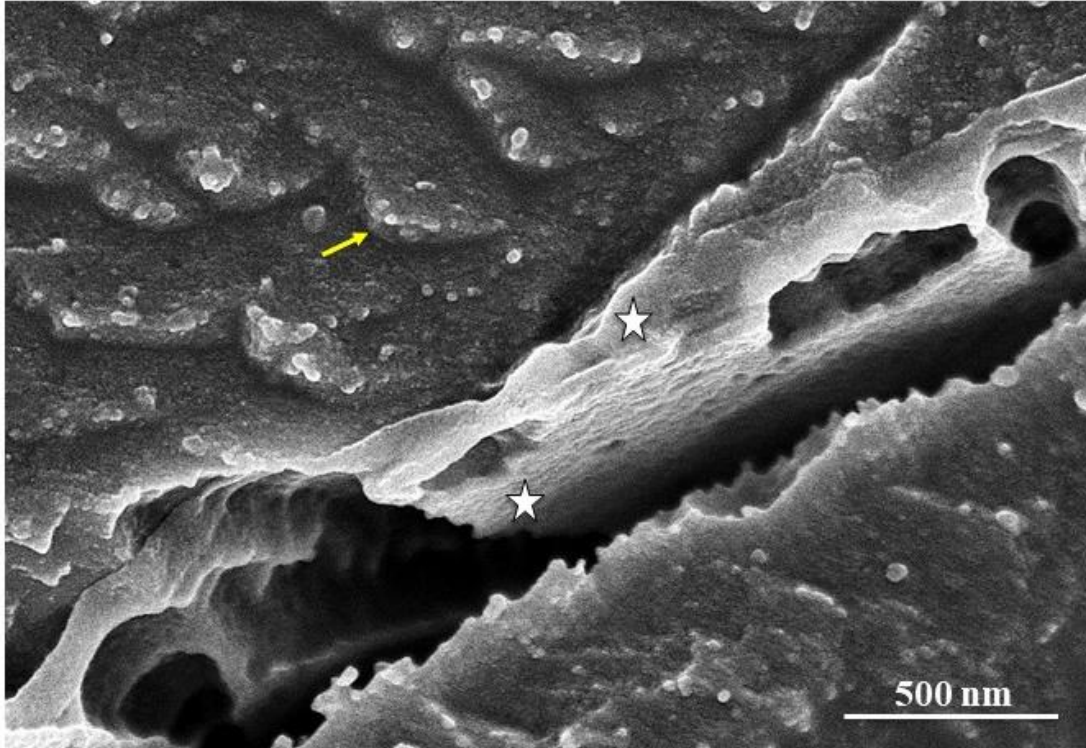


Figure S2.4.14. The rhombohedral shape (yellow arrow) of biocrystals in *L. neozelanica*. SEM images of microtome knife polished and etched shell surfaces. White stars point to the occluded biopolymer membrane.

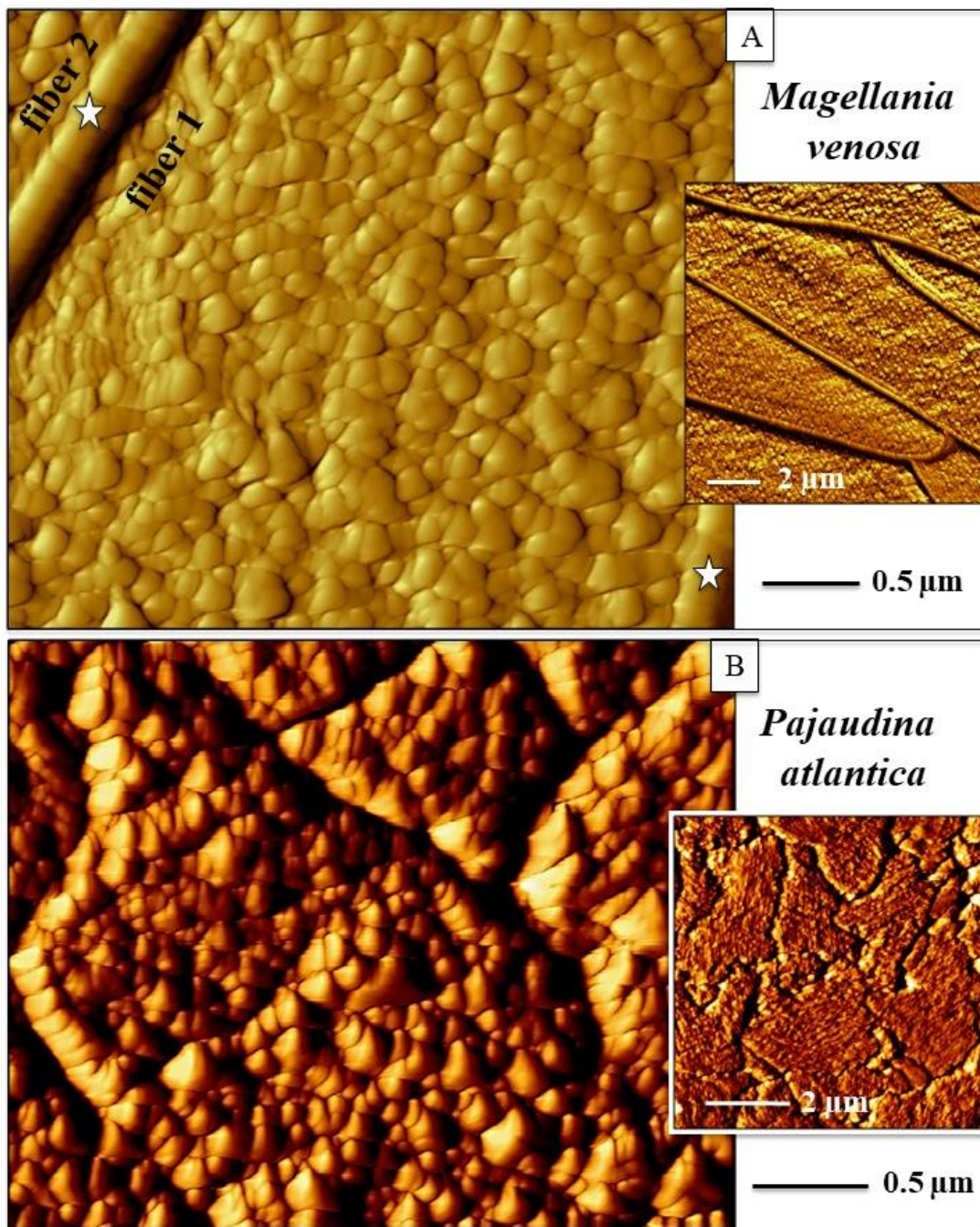
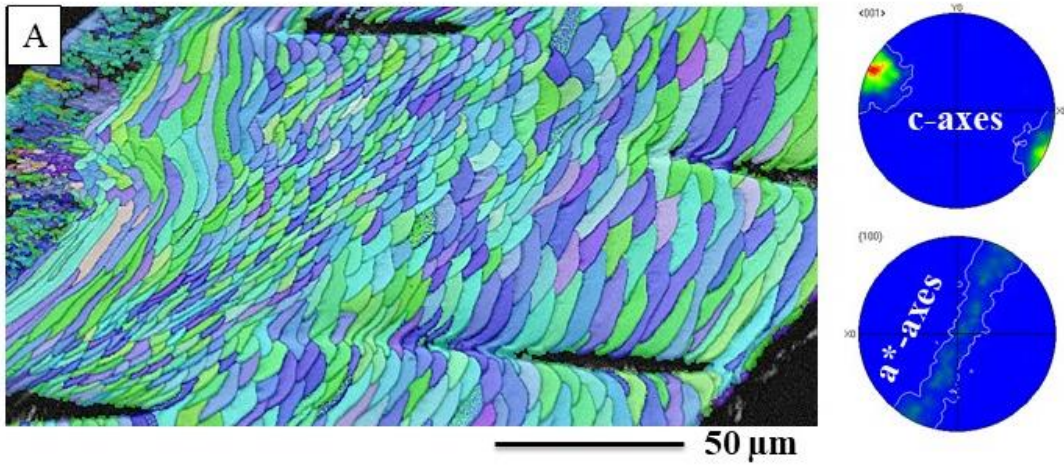


Figure S2.4.15. Vertical deflection AFM images of terebratulid fibers (A) and thecideide mineral units/crystals (B). White stars in (A) point to the presence of a membrane that delineates neighboring fibers. Note the absence of biopolymer membranes between mineral units in the thecideide shell (B). Even though biocrystal morphologies, sizes and the shell microstructure of the two brachiopod taxa differ significantly, the submicrometer internal structure of the biocrystals that comprise the shells is comparable and constitute of 200 to 400 nm sized crystallites.

Magellania venosa



Liothyrella neozelanica

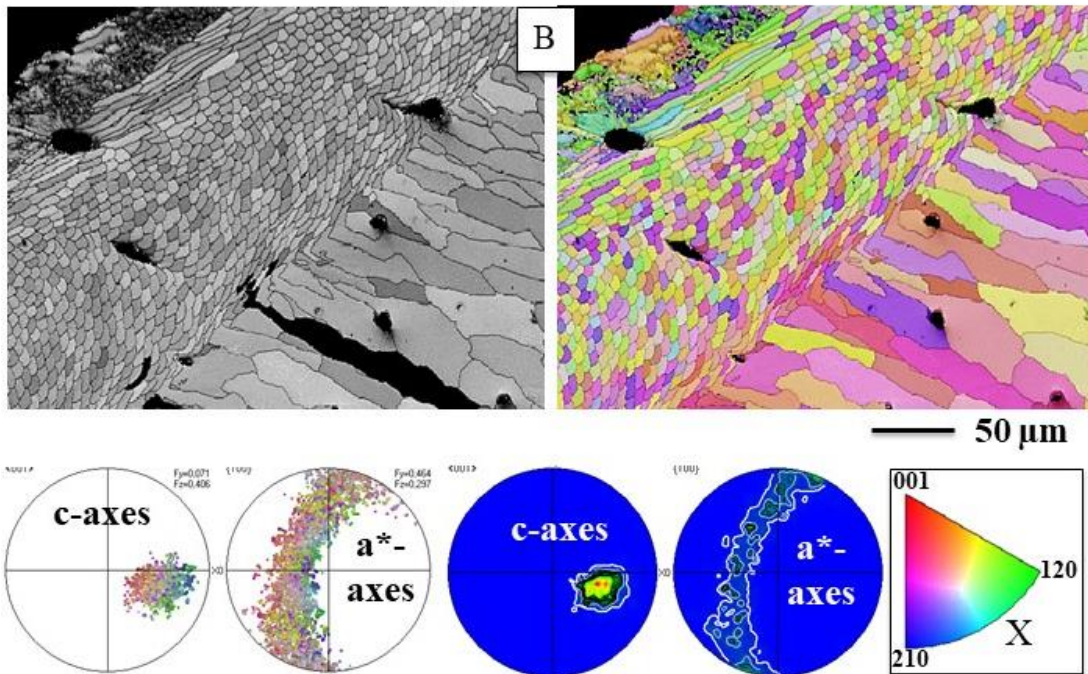


Figure S2.4.16. Microstructure and texture of primary, fibrous and columnar layers in *M. venosa* (A) and *L. neozelanica* (B). Both have an axial texture. The color-code for A is given in Fig. S2.4.17, for B in Fig. S2.4.16.

Pajaudina atlantica

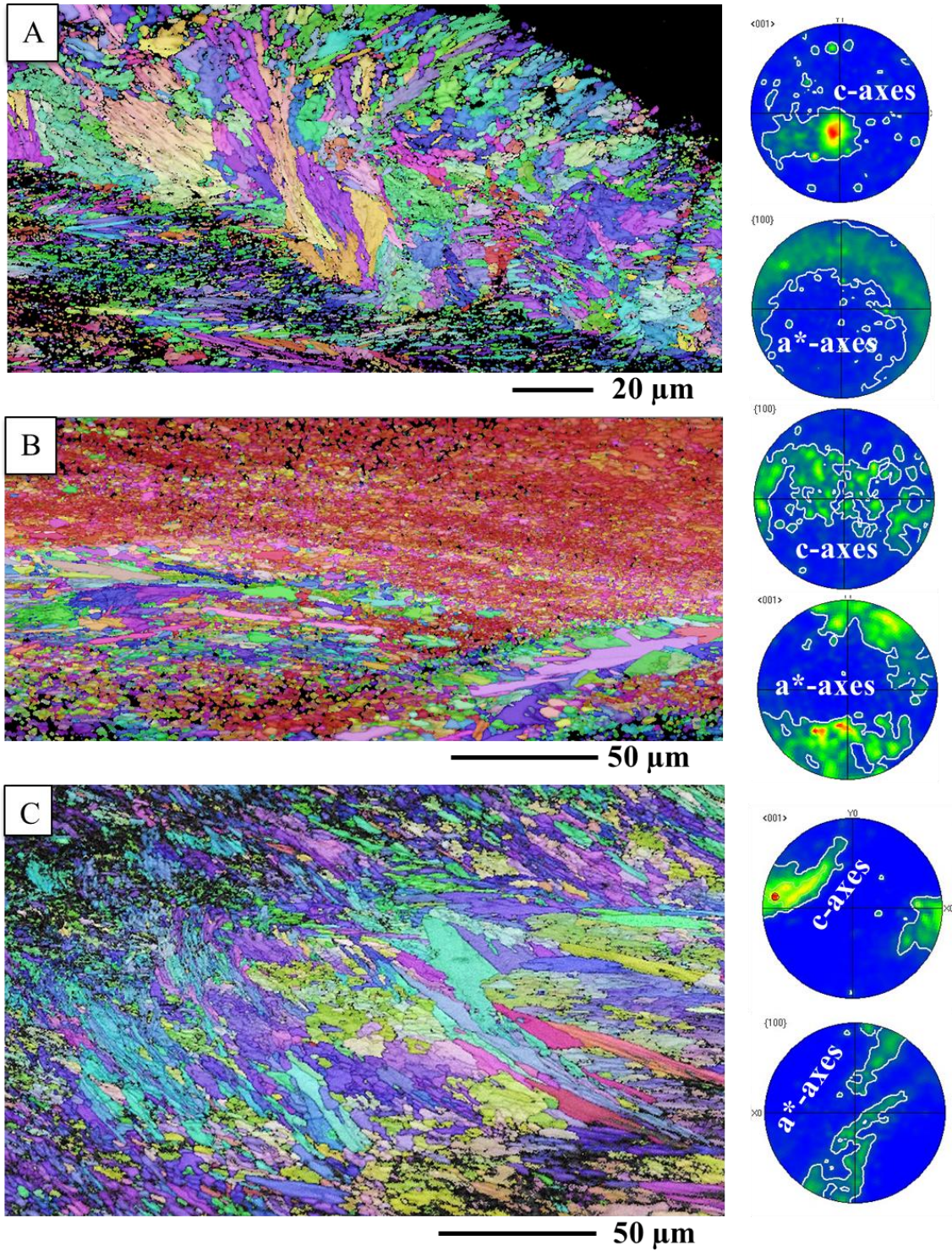


Figure S2.4.18. Microstructure and texture of the shell of the thecideid species *P. atlantica*. Well visible is the unstructured microstructure (EBSD maps) and the weak texture (the pole figures). The color-code for A and C is given in Fig. S2.4.17, for B in Fig. S2.4.16.

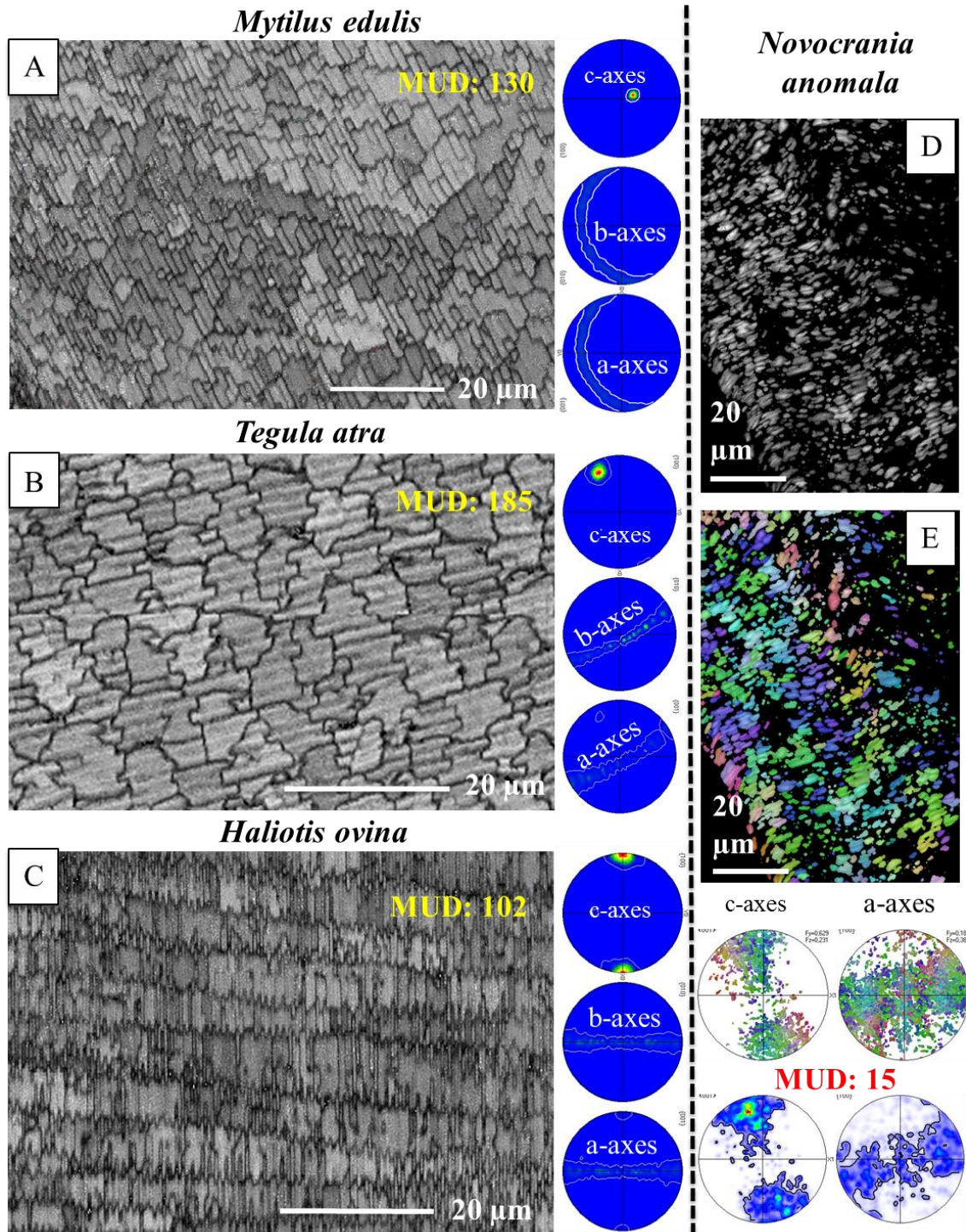


Figure S2.4.19. Comparison of microstructure and texture between bivalve, gastropod nacre and *N. anomala* shell microstructure and texture. A, B, C, D: EBSD band contrast images, E: EBSD calcite orientation map. *N. anomala* forms its shell of small tabular units, crystals (D). These are often compared to nacre tablets in bivalves and gastropods. Accordingly, the shell structure of *N. anomala* is addressed as a ‘semi-nacreous’ structure/microstructure (Engaland et al. 2007, Perez-Huerta et al. 2007). The comparison shown in the figure proves that, even though made of tablet-shape resembling crystals, the structure of *N. anomala* shells has nothing to do with nacre when based on microstructure, texture, strength of preferred crystallographic orientation (see the difference in MUD value). The color-code for E is given in Fig. S2.4.16.

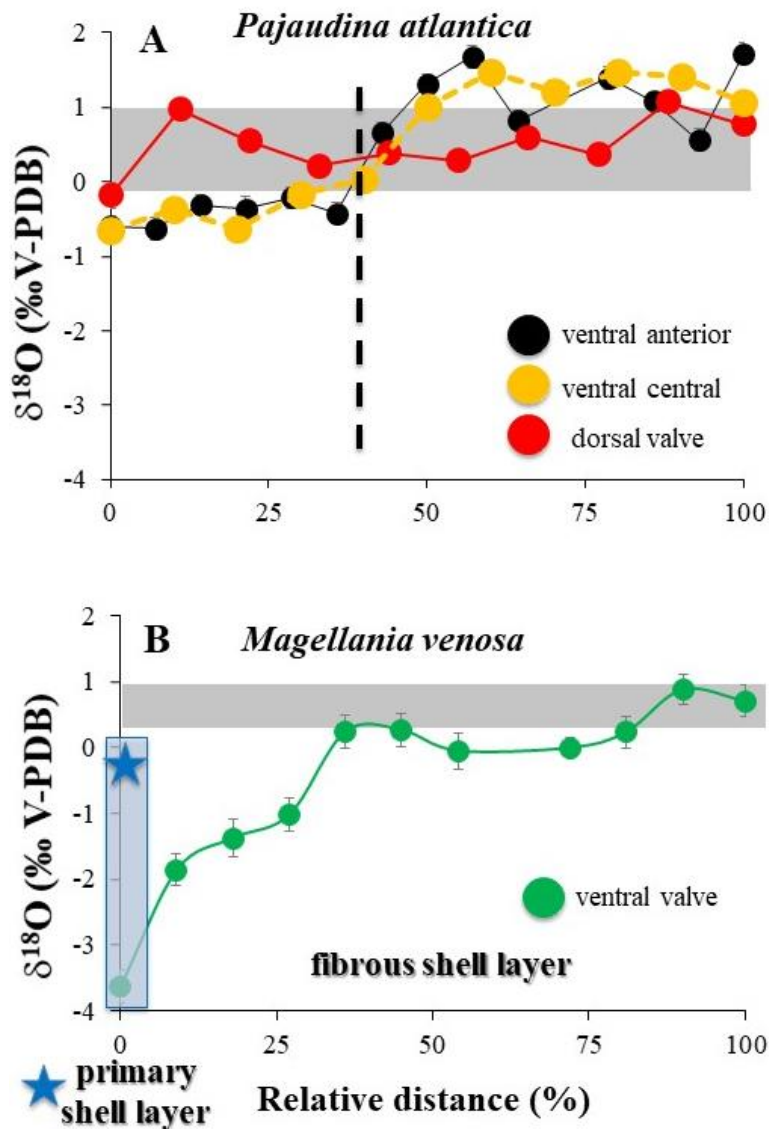


Figure S2.4.20. Oxygen isotope composition along cross-sections through the shell of *P. atlantica* and *M. venosa*. Error bars represent the standard deviation. The grey field in the figures indicates the region of $\delta^{18}\text{O}$ where inorganic calcite precipitates in equilibrium with seawater. The calculation of the latter is based on the equation given by Watkins et al. (2013), for the localities where the brachiopods were sampled from. The relative distance along the shell cross-section is calculated such that 0% corresponds to outermost, 100% to innermost layers, respectively. For further information see Milner Garcia 2018.

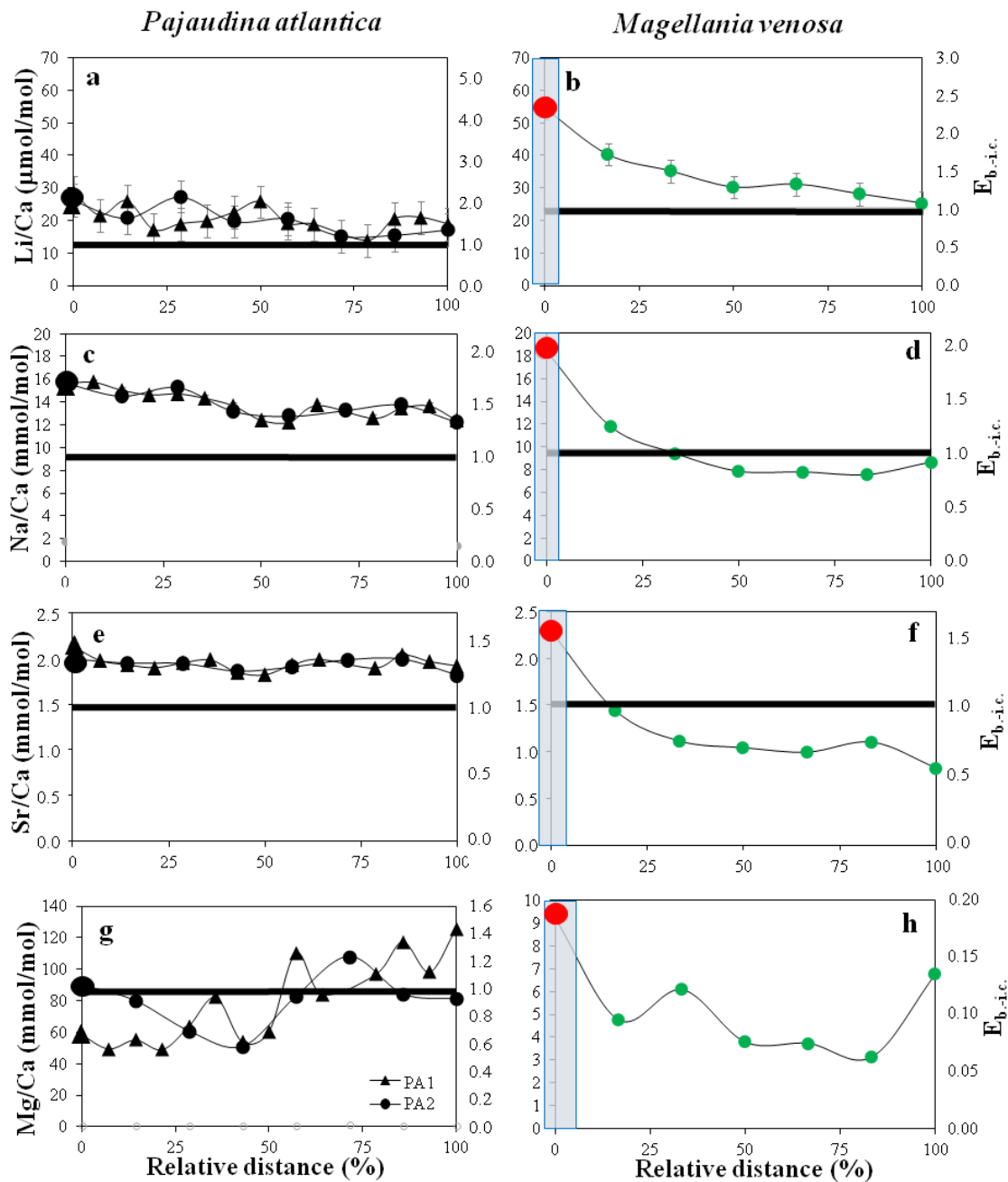


Figure S2.4.21. Li/Ca, Na/Ca, Mg/Ca and Sr/Ca variations along shell cross-sections comprising outermost and innermost shell portions of the ventral valve of *P. atlantica* and *M. venosa*, respectively. The black line in the diagrams marks the equilibrium value (see also Okumura and Kitano 1986; Oomori 1987; Marriott et al 2004; Gabitov and Watson 2006). Error bars represent the standard deviation. The relative distance along the shell cross-section is calculated such that 0% corresponds to the outermost and 100% to the innermost part of the shell, respectively. The blue rectangle indicates the extent of the primary layer in *M. venosa*. Further information is given in Milner Garcia 2018.

Chapter 3. Concluding Summary and Outlook

3.1. Concluding Summary

The research done for this thesis covers three main topics: (1) biomineralization processes for calcite nucleation and fibre formation of the fibrous layer of modern terebratulide brachiopods, (2) a detailed study of the evolution of thecideide microstructure, and (3) a comparison and review of modern brachiopod shell micro and nanostructure.

Chapter 2.1 – 2.2 summarizes the characterization of the mantle epithelium of *Magellania venosa*, a terebratulide brachiopod. We performed a highly detailed study of the different areas of the epithelium paying special attention to the outer mantle epithelium (OME), as the latter is in closest contact to the shell. This biological approach was done using TEM imaging of chemically fixed and HPF-FS samples, FE-SEM imaging, EBSD measurements and AFM imaging techniques.

Chapter 2.1 covers in higher detail the whole mantle epithelium of *Magellania venosa*, outer and inner mantle epithelial cells, under the primary and fibrous layer and inside the punctae in the commissure and central shell regions. We performed a qualitative study describing the diverse structures, cell connections and organelles we observed. This was done using large TEM panorama images containing up to 350 images of 8000 magnification. With these images we were able to have an overview of the general structure of the mantle epithelium and at the same time we could describe nanostructures. The goal was to have a better understanding of the possible biomineralization processes, mineral transport and shell secretion in brachiopod shells and the role of the outer mantle epithelium in contact to the shell. With this, the study pointed out the possible role of the OME organelles, the description of the extracellular space, the relations between the outer mantle epithelial cells and its spatial relation to the growing shell.

The results show that the OME ultrastructure at the commissure differs significantly from that at central shell regions. While at central shell regions the OME is single cell layered, it consists of several cell layers at the commissure. Regarding the morphology of the cells at the commissure, in longitudinal sections, they form long, thin lateral extensions parallel to the shell. In cross section they are roundish and they become larger the closer they are to the connective tissue. At central shell regions, OME cells are considerably thinner in comparison to cells at the commissure. Especially longitudinal sections at forming calcite fibre cells can be only a few tens of nm thick. The organelle quantitative counting shows no statistical significance between commissure and the central shell regions when they are normalized to the same volume. Only the amount of mitochondria, endo-lysosomes and vesicles is significantly higher at the commissure. There is no evidence of any specific organelle related directly to shell secretion.

We observed that frequently more than one cell contributes to the formation of a calcite fibre at the same time in both commissure and central shell regions; therefore, fibre secretion, growth and shape generation requires communication of adjacent OME cells. In addition, the cells interdigitate with each other and there is a high abundance of gap junctions between cells, also supporting the necessary communication and tight

cooperation of neighbouring OME cells for the coordinated secretion of organic membrane and mineral. In addition, TEM and SEM images on chemically fixed and HPF-FS samples show that the extracellular space is either extremely narrow (few nanometres wide) or even non-existent under fibres that are under secretion. This indicates that fibre formation in *Magellania venosa* is under tight cellular control. Furthermore, the space is so small that no organelles can fit into it.

All this new data lead us to support a mineral transport mechanism in young/juvenile *Magellania venosa*, where cells secrete calcium and hydrogen carbonate via ion transport mechanisms (Fig. 3.1) rather than mineral transport via organelles (such as vesicles).

In chapter 2.2 the study focused on the OME under the fibrous layer in the central shell region of brachiopod shells and on fibre shape formation. The biological information was supported by the FE-SEM, EBSD and AFM results of the hard tissue. Fibre and extracellular organic matrix membranes secretion as well as fibre shape formation in the modern brachiopod *Magellania venosa* is a dynamic process induced and coordinated by the OME. We observed in AFM that the fibres are not individually and completely sheathed by separate organic membranes. The TEM results showed that the extracellular organic membrane is secreted by the OME only onto the proximal, convex surface of a fibre once the fibre is finished. In addition, we distinguished those areas where there is active secretion of the fibres and those where there is no secretion and the fibres are finished. The secretion of calcite by epithelial cells occurs only at sites where the extracellular organic membrane at the proximal, convex surface of the fibre is absent. Once the extracellular membrane at the base of fibres is secreted, the outer mantle epithelium cells are attached to it by apical hemidesmosomes. This keeps the OME close to the shell and stabilizes those regions that are still in active secretion. Calcite secretion is suspended where the proximal organic membrane of the fibre is formed. The secretion continues in locations where OME cells reabsorbed the hemidesmosomes and detach from the extracellular membrane of a previously finished fibre. We developed a model that shows the brachiopod fibre formation as a cyclic sequence of processes occurring at the apical OME cell membrane. The model is shown in Figure 11 of chapter 2.2. and Figures 8 and 9 of chapter 2.1 of this thesis.

By studying the relations of the individual fibres of the fibrous layer of rhynchonelliform brachiopod shells, we concluded that it has an overall plywood-like organization. The arrangement of the basic mineral units, the fibres, can be compared to an ‘anvil-type’ arrangement of calcite fibres. It also resembles the “brick wall” arrangement of aragonite tablets in bivalve nacre, but rather than being simply rectangular “bricks”, the mineral units have the characteristic cross section generated by the simultaneous growth of parallel brachiopod fibres.

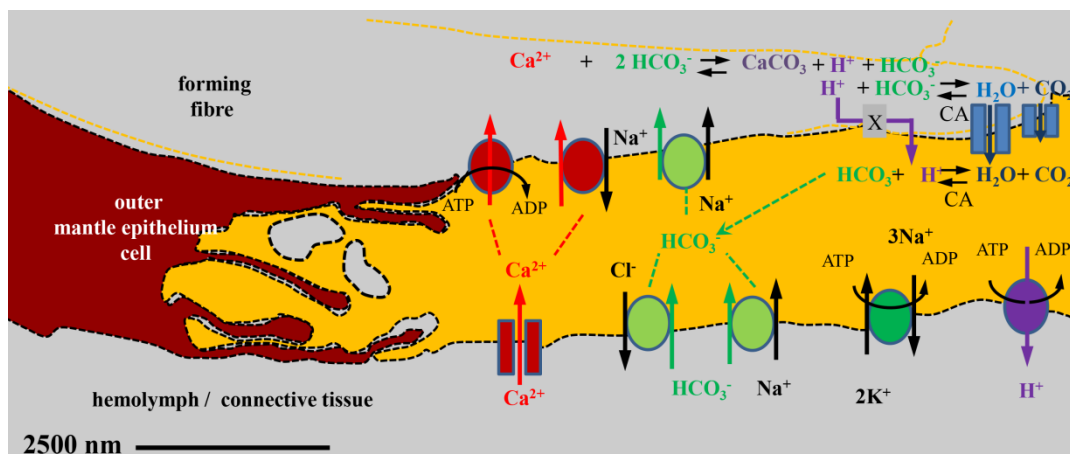


Figure 3.1. Conceptual model for calcite secretion in the shell of modern terebratulid brachiopods based on Fig. 2.1.13. See detailed information in Chapter 2.1.

The detailed description of the heterogranular microstructure of thecideide brachiopods, and its evolution from the late Triassic up to today, is described in the chapters 2.3 – 2.4.

Chapter 2.3 covers the study of the shell microstructure of thecideide specimens from the Later Triassic, when they first appear, to present times, with the objective of understanding the appearance and evolution of the “heterogranular microstructure”. For this, we analyzed with FE-SEM imaging and EBSD the distribution of the crystal units and all their different morphologies and the general texture of the shells. The results show for Triassic and Jurassic specimens the presence of fibres but with the first appearance of large crystal units within the shell. Upper Jurassic species represent transitional forms composed by a combination of stacks of acicles on external shell portions and of a remnant of the fibrous layer next to the soft tissue of the animal. The presence of acicles crystals will prevail up to modern species. The fibres disappear subsequently from the Cretaceous to modern times and the acicular, granular and polygonal crystals, embedded in a matrix of nanocrystallites, prevailed from the Cretaceous to modern times developing minor changes. In addition there is a decrease in the regularity of biocrystal shape, mineral unit size, and the strength of calcite co-orientation, represented by the MUD values, from the Late Triassic to Recent species.

The change in microstructure and texture was interpreted as an ecological strategy to exploit different niches, the attachment to hard substrates.

The chapter 2.4 review the shell microstructures of the modern brachiopods with Ca-carbonated shell. The review contained a compilation of calcite and organic matrix assembly on nano-, micro- and micrometer scale for 14 brachiopod species. The conclusions are based on AFM, EBSD, STEM, and FE-SEM measurements and imaging of polished and etched samples where the organics were fixed.

Chapter 2.4 showed the differences in composite hard tissue organization for taxa with different lifestyles, highlighting, thecideide shell characteristics. We compared the shell texture between species that live attached by a pedicle and those that live cemented with a valve to the substrate/sediment. For Thecideida, we contrasted their shell structure with the primary shell-layer of rhynchonellide and terebratulide taxa. Thecideide shell microstructure is defined as a stand-alone microstructure, specific for

this order and non comparable with the primary layer. This conclusion is also support with preliminary geochemical data. An important part of this review chapter is the composite nature and hierarchical architecture of brachiopod shells (we discussed up to six levels of hierarchy for the entire shell) as well as the function of the shell as a biomaterial.

We analyzed, for all four orders, the relation between each type of biocrystal (dendrites, fibers, columns, platelets, and, polygonal crystals) and the organic matrices within the shell. It is illustrated, in particular, the case of the columnar layer. Column- and prism-shaped biocrystals form through crystal competition and are the closest analogs to non-biologic carbonate. We furthermore visualize the nanostructure of calcite assembly in rhynchonellide fibers and discussed, for representatives of Rhynchonelliformea, the feasibility to use the shells as archives for proxies for paleoenvironment reconstruction. In addition, we showed the nanometer scale structure of modern rhynchonellide and terebratulide fibers as a reference for the assessment of overprint of fossil equivalents.

The review covers, shown by representatives of extant calcite secreting brachiopod orders, the diversity of calcite crystal assembly necessary for shell formation and summarizes the current knowledge on brachiopod shell structure, microstructure and, texture.

3.2. Outlook

The different processes used for carbonate precipitation of biominerals are complex and many questions are unanswered. A biological approach investigating the mantle epithelium ultrastructure of brachiopods or that of other animals with a carbonate exoskeleton helps to understand some of these processes. Although we provide some answers, this dissertation has opened new research perspectives.

1. A complete understanding of the relation between the outer mantle epithelium and the brachiopod shell.

Understanding the Outer Mantle Epithelium (OME) and its relation with extrapallial space is essential to comprehend the calcium carbonate precipitation and the pathways for Ca^+ , HCO_3^- and H^+ transport. At the same time it gives information for understanding (1) morphologies of the individual calcite crystal units of the shell and (2) the distribution of the organics in the shell. Our research is a small part of the huge panorama of the biominerals and biomineralization processes.

Investigation of the cell/mineral contact was not done for many organisms. The references are sometimes old and some interpretations are vague or are based on general hypotheses due to limitation of techniques that were available at that moment as well as the complicated sample preparation. Our work was done only for the primary and fibrous layer of the brachiopod shell and in 2D. Future work should be done on the columnar layer as well and in 3D. The analytical techniques should include FE-SEM, TEM imaging of FIB and HPF-FS samples. The sample preparation as well as the qualitative description we performed and its application for the interpretation of shell secretion may serve as a guide for understanding OME and shell secretion in other organisms. Presumably, differences in the OME below the different microstructures may be observed. The differences will lead to more precise defined coherent models of ion transport in brachiopod shells. It is possible that both types of material transfer, ion as well as vesicle transport, can be expected for the secretion of brachiopod shells, depending on the different microstructures.

2. Investigating the dimension of extrapallial space in other invertebrate groups such as molluscs

The extrapalleal space is the space between the mineralized shell and the outer mantle epithelium. The dimensions of the extrapallial space defines which pathways the Ca^+ and HCO_3^- ions can follow and defines the available space for biomineralization of the shell. In terms of sample preparation, the attachment of OME tonofilaments to the shell, allows hard and soft tissue to stay in contact. This condition makes brachiopods very useful animals to understand some biomineralization processes. This type of research becomes more complicated in other organisms such as molluscs, as here the mantle detaches easily from the shell. In addition, we observe too that techniques such as High Pressure Frozen – Freeze Substituted and embedding with methacrylate are good allies to preserve areas where the tonofilaments are not attached to the hard tissue.

Sample preparation is complicated and the current technical approach that one can use is limited. However, research in this direction can be applied to different

invertebrate groups, as bivalves or gastropods, may contribute to decipher (1) the way organics are organized during shell biomineralization and (2) detailed processes of biomineralization.

3. Investigation of the biological function of the punctae

Punctae are specific features of some brachiopod shells and their possible role in shell secretion or in the life of the animal is still under debate. They are complicated structures that form at the very commissure of the animal, in the outermost part of the OME. They cross the shell thickness connecting the mantle epithelium and the periostracum. We presented 2D qualitative and quantitative analysis of these structures in our work. Studies on the relation between the mantle and the periostracum, as well as 3D analysis of the organelles, may be very useful to understand the role of punctae in brachiopod shells. The functions could be related with the repair of external damages on the shell or with the expulsion of dead cells or organelles through the periostracum (as many late stage lysosomes were observed at the upper part of punctae in this study).

4. Distribution of organic matrices within the shell

The weight percent of organics in the shell is very small but plays a very important role in the formation of the biological mineral units. Many studies were done on the different proteins within brachiopod shells as the protocols for protein identification are well known. In addition, during the last decade the physical distribution of the mayor organic matrices, along with nanometre-fibrils, is starting to be understood. At the same time it is known that not all the observed organics are proteins. Future work should be carried out distinguish the different biopolymers in the shell and the possible role and presence of chitin within brachiopod shells.

5. Using EBSD as a tool to track microstructure evolution through the geological time.

We see that EBSD is a useful technique to track microstructures through geological time. Using it, we can understand the formation and appearance of the individual crystallites and track textures and morphologies in structural materials through geologic time. Combining EBSD and isotopic and elemental analysis with the use of modern samples as references, we can understand the correlation between microstructures and water conditions. Studies in this direction may lead to interpret the results in terms of how animals print the changes on water conditions into their shell microstructures. This new perspective of approaching the shell microstructure can be applied to well-studied groups of animals such as bivalves and gastropods. Results in this direction will help to understand the effect that the seawater composition as well as the temperature have on the precipitation of biomineral crystallites. Mimicking some conditions with cultured animals and in laboratory can be another way of moving towards this field of research. The results can add information to interpret more accurately the geological record and extinctions.

6. Relation between the different microstructures or layers in the brachiopod shell.

Modern brachiopod shells are composed by layers with different properties depending on their microstructures and their organic content. How the animal changes the type of microstructure at secretion and how the transitions between the different layers are, are questions that still remain to be understood. We know how the outer mantle epithelium is under the primary and the fibrous layer and we understand better the crystallographic transition between these two layers. For the biological studies, the main difficulty is reaching the right moment to prepare the sample so that the transition can be well observed. The same problem appears for sample preparation for EBSD and FE-SEM. Our hypothesis is that, studying larvae as well as adult animals and applying high resolution techniques, new research in this direction will help to understand why the animals secrete “suddenly” a different concentration of calcium and organic material that originates in new crystal morphologies. The studies presented in this dissertation offered some ways to deal with this line of research and the approaches used can be applied not only to brachiopods but also to the hard tissue of other invertebrate groups.

As it is summarized above, the study of the mantle epithelium, the microstructures, as well as its composition and the formation of their crystal units bring important light into the biomineralization processes for Ca^+ and HCO_3^- transport.

This dissertation covers only a small range of questions with focus on brachiopods. The field of biominerals is wide and an infinite number of questions remain unanswered. The studies in this thesis bring some new ways and lights to approach biomineralization processes and to understand microstructures in and of brachiopods. The knowledge gained with this study is expected to be applicable to other organisms such as molluscs and gastropods, as well.

Bibliography

- Addadi, L., Raz, S., Weiner, S., 2003. Taking advantage of disorder: amorphous calcium carbonate and its roles in biomineralization. *Advanced Materials* 15, 959-970.
- Ahearn, G.A., Mandal, P.K., Mandal, A., 2004. Calcium regulation in crustaceans during the molt cycle: a review and update. *Comparative Biochemistry and Physiology* 137, 247-257.
- Aizenberg, B.J., Lambert, G., Addadi, L., Weiner, S., 1996. Stabilization of Amorphous Calcium Carbonate by Specialized Macromolecules in Biological and Synthetic Precipitates. *Advanced Materials* 8, 222-226.
- Al-Aasm, I.S., Veizer, J.J., 1982. Chemical stabilization of low-magnesium calcite: an example of brachiopods. *Journal of Sedimentary Petrology* 52, 1101-1109.
- Allemand, D., Ferrier-pagès, C., Furla, P., Houlbrèque, F., Darwin, C., 2004. Biomineralisation in reef-building corals: from molecular mechanisms to environmental control. *Comptes Rendus Palevol* 3, 453-467.
- Angiolini, L., Jadoul, F., Leng, M.J., Stephenson, M.H., Rushton, J., Chenery, S., Crippa, G., 2009. How cold were the Early Permian glacial tropics? Testing sea-surface temperature using the oxygen isotope composition of rigorously screened brachiopod shells. *Journal of the Geological Society of London* 166, 933-945.
- Auclair, A.C., Joachimski, M.M., Lécuyer, C., 2003. Deciphering kinetic, metabolic, and environmental controls on stable isotope fractionations between seawater and the shell of *Terebratalia transversa* (Brachiopoda). *Chemical Geology* 202, 59-78.
- Audino, J.A., Marian, J.E.A.R., Wanninger, A., Lopes, S.G.B.C., 2015. Mantle margin morphogenesis in *Nodipecten nodosus* (Mollusca: Bivalvia): new insights into the development and the roles of bivalve pallial folds. *BMC Developmental Biology* 15, 1-22
- Backhaus, E., 1959. Monographie der cretacischen Thecideidae (Brach). *Mitteilungen aus dem Geologischen Staatsinstitut in Hamburg* 28, 5-90
- Bajnai, D., Fiebig, J., Tomašových, A., Milner Garcia, S., Rollion-Bard, C., Raddatz, J., Löffler, N., Primo-Ramos, C., Brand, U., 2018. Assessing kinetic fractionation in brachiopod calcite using clumped isotopes. *Scientific Reports* 8, 533.
- Baker, P.G., 1990. The classification, origin and phylogeny of thecideidine brachiopods. *Palaeontology* 33, 175-91.
- Baker, P.G., 2006. Thecideida. In Kaesler, R.L. (ed.): *Treatise on Invertebrate Paleontology Part H. Brachiopoda 5 (revised)*, Geological Society of America, Boulder, and University of Kansas Press, Lawrence, Kansas, pp. 1938-1943.
- Baker, P.G., Laurie, K., 1978. Revision of Aptian thecideidine brachiopods of the Faringdon Sponge Gravels. *Palaeontology* 21, 555-570.

- Baker, P.G., Logan, A., 2011: Support from early juvenile Jurassic, Cretaceous and Holocene thecideoid species for a postulated common early ontogenetic development pattern in thecideoid brachiopods. *Palaeontology* 54, 111-131.
- Barthelat, F., Mirkhalaf, M., 2013. The quest for stiff, strong and tough hybrid materials : an exhaustive exploration. *Journal of the Royal Society Interface* 10, 20130711.
- Bates, N.R., Brand, U., 1991. Environmental and physiological influences on isotopic and elemental compositions of brachiopod shell calcite: Implications for the isotopic evolution of Paleozoic oceans. *Chemical Geology* 94, 67-78.
- Baumgarten, S., Laudien, J., Jantzen, C., Häussermann, V., 2014. Population structure, growth and production of a modern brachiopod from the Chilen fjord region. *Marine Ecology* 35, 401-413.
- Beck, W.C., Grossman, E.L., Morse, J.W., 2005. Experimental studies of oxygen isotope fractionation in the carbonic acid system at 15, 25, and 40 °C. *Geochimica et Cosmochimica Acta* 69, 3493-3503.
- Beniash, E., Aizenberg, J., Addadi, L., Weiner, S., 1997. Amorphous calcium carbonate transforms into calcite during sea urchin larval spicule growth. *Proceedings of the Royal Society of London B* 264, 461-465.
- Beniash, E., Addadi, L., Weiner, S., 1999. Cellular control over spicule formation in sea urchin embryos a structural approach. *Journal of Structural Biology* 125, 50-62.
- Bentov, S., Brownlee, C., Erez, J., 2009. The role of seawater endocytosis in the biomineralization process in calcareous foraminifera. *PNAS*, 106, 21500-21504.
- Bittner, A., 1890. Brachiopoden der Alpen Trias. *Abhandlungen der Kaiserlich-Königlichen Geologischen Reichsanstalt* 14, 1-325.
- Bitner, M.A., 2000. Biodiversity of shallow-water brachiopods from New Caledonia, SW Pacific, with description of a new species. *Scientia Marina* 74, 643-657.
- Böhn, F., Gussone, N., Eisenhauer, A., Dullo, W.C., Reynaud, S., Paytan, A., 2006. Calcium isotope fractionation in modern scleractinian corals. *Geochimica et Cosmochimica Acta* 70, 4452-4462.
- Boskey, A. L., 1998. Biomineralization: conflicts, challenges, and opportunities. *Journal of Cellular Biochemistry*, Supplement 30–31, 83–91.
- Braissant, O., Decho, A.W., Dupraz, C., Glunk, C., Przekop, K.M., Visscher, P.T., 2007. Exopolymeric Substances of Sulfate-Reducing Bacteria: Interactions with Calcium at Alkaline pH and Implication for Formation of Carbonate Minerals. *Geobiology* 5, 401-411.
- Brand, U., Logan, A., Hiller, N., Richardson, J., 2003. Geochemistry of modern brachiopods: applications and implications for oceanography and paleoceanography. *Chemical Geology* 198, 305-334
- Brand, U., Logan, A., Bitner, M.A., Griesshaber, E., Azmy, K., Buhl, D., 2011. What is the Ideal Proxy of Palaeozoic Seawater chemistry? *Memoirs of the Association of Australasian Palaeontologists* 41, 9-24.

- Brand, U., Bitner, M.A., Logan, A., Azmy, K., Crippa, G., Angiolini, L., Colin, P., Griesshaber, E., Harper, E., Ruggiero, E., Häussermann, V., Bitner, U., Ruggiero, T., Häussermann, E., 2019. Brachiopod-based oxygen-isotope thermometer: Update and review. *Rivista Italiana di Paleontologia e Stratigrafia* 125, 775-787.
- Brazeau, M.D., Guillerme, T., Smith, M.R., 2019. An algorithm for morphological phylogenetic analyses with inapplicable data. *Systematic Biology* 68, 619-631.
- Brečević, L., Nielsen, A.E., 1989. Solubility of amorphous calcium carbonate. *Journal of Crystal Growth* 98, 504-510.
- Cameron, J.N., Wood, C.M., 1985. Apparent H⁺ excretion and CO₂ dynamics accompanying carapace mineralization in the blue crab (*Callinectes sapidus*) following moulting. *Journal of Crystal Growth* 114, 181-196.
- Carlson, S. J., 1995. Phylogenetic relationships among extant brachiopods. *Cladistics* 11, 131-197.
- Carlson, S.J., 2007. Recent research on brachiopod evolution. In: Kaesler, R.L., Selden, P.A. (eds.): *Treatise on Invertebrate Paleontology Part H. Brachiopoda* 6, Geological Society of America, Boulder, Colorado and University of Kansas Press, Lawrence, Kansas, pp. 2878-2900.
- Carlson, S. J., 2016. The Evolution of Brachiopoda. *Annual Review of Earth and Planetary Sciences* 44, 409-438.
- Carpenter, S.J., Lohmann, K.C., Holden, P., Walter, L.M., Hoston, T. and Halliday, A.N., 1991. Delta 18O values, 87Sr/86Sr and Sr/Mg ratios of late Devonian abiogenic marine calcite: Implications for the composition of ancient seawater. *Geochimica et Cosmochimica Acta* 55, 1991-2010.
- Carpenter, S.J., Lohmann, K.C., 1995. ¹⁸O and ¹³C values of modern brachiopod shells. *Geochimica et Cosmochimica Acta* 59, 3749-3764.
- Cartwright, J.H.E., Checa, A.G., 2007. The dynamics of nacre self-assembly. *Journal of the Royal Society Interface* 4, 491-504
- Cartwright, J., Checa, A., Gale, J.D., Gebauer, D., Sainz-Díaz, C., 2012. Calcium Carbonate Polyamorphism and Its Role in Biomineralization: How Many Amorphous Calcium Carbonates Are There? *Angewandte Chemie International Edition in English* 51, 11960-11970.
- Carter, J.G., 1990a. *Skeletal Biomineralization, Patterns, Processes and Evolutionary Trends, Volume 1*. Van Nostrand Reinhold and Company, New York, 832 pp.
- Carter, J.G., 1990b. *Skeletal Biomineralization, Patterns, Processes and Evolutionary Trends, Volume 2*. Van Nostrand Reinhold and Company, New York, 301 pp.
- Carter, J. G., Harries, P., Malchus, N., Sartori, A., Anderson, L., Bieler, R., Bogan, A., Coan, E., Cope, J., Cragg, S., Garcia-March, J., Hylleberg, J., Kelley, P., Kleemann, K., Kriz, J., McRoberts, C., Mikkelsen, P., Pojeta, Jr. J., Skelton, P.W., Temkin, I., Yancey, T., Zieritz, A., 2012. *Illustrated Glossary of the Bivalvia in Treatise Online*, no. 48, Part N (Revised) Volume 1. Lawrence, University of Kansas, 209 pp.
- Casella, L.A., Griesshaber, E., Yin, X., Ziegler, A., Mavromatis, V., Müller, D., Ritter, A., Hippler, D., Harper, E.M., Dietzel, M., Immenhauser, A., Schöne, B.R., Angiolini, L.,

- Schmahl, W.W., 2017. Experimental diagenesis: insights into aragonite to calcite transformation of *Arctica islandica* shells by hydrothermal treatment. *Biogeosciences* 14, 1461-1492.
- Casella, L.A., Griesshaber, E., Simonet-Roda, M., Ziegler, A., Mavromatis, V., Henkel, D., Laudien, J., Häussermann, V., Neuser, R.D., Angiolini, L., Dietzel, M., Eisenhauer, A., Immenhauser, A., Brand, U., Schmahl, W.W., 2018a. Micro- and nanostructures reflect the degree of diagenetic alteration in modern and fossil brachiopod shell calcite: a multi-analytical screening approach (CL, FE-SEM, AFM, EBSD). *Palaeogeography. Palaeoclimatology. Palaeoecology* 502, 13-30.
- Casella, L.A., Simonet Roda, M., Angiolini, L., Ziegler, A., Schmahl, W.W., Brand, U., Griesshaber, E., 2018b. Archival biogenic micro- and nanostructure data analysis: Signatures of diagenetic systems Data in Brief Archival biogenic micro- and nanostructure data analysis: Signatures of diagenetic systems. *Data Brief* 19, 299-311.
- Casella, L.A., He, S., Griesshaber, E., Fernández-Díaz, L., Greiner, M., Harper, E.M., Jackson, D., Ziegler, A., Mavromatis, V., Dietzel, M., Eisenhauer, A., Immenhauser, Veintemillas-Verdaguer, S., Brand, U., Schmahl, W.W., 2018c. Hydrothermal alteration of aragonitic biocarbonates: assessment of micro- and nanostructural dissolution-reprecipitation and constraints of diagenetic overprint from quantitative statistical grain-area analysis. *Biogeosciences* 15, 7451-7484.
- Checa, A.G., Salas, C., Harper, E.M., Bueno-Pérez, J.D.D., 2014. Early Stage Biomineralization in the Periostracum of the “Living Fossil” Bivalve *Neotrigonia*. *PLOS One* 9, e90033.
- Checa, A. 2018. Physical and Biological Determinants of the Fabrication of Molluscan Shell Microstructures. *Frontiers in Marine Science* 5, 353.
- Checa, A., Harper, E., Gonzalez Segura, A., 2018. Structure and crystallography of foliated and chalk shell microstructures of the oyster *Magallana*: The same materials grown under different conditions. *Scientific Reports* 8, 7507.
- Checa, A. G., Cartwright, J. H. E. Willinger, M. 2009. The key role of the surface membrane in why gastropod nacre grows in towers. *PNAS* 106, 38-43.
- Checa, A. G., Macías, E., Harper, E. M. Cartwright, J. H. E. 2016. Organic membranes determine the pattern of the columnar prismatic layer of mollusc shells. *Proceedings of the Royal Society B* 283, 20160032.
- Checa, A., Salas, C., Rodriguez-Navarro, A., Grenier, C., Lagos, N., 2019. Articulation and growth of skeletal elements in balanid barnacles (Balanidae, Balanomorpha, Cirripedia). *Royal Society Open Science* 6, 190458.
- Checa, A., Yanez-Avila, M., Gonzalez-Segura, A., Varela-Feria, F., Griesshaber, E., Schmahl, W.W., 2019. Bending and branching of calcite laths in the foliated microstructure of pectinoidean bivalves occurs at coherent crystal lattice orientation. *Journal of Structural Biology* 205, 7-17.
- Clapham, M.E., Bottjer, D.J., 2007. Prolonged permian triassic ecological crisis recorded by molluscan dominance in the Late Permian offshore assemblages. *Proceedings of the National Academy of Sciences* 104, 12971-12975.
- Clastro-Claros, J.D., Checa, A., Lucena, C., Pearson, J.R., Salas, C., 2020. Shell-aductor muscle attachment and Ca²⁺ transport in the bivalves *Ostrea stentina* and *Anomia ephippium*.

- Cohen, B.L. 2007. The brachiopod genome. In Selden, P.A.(ed.): Treatise on invertebrate paleontology. Part H (supplement), Brachiopoda 6 (Revised). Geological Society of America, Boulder, Colorado and University of Kansas Press, Lawrence, Kansas, pp. 2356 - 2372.
- Cohen, P.A., Schopf, J.W., Butterfield, N.J., Kudryavtsev, A.B., MacDonald, F.A., 2011. Phosphate biomineralization in mid-Neoproterozoic protists. *Geology* 39, 539–542.
- Corni, I., et al. 2012. A review of experimental techniques to produce a nacre-like structure. *Bioinspiration and Biomimetics* 7, 031001.
- Crenshaw, M.A., 1980. Mechanisms of shell formation and dissolution. In Rhoads, D.C., Lutz, R.A., (eds.): *Skeletal Growth of Aquatic Organisms*. Plenum Publishing Corporation, New York, pp. 115-132.
- Crippa, G., Ye, F., Malinverno, C., Rizzi, A., 2016. Which is the best method to prepare invertebrate shells for SEM analysis? Testing different techniques on recent and fossil brachiopods. *Bollettino della Societa Paleontologica* 55, 111-125.
- Crippa, G., Griesshaber, E., Checa, A.G., Harper, E., Simonet Roda, M., Schmahl, W.W., 2020a. Orientation patterns of the aragonitic crossed-lamellar, myostracal and fibrous microstructures of modern *Glycymeris* shells. *Journal of Structural Biology* 212, 107653.
- Crippa, G., Griesshaber, E., Checa, A.G., Harper, E.M., Simonet Roda, M., Schmahl, W.W., 2020b. SEM, EBSD, laser confocal microscopy and FE-SEM data from modern *Glycymeris* shell layers. *Data Brief* 33, 106547.
- Criss, R. E., 1999. Principles of stable isotope distribution. Oxford University Press, New York, 264 pp.
- Cross, E.L., Harper, E.M., Peck, L.S., 2018. A 120-year record of resilience to environmental change in brachiopods. *Global Change Biology* 24, 2262-2271.
- Cross, E.L., Peck, L.S., Lamare, M.D., Harper, E.M., 2016. No ocean acidification effects on shell growth and repair in the New Zealand brachiopod *Calloria inconspicua* (Sowerby, 1846). *ICES Journal of Marine Sciences* 73, 920-926.
- Cross, E L, Peck L S, Harper E M. 2015. Ocean acidification does not impact shell growth or repair of the Antarctic brachiopod *Liothyrella uva* (Broderip, 1833). *Journal of Experimental Marine Biology and Ecology* 462, 29-35.
- Cusack, M., Dauphin, Y., Chung, P., Pérez-Huerta, A., Cuif, J. P., 2008. Multiscale structure of calcite fibres of the shell of the brachiopod *Terebratulina retusa*. *Journal of Structural Biology* 164, 96-100.
- Cusack, M., Williams, A., 2007. Biochemistry diversity of brachiopod shells. In: Kaesler, R., (ed.): *Treatise on Invertebrate Paleontology*. Part H, Brachiopoda 1, Geological Society of America, Boulder, Colorado and University of Kansas Press, Lawrence, Kansas, pp. 2373-2395.

- Cusack, M., 2001. Biomineralization in brachiopod shells. *Paleontological Society Papers* 7, 105-116.
- Dagys, A.S., 1972. Ultrastructure of thecospirid shells and their position in brachiopod systematics. *Paleontological Journal* 6, 359-369.
- Decho, A. W., 2010. Overview of Biopolymer-Induced Mineralization: What Goes on in Biofilms? *Ecological engineering* 36, 137–144.
- Delaney, M.L., Popp, B.N., Lepzelter, C.G., Anderson, T.F., 1989. Lithium-to calcium ratios in modern, Cenozoic and Paleozoic articulate brachiopod shells. *Paleoceanography* 4, 681-691.
- De Nooijer, L.J., Spero, H J., Erez, J., Bijma, J., Reichart, G. J., 2014. Biomineralization in perforate foraminifera. *Earth-Science Reviews* 135, 48-58.
- DePaolo, D.J., 2011. Surface kinetic model for isotopic and trace element fractionation during precipitation of calcite from aqueous solutions. *Geochimica et Cosmochimica Acta* 75, 1039-1056.
- Deville, S., Saiz, E., Nalla, R. K. Tomsia, A. P., 2006. Freezing as a Path to Build Complex Composites. *Science* 311, 515-518
- DeVol, R.T., Sun, C.-Y., Marcus, M.A., Coppersmith, S.N., Myneni, S.C.B., Gilbert, P.U.P.A., 2015. Nanoscale Transforming Mineral Phases in Fresh Nacre. *Journal of the American Chemical Society* 137, 13325-13333.
- Devi, R.S., Aravind Kumar, S., Bhuvanesh, E., Kavya,C., 2017. Biomaterial and its medical applications. *International Journal of Advance Research and Innovative Ideas in Education* 3, 489-498.
- Dixon, G. 1789. A voyage around the world; but more particularly to the North-West coast of America; performed in 1785, 1786, 1787 and 1788, in the King George and Queen Charlotte, Captains Portlock and Dixon. *Geo. Goulding*, 527 pp.
- Dunlop, J.W.C. Fratzl, P. 2010: Biological Composites. *Annual Review of Materials Research* 40, 1-24.
- Dupraz, C., Reid, R.P., Braissant, O., Decho, A. W., Norman, R. S., Visscher, P.T., 2009. Processes of Carbonate Precipitation in Modern Microbial Mats. *Earth-Science Reviews* 96, 141–162.
- Elliot, G.F. 1953. The classification of the cidean brachiopods. *The Annals and Magazine of Natural History* 6, 693-701.
- Emmrich, H., 1855. II. Notiz über den Alpenkalk der Lienzer Gegend. *Jahrbuch der Geologischen Bundesanstalt* 6, 444-450.
- England, J., Cusack, M., Dalbeck, P., Pérez-Huerta, A., 2007. Comparison of the crystallographic structure of semi nacre and nacre by Electron Backscatter Diffraction. *Crystal Growth and Design* 7, 307-310.
- Eptsein, S., Buchsbaum, R., Lowenstam, H.A., Urey, H.C., 1951. Carbonate-water isotopic temperature scale. *Bulletin of the Geological Society of America* 62, 417-426.

- Ercole, C., Bozzelli, P., Altieri, F., Cacchio, P., Del Gallo, M., 2012. Calcium Carbonate Mineralization: Involvement of Extracellular Polymeric Materials Isolated from Calcifying Bacteria. *Microscopy and Microanalysis* 18, 829–839.
- Fabritius, H., Ziegler, A., 2003. Analysis of Ca CO₃ deposit formation and degradation during the molt cycle of the terrestrial isopod *Porcellio scaber* (Crustacea, Isopoda). *Journal of Structural Biology* 142, 281-291.
- Fabritius, H., Walther, P., Ziegler, A., 2005 Architecture of the organic matrix in the sternal CaCO₃ deposits of *Porcellio scaber* (Crustacea, Isopoda). *Journal of Structural Biology* 150, 190-199.
- Falini, G., Albeck, S., Weiner, S., Addadi, L., 1996. Control of aragonite or calcite polymorphism by mollusk shell macromolecules. *Science* 271, 67-69.
- Fallini, G., Fermani, S., Goffredo, S., 2015. Seminars in Cell Developmental Biology Coral biomineralization: A focus on intra-skeletal organic matrix and calcification. *Seminars in Cell and Developmental Biology* 46, 17-26.
- Fang, Z., Feng, Q., Chi, Y., Xie, L., Zhang, R., 2008. Investigation of cell proliferation and differentiation in the mantle of *Pinctada fucata* (Bivalve, Mollusca). *Marine Biology* 153, 745-754.
- Finnegan, S., Rasmussen, C., M.Ø, Harper, D.A.T., 2016. Biogeographic and bathymetric determinants of brachiopod extinction and survival during the Late Ordovician mass extinction. *Proceedings of the Royal Society B* 283, 20160007.
- Flik, G., Verboost, P.M., Atsma, W., 1994. Calcium transport in gill plasma membranes of the crab *Carcinus maenas*: evidence for carriers driven by ATP and a Na⁺ gradient. *Journal of Crystal Growth* 195, 109-122.
- Fortin, D., Ferris, F.G., Beveridge, T.J., 1997. Surface-Mediated Mineral Development by Bacteria. *Reviews in Mineralogy and Geochemistry* 35, 161-180.
- Fratzl, P., Weinkarmer, R., 2007: Nature's hierarchical materials. *Progress in Material Science* 52, 1263-334.
- Frisia, S., 1990: TEM investigation of the shell of the brachiopod *Thecospira tyrolensis* (Loretz): A clue to understanding growth and replacement of prismatic and/or fibrous low mg-calcite? *Rivista Italiana di Paleontologia e Stratigrafia* 96, 77-92.
- Gabitov, R.I., Watson, E.B., 2006. Partitioning of strontium between calcite and fluid. *Geochemistry, Geophysics, Geosystems* 7, Q11004.
- Gal, A., Kahil, K., Vidavsky, N., De Vol, R.T., Gilbert, P.U.P.A., Fratzl, P., Weiner, S., Addadi, L., 2014. Particle Accretion Mechanism Underlies Biological Crystal Growth from an Amorphous Precursor Phase. *Advanced Functional Materials*. 24, 5420-5426.
- Garbelli, C., Angiolini, L., Shen, S.Z., 2017: Biomineralization and global change: A new perspective for understanding the end-Permian extinction. *Geology* 45, 19-22.
- Garbelli, C., Angiolini, L., Jadoul, F., Brand, U., 2012. Micromorphology and differential preservation of Upper Permian brachiopod low-Mg calcite. *Chemical Geology* 299, 1-10.

- Garbelli, C., Angiolini, L., Brand, U., Jadoul, F., 2014. Brachiopod fabric, classes and biogeochemistry: implications for the reconstruction and interpretation of seawater carbon- isotope curves and records. *Chemical Geology* 371, 60-67.
- Garbelli, C., Angiolini, L., Brand, U., Jadoul, F., 2014. Brachiopod fabric, classes and biogeochemistry: Implications for the reconstruction and interpretation of seawater carbon-isotope curves and records. *Chemical Geology* 371, 60-67.
- Garbelli, C., 2017. Shell microstructures in lopingian brachiopods: Implications for fabric evolution and calcification *Rivista Italiana di Paleontologia e Stratigrafia* 123, 541-560.
- Gaspard, D., Marie, B., Luquet, G., Marin, F., 2008. Biochemical characteristics of the soluble organic matrix from the shell of three recent terebratulid brachiopod species. *Fossils and Strata* 98, 269-275.
- Gaspard, D., Nouet, J., 2016. Hierarchical architecture of the inner layers of selected extant rhynchonelliform Brachiopod. *Journal of Structural Biology* 196, 197-205.
- Giraud-Guille, M.-M., 1984. Calcification initiation sites in the crab cuticle: the interprismatic septa. *Cell Tissue Research* 236, 413-420.
- Goetz, A.J., Griesshaber, E., Neuser, R.D.L., Harper, E., Schmahl, W.W., 2009. Calcite morphology, texture and hardness in the distinct layers of rhynchonelliform brachiopod shells. *European Journal of Mineralogy* 21, 303-315.
- Goetz, A.J., Steinmetz, D.R., Griesshaber, E., Zaefferer, S., Raabe, D., Kelm, K., Irsen, S., Sehrbrock, A., Schmahl, W.W., 2011. Interdigitating biocalcite dendrites form a 3-D jigsaw structure in brachiopod shells. *Acta Biomaterialia* 7, 2237-2243.
- Goetz, A. J., Griesshaber, E., Abel, R., Fehr, Th., Ruthensteiner, B., Schmahl, W.W., 2014. Tailored order: The mesocrystalline nature of sea urchin teeth. *Acta Biomaterialia* 10, 3885-3898.
- Gothmann, A.M., Bender, M.L., Blättler, C.L., Swart, P.K., Giri, S.J., Adkins, J.F., Stolarski, J., Higgins, J.A., 2016. Calcium isotopes in scleractinian fossil corals since the Mesozoic: Implications for vital effects and biomineralization through time. *Earth and Planetary Science Letters* 444, 205-214.
- Gotliv, B-A., Addadi, L., Weiner, S., 2003. Mollusk shell acidic proteins: in search of individual functions. *ChemBioChem* 4, 522-529
- Grant, R.E., 1972. The lophophore and feeding mechanism of the Productidina (Brachiopoda). *Journal of Paleontology* 46, 213-250.
- Greenaway, P., Dillaman, R.M., Roer, R.D., 1995. Quercetin-dependent ATPase activity in the hypodermal tissue of *Callinectes sapidus*, during the moult cycle. *Comparative Biochemistry and Physiology* 111A, 303-312.
- Grégoire, C., Duchateau, G.H., Florkin, M., 1955. La trame protidique des nacres et des perles. *Annales de l'Institut océanographique Monaco* 31, 1-36.
- Greiner, M., Yin, X., Fernández-Díaz, L., Griesshaber, E., Weitzel, F., Ziegler, A., Veintemillas-Verdaguer, S., Schmahl, W.W., 2018. Combined Influence of Reagent

Concentrations and Agar Hydrogel Strength on the Formation of Biomimetic Hydrogel-Calcite Composite. *Crystal Growth and Design* 18, 1401-1414.

- Griesshaber, E., Schmahl, W.W., Neuser, R.D., Job, R., Bluem, M., Brand, U., 2005. Microstructure of brachiopod shells - an inorganic/organic fibre composite with nanocrystalline protective layer. In: Katti, K., Ulm, F.J., Hellmich, C., Viney, C. (eds.): *Mechanical Properties of Bio-Inspired and Biological Materials*, Materials Research Society *Symposium Proceedings*, pp. 99-104.
- Griesshaber, E., Schmahl, W.W., Neuser, R., Pettke, T., Blüm, M., Mutterlose, J. Brand, U., 2007. Crystallographic texture and microstructure of terebratulide brachiopod shell calcite: An optimized materials design with hierarchical architecture. *American Mineralogist* 92, 722-734.
- Griesshaber, E., Kelm, K., Sehrbrock, A., Mader, W., Mutterlose, J., Brand, U., Schmahl, W. W., 2009. Amorphous calcium carbonate in the shell material of the brachiopod *Megerlia truncate*. *European Journal of Mineralogy* 21, 715-723.
- Griesshaber, E., Goetz, A. J., Howard, L., Ball, A., Ruff, S., Schmahl, W. W., 2012. Crystal architecture of the tooth and jaw bone (pyramid) of the sea urchin *Paracentrotus lividus*. *Bioinspired Biomimetic and Nanobiomaterials* 1, 133-139.
- Griesshaber, E., Schmahl, W.W., Ubhi, H.S., Huber, J., Nindiyasari, F., Maier, B., Ziegler, A., 2013. Homoepitaxial meso- and microscale crystal co-orientation and organic matrix network structure in *Mytilus edulis* nacre and calcite. *Acta Biomaterialia* 9, 9492-9502.
- Griesshaber, E., Yin, X., Ziegler, A., Kelm, K., Checa, A., Eisenhauer, A., Schmahl, W. W., 2017. Patterns of mineral organization in carbonate biological hard materials. In Heuss-Assbichler, S., Amthauer, G., John, M. (eds.): *Highlights in applied mineralogy*. De Gruyter, pp. 245-272.
- Grossman, E. L., Zhang, C., Yancey, T. E., 1991. Stable-isotope stratigraphy of brachiopods from Pennsylvanian shales in Texas. *Geological Society of America Bulletin* 103, 953-965.
- Grossman, E.L, Mii, H., Yancey, T.E., 1993. Stable isotopes in late Pennsylvanian brachiopods from the United States: Implications for Carboniferous paleoceanography. *Geological Society of America Bulletin* 103, 953-965.
- Grossman, E.L., Mii, H.-S., Zhang, C., Yancey, T.E., 1996. Chemical variation in pennsylvanian brachiopod shells-diagenetic. Taxonomic, microstructural, and seasonal effects. *International Journal of Sediment Research* 66, 1011-1022.
- Gussone, N., Langer, G., Eisenhauer, A., 2006. Cellular calcium pathways and isotope fractionation in *Emiliana huxleyi*. *Geology* 34, 625-628.
- Hagedorn, M., Ziegler, A., 2002. Analysis of Ca^{2+} uptake into the smooth endoplasmic reticulum of permeabilised sternal epithelial cells during the moulting cycle of the terrestrial isopod *Porcellio scaber*. *Journal of Crystal Growth* 205, 1935-1942.
- Hagedorn, M., Weihrauch, D., Towle, D.W., Ziegler, A., 2003. Molecular characterisation of the smooth endoplasmic reticulum Ca^{2+} -ATPase of *Porcellio scaber* and its expression in sternal epithelia during the moult cycle. *Journal of Crystal Growth* 206, 2167-2175.

- Harper, E.M., Checa, A., 2017. Physiological versus Biological Control in Bivalve Calcite Prisms: Comparison of Euheterodonts and Pteriomorphs. *Biological Bulletin* 232, 19-29.
- Harper, D.A.T., Drachen, A., 2010. The Orthida: the rise and fall of a great Palaeozoic clade. *Special Papers in Palaeontology* 84, 107-117.
- Harper, D.A.T., Renbin, Z., Jisuo, J., 2015. The Great Ordovician Biodiversification Event: reviewing two decades of research on diversity's big bang illustrated by mainly brachiopod data. *Palaeoworld* 24, 75-85.
- Harper, D.A.T., Popov, L.E., Holmer, L.E., 2017. Brachiopods: origin and early history. *Palaeontology* 60, 609-631.
- He, W.H., Shi, G. R., Zhang, K.X., Yang, T.-L., Shen, S.-Z., Zhang, Y., 2019. Brachiopods around the Permian-Triassic Boundary of South China. *New Records of the Great Dying in South China*. Springer, 261 pp.
- Henkes, G. A., Passey, B., Grossman, E., Shenton, B., Yancey, T., Perez-Huerta, A., 2018. Temperature evolution and the oxygen isotope composition of Phanerozoic oceans from carbonate clumped isotope thermometry. *Earth and Planetary Science Letters* 490, 40-50.
- Hermoso, M., Lefeuvre, B., Minoletti, F., de Raféñis, M., 2017. Extreme strontium concentrations reveal specific biomineralization pathways in certain coccolithophores with implications for the Sr / Ca paleoproductivity proxy. *PLoS One* 12, e0185655.
- Huber, J., Griesshaber, E., Nindiyasari, F., Schmahl, W.W., Ziegler, A., 2015. Functionalization of biomineral reinforcement in crustacean cuticle: calcite orientation in the partes incisivae of the mandibles of *Porcellio scaber* and the supralittoral species *Tylos europaeus* (Oniscidea, Isopoda). *Journal of Structural Biology* 190, 173-191.
- Immenhauser, A., Schöne, B.R., Hoffmann, R., Niedermayr, A., 2016. Mollusc and brachiopod hard parts: Intricate archives of their marine environment. *Sedimentology* 63, 1-59.
- Inoue, M., Gussone, N., Koga, Y., Iwase, A., Suzuki, A., Sakai, K., Kawahata, H., 2015. Science Direct Controlling factors of Ca isotope fractionation in scleractinian corals evaluated by temperature, pH and light controlled culture experiments. *Geochimica et Cosmochimica Acta* 167, 80-92.
- Jackson, A.P., Vincent, J.F., Turner, R.M., 1988. The mechanical design of nacre. *Proceedings of the Royal Society of London. Series B* 234, 415- 440
- Jacob, D.E., Wirth, R., Soldati, A.L., Wehrmeister, U., Schreiber, A., 2011. Amorphous calcium carbonate in the shells of adult Unionoida. *Journal of Structural Biology* 173, 241-249.
- Jaecks, G.S., Carlson, S.J., 2001. How phylogenetic inference can shape our view of heterochrony: examples from thecideide brachiopods. *Paleobiology* 27, 205-225.
- Kamat, S., Su, X., Ballarini, R., Heuer, A.H., 2000. Structural basis for the fracture toughness of the shell of the conch *strombus gigas*. *Nature* 405, 1036-1040
- Khan, M.Y., Chen, M-H., 2019. A Review on Role of biomaterials in biomedical field. *International Journal of Bio-Pharma Research* 8, 2788-2793.

- Khim, B.-K., Sik Woo, K., Je, J.G., 2000. Stable isotope profiles of bivalve shells: Seasonal temperature variations, latitudinal temperature gradients and biological carbon cycling along the east coast of Korea. *Continental Shelf Research* 20, 843-861.
- Kniprath, E., 1978. Growth of the Shell-field in *Mytilus* (Bivalvia). *Zoologica Scripta* 7, 119-120.
- Kniprath, E., 1975. Das Wachstum des Mantels von *Lymnaea stagnalis* (Gastropoda). *Cytobiologie* 10, 260-267.
- Knoll, A.H., 2003. Biomineralization and evolutionary history. In Dove, P.M., DeYoreo, J.J., Weiner, S., (eds.): *Biomineralization - Reviews in Mineralogy and Geochemistry* Vol. 54. The Mineralogical Society of America, pp. 329-356.
- Korte, C., Kozur, H. W., Veizer, J., 2005. $\delta^{13}\text{C}$ and $\delta^{18}\text{O}$ values of Triassic brachiopods and carbonate rocks as proxies for coeval seawater and palaeotemperature. *Palaeogeography, Palaeoclimatology, Palaeoecology* 226, 287-306.
- Krawczyński, C., 2008. The Upper Oxfordian (Jurassic) thecideide brachiopods from the Kujawy area, Poland. *Acta Geologica Polonica* 58, 395-406.
- Kreplak L., Fudge D., 2007. Biomechanical properties of intermediate filaments: from tissues to single filaments and back. *BioEssays* 29, 26-35.
- Kumar, R., 1995. Calcium transport in epithelial cells of the intestine and kidney. *Journal of Cellular Biochemistry* 57, 392-398.
- Lane, N. J., Harrison, J. B., 1979. An unusual cell surface modification: a double plasma membrane. *Journal of Cell Science* 39, 355-372.
- Langer, G., Gussone, N., Kiel, D., Eisenhauer, A., 2007. Calcium isotope fractionation during coccolith formation in *Emiliania huxleyi*: Independence of growth and calcification rate. *Geochemistry, Geophysics, Geosystems* 8, Q05007.
- Lee, D. E., Robinson, J. H., Witman, J. D., Copeland, S. E., Harper, E. M., Smith, F., Lamare, M., 2011. Observations on recruitment, growth and ecology in a diverse living brachiopod community, doubtful Sound, Fiordland, New Zealand. *Special Papers in Palaeontology*, 84, 177-191.
- Levi-Kalisman, Y., Falini, G., Addadi, L., Weiner, S., 2001. Structure of the nacreous organic matrix of a bivalve mollusk shell examined in the hydrated state using cryo-TEM. *Journal of Structural Biology* 135, 8-17.
- Lian, B., Chen, J., Ji, J., Teng, H.H., 2006. Carbonate biomineralisation induced by soil bacterium *Bacillus megaterium*. *Geochimica et Cosmochimica Acta* 70, 5522-5535.
- Liow, L.H., Reitan, T., Harnik, P.G., 2015. Ecological interactions on macroevolutionary time scales: clams and brachiopods are more than ships that pass in the night. *Ecology Letters* 18, 1030-1039.
- Liu, Y.-W., Eagle, R.A., Aciego, S.M., Gilmore, R.E., Ries, J.B., 2018. A coastal coccolithophore maintains pH homeostasis and switches carbon sources in response to ocean acidification. *Nature Communications* 9, 2857.

- Logan, A., 1988. A new thecideid genus and species (Brachiopoda, Recent) from the southeast North Atlantic. *Journal of Paleontology* 62, 546-551.
- Logan, A., 2007. Geographic distribution of extant articulated brachiopods. In Kaesler, R.L. (ed.): *Treatise on Invertebrate Paleontology, Part H, Brachiopoda 6*, (revised). Geological Society of America, Boulder, Colorado and University of Kansas Press, Lawrence, Kansas, pp. 2822-2855.
- Loretz, H., 1875. Einige Petrefacten der alpinen Trias aus den Südalpen. *Zeitschrift der Deutschen Geologischen Gesellschaft* 27, 784-841.
- Lowenstam, H.A., 1961. Mineralogy, O18/O16 ratios, and Strontium and Magnesium contents of recent and fossils brachiopods and their bearing on the history of the oceans. *Journal of Geology* 69, 241-260.
- Lowenstam, H.A., 1981. Minerals formed by organisms. *Science* 211, 1126-1131.
- Lowenstam, H.A., Weiner, S., 1989. *On Biomineralization*. Oxford University Press, New York, 336 pp.
- Lucu, C., 1994. Calcium Transport Across Isolated Gill Epithelium of *Carcinus*. *Journal of Experimental Zoology* 268, 339-346.
- Lüter, C., 2005. The first modern species of the unusual brachiopod *Kakanuiella* (Thecideidae) from New Zealand deep waters. *Systematics and Biodiversity* 3, 105-111.
- Mackinnon, D.I., 1974. The shell structure of spiriferide Brachiopoda. *Bulletin of the British Museum of Natural History (Geology)* 25, 189-261.
- Macdonald, J., Freer, A., Cusack, M., 2010. Attachment of oysters to natural substrata by biologically induced marine carbonate cement. *Marine Biology* 157, 2087-2095.
- Macías-Sánchez, E., Willinger, M.G., Pina, C.M., Checa, A.G., 2017. Transformation of ACC into aragonite and the origin of the nanogranular structure of nacre. *Scientific Reports* 7, 12728.
- Maloof, A.C., Rose, C.V., Beach, R., Samuels, B.M., Calmet, C.C., Erwin, D.H., Poirier, G.R., Yao, N., Simons, F.J., 2010. Possible animal-body fossils in pre-Marinoan limestones from South Australia. *Nature Geoscience*. 3, 653–659.
- Mann, S., 1983. Mineralization in biological systems. *Structure and Bonding* 54, 125-174.
- Mann, S., 2001. *Biomineralization: Principles and Concepts in Bioinorganic Materials Chemistry*. Oxford University Press, New York, 210 pp.
- Maier, B.J., Griesshaber, E., Alexa, A., Ziegler, A., Ubhi, H.S., Schmahl, W.W., 2014. Biological control of crystallographic architecture: Hierarchy and co-alignment parameters. *Acta Biomaterialia* 10, 3866-3874.
- Marriott, C.S., Henderson, G.M., Belshaw, N.S., Tudhope, A.W., 2004. Temperature dependence of $\delta^7\text{Li}$, $\delta^{44}\text{Ca}$ and Li/Ca during growth of calcium carbonate. *Earth and Planetary Science Letters* 222, 615-624.

- Marshall, A.T., Clode, P.L., Russell, R., Prince, K., Stern, R., 2007. Electron and ion microprobe analysis of calcium distribution and transport in coral tissues. *Journal of Crystal Growth* 210, 2453-2463.
- Mayer, G., 2005. Rigid biological systems as models for synthetic composites. *Science* 310, 1144-1147.
- Mayer, G., Sarikaya, M., 2002. Rigid biological composite materials: structural examples for biomimetic design. *Experimental Mechanics* 42, 395-403.
- McClelland, H.L.O., Bruggeman, J., Hermoso, M., Rickaby, R.E.M., 2017. The origin of carbon isotope vital effects in coccolith calcite. *Nature Communications* 8, 14511.
- McConnaughey, T., 1989. ^{13}C and ^{18}O isotopic disequilibrium in biological carbonates: II. In vitro simulation of kinetic isotope effects. *Geochimica et Cosmochimica Acta* 53, 163-171.
- McGhee, G. R., 1980. Shell form in the biconvex articulate Brachiopoda: a geometric analysis. *Paleobiology* 6, 57-76.
- McGhee, G.R. Jr., 1999. The theoretical enigma of non-biconvex brachiopod shell form. In Savazzi, E. (ed.): *Functional morphology of the invertebrate skeleton*. Wiley Sons, Chichester, New York, pp. 429-433.
- Mejía, M., Paytan, A., Eisenhauer, A., Böhm, F., Kolevica, A., Bolton, C., Méndez-Vicente, A., Abrevaya, L., Isensee, K., 2018. Controls over $\delta 44/40\text{Ca}$ and Sr/Ca variations in coccoliths: New perspectives from laboratory cultures and cellular models. *Earth and Planetary Science Letters* 481, 48-60.
- Merkel, C., Griesshaber, E., Kelm, K., Neuser, R., Jordan, G., Logan, A., Mader, W., Schmahl, W.W., 2007. Micromechanical properties and structural characterization of modern inarticulated brachiopod shells. *Journal of Geophysical Research* 112, G02008.
- Merkel, C., Deuschle, J., Griesshaber, E., Enders, S., Steinhäuser, E., Hochleitner, R., Brand, U., Schmahl, W.W., 2009. Mechanical properties of modern calcite (*Mergerlia truncata*) and phosphate-shelled brachiopods (*Discradisca stella* and *Lingula anatina*) determined by nanoindentation. *Journal of Structural Biology* 168, 396-408.
- Merz, W.A., 1967. Die Streckenmessung an gerichteten Strukturen im Mikroskop und ihre Anwendung zur Bestimmung von Oberflächen-Volumen-Relationen. *Knochengewebe. Mikroskopie* 22, 132-142.
- Meyers, M. A., Chen, P.-Y., Lin, A.Y.-M., Seki, Y., 2008. Biological materials: Structure and mechanical properties. *Progress in Materials Science* 53, 1-206.
- Michalik, J., 1976. Two representatives of Strophomenida (Brachiopoda) in the uppermost Triassic of the West Carpathians. *Geologica Carpathica* 27, 79-96.
- Milner Garcia, S., 2018. Evaluation of the biomineralization and chemical differentiation in brachiopods. Dissertation, Sorbonne Université, Paris.
- Moor, M.B., Bonny, O., 2016. Ways of calcium reabsorption in the kidney. *American Journal of Physiology-Renal Physiology* 310, 1337-1350.

- Morse, J. W., Wang, Q., Tsio, N. Y., 1997. Influences of temperature and Mg:Ca ratio on CaCO₃ precipitates from seawater. *Geology* 25, 85-87.
- Naleway, S., Porter, M., Mckittrick, J., Meyers, M., 2015. Structural design elements in biological materials: application to bioinspiration. *Advanced Materials* 27, 5455-5476.
- Nassif, N., Pinna, N., Gehrke, N., Antonietti, M., Jäger, C., Cölfen, H., 2005. Amorphous layer around aragonite platelets in nacre. *PNAS* 102, 12653-12655.
- Nebelsick, J.D., Bassi, D., Rasser, M.W., 2011. Cryptic relicts from the past: Paleoecology and taphonomy of encrusting thecideid brachiopods in Paleogene carbonates. *Annalen des Naturhistorischen Museums in Wien* 113, 525-542.
- Neufeld, D.S., Cameron, J.N., 1993. Transepithelial movement of calcium in crustaceans. *Journal of Crystal Growth* 184, 1-16.
- Niebel, T. P., Bouville, F., Kokkinis, D., Studart, A., R. 2016. Role of the polymer phase in the mechanics of nacre-like composites. *Journal of the Mechanics and Physics of Solids* 96, 133-146.
- Nielsen, L.C., Druhan, J.L., Yang, W., Brown, S.T., DePaolo, D.J., 2012. Calcium Isotopes as Tracers of Biogeochemical Processes. In Baskaran, M. (ed.): *Handbook of Environmental Isotope Geochemistry. Advances in Isotope Geochemistry*. Springer, Berlin, pp. 105-124.
- Nielsen, J. K., Błażejowski, B., Gieszczyk, P., Nielsen, J. K., 2013. Carbon and oxygen isotope records of Permian brachiopods from relatively low and high palaeolatitudes: climatic seasonality and evaporation. *Geological Society, London, Special Publications* 376, 387 LP-406.
- Nindiyasari, F., Ziegler, A., Griesshaber, E., Fernández-Díaz, L., Huber, J., Walther, P., Schmahl, W.W., 2015. Effect of hydrogel matrices on calcite crystal growth morphology, aggregate formation, and co-orientation in biomimetic experiments and biomineralization environments. *Crystal Growth and Design* 15, 2667-2685.
- Nudelman, F., Shimoni, E., Klein, E., Rousseau, M., Bourrat, X., Lopez, E., Addadi, L., Weiner, S., 2008. Forming Nacreous Layer of the Shells of the Bivalves *Atrina rigida* and *Pinctada margaritifera*. *Journal of Structural Biology* 162, 290-300.
- Oppenheimer-Shaanan, Y., Sibony-Nevo, O., BloomAckermann, Z., Suissa, R., Steinberg, N., Kartvelishvily, E., Brumfeld, V., Kolodkin-Gal, I., 2016. Spatio-Temporal Assembly of Functional Mineral Scaffolds within Microbial Biofilms. *Npj Biofilms and Microbiomes* 2, 15031.
- Pajaud, D., 1970. Monographies des Thécidées (Brachiopodes). *Mémoires de la Société géologique de France* 112, 1-349.
- Pajaud, D., 1974. *Écologie des Thécidées*. *Lethaia* 7, 203-218.
- Pan, N., 2014. Exploring the significance of structural hierarchy in material systems — A review. *Applied Physics Reviews* 1, 1-31.

- Parkinson, D., Curry, G.B., Cusack, M., Fallick, A.E., 2005. Shell structure, patterns and trends of oxygen and carbon stable isotopes in modern brachiopod shells. *Chemical Geology* 219, 193-235.
- Payne, J., Clapham, M., 2012. End-Permian mass extinction in the oceans: an ancient analog for the 21st century? *Annual Review of Earth and Planetary Sciences* 40, 89-111.
- Peck, L., 2007. Earth and Environmental Science Transactions of the Royal Royal Society of Edinburgh: Brachiopods and climate change Brachiopods and climate change. *Earth and Environmental Science Transactions of The Royal Society of Edinburgh* 98, 451-456.
- Peck, L.S., Harper, E.M., 2010. Variation in size of living articulated brachiopods with latitude and depth. *Marine Biology* 157, 2205-2213.
- Peck, L.S., Brockington, S., Brey, T., Trans, P., Lond, R.S., Peck, L.S., Brockington, S., Brey, T., 1997. Growth and metabolism in the Antarctic brachiopod *Liothyrella uva*. *Philosophical Transactions of the Royal Society B: Biological Sciences* 352, 851-858.
- Pereira-Mouriès, L., Almeida, M-J., Ribeiro, C., Peduzzi, J., Barthélemy, M., Milet, C., Lopez, E., 2002. Soluble silk-like organic matrix in the nacreous layer of the bivalve *Pinctada maxima*. *FEBS* 269, 4994-5003.
- Pérez-Huerta, A., Cusack, M., England, J., 2007. Crystallography and diagenesis in fossil Craniid brachiopods. *Palaeontology* 50, 757-763.
- Peter, N.J., Griesshaber, E., Reisecker, Ch., Hild, S., Oliveira, M.V.G., Ziegler, A., Schmahl, W.W., Arzt, E., Schneider, A.S., 2020. Microstructure, texture and material property relationships in mollusc shells. Submitted to *Acta Biomater.*
- Politi, Y., Metzler, R.A., Abrecht, M., Wilt, F.H., Sagi, I., Addadi, L., Weiner, S., Politi, Y., Metzler, R.A., Abrecht, M., Gilbert, B., Wilt, F.H., Addadi, L., Weiner, S., Gilbert, P.U.P.A., 2008. Transformation mechanism of amorphous calcium carbonate into calcite in the sea urchin larval spicule. *PNAS* 105, 17362-17366.
- Porter, S., 2011. The rise of predators. *Geology* 39, 607-608.
- Politi, Y., Arad, T., Klein, E., Weiner, S., Addadi, L., 2004. Sea Urchin Spine Calcite Forms via a Transient Amorphous Calcium Carbonate Phase. *Science* 306, 1161-1164.
- Pretet, C., Samankassou, E., Felis, T., Reynaud, S., Böhm, F., Eisenhauer, A., Ferrier-pagès, C., Gattuso, J., Camoin, G., 2013. Constraining calcium isotope fractionation ($\delta^{44/40}\text{Ca}$) in modern and fossil scleractinian coral skeleton. *Chemical Geology* 340, 49-58.
- Queiroz, A.C., Santos, J.D., Monteiro, F.J., Gibson, I.R., Knowles, J.C., 2001. Adsorption and release studies of sodium ampicillin from hydroxyapatite and glass-reinforced hydroxyapatite composites. *Biomaterials* 22, 393-1400.
- Quenstedt, F.A., 1858. *Der Jura*. Laupp, Tübingen, 842 pp.
- Reddin, C. J., Kocsis, T., Kocsis, Á. T., Kiessling, W., 2018. Marine invertebrate migrations trace climate change over 450 million years. *Global Ecology and Biogeography* 27, 704-713.

- Rezaie, H.R., Bakhtiari, L., Öchsner, A., 2015. Biomaterials and their applications. Springer International Publishing, 49 pp.
- Richardson, J.R., 1997. Ecology of articulated brachiopods. In Kaesler RL (ed.): Treatise on Invertebrate Palaeontology. Part H, Brachiopoda 1 (Revised). Geological Society of America, Boulder, Colorado and University of Kansas Press, Lawrence, Kansas, pp. 441-462.
- Richie, R. O., 2011. The conflicts between strength and toughness. *Nature Materials* 10, 817-822.
- Risso, A., 1826. Histoire naturelle des principales productions de l'Europe méridionale, et particulièrement de celles des environs de Nice et des Alpes Maritimes. IV. Aperçu sur l'Histoire Naturelle des mollusques et des coquilles de l'Europe Méridionale 7, 439.
- Rosenberg, G. D., Hughes, W. W., Tkachuk, R. D., 1988. Intermediary metabolism and shell growth in the brachiopod *Terebratalia transversa*. *Lethaia* 21, 219-230.
- Roark, A., Grossman, E.L., Lebold, J., 2015. Low seasonality in central equatorial Pangea during a late Carboniferous highstand based on high-resolution isotopic records of brachiopod shells. *Geological Society of America Bulletin* 128, 597-608.
- Roduit, N., (accessed 06 December 2020). JMicroVision: Image analysis toolbox for measuring and quantifying components of high-definition images. Version 1.3.1. <https://jmicrovision.github.io>
- Roer, R.D., 1980. Mechanisms of resorption and deposition of calcium in the carapace of the crab *Carcinus maenas*. *Journal of Crystal Growth* 88, 205-218.
- Roer, R., Dillaman, R., 1984. The structure and calcification of the crustacean cuticle. *American Zoologist* 24, 893-909.
- Rollion-Bard, C., Mangin, D., Champenois, M., 2007. Development and application of oxygen and carbon isotopic measurements of biogenic carbonates by ion microprobe. *Geostandards and Geoanalytical Research* 31, 39-50.
- Rollion-Bard, C., Marin-Carbonne, J., 2011. Measurements of SIMS matrix effects on oxygen isotopic compositions in carbonates. *Journal of Analytical Atomic Spectrometry* 26, 1285-1289.
- Rollion-Bard, C., Chaussidon, M., France-Lanord, C., 2011. Biological control of internal pH in scleractinian corals: Implications on paleo-pH and paleo-temperature reconstructions. *Comptes rendus Geoscience* 343, 397-405.
- Rollion-Bard, C., Saulnier, S., Vigier, N., Schumacher, A., Chaussidon, M., Lécuyer, C., 2016. Variability in magnesium, carbon and oxygen isotope compositions of brachiopod shells: Implications for paleoceanographic studies. *Chemical Geology* 423, 49-60.
- Rollion-Bard, C., Milner Garcia, S., Burckel, P., Angiolini, L., Jurikova, H., Tomašových, A., Henkel, D., 2019. Assessing the biomineralization processes in the shell layers of modern brachiopods from oxygen isotopic composition and elemental ratios: Implications for their use as paleoenvironmental proxies. *Chemical Geology* 524, 49-66.

- Romanin, M., Crippa, G., Ye, F., Brand, U., Bitner, M.A., Gaspard, D., Häussermann, V., Laudien, J.A., 2018. Sampling strategy for recent and fossil brachiopods: 1321 selecting the optimal shell segment for geochemical analyses. *Rivista Italiana di Paleontologia e Stratigrafia* 124, 343-359.
- Rosenberg, G.D., Hughes, W.W., Tkachuck, R.D., 1988. Intermediary metabolism and shell growth in the brachiopod *Terebratalia transversa*. *Lethaia* 21, 219-230.
- Rousseau, M., 2018. Nacre: a biomineral, a natural biomaterial, and a source of bio-inspiration. In Heuss-Assbichler, S., Amthauer, G., John, M. (eds.): *Highlights in applied mineralogy*. De Gruyter, pp. 285-300.
- Rowell, A.J., Grant, R. E., 1987. Phylum Brachiopoda in *Fossil Invertebrates*. Boardman, R.S., Cheetham, A.H., Rowell, A.J. (eds.), Blackwell Scientific Publications, pp. 445-496.
- Rudwick, M. J. S., 1959. The growth and form of brachiopod shells. *Geological Magazine* XCVI.
- Rudwick, M.J.S., 1968. The feeding mechanisms and affinities of the Triassic brachiopods *Thecospira Zugmayer* and *Bactrynum Emmrich*. *Palaeontology* 11, 329-360.
- Rudwick, M.J.S., 1970. *Living and fossil brachiopods*. Hutchinson University Library, London, 199 pp.
- Saenz, A., Brostow, W., Rivera-Muñoz, E., 1999. Ceramic biomaterials: An introductory overview. *Journal of Materials Education* 21, 297-306.
- Samtleben, C., Munnecke, A., Bickert, T., 2001. Shell succession, assemblage and species dependent effects on the C r O-isotopic composition of brachiopods — examples from the Silurian of Gotland. *Chemical Geology* 175, 61-107.
- Sánchez-Román, M., Rivadeneyra, M.A., Vasconcelos, C., McKenzie, J.A., 2007. Biomineralization of Carbonate and Phosphate by Moderately Halophilic Bacteria. *FEMS Microbiology Ecology* 61, 273-284.
- Sarikaya, M., 1999. Biomimetics: Materials fabrication through biology. *Proceedings of the National Academy of Sciences of the United States of America* 96, 14183–14185.
- Schlotheim, E.F., 1813. Beiträge zur Naturgeschichte der Versteinerungen in geognostischer Hinsicht. In Leonhard, C. C. (ed.): *Taschenbuch für die gesammte Mineralogie mit Hinsicht auf die neuesten Entdeckungen*, Volume 7. Hermannsche Buchhandlung, Frankfurt am Main, 340 pp.
- Schmahl, W.W., Griesshaber, E., Neuser, R., Lenze, A., Job, R. Brand, U., 2004. The microstructure of the fibrous layer of terebratulide brachiopod shell calcite. *European Journal of Mineralogy* 16, 693-697.
- Schmahl, W.W., Griesshaber, E., Merkel, C., Kelm, K., Deuschle, J., Neuser, R.D., Goetz, A.J., Sehrbrock, A., Mader, W., 2008. Hierarchical fibre composite structure and micromechanical properties of phosphatic and calcitic brachiopod shell biomaterials - an overview. *Mineral Magazine* 72, 541-562.
- Schmahl, W.W., Griesshaber, E., Kelm, K., Goetz, A., Jordan, G., Ball, A., Xu, D., Merkel, C. Brand, U. 2012: Hierarchical structure of marine shell biomaterials: biomechanical

- functionalization of calcite by brachiopods. *Zeitschrift für Kristallographie* 227, 793-611.
- Schwartz, A., Kumar, M., Adams, B., Field, D., 2000. *Electron Backscatter Diffraction in Materials Science*. Springer, Boston, MA, 393 pp.
- Seidl, B., Ziegler, A., 2012. Electron microscopic and preparative methods for the analysis of isopod cuticle. *Zookeys* 176, 73-85.
- Seidl, B., Reisecker, C., Hild, S., Griesshaber, E., Ziegler, A., 2012. Calcite distribution and orientation in the tergite exocuticle of the isopods *Porcellio scaber* and *Armadillidium vulgare* (Oniscidea, Crustacea). *Zeitschrift für Kristallographie* 227, 777-792.
- Seidl, B., Griesshaber, E., Fabritius, H. O., Reisecker, C., Hild, S., Taiti, S., Schmahl, W., Ziegler, A., 2018. Tailored disorder in calcite organization in tergite cuticle of the supralittoral isopod *Tylos europaeus*, Arcangeli, 1938. *Journal of Structural Biology* 204, 464-480.
- Shirakawa, M.A., Cincotto, M.A., Atencio, D., Gaylarde, C.C., John, V.M., 2011. Effect of Culture Medium on Biocalcification by *Pseudomonas Putida*, *Lysinibacillus Sphaericus* and *Bacillus Subtilis*. *Brazilian Journal Microbiology* 42, 499-507.
- Simkiss, K., Wilbur, K.M., 1979. *Biom mineralization - Cell Biology and mineral deposition*. Academic Press, San Diego, California, 337 pp.
- Simkiss, K., 1986. The processes of biomineralization in lower plants and animals-an overview. In Leadbeater, B.S.C., Riding, R., (eds): *Biom mineralization in Lower Plants and Animals*. Vol 30. Oxford University Press, NY, pp. 19-37.
- Simkiss, K., 1996. Calcium transport across calcium-regulated cells. *Physiological and Biochemical Zoology* 69, 343-350.
- Simonet Roda, M., Ziegler, A., Griesshaber, E., Yin, X., Rupp, U., Greiner, M., Henkel, D., Häusermann, V., Eisenhauer, A., Laudien, J. Schmahl, W.W., 2019a. Terebratulide brachiopod shell biomineralization by mantle epithelial cells. *Journal of Structural Biology* 207, 136-157.
- Simonet Roda, M., Griesshaber, E., Ziegler, A., Rupp, U., Yin, X., Henkel, D., Häusermann, V., Laudien, J., Brand, U., Eisenhauer, A., Checa, A.G. Schmahl, W.W., 2019b. Calcite fibre formation in modern brachiopod shells. *Scientific Reports* 9, 598.
- Simonet Roda M., Griesshaber, E., Henkel, D., Häusermann, V., Ziegler, A., Eisenhauer, A., Schmahl, W.W., 2020. Characterization of the biomineral microstructure of the modern brachiopod *Pajaudina atlantica*. *Lethaia*, accepted.
- Simonet Roda, M., Griesshaber, E., Angiolini, L., Rollion-Bard, C., Milner, S., Ye, F., Henkel, D., Häusermann, V., Eisenhauer, A., Brand, U., Gnägi, H., Schmahl, W.W., 2020b. Diversity of mineral and biopolymer assembly in modern terebratulide, rhynchonellide, thecideide and craniide brachiopod shells. Submitted.
- Sowerby, G.B., 1823. *The Genera of Recent and Fossil Shells, for the use of students in Conchology and Geology*. Stirling, London, 578 pp.

- Srivastav, A., 2011. An Overview of Metallic Biomaterials for Bone Support and Replacement. In Laskovski, A.N., (ed.): Biomedical Engineering, trends in material Science. InTech, pp. 153-168
- Stevens, K., Griesshaber, E., Casella, L.A., Iba, Y., Mutterlose, J., 2017. Belemnite biomineralization, development and geochemistry: the complex rostrum of *Neohibolites minimus*. *Palaeogeography, Palaeoclimatology, Palaeoecology* 468, 388-402.
- Stigall, A. L., 2018. How is biodiversity produced? Examining speciation processes during the GOBE. *Lethaia* 51, 165-172.
- Studart, A. R., 2012. Towards High-performance bioinspired composites. *Advanced Materials* 24, 5024-5044.
- Studart, A. R., 2013. Biological and bioinspired composites with spatially tunable heterogeneous architectures. *Advanced Functional Materials*. 23, 4423-4436.
- Studart, A. R., Erb, R. M., 2014. Bioinspired materials that self-shape through programmed microstructures. *Royal Society of Chemistry* 10, 1284-1294.
- Swart, P. K., 2015. The geochemistry of carbonate diagenesis: The past, present and future. *Sedimentology* 62, 1233-1304.
- Takayanagi, H., Asami, R., Abe, O., Miyajima, T., Kitagawa, H., Sasaki, K., Iryu, Y., 2013. Intraspecific variations in carbon-isotope and oxygen-isotope compositions of a brachiopod *Basiliola lucida* collected off Okinawa-jima, southwestern Japan. *Geochimica et Cosmochimica Acta* 115, 115-136.
- Tambutté, S., Holocomb, M., Ferrier-Pagés, C., Reynaud, S., Tambutté, E., Zoccola, D., Allemand, D., 2011. Coral biomineralization: From the gene to the environment. *Journal of Experimental Marine Biology and Ecology* 408, 58-78.
- Temereva, E.N., 2017. Ultrastructure of the coelom in the brachiopod *Lingula anatina*. *Journal of Morphology* 278, 997-1011.
- Temereva, E.N., Kuzmina, T. V, 2017. The first data on the innervation of the lophophore in the rhynchonelliform brachiopod *Hemithiris psittacea* : what is the ground pattern of the lophophore in lophophorates ? *BMC Evolutionary Biology* 17, 1-12.
- Thunberg, C. P., 1793. Tekning och Beskrifning på en stor Ostronsort ifrån Japan. *Kongliga Vetenskaps Academiens Nya Handlingar* 14, 140-142.
- Tourney, J., Ngwenya, B.T., 2009. Bacterial extracellular polymery substances (EPS) mediate CaCO₃ morphology and polymorphism. *Chemical Geology* 262, 134-146.
- Toyofuku, T., Matsuo, M. Y., De Nooijer, L. J., Nagai, Y., Kawada, S., Fujita, K., Reichart, G., Nomaki, H., Tsuchiya, M., Sakaguchi, H., Kitazato, H., 2017. Proton pumping accompanies calcification in foraminifera. *Nature Communications* 8, 14145.
- Tretsch, H., 1950. Observations on Vickers microhardness in calcite. *Mikroskopie* 5, 172-183.
- Ullmann, C.V., Frei, R., Korte, C., Lüter, C., 2017. Element/Ca, C and O isotope ratios in modern brachiopods: Species-specific signals of biomineralization. *Chemical Geology* 460, 15-24.

- Urey, H.C., Lowenstam, H.A., Epstein, S., Mckinney, C.R., 1951. Measurements of paleotemperatures and temperatures of the upper Cretaceous of England, Denmark, and the southeastern United States. *Geological Society of America Bulletin* 62, 399-416.
- Veizer, J., Fritz, P., Jones, B., 1986. Geochemistry of brachiopods: Oxygen and carbon isotopic records of Paleozoic oceans. *Geochimica et Cosmochimica Acta* 50, 1679-1696.
- Veizer, J. et al., 1999. $^{87}\text{Sr}/^{86}\text{Sr}$, $\delta^{13}\text{C}$ and $\delta^{18}\text{O}$ evolution of Phanerozoic seawater. *Chemical Geology* 161, 59-88.
- Veizer, J., Godderis, Y., François, L. M., 2000. Evidence for decoupling of atmospheric CO_2 and global climate during the Phanerozoic eon. *Nature* 408, 698.
- Veizer, J., Prokoph, A., 2015. Temperatures and oxygen isotopic composition of Phanerozoic oceans. *Earth-Science Reviews* 146, 92-104.
- Vinn, O., 2013. Occurrence formation and function of organic sheets in the mineral tube structures of Serpulidae (Polychaeta Annelida). *PLoS ONE*. 8, e75330.
- Von Allmen, K., Nägler, T.F., Pettke, T., Hippler, D., Griesshaber, E., Logan, A., Eisenhauer, A., Samankassou, E., 2010. Stable isotope profiles (Ca, O, C) through modern brachiopod shells of *T. septentrionalis* and *G. vitreus*: implications for calcium isotope paleo-ocean chemistry. *Chemical Geology* 269, 210-219.
- Wählich, F. C. et al. 2014. Surviving the surf: The tribomechanical properties of the periostracum of *Mytilus* sp. *Acta Biomaterialia* 10, 3978-3985.
- Walther, P., Ziegler, A., 2002. Freeze substitution of high-pressure frozen samples: the visibility of biological membranes is improved when the substitution medium contains water. *Journal of Microscopy* 208, 3-10.
- Walther, P., 2008. High-Resolution cryoscanning electron microscopy of biological samples. In Schatten, H., Pawley, J.B., (eds.): *Biological Low-Voltage Scanning Electron Microscopy* Springer, New York, pp. 245-261.
- Wang, S. et al. 2015. Nanostructured individual nacre tablet: a subtle designed organic-inorganic composite. *Cryst. Eng. Comm*, 17, 2964-2968.
- Watkins, J.M., Nielsen, L.C., Ryerson, F.J., DePaolo, D.J., 2013. The influence of kinetics on the oxygen isotope composition of calcium carbonate. *Earth and Planetary Science Letters* 375, 349-360.
- Wegst, U. G. K., Bai, H., Saiz, E., Tomsia, A. P., Ritchie, R. O., 2014. Bioinspired structural materials. *Nat. Mater.* 14, 23-36.
- Wegst, U. G. K., Bai, H., Saiz, E., Tomsia, A. P., Ritchie, R. O., 2015. Bioinspired structural materials. *Nature Materials* 14, 23-36.
- Weiner, S., Traub, W., 1980. X-ray diffraction study of the insoluble organic matrix of mollusk shells. *FEBS Letters* 111. 311-316.
- Weiner, S., Traub, W., 1984. Macromolecules in mollusk shells and their functions in biomineralization. *Transactions of the Royal Society B* 304, 421-438.

- Weiner, S., Wagner, H. D., 1998. The material bone: structure-mechanical function relations. *Annual Review of Materials Research* 28, 271-298.
- Weiner, S., Dove, P.M., 2003. An overview of biomineralization processes and the problem of the vital effect. In: Dove, P.M., De Yoreo, J.J., Weiner, S. (eds.): *Biomineralization - Reviews in Mineralogy and Geochemistry* Vol. 54. The Mineralogical Society of America, pp. 1-29.
- Weiner, S., Addadi, L., 2011. Crystallization Pathways in Biomineralization. *Annual Review of Earth and Planetary Sciences* 41, 21-40.
- Weiner, S., Talmon, Y., Traub, W., 1983. Electron diffraction of mollusc shell organic matrices and their relationship to the mineral phase. *International Journal of Biological Macromolecules* 5, 325-328.
- Weiner, S., Levi-kalishman, Y., Raz, S., Addadi, L., 2003. Biologically Formed Amorphous Calcium Carbonate. *Connective Tissue Research* 44, 214-218.
- Weiss, I.M., Tuross, N., Addadi, L., 2002. Mollusc Larval Shell Formation: Amorphous Calcium Carbonate Is a Precursor Phase for Aragonite. *Journal of Experimental Zoology* 293, 478-491.
- Wenzel, B., Lécuyer, C., Joachimski, M.M., 2000. Comparing oxygen isotope records of Silurian calcite and phosphate - $\delta^{18}\text{O}$ compositions of brachiopods and conodonts. *Geochimica et Cosmochimica Acta* 64, 1859-1872.
- Wheatly, M.G., 1999. Calcium homeostasis in crustacea: the evolving role of branchial, renal, digestive and hypodermal epithelia. *Journal of Experimental Zoology* 283, 620-640.
- Wheatly, M.G., Zhang, Z., Weil, J.R., Rogers, J.V., Stiner, L.M., 2001. Novel subcellular and molecular tools to study Ca^{2+} transport mechanisms during the elusive moulting stages of crustaceans: flow cytometry and polyclonal antibodies. *Journal of Experimental Zoology* 204, 959-966.
- Wheatly, M.G., Gao, Y., Gillen, C.M., 2007. Paradox of epithelial cell calcium homeostasis during vectorial transfer in crayfish kidney. *General and Comparative Endocrinology* 152, 267-272.
- Williams, A., 1953. North American and European stropheodontids: their morphologies and systematic. *Memoirs - Geological Society of America* 56, 1-67.
- Williams, A., 1966. Growth and structure of the shell of living articulate brachiopod. *Nature* 211, 1146-1148.
- Williams, A., 1968. A history of skeletal secretion among articulate brachiopods. *Lethaia* 1, 268-87.
- Williams, A., 1968. Evolution of the shell structure of articulate brachiopods. *Special Papers in Palaeontology* 2, 1-55.
- Williams, A., 1968. Shell structure of the Billingsellacean brachiopods. *Palaeontology* 11, 486-490.
- Williams, A., Wright, A.D., 1970. Shell structure of the Craniacea and other calcareous inarticulate Brachiopoda. *Special Papers in Palaeontology* 7, 1-51.

- Williams, A., 1973. The secretion and structural evolution of the shell of Thecideidine brachiopods. *Philosophical Transactions of the Royal Society B* 264, 439-478.
- Williams, A., 1997. Shell structure. In: Kaesler RL (ed.) *Treatise on Invertebrate Palaeontology. Part H, Brachiopoda 1 (Revised)*. Geological Society of America, Boulder, Colorado and University of Kansas Press, Lawrence, Kansas, pp. 267-320.
- Williams, A., Carlson, S.J., Brunton, C.H., 2000. Brachiopod Classification. In: Kaesler RL (ed.) *Treatise on Invertebrate Paleontology. Part H, Brachiopoda 2 (Revised)*. Geological Society of America, Boulder, Colorado and University of Kansas Press, Lawrence, Kansas, pp. 1-29.
- Williams, A., Brunton, C.H.C., Cocks, L.R.M. 2000. Strophomenata. In Kaesler, R.L. (ed.): *Treatise on Invertebrate Paleontology. Part H, Brachiopoda 2 (Revised)*. Geological Society of America, Boulder, Colorado and University of Kansas Lawrence, pp. 215-708.
- Williams, A., Carlson, S.J., 2007. Affinities of brachiopods and trends in their evolution. In: Selden PA (ed.) *Treatise on invertebrate Paleontology, Part H, Brachiopoda 6 (Revised)*. Geological Society of America, Boulder, Colorado and University of Kansas Press, Lawrence, Kansas, pp. 2822-2877.
- Williams, A., Cusack, M., 2007. Chemicostructural diversity of the brachiopod shell. In: Selden PA (ed.) *Treatise on Invertebrate Paleontology. Part H, Brachiopoda 6 (Revised)*, Geological Society of America, Boulder, Colorado and University of Kansas Press, Lawrence, Kansas, pp. 2397-2521.
- Yamamoto, K., Asami, R., Iryu, Y., 2010. Within-shelf variations in carbon and oxygen isotope compositions of two modern brachiopods from subtropical shelf environments off Amami-o-shima, southwestern Japan. *Geochemistry, Geophysics, Geosystems* 11, 1-16.
- Yamamoto, K., Asami, R., Iryu, Y., 2013. Correlative relationships between carbon-and oxygen-isotope records in two cooltemperate brachiopod species off Otsuchi Bay, northeastern Japan. *Paleontological Research* 17, 12-26.
- Ye, F., Crippa, G., Garbelli, C., Griesshaber, E., 2018a. Microstructural data of six modern brachiopod species : SEM, EBSD, morphometric and statistical analyses. *Data in Brief* 18, 300-318.
- Ye, F., Crippa, G., Angiolini, L., Brand, U., Capitani, G., Cusack, M., Garbelli, C., Griesshaber, E., Harper, E., Schmahl, W.W., 2018b. Mapping of modern brachiopod microstructure: A tool for environmental studies. *Journal of Structural Biology* 201, 221-236.
- Ye, F., Jurikova, H., Angiolini, L., Brand, U., Crippa, G., Henkel, D., Laudien, J., Hiebenthal, C., Smajgl, D., 2019. Variation in brachiopod microstructure and isotope geochemistry under low pH-ocean acidification-conditions. *Biogeosciences Discussions* 16, 617-642.
- Ye, F., Angiolini, L., Garbelli, C., Shen, S., 2020. Shell fabric of Palaeozoic brachiopods: patterns and trends. *Lethaia* 000, 1-21.
- Yin, X., Ziegler, A., Kelm, K., Hofmann, R., Watermeyer, P., Alexa, P., Villinger, C., Rupp, U., Schlüter, L., Reusch, T., Griesshaber, E., Schmahl, W.W., 2017. Formation and

- mosaicity of coccolith segment calcite of the marine algae *Emiliana huxleyi*. *Journal of Phycology* 54, 85-104.
- Yin, X., Griesshaber, E., Fernández-Díaz, L., Ziegler, A., García-García, F., Schmahl, W.W. 2019. Influence of Gelatin-Agarose Composites and Mg on Hydrogel-Carbonate Aggregate Formation and Architecture. *Crystal Growth and Design* 19, 5696-5715.
- Yin, X., Weitzel, F., Griesshaber, E., Fernández-Díaz, L., Jimenez-Lopez, C., Ziegler, A., Rodriguez-Navarro, A., Schmahl, W.W., 2020. Bacterial EPS in Agarose Hydrogels Directs Mineral Organization in Calcite Precipitates: Species-Specific Biosignatures of *Bacillus subtilis*, *Mycobacterium phley*, *Mycobacterium smagmatis*, and *Pseudomonas putida* EPS. *Crystal Growth and Design* 20, 4402-4417.
- Zeebe, R.E., Wolf-Gladrow, D., 2001. CO₂ in seawater: equilibrium, kinetics, isotopes (No. 65). Gulf Professional Publishing, 360 pp.
- Ziegler, A. 1997. Immunocytochemical localization of Na⁺, K⁺-ATPase in the calcium-transporting sternal epithelium of the terrestrial isopod *Porcellio scaber* Latr. (Crustacea). *Journal of Histochemistry and Cytochemistry* 45, 437-446.
- Ziegler, A. 2002. X-ray microprobe analysis of epithelial calcium transport. *Cell Calcium* 31, 307-321.
- Ziegler, A., Weihrauch, D., Towle, D.W., Hagedorn, M., 2002. Expression of Ca²⁺-ATPase and Na⁺/Ca²⁺-exchanger is upregulated during epithelial Ca²⁺ transport in hypodermal cells of the isopod *Porcellio scaber*. *Cell Calcium* 32, 131-141.
- Ziegler, A., Weihrauch, D., Hagedorn, M., Towle, D.W., Bleher, R., 2004. Expression and polarity reversal of V-type H⁺-ATPase during the mineralization-demineralization cycle in *Porcellio scaber* sternal epithelial cells. *Journal of Experimental Biology* 207, 1749-1756.
- Ziegler, A., Fabritius, H., Hagedorn, M., 2005. Microscopical and functional aspects of calcium-transport and deposition in terrestrial isopods. *Micron* 36, 137-153
- Ziveri, P., Stoll, H., Probert, I., Klaas, C., Geisen, M., Ganssen, G., Young, J., 2003. Stable isotope “vital effects” in coccolith calcite. *Earth and Planetary Science Letters* 210, 137-149.

Appendices

Appendix I. Material description

Modern brachiopods

Magellania venosa (Dixon, 1789)

Class Rhynchonellata - Order Terebratulida - Family Terebratellidae

Magellania venosa is a benthic marine brachiopod which lives in a depth range of 2 - 3010 meter (Foster, 1989). This species can be found in temperate water of the Southeast Pacific and Southwest Atlantic and they commonly live fixed to hard substrate, such as corals or rocks, with a pedicle (Häussermann and Försterra, 2009).

The investigated samples were originally obtained from Comau Fjord, located in southern Chile, in collaboration with Huinay Scientific Field Station. Afterwards they were cultured at GEOMAR, Helmholtz Centre for Ocean Research, Kiel (Germany), in tanks where the original ocean water conditions of Comau Fjord were imitated (Fig. A1). The samples were taken at 21 meters depth, the water temperature was of 11 °C average and the salinity of 30.3 PSU.

Our objective was to study for this species the hard and soft tissues as well as the relation of the latter. Especially for the soft tissues the preservation state of the individuals needed to be extremely high. The brachiopods were provided alive in water with the culturing conditions. The samples were kept alive for chemical preparation in order to preserve the ultrastructure as well as possible.

We selected juvenile specimens for chemical fixation and high pressure freezing – freeze substitution, as in these stages the growth rate is higher (Baumgarten et al., 2013). For measuring the size of the individuals we took the length of their longitudinal axes. The samples were between 5 and 7 millimeters long for chemical fixation and 4-5 millimeters for High Pressure Freezing preparation. The soft tissue was studied following the latter methods under TEM and SEM. The hard tissue was characterized with SEM and EBSD.

Pajaudina atlantica (Logan, 1988)

Class Rhynchonellata - Order Thecideida – Family Thecideidae

Pajaudina atlantica is a benthic marine brachiopod which lives in a range of 5-1000 meter water depth in subtropical environment (Logan, 1988). The species distribution covers the Eastern Central Atlantic. The individuals used for this work were sampled at the Canary Islands. They commonly live fixed to hard substrates and they grow cemented to the neighboring individuals. Their valves are very thick and compact in relation with their own shell proportions.

The investigated specimens were sampled in Punta Malpique, Palma (Canary Islands) at 14 meters water depth. The water conditions were 22 °C and the salinity was 36.3 PSU. The sampling and subsequent culturing and collection were done by Daniela Henkel and Hana Jurikova from GEOMAR, Helmholtz Centre for Ocean Research, Kiel, Germany (Fig. A2).



Figure A1. Photograph provided by Daniela Henkel (GEOMAR, Helmholtz Centre for Ocean Research, Kiel, Germany) of *Magellania venosa* in a culturing tank.

For this species we were interested in the microstructure of the shell and the elemental and isotopic characterization. Samples of 3-4 mm length were characterized with SEM, EBSD and AFM. Trace element compositions were measured using laser ablation coupled to an ICP-MS (Inductively Coupled Plasma Mass Spectrometry). The samples used for ICP-MS analysis measured in the longitudinal axes 16 mm.



Figure A2. Photograph provide by Daniela Henkel (GEOMAR, Helmholtz Centre for Ocean Research, Kiel, Germany) of *Pajaudina atlantica* in situ.

Others

From the four different extant orders that secrete calcitic shell (Craniidae, Rhynchonellidae, Thecideidae and Terebratulidae). Some species were selected for Chapter 2.4. In these samples we performed FE-SEM, STEM, AFM and EBSD measurements. These samples are compiled in Figure S 2.4.1.

Fossil brachiopods

We worked with fossil thecideide brachiopods of different ages, from the Late Triassic to Pleistocene. The study was focused in their shell microstructures that were characterize with SEM and EBSD. In addition, we preformed some EDX and Catodoluminiscense measurements.

The data was compare with the one obtained from modern thecideide representatives as *Pajaudina atlantica* or *Kakanuella chatamensis*.

We selected up to two well preserve samples per species. Their name, age and sampling location can be found in the following table.

Table A1. Samples information and numbers for fossil thecideide.

Species	Age	Original location	Depository number	Repository
<i>Thecospira tenuistriata</i> Bittner, 1890	Late Triassic	Alpe di Specie, Italy	MPU5784-4 MPU5804	Museo di Paleontologia Dipartimento di Scienze della Terra Università degli Studi di Milano
<i>Thecospira tyrolensis</i> (Loretz, 1875)	Late Triassic	Alpe di Specie, Italy	MPU5484-4	Museo di Paleontologia Dipartimento di Scienze della Terra Università degli Studi di Milano
<i>Bactrynum bicarinatum</i> (Emmrich, 1855)	Late Triassic	Elberg Austria	E100-18-17	Ludwig Maximilian University of Munich
<i>Neothecidella ulmensis</i> (Quenstedt, 1858)	Late Jurassic (middle Oxfordian)	Bałtów, Poland	LMU-NU01	Ludwig Maximilian University of Munich
<i>Thecidiopsis digitata</i> (Sowerby, 1823)	Late Cretaceous	Petersberg, Maastricht, Netherlands	LMU-TD01	Ludwig Maximilian University of Munich
<i>Thecidea papillata</i> (Schlotheim, 1813)	Late Cretaceous	Symphorien, Mons, Belgium	LMU-TPLC01	Ludwig Maximilian University of Munich
<i>Thecidea papillata</i> (Schlotheim, 1813)	Paleocene	Ciply near Mons, Belgium	LMU-TPP01	Ludwig Maximilian University of Munich
<i>Lacazella mediterranea</i> (Risso, 1826)	Late Eocene	Dnipropetrovsk, Ukraine	LMU-LME01	Ludwig Maximilian University of Munich
<i>Lacazella mediterranea</i> (Risso, 1826)	Late Oligocene	Peyrere Aquitaine Basin, France	LMU-LMO01	Ludwig Maximilian University of Munich
<i>Thecidellina</i> sp.	Pleistocene	Curaçao, Caribbean	UF 325201	Ludwig Maximilian University of Munich
<i>Pajaudina atlantica</i> Logan, 1988	Recent	Palma, Canary Islands, Spain	LMU-PA008	Ludwig Maximilian University of Munich
			LMU-PA009	
			LMU-PA010	
			LMU-PA011	

Appendix II. Applied Methods

Transmission electron microscopy (TEM)

A Zeiss 912 TEM (Zeiss, Jena, Germany) equipped with an Omega energy filter, a goniometer stage and a 2k x 2k pixel camera (TRS, Moorenweis, Germany) was used to image the sections at 8000 times magnification and 120 kV acceleration voltage using only elastically scattered electrons. To screen a large area of the outer mantle epithelium, at high resolution up to 300 images were recorded at rectangular grids. The images were then aligned into large composite images using the TRS software. These composite images were used for the structural and numerical analysis.

High Pressure Freezing and Freeze Substitution (HPF-FS)

In the high pressure freeze living animals or material are rapidly chilled to liquid nitrogen temperature while exposed simultaneously to 2100 bar pressure. The animals become frozen as “vitreous ice” ideally preventing the formation of any detectable ice crystals. This rapid freezing preserves the animal’s true shape of all cell organelles.

This method gives improved views of intercellular junctions, including gap junctions, septate junctions and basal lamina. (<http://45.63.20.54/EMmethods/HPF.htm>)

The method was not easy to apply to our samples as the shells are consisted of materials with very different properties (hard and soft tissues) that are in very close contact to each other. Small organelles and the contact between shell and the outer mantle epithelium were especially difficult to preserve using this method. The well preserved samples, showed very good preservation of the membranes and in addition, different junctions could be differentiated.

Field emission scanning electron microscopy (FE-SEM)

Samples were mounted on aluminum holders using self-adhesive carbon pads and conductive glue. Samples were then coated with 4 nm of carbon using a BAF 300 (BAL-TEC, Balzers, Liechtenstein). Samples were analyzed with a Hitachi S5200 field emission scanning electron microscope (FE-SEM) using the converted backscattered electron signal to obtain so called composite rich images (Walther, 2008) using 20 μ A emission current and 3kV acceleration voltage in analysis mode of the microscope.

Electron backscatter diffraction (EBSD)

Once the samples are highly polished, they are coated with 4– 6 nm of carbon for EBSD and EDX measurements and mapping. EBSD measurements were carried out on a Hitachi SU5000 field emission SEM, equipped with an Oxford EBSD detector. The SEM was operated at 15-20 kV and measurements were indexed with the CHANNEL 5 HKL software (Schmidt and Olesen, 1989, Randle and Engler, 2000). The EBSD measurements are presented with colour-coded crystal orientation maps, with their corresponding pole figures, and with band contrast measurements. Band contrast data gives the signal strength of the EBSD–Kikuchi diffraction pattern and is displayed as a greyscale component of EBSD scanning maps. A high strength of the EBSD signal, when a crystal is detected, presents bright colours. In comparison, organic matter appears dark/black colours as it gives only poor or non-existing signal. The pole figures

give information about co-orientation statistics of the different points measured on the selected area. From the plotted points we obtain the Multiple of Uniform random Distribution or MUD value. This value is a measure of crystal co-orientation and can be translate into texture sharpness of the scanned area. The co-orientation in the shell is high when the MUD values are high whereas low MUD values indicate a low or arbitrary co-orientation.

EBSD is an automated micro-diffraction method which provides space-resolved information on the phase state of the samples and crystallite orientation of the constituting mineral. EBSD band contrast images highlight the shell microstructures.

Atomic Force Microscopy (AFM)

Samples were measured in contact mode with a JPK NanoWizard II AFM using silicon cantilevers. The measurements of height, lateral and vertical deflection traces were processed with the NanoWizard® IP image processing software and Gwyddion free and open source software. We used the “Gold” scale for colouring the measurements. The height trace shows the surface height of the measured area, while lateral and vertical deflection traces are the result of the lateral and vertical interactions between the cantilever tip and the sample surface. With lateral deflection traces, the properties of the different materials can be observed in the shell. While bright/yellow areas match with the location of the organic membranes darker areas correspond to crystallite regions (calcite fibres). The AFM results were present with vertical and lateral deflection trace measurements.

Morphometry

For the morphometric analysis, we performed a point-counting of organelles with the free software Fiji and JMicroVision aiming to have a rough idea of the organelles distribution and their relation with the shell secretion processes. The analyses were done in 2D panorama images, compound of 120 to 300 images, of 8000 magnification each.

Out of more than 150 sections and 60 panorama images we selected 18 panorama images and 48 areas within them. For the selection we took the preservation of the OME into account to avoid mechanical destruction or areas showing some biological stress and also considered a consistent statistical representation of the region each area they represent. For this, we compare the TEM data with the one obtained (1) via other methods (SEM, HPF-FS and lower magnification TEM images) and (2) gathered in previous studies (Williams, 1966, 1968a, 1968b and 1997). The statistics were made in 2 different individuals

For the quantitative analysis, we distinguished four different regions of the OME. In the central part, we compared OME that is not attached to the organic membrane of calcite fibres (cr-s, secreting OME of the central region) with those attached to the organic membranes with tonofilaments (cr-a, non-secreting OME of the central region). In addition, we quantified the thin epithelium at the middle region of the punctae (pt) as an additional reference of a non-mineral secreting area of the epithelium. Finally, we compared the multi-cell layered OME of the part of the commissure underneath calcite fibres (com) with the single-cell layered OME of the central region (cr-all).

The volume fraction of various organelles were determined by counting randomly positioned points on predefined structures (classes) within pre-defined test fields using the open source software JMicroVision Image analysis system (Roudit, 2008). The organelles were divided into 16 different classes: cytoplasm, tonofilaments, nucleus, mitochondria, lysosomes-endosomes (dark and white), vesicles (dark and white), Golgi apparatus, Golgi vesicles, rough endoplasmic reticulum (rER), smooth endoplasmic reticulum (sER), multivesicular bodies, glycogen, others, and extracellular space (Figs. A3-A7).

The number of random points was set either to 250 or 500 depending on the size of the test field. Test areas were defined using the implemented “area editor” so the regions outside the epithelium were at a minimum. Evolution plots created by the software (see fig.3) were used to evaluate the representativeness of the calculated volume fractions of organelles.

For each test field the length of the epithelium “ E_L (μm)” and the testfield area “ A_T (μm^2)” was determined and the percentages of the various classes “ A_p (%)” in “ A_T ” were measured.

The absolute area “ A_O ” of each class was calculated by

$$A_O = A_T * (A_p / 100) (\mu\text{m}^2)$$

The areas of the extracellular space and the nucleus were excluded by calculating the area of the cytoplasm “ A_C ” within the test field by

$$A_C = (\sum A_O - A_{O(\text{nucleus})} - A_{O(\text{extracellular space})}) (\mu\text{m}^2)$$

The volume fraction of each class “ V_O ” of the cytoplasm without the nucleus equals the area fraction “ A ” and was calculated by

$$V_O = A = (A_O / A_C) * 100 (\%)$$

From the area fraction “ A ” of classes, we calculated the absolute volume V_A of classes per $10 \mu\text{m}^2$ epithelium area by

$$V_A (\mu\text{m}^3 / \mu\text{m}^2) = A_O / E_L * 10 (\mu\text{m}^2 / \mu\text{m})$$

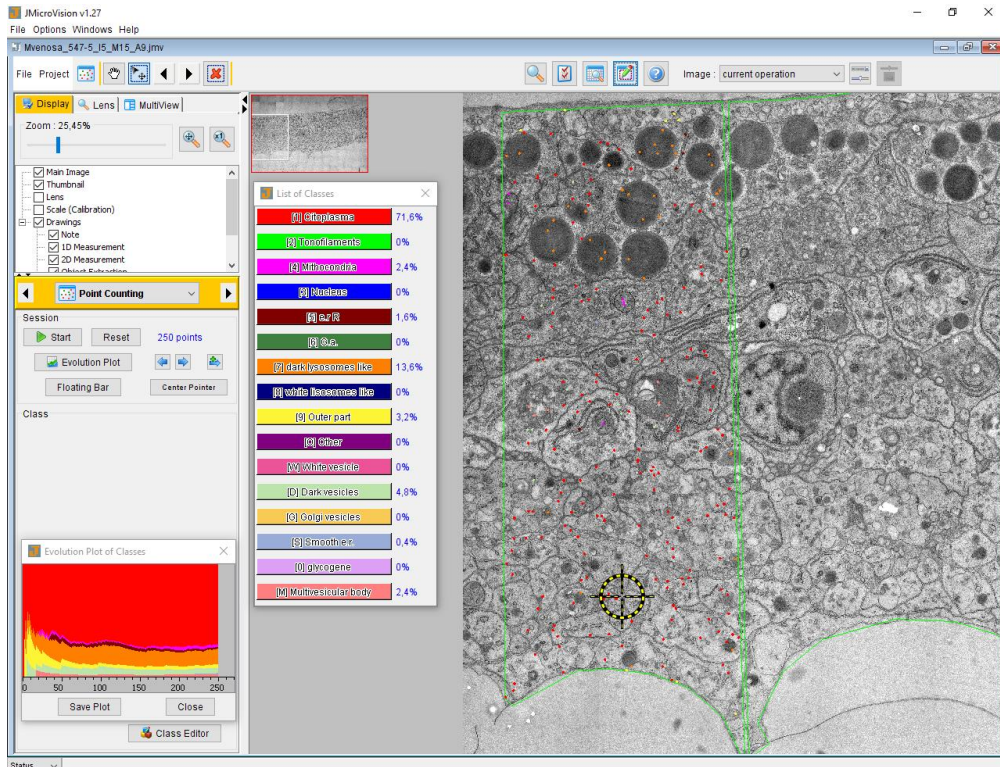


Figure A3. “Point Counting” in *M. venosa* outer epithelium at the region of the commissure. The areas were previously selected manually (in green) as well as the “List of classes”. The pointer (in yellow and black) jumps from one point to another automatically, once the point is classified inside one of the classes, creating a random/non-selective net. The “Evolution Plot of classes” shows when the percentages of the different classes get stable.

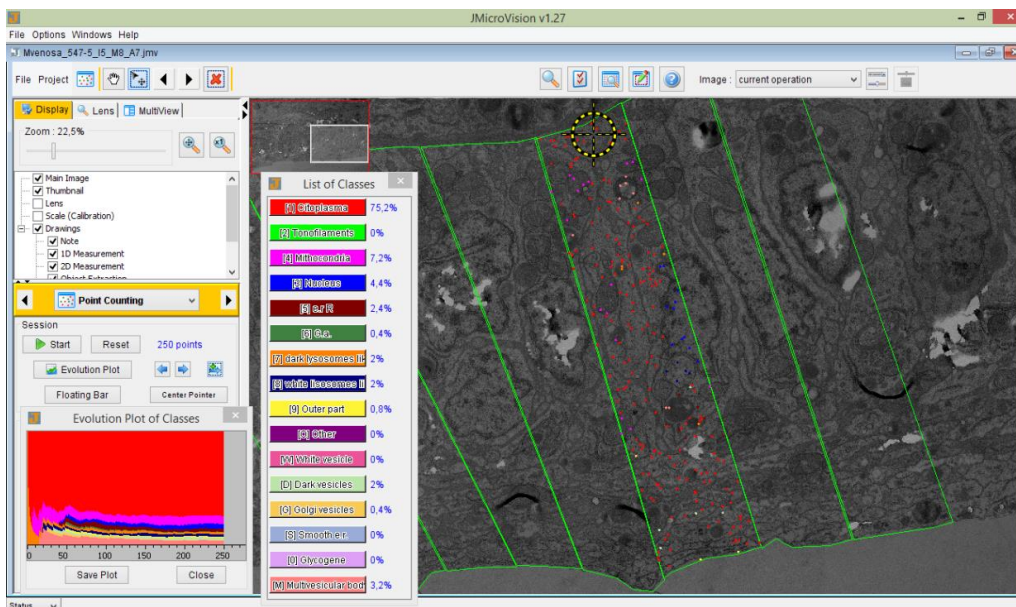


Figure A4. Overview of the “Point Counting” option of JMicroVision program in a selected area of *M. venosa* outer epithelium at the commissure.

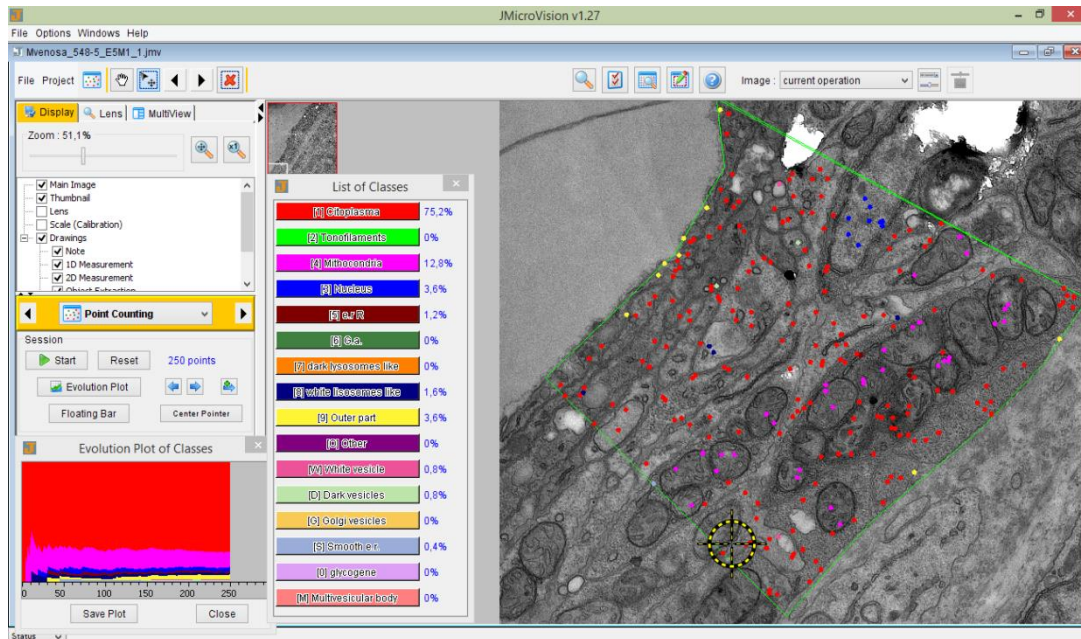


Figure A5. Detail of “Point Counting” in *M. venosa* outer epithelium at the region of the commissure.

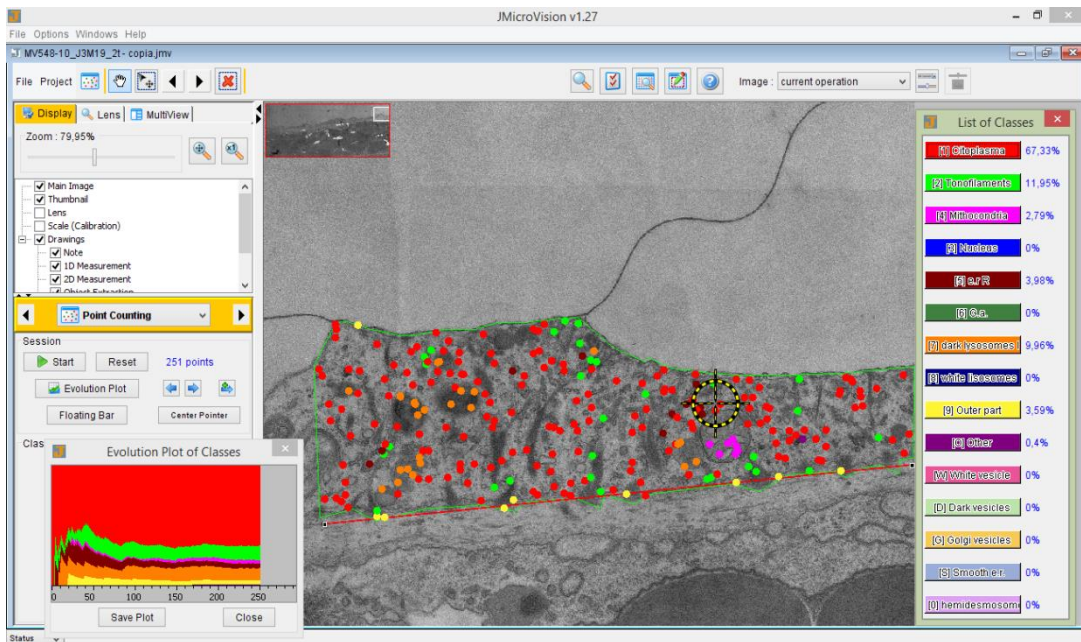


Figure A6. Detail of “Point Counting” in *M. venosa* outer epithelium at the central shell region.

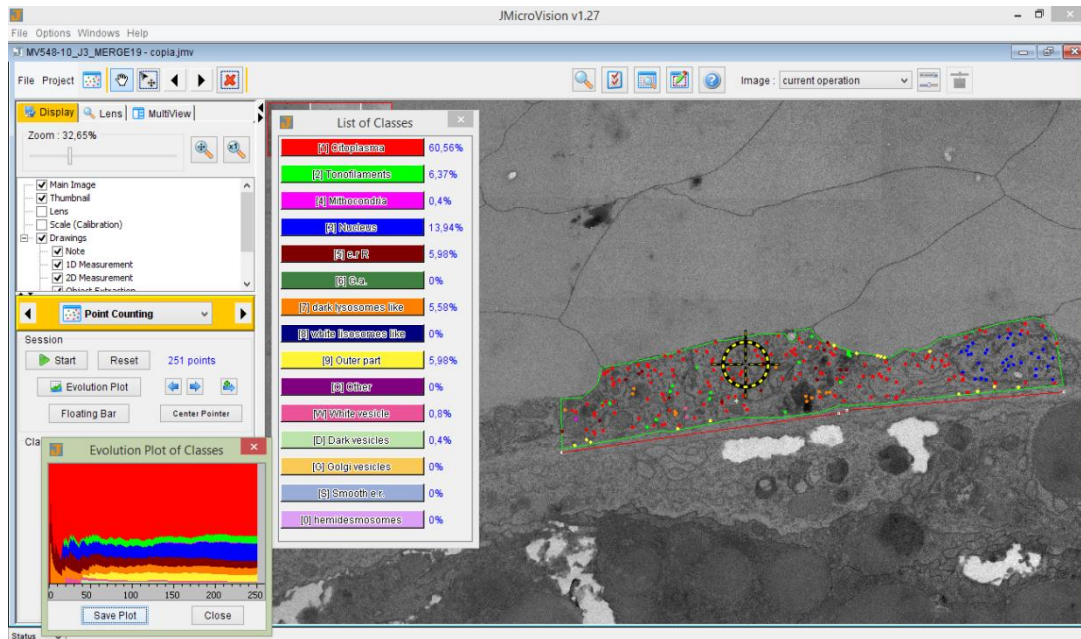


Figure A7. Overview of “Point Counting” option in *M. venosa* outer epithelium at the central shell region.

For calculating the area of the apical and basal plasma membranes as well as for the outer membrane of the mitochondria we followed the method of Merz (1967). The Merz grid plugin for ImageJ/Fiji (Research Services Branch, National Institute of Mental Health, Bethesda, MD, USA), was superimposed an array of coherent semicircular lines to the images (Figs. A8-A9). The profile length “ L_p ” of the plasma membrane (apical and basal cell membrane) and the outer membrane of the mitochondria was determined by counting the intersections of the Merz grid lines with the membranes inside the test fields. L_p was calculated by:

$$L_p = Nd (\mu\text{m})$$

with “N” as the number of intersections between the grid lines and the membranes and “d” the diameter of the semicircles in each test field.

L_p was normalised to $1\mu\text{m}$ epithelium length by

$$L = L_p/E_L \text{ with "E}_L\text{" the epithelial length within the test field.}$$

The areas of the membranes “ A_M ” per μm^2 area of epithelium was calculated by

$$A_M = L \times 1.273 (\mu\text{m}^2) \text{ (Merz, 1967)}$$

All calculations were done using Microsoft Excel for Mac version 15.33.

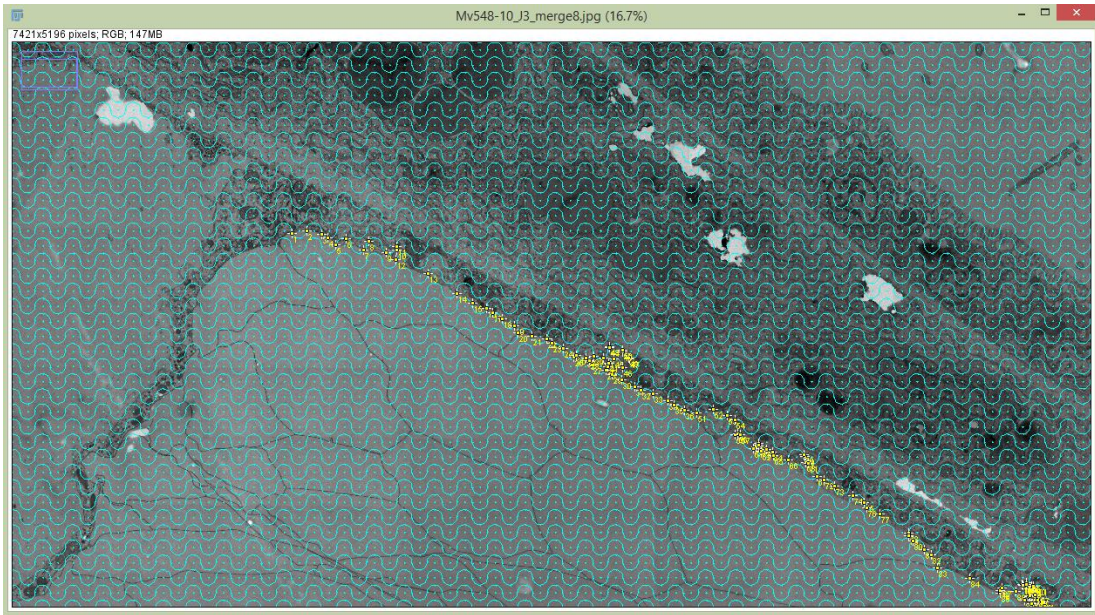


Figure A8. Overlap of the Merz grid on a TEM panorama image. In yellow the points of intersections between the grid and the apical membrane of the epithelium at the central shell region of *M. venosa*.

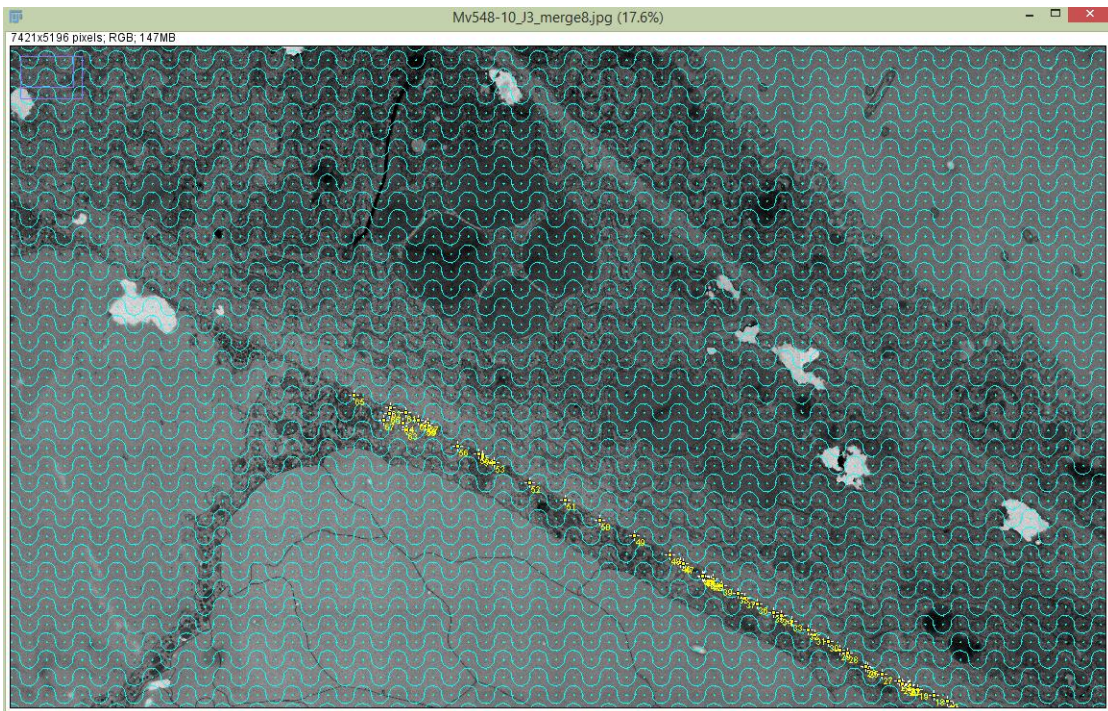


Figure A9. Overlap of the Merz grid on a TEM panorama image. In yellow the points of intersections between the grid and the the basal membrane of the epithelium at the central shell region of *M. venosa*.

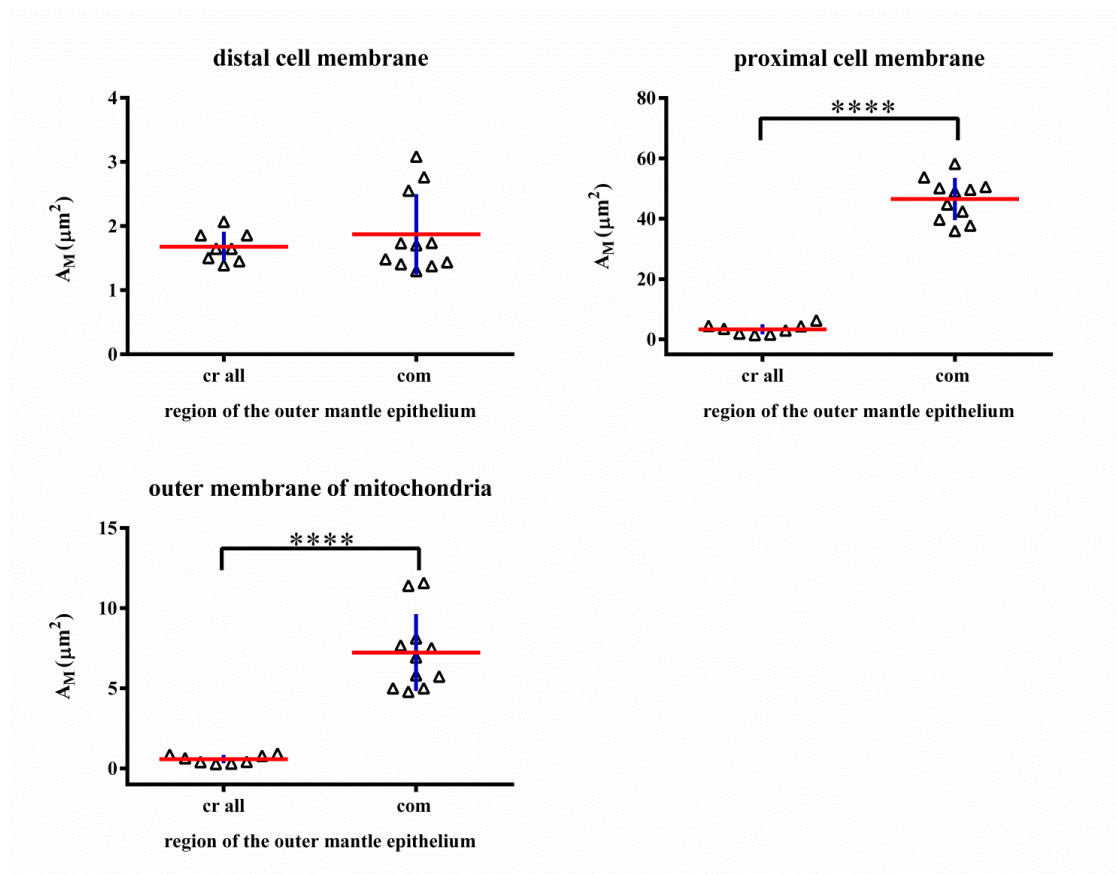
Statistical analysis

To facilitate the comparison of the TEM data obtained for the different regions of the OME and to see if it was representative, we performed some statistical analyses.

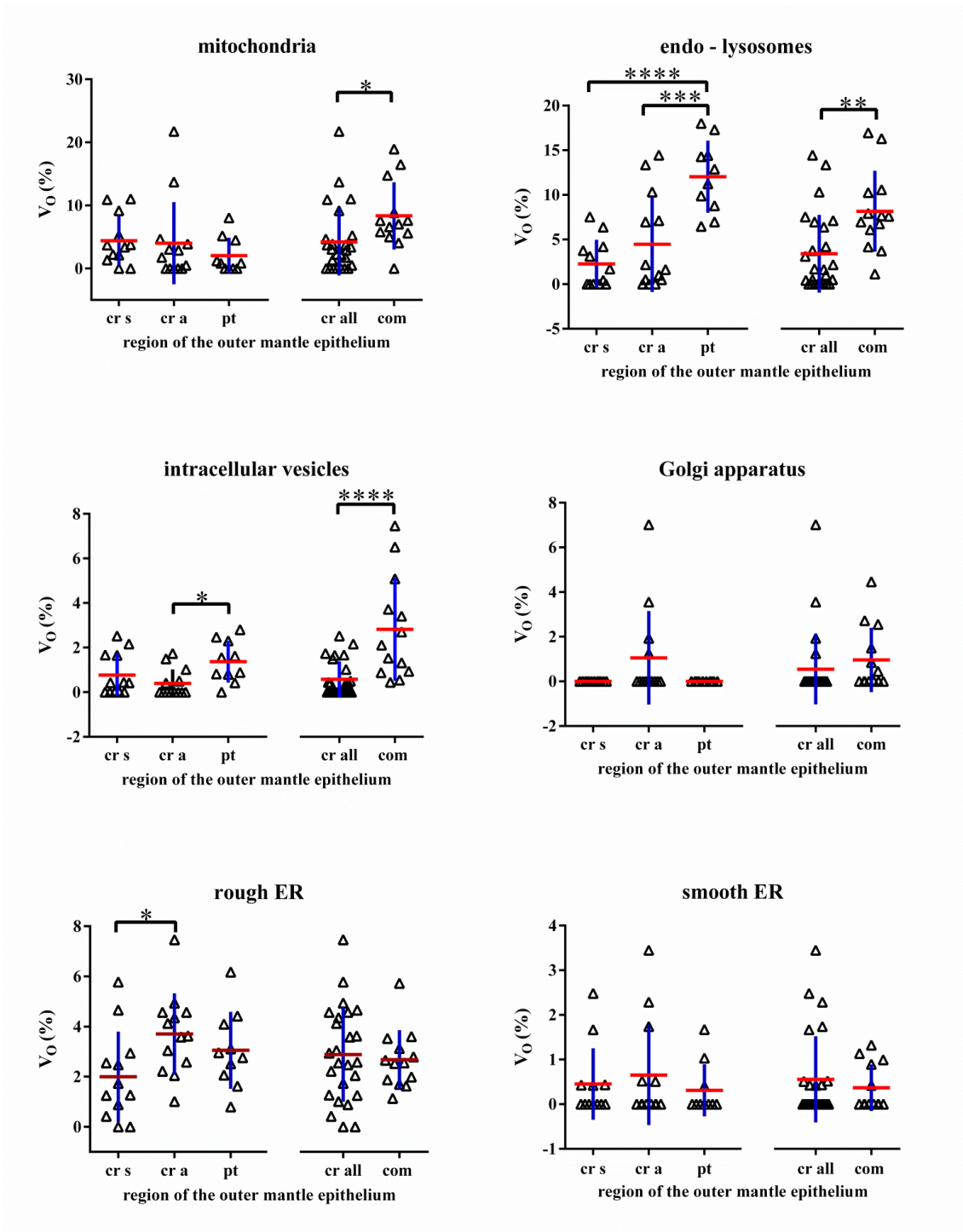
GraphPad Prism software version 6.00 for Mac (GraphPad Software, La Jolla California USA, www.graphpad.com) was used for the statistical analysis and graphical representation. Means and standard deviations were calculated for the volume fractions V_O , the absolute volume of each class was normalized to $10\mu\text{m}^2$ of epithelium V_A , and the membrane areas were normalized to one square micrometer epithelium A_M for the apical and basal cell membrane, and the outer membrane of the mitochondria.

One way ANOVA was used to test the significance of differences in the mean values for the volume fraction V_O and area per $10\mu\text{m}$ epithelial lengths of classes A_O . To account for multiple comparisons, Sidiak's multiple comparisons test were used to assign significant differences between the mean values for the mineral secreting central region (cr-s), the non-secreting attached areas of the central region (cr-a) and the middle region of the punctae (pt). T-tests were used to assign significant differences between the mean values of the pooled central regions and the commissure for V_O , V_A and A_M .

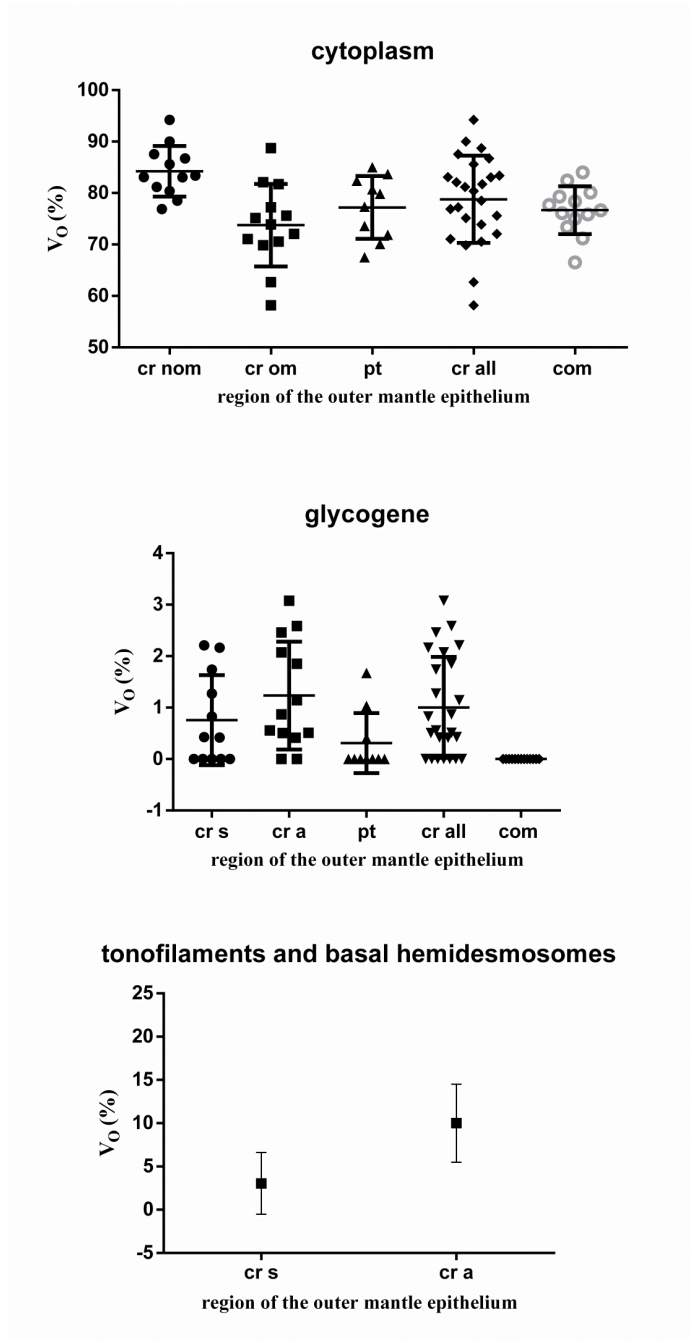
Some results were already published in Simonet Roda et al. 2019a; here it is added all the significant and non-significant statistical analysis obtained for the different organelles for the different shell regions. The raw data used for Graphs 1 to 5 is included in Appendix V.



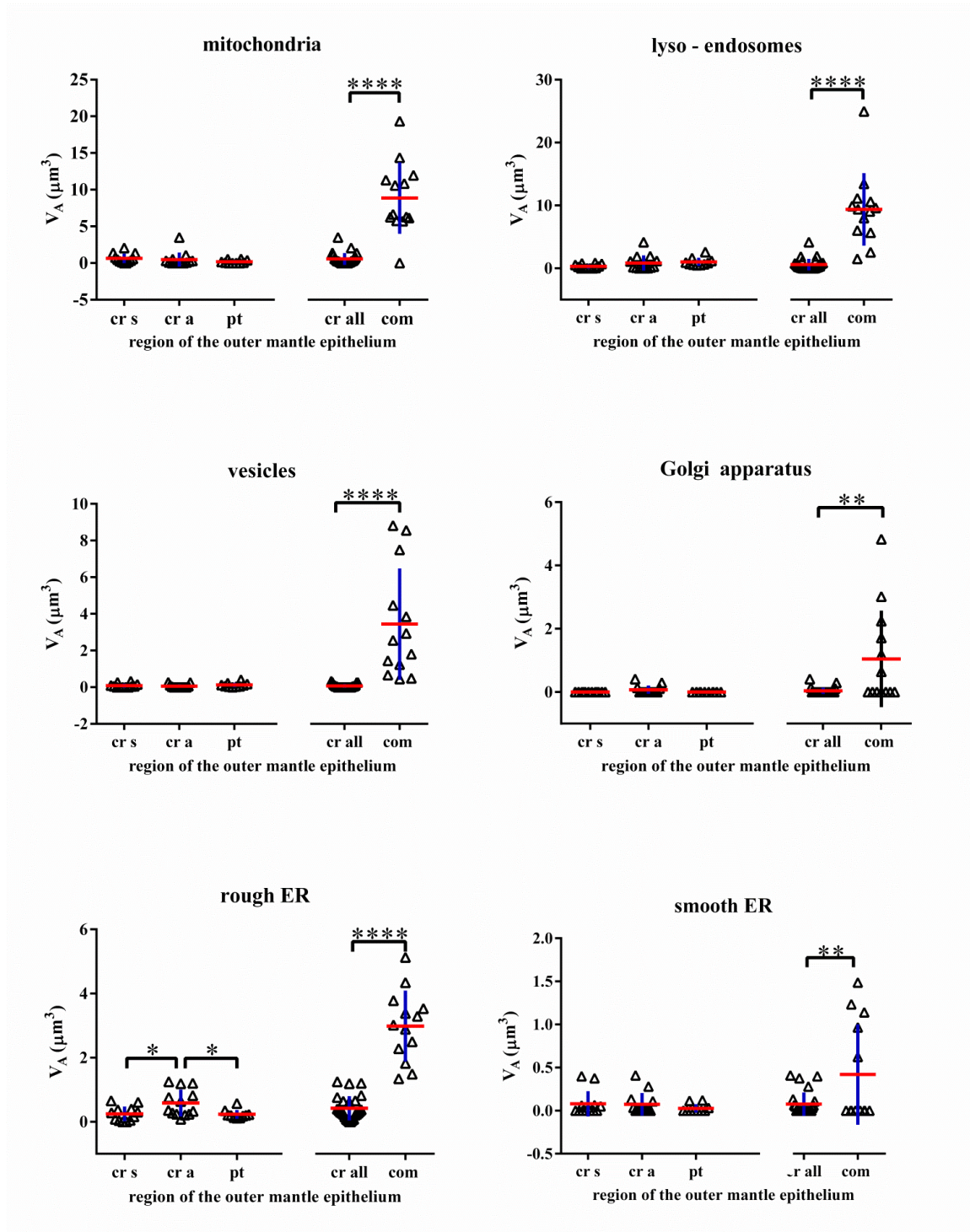
Graph A1. Membrane area per $10\mu\text{m}^2$ of: apical and proximal cell membrane and membrane area of the outer membrane of mitochondria. Results were obtained for the central shell portion (secreting and not secreting: cr all) and the commissure (com). Results are plotted with the mean (indicated with horizontal red lines in the graphs) and the standard deviation (indicated with vertical blue lines in the graphs). Stars indicate significant differences of mean values for a given organelle between different outer mantle epithelium regions: ****: $P \leq 0.0001$.



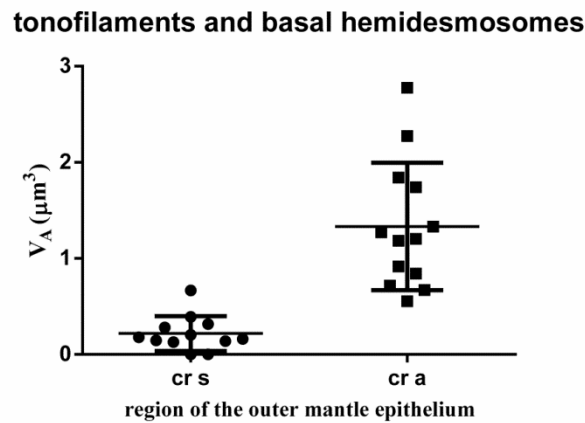
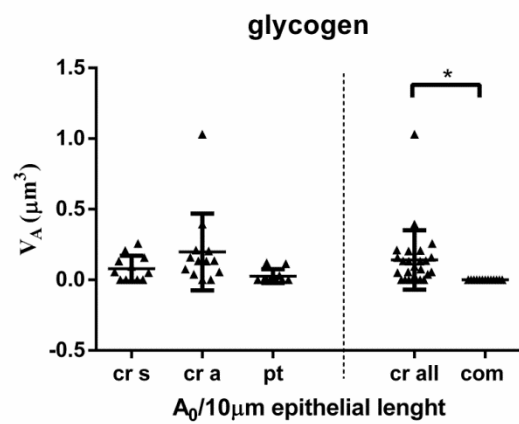
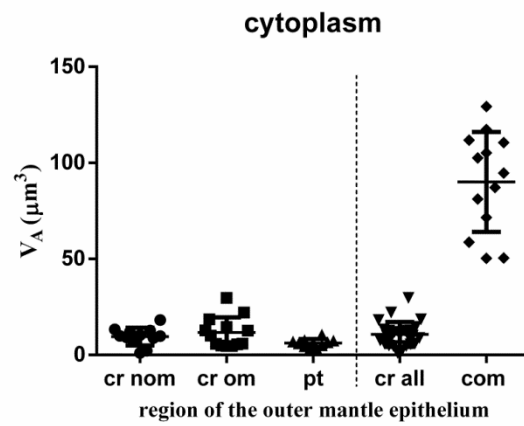
Graph A2. Volume fraction in percentage of membrane-bound organelles: mitochondria, endo-lysosomes, intracellular vesicles, Golgi apparatus, and rough and smooth endoplasmatic reticulum (ER) in different regions of the outer mantle epithelium. Central shell region that can secrete mineral is indicated as “cr s”, central shell region not involved in secretion as “cr a”, punctum as “pt”, secreting plus not secreting central shell portions as “cr all” and commissure as “com”. Stars indicate significant differences of mean values for a given organelle between different outer mantle epithelium regions: *: $P \leq 0.05$; **: $P \leq 0.01$; ***: $P \leq 0.001$; ****: $P \leq 0.0001$.



Graph A3. Volume fraction, in percentage, for cytoplasm, glycogen and tonofilaments plus hemidesmosomes within the different regions of the outer mantle epithelium. Central shell region that can secrete mineral is indicated as “cr s”, central shell region not involved in secretion as “cr a”, punctum as “pt”, secreting plus not secreting central shell portions as “cr all” and commissure as “com”.



Graph A4. Volume of organelles (mitochondria, lyso- endosomes, vesicles, Golgi apparatus, rough endoplasmatic reticulum (rough ER), smooth endoplasmatic reticulum (smooth ER)) in the cells of $10 \mu\text{m}^2$ of the outer mantle epithelium for different OME regions: Results are plotted with the mean (indicated with horizontal red lines in the graphs) and the standard deviation (indicated with vertical lines in the graphs). Stars indicate the significant differences of mean values for a given organelle between different outer mantle epithelium regions: *: $P \leq 0.05$; **: $P \leq 0.01$; ***: $P \leq 0.001$; ****: $P \leq 0.0002$.



Graph A5. Volume of cytoplasm, glycogen, tonofilaments and basal hemidesmosomes in the cells of $10\ \mu\text{m}^2$ of the outer mantle epithelium for different OME regions: Results are plotted with the mean (indicated with horizontal red lines in the graphs) and the standard deviation (indicated with vertical lines in the graphs). Stars indicate a significant difference of mean values for a given organelle between different outer mantle epithelium regions: *: $P \leq 0.05$

Appendix III. Sample Preparation Procedures

Chemical fixation and decalcification

Aiming to preserve the epithelium as it is during secretion of the shell, the living samples were treated following a specific protocol for organic fixation, out of 8 individuals. A total of 40 pieces of the shell with the mantle tissue attached were dissected from central and commissure regions of both the brachial (ventral) and pedicular (dorsal) valves.

For the fixation we used Paraformaldehyde (PFA) and Glutaraldehyde (GA). While PFA penetrates faster the tissues, GA has a slower action but it lead to a better preservation of the ultrastructure. Both chemicals were diluted in a saline buffer (0.35 mol L^{-1} saccharose and 0.17 mol L^{-1} NaCl in 0.2 mol L^{-1} Na-cacodylate buffer with a pH of 7.7) to imitate the water conditions where the animals lived.

During the embedding process we used different chemicals as OsO_4 and uranyl acetate to increase the contrast of the proteins and membranes. With this protocol the different organelles and the cell can be easily seen and distinguish under the TEM.

Two different fixation media were used in two different animals to observe if the preservation improved by increasing the concentration of PFA and GA. The preservation was good in both cases and no differences could be observed. Fixation medium A was prepared by mixing equal volumes of filtered seawater from the culture of *Magellania venosa* containing 2% paraformaldehyde and 2% glutaraldehyde with a solution of 0.35 mol L^{-1} saccharose and 0.17 mol L^{-1} NaCl in 0.2 mol L^{-1} Na-cacodylate buffer (pH 7.7). Fixation medium B was prepared in the same way, however, with 3.2% paraformaldehyde and 4% glutaraldehyde in the filtered seawater. No differences in the preservation of the structure were observed between the fixation procedures. After 17 hours in fixation solution at $4 \text{ }^\circ\text{C}$, 8 samples, one from each region and valve of the animals, were decalcified for 14 days in a solution containing 0.25 mol L^{-1} HEPES as buffering agent, 0.05 mol L^{-1} EDTA and 1% glutaraldehyde. All samples were washed three times with 0.1 M Na-cacodylate buffer (7.7 pH) and postfixed in the same buffer containing 1% OsO_4 and 0.9% $\text{K}_4\text{Fe}(\text{CN})_6 \cdot 3\text{H}_2\text{O}$ for one hour. $\text{K}_4\text{Fe}(\text{CN})_6 \cdot 3\text{H}_2\text{O}$ is used to change the redox of the reaction. After washing with bidest-distilled water the samples were dehydrated in an ascending series of isopropanol solutions (30, 50, 70 and 90%), and contrasted with 2% uranyl acetate (in 100 % ethanol for 30 minutes, washed 3 times for 30 minutes each in 100% isopropanol and two times for 5 minutes in propylenoxid and embedded in EPON resin. To avoid detachment of the OME from the edge of the commissure two *M. venosa* were chemically fixed in whole by injecting fixation solution A through the pedicle opening, samples were then kept in fixation solution. After several month, regions of the commissure were dissected off and postfixed and dehydrated in the same way as described above before embedding in EPON resin. Due to the prolonged fixation time part of the shell mineral had dissolved.

High Pressure Freezing and Freeze Substitution

M. venosa samples, no longer than 6 mm, were dissected in sea water of the culture. Shell pieces with the mantle epithelium attached were cut from the commissure and central region of both valves using scalpels. Samples were transferred to hexadecane

and placed in aluminium planchets with an outer diameter of 3 mm and a 200 µm deep cavity. The planchets were covered with the flat side of another planchet. Samples were then high pressure frozen with a Wohlwend HPF Compact 01 high-pressure freezer (Engineering Office M. Wohlwend GmbH) within 30 ms at a pressure of 2.3×10^8 Pa. The planchet sandwiches were then opened and freeze substituted overnight in 0.2% OsO₄, 0.1% uranyl acetate and 5% H₂O in acetone from -90°C to 20°C (Walther and Ziegler, 2002). Samples were then embedded in EPON. Embedded samples were cut open using a diamond trimming knife (Diatome, Liechtenstein) and a Reichert Ultracut ultra microtome (Leica) to expose the mineralised shell. Part of these samples were then decalcified with EDTA as described above and re-embedded in Epon to facilitate thin sectioning for TEM analysis.

For Transmission electron microscopy

Ultrathin 60 nm thick sections were cut from chemically fixed and from high pressure frozen and freeze substituted decalcified samples using a diamond knife and the ultra-microtome. The sections were placed on carbon stabilized Formvar-coated copper hole grids and stained with 0.3% lead citrated.

For Scanning Electron Microscopy

For FE-SEM, EBSD and EDX analyses

We worked with two different preparations methods:

1. Embedding in epoxy resin and polishing of the surface by sequential of mechanical grinding. The polishing was performed with special grinding sheets with different grain sizes down to 1 µm. The last step is a process of etch-polishing with colloidal alumina (particle size ~ 0.06 µm) in a vibratory polisher.
2. Non-decalcified EPON embedded samples from animals that were chemically fixed as a whole, were polished by microtome following the protocol of Fabritius et al. 2005. This protocol consists in successively advancing the knife for 70, 40, 20, 10 and 5 nm 15 times for each step.

For Atomic Force Microscopy

For AFM imaging, shell pieces of modern *Magellania venosa* shells were cut in longitudinal section from the umbo to the commissure and embedded in epoxy resin. Embedded sample surfaces were polished in 5 sequential mechanical steps down to a grain size of 1 µm. For the final step, etch-polishing was applied for three hours with a colloidal alumina suspension in a vibratory polisher. Subsequently, the samples were washed in Milli-Q water in an ultrasonic bath and rinsed with 80% ethanol.

Appendix IV. Control tables for chemical experiments

Magellania venosa - South Chile (Huinay)

1. Chemical fixation and decalcification May 2016

Chemical fixation

Fixation solution A

Part 1 (2% PFA 2% GA) in filtered seawater

Part 2 (0.35M Saccharose 0.17M NaCl) in
Na- cacodylate buffer : Bidest = 1:1

Na- cacodylate buffer pH = 7.7

Fixation solution B

Part 1 (3.2% PFA 4% GA) in filtered seawater

Part 2 (0.35M Saccharose 0.17M NaCl) in
Na- cacodylate buffer : Bidest = 1:1

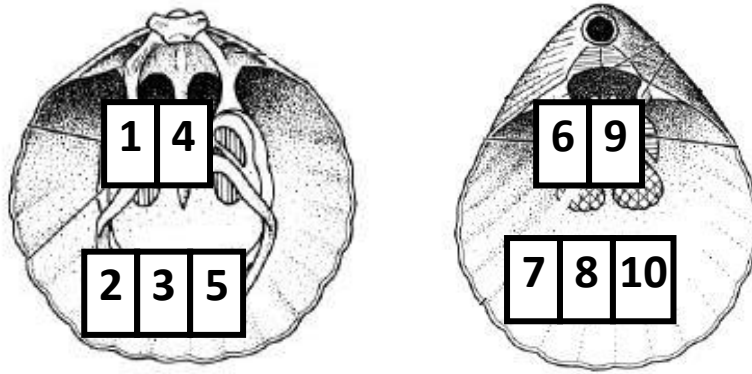
Na- cacodylate buffer pH = 7.7

Sample's number	Shell piece number	valve	Part of the valve	Fixation	Preparation	Fixation	Notes
547	1	dorsal	Middle	A	Embedding	18.05.16 (DN*)	
	2	dorsal	Rim	A	Embedding	18.05.16 (DN*)	
	3	dorsal	Rim	A	Embedding	18.05.16 (DN*)	*
	4	dorsal	Middle	A	Decalcification* Embedding	18.05.16 (DN*)	*
	5	dorsal	Rim	A	Decalcification* Embedding	18.05.16 (DN*)	*
	6	ventral	Middle	A	Embedding	18.05.16 (DN*)	
	7	ventral	Rim	A	Embedding	18.05.16 (DN*)	
	8	ventral	Rim	A	Embedding	18.05.16 (DN*)	
	9	ventral	Middle	A	Decalcification* Embedding	18.05.16 (DN*)	
	10	ventral	Rim	A	Decalcification*	18.05.16	

					Embedding	(DN*)	
548	1	dorsal	Middle	B	Embedding	18.05.16 (DN*)	
	2	dorsal	Rim	B	Embedding	18.05.16 (DN*)	*
	3	dorsal	Rim	B	Embedding	18.05.16 (DN*)	
	4	dorsal	Middle	B	Decalcification* Embedding	18.05.16 (DN*)	
	5	dorsal	Rim	B	Decalcification* Embedding	18.05.16 (DN*)	
	6	ventral	Middle	B	Embedding	18.05.16 (DN*)	
	7	ventral	Rim	B	Embedding	18.05.16 (DN*)	
	8	ventral	Rim	B	Embedding	18.05.16 (DN*)	
	9	ventral	Middle	B	Decalcification* Embedding	18.05.16 (DN*)	*
	10	ventral	Rim	B	Decalcification* Embedding	18.05.16 (DN*)	
	5	dorsal		B	Critical point drying	18.05.16 (DN*)	
	6	ventral		B	Critical point drying	18.05.16 (DN*)	

- (*) indicates an orientation of the shell piece perpendicular to the commissure in the Epon for TEM sections. The other samples are orientated parallel to the commissure.
- DN* is “during night”.
- Decalcification*: The samples were in decalcification solution (0.25 M HEPES + 0.05 EDTA + 1% GA) for 14 nights (19.05.2016 – 02.06.2016) in the refrigerator before embedded in EPON.
- The animal 3 was used for critical point drying

The shell piece number refers to the area in the shell where the piece was cut for each animal (shown in the scheme below).



2. High Pressure Freezing in May 2017

(Samples in 200µm depth Aluminum holders)

The samples are stored in liquid nitrogen at the Center for Electron Microscopy, University of Ulm (Germany). The “location of the samples” refers to storage and vial number where the samples were deposited.

	size of the animal	location of the samples	Sample number	valve	region	preparation	notes
Animal 1	6 mm	112-K9 Vial E17	1	Dorsal	Commissure		
		112-K9 E18	2	Dorsal	central		300µm depth Aluminum holder
			3				Possibly too thick
		112-K9 E19	4	Ventral	Commissure		
		112-K9 E20	5	Ventral	Central part with commissure		Small
6							
Animal 2 (The upper shell broke)	6mm	157-K3 E21 (2 samples vial 19 FS)	7	Ventral	Commissure	FS* (04.12.2017)	Triangular shape
			8			FS* (04.12.2017)	
			9				
			10				
		85-K3 E22	11	Ventral	Central with commissure		
			12				
Animal	6mm	85-K3	13	Dorsal	Commissure		

3		E23	14						
		85-K3	15	Dorsal	Central with commissure				
		E24	16						
		85-K3	17	Ventral	Commissure				
		E25	18						
		85-K3	19	Ventral	Central with commissure				
		E26	20	Ventral					
		Animal 4	6mm	157-K3	21	Dorsal	Commissure		
				E27	22				
					23				
157-K3	24			Dorsal	Central with commissure				
E28	25								
157-K3 E29	26			Ventral	Commissure				
	27								
	28						Broken shell		
	29								
112-K9	30			Ventral	central	FS* (04.12.2017)			
E30 (2 samples vial 20 FS)	31					FS* (04.12.2017)			
	32								
	33								
Animal 5	5 mm			157-K3	34	Dorsal	Commissure		
		E31	35						
			36						
		11-K4	37	Dorsal	Central				
		E32	38		Central with commissure				
		11-K4	39	Ventral	Commissure	FS* (04.12.2017)			
		E33 (2 samples vial 21 FS)	40			FS* (04.12.2017)			
			41						
			42						
		11-K4	43	Ventral	Central with commissure	FS* (04.12.2017)			

	E34 (2 samples vial 22 FS)	44	Central	FS* (04.12.2017)	Triangular shape
		45			
		46			

FS* "Free substitute"

Pajaudina atlantica - Palma de Mallorca (Spain)

Chemical fixation in March 2016

a) **Fixation solution A**

Part 1 (2% PFA 2% GA) in filtered seawater

Part 2 (0.35M Saccharose 0.17M NaCl) in Na- cacodylate buffer: Bidest (1:1) with a pH 7.6

b) **Fixation solution B**

Part 1 (3.2% PFA 4% GA) in filtered seawater

Part 2 (0.35M Saccharose 0.17M NaCl) Na- cacodylate buffer pH 7.6

Decalcification

c) 02.03.2016 0.25 M HEPES + 0.05 EDTA in the refrigerator

d) 03.03.2016 0.25 M HEPES + 0.05 EDTA + 1% GA in the refrigerator

Specimen number	Sample specific number	Valve	Fixation	Notes	Preparation	Sample	Decalcification
455	1	Brachial	A		Decalcification		03.03.16
	2	Pedicle	B		Epithelial embedding	455-1 distal 455-2 proximal with eggs 455-3 distal 455-4 proximal	
	3	Brachial	A		Decalcification		02.03 03.03.16 +
	4	Pedicle	B		Decalcification		03.03.16

					Epithelial embedding	Discarded	
	5	Pedicle	B		Epithelial embedding		
456	1	Pedicle	A	Hinge	Decalcification		03.03.16
					Epithelial embedding	456-5 distal 456-6 proximal	
	2	Pedicle	A		Epithelial embedding	456-1 distal 456-2 distal + proximal with eggs	
	3	Brachial	B		Decalcification		02.03 + 03.03.16
	4	Pedicle	A		Epithelial embedding	456-3 distal 456-4 proximal	
					LM image	Proximal part	
	5	Brachial	B		Decalcification		03.03.16
457	1	Pedicle	A		Critical point drying		
	2	Pedicle	B		Epithelial embedding	457-1 distal	
Epithelial Decalcification					457-2 proximal	03.03.16	
457	3	Brachial	A		Critical point drying		
	4	Brachial	B		Decalcification		02.03 + 03.03.16
458	1	Brachial	A	Not good	Critical point drying		
	2	Pedicle	B		Epithelial embedding	458-2 distal 458-3 proximal	
					Epithelial Decalcification	458-4 proximal	03.03.16
	3	Brachial	A		Decalcification	458-1	03.03.16
	4	Pedicle	B		Critical point drying		
459	1	Pedicle	A	Entire	Decalcification		02.03 + 03.03.16
	2	Brachial	B	Entire	Decalcification		02.03 + 03.03.16

Appendix V. Morphological analysis raw data

Organelles counting

Table A2. Data, in percentage, of the organelles at the areas of outer mantle were the scretiontakes place. The counting was done using JMicroVision (see Appendix II).

Outer epithelium under secretion	Sample 548-10_J3M19			Sample 548-4_F2M3			Sample 548-10_J3M8			Sample 547-10_I2M15			Sample 547-10_I2M14
	1nt	2nt	3nt	1nt	2nt	1nt	2nt	3nt	1nt	2nt	3nt	1nt	
Epithelium length (µm)	9,772	10,147	11,226	12,453	15,223	9,877	11,313	5,293	7,055	9,69	11,729	16,367	
Area (µm)	12,884	11,8	11,008	3,478	3,974	14,673	14,428	7,084	11,323	16,133	27,559	17,043	
Citoplasma	78,4	78,8	77,6	76,8	39,2	80,8	78,4	73,2	82,8	76	77,2	85,2	
Tonofilamentes	2,4	1,2	4	6,4	5,6	0	1,6	1,2	0,8	4	1,2	0	
Nucleous	0	5,6	0	0	0	0	0	0	0	0	0	0	
Mitocondria	10,4	1,2	3,6	0	0	3,2	2	10,4	4,8	3,6	8,8	2	
Rough Endoplasmic Reticulum	1,2	5,2	0,4	1,6	0	4,4	2,4	2,8	0	2,4	1,2	0,8	
Golgi aparat	0	0	0	0	0	0	0	0	0	0	0	0	
Dark lysosomes like	0	2,8	6,4	0	0	1,6	6	4	0,4	0	3,2	0	
White lysosomes like	0	0	0,8	0	0	0	0	0	0	0	0,4	0	
Other	0,8	0,4	1,2	3,6	0,4	4	2,4	1,2	1,2	6	1,6	0,4	
White vesicles	0	0	0,8	2	0	0	0,4	2,4	0	0,4	0,4	0	
Dark vesicles	0	0,4	0,8	0	0	0	0	0	0	1,2	0	0	
Golgi vesicles	0	0	0	0	0	0	0	0	0	0	0	0	
Smooth Endoplasmic Reticulum	0	0	0	0	0	0,4	0,4	0	0,4	2,4	1,6	0	
Glycogen	1,2	0	0	2	0	0	0,4	0	1,6	0,8	0,4	2	
outer part	5,6	4,4	4,4	7,6	54,8	5,6	6	4,8	8	3,2	4	9,6	
TOTAL	100	100	100	100	100	100	100	100	100	100	100	100	

Table A3. Data, in percentage, of the organelles at the areas of outer mantle where the secretion of the fibres is finished takes place. The counting was done using JMicroVision (see Appendix II).

Outer epithelium under complete fibres	Sample 548-4_F2M2				Sample 548-10_I3M19		Sample 548-4_F2M3		Sample 547-10_I2M15		Sample 547-10_I2M14		
	3t	1a(t)	1c(t)	1b(t)	1t	2t	1t	2t	3t	1t	2t	1t	2t
Epithelium length (µm)	5,923	9,927	7,101	9,733	15,983	7,607	4,147	8,989	11,866	3,408	2,989	3,499	2,512
Area (µm)	5,273	11,119	6,028	10,087	33,374	14,47	6,821	6,189	11,745	9,055	9,504	12,025	5,136
Citoplasma	53,15	53,2	58	55,6	60,56	67,33	61,2	68	56,8	69,65	69,5	86,5	71,5
Tonofilamentes	9,45	6	10,8	16,8	6,37	11,95	7,2	10,4	5,6	10,45	4	3,5	9
Nucleous	0	9,6	0	0	13,94	0	0	0	16,4	0	7	0	7,5
Mitochondria	3,54	0	3,6	2,4	0,4	2,79	21,2	1,6	10,8	0	0	0	0
Rough Endoplasmic Reticulum	2,36	3,2	2,8	0,8	5,98	3,98	2	4	2,4	4,48	2	3,5	4
Golgi aparat	0	0	0	2,8	0	0	0	0	0	0	0	0	0
Dark lysosomes like	12,2	0	0	0,4	5,58	9,96	1,6	2	0,8	6,97	13	0	0
White lysosomes like	0	0	0	0	0	0	0	0	0	0	0	0,5	0
Other	5,12	1,2	0	0	0	0	1,6	2	1,6	4,48	1	0,5	0
White vesicles	0	0	0	0	0,8	0	0,4	1,2	0,4	0,5	0	0	0
Dark vesicles	0	0	0	0	0,4	0	0	0,4	0	0,5	0	0	0
Golgi vesicles	0	0	0	0	0	0	0	0	0	0	0	0	0
Smooth Endoplasmic Reticulum	3,15	0	0,4	0	0	0	0	1,6	0	0,5	0	0	2
Glycogen	2,36	1,2	1,6	0	0	0,4	2,4	0,8	0,4	0,5	0,5	3	1
outer part	8,66	25,6	22,8	21,2	5,98	3,59	2,4	8	4,8	1,99	3	2,5	5
TOTAL	99,99	100	100	100	100,01	100	100	100	100	100,02	100	100	100

Table A4. Data, in percentage, of the organelles at the areas of outer mantle attached to the puctae walls. The counting was done using JMicroVision (see Appendix II).

Outer epithelium inside the Punctae	Sample 547-10_I2M12				Sample 547-10_I2M13			Sample 548-10_J3M8		
	P1	P2	P3	P4	P5	P6	P7	P8	P9	P10
Epithelium length (µm)	22,628	24,761	12,256	23,762	7,892	17,284	18,514	13,605	14,878	26,849
Area (µm)	16,579	11,862	17,509	20,529	6,189	13,05	17,74	9,694	21,145	15,212
Citoplasma	69,6	80,4	73,6	80,4	84	80	77,6	64	54,4	62,4
Tonofilaments	0	0	0	0	0	0	0	0	0	0
Nucleous	0	0	0	0	0	0	0	0	16	0
Mitochondria	0	0	1,2	4,4	0,8	0,8	0	7,6	4	0
Rough Endoplasmic Reticulum	2,8	4,4	0,8	4	1,6	2,4	6	2,8	1,6	2,4
Golgi aparat	0	0	0	0	0	0	0	0	0	0
Dark lysosomes like	11,6	11,2	18	6,8	6,4	8,4	9,6	16,4	11,2	12,4
White lysosomes like	0	0	0	0	0	0	0	0	0	0
Other	0,8	0	0,4	0	0	0	0	0	1,6	5,6
White vesicles	0,8	0,8	2,4	0,8	1,6	0,4	2,4	0	0,8	1,2
Dark vesicles	0	0	0,4	0	0	0	0	0	0,4	0,8
Golgi vesicles	0	0	0	0	0	0	0	0	0	0
Smooth Endoplasmic Reticulum	0	0	0	0	0,4	1,6	0	0	0,8	0
Glycogen	4,4	2,8	3,2	1,2	4	2	1,6	4	2,8	2
outer part	10	0,4	0	2,4	1,2	4,4	2,8	5,2	6,4	13,2
	100	100	100	100	100	100	100	100	100	100

Table A5. Data, in percentage, of the organelles at the areas of outer mantle in the commissure. The counting was done using JMicroVision (see Appendix II).

Outer epithelium in commissure	Mvenosa_547-5_I5_M8				Mvenosa_548-5_E5M1_1	Mvenosa_547-5_I5_M12			Mvenosa_547-5_I5_M15	Mvenosa_547-5_I5_M13(169)	
	A8	A7	A5	A3	B1	A13	A15	A17	A9	A22	A19
Epithelium length (µm)	4,308	2,944	2,568	3,439	4,1	3,266	4,316	4,671	5,673	4,234	4,541
Area (µm)	35,956	41,963	37,746	31,35	19,733	58,979	67,964	74,822	88,568	78,688	68,475
Citoplasma	60,4	61,2	75,2	55,2	75,2	71,6	66,8	73,2	71,6	55,2	62,8
Tonofilamentes	0	0	0	0	0	0	0	0	0	0	0
Nucleous	8,4	18,8	4,4	24	3,6	13,2	11,6	10,4	2,4	25,2	20,8
Mitochondria	17,2	4	7,2	12,4	12,8	6	7,6	3,6	0	10,4	4,4
Rough Endoplasmic Reticulum	5,2	1,6	2,4	2	1,2	1,6	2,4	3,2	1,6	0,8	2
Golgi aparat	0	0,8	0,4	0	0	0	0	0,4	0	0	1,2
Dark lysosomes like	5,2	4	2	0,4	0	3,2	0,8	4,8	13,6	0,8	5,2
White lysosomes like	1,2	0,8	2	0	1,6	0	2,4	0,4	0	0	0,8
Other	0	0	0	0	0	0	0	0	0	0	0
White vesicles	0	0,8	0	0	0,8	0	0	0	0	0,4	0,4
Dark vesicles	0,8	5,2	2	2,8	0,8	0,8	5,6	2,4	4,8	2	0,8
Golgi vesicles	0	0,4	0,4	0	0	0	0	0	0	0	0,8
Smooth Endoplasmic Reticulum	0	0,8	0	0	0,4	0	0	0	0,4	0,8	0
Glycogen	0	0	0	0	0	0	0	0	0	0	0
outer part	0,8	0,8	0,8	0,8	3,6	1,6	2,4	0,8	3,2	4,4	0,8
Multivesicular body	0,8	0,8	3,2	2,4	0	2	0,4	0,8	2,4	0	0
TOTAL	100	100	100	100	100	100	100	100	100	100	100

Table A6. Data of the apical and basal epithelial length obtained from in different TEM panorama images. Using Fiji software we counted the apical and basal intersections of the outer mantle epithelium with a merz grid (see Appendix II).

Image	Apical Epith. Lenth (µm)	Basal Epith. Lenth (µm)	part of the shell	apical Intersecctions	basal Intersecctions	x10nm	merz grid constant in nm
548-4_F2M2	35,343	34,962	central	70	69	6463,039	646,3039
548-4_F2M3	54,588	52,67	central	90	96	6390,481	639,0481
548-4_F4M4	55,266	52,128	central	95	124	6493,165	649,3165
548-10_J3M8	42,572	41,036	central	66	135	7109,61	710,961
548-10_J3M16	40,007	38,53	central	58	122	10792,181	1079,2181
548-10_J3M19	57,291	55,717	central	115	220	7066,901	706,6901
547-10_I2M14	74,753	72,567	central	118	399	8969,393	896,9393
547-10_I2M15	43,873	42,537	central	61	166	9020,409	902,0409
547-5_I5_M8 A1	7,697	9,52	rim	22	478	5900,208	590,0208
547-5_I5_M8 A2	8,684	8,693	rim	32	460	5900,208	590,0208
547-5_I5_M12 A3	6,923	6,529	rim	19	261	8331,622	833,1622
547-5_I5_M12 A4	6,841	6,923	rim	9	235	8331,622	833,1622
547-5_I5_M12 A5	6,816	6,781	rim	9	286	8331,622	833,1622
547-5_I5_M13-2_A6	5,734	5,388	rim	10	315	7223,363	722,3363
547-5_I5_M13-2_A7	5,418	5,276	rim	10	285	7223,363	722,3363
547-5_I5_M13-2_A8	4,896	4,677	rim	13	296	7223,363	722,3363
548-5_E5M5_A9	5,218	4,697	rim	9	306	5898,36	589,836
548-5_E5M5_A10	7,557	7,5	rim	13	505	5898,36	589,836
548-5_E5M5_A11	7,683	7,588	rim	15	507	5898,36	589,836

Table A7. Data of the apical and basal epithelial length obtained from in different TEM panorama images. Using Fiji software we counted the intersections of the apical and basal membrane and the mitochondria membrane with a merz grid to calculate there are and profile length (see Appendix II).

Area per (μm^2)			Profile length (μm)			Image name	part of the shell
Apical Memb	Basal Mebrane	Mitochondria	Apical Memb	Basal Mebrane	Mitochondria		
1,629520429	1,623745657	1,606241566	1,280063181	1,275526832	1,261776564	548-4_F2M2	central
1,341242413	1,482756602	1,430658573	1,053607551	1,16477345	1,123848055	548-4_F2M3	central
1,420857144	1,966235193	1,854592483	1,116148581	1,544568102	1,456867622	548-4_F4M4	central
1,403117573	2,977439386	2,870013217	1,102213333	2,338915464	2,254527271	548-10_J3M8	central
1,991726178	4,350092038	4,189492995	1,564592441	3,417197202	3,291039273	548-10_J3M16	central
1,805796673	3,552158756	3,454567548	1,418536271	2,79038394	2,713721562	548-10_J3M19	central
1,802373684	6,278055974	6,094466949	1,415847356	4,931701472	4,787483856	547-10_I2M14	central
1,596566955	4,481215857	4,344755975	1,254176712	3,520200987	3,413005479	547-10_I2M15	central
2,146826364	37,7126173	46,64468191	1,686430765	29,62499395	36,64154117	547-5_I5_M8 A1	rim
2,767743817	39,74512597	39,78631737	2,174189959	31,22162291	31,25398065	547-5_I5_M8 A2	rim
2,910832606	42,39862773	39,9856479	2,286592778	33,30607049	31,41056395	547-5_I5_M12 A3	rim
1,395342688	36,00240328	36,43394795	1,096105803	28,28154225	28,62054042	547-5_I5_M12 A4	rim
1,400460582	44,73322924	44,50352515	1,100126144	35,14000726	34,95956414	547-5_I5_M12 A5	rim
1,603652093	53,75895409	50,51504092	1,259742414	42,2301289	39,68188603	547-5_I5_M13-2_A6	rim
1,697183665	49,67157341	48,36973446	1,333215762	39,01930354	37,99664922	547-5_I5_M13-2_A7	rim
2,441573413	58,19587268	55,59274847	1,917968117	45,71553235	43,67065866	547-5_I5_M13-2_A8	rim
1,295084525	48,91708234	44,03287385	1,017348409	38,42661614	34,58984592	548-5_E5M5_A9	rim
1,291676057	50,55798935	50,17664684	1,014670901	39,715624	39,41606193	548-5_E5M5_A10	rim
1,465953198	50,16956281	49,54921809	1,151573604	39,4104971	38,92318782	548-5_E5M5_A11	rim

Acknowledgment



I want to thank my Doktoerlern for their guidance and for giving me the opportunity to come to Germany.

Tina, thank you for always being there and for bringing so much happiness with all those memes. To whom I consider my “Dokortante”. Xiaofei thank you for you guidance and friendship during these years, especially for those days in Ulm. Viola, Pluto, Michi, Moritz, Laura, thank for those lunch-breaks and everything that come with them. To all my PhD colleagues, thank you for the last 5 years.

Andreas, Uli, Paul, Renate, and everyone from the Central Facility for Electron Microscopy (Ulm University). Thanks to this great team I had the chance of learning and to do what I thought was impossible for me. Thank you for taking me in during those many weeks and for letting me considers Ulm as a second home in Germany.

BASE-LiNE Earth troupe, I will never be able to thank you enough. Daniela and Toni thank you for giving me the chance of work inside this ITN and have the opportunity of having not only a huge scientific network but also very good friends. Tomi, Sara, Facheng, Rita, Hana, Amin, Isaac and all, thank you.

A mi familia, especialmente a mis abuelos que siempre han confiado en mí incluso cuando yo lo creía imposible, gracias por estar siempre ahí en silencio rezando, ayudando a despejarme o simplemente con algún chiste malo. María y Carmen, gracias por ser mis muletas estos años. A todos mis amigos (almerienses, granainos, madrileños, americanos,...), en particular a Addi, Irene y Eloy, gracias por todo vuestro apoyo y por ayudarme a reírme hasta de mi sombra.

There are still many people I should thank. As Bilbo Baggins would say: Five years is far too short a time to live among such excellent and admirable people. I don't know half of you half as well as I should like, and I like less than half of you half as well as you deserve. But, I, uh, I have things to do. I've put this off for far too long. I regret to announce — this is the end. I am going now. I bid you all a very fond farewell. Thank you and goodbye.

List of publications

2020

Simonet Roda, M., Griesshaber, E., Angiolini, L., Harper, D.A.T., Jansen, U., Bitner, M.A., Henkel, D., Manzanero, E., Müller, T., Tomašových, A., Eisenhauer, A., Ziegler, A. and Schmahl, W.W. The evolution of thecideide microstructures and textures: traced from Triassic to Holocene. *Lethaia*.

Simonet Roda, M., Griesshaber, E., Angiolini, L., Rollion-Bard, C., Milner, S., Ye, F., Henkel, D., Häussermann, V., Eisenhauer, A., Brand, U., Gnägi, H., Schmahl, W.W., 2020b. Diversity of mineral and biopolymer assembly in modern terebratulide, rhynchonellide, thecideide and craniide brachiopod shells. Submitted to *Marine Biology*.

Griesshaber, E., **Simonet Roda, M.**, Crippa, G., Schmahl, W.W., and Ziegler, A. Carbonate Biomaterial Functionalization Through Crystallite Organization By. To Be Submitted To *Acta Biomaterialia*.

Crippa, G., Griesshaber, E., Checa, A.G., Harper, E., **Simonet Roda, M.** and Schmahl, W.W. 2020: Orientation Patterns Of The Aragonitic Crossed-Lamellar, Myostracal And Fibrous Microstructures Of Modern Glycymeris Shells. *Journal of Structural Biology*, 212, 107653.

Crippa, G., Griesshaber, E., Checa, A.G., Harper, E.M., **Simonet Roda, M.** and Schmahl, W.W. 2020: SEM, EBSD, laser confocal microscopy and FE-SEM data from modern Glycymeris shell layers, Data in Brief 33:106547.

2019

Simonet Roda, M., Ziegler, A., Griesshaber, E., Yin, X., Rupp, U., Greiner, M., Henkel, D., Häussermann, V., Eisenhauer, A., Laudien, J. And Schmahl, W.W. 2019a : Terebratulide Brachiopod Shell Biomineralization By Mantle Epithelial Cells. *Journal Of Structural Biology*, 207, 136-157.

Simonet Roda, M., Griesshaber, E., Ziegler, A., Rupp, U., Yin, X., Henkel, D., Häussermann, V., Laudien, J., Brand, U., Eisenhauer, A., Checa, A.G. And Schmahl, W.W. 2019b Calcite Fibre Formation In Modern Bra-Chiopod Shells. *Scientific Reports*, 9, 598.

2018

Casella, L.A., Griesshaber, E., **Simonet Roda, M.**, Ziegler, A., Mavromatis, V., Henkel, D., Laudien, J., Häussermann, V., Neuser, R.D., Angiolini, L., Dietzel, M., Eisenhauer, A., Immenhauser, A., Brand, U. And Schmahl, W.W. 2018: Micro- And Nanostructures Reflect The Degree Of Diagenetic Alteration In Modern And Fossil Brachiopod Shell Calcite: A Multi-Analytical Screening Approach (CL, FE-SEM, AFM, EBSD). *Palaeogeography. Palaeoclimatology. Palaeoecology*, 502, 13-30.

Casella, L.A., **Simonet Roda, M.**, Angiolini, L., Ziegler, A., Schmahl, W.W., Brand, U., Griesshaber, E. 2018: Archival biogenic micro- and nanostructure data analysis: signatures of diagenetic systems. *Data Brief*, 19, 299-311.

Conference Contributions

- Simonet Roda, M.** and Manzanero, E. 2019: Making science accessible to everyone – when scientists and artists work together: the case of brachiopods -. at the 4rd IIMERP - International Meeting of Early-Staged Researchers in Palaeontology (Cuenca, Spain) - Oral presentation
- Simonet Roda, M.**, Griesshaber, E., Ziegler, A., Rupp, U., Yin, X., Henkel, D., Häussermann, V., Laudien, J., Brand, U., Eisenhauer, A., Checa, A., and Schmahl, W.W. 2019: Insight to biomineralization processes in the secondary layer of *Magellania venosa* – at the 15th BIOMIN - International Symposium on Biomineralization (Munich, Germany) - Oral presentation.
- Schmahl, W.W., Griesshaber, E., Ziegler, A., **Simonet Roda, M.**, Henkel, D. 2019: Pattern formation of interlocking calcite fibre hybrid composite in brachiopod shells poster - at the 15th BIOMIN - International Symposium on Biomineralization (Munich, Germany) - Poster presentation
- Griesshaber, E., Schmidt, R., Schmidt, T., Steffen, R., Gnägi, H., **Simonet Roda, M.**, Ziegler, A., Schmahl, W.W. Nanoscale structuring of modern brachiopod calcite fibres - at the 15th BIOMIN - International Symposium on Biomineralization (Munich, Germany) - Poster presentation
- Simonet Roda, M.**, Ziegler, A., Griesshaber, E., Henkel, D., Häussermann, V., Eisenhauer, A., and Schmahl, W.W., 2019: New insights into the vital effect during brachiopod shell formation and its relevance to the geochemical record –at the The Palaeontological Association – 63rd Annual Meeting (Valencia, Spain) - Oral presentation:
- Simonet Roda, M.**, Milner, S., Müller, T., Griesshaber, E., Jurikova, H., Rollion-Bard, C., Angiolini, L., Ye, F., Bitner, M. A., Henkel, D., Tomašových, A., Eisenhauer, A., Harper, D., Jansen, U., and Schmahl, W.W. 2018: The evolution of theicideide brachiopod shell microstructure from Triassic to modern times - at the 8th IBC - International Brachiopod Congress (Milano, Italy) - Oral presentation. (In *Permophiles Issue #66 Supplement 1*).
- Simonet Roda, M.**, Yin, X., Cross, E., Harper, L., Ziegler, A., Schmahl, W. W., Peck, L., and Griesshaber, E. 2018: Microstructure formation in the shell of the Antarctic brachiopod *Liothyrella uva* (Broderip 1833): transition from larval to juvenile stages - at the 8th IBC - International Brachiopod Congress (Milano, Italy) – Poster presentation. (In *Permophiles Issue #66 Supplement 1*).
- Ziegler A., **Simonet Roda M.**, Griesshaber E., Henkel D., Häussermann V., Eisenhauer A., Laudin J., and Schmahl W.W. 2018: Mechanisms of calcite fibre formation in *Magellania venosa*.- at the 8th IBC - International Brachiopod Congress (Milano, Italy) - Oral presentation. (In *Permophiles Issue #66 Supplement 1*).
- Mages V., Casella L., **Simonet Roda M.**, Ye F., Crippa G., E. Griesshaber, Angiolini L. and Schmahl W. W., 2018: The intermediate stages of diagenetic overprint deduced from hydrothermally altered and fossil brachiopod shells - at the 8th IBC - International Brachiopod Congress (Milano, Italy) - Oral presentation. (In *Permophiles Issue #66 Supplement 1*).
- Simonet Roda, M.**, Griesshaber, E., Henkel, D., Häussermann, V., Ziegler, A., Eisenhauer, A. and Schmahl, W.W. 2018: Characterization of the biomineral microstructure of the modern brachiopod *Pajaudina atlantica* and its relevance for the fossil record. – at the 3rd IIMERP - International Meeting of Early-Staged Researchers in Palaeontology

(Opole, Poland) - Oral presentation:

- Simonet Roda, M.**, Milner, S., Müller, T., Griesshaber, E., Jurikova, H., Rollion-Bard, C., Angiolini, L., Ye, F., Bitner, M. A., Henkel, D., Tomašových, A., Eisenhauer, A., Harper, D., Jansen, U., and Schmahl, W.W. 2018: The evolution of theicideid brachiopod shell microstructure.- at the 3rd IIMERP - International Meeting of Early- Staged Researchers in Palaeontology (Opole, Poland) – Poster presentation.
- Simonet Roda, M.**, Ziegler, A., Griesshaber, E., Henkel, D., Häusermann, V., Eisenhauer, A., and Schmahl, W. W. 2017: New insights into shell formation of the modern brachiopod *Magellania venosa* – at the 14th BIOMIN - International Symposium on Biomineralization (Tsukuba, Japan) - Oral presentation.
- Simonet Roda, M.**, Griesshaber, E., Henkel, D., Häusermann, V., Ziegler, A., Eisenhauer, A., and Schmahl, W.W. 2017: A new biomineral microstructure detected in modern brachiopod shells – at the at the 14th BIOMIN - International Symposium on Biomineralization (Tsukuba, Japan) – Poster presentation.
- Simonet Roda, M.**, López-Cabrera, J. and Sequero-López, C. 2015: Reconstrucción paleoambiental de los miembros Azagador y Abad Inferior del margen sureste de la Cuenca de Sorbas (Almería) – at the XIII EJIP-Encuentro de Jóvenes Investigadores en Paleontología / Meeting of Young Paleontology Researchers (Madrid, Spain) – Oral presentation.

